TU/e EINDHOVEN UNIVERSITY OF TECHNOLOGY

On the Development of Membrane Reactor Technology for Ammonia Synthesis

Citation for published version (APA):
Gargiulo, I. (2026). *On the Development of Membrane Reactor Technology for Ammonia Synthesis: from materials to reactor design and scale-up*. [Phd Thesis 1 (Research TU/e / Graduation TU/e), Chemical Engineering and Chemistry]. Eindhoven University of Technology.

Document status and date:
Published: 26/10/2026

Document Version:
Publisher's PDF, also known as Version of Record (includes final page, issue and volume numbers)

Please check the document version of this publication:

• A submitted manuscript is the version of the article upon submission and before peer-review. There can be important differences between the submitted version and the official published version of record. People interested in the research are advised to contact the author for the final version of the publication, or visit the DOI to the publisher's website.
• The final author version and the galley proof are versions of the publication after peer review.
• The final published version features the final layout of the paper including the volume, issue and page numbers.

Link to publication

General rights
Copyright and moral rights for the publications made accessible in the public portal are retained by the authors and/or other copyright owners and it is a condition of accessing publications that users recognise and abide by the legal requirements associated with these rights.

• Users may download and print one copy of any publication from the public portal for the purpose of private study or research.
• You may not further distribute the material or use it for any profit-making activity or commercial gain
• You may freely distribute the URL identifying the publication in the public portal.

If the publication is distributed under the terms of Article 25fa of the Dutch Copyright Act, indicated by the "Taverne" license above, please follow below link for the End User Agreement:

www.tue.nl/taverne

Take down policy
If you believe that this document breaches copyright please contact us at:

openaccess@tue.nl

providing details and we will investigate your claim.

Download date: 17. Nov. 2026

On the Development of Membrane Reactor Technology for Ammonia Synthesis:
from materials to reactor design and scale-up

PROEFSCHRIFT

ter verkrijging van de graad van doctor aan de Technische Universiteit Eindhoven, op gezag van de rector magnificus prof.dr. S.K. Lenaerts, voor een commissie aangewezen door het College voor Promoties, in het openbaar te verdedigen op maandag 26 oktober 2026 om 11:00 uur

door

Iolanda Gargiulo

Geboren te Castellammare di Stabia, Italië

Dit proefschrift is goedgekeurd door de promotoren en de samenstelling van de promotiecommissie is als volgt:

Voorzitter:	prof.dr.ir. J.A.M. Kuipers
1e promotor:	prof.dr.ir. F. Gallucci
2e promotor:	prof.dr.ir. J. van der Schaaf
Leden:	dr. M.F. Neira D'Angelo
	prof.dr.ir. M. van Sint Annaland
	prof.dr. D. Alique Amor (Universidad Rey Juan Carlos)
	prof.dr.ir. E. Curcio (Università della Calabria)
Adviseur:	dr. A. Vita (Istituto di Tecnologie Avanzate per l' Energia "Nicola Giordano")

Het onderzoek of ontwerp dat in dit proefschrift wordt beschreven is uitgevoerd in overeenstemming met de TU/e Gedragscode Wetenschapsbeoefening.

"So,
I will water these seeds
until fields of love grow
flower at my feet"

- Dylan Edward

The research described in this thesis has been carried out in the framework of the European project AMBHER. This project has received funding from the European Union's Horizon Europe research and innovation programme under grant agreement No 101058565. The content of publication is the sole responsibility of the author(s). The European Commission or its services cannot be held responsible for any use that may be made of the information it contains.





Copyright © 2026 by Iolanda Gargiulo, Eindhoven, The Netherlands.

All rights reserved. No part of the material protected by this copyright notice may be reproduced or utilised in any form or by any means, electronic or mechanical, including photocopying, recording or by any information storage and retrieval system, without the prior permission of the author.

A catalogue record is available from the Eindhoven University of Technology Library.

ISBN: 978-90-386-6805-5

Cover design concept by Iolanda Gargiulo
Cover design by Meng-Han Cheng
Printed by Proefschriftspecialist

CONTENTS

LIST OF ABBREVIATIONS I

SUMMARY V

CHAPTER 1 : General introduction 1

1.1 Context and motivation for the energy and industrial transition 1

1.2 Ammonia: properties, uses, and role as a hydrogen carrier 4

1.3 Conventional ammonia synthesis: the Haber-Bosch process 5

1.3.1 Catalysts for ammonia synthesis: from iron to ruthenium and beyond 6

1.3.2 Periodic open cellular structures (POCS) as structured catalyst supports 7

1.4 Towards intensified and decentralised ammonia synthesis: the role of membrane reactors 8

1.4.1 Membrane reactor concepts and configurations 10

1.5 NH_3-selective membranes: carbon molecular sieve (CMS) and beyond 11

1.5.1 Gas transport mechanisms and modelling 13

1.6 Modelling strategies for membrane reactors 14

1.7 Thesis outline 15

CHAPTER 2: Modelling of a packed bed membrane reactor for ammonia synthesis: on the role of membrane performance and operating conditions 33

2.1 Introduction 34

2.2 Reactor configuration and reaction kineticS 34

2.2.1 Packed bed membrane reactor configuration 34

2.2.2 Ammonia synthesis reaction and kinetic model 35

2.3 Mathematical formulation of the reactor model 37

2.4 Simulation results 40

2.4.1 Validation of the packed bed reactor 41

2.4.2 Validation of the permeation module 42

2.4.3 Study of the membrane performance 44

2.4.4 Ideal membrane case study 45

2.4.5 Real membrane case study 47

2.4.6 Operating parameter study: sweep-gas-to-feed flow ratio and transmembrane pressure difference 50

2.4.7 Heat management study: effect of temperature 52

2.4.8 On the effect of sweep-gas H_2:N_2 molar ratio 54
2.4.9 Packed bed membrane reactor vs. packed bed reactor 55
2.5 Conclusions 57
CHAPTER 3: Carbon molecular sieve (CMS) membranes for ammonia synthesis: experimental and theoretical analysis of transport mechanisms 71
3.1 Introduction 72
3.2 Experimental 79
3.2.1 Membrane preparation 79
3.2.2 Gas permeation experimental setup 80
3.2.3 Permporometer setup 83
3.2.4 Confocal laser microscope 84
3.2.5 Scanning electron microscopy (SEM) 84
3.3 Mathematical model 84
3.3.1 Modified Knudsen diffusion model 85
3.3.2 Molecular sieving model 86
3.3.3 Surface diffusion model 87
3.3.4 Fitting parameters 88
3.4 Results and discussion 88
3.4.1 Effect of carbonisation temperature on CMS membranes 89
3.4.2 Effect of metal addition on CMS membranes: pure gas tests 93
3.4.3 Effect of metal addition on CMS membranes: mixed-gas tests 96
3.4.4 Gas transport mechanism analysis 100
3.5 Conclusions 103
CHAPTER 4: Activated triply periodic minimal surfaces (TPMS) Gyroid supports for efficient ammonia synthesis in membrane-integrated reactors 119
4.1 Introduction 120
4.2 Experimental: materials and preparation 120
4.2.1 TPMS Gyroid supports: manufacturing and catalytic activation by dip/spin coating 120
4.2.2 Carbon molecular sieve (CMS) membrane fabrication 122
4.3 Characterisation techniqueS 123
4.3.1 TPMS Gyroid catalyst and coating slurry 123
4.3.2 CMS membrane 123
4.3.3 Experimental setup 124
4.4 Operating conditions and Key Performance Indicators for reactor

performance 126
4.5 Results and discussion 127
4.5.1 TPMS Gyroid catalyst: morphological characterisation 127
4.5.2 CMS membrane: separation performance and morphological characterisation 128
4.5.3 Effect of temperatures and pressures on the SCR 130
4.5.4 Effect of H_2:N_2 molar feed ratio on the SCR 131
4.5.5 Effect of WHSV on the SCR 133
4.5.6 Effect of temperature, pressure and sweep-gas-to-feed flow ratio on the SCMR 133
4.5.7 Effect of WHSV on the SCMR 138
4.5.8 Influence of POCS geometry: Gyroid vs. BCC 139
4.6 Comparison between model predictions and experimental results 140
4.7 Conclusions 141
CHAPTER 5: A 2D model for membrane reactors in ammonia synthesis: radial transport effects and scale-up design criteria 149
5.1 Introduction 150
5.2 Development of the 2D non-isothermal PBMR model 152
5.2.1 Reactor geometry 152
5.2.2 Reaction kinetics and membrane flux 154
5.2.3 Preliminary transport analysis: screening negligible mass- and heat-transfer resistances 154
5.2.4 Model assumptions 157
5.2.5 Modelling equations 158
5.2.6 Boundary conditions 159
5.2.7 Numerical implementation 160
5.2.8 Dimensionless framework: concentration polarisation and Sherwood correction 160
5.2.9 Mechanistic closure: the reaction-screened diffusion layer 164
5.2.10 Key performance indicators for 1D-2D model comparison 165
5.3 Results and discussion 166
5.3.1 Verification and validation of sub-models 166
5.3.2 1D-2D discrepancies across key performance indicators (KPIs) 168
5.3.3 Physical origin of divergence from 2D fields 174
5.3.4 Empirical Sherwood number correction for radial mass transfer 178
5.3.5 Application of Sherwood optimal correction for CP prediction 181
5.3.6 Mechanistic validation: reaction screening, not hydrodynamics 182
5.3.7 Towards scale-up: operating condition and geometry design criteria 185
5.4 Conclusions 187
CHAPTER 6: On the scaling-up of 3D-printed metallic POCS structured catalysts membrane reactors 214

6.1 Introduction 215
6.2 Experimental: materials and preparation 216
6.2.1 POCS design and fabrication: Gyroid and BCC geometry 216
6.2.2 Catalyst slurry preparation 217
6.2.3 POCS activation by dip-spin coating 218
6.2.4 Membrane fabrication 219
6.3 Characterisation techniques 219
6.3.1 Morphological and rheological characterisation of POCS supports and washcoat slurry 219
6.3.2 Unsupported carbon membrane material characterisation 219
6.3.3 Experimental setup for multi-membrane reactor testing 220
6.4 Operating conditions and key performance indicators for reactor performance 222
6.5 Results and discussion 223
6.5.1 POCS catalysts: slurry rheology and batch reproducibility 223
6.5.2 POCS catalysts: optical characterisation 224
6.5.3 Chemical and structural characterisation of the CMS membrane material 225
6.5.4 POCS geometry comparison in a conventional reactor: Gyroid vs. BCC performance 228
6.5.5 POCS geometry comparison in a membrane reactor: Gyroid vs. BCC performance 230
6.5.6 Effect of sweep gas configuration and pressure on membrane reactor performance 232
6.5.7 Influence of transmembrane ΔP on membrane reactor performance 236
6.5.8 Scaling the membrane contribution: 1 vs. 4 membrane configuration 238
6.6 Conclusions 240
CHAPTER 7: Techno-economic analysis of a small-scale green ammonia plant: conventional vs. membrane-assisted process 249
7.1 Introduction 250
7.2 Methodology 251
7.2.1 Process design choice and system boundaries 251
7.2.2 Process design modelling 253
7.2.3 Technical key performance indicators (KPIs) 262
7.2.4 Economic parameters 263
7.3 Results and discussion 269
7.3.1 Traditional ammonia synthesis process: PBR design 269
7.3.2 Traditional ammonia synthesis process: process implementation 272
7.3.3 Membrane-assisted ammonia synthesis process: PBMR design 274

7.3.4 Membrane parameter sensitivity analysis 278
7.3.5 Adsorption and desorption temperature optimisation 282
7.3.6 Membrane-assisted ammonia synthesis process: process implementation 283
7.4 Technical analysis 285
7.5 Economic analysis 287
7.6 Sensitivity analysis 290
7.7 Regulatory and policy scenario analysis 294
7.8 Conclusions 296
CHAPTER 8: Conclusions & Outlook 308
8.1 Conclusions 308
8.2 Outlook and recommendations for future work 312
LIST OF PUBLICATIONS 316
ACKNOWLEDGEMENTS 320
CURRICULUM VITAE 330

LIST OF ABBREVIATIONS

Abbreviation	Definition
1D, 2D,3D	One-dimensional, two-dimensional, three-dimensional
ASU	Air separation unit
BCC	Body-centred cubic
BEC	Bare erected cost
BPR	Back pressure regulator
CAD	Computer-aided design
CAGR	Compound annual growth rate
CAPEX	Capital expenditure
CBAM	Carbon Border Adjustment Mechanism
CCF	Capital charge factor
CCUS	Carbon capture, utilisation, and storage
CGE	Cold gas efficiency
CEPCI	Chemical Engineering Plant Cost Index
CMR	Catalytic membrane reactor
CMS	Carbon molecular sieve
COF	Covalent organic framework
CP	Concentration polarisation
EDX	Energy-dispersive X-ray spectroscopy
EoS	Equation of state
EPC	Engineering, procurement and construction
ETS	(EU) Emissions Trading System
FBMR	Fluidised bed membrane reactor
GC	Gas chromatography
GHSV	Gas hourly space velocity
HB	Haber-Bosch
HP	High pressure
ICCT	International Council on Clean Transportation
IEA	International Energy Agency
IQR	Interquartile range
KBR	Kellogg Brown & Root

KPI	Key performance indicator
LCOA	Levelized cost of ammonia
LHV	Lower heating value
LOHC	Liquid organic hydrogen carrier
LPBF	Laser powder bed fusion
MAE	Mean absolute error
MAPE	Mean absolute percentage error
MFC	Mass flow controller
MOF	Metal-organic framework
OEA	Organic elemental analysis
OPEX	Operating expenditure
P&ID	Piping and instrumentation diagram
PBMR	Packed bed membrane reactor
PBR	Packed bed reactor
PFD	Process flow diagram
PI	Pressure indicator
POCS	Periodic open cellular structure
PSD	Pore size distribution
PSO	Particle swarm optimisation
PT	Pressure transmitter
PtA	Power-to-ammonia
RMR	Recycle membrane reactor
SCMR	Structured catalyst membrane reactor
SCR	Structured catalyst reactor
SEBM	Selective electron beam melting
SEM	Scanning electron microscopy
SMES	Superconducting magnetic energy storage
SMR	Steam methane reforming
STHE	Shell-and-tube heat exchanger
SW	Sweep-gas-to-feed flow ratio
TC	Temperature controller
TDPC	Total direct plant cost
TE	Temperature sensor
TIC	Total installation cost

TOC	Total overnight cost
TPMS	Triply periodic minimal surface
TRL	Technology readiness level
TSA	Temperature swing adsorption
WHSV	Weight hourly space velocity
XPS	X-ray photoelectron spectroscopy

SUMMARY

The rapid expansion of renewable electricity has renewed interest in hydrogen as a versatile energy carrier. However, its large-scale deployment is still constrained by the challenges of storing and transporting it safely and efficiently. As a result, considerable effort is being devoted to alternative energy carriers that can store hydrogen in chemically bound form while offering higher volumetric energy density and more practical logistics.

Ammonia (NH_3) has emerged as one of the most promising candidates, combining a high hydrogen (H_2) content with relatively simple liquefaction, a well-established global infrastructure for storage and shipping, and the possibility of reconversion to hydrogen or direct use as a fuel. These features make ammonia attractive not only for large export-import corridors and maritime applications, but also for decentralised energy systems, where regional or local synthesis, storage and utilisation can provide a flexible link between variable renewable electricity supply and distributed demand.

Currently, ammonia is produced almost entirely via the mature Haber-Bosch process, which uses fossil-based hydrogen and operates at 100-300 bar and 400-500 °C. This route is highly energy- and carbon-intensive, emitting on the order of 2.4 tons of CO_2 per ton of ammonia in typical natural gas-based plants. Furthermore, it is optimised for very large, baseload units that do not scale down easily or flexibly to serve decentralised, renewable-driven production. In addition, ammonia synthesis is a thermodynamically limited reaction: the combination of high temperature and fixed stoichiometry strongly constrains the achievable equilibrium conversion, resulting in high operating pressures and extensive recycling to attain industrially relevant yields.

In this context, membrane reactors emerge as a particularly attractive option since they integrate reaction and separation in a single, compact unit, replacing the conventional sequence of synthesis, cooling and separation stages. By selectively withdrawing ammonia as it forms, they maintain a favourable reaction driving force and reach high conversions at milder pressures and temperatures, lowering energy demand and associated CO_2 emissions. At the same time, their modular nature and reduced operating severity make them better suited to decentralised, renewable-driven ammonia plants, where H_2 from electrolysis and fluctuating power supply call for smaller, flexible process units rather than traditional Haber-Bosch plants.

The present thesis investigates membrane reactor technology for ammonia synthesis across multiple scales, from the design and characterisation of membrane materials to the experimental proof of concept of the membrane reactor and its assessment at process level.

A general introduction and motivation for the thesis is presented in **Chapter 1**,

starting from the global energy transition context and the need to decarbonise energy-intensive industries. It discusses the role of hydrogen and ammonia as energy carriers, highlighting the advantages and limitations of conventional Haber-Bosch synthesis. On this basis, the chapter introduces intensified and decentralised ammonia synthesis concepts, with a particular focus on membrane reactors to mitigate thermodynamic limitations and improve process efficiency, establishing the background and conceptual framework for the research questions addressed in the rest of the thesis.

Chapter 2 presents the development and analysis of a non-isothermal one-dimensional (1D) packed bed membrane reactor (PBMR) model for ammonia synthesis, integrating in-situ ammonia separation via NH_3-selective membranes and a sweep-gas-assisted permeate side. Through systematic parametric studies, the chapter identifies the required membrane permeance and selectivity, as well as optimal temperature, sweep-gas-to-feed flow ratio and transmembrane pressure difference, to overcome equilibrium limitations and improve H_2 conversion, NH_3 recovery and purity. The results show that, for suitable combinations of membrane performance and operating conditions, the membrane reactor can significantly outperform a conventional packed bed reactor (PBR) while operating under milder conditions. On this basis, carbon molecular sieve (CMS) membranes emerge as particularly promising candidates, owing to their chemical and mechanical robustness under ammonia synthesis conditions.

Building on these findings, **Chapter 3** presents a comprehensive experimental and theoretical investigation of phenolic-resin-derived, metal-doped carbon molecular sieve membranes for ammonia separation, focusing on how carbonisation temperature and transition metal doping influence membrane structure and gas transport. The chapter describes membrane fabrication via dip-coating and controlled carbonisation temperature, permeation experiments with pure and mixed gases under ammonia-synthesis-relevant conditions, and detailed membrane characterisation using permporometry, confocal laser microscopy and scanning electron microscopy (SEM), combined with a transport model that couples molecular sieving, surface diffusion and (micro-)Knudsen diffusion to elucidate the dominant mechanisms. The results show that higher carbonisation temperatures promote tighter ultra-microporous structures and more pronounced molecular-sieving behaviour, while lower temperatures and suitable metal dopants (Cu and Ni) enhance ammonia surface diffusion contributions, identifying Cu-based membranes carbonised at 500-550 °C as the most promising candidates for NH_3 separation under the targeted conditions. Although the achieved separation performance does not yet meet target levels for process-scale implementation, the study provides a mechanistic basis and experimentally validated modelling tools for the future optimisation of CMS membranes for ammonia synthesis.

Chapter 4 investigates a structured catalyst membrane reactor (SCMR) concept in

which a Cu-CMS membrane is integrated within an activated triply periodic minimal surface (TPMS) Gyroid support uniformly coated with a Ru-based catalyst. For comparison, an equivalent structured catalyst reactor (SCR) without a membrane was also tested under matching conditions. The chapter evaluates this Gyroid-based membrane reactor under various weight hourly space velocities (WHSVs), temperatures, pressures, H_2:N_2 feed ratios and sweep-gas flow rates, identifying baseline conditions that approach thermodynamic equilibrium while minimizing hydrogen poisoning on Ru. By varying sweep-gas-to-feed flow ratio and pressure, it quantifies their effects on H_2 conversion, NH_3 production rate, yield, and recovery, revealing clear trade-offs between production rate and product recovery. Under optimal conditions, the SCMR achieves H_2 conversion above the equilibrium limit of the corresponding non-membrane case and delivers comparable performance at lower temperatures than the structured catalyst reactor without a membrane. Finally, the chapter compares different periodic open cellular structures (POCS) geometries (i.e. Gyroid and Body-centred cubic (BCC)) under optimal membrane reactor conditions, confirming that both deliver similar ammonia production performance and together provide a strong experimental proof of concept for structured catalyst membrane reactors as intensified, milder-condition options for ammonia synthesis and future scale-up. Although the membrane selectivity and permeance achieved here do not yet match the targets defined in Chapter 2, the SCMR experiments clearly demonstrate the feasibility of the concept and confirm sweep-gas operation as an effective lever to enhance performance under realistic conditions.

Chapter 5 develops a fully two-dimensional (2D), non-isothermal PBMR model for ammonia synthesis to resolve radial transport effects and concentration polarisation that are inherently neglected in 1D descriptions, with the specific aim of understanding scale-up behaviour. The model is validated against kinetic and permeation data and applied over a wide range of operating conditions and geometries to systematically compare 1D and 2D predictions and to identify when 1D models become unreliable, especially under strong permeation and near-equilibrium conditions. The 2D framework helps explain how concentration polarisation arises and why classical Sherwood correlations fail under reaction-permeation coupling. Importantly, the Sherwood numbers derived from the 2D results are introduced as an effective closure for the present design space, rather than general hydrodynamic correlations. They provide quantitative guidelines for scale-up and modular design, clarifying under which conditions radial diffusion and concentration polarisation become rate-limiting. When applied within this domain, the corrected 1D model reproduces the ammonia concentration at the membrane wall predicted by the 2D model.

Building on the scale-up analysis developed in Chapter 5, **Chapter 6** extends the structured catalyst membrane reactor (SCMR) concept towards experimental scale-up by testing larger Gyroid and BCC POCS catalysts, with and without

integrated carbon membranes, across an increased number of membrane modules and an expanded range of operating conditions. It first characterises and scales up the POCS catalysts in membrane-free operation, clarifying how WHSV and pressure control the transition from kinetically controlled to thermodynamically limited regimes and confirming comparable catalytic performance for both geometries. Building on this baseline, the same POCS configurations are then operated as SCMRs with sweep gas, showing that membrane integration systematically enhances ammonia production relative to the SCR configuration and that increasing membrane surface within the reactor volume leads to higher ammonia production and stronger equilibrium shifting. Together, these results demonstrate that POCS supports can be scaled up without loss of catalytic performance, that sweep-gas-assisted SCMRs effectively relax thermodynamic constraints at larger scale, and that reactor production rate increases favourably with membrane area.

Chapter 7 shifts the focus to a full process-scale techno-economic assessment of ammonia synthesis via membrane reactor technology, addressing whether the intensification demonstrated in previous chapters translates into an economically favourable process at small, decentralised scale. A conventional PBR and a PBMR are each optimised within a full process model, first by screening reactor geometry and operating conditions, then by optimizing the membrane-specific parameters (sweep-gas-to-feed flow ratio, transmembrane pressure difference, permeate composition, membrane number). A central methodological contribution of this chapter is replacing the conventional condensation-based ammonia separation step with adsorption-based separation using a Zeolite-13X sorbent. The optimised PBMR achieves a lower levelized cost of ammonia (LCOA) than the PBR, together with higher power-to-ammonia efficiency and H_2 conversion, through a broad reduction in both capital and operating cost. Sensitivity analysis identifies hydrogen price as the dominant economic lever. Relative to condensation-based separation, the adsorption-assisted configuration improves efficiency and reduces cost simultaneously, confirming that separation technology is decisive for economic competitiveness.

Finally, the main conclusions of this thesis and the associated research outlook are summarised in **Chapter 8**.

CHAPTER 1

General introduction

1.1 CONTEXT AND MOTIVATION FOR THE ENERGY AND INDUSTRIAL TRANSITION

Total energy-related CO_2 emissions reached an all-time high of 37.8 Gt_{CO2} in 2024, as shown in **Figure 1.1**. While industrial process emissions declined by 2.3% (62 Mt_{CO_2}), emissions from fuel combustion rose by approximately 1% (357 Mt_{CO_2}) [1]. The transition to a low-carbon, resource-efficient economy requires not only cleaner energy sources but a fundamental re-design of industrial processes [2]. The urgency of this transition is underscored by accelerating climate change and the growing frequency and intensity of extreme weather events worldwide (**Figure 1.2**) [3,4].

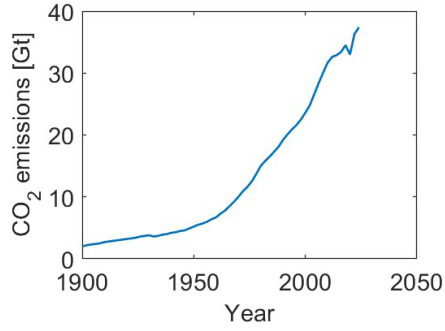


Figure 1.1 Global CO_2 emissions from fossil fuel combustion and industrial processes and their annual change (1900-2023). Data: IEA [1]

Under the Paris Agreement, the international community committed to limiting global warming to well below 2 °C above pre-industrial levels, while pursuing efforts to restrict the temperature increase to 1.5 °C [5,6]. Achieving these goals requires global greenhouse gas emissions to fall by roughly half by 2030 and reach net zero around mid-century [7]. Within the European Union (EU), the renewable share of gross final energy consumption reached 22% in 2020, exceeding the 2020 target by two percentage points [8]. The EU is projected to achieve sharp reductions in electricity emission intensity, declining from 170 $g_{CO_2} \cdot kWh^{-1}$ in 2025 to 90 $g_{CO_2} \cdot kWh^{-1}$ in 2030. Global CO_2 intensity from electricity generation contracted by an estimated 3% in 2025, after a 2.6% reduction in 2024. An increasing share of renewables and robust output in nuclear energy generation are driving this trend [9]. Reaching these climate objectives relies on a comprehensive energy transition in which fossil-based supply chains are progressively replaced by low-carbon energy

carriers and more efficient end-use technologies [10,11]. A central pillar of this transition is the deep decarbonisation of industry through direct and indirect electrification, coupled with the large-scale deployment and system integration of renewable electricity sources such as wind and solar [12,13].

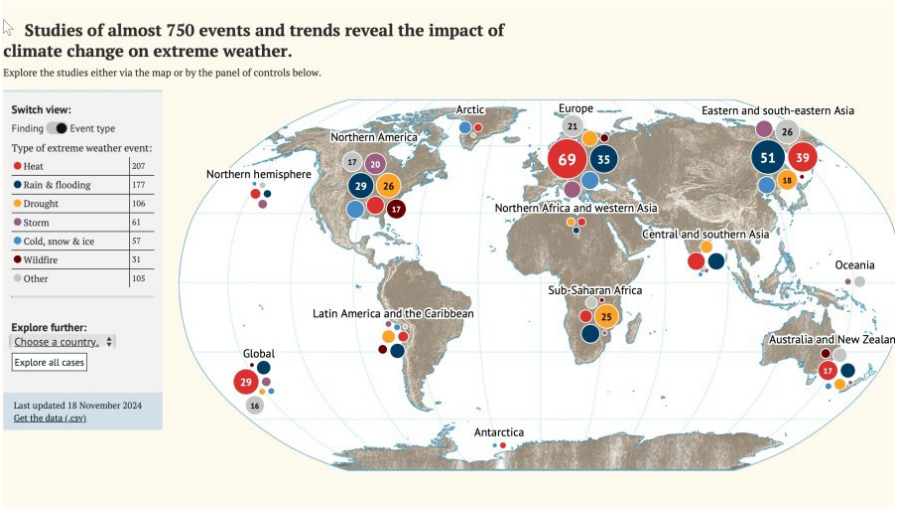


Figure 1.2 Carbon Brief map of 600 studies covering nearly 750 extreme weather events found 74% of them were either intensified or made more likely due to human-caused climate change [4]

Enhancing energy efficiency, decarbonising power generation, promoting electrification, and implementing carbon capture, utilisation, and storage (CCUS) represent crucial pillars of deep decarbonisation [14].

Within this framework, the chemical and petrochemical industry is of primary importance. As a major consumer of energy and fossil feedstocks, it accounts for several percent of global anthropogenic emissions [15,16]. Consequently, the sector represents an essential target for substituting fossil inputs with renewable electricity and low-carbon energy carriers [17].

However, the increased reliance on renewable energy also introduces several challenges, including intermittency and reliability issues [18], limitations in energy storage [19], high upfront investment costs, and grid integration and infrastructure constraints. The intermittent nature of renewable sources complicates the management of available electricity, since the load is difficult to predict on a daily basis [20]. Addressing these issues requires scalable energy storage technologies capable of buffering variable generation. In this context, energy-storage technologies play a central role and can be broadly grouped into mechanical (e.g. pumped hydro, compressed air), thermal (sensible, latent and thermochemical) [21–23], electrochemical (batteries and flow batteries) [24–27], electrical (supercapacitors, SMES) [28,29], and chemical options, including hydrogen and hydrogen-based

energy carriers [30,31]. Each class offers distinct characteristics in terms of storage duration, power and energy density, cost and response time [32].
Among the available options, hydrogen produced via water electrolysis provides a zero-carbon chemical vector that can store large energy quantities over extended durations, at capacities where conventional battery technologies become technically and economically challenging [33]. Although hydrogen possesses a high gravimetric energy density (143 $MJ \cdot kg^{-1}$ vs. ~44 $MJ \cdot kg^{-1}$ for gasoline), its low ambient density (~0.09 $kg \cdot m^{-3}$) results in poor volumetric energy density. Transporting and storing hydrogen requires cryogenic cooling (−253 °C) or compression to 350-700 bar, which incurs severe energy penalties, high capital expenditure, safety risks, and material embrittlement [34].

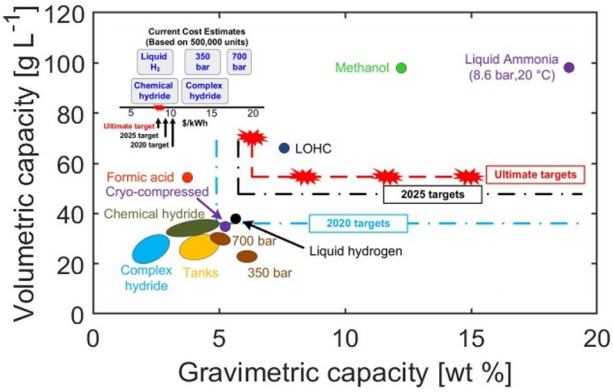


Figure 1.3 Graphical comparison of volumetric and gravimetric hydrogen capacities for selected storage methods and materials, including the US DOE 2025 targets for reference [61]

A comprehensive overview of hydrogen energy sources and storage options is provided in the study of Niaz et al. [35]. The discussed hydrogen production routes include biological processes, wind-powered systems, thermolysis and electrolysis of water, photo-splitting of water, reforming of fossil fuels, and methanol-based processes. Storage methods encompass compressed and liquid hydrogen [36–38] as well as various chemical and materials-based strategies such as ammonia [39,40], methanol [41,42], metal hydrides [43,44], formic acid [45,46], carbohydrates [47,48], other liquid organic hydrogen carriers (LOHCs) [49,50], and physisorption in porous or structured media: carbon materials [51,52], zeolites [53,54], glass microspheres [55], organotransition-metal complexes, metal-organic frameworks (MOFs) [56–58], and covalent organic frameworks (COFs) [59].
The different storage technologies are systematically compared in **Figure 1.3**. Among these candidates, ammonia offers a unique combination of high gravimetric and volumetric storage capacity without releasing CO_2 at the point of use [60].

1.2 AMMONIA: PROPERTIES, USES, AND ROLE AS A HYDROGEN CARRIER

Ammonia is a carbon-free molecule with several favourable physical and thermodynamic characteristics: (1) although technically flammable, it has a relatively high lower flammability limit and a narrow flammable range; (2) at room temperature its vapour pressure is on the order of 0.9 MPa, enabling liquefaction (-33 °C at atmospheric pressure or near-ambient temperature at ~10 bar) and storage in comparatively simple, moderately pressurised vessels; and (3) liquid ammonia combines a relatively high hydrogen content (about 17.6 wt%) with a volumetric energy density of around 12.7 $MJ \cdot L^{-1}$, exceeding that of liquid hydrogen (~8.5 $MJ \cdot L^{-1}$) and compressed hydrogen at 69 MPa and 25 °C (~4.5 $MJ \cdot L^{-1}$) [62–64].

Under standard conditions, ammonia is a colourless gas with a characteristic pungent odour [65], detectable at concentrations of only a few parts per million. At the molecular level, ammonia is a simple inorganic compound consisting of one nitrogen atom covalently bonded to three hydrogen atoms, adopting a trigonal pyramidal geometry with a bond angle of about 106-107° [66]. **Table 1.1** provides a general overview of the properties of ammonia.

Table 1.1 NH_3 basic physicochemical properties

Property	Units	Value
Critical temperature	°C	132.4
Critical pressure	bar	113.3
Density (gas, 0 °C, 1 atm)	$g \cdot L^{-1}$	~0.77
Density (liquid, -33.4 °C, 1 atm)	$g \cdot mL^{-1}$	~0.682
Vapour density (air = 1)	-	~0.597
pK_a of NH_4^+ (25 °C)	-	~9.25
Solubility in water (20 °C)	wt%	~33-34
Flammability limits in air	vol%	~16-25
Auto-ignition temperature	°C	~650

The global ammonia market reached USD 224 billion in 2024 and is projected to reach USD 313 billion by 2030 (5.9% CAGR) [67]. Around 70% of global production is used to manufacture nitrogen-based fertilisers that are critical for crop yields and global food security, while the remaining share serves diverse industrial applications such as explosives, refrigeration, textiles, plastics, and synthetic fibres [68,69]. Driven by the energy transition, ammonia is increasingly evaluated as a zero-carbon maritime fuel, power-generation combustible, and long-distance hydrogen vector [70].

1.3 CONVENTIONAL AMMONIA SYNTHESIS: THE HABER-BOSCH PROCESS

Ammonia is synthesised industrially via the exothermic, reversible Haber-Bosch reaction (Equation (1.1)):

$$N_2 + 3H_2 \leftrightarrow 2NH_3 \quad \Delta H_{298K} = -92\ kJ\ mol^{-1} \tag{1.1}$$

Since ammonia synthesis is a reversible and equilibrium-limited reaction, high pressures are required to shift the equilibrium toward ammonia formation and achieve reasonable conversions (**Figure 1.4**).

However, activating the stable N≡N bond (945 kJ·mol^{-1}) requires temperatures of 400-500 °C over conventional iron catalysts. At these temperatures, chemical equilibrium restricts single-pass conversion to 20-35%, requiring synthesis loop pressures of 100-200 bar and extensive unreacted gas recycling [71]. In conventional natural-gas-based plants (1,000-1,500 ton·day^{-1}), production comprises syngas generation, purification, and the synthesis loop (**Figure 1.5**).

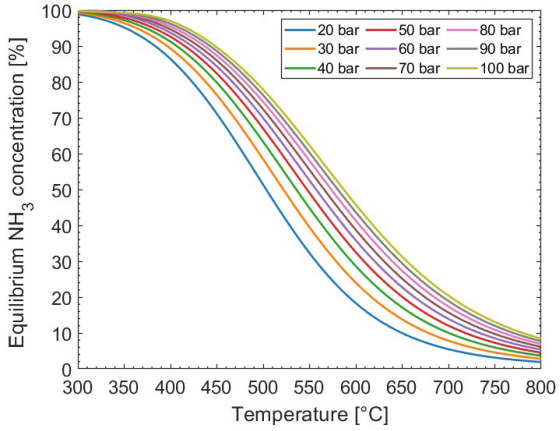


Figure 1.4 Equilibrium NH_3 concentration vs. temperature at different pressure, calculated in Aspen Plus with an RGibbs reactor

Natural gas is desulfurised and reformed [72] via primary steam methane reforming (SMR, 850-900 °C, 25-35 bar) and secondary reforming with air to introduce nitrogen. The syngas is treated via high- and low-temperature water-gas shift reactors, CO_2 absorption, and methanation to eliminate carbon oxides that poison downstream catalysts. The purified synthesis gas, adjusted to an approximately stoichiometric H_2:N_2 ratio, is compressed and routed to multi-bed adiabatic converters with inter-bed cooling. Ammonia is separated by condensation at −10 to −25 °C via mechanical refrigeration, and unreacted gases are recycled [73,74].

Major licensors - including KBR (formerly Kellogg), Topsoe, Thyssenkrupp Uhde, Casale, and Linde - dominate modern commercial plant design [72,76].

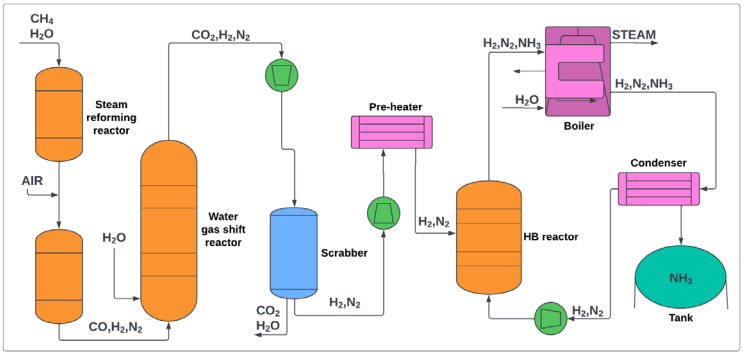


Figure 1.5 Process Flow Diagram of the Haber-Bosch Process [75]

KBR's Purifier technology combines two-step reforming with cryogenic purification to reduce energy consumption to 6.6-6.7 Gcal·$t^{-1}_{NH_3}$ NH_3, while Thyssenkrupp Uhde's dual-pressure loop enhances capacity and thermal efficiency [77].

1.3.1 Catalysts for ammonia synthesis: from iron to ruthenium and beyond

Conventional iron catalysts are derived from magnetite (Fe_3O_4) or wüstite ($Fe_{1-x}O$) promoted structurally by Al_2O_3 and CaO to prevent sintering, and electronically by K_2O to facilitate N_2 dissociative chemisorption [78]. On iron catalysts, N_2 dissociation is strictly rate-determining without significant site-blocking by other adspecies, resulting in peak reaction rates near the stoichiometric ratio [79].

Early work by Ozaki and co-workers and later volcano-type analyses showed that the catalytic activity for ammonia synthesis correlates with nitrogen adsorption strength, with Fe, Ru and Os located near the top of the volcano and thus exhibiting the highest intrinsic activities among transition metals. Since then, a wide variety of Ru catalysts has been proposed, including systems supported on basic oxides (MgO [80], BaO, La_2O_3, CeO_2 [81]) and carbon [82], often promoted with strongly basic alkali or alkaline-earth cations, which are crucial for electron donation and N_2 activation [83–85]. Cs- or K-promoted Ru/MgO, for example, can achieve high activities under comparatively mild conditions and shows markedly enhanced rates upon increasing support basicity [86]. Ru-based catalysts are generally less sensitive than iron to poisoning by water, carbon oxides and ammonia, and maintain high activity even at elevated NH_3 concentrations [87].

The kinetic behaviour of ruthenium catalysts differs significantly from that of conventional iron systems. While iron catalysts usually exhibit an optimum rate close to the stoichiometric H_2:N_2 feed ratio of about 3:1, Ru catalysts suffer from hydrogen inhibition, where strong hydrogen chemisorption blocks active sites for rate-determining N_2 activation. Consequently, the ammonia formation rate on Ru exhibits a negative reaction order with respect to hydrogen partial pressure and

increases with nitrogen partial pressure, making lower, nitrogen-rich H_2:N_2 ratios (e.g., 1:1 to 2:1) kinetically beneficial [82]. Recent kinetic studies, for instance on Ru/CeO_2, confirm this strong rate sensitivity and demonstrate substantial activity gains when the mixture is shifted towards higher N_2 fractions, in contrast to iron catalysts that are less responsive except at low temperature and high pressure. In practice, however, operating below the stoichiometric 3:1 ratio makes hydrogen the limiting reactant and causes unreacted N_2 to accumulate in recycle loops, which constrains commercial synthesis loops to compromise at H_2:N_2 ratios around 2.2:1 rather than operating at the kinetically optimal composition [88].
Further investigations have explored Fe-, Ru-, Co-, Mo- and Ni-based materials on a variety of supports in combination with different promoter oxides, leading to a broad portfolio of alternative systems. Many of these can be grouped into classes such as electrides (e.g. $Ru/C_{12}A_7{:}e^-$), hydrides (e.g. CaH_2, BaH_2, alkali hydrides, Ca_2NH), nitrides (e.g. Mo_2N, MnN, TiN, VN, CrN), intermetallic/alloy catalysts (Fe, Co, Ni, Mo) and carbon-supported nanocatalyst, which typically provide highly electron-donating or hydrogen-donating environments that stabilise active nitrogen-containing intermediates and enable high rates at lower temperature and pressure [89].

1.3.2 Periodic open cellular structures (POCS) as structured catalyst supports

While more active Fe- and Ru-based formulations have been developed, most industrial ammonia catalysts are still used as packed beds of pellets or rings, which can limit heat and mass transfer, increase pressure drop, and restrict reactor design flexibility under intensified operating conditions [90]. This has motivated growing interest in structured catalyst architectures - such as monoliths, foams and periodic cellular structures - that aim to better couple reaction, transport and heat management within the reactor.
In particular, periodic open cellular structures (POCS) are lattice materials consisting of an ordered assembly of interconnected unit cells made of solid ligaments (struts) and open windows (**Figure 1.6**); the cells have a well-defined geometry and tile space in a regular three-dimensional frame [91,92]. Additive manufacturing techniques, such as selective laser melting (SLM) and selective electron beam melting (SEBM), enable the fabrication of metallic POCS with tailored unit cell topologies, strut thicknesses, and porosities [93,94].
The use of such tailor-made catalyst supports holds great potential for process intensification in the chemical process industries [94]. The highly regular morphology of POCS allows their morphological, fluid-dynamic and heat-transport properties to be predicted a priori from the unit-cell geometry, so the catalyst support can be designed and optimised for a given application in advance [95,96].
Structured cellular supports, including POCS and open-cell foams, have already been

widely employed in experimental studies [97,98]. In the work of Richard et al. [99], the authors investigated the impact of POCS design parameters (e.g., porosity, cell type) and flow conditions on external mass transfer for ammonia decomposition. Fratalocchi et al. [100] experimentally demonstrated at lab scale that the heat transfer performance of fixed-bed Fischer-Tropsch reactors can be enhanced by replacing conventional packings with periodic open cellular structures, particularly high conductivity metals such as aluminium.

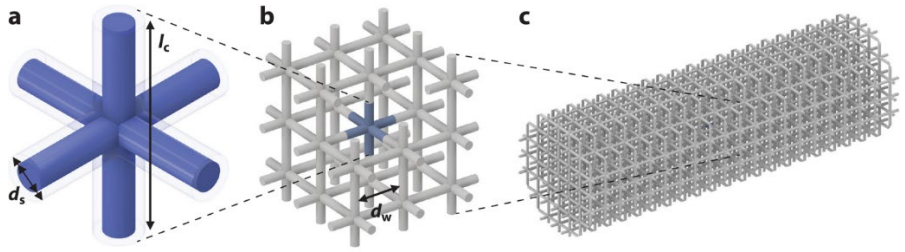


Figure 1.6 Schematic representation of the periodic open cellular structure (POCS): (a) cubic single-unit cell with strut diameter, (b) composite of some unit cells with marked window diameter, (c) resulting structured insert [90]

For ammonia synthesis, POCS offer the possibility to combine high catalyst effectiveness with improved thermal management and low, well-defined pressure drop, which is especially attractive for compact, high-pressure reactors and for intensified concepts such as membrane reactors. In this context, POCS can serve as a platform to integrate catalytic function, heat transfer and, where relevant, separation in a single structured device. Among the various POCS architectures, triply periodic minimal surfaces (TPMS) (i.e. Gyroid lattice) and strut-based Body-centred cubic (BCC) lattice represent a particularly attractive subclass, offering smooth, continuous channels, high specific surface area and excellent mechanical stability, while remaining compatible with metal additive manufacturing.

1.4 TOWARDS INTENSIFIED AND DECENTRALISED AMMONIA SYNTHESIS: THE ROLE OF MEMBRANE REACTORS

According to the International Energy Agency, global ammonia production in 2020 consumed about 8.6 EJ of industrial energy, over 95% of which came from fossil fuels, and accounted for roughly 20% of the chemical sector's energy use and 35% of its CO_2 emissions [69]. Despite more than a century of optimisation, conventional packed bed Haber-Bosch reactors remain constrained by thermodynamic equilibrium, which limits single-pass conversion and necessitates operation at high pressure with extensive gas recycling. In recent years, electrocatalytic ammonia synthesis has attracted increasing attention as a novel production route that could

offer higher energy efficiency and lower environmental impact, particularly for small-scale, distributed plants supplied by renewable electricity [101].
Emerging electrochemical synthesis routes span high-temperature solid-oxide electrolysers (400-750 °C), intermediate molten-salt or composite-membrane systems (100-500 °C), and low-temperature liquid- or solid-state electrolytes (< 100 °C) [102]. Another emerging route is non-thermal plasma synthesis, where energetic plasma species activate nitrogen through vibrational and electronic excitation, enabling operation at milder bulk temperatures and pressures than conventional thermal catalysis to lower activation energy [103]. However, material degradation, competitive hydrogen evolution, high specific energy consumption, and very low ammonia formation rates still prevent this technology from competing with Haber-Bosch at industrial scale, and no catalyst has yet demonstrated sufficiently high activity and selectivity under mild conditions [104]. Moreover, such distributed systems lose economies of scale, and the high capital intensity of conventional Haber-Bosch technology can inhibit widespread deployment of small plants [105].
Improving the sustainability of ammonia production, both environmentally and economically, hinges on intensifying the synthesis loop, either increasing productivity under current operating conditions or achieving equivalent output under milder conditions to reduce energy and resource demand per ton of ammonia [106].

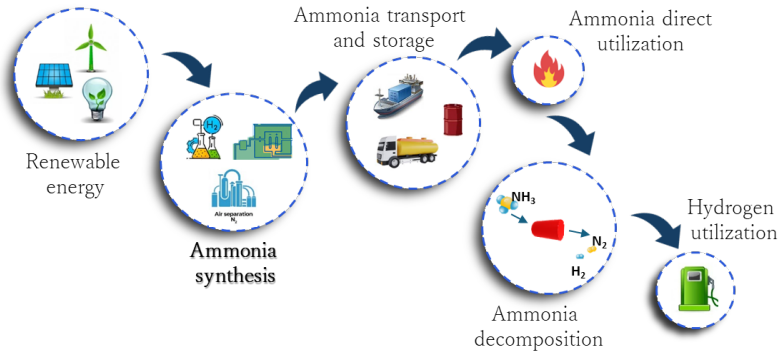


Figure 1.7 Schematic of the renewable-to-ammonia value chain, showing ammonia synthesis from renewable energy, its transport and storage, direct use as a fuel, and decomposition for hydrogen utilisation

Decentralised ammonia production based on modular, smaller-capacity units is particularly appealing to match geographically isolated or variable renewable energy sources but requires reactor concepts that combine high efficiency with reduced size and complexity [107–109]. **Figure 1.7** illustrates an ammonia-based Power-to-X pathway: renewable electricity is converted into green hydrogen via water electrolysis, which serves as a low-carbon feedstock for ammonia synthesis, transport, storage, and end-use power or hydrogen delivery [110].

As previously discussed in Section 1.3, ammonia synthesis is an inherently reversible reaction strongly constrained by thermodynamic equilibrium. In this context, membrane reactors have gained considerable attention, as they offer a means to intensify reversible reactions by combining catalytic reaction and selective product separation into a single unit, thereby relaxing the thermodynamic equilibrium constraint according to Le Châtelier's principle [111–116]. At equilibrium, the macroscopic state variables no longer change with time, even though the reaction remains microscopically active; kinetically, this corresponds to a dynamic state where the forward and reverse reaction rates are equal, and the net rate of conversion is zero [117]. By continuously removing ammonia from the synthesis zone as it forms, membrane reactors shift the apparent equilibrium forward, increase single-pass conversion, simplify downstream separation, and enable resource-efficient ammonia production under milder, decentralised operating conditions [118,119].

1.4.1 Membrane reactor concepts and configurations

Membrane reactors can be classified into different types based on the function of the membrane, namely extractor-, distributor- and contactor-type configurations [120]. In a distributor-type membrane reactor, one or more reactants are fed through the membrane into the reaction zone to establish controlled concentration profiles, enhance selectivity, or improve operational safety [121]. In a contactor-type reactor, the membrane matrix defines the reaction zone, bringing reactants into contact via diffusion across a catalytically active layer. The extractor-type configuration is the most relevant for equilibrium-limited reactions, where the membrane selectively withdraws products to shift conversion beyond conventional thermodynamic limits. When the membrane provides only a separation function (selective supply of reactants and/or removal of products) and the catalyst is placed in a fixed or fluidised bed, the system is referred to as a packed bed membrane reactor (PBMR) or fluidised-bed membrane reactor (FBMR), respectively [122].

In a PBMR configuration, the reactor produces two outlet streams (**Figure 1.8**): in our case, an ammonia-enriched permeate stream and a retentate stream, comprising the non-permeated gas leaving the catalytic side and typically used to quantify conversion and selectivity. Transmembrane ammonia transport is driven by the chemical potential gradient (partial pressure difference) across the membrane. A sweep gas is introduced on the permeate side as an inert carrier to lower the permeate ammonia partial pressure, thereby sustaining the transmembrane driving force while assisting reactor thermal management [123].

To date, research on ammonia synthesis membrane reactors is still relatively sparse and dominated by modelling and process-simulation studies [124–127], with only a limited number of experimental studies available. Among them, Wakimoto et al. [128] demonstrated that a recycle membrane reactor (RMR) operating at 350 °C and 0.2 MPa, achieved a permeate NH_3 mole fraction of 0.10-0.45, clearly beyond the

equilibrium composition. Similarly, Yan et al. [129] reported a catalytic membrane reactor achieving N_2 and H_2 conversions in the range of approximately 7-10% and NH_3 yields of roughly 7-9%, clearly exceeding the near-equilibrium values (~1%) obtained in the PBR.

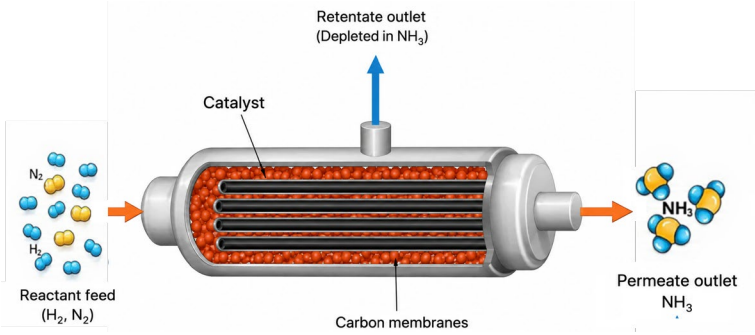


Figure 1.8 Schematic of the proposed membrane reactor for ammonia synthesis, illustrating N_2-H_2 feed conversion to ammonia with simultaneous product removal through the membrane

However, packed bed reactors typically exhibit poor-to-moderate radial heat-transfer rates and significant thermal gradients during exothermic synthesis, motivating the development of multi-tubular reactor architectures to ensure efficient heat removal and reliable scale-up [130].

1.5 NH_3-SELECTIVE MEMBRANES: CARBON MOLECULAR SIEVE (CMS) AND BEYOND

Membranes can be classified in many ways, including by material, morphology, geometry, preparation method and separation mechanism. In terms of materials, they may be organic (polymeric) or inorganic (ceramic/metallic), solid or liquid, and charged or neutral; their structure can be homogeneous or heterogeneous, symmetric or asymmetric [131]. For membrane reactors in catalytic systems, the key requirement is stability under reaction conditions: polymeric membranes generally show limited resistance to high temperatures, aggressive solvents, and oxidative environments [132], whereas inorganic membranes can withstand higher temperatures and harsher chemical conditions and thus offer superior robustness [120]. Inorganic membranes are usually subdivided into dense and porous types; porous membranes are further classified by IUPAC into microporous (d_p < 2 nm), mesoporous (2 nm < d_p < 50 nm) and macroporous (d_p > 50 nm) [133]. Typical module geometries include plate-and-frame, tubular, hollow-fibre, and spiral-wound designs, with tubular modules being considered in this work.

Among inorganic systems, carbon membranes - and especially carbon molecular sieve (CMS) membranes - have emerged as leading candidates for gas separation

because they combine high selectivity and relatively high permeability with excellent thermal and chemical stability and a narrowly distributed microporous structure. CMS membranes are obtained by pyrolysis and carbonisation of polymeric precursors [134] such as polyimides [135,136], polyetherimide [137,138], and phenolic resin [139–143]; the precursor chemistry and carbonisation conditions determine the resulting pore architecture and thus the separation performance [144]. Phenolic resins, particularly phenol-formaldehyde resins, are attractive CMS precursors due to their high carbon yield, low cost and ability to form molecular-sieving carbons after thermal treatment [145,146], with structure and properties depending on the formaldehyde/phenol ratio, catalyst, pH, and temperature; two main types are distinguished: resol and novolac resins [147]. Carbonisation of such polymers in inert or vacuum atmospheres proceeds through three temperature regimes: (1) annealing at approximately 100-400 °C, (2) intermediate heating at about 400-500 °C, and (3) pyrolysis to form carbon at 500-1,000 °C [148]. During these steps, extensive cross-linking suppresses the formation of large graphitic crystallites and produces non-graphitizing carbons with narrow pore-size distributions, which are crucial for molecular sieving [149]. Process parameters such as heating rate, final temperature, soak time and gas atmosphere, together with pre- and post-treatments (thermostabilizing, oxidation, chemical vapour deposition), strongly influence the microstructure and gas transport properties of CMS membranes [150,151]. In composite configurations, the porous support also plays a crucial role: as noted by Ma et al. [152], the overall performance depends on matching the thickness of the carbon layer to the support porosity, since varying the coating thickness on the same support can significantly change flux at essentially unchanged selectivity [143]. A common fabrication route is therefore to deposit a thin polymer film from solution onto a porous support and subsequently carbonise it under controlled conditions to obtain the CMS separation layer.

Recent data compiled by Genduso et al. [153] show that state-of-the-art CMS membranes can achieve hydrogen permeabilities in the range of roughly 10^2-10^3 Barrer with H_2/CH_4 and H_2/CO_2 selectivities frequently well above 100 and, in some cases, approaching or exceeding 1000. For CO_2 selective CMS membranes, the same review reports CO_2 permeabilities on the order of 10^3-10^4 Barrer, combined with CO_2/CH_4 and CO_2/N_2 selectivities typically between about 50 and 400. For ammonia applications, Yarema et al. [154] distinguish mainly between polymeric (including facilitated-transport and ionic-liquid-based) membranes and inorganic systems. Polymeric and hybrid membranes can achieve very high NH_3/H_2 and NH_3/N_2 selectivities at low to moderate temperatures, but their limited thermal and chemical stability under hot, reactive $NH_3/H_2/N_2$ mixtures prevents straightforward application at ammonia-synthesis conditions. In contrast, inorganic membranes - particularly porous ceramics and carbon molecular sieve membranes - offer the thermal and chemical robustness required for operation at 350-500 °C and

elevated pressures, while still providing significant NH_3 selectivity through a combination of molecular sieving and strong sorption interactions [154].
According to Yan and Tsuru [155], NH_3 permselective membranes span a wide performance space: polymeric and ion-exchange membranes show NH_3/N_2 and NH_3/H_2 selectivities from about 10 up to a few hundred at low temperature, ionic-liquid-based hybrid membranes can exceed selectivities of 100-1000 with NH_3 permeances of roughly 10-100 GPU; and recent organosilica-type inorganic membranes reach NH_3/H_2 and NH_3/N_2 selectivities of 50-500 at 50-300 °C. Zeolite and silica-type inorganic membranes have been explored for ammonia separation, with early γ-alumina-supported organosilica and silica layers reporting NH_3 permeances around 10^{-7}-10^{-6} $mol \cdot m^{-2}\ s^{-1}\ Pa^{-1}$ and NH_3/N_2 or NH_3/H_2O separation factors of approximately 5-15. More recent FAU- and SAPO-34-based zeolite membranes achieved NH_3/N_2 separation factors exceeding 2,000 and NH_3/H_2S values above 3000 by exploiting strong adsorption of ammonia in the microporous framework. Padinjarekutt et al. [156] studied a Na^+-gated NaA zeolite nanochannel membrane, demonstrating NH_3/H_2 selectivity up to about 4,280 and NH_3/N_2 selectivity >10,000 at up to 250 °C and 35 bar in $NH_3/H_2/N_2$ mixtures. Despite these encouraging figures, both reviews emphasise that most NH_3-selective membranes still face important limitations, including restricted operational temperature windows (especially for polymers and ILs), trade-offs between selectivity and permeance, and outstanding challenges in achieving long-term hydrothermal and chemical stability [157]. Consequently, developing membranes that combine sufficient NH_3 selectivity and permeance with long-term stability and scalable module design under ammonia-synthesis conditions remains a key barrier to industrial implementation.

1.5.1 Gas transport mechanisms and modelling

Gas transport across porous and CMS membranes proceeds through several mechanisms that depend on pore size, connectivity and surface chemistry, with viscous (Poiseuille) flow, Knudsen diffusion, adsorption-surface diffusion and molecular sieving typically identified as the dominant regimes [149].
Viscous (Poiseuille) flow dominates where the pore diameter (typically d_p > 50 nm) exceeds the molecular mean free path and bulk flow is driven by the pressure gradient [158]. As pore size decreases into the mesoporous range, Knudsen diffusion takes over once molecule-wall collisions become more frequent than intermolecular collisions, that is, once the mean free path of the gas molecules exceeds the characteristic pore dimension [159]. At smaller scales still, within the micropores (d_p = 0.5-2 nm) of these membranes, selective adsorption-diffusion becomes the dominant transport pathway: species with stronger affinity for the pore walls form a mobile adsorbed layer and diffuse preferentially along the pore surface.

Finally, in the ultramicroporous domain (d_p = 0.25-0.5 nm), transport is governed by strict molecular sieving, whereby only molecules smaller than the pore aperture are permitted to pass through [160,161]. Mass transport modelling in carbon membranes has been comprehensively reviewed by Sahin and co-workers, among others, spanning approaches from simplified solution-diffusion and Fickian resistance-network descriptions to more rigorous Maxwell-Stefan and Dusty Gas formulations, as well as molecular simulation techniques.

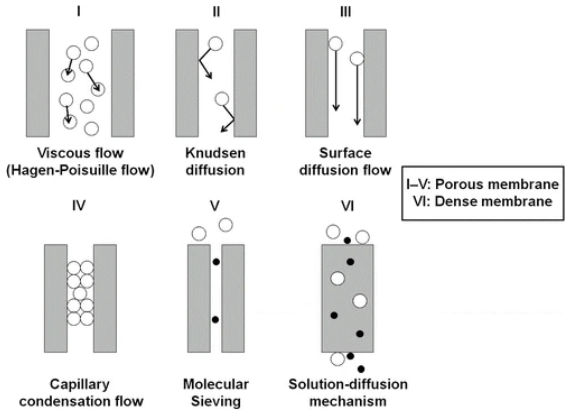


Figure 1.9 Mechanisms of transport for gas molecules through a porous/dense membrane [158]

These studies conclude that accurate prediction of CMS performance generally requires models that capture the coupled contributions of Knudsen, surface and activated diffusion across the relevant pore-size spectrum and incorporate realistic adsorption isotherms [162]. For example, Kruse et al. modelled high-pressure gas permeation through CMS layers using a Maxwell-Stefan framework driven by fugacity gradients, explicitly coupled with experimentally measured adsorption data, and achieved good agreement with experimental results over broad ranges of pressure and composition [163].

1.6 MODELLING STRATEGIES FOR MEMBRANE REACTORS

Mathematical modelling of chemical reactors is a cornerstone of modern process design and development. Advances in numerical methods, computational hardware and specialised software nowadays allow detailed representation of both steady-state and dynamic reactor behaviour, so that transport and reaction phenomena can be analysed in silico before any unit is built [164]. Modelling of membrane reactors has become an active research field and provides an effective tool for process design, evaluation and optimisation, as demonstrated by a substantial body of work [165]. In practice, reactor models are used to (1) improve understanding of the process and

reaction system by examining internal profiles and dynamics, and (2) optimize operating conditions and design variables by virtually testing alternative scenarios without extensive experimental campaigns [117].

For membrane reactors, modelling approaches range from simplified one-dimensional plug-flow descriptions [166–168] to detailed two- [169–171], and three-dimensional formulations [172,173] that explicitly account for reaction kinetics, multicomponent diffusion, heat transfer and membrane permeation [174,175]. One-dimensional axial models are widely employed for preliminary design, parameter estimation and process level studies, whereas two- or three-dimensional models are required when radial temperature or concentration gradients, flow maldistribution or concentration polarisation near the membrane significantly affect performance. Recent work has proposed criteria based on dimensionless groups, such as Péclet and Damköhler numbers, to indicate when a 1D description is sufficient and when higher-dimensional models are necessary [176]. In many catalytic fixed-bed systems, appropriately formulated 1D models provide accurate predictions of overall conversion and peak temperatures, while 2D models add important information on radial profiles and may become essential for detailed design or for systems with strong heat- and mass-transfer limitations [117,177].

Following the classical classification by Froment and Bischoff, reactor models can be divided into pseudo-homogeneous and heterogeneous formulations. In pseudo-homogeneous models, fluid and catalyst particles are treated as a single effective phase with averaged properties, whereas heterogeneous models explicitly distinguish between fluid and solid phases and may include intraparticle transport resistances to capture diffusion-reaction interactions inside the catalyst [178].

1.7 THESIS OUTLINE

This thesis presents a combined theoretical and experimental investigation of catalytic membrane reactors for ammonia synthesis, progressing from fundamental modelling and materials development to experimental proof of concept, scale-up, and process-level economic assessment.

Chapter 2 develops a 1D non-isothermal packed bed membrane reactor model for ammonia synthesis, aimed at assessing the feasibility and potential benefits of membrane-assisted operation compared to a conventional packed bed. The model is used to explore how membrane permeance and selectivity, together with operating conditions, affect H_2 conversion, NH_3 recovery and purity, and to define target membrane performance windows.

Chapter 3 experimentally and theoretically characterizes carbon molecular sieve (CMS) membranes linking carbonisation temperature and polymer functionalisation, including metal doping, to membrane microstructure. A multi-mechanism transport

model is used to quantify the relative contributions of gas transport mechanisms, and to identify promising CMS membrane designs for integration into the reactor studies developed in the subsequent chapters.

Chapter 4 demonstrates a proof of concept structured catalyst membrane reactor (SCMR) integrating a Cu-carbon membrane with manufactured POCS Gyroid-BCC catalyst support. The effect of key operating variables, such as temperature, pressure, H_2:N_2 feed ratio, weight hourly space velocity (WHSV), and particularly the sweep gas flow, is systematically evaluated. The one-dimensional packed bed membrane reactor model developed in Chapter 2 is employed to interpret these experiments and benchmark the observed performance.

Chapter 5 introduces a 2D non-isothermal packed bed membrane reactor model capturing axial and radial transport phenomena, with emphasis on concentration polarisation, radial diffusion and its interplay with membrane spacing and permeation, in multi-membrane packed bed configurations. The 2D model is used to map the regimes in which conventional 1D descriptions fail, to derive a reaction-enhanced Sherwood correction for ammonia mass transfer, and to formulate geometry and operating window design criteria for scale-up from a single-tube to multi-tubular membrane reactors.

Chapter 6 extends the experimental investigation to a multi-tubular membrane reactor containing a bundle of four membranes and structured catalyst supports, addressing practical aspects such as mechanical integration and flow distribution under small pilot-scale conditions. The influence of membrane number, membrane area, sweep-gas-to-feed flow ratio, and transmembrane pressure difference on H_2 conversion, NH_3 production rate and recovery is systematically assessed and compared with the single-membrane results of Chapter 4 to evaluate the robustness of the proposed scale-up strategies.

Chapter 7 presents a techno-economic analysis comparing a conventional packed bed reactor against a packed bed membrane reactor integrated with adsorption-based ammonia separation, in place of the condensation-based separation typically adopted in earlier assessments. Both configurations are optimised within a full process model, first by screening reactor geometry and operating conditions, then by optimizing the membrane-specific parameters. The chapter quantifies the resulting differences in levelized cost of ammonia and power-to-ammonia efficiency, identifying hydrogen feedstock price as the dominant economic driver. These results are benchmarked against previous techno-economic work to assess whether adsorption-based separation unlocks cost benefits beyond the efficiency gains already established at reactor scale.

Finally, **Chapter 8** summarizes the main conclusions of the research and provides perspectives for future work to further enhance and scale up the membrane reactor technology.

REFERENCES

[1] CO2 Emissions – Global Energy Review 2025 – Analysis - IEA, (n.d.). https://www.iea.org/reports/global-energy-review-2025/co2-emissions.

[2] J. Busch, T.J. Foxon, P.G. Taylor, Designing industrial strategy for a low carbon transformation, Environ. Innov. Soc. Transit. 29 (2018) 114–125. https://doi.org/10.1016/j.eist.2018.07.005.

[3] M.K. Jha, M. Dev, Impacts of Climate Change, Studies in Computational Intelligence 1165 (2024) 139–159. https://doi.org/10.1007/978-3-031-70102-3_10.

[4] Carbon Brief releases sixth version of extreme weather event interactive map, (n.d.). https://www.intellinews.com/carbon-brief-releases-sixth-version-of-extreme-weather-event-interactive-map-353993/.

[5] M.J. Regufe, A. Pereira, A.F.P. Ferreira, A.M. Ribeiro, A.E. Rodrigues, "Current Developments of Carbon Capture Storage and/or Utilization–Looking for Net-Zero Emissions Defined in the Paris Agreement", *Energies* 2021, Vol. 14, 14 (2021). https://doi.org/10.3390/en14092406.

[6] M.J.B. Kabeyi, O.A. Olanrewaju, "Sustainable Energy Transition for Renewable and Low Carbon Grid Electricity Generation and Supply", *Front. Energy Res.* 9 (2022) 743114. https://doi.org/10.3389/fenrg.2021.743114.

[7] I. Elegbeleye, O. Oguntona, F. Elegbeleye, "Green Hydrogen: Pathway to Net Zero Green House Gas Emission and Global Climate Change Mitigation", *Hydrogen 2025*, Vol. 6, 6 (2025). https://doi.org/10.3390/hydrogen6020029.

[8] M. Simionescu, W. Strielkowski, M. Tvaronavičiene, "Renewable Energy in Final Energy Consumption and Income in the EU-28 Countries", *Energies 2020*, Vol. 13, 13 (2020). https://doi.org/10.3390/en13092280.

[9] Emissions – Electricity 2026 – Analysis - IEA, (n.d.). https://www.iea.org/reports/electricity-2026/emissions.

[10] T. Nasiri, M. Moeini-Aghtaie, M. Foroughi, M. Azimi, "Energy optimization of multi-carrier energy systems to achieve a low carbon community", J. *Clean. Prod.* 390 (2023) 136154. https://doi.org/10.1016/j.jclepro.2023.136154.

[11] X. Chen, "Green and low-carbon energy-use", (2024). https://doi.org/10.59717/j.xinn-energy.2024.100003.

[12] M. Wei, C.A. McMillan, S. de la Rue du Can, "Electrification of Industry: Potential, Challenges and Outlook", *Current Sustainable/Renewable Energy Reports* 6 (2019) 140–148. https://doi.org/10.1007/s40518-019-00136-1.

[13] D.S. Renné, "Progress, opportunities and challenges of achieving net-zero emissions and 100% renewables", *Solar Compass* 1 (2022) 100007. https://doi.org/10.1016/j.solcom.2022.100007.

[14] Z. Wang, Y. Sun, H. Kong, C. Xia-Bauer, "An in-depth review of key technologies and pathways to carbon neutrality: classification and assessment of decarbonization technologies", *Carbon Neutrality* 2025 4:1 4 (2025) 15-. https://doi.org/10.1007/s43979-025-00129-8.

[15] E. Worrell, "Industrial Energy Use, Status and Trends", *Encyclopedia of Energy* (2004) 395–406. https://doi.org/10.1016/b0-12-176480-x/00196-0.

[16] A. Boulamanti, J.A Moya, "Energy efficiency and GHG emissions: Prospective scenarios for the Chemical and Petrochemical Industry", (2017). https://doi.org/10.2760/630308.

[17] G. Centi, G. Iaquaniello, S. Perathoner, "Chemical engineering role in the use of renewable energy and alternative carbon sources in chemical production", *BMC Chemical Engineering* 2019 1:1 1 (2019) 5-. https://doi.org/10.1186/s42480-019-0006-8.

[18] M. Y. Suberu, M. W. Mustafa, N. Bashir, "Energy storage systems for renewable energy power sector integration and mitigation of intermittency", *Renewable and Sustainable Energy Reviews* 35 (2014) 499–514. https://doi.org/10.1016/j.rser.2014.04.009.

[19] M.A. Basit, S. Dilshad, R. Badar, S.M. Sami ur Rehman, "Limitations, challenges, and solution approaches in grid-connected renewable energy systems", *Int. J. Energy Res.* 44 (2020) 4132–4162. https://doi.org/10.1002/er.5033.

[20] Wood Mackenzie, "How to address risk from the intermittency of renewable energy in power markets", (n.d.). https://www.woodmac.com/news/opinion/how-to-address-risk-from-the-intermittency-of-renewable-energy-in-power-markets/.

[21] A. V. Olympios, J.D. McTigue, P. Farres-Antunez, A. Tafone, A. Romagnoli, Y. Li, Y. Ding, W.D. Steinmann, L. Wang, H. Chen, C.N. Markides, "Progress and prospects of thermo-mechanical energy storage—a critical review", *Progress in Energy* 3 (2021) 022001. https://doi.org/10.1088/2516-1083/abdbba.

[22] K.R. Gautam, G.B. Andresen, M. Victoria, "Review and Techno-Economic Analysis of Emerging Thermo-Mechanical Energy Storage Technologies", *Energies* 2022, Vol. 15, 15 (2022). https://doi.org/10.3390/en15176328.

[23] A.H. Alami, "Mechanical Energy Storage for Renewable and Sustainable Energy Resources", (2020). http://link.springer.com/10.1007/978-3-030-33788-9.

[24] R. Ye, D. Henkensmeier, S.J. Yoon, Z. Huang, D.K. Kim, Z. Chang, S. Kim, R. Chen, "Redox Flow Batteries for Energy Storage: A Technology Review", *Journal of Electrochemical Energy Conversion and Storage* 15 (2018) 10801–10802. https://doi.org/10.1115/1.4037248.

[25] D. N. Buckley, C. O'Dwyer, N. Quill, R.P. Lynch, "Electrochemical Energy Storage", *Issues in Environmental Science and Technology* 2019-January (2018) 115–149. https://doi.org/10.1039/9781788015530-00115.

[26] Y. Arellano-Prieto, E. Chavez-Panduro, P. S. Rossi, F. Finotti, "Energy Storage Solutions for Offshore Applications", *Energies* 2022, Vol. 15, 15 (2022). https://doi.org/10.3390/en15176153.

[27] G.L. Soloveichik, "Battery technologies for large-scale stationary energy storage", *Annu. Rev. Chem. Biomol. Eng.* 2 (2011) 503–527. https://doi.org/10.1146/annurev-chembioeng-061010-114116.

[28] M.H. Ali, B. Wu, R.A. Dougal, "An overview of SMES applications in power and energy systems", *IEEE Trans. Sustain. Energy* 1 (2010) 38–47. https://doi.org/10.1109/TSTE.2010.2044901.

[29] J.X. Jin, "Emerging SMES technology into energy storage systems and smart grid applications", *Green Energy and Technology* (2014) 77–125. https://doi.org/10.1007/978-981-4585-30-9_4.

[30] A.M. Abdalla, S. Hossain, O.B. Nisfindy, A.T. Azad, M. Dawood, A.K. Azad, "Hydrogen as an energy carrier", *Energy Convers. Manag.* 165 (2018) 31–61. https://doi.org/10.1016/j.enconman.2018.03.088.

[31] N. Stetson, M. Wieliczko, "Hydrogen technologies for energy storage: A perspective, *MRS Energy & Sustainability* 7 (2020) E41. https://doi.org/10.1557/mre.2020.43.

[32] "Four Types of Energy Storage: Batteries, Mechanical, Thermal, Hydrogen", (n.d.). https://ffdpower.com/the-four-major-types-of-energy-storage-electrochemical-mechanical-thermal-hydrogen/.

[33] Q. Hassan, S. Algburi, A.Z. Sameen, M. Jaszczur, H.M. Salman, "Hydrogen as an energy carrier: properties, storage methods, challenges, and future implications", *Environment Systems and Decisions* 2023 44:2 44 (2023) 327–350. https://doi.org/10.1007/s10669-023-09932-z.

[34] S. Guan, S. Shen, Y. Dou, W. Chen, J. Shen, B. Ye, W.G. Cui, W. Zhong, Z. Li, H. Pan, D. Wang, "Progress and perspectives on hydrogen storage and release in the negative hydrogen medium", *Energy Environ. Sci.* 18 (2025) 9324–9372. https://doi.org/10.1039/d5ee04149j.

[35] S. Niaz, T. Manzoor, A.H. Pandith, "Hydrogen storage: Materials, methods and perspectives", *Renewable and Sustainable Energy Reviews* 50 (2015) 457–469. https://doi.org/10.1016/j.rser.2015.05.011.

[36] A. Naquash, N. Agarwal, M. Lee, "A Review on Liquid Hydrogen Storage: Current Status, Challenges and Future Directions", *Sustainability* 2024, Vol. 16, 16 (2024). https://doi.org/10.3390/su16188270.

[37] L. Fang, X. Dong, H. Wang, M. Gong, "Economic analysis of compressed gaseous hydrogen, liquid hydrogen, and cryo-compressed hydrogen storage methods for large-scale storage and transportation", *Int. J. Hydrogen Energy* 162 (2025) 150725. https://doi.org/10.1016/j.ijhydene.2025.150725.

[38] M. Aziz, "Liquid Hydrogen: A Review on Liquefaction, Storage, Transportation, and

Safety", *Energies* 2021, Vol. 14, 14 (2021). https://doi.org/10.3390/en14185917.

[39] K.E. Lamb, M.D. Dolan, D.F. Kennedy, "Ammonia for hydrogen storage; A review of catalytic ammonia decomposition and hydrogen separation and purification", *Int. J. Hydrogen Energy* 44 (2019) 3580–3593. https://doi.org/10.1016/j.ijhydene.2018.12.024.

[40] F. Chang, W. Gao, J. Guo, P. Chen, "Emerging Materials and Methods toward Ammonia-Based Energy Storage and Conversion", *Advanced Materials* 33 (2021) 2005721. https://doi.org/10.1002/adma.202005721.

[41] D. Bellotti, M. Rivarolo, L. Magistri, "Economic feasibility of methanol synthesis as a method for CO2 reduction and energy storage", *Energy Procedia* 158 (2019) 4721–4728. https://doi.org/10.1016/j.egypro.2019.01.730.

[42] E. Moioli, R. Mutschler, A. Züttel, "Renewable energy storage via CO2 and H2 conversion to methane and methanol: Assessment for small scale applications", *Renewable and Sustainable Energy Reviews* 107 (2019) 497–506. https://doi.org/10.1016/j.rser.2019.03.022.

[43] E. Nemukula, C.B. Mtshali, F. Nemangwele, "Metal Hydrides for Sustainable Hydrogen Storage: A Review", *Int. J. Energy Res.* 2025 (2025) 6300225. https://doi.org/10.1155/er/6300225.

[44] A. Schneemann, J.L. White, S. Kang, S. Jeong, L.F. Wan, E.S. Cho, T.W. Heo, D. Prendergast, J.J. Urban, B.C. Wood, M.D. Allendorf, V. Stavila, "Nanostructured Metal Hydrides for Hydrogen Storage", *Chem. Rev.* 118 (2018) 10775–10839. https://doi.org/10.1021/acs.chemrev.8b00313.

[45] D. Mellmann, P. Sponholz, H. Junge, M. Beller, "Formic acid as a hydrogen storage material – development of homogeneous catalysts for selective hydrogen release", *Chem. Soc. Rev.* 45 (2016) 3954–3988. https://doi.org/10.1039/c5cs00618j.

[46] A.K. Singh, S. Singh, A. Kumar, "Hydrogen energy future with formic acid: a renewable chemical hydrogen storage system", *Catal. Sci. Technol.* 6 (2015) 12–40. https://doi.org/10.1039/c5cy01276g.

[47] J.E. Kim, Y.H.P. Zhang, "Use of carbohydrates for hydrogen storage", Compendium of Hydrogen Energy: Hydrogen Storage, Distribution and Infrastructure: Volume 2 "107 (2016) 219–241. https://doi.org/10.1016/B978-1-78242-362-1.00009-2.

[48] Y.H.P. Zhang, J.R. Mielenz, "Renewable Hydrogen Carrier — Carbohydrate: Constructing the Carbon-Neutral Carbohydrate Economy", *Energies* 2011, Vol. 4, Pages 254-275 4 (2011) 254–275. https://doi.org/10.3390/en4020254.

[49] T.H. Le, N. Tran, H.J. Lee, "Development of Liquid Organic Hydrogen Carriers for Hydrogen Storage and Transport", I*nternational Journal of Molecular Sciences* 2024, Vol. 25, 25 (2024). https://doi.org/10.3390/ijms25021359.

[50] P.M. Modisha, C.N.M. Ouma, R. Garidzirai, P. Wasserscheid, D. Bessarabov, "The

Prospect of Hydrogen Storage Using Liquid Organic Hydrogen Carriers", *Energy & Fuels* 33 (2019) 2778–2796. https://doi.org/10.1021/acs.energyfuels.9b00296.

[51] L. Zubizarreta, A. Arenillas, J.J. Pis, "Carbon materials for H2 storage", *Int. J. Hydrogen Energy* 34 (2009) 4575–4581. https://doi.org/10.1016/j.ijhydene.2008.07.112.

[52] M. Bastos-Neto † ,C. Patzschke, M. Lange, J. Möllmer, A. Möller, S. Fichtner, C. Schrage, D. Lässig, J. Lincke, R. Staudt, H. Krautscheid, R. Gläser, "Assessment of hydrogen storage by physisorption in porous materials", *Energy & Environmental Science* DOI:10.1039/C2EE22037G.

[53] B. Taşğın, J. Ryšavý, T. Sangeetha, W.-M. Yan, "Green Energy and Fuel Research Hydrogen Storage in Zeolites: A Mini Review of Structural and Chemical Influences on Adsorption Performance", *Green Energy and Fuel Research* (2025). https://doi.org/10.53941/gefr.2025.100005.

[54] P.A. Anderson, "Storage of hydrogen in zeolites", *Solid-State Hydrogen Storage: Materials and Chemistry* (2008) 223–260. https://doi.org/10.1533/9781845694944.3.223.

[55] J. Zhang, Y. Zhou, C. Li, Z. Wang, "Advancements in Solid-State Hydrogen Storage: A Review on the Glass Microspheres", *Review Langmuir* 40 (2024) 10433–10448. https://doi.org/10.1021/acs.langmuir.4c01006.

[56] J.L.C. Rowsell, O.M. Yaghi, "Strategies for Hydrogen Storage in Metal–Organic Frameworks", *Angew. Chem. Int. Ed.* 44 (2005) 4670–4679. https://doi.org/10.1002/anie.200462786.

[57] M.P. Suh, H.J. Park, T.K. Prasad, D.W. Lim, "Hydrogen Storage in Metal–Organic Frameworks", *Chem. Rev.* 112 (2011) 782–835. https://doi.org/10.1021/cr200274s.

[58] B. Panella, "Hydrogen storage by physisorption on porous materials", (2006).

[59] E. Klontzas, E. Tylianakis, G.E. Froudakis, "Hydrogen Storage in 3D Covalent Organic Frameworks. A Multiscale Theoretical Investigation", *Journal of Physical Chemistry* 112 (2008) 9095–9098. https://doi.org/10.1021/jp711326g.

[60] A.S. Mekonnin, K. Wacławiak, M. Humayun, S. Zhang, H. Ullah, "Hydrogen Storage Technology, and Its Challenges: A Review", *Catalysts* 2025, Vol. 15, 15 (2025). https://doi.org/10.3390/catal15030260.

[61] P.K. Panigrahi, B. Chandu, M.R. Motapothula, N. Puvvada, "Potential Benefits, Challenges and Perspectives of Various Methods and Materials Used for Hydrogen Storage", *Energy & Fuels* 38 (2024) 2630–2653. https://doi.org/10.1021/acs.energyfuels.3c04084.

[62] Y. He, B. Guan, Z. Zhuang, J. Chen, L. Zhu, Z. Ma, X. Hu, C. Zhu, S. Zhao, K. Shu, H. Dang, T. Zhu, Z. Huang, "Advances in ammonia (NH3) adsorption and storage: materials, mechanisms, and applications", *Adsorption* 2025 31:2 31 (2025) 48-. https://doi.org/10.1007/s10450-025-00601-y.

[63] Y. Kojima, M. Yamaguchi, "Ammonia as a hydrogen energy carrier", *Int. J. Hydrogen Energy* 47 (2022) 22832–22839. https://doi.org/10.1016/j.ijhydene.2022.05.096.

[64] M. Aziz, A. TriWijayanta, A.B.D. Nandiyanto, "Ammonia as Effective Hydrogen Storage: A Review on Production, Storage and Utilization", *Energies* 2020, Vol. 13, 13 (2020). https://doi.org/10.3390/en13123062.

[65] T. Rajabloo, "Ammonia, production, applications, and the effect of its phase-out", (2022).

[66] Molecular Geometry, Lewis Structure, & Bond Angle of Ammonia, (n.d.). https://www.chemistrylearner.com/molecular-geometry/nh3-molecular-geometry.

[67] Ammonia Market Size, Share & Trends Analysis Report, 2030, (n.d.). https://www.grandviewresearch.com/industry-analysis/ammonia-market.

[68] A.E. Yüzbaşıoğlu, C. Avşar, A.O. Gezerman, "The current situation in the use of ammonia as a sustainable energy source and its industrial potential", *Current Research in Green and Sustainable Chemistry* 5 (2022) 100307. https://doi.org/10.1016/j.crgsc.2022.100307.

[69] Executive Summary – Ammonia Technology Roadmap – Analysis - IEA. https://www.iea.org/reports/ammonia-technology-roadmap/executive-summary.

[70] D. Erdemir, I. Dincer, "A perspective on the use of ammonia as a clean fuel: Challenges and solutions", *Int. J. Energy Research* (2020). https://doi.org/10.1002/er.6232.

[71] C.D. Demirhan, W.W. Tso, J.B. Powell, E.N. Pistikopoulos, "Sustainable ammonia production through process synthesis and global optimization", *AIChE Journal* 65 (2019) e16498. https://doi.org/10.1002/aic.16498.

[72] A.I. Amhamed, S.S. Qarnain, S. Hewlett, A. Sodiq, Y. Abdellatif, R.J. Isaifan, O.F. Alrebei, "Ammonia Production Plants—A Review", *Fuels* 2022, Vol. 3, Pages 408-435 3 (2022) 408–435. https://doi.org/10.3390/fuels3030026.

[73] C. Smith, A.K. Hill, L. Torrente-Murciano, "Current and future role of Haber–Bosch ammonia in a carbon-free energy landscape", *Energy Environ. Sci.* 13 (2020) 331–344. https://doi.org/10.1039/c9ee02873k.

[74] M. Appl, "50th Anniversary of the IFA Technical Conference", Sevilla, Spain (1997), pp. 25-26

[75] M.L. Carreon, "Plasma catalytic ammonia synthesis: State of the art and future directions", *J. Phys. D Appl. Phys.* 52 (2019). https://doi.org/10.1088/1361-6463/ab3b2c.

[76] N. Erfani, L. Baharudin, M. Watson, "Recent advances and intensifications in Haber-Bosch ammonia synthesis process", *Chemical Engineering and Processing - Process Intensification* 204 (2024) 109962. https://doi.org/10.1016/j.cep.2024.109962.

[77] J.R. Venkat Pattabathula, "Introduction to Ammonia Production", (2016) 256.

[78] J. Humphreys, R. Lan, S. Tao, "Development and Recent Progress on Ammonia Synthesis Catalysts for Haber–Bosch Process", *Advanced Energy and Sustainability Research* 2 (2021) 2000043. https://doi.org/10.1002/aesr.202000043.

[79] N. Cherkasov, A.O. Ibhadon, P. Fitzpatrick, "A review of the existing and alternative methods for greener nitrogen fixation", *Chemical Engineering and Processing: Process Intensification* 90 (2015) 24–33. https://doi.org/10.1016/j.cep.2015.02.004.

[80] F. Rosowski, A. Hornung, O. Hinrichsen, D. Herein, M. Muhler, G. Ertl, "Ruthenium catalysts for ammonia synthesis at high pressures: Preparation, characterization, and power-law kinetics", *Applied Catalysis A* 151 (1997) 443–460. https://doi.org/10.1016/S0926-860X(96)00304-3.

[81] B. Lin, B. Fang, Y. Wu, C. Li, J. Ni, X. Wang, J. Lin, C.T. Au, L. Jiang, "Enhanced Ammonia Synthesis Activity of Ceria-Supported Ruthenium Catalysts Induced by CO Activation", *ACS Catal.* 11 (2021) 1331–1339. https://doi.org/10.1021/acscatal.0c05074.

[82] I. Rossetti, N. Pernicone, F. Ferrero, L. Forni, "Kinetic Study of Ammonia Synthesis on a Promoted Ru/C Catalyst", *Ind. Eng. Chem. Res.* 45 (2006) 4150–4155. https://doi.org/10.1021/ie051398g.

[83] M. Kitano, S. Kanbara, Y. Inoue, N. Kuganathan, P. V. Sushko, T. Yokoyama, M. Hara, H. Hosono, "Electride support boosts nitrogen dissociation over ruthenium catalyst and shifts the bottleneck in ammonia synthesis", *Nature Communications* 2015 6:1 6 (2015) 6731-. https://doi.org/10.1038/ncomms7731.

[84] N. Saadatjou, A. Jafari, S. Sahebdelfar, "Ruthenium Nanocatalysts for Ammonia Synthesis: A Review", *Chem. Eng. Commun.* 202 (2015) 420–448. https://doi.org/10.1080/00986445.2014.923995.

[85] H. Fang, D. Liu, Y. Luo, Y. Zhou, S. Liang, X. Wang, B. Lin, L. Jiang, "Challenges and Opportunities of Ru-Based Catalysts toward the Synthesis and Utilization of Ammonia", *ACS Catal.* 12 (2022) 3938–3954. https://doi.org/10.1021/acscatal.2c00090.

[86] R. Javaid, T. Nanba, "Stability of Cs/Ru/MgO Catalyst for Ammonia Synthesis as a Hydrogen and Energy Carrier", *Energies* 2022, Vol. 15, 15 (2022). https://doi.org/10.3390/en15103506.

[87] X. Chen, Y. Zhou, Z. Jia, X. Yuan, L. Fu, L. Liu, Y. Chen, Y. Wu, "Recent progress towards advanced catalysts for efficient thermocatalytic ammonia synthesis", *J. Power Sources* 670 (2026) 239490. https://doi.org/10.1016/j.jpowsour.2026.239490.

[88] D.E. Brown, T. Edmonds, R.W. Joyner, J.J. McCarroll, S.R. Tennison, The Genesis and Development of the Commercial BP Doubly Promoted Catalyst for Ammonia Synthesis, Catalysis Letters 2014 144:4 144 (2014) 545–552. https://doi.org/10.1007/s10562-014-1226-4.

[89] V.S. Marakatti, E.M. Gaigneaux, "Recent Advances in Heterogeneous Catalysis for Ammonia Synthesis", *Chem Cat Chem* 12 (2020) 5838–5857.

https://doi.org/10.1002/cctc.202001141.

[90] L. Eckendörfer, D. Rudolf, A. Brix, M. Börnhorst, H. Freund, "Periodic Open Cellular Structures in Chemical Engineering: Application in Catalysis and Separation Processes", *Annu. Rev. Chem. Biomol. Eng.* 15 (2024) 163–186. https://doi.org/10.1146/annurev-chembioeng-101121-085630.

[91] M. Iwaniszyn, "Periodic Open Cellular Structures (POCS) as Catalyst Supports—A Review", *Energies* 2022, Vol. 15, 15 (2022). https://doi.org/10.3390/en15207703.

[92] C. Ferroni, M. Bracconi, M. Ambrosetti, M. Maestri, G. Groppi, E. Tronconi, "A Fundamental Investigation of Gas/Solid Heat and Mass Transfer in Structured Catalysts Based on Periodic Open Cellular Structures (POCS)", *Ind. Eng. Chem. Res.* 60 (2021) 10522–10538. https://doi.org/10.1021/acs.iecr.1c00215.

[93] E. Bianchi, W. Schwieger, H. Freund, "Assessment of Periodic Open Cellular Structures for Enhanced Heat Conduction in Catalytic Fixed-Bed Reactors", *Adv. Eng. Mater.* 18 (2016) 608–614. https://doi.org/10.1002/adem.201500356.

[94] C. Ferroni, F.S. Franchi, M. Ambrosetti, M. Bracconi, G. Groppi, M. Maestri, E. Tronconi, "Numerical and Experimental Investigation of Pressure Drop in Periodic Open Cellular Structures for Intensification of Catalytic Processes", *ACS Engineering Au* (2022). https://doi.org/10.1021/ACSENGINEERINGAU.1C00034.

[95] C. Sinn, J. Wentrup, G.R. Pesch, J. Thöming, L. Kiewidt, "Structure-heat transport analysis of periodic open-cell foams to be used as catalyst carriers", *Chemical Engineering Research and Design* 166 (2021) 209–219. https://doi.org/10.1016/j.cherd.2020.12.007.

[96] C. Busse, H. Freund, W. Schwieger, "Periodic open cellular structures (POCS) as catalyst support for intensified heat transport in the partial oxidation of methanol to formaldehyde", *Chemical Engineering Journal* 489 (2024) 151139. https://doi.org/10.1016/j.cej.2024.151139.

[97] C. Italiano, G. Marino, M. Thomas, B. Hary, S. Nardone, S. Richard, A. Saker, D. Tasso, N. Meynet, P. Olivier, F. Gallucci, A. Vita, "Combined dip/spin coating deposition of Ni/CeO2 and Ni/CeO2-Al2O3 onto 3D printed AlSi10Mg Periodic Open Cellular Structures (POCS)", *Applied Surface Science AdvanceS* 27 (2025) 100731. https://doi.org/10.1016/j.apsadv.2025.100731.

[98] C. Italiano, G. Marino, M. Thomas, B. Hary, S. Nardone, S. Richard, A. Saker, D. Tasso, N. Meynet, P. Olivier, F. Gallucci, A. Vita, "Carbon-Free H2 Production from Ammonia Decomposition over 3D-Printed Ni-Alloy Structures Activated with a Ru/Al2O3 Catalyst", *Processes* 2024, Vol. 12, 12 (2024). https://doi.org/10.3390/pr12122663.

[99] S. Richard, D. Tasso, M. Rajana, A. Saker, N. Meynet, B. Hary, S. Nardone, G. Marino, C. Italiano, A. Vita, F. Gallucci, "Modelling the feasibility of membrane integration into periodic open cellular structures for ammonia decomposition", *Chemical Engineering Journal* 521 (2025) 166903.

https://doi.org/10.1016/j.cej.2025.166903.

[100] L. Fratalocchi, G. Groppi, C.G. Visconti, L. Lietti, E. Tronconi, "Adoption of 3D printed highly conductive periodic open cellular structures as an effective solution to enhance the heat transfer performances of compact Fischer-Tropsch fixed-bed reactors", *Chemical Engineering Journal* 386 (2020). https://doi.org/10.1016/j.cej.2019.123988.

[101] Y. Wu, M. Zhang, Z. Zhao, W. Song, J. Yan, J. Wen, A. Mahmood Ali, X. Ge, H. Zhang, "Recent Progress and Future Outlook on Catalysts for Ammonia Electrosynthesis: Materials, Structural Design, and Reaction Efficiency", *Energy & Fuels* 39 (2025) 1507–1540. https://doi.org/10.1021/acs.energyfuels.4c05425.

[102] K.H.R. Rouwenhorst, P. M. Krzywda, N. E. Benes, G. Mul, L. Lefferts, "Ammonia Production Technologies", (2021). https://doi.org/10.1016/B978-0-12-820560-0.00004-7.

[103] K.H.R. Rouwenhorst, Y. Engelmann, K. Van 'T Veer, R.S. Postma, A. Bogaerts, L. Lefferts, "Plasma-driven catalysis: Green ammonia synthesis with intermittent electricity", *Green Chemistry* Vol. 22, 19 (2020) 6258–6287. https://doi.org/10.1039/d0gc02058c.

[104] X. Cui, C. Tang, Q. Zhang, "A Review of Electrocatalytic Reduction of Dinitrogen to Ammonia under Ambient Conditions", *Advanced energy Materials* Vol. 8, (2018). https://doi.org/10.1002/aenm.201800369.

[105] M.J. Palys, A. McCormick, E.L. Cussler, P. Daoutidis, "Modeling and Optimal Design of Absorbent Enhanced Ammonia Synthesis", *Processes*, Vol. 6, 6 (2018). https://doi.org/10.3390/PR6070091.

[106] A. Tripodi, F. Conte, I. Rossetti, "Process Intensification for Ammonia Synthesis in Multibed Reactors with Fe-Wustite and Ru/C Catalysts", *Ind. Eng. Chem. Res.* Vol. 60 (2021) 908–915. https://doi.org/10.1021/acs.iecr.0c05350.

[107] A. Valera-Medina, R. Banares-Alcantara, "Techno-economic challenges of green ammonia as energy vector", (2021).

[108] E. Spatolisano, D. Figini, "Absorption-enhanced Haber-Bosch for small-scale green NH3 production. A feasibility study", *Energy Conversion and Management* Vol. 337 (2025). https://doi.org/10.1016/j.enconman.2025.119904.

[109] M. Wang, M. Khan, I. Mohsin, Md. G. Kibria, J. Wicks, A. H. Ip, K. Z. Sumon, C. T. Dihn, E. H. Sargent, I. D. Gates, "Can sustainable ammonia synthesis pathways compete with fossil-fuel based Haber–Bosch processes? -, *Energy Environ. Sci.* (n.d.). https://doi.org/DOI:10.1039/D0EE03808C.

[110] Why is the transition away from fossil raw materials not happening faster? | Neste.

[111] V. Cechetto, L. Di Felice, R. G. Martinez, A. A. Plazaola, F. Gallucci, Ultra-pure hydrogen production via ammonia decomposition in a catalytic membrane reactor, Int. J. Hydrogen Energy 47 (2022) 21220–21230.

https://doi.org/10.1016/j.ijhydene.2022.04.240.

[112] M.A. Habib, A. Harale, S. Paglieri, F.S. Alrashed, A. Al-Sayoud, M.V. Rao, M.A. Nemitallah, S. Hossain, M. Hussien, A. Ali, M.A. Haque, A. Abuelyamen, M.R. Shakeel, E.M.A. Mokheimer, R. Ben-Mansour, "Palladium-Alloy Membrane Reactors for Fuel Reforming and Hydrogen Production: A Review", *Energy & Fuels* 35 (2021) 5558–5593. https://doi.org/10.1021/acs.energyfuels.0c04352.

[113] F. Dalena, A. Senatore, M. Basile, S. Knani, A. Basile, A. Iulianelli, "Advances in Methanol Production and Utilization, with Particular Emphasis toward Hydrogen Generation via Membrane Reactor Technology", *Membranes* 2018, Vol. 8, 8 (2018). https://doi.org/10.3390/membranes8040098.

[114] A. Iulianelli, S. Liguori, J. Wilcox, A. Basile, "Advances on methane steam reforming to produce hydrogen through membrane reactors technology: A review", *Catal. Rev. Sci. Eng.* 58 (2016) 1–35. https://doi.org/10.1080/01614940.2015.1099882.

[115] A. Iulianelli, C. Pirola, A. Comazzi, F. Galli, F. Manenti, A. Basile, "Water gas shift membrane reactors", *Membrane Reactors for Energy Applications and Basic Chemical Production* (2015) 3–29. https://doi.org/10.1016/B978-1-78242-223-5.00001-7.

[116] F. Gallucci, S. Poto, M.A.L. Tanco, D.A.P. Tanaka, "Production of Methanol by CO2 Hydrogenation Using a Membrane Reactor", *Catalysts* 2026, Vol. 16, 16 (2026) 53. https://doi.org/10.3390/catal16010053.

[117] M. De Falco, A. Basile, "Mathematical modelling of membrane reactors: overview of strategies and applications for the modelling of a hydrogen-selective membrane reactor", Handbook of Membrane Reactors 1 (2013) 435–463. https://doi.org/10.1533/9780857097330.3.435.

[118] Y. Feng, Y. Ling, Y. Wang, P. Li, R. Xiao, G. Yang, T. Li, "Membrane reactors for sustainable production of fuels and value-added chemicals: Innovations, challenges and future directions", *Renewable and Sustainable Energy Reviews* 219 (2025) 115846. https://doi.org/10.1016/j.rser.2025.115846.

[119] S. Hafeez, S.M. Al-Salem, G. Manos, A. Constantinou, "Fuel production using membrane reactors: a review", *Environmental Chemistry Letters* 5 18 (2020) 1477–1490. https://doi.org/10.1007/s10311-020-01024-7.

[120] R. Dittmeyer, J. Caro, "Catalytic Membrane Reactors", Handbook of Heterogeneous Catalysis (2008) 2198–2248. https://doi.org/10.1002/9783527610044.hetcat0117.

[121] J. Caro, "Chemical Membrane Reactors", *Chem. Ing. Tech.* 96 (2024) 1537–1544. https://doi.org/10.1002/cite.202400033.

[122] E. Drioli, E. Fontananova, "Membrane Reactors", Ullmann's Encyclopedia of Industrial Chemistry (2010). https://doi.org/10.1002/14356007.d16_d01.pub2.

[123] R.Y. Chein, Y.C. Chen, J.N. Chung, "Sweep gas flow effect on membrane reactor performance for hydrogen production from high-temperature water-gas shift reaction", *J. Memb. Sci.* 475 (2015) 193–203.

https://doi.org/10.1016/j.memsci.2014.09.046.

[124] Z. Zhang, J.D. Way, C.A. Wolden, "Design and operational considerations of catalytic membrane reactors for ammonia synthesis", *AIChE Journal* 67 (2021) e17259. https://doi.org/10.1002/aic.17259.

[125] L. Ye, H. Li, K. Xie, "Sustainable ammonia production enabled by membrane reactor", *Nature Sustainability* 2022 5:9 5 (2022) 787–794. https://doi.org/10.1038/s41893-022-00908-6.

[126] G. Chehade, I. Dincer, "A modular membrane reactor concept for intensified ammonia synthesis", *Chemical Engineering Journal* 519 (2025) 165119. https://doi.org/10.1016/j.cej.2025.165119.

[127] E. Kucuk, H. Hasan Koybasi, A.K. Avci, "Beyond equilibrium ammonia synthesis in a membrane and heat exchange integrated microreactor: A modeling study", *Fuel* 357 (2024) 129858. https://doi.org/10.1016/j.fuel.2023.129858.

[128] K. Wakimoto, W.W. Yan, M. Hattori, M. Hara, N. Moriyama, H. Nagasawa, M. Kanezashi, T. Tsuru, "Green ammonia production via recycle membrane reactor: Experiment and process simulation", *Chemical Engineering Journal* 496 (2024) 153754. https://doi.org/10.1016/j.cej.2024.153754.

[129] W.W. Yan, N. Moriyama, H. Nagasawa, M. Kanezashi, T. Tsuru, "Green ammonia production via a catalytic membrane reactor: Proof of concept through experiments and simulations", *AIChE Journal* 71 (2025) e18863. https://doi.org/10.1002/aic.18863.

[130] A.E.M. Adris, J.R. Grace, "Characteristics of Fluidized-Bed Membrane Reactors: Scale-up and Practical Issues", *Ind. Eng. Chem. Res.* 36 (1997) 4549–4556. https://doi.org/10.1021/ie970108w.

[131] M.A. Abd El-Ghaffar, H.A. Tieama, "A Review of Membranes Classifications, Configurations, Surface Modifications, Characteristics and Its Applications in Water Purification", *Chemical and Biomolecular Engineering* 2 (2017) 57–82. https://doi.org/10.11648/j.cbe.20170202.11.

[132] I.F.J. Vankelecom, "Polymeric Membranes in Catalytic Reactors", *Chem. Rev.* 102 (2002) 3779–3810. https://doi.org/10.1021/cr0103468.

[133] F. Gallucci, A. Basile, F. Hai, "Introduction - A review of membrane reactors", Membranes for Membrane Reactors: Preparation, Optimization and Selection (2011). https://doi.org/10.1002/9780470977569.ch

[134] R. Xu, L. He, L. Li, M. Hou, Y. Wang, B. Zhang, C. Liang, T. Wang, "Ultraselective carbon molecular sieve membrane for hydrogen purification", J*ournal of Energy Chemistry* 50 (2020) 16–24. https://doi.org/10.1016/j.jechem.2020.03.008.

[135] P.S. Tin, Y. Xiao, T.S. Chung, "Polyimide-carbonized membranes for gas separation: Structural, composition, and morphological control of precursors", *Separation and Purification Reviews* 35 (2006) 285–318.

https://doi.org/10.1080/15422110601003481.

[136] Y. Xiao, T.S. Chung, M.L. Chng, S. Tamai, A. Yamaguchi, "Structure and Properties Relationships for Aromatic Polyimides and Their Derived Carbon Membranes: Experimental and Simulation Approaches", *Journal of Physical Chemistry B* 109 (2005) 18741–18748. https://doi.org/10.1021/jp050177l.

[137] M.G. Sedigh, L. Xu, T.T. Tsotsis, M. Sahimi, "Transport and Morphological Characteristics of Polyetherimide-Based Carbon Molecular Sieve Membranes", *Ind. Eng. Chem. Res.* 38 (1999) 3367–3380. https://doi.org/10.1021/ie9806592.

[138] M.G. Sedigh, M. Jahangiri, P.K.T. Liu, M. Sahimi, T.T. Tsotsis, "Structural characterization of polyetherimide-based carbon molecular sieve membranes", *AIChE Journal* 46 (2000) 2245–2255. https://doi.org/10.1002/aic.690461116.

[139] M. Teixeira, M.C. Campo, D.A. Pacheco Tanaka, M.A. Llosa Tanco, C. Magen, A. Mendes, "Composite phenolic resin-based carbon molecular sieve membranes for gas separation", *Carbon N. Y.* 49 (2011) 4348–4358. https://doi.org/10.1016/j.carbon.2011.06.012.

[140] T.A. Centeno, A.B. Fuertes, "Supported carbon molecular sieve membranes based on a phenolic resin", *J. Memb. Sci.* 160 (1999) 201–211. https://doi.org/10.1016/S0376-7388(99)00083-6.

[141] T.A. Centeno, J.L. Vilas, A.B. Fuertes, "Effects of phenolic resin pyrolysis conditions on carbon membrane performance for gas separation", *J. Memb. Sci.* 228 (2004) 45–54. https://doi.org/10.1016/j.memsci.2003.09.010.

[142] W.N.W. Salleh, A.F. Ismail, T. Matsuura, M.S. Abdullah, "Precursor selection and process conditions in the preparation of carbon membrane for gas separation: A review", *Separation and Purification Reviews* 40 (2011) 261–311. https://doi.org/10.1080/15422119.2011.555648.

[143] K. Briceño, A. Iulianelli, D. Montané, R. Garcia-Valls, A. Basile, "Carbon molecular sieve membranes supported on non-modified ceramic tubes for hydrogen separation in membrane reactors", *Int. J. Hydrogen Energy* 37 (2012) 13536–13544. https://doi.org/10.1016/j.ijhydene.2012.06.069.

[144] W.N.W. Salleh, A.F. Ismail, "Carbon membranes for gas separation processes: Recent progress and future perspective", *Journal of Membrane Science and Research* 1 (2015) 2–15.

[145] S.M. Saufi, A.F. Ismail, "Fabrication of carbon membranes for gas separation—a review", *Carbon N. Y.* 42 (2004) 241–259. https://doi.org/10.1016/j.carbon.2003.10.022.

[146] W. Wei, G. Qin, H. Hu, L. You, G. Chen, "Preparation of supported carbon molecular sieve membrane from novolac phenol–formaldehyde resin", *J. Memb. Sci.* 303 (2007) 80–85. https://doi.org/10.1016/j.memsci.2007.06.055.

[147] M.A. Llosa Tanco, D.A. Pacheco Tanaka, S.C. Rodrigues, M. Texeira, A. Mendes,

"Composite-alumina-carbon molecular sieve membranes prepared from novolac resin and boehmite. Part I: Preparation, characterization and gas permeation studies", *Int. J. Hydrogen Energy* 40 (2015) 5653–5663. https://doi.org/10.1016/j.ijhydene.2015.02.112.

[148] M.A. Llosa Tanco, D.A. Pacheco Tanaka, A. Mendes, "Composite-alumina-carbon molecular sieve membranes prepared from novolac resin and boehmite. Part II: Effect of the carbonization temperature on the gas permeation properties", *Int. J. Hydrogen Energy* 40 (2015) 3485–3496. https://doi.org/10.1016/j.ijhydene.2014.11.025.

[149] A. F. Ismail, D. Rana, T. Matsuura, H. C. Foley, "Carbon-based Membranes for Separation Processes".

[150] J.J. Li, W. Wei, Q. Lin, J.Y. Zhang, "Effects of Pyrolysis Temperature on the Properties of Phenol-Formaldehyde Resin Based Carbon Molecular Sieve Membrane", *Materials Science Forum* 848 (2016) 738–742. https://doi.org/10.4028/www.scientific.net/MSF.848.738.

[151] S.C. Rodrigues, R. Whitley, A. Mendes, "Preparation and characterization of carbon molecular sieve membranes based on resorcinol–formaldehyde resin", *J. Memb. Sci.* 459 (2014) 207–216. https://doi.org/10.1016/j.memsci.2014.02.013.

[152] X. Ma, B.K. Lin, X. Wei, J. Kniep, Y.S. Lin, "Gamma-Alumina Supported Carbon Molecular Sieve Membrane for Propylene/Propane Separation", *Ind. Eng. Chem. Res.* 52 (2013) 4297–4305. https://doi.org/10.1021/ie303188c.

[153] G. Genduso, W. Ogieglo, Y. Wang, I. Pinnau, "Carbon molecular sieve gas separation materials and membranes: A comprehensive review", *J. Memb. Sci.* 699 (2024). https://doi.org/10.1016/j.memsci.2024.122533.

[154] G. Yarema, J. Yang, A. Warty, Z. Liu, L. Hu, D. Liu, "Membrane Reactors for Ammonia Production: Insights into Ammonia-Separative Membranes, Synthesis Catalysts, and Their Integration", *ACS Nano* 19 (2025) 39535–39563. https://doi.org/10.1021/acsnano.5c12610.

[155] W.W. Yan, T. Tsuru, "Overview: Insight into NH3 permselective membranes and their application to a membrane reactor for efficient ammonia production", *Sep. Purif. Technol.* 370 (2025) 133275. https://doi.org/10.1016/J.SEPPUR.2025.133275.

[156] S. Padinjarekutt, H. Li, S. Ren, P. Ramesh, F. Zhou, S. Li, G. Belfort, M. Yu, "Na+-gated nanochannel membrane for highly selective ammonia (NH3) separation in the Haber-Bosch process", *Chemical Engineering Journal* 454 (2023) 139998. https://doi.org/10.1016/j.cej.2022.139998.

[157] R. Shindo, K. Nagai, "Gas Separation Membranes", Encyclopedia of Polymeric Nanomaterials (2013) 1–8. https://doi.org/10.1007/978-3-642-36199-9_134-1.

[158] S.T. Oyama, M. Yamada, T. Sugawara, A. Takagaki, R. Kikuchi, "Review on mechanisms of gas permeation through inorganic membranes", *Journal of the Japan Petroleum Institute* 54 (2011) 298–309. https://doi.org/10.1627/jpi.54.298.

[159] J.B.S. Hamm, A. Ambrosi, J.G. Griebeler, N.R. Marcilio, I.C. Tessaro, L.D. Pollo, "Recent advances in the development of supported carbon membranes for gas separation", *Int. J. Hydrogen Energy* 42 (2017) 24830–24845. https://doi.org/10.1016/j.ijhydene.2017.08.071.

[160] J.A. Medrano, M.A. Llosa-Tanco, D.A. Pacheco-Tanaka, F. Gallucci, "Transport Mechanism and Modeling of Microporous Carbon Membranes", *Current Trends and Future Developments on (Bio-) Membranes: Microporous Membranes and Membrane Reactors* 130 (2019) 39–58. https://doi.org/10.1016/B978-0-12-816350-4.00002-7.

[161] L. Forster, C. D'Agostino, M.A. Llosa-Tanco, V. Spallina, C. Brencio, F. Gallucci, M. Lindley, S.J. Haigh, D.A. Pacheco-Tanaka, "Tailoring pore structure and surface chemistry of microporous Alumina-Carbon Molecular Sieve Membranes (Al-CMSMs) by altering carbonization temperature for optimal gas separation performance: An investigation using low-field NMR relaxation measurements", *Chemical Engineering Journal* 424 (2021) 129313. https://doi.org/10.1016/j.cej.2021.129313.

[162] Z. Sahin, D. Emmery, A.R. Mamaghani, M. Gazzani, F. Gallucci, "Mass transport in carbon membranes", *Current Op. Chem. Eng.* (2023). https://doi.org/10.1016/j.coche.2022.100896.

[163] N. Kruse, Y. Schießer, N. Reger-Wagner, H. Richter, I. Voigt, G. Braun, J.U. Repke, "High pressure adsorption, permeation and swelling of carbon membranes – Measurements and modelling at up to 20 MPa", *J. Memb. Sci.* 544 (2017) 12–17. https://doi.org/10.1016/j.memsci.2017.09.004.

[164] M.G. Slin'ko, "History of the development of mathematical modeling of catalytic processes and reactors", *Theoretical Foundations of Chemical Engineering* 41 (2007) 13–29. https://doi.org/10.1134/S0040579507010022.

[165] L. Grazia, "Mathematical modeling of an integrated membrane reactor for steam reforming", *Int. J. Res. Eng. Technol.* 05 (2016).

[166] M.A. Murmura, S. Cerbelli, M.C. Annesini, "Modeling Fixed Bed Membrane Reactors for Hydrogen Production through Steam Reforming Reactions: A Critical Analysis", *Membranes* 2018, Vol. 8, 8 (2018). https://doi.org/10.3390/membranes8020034.

[167] G. Di Marcoberardino, F. Sosio, G. Manzolini, S. Campanari, "Fixed bed membrane reactor for hydrogen production from steam methane reforming: Experimental and modeling approach", *Int. J. Hydrogen Energy* 40 (2015) 7559–7567. https://doi.org/10.1016/j.ijhydene.2014.11.045.

[168] D. Mendes, S. Sá, S. Tosti, J.M. Sousa, L.M. Madeira, A. Mendes, "Experimental and modeling studies on the low-temperature water-gas shift reaction in a dense Pd-Ag packed-bed membrane reactor", *Chem. Eng. Sci.* 66 (2011) 2356–2367. https://doi.org/10.1016/j.ces.2011.02.035.

[169] T.P. Tiemersma, C.S. Patil, M. Van Sint Annaland, J.A.M. Kuipers, "Modelling of

packed bed membrane reactors for autothermal production of ultrapure hydrogen", *Chem. Eng. Sci.* 61 (2006) 1602–1616. https://doi.org/10.1016/j.ces.2005.10.004.

[170] C. Fukuhara, A. Igarashi, "Two-dimensional simulation of a membrane reactor for dehydrogenation of ethylbenzene, considering heat and mass transfer", *Journal of Chemical Engineering of Japan* 36 (2003) 530–539. https://doi.org/10.1252/jcej.36.530.

[171] M.A. Murmura, S. Cerbelli, L. Manozzi, M.C. Annesini, "Toward Minimal Complexity Models of Membrane Reactors for Hydrogen Production", *Membranes* 2022, Vol. 12, 12 (2022). https://doi.org/10.3390/MEMBRANES12111115.

[172] Y. Yu, Z. Bian, W. Tan, Q. Zhong, "CFD modelling and simulation of a zeolite catalytic membrane reactor for low temperature water-gas shift reaction", *Chemical Engineering and Processing - Process Intensification* 178 (2022). https://doi.org/10.1016/j.cep.2022.108994.

[173] M.S. Salehi, M. Askarishahi, H.R. Godini, O. Görke, G. Wozny, "Sustainable Process Design for Oxidative Coupling of Methane (OCM): Comprehensive Reactor Engineering via Computational Fluid Dynamics (CFD) Analysis of OCM Packed-Bed Membrane Reactors", *Ind. Eng. Chem. Res.* 55 (2016) 3287–3299. https://doi.org/10.1021/acs.iecr.5b03292.

[174] A. H. Kassi, T.A. Al-Hattab, "A Review: Membrane Reactor for Hydrogen Production: Modeling and Simulation, *Engineering Chemistry* (2023). https://doi.org/10.4028/p-XakNe1.

[175] A. C. Faria, C. V. Miguel, A.E. Rodrigues, L.M. Madeira, "Modeling and Simulation of a Steam-Selective Membrane Reactor for Enhanced CO2 Methanation", *Ind. Eng. Chem. Res.* 59 (2020) 16170–16184. https://doi.org/10.1021/acs.iecr.0c02860.

[176] J. Zhu, X. Cui, S.S. Araya, "Comparison between 1D and 2D numerical models of a multi-tubular packed-bed reactor for methanol steam reforming", *Int. J. Hydrogen Energy* 47 (2022) 22704–22719. https://doi.org/10.1016/j.ijhydene.2022.05.109.

[177] S.T.B. Lundin, W.J. Movick, A. Ikeda, Y. Hasegawa, C.A. Wolden, J.D. Way, "Modeling of an ammonia decomposition membrane reactor including purity with complex geometry and non-isothermal behavior", *J. Memb. Sci.* 693 (2024). https://doi.org/10.1016/j.memsci.2023.122345.

[178] Y. Nalbant Atak, C.O. Colpan, A. Iulianelli, "A review on mathematical modeling of packed bed membrane reactors for hydrogen production from methane", *Int. J. Energy Res.* 45 (2021) 20601–20633. https://doi.org/10.1002/er.7186

CHAPTER 2

Modelling of a packed bed membrane reactor for ammonia synthesis: on the role of membrane performance and operating conditions

ABSTRACT:
This chapter presents the development of a non-isothermal 1D packed bed membrane reactor (PBMR) model for ammonia synthesis over a ruthenium-based catalyst, coupled with in-situ ammonia separation using NH_3-selective membranes. The kinetic model was first validated against experimental data obtained from a conventional packed bed reactor and subsequently applied to evaluate the feasibility and performance of the membrane-assisted configuration. The study focuses on identifying the membrane properties required to enhance reactor efficiency in terms of H_2 conversion, NH_3 purity, and NH_3 recovery.
Under isothermal conditions, the results indicate that a membrane permeance $\mathcal{P}_{NH_3}$ > 10^{-7} mol·Pa^{-1}m^{-2}s^{-1} and a selectivity S_{NH_3/H_2} = 50 are required to significantly boost H_2 conversion. On the other hand, a selectivity S_{NH_3/N_2} = 100 was selected as a trade-off value influencing NH_3 purity and NH_3 recovery. Parametric analysis further reveals that both the sweep-gas-to-feed flow ratio (SW) and the transmembrane pressure difference (ΔP) strongly influence reactor performance, with optimal conditions identified at a sweep-gas-to-feed flow ratio SW = 6 and ΔP = 20 bar. In the adiabatic case, the integration of heat exchange between the feed and sweep streams was investigated, highlighting the role of the sweep gas as an effective cooling medium. Optimal performance was achieved at a permeate inlet temperature of 200 °C, resulting in a H_2 conversion of 93.0%, NH_3 recovery of 99.2%, and NH_3 purity of 5.7%. Overall, the model demonstrates that an adiabatic packed bed membrane reactor with integrated heat management can surpass the equilibrium limitations of conventional packed bed reactors, offering a promising route for intensified ammonia synthesis.

This chapter is based on the following journal article:
"Modelling of a packed bed membrane reactor for ammonia synthesis: on the role of membrane performance and operating conditions", **I. Gargiulo**, G. Anello, S. Richard, F. Gallucci, *Int. J. Hydrogen Energy*, 2025.

2.1 INTRODUCTION

This chapter focuses on the development and analysis of a one-dimensional membrane reactor model for ammonia synthesis. Several studies have explored the potential of membrane reactors for ammonia synthesis under different configurations and assumptions. For instance, Zhang et al. investigated an isothermal packed bed membrane reactor employing conventional iron-based catalysts, highlighting the importance of membrane selectivity for process intensification. Their results indicated that an ammonia-to-nitrogen selectivity higher than 10 and an ammonia-to-hydrogen selectivity higher than 4 are required to achieve meaningful performance improvements. However, the effects of reaction heat were not considered, despite the strongly exothermic nature of ammonia synthesis and its implications for reactor performance and membrane stability. The heat released by the reaction can therefore influence the system both kinetically and thermodynamically, as well as the stability and selectivity of the membrane [1]. More recently, Kucuk et al. modelled a structured microreactor, whose channels were coated with iron-based catalyst, with heat exchange and membrane ($ZnCl_2$ immobilised molten-salt) separation integrated. The proposed system achieved a 47% N_2 conversion, surpassing the corresponding equilibrium conversion of the conventional system (40%); thus the reported results support the possibility of overcoming the thermodynamic limits in the conventional Haber-Bosch process [2]. Building on these insights, this chapter presents a non-isothermal, one-dimensional model of a packed bed membrane reactor for ammonia synthesis, aimed at identifying the minimum membrane specifications in terms of ammonia membrane permeance and perm-selectivity, required for improved reactor performance. A subsequent parametric study then evaluates the effect of key operating conditions, including temperature, pressure, and sweep-gas-to-feed flow ratio, on reactor performance. The overall objective is to demonstrate the feasibility of membrane-assisted ammonia synthesis under milder operating conditions, and to establish a benchmark for future membrane technology development.

2.2 REACTOR CONFIGURATION AND REACTION KINETICS

2.2.1 Packed bed membrane reactor configuration

The membrane reactor design proposed in this chapter is illustrated in **Figure 2.1**, consisting of a shell-and-tube configuration. The inner tube represents a tubular membrane (or membrane bundle), while catalyst particles occupy the shell side. This configuration establishes two distinct zones: the retentate side, where the feed is introduced and the reaction proceeds along the reactor length, and the permeate side, where gases selectively permeate across the membrane.

Unlike the inert sweep gas configuration introduced in Chapter 1, in this model the permeate side is swept with a stream containing H_2 and N_2 rather than an inert carrier such as Ar. This choice reflects the operating conditions of a decentralised ammonia plant, where unreacted feed or recycled synthesis-loop gas is more readily available on-site than a dedicated inert diluent. Moreover, the H_2 and N_2-rich sweep lowers the ammonia partial pressure on the permeate side, maintaining a large transmembrane driving force for ammonia removal and thereby shifting the synthesis equilibrium toward higher conversion. At the same time, the elevated H_2 and N_2 partial pressures on the permeate side reduce the driving force for their own permeation, limiting reactant loss through the membrane while keeping the permeate composition compatible with recycle.

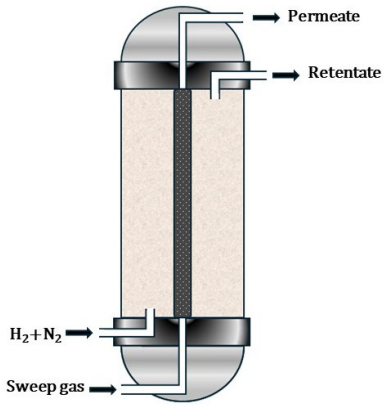


Figure 2.1 Schematic of a packed bed membrane reactor with retentate and permeate streams

The sweep gas H_2:N_2 molar ratio and its flow rate relative to the fresh feed, expressed as the sweep-gas-to-feed flow ratio (SW), are initially set equal to those of the retentate feed. Once the required membrane performance has been established (Section 2.4.3), both the composition and SW are treated as independent operating variables and are varied systematically in the parametric study of Section 2.4.6. Because the sweep gas is injected on the permeate side, it unavoidably dilutes the permeated ammonia. A co-current arrangement between the feed and the sweep gas was adopted throughout this study, selected primarily to manage the strongly exothermic nature of ammonia synthesis. In this configuration, the coolest sweep gas enters alongside the fresh feed at the point of highest reaction rate and heat release, moderating the peak reactor temperature and yielding a smoother axial thermal profile than a counter-current arrangement, where the coldest sweep would instead act at the reactor outlet rather than the high-heat-release inlet zone.

2.2.2 Ammonia synthesis reaction and kinetic model

The kinetic model of the ammonia synthesis reaction was obtained from a previous

study by Rossetti et al. that utilised a Ru/C catalyst [3].

Table 2.1 Equations utilised to determine parameters in the kinetic expression of Rossetti et al. [3]

Parameter	Units	Equations
k_f	mol·$L_{cat}^{-1}h^{-1}$	$9.02 \cdot 10^8 exp(\frac{-23.0}{RT})$
K_a	-	$exp\left(-2.691122\, log_{10}T - 5.519265 \cdot 10^{-5}T + 1.848863 \cdot 10^{-7}T^2 + \frac{2001.6}{T} + 2.6899\right)$
a_{N_2}	atm	$\frac{1-\eta\,\beta(q)}{1+q-2\,\eta\,\beta(q)} P\,\gamma_{N_2}$
a_{H_2}	atm	$\frac{q-3\,\eta\,\beta(q)}{1+q-2\,\eta\,\beta(q)} P\,\gamma_{H_2}$
a_{NH_3}	atm	$\frac{2\,\eta\,\beta(q)}{1+q-2\,\eta\,\beta(q)} P\,\gamma_{NH_3}$
η	-	$a(\frac{y}{1+y})$
γ_{N_2}	-	$0.93431737 + 0.3101804 \cdot 10^{-3}T + 0.295896 \cdot 10^{-3}P - 0.2707279 \cdot 10^{-6}T^2 + 0.4775207 \cdot 10^{-6}P^2$
γ_{H_2}	-	$exp\Big[exp(-3.8402T^{0.125} + 0.541)\,P - exp(-0.1263T^{0.5} - 15.98)\,P^2 + 300\,exp(-0.011901T - 5.941)\left(exp\left(-\frac{P}{300}\right) - 1\right)\Big]$
γ_{NH_3}	-	$0.1438996 + 0.2028538 \cdot 10^{-2}T - 0.4487672 \cdot 10^{-3}P - 0.1142945 \cdot 10^{-5}T^2 + 0.2761216 \cdot 10^{-6}P^2$
K_{H_2}	-	$exp\left(\frac{-56.9024}{R} + \frac{37656}{RT}\right)$
K_{NH_3}	-	$exp\left(\frac{-34.7272}{R} + \frac{29228}{RT}\right)$

The overall structure of the reaction rate is derived from the classical Temkin equation, incorporating an additional adsorption term, as expressed in Equation (2.1).

$$\frac{d\eta}{d\tau} = k_f \lambda(q) \frac{(a_{N_2})^{0.5}\left[\frac{(a_{H_2})^{0.375}}{(a_{NH_3})^{0.25}}\right] - \frac{1}{Ka}\left[\frac{(a_{NH_3})^{0.75}}{(a_{H_2})^{1.125}}\right]}{1 + K_{H_2}(a_{H_2})^{0.3} + K_{NH_3}(a_{NH_3})^{0.2}} \tag{2.1}$$

where $\frac{d\eta}{d\tau}$ expresses the reaction rate of the limiting reactant in mol·L_{cat}^{-1} h^{-1}, a_i are the partial activities of the involved species, K_a is the reaction equilibrium constant, K_{H_2} and K_{NH_3} are the adsorption equilibrium constants of hydrogen and ammonia respectively, q is the H_2:N_2 molar feed ratio. Therefore $\lambda(q)$ was set to 1 when H_2:N_2 = 3 and to 3 when H_2:N_2 = 1.5.

The aforementioned parameters are determined according to the equations shown in **Table 2.1**, where $\beta(q) = 1$ if $q = 3$, $\beta(q) = 0.5$ if $q = 1.5$. η is the fractional conversion depending on y, which is the outlet mole fraction of NH_3; the parameter a is set to 2 if $q = 3$ and 2.5 if $q = 1.5$.

2.3 MATHEMATICAL FORMULATION OF THE REACTOR MODEL

The packed bed membrane reactor was described using a one-dimensional, steady-state, pseudo-homogeneous model. The key modelling assumptions are summarised below:

- Plug flow behaviour is assumed, with negligible radial gradients in both concentration and temperature, assuring $\frac{D/2}{L} \ll Re \cdot Sc \ll \frac{L}{D/2}$
- Steady-state conditions
- Negligible pressure drops on the permeate side
- The membrane material is considered inert
- Pseudo-homogeneous reactor description (no separate solid- and gas-phase balances)
- Negligible intra-particle and external mass- and heat-transport limitations inside and around the catalyst pellets
- No catalytic activity on the permeate side

As expected, these assumptions inherently introduce certain limitations. For example, the pseudo-homogeneous model assumes constant catalyst properties and neglects any radial gradients. To minimise the impact of these simplifications, as noted in Section 2.4.1, the study was conducted using a small-scale reactor. Moreover, assuming steady-state conditions neglects the possibility of accounting for possible fluctuations in concentrations, temperature, and pressure. In membrane-assisted systems, such variations would also lead to fluctuations in partial pressure and concentration gradients, thereby reducing permeate flux and overall separation efficiency. These limitations are acceptable for the scope of this chapter, which focuses on identifying membrane performance targets and optimal operating conditions for a laboratory-scale reactor. The implications for larger-scale systems are addressed in Chapter 5 through a two-dimensional description that includes radial diffusion and concentration polarisation.

The 1D model consists of coupled mass, energy, and momentum balances for the retentate and permeate sides, together with constitutive equations for reaction rate, membrane permeation and heat transfer. The resulting system of ordinary differential equations (ODEs) was solved in *MATLAB R2022a* using the *ode15s* solver, together with algebraic equations for reaction kinetics and temperature-

dependent gas properties.

Governing equations:

For each gas component i (H_2,N_2,NH_3), the molar flow rates along the reactor length L on the retentate (F_i^R) and permeate (F_i^P) sides are described by Equations (2.2)-(2.3):

$$\frac{dF_i^R}{dL} = \vartheta_i\,(r_i)\,\rho_c\,(1-\varepsilon)\,\frac{\pi}{4}\left(D_r^{i\,2} - D_m^{O\,2}\right) - J_i\,(\pi\,D_m^O) \tag{2.2}$$

$$\frac{dF_i^P}{dL} = J_i\,(\pi\,D_m^O) \tag{2.3}$$

where ϑ_i is the stoichiometric coefficient of component i, r is the ammonia synthesis reaction rate (mol·L_{cat}^{-1} h^{-1}), ρ_c is the catalyst bed density, ε is the bed porosity, D_r^i and D_m^O are the inner reactor diameter and outer membrane diameter, respectively, and J_i is the transmembrane molar flux of component i.

The flux through the membrane is expressed as a pressure-driven process:

$$J_i = \mathcal{P}_i\,(P_i^R - P_i^P) \tag{2.4}$$

where $\mathcal{P}_i$ is the permeance of component i and P_i^R and P_i^P are the partial pressures on the retentate and permeate sides, respectively. The pressure difference is defined as positive when the flow proceeds from the retentate to the permeate side. This convention ensures that a positive flux corresponds to net transport of component i from the reaction zone towards the permeate. With this definition, the results of this study are representative of all pressure-driven membrane separations that could be applied for in-situ NH_3 recovery in the reactor. At the same time, the functional form of Equation (2.4) - in particular the dependence of permeance on temperature, pressure, and composition - is membrane-specific and reflects the underlying transport mechanism (e.g. molecular sieving, surface diffusion, Knudsen diffusion, or solution-diffusion). In this chapter, a simplified pressure-driven formulation with constant permeance is adopted as a first approximation, consistent with the experimental validation under non-reactive conditions at fixed temperature (Section 2.4.1). A more detailed, temperature- and composition-dependent description of the membrane flux for the carbon molecular sieve membranes is introduced in Chapter 3 and incorporated into the two-dimensional model of Chapter 5.

Similarly, energy balance equations are formulated for both the retentate and permeate sides:

$$\sum_i F_i^R\,Cp_i^R\,\frac{dT^R}{dL} = (r)\,(-\Delta H)_{T^R}\,\rho_c\,(1-\varepsilon)\,\frac{\pi}{4}\left(D_r^{i\,2} - D_m^{O\,2}\right) - U\,\pi\,D_m^i\,(T^R - T^P) \tag{2.5}$$

$$\sum_i F_i^P\,Cp_i^P\,\frac{dT^P}{dL} = U\,\pi\,D_m^i\,(T^R - T^P) \tag{2.6}$$

where T^R and T^P are the retentate and permeate temperatures, $C_{p,i}$ are the component heat capacities, ΔH is the reaction enthalpy, and U is the overall heat-transfer coefficient. The coefficient U accounts for convection on the permeate side, conduction through the membrane and support, and convection on the retentate side:

$$U = \left(\frac{1}{h^P} + \frac{\frac{D_m^i}{2\ln\left(\frac{D_m^o}{D_m^i}\right)}}{k} + \frac{D_m^i}{D_m^o}\frac{1}{h^R} \right)^{-1} \tag{2.7}$$

The heat transfer coefficient in the reaction zone (h^R) was calculated using the correlation proposed by Li and Finlayson for packed beds [4] (Equation (2.10)), based on the Reynolds and Prandtl numbers given in Equation (2.8)-(2.9):

$$Re^R = \frac{d_p G^R}{{\mu_{mix}}^R} \tag{2.8}$$

$$Pr^R = \frac{{\mu_{mix}}^R cp_{mix}^R}{\lambda_{mix}^R} \tag{2.9}$$

$$Nu^R = 0.17\, {Re^R}^{0.79} \left(\frac{{Pr}^R}{0.7}\right)^{1/3} = \frac{h^R\, d_p}{\lambda_{mix}^R} \tag{2.10}$$

For the permeate zone, the heat transfer coefficient (h^P) was calculated using the Dittus-Boelter correlation (Equation (2.13)), which considers a smooth concentric annulus [5]. In this case, Reynolds and Prandtl number, are given in Equation (2.11)-(2.12):

$$Re^P = \frac{D_m^i G^P}{{\mu_{mix}}^P} \tag{2.11}$$

$$Pr^P = \frac{{\mu_{mix}}^P cp_{mix}^P}{\lambda_{mix}^P} \tag{2.12}$$

$$Nu^P = 0.023\, {Re^P}^{0.8}\, {Pr^P}^{0.4} = \frac{h^P\, D_m^i}{\lambda_{mix}^P} \tag{2.13}$$

The mass fluxes G^R and G^P in the retentate and permeate are defined as:

$$G^R = \frac{F_{tot}^R\, M_{mix}^R}{A} \tag{2.14}$$

$$G^P = \frac{F_{tot}^P\, M_{mix}^P}{A_m^i} \tag{2.15}$$

The effective thermal conductivity k of the carbon-based membrane layer on the α-Al_2O_3 support was computed using the correlation proposed by Poto et al. [6], and should be updated for different membrane materials or configurations.

All gas properties (density, viscosity, heat capacity, thermal conductivity) were

treated as temperature-dependent and are reported in Appendix A.2.9.
Pressure drop was considered only on the retentate side and was described using the Ergun equation:

$$\frac{dP^R}{dL} = -\left(\frac{150\,\mu_{mix}\,u\,(1-\varepsilon)^2}{\varepsilon^3\,d_{particle}^2} + \frac{1.75\,(1-\varepsilon)\,\rho_{mix}\,u^2}{\varepsilon^3\,d_{particle}}\right)\cdot 10^{-5} \qquad (2.16)$$

Where μ_{mix} and ρ_{mix} are the mixture viscosity and density, u is the superficial velocity based on the empty cross-section of the reactor, and $d_{particle}$ is the catalyst particle diameter.

Boundary conditions

At the reactor inlet ($L = 0$), the following boundary conditions were imposed:
$T^R = T^R(0)$
$T^P = T^P(0)$
$F_i^R = F_i^R(0), \quad i = 1,2,3$
$F_i^P = F_i^P(0) \quad i = 1,2,3$
$P^R = P^R(0)$
The permeate pressure was set according to the chosen transmembrane pressure difference ΔP.

2.4 SIMULATION RESULTS

With the governing equations and boundary conditions defined above, the model fully describes the axial profiles of composition, temperature, and pressure in the packed bed membrane reactor. Reactor performance was assessed in terms of H_2 conversion, NH_3 recovery, and NH_3 purity.
H_2 conversion (Equation (2.17)) was defined to account for the non-ideal membrane behaviour, including possible hydrogen and nitrogen permeation and back-permeation:

$$\%\,X_{H_2} = \frac{F_{H_2,in}^R - F_{H_2,out}^R - F_{H_2,tm}}{F_{H_2,in}^R - F_{H_2,tm}^*} \times 100 \qquad (2.17)$$

where:
$F_{H_2,tm} = F_{H_2,out}^P - F_{H_2,in}^P$
$F_{H_2,tm}^* = F_{H_2,out}^P - F_{H_2,in}^P \qquad$ only if $F_{H_2,tm}^* \leq 0$
This represents a loss of reactants from the retentate, which must be accounted for when defining conversion. As shown in **Figure 2.2**, the transmembrane molar flow of hydrogen, previously defined as $F_{H_2,tm}$, is taken as positive when hydrogen exits the reaction zone (from retentate to permeate) and is therefore subtracted from the total available hydrogen in the retentate.
However, if the hydrogen partial pressure on the permeate side exceeds that on the retentate side, back-permeation may occur. In this scenario, hydrogen flows from the permeate back into the retentate, effectively increasing the amount of reactant

available for reaction. To maintain a consistent and physically meaningful definition of conversion, this additional hydrogen must be included in the total reacting hydrogen. In the model, back-permeation corresponds to a negative net flux of hydrogen into the retentate according to the adopted sign convention; this quantity is denoted as $F_{H_{2,bp}}$.

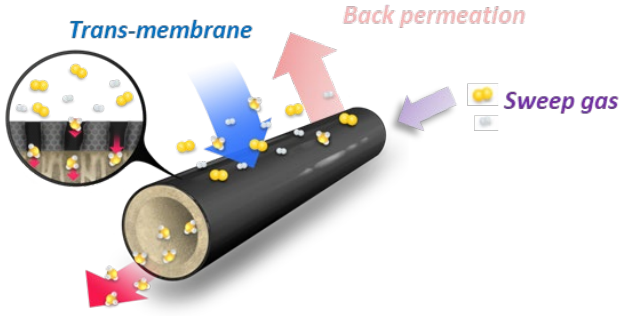


Figure 2.2 Schematic representation of gas flow through porous membrane

In addition to H_2 conversion, NH_3 recovery and purity, defined in Equations (2.18) and (2.19), were used to assess the performance of the PBMR. The parameter $NH_3\ recovery$ indicates the fraction of produced ammonia that can be collected on the permeate side relative to the amount produced in the retentate, while $NH_3\ purity$ indicates the ammonia mole fraction in the permeate stream. These parameters provide critical information for the design and optimization of downstream separation units.

$$\%\ NH_3\ recovery = \frac{F^P_{NH_3}}{F^R_{NH_3} + F^P_{NH_3}} \times 100 \tag{2.18}$$

$$\%\ NH_3\ purity = \frac{F^P_{NH_3}}{F^P_{N_2} + F^P_{H_2} + F^P_{NH_3}} \times 100 \tag{2.19}$$

2.4.1 Validation of the packed bed reactor

Before analysing the reactor's performance, the mathematical model was first validated against experimental data reported by Rossetti et al. [3]. This was based on a data set comprising 19 kinetic tests conducted at temperatures between 370 and 460 °C and pressures between 50 and 100 bar, with two different H_2:N_2 feed ratios, i.e. 1.5 and 3, and gas hourly space velocity (GHSV), ranging from 0.5 to $4{\cdot}10^5\ h^{-1}$. To ensure the validity of the mathematical model, a sensitivity study was performed by varying the bed porosity (ε) and consequently the effective active bed length (which is not reported by Rossetti et al.). As illustrated in **Figure 2.3**, bed porosity values between 0.3 and 0.5 were investigated. The results indicate that changes in bed porosity have a negligible effect on the final predictions, which can be attributed

to the fast reaction kinetics that allow the system to rapidly approach a quasi-steady state, enabling the reactants to equilibrate quickly along the bed.

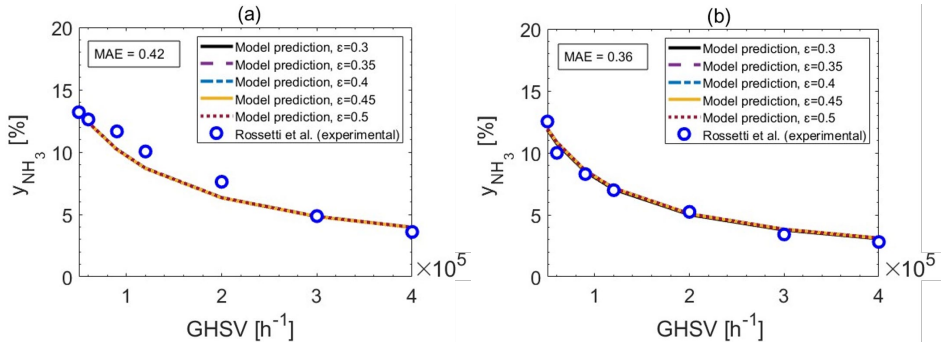


Figure 2.3 Model prediction of ammonia outlet molar fraction from experimental tests at 430 °C and 100 bar for GHSV = (0.5-4)·10^5 h^{-1} for: (a) H_2:N_2=1.5 (b) H_2:N_2=3

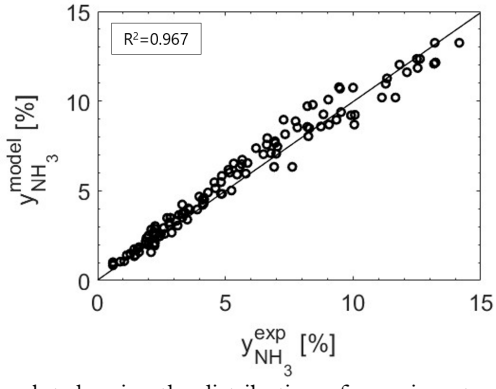


Figure 2.4 Parity plot showing the distribution of experiments vs. model prediction

To assess the model's accuracy, the Mean Absolute Error (MAE) was adopted as the principal validation metric and was calculated as follows:

$$MAE = \frac{1}{n}\sum_{i=1}^{n}\left|y_{NH_3}^{exp} - y_{NH_3}^{model}\right| \tag{2.20}$$

Where n represents the number of data points in each test set. Additionally, a parity plot was used to visualise all the data in a single representation, allowing a direct comparison between the experimental values and the model predictions and highlighting the overall agreement across all test conditions (**Figure 2.4**). Further details of the validation for all remaining tests are provided in the Appendix A.2.1.

2.4.2 Validation of the permeation module

Once the packed bed reactor model was validated, it was extended to include a membrane, by incorporating Equations (2.3)-(2.4). In this extended configuration,

the permeation process was described solely in terms of pressure driving forces, without explicit temperature dependence. This choice reflects the fact that the permeation model (Equation (2.4)) was validated using experimental data collected at a fixed temperature of 300 °C, close to the target reaction range (370-460 °C).
In this overview, the choice of an ammonia permeable membrane for a membrane reactor is critical, and various membrane types can be considered.

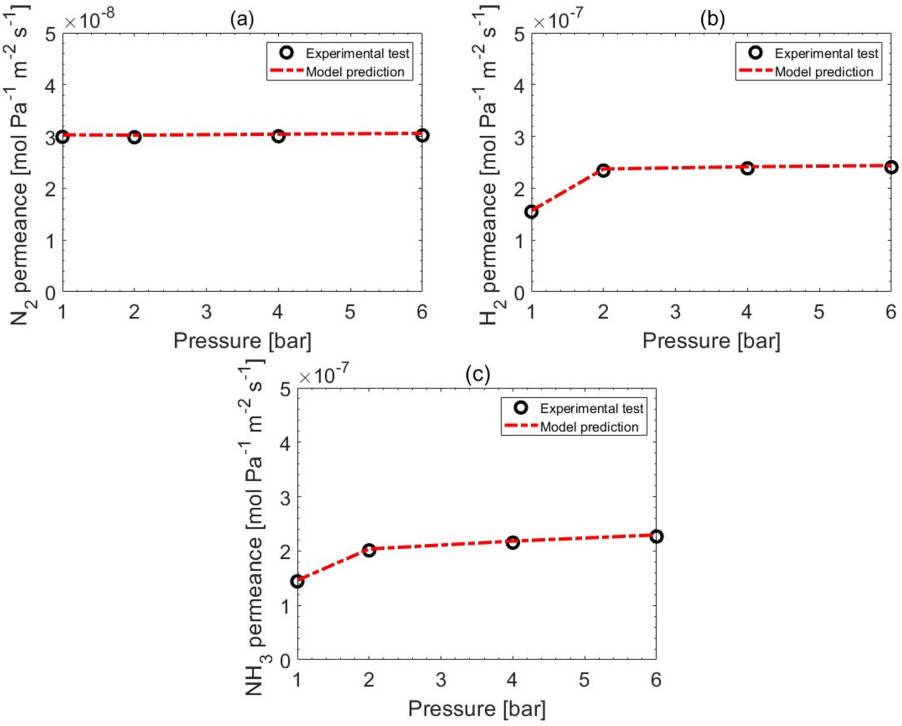


Figure 2.5 Permeation module validation with experimental test at ΔP = (1-6) bar and 300 °C for: (a) pure N_2 permeance, (b) pure H_2 permeance and (c) pure NH_3 permeance

The selection of a membrane is influenced by various factors, including operating conditions (such as temperature, pressure), feedstock composition, and the required product purity.
Additionally, chemical resistance and long-term stability are crucial considerations. Membrane materials that have been investigated for ammonia synthesis and separation include molten-salt based membrane [7], polymeric membranes [8], ceramic membranes such as zeolite membranes [9,10], and silica membranes [11].
This work focuses on inorganic porous membranes, particularly carbon membranes supported on ceramic substrates [12], due to their high chemical resistance, cost-effectiveness and tuneable pore structure and surface chemistry. Although no prior studies in the literature have reported their use under ammonia synthesis conditions, the application of these membranes for ammonia separation was investigated in this

work and is central to the membrane reactor technology developed in this thesis. A more detailed description of these membranes is provided in Chapter 3. From this phase of the research, experimental gas permeation tests were carried out in the laboratory to evaluate the membrane's performance under relevant conditions, i.e., at high temperatures and under different pressure differentials.Given the availability of data obtained from these tests, they were integrated into the mathematical model to assess its accuracy and predictive capability. Specifically, under non-reactive conditions, the model successfully predicted the permeance of each component as a function of the transmembrane pressure difference (as shown in **Figure 2.5**). It is worth emphasising that the approximately constant permeance observed with increasing transmembrane pressure difference in **Figure 2.5** should not be interpreted as a negligible effect of pressure on permeation. By definition, permeance is the flux normalised by the pressure driving force (Equation (2.4)); a constant permeance therefore indicates that the permeation flux increases approximately linearly with ΔP, rather than that the flux is insensitive to it.

2.4.3 Study of the membrane performance

Preliminary studies were conducted on the isothermal membrane reactor to investigate how the membrane's performance would impact the reactor's capabilities in terms of H_2 conversion, NH_3 recovery and purity. All the operating conditions and design specifications of the reactor selected for this study are detailed in **Table 2.2**, where:

- Temperature and pressure were set at the lower boundary of the range for which the kinetic law was determined
- A sub-stoichiometric feed ratio was selected to mitigate hydrogen poisoning on the Ru-based catalyst; in this case, the conversion is reported in terms of H_2 conversion, being the limiting reagent
- Reactor length and diameter were chosen to ensure $L/D_r^i > 30$, minimizing radial dispersion [13]
- The sweep-gas-to-feed flow ratio (SW) was selected to match the feed flow in the retentate
- The Péclet number was employed to determine the appropriate axial velocity such that axial dispersion could be neglected

Under these conditions, the presence of axial dispersion would imply a deviation from ideal plug flow, introducing back-mixing along the reactor length and potentially reducing overall conversion. In membrane systems, this would further diminish the effective driving force for separation, negatively impacting overall performance.

Table 2.2 Packed bed membrane reactor parameters in isothermal conditions

Parameters	Symbol	Units	Value
Retentate temperature	T_{in}^{R}	°C	370
Retentate pressure	P_{in}^{R}	bar	50
H_2:N_2 feed ratio (ret. & perm.)	q	$mol_{H_2} \cdot mol_{N_2}^{-1}$	1.5
Sweep-gas-to-feed flow ratio	SW	-	1
Pressure difference across the membrane	ΔP	bar	0
Reactor length	L	m	1
Reactor diameter	D_r^i	m	0.033
Gas hourly space velocity	$GHSV$	h^{-1}	35
Bed porosity	ε	$m_v^3 \cdot m_r^{-3}$	0.4
Catalyst bed density	ρ_c	$kg \cdot m_c^{-3}$	590

2.4.4 Ideal membrane case study

In assessing potential membrane performance benchmarks, membrane selectivity (S_{NH_3/H_2}, S_{NH_3/N_2}, S_{H_2/N_2}) and component permeances were used as key performance indicators. A detailed definition of these performance metrics is provided in Chapter 3. A literature survey on hypothetical membranes suitable for ammonia separation indicated that ceramic membranes, in particular silica and zeolite membranes, are promising candidates for ammonia separation. Therefore their reported performance was chosen as a reference. For instance, Camus et al. reported NH_3 permeances $\mathcal{P}_{NH_3}$~10^{-8}-10^{-7} $mol \cdot Pa^{-1}m^{-2}s^{-1}$ at 80 °C and 10 bar [10], meanwhile Kanezashi et al. observed permeances around $\mathcal{P}_{NH_3}$~10^{-9} $mol \cdot Pa^{-1}m^{-2}s^{-1}$ for silica membranes across a wide temperature range [11]. Accordingly, the initial NH_3 permeance range investigated in this work was set to $\mathcal{P}_{NH_3}$= [0-10^{-6}] $mol \cdot Pa^{-1}m^{-2}s^{-1}$. In this context it is important to identify the limitations associated with them, namely silica-based and zeolite-based membranes. Silica membranes, despite their good ammonia selectivity, are prone to cracking or failure under mechanical stress or thermal cycling. Additionally, producing defect-free silica membranes is often expensive. Zeolite membranes, on the other hand, may suffer from ammonia adsorption during prolonged operation, potentially blocking active pores and reducing separation efficiency. Their synthesis is also costly, requiring high-purity precursors and precise fabrication conditions.

The membrane was initially considered to be ideal, with a pore size distribution designed to allow only ammonia and hydrogen to pass, owing to their small and similar kinetic diameters (0.26 nm and 0.29 nm respectively). Thus, during the simulations, nitrogen permeation was neglected, resulting in S_{H_2/N_2}= ∞ and

$S_{NH_3/N_2} = \infty$. From a transport-mechanism standpoint, molecular sieving would be the preferred separation mechanism, relying on differences in kinetic diameter. In contrast, if the pores are larger and not strictly tailored for ammonia passage, transport may shift toward Knudsen diffusion [12] for which the Knudsen ideal selectivity $S_{NH_3/H_2} = \sqrt{M_{H_2}/M_{NH_3}} = 0.34$ is valid. This value was taken as lower bound to set the selectivity range to study, which turned out to be S_{NH_3/H_2} = [0-50]. Assuming complete nitrogen rejection, and thus infinite H_2/N_2 and NH_3/N_2 selectivities, corresponds to a limiting condition that no real membrane can achieve, since even highly selective microporous membranes retain a finite nitrogen permeance. Consequently, a non-zero nitrogen flux will always occur, and the actual selectivities remain finite. This ideal case is therefore used purely as a theoretical upper-bound benchmark, establishing the maximum achievable reactor performance independently of any specific membrane material. Finite, realistic selectivities and permeances, including those of the CMS membranes characterised experimentally in Chapter 3, are systematically explored in Subsection 2.4.5, where actual reactor performance is expected to fall below this ideal benchmark.

From this initial study, H_2 conversion is significantly influenced by NH_3 permeance, as shown in **Figure 2.6**(a). The increasing trend reaches a plateau when $\mathcal{P}_{NH_3}$ = $4{\cdot}10^{-7}$ mol·Pa^{-1}m^{-2}s^{-1}, at which point the reaction and permeation zones approach thermodynamic equilibrium. In all cases, the achieved conversion exceeds that of the conventional packed bed reactor (31.4%), and further increases in NH_3 permeance beyond this value yield no significant improvement, in line with previous literature [1].

Figure 2.6(b) plots the ammonia transmembrane molar flow ($F_{NH_3,tm}$) as a function of permeance $\mathcal{P}_{NH_3}$ at different selectivities S_{NH_3/H_2}. The results show that the ammonia molar flow does not increase significantly with the selectivity, indicating that this molar flow depends primarily on NH_3 permeance rather than the selectivity of the membrane. Although an increase in permeance is observed, it is insufficient to markedly enhance ammonia transport across the membrane or to further improve H_2 conversion. Afterward, the study focused on hydrogen back-permeating from the permeate to the retentate, i.e. $F_{H_{2,bp}}$. As shown in **Figure 2.6**(c) this molar flow becomes more negative (i.e., back-permeation increases) with increasing NH_3 permeance, whereas it becomes less negative as selectivity increases.

This behaviour can be explained by the fact that an increase in S_{NH_3/H_2}, results in less hydrogen loss from the retentate side, maintaining a higher hydrogen partial pressure and reducing the driving force for hydrogen to permeate back from the permeate to the retentate. Avoiding excessive hydrogen accumulation in the retentate is crucial from a catalyst-stability perspective, while hydrogen loss in the permeate requires additional sweep-gas reintegration.

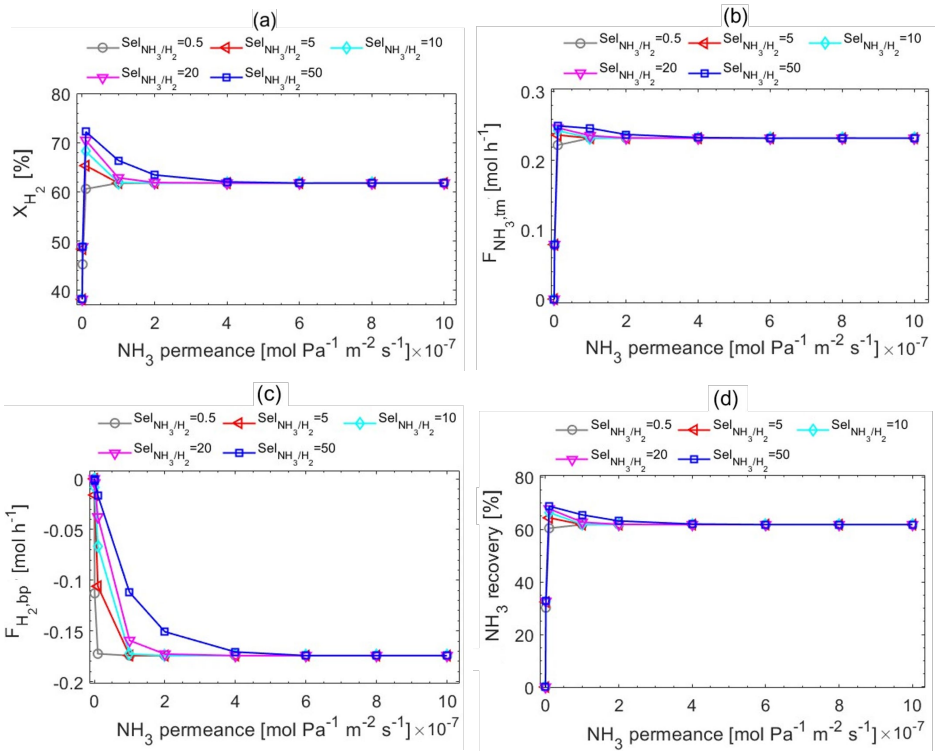


Figure 2.6 Study of the impact of membrane performance with respect to NH_3 permeance and parametric to S_{NH_3/H_2} on: (a) H_2 conversion, (b) NH_3 transmembrane flow, (c) H_2 back-permeation flow and (d) NH_3 recovery

Moreover, lower hydrogen back-permeation keeps the ammonia partial pressure in the permeate lower, thereby enhancing ammonia permeation. Consequently, as shown in **Figure 2.6**(d), higher S_{NH_3/H_2} enables a higher NH_3 recovery, reaching a maximum at $\mathcal{P}_{NH_3} = 10^{-8}$ mol·Pa^{-1}m^{-2}s^{-1}. This permeance value, together with a selectivity of 50, was selected as a temporary membrane performance target for this initial (ideal-case) screening.

2.4.5 Real membrane case study

Following this initial optimisation, nitrogen permeation was also included in the analysis, and the influence of the ammonia-to-nitrogen selectivity (S_{NH_3/N_2}) was examined. A broad range of selectivity values was selected based on literature studies. As shown in **Figure 2.7**(a) there is no significant correlation between conversion and selectivity, even with a three-orders-of-magnitude increase, which is consistent with the findings reported by Zhang et al. [1].

Instead, the amount of nitrogen lost from the retentate side, denoted as $F_{N_{2,tm}}$, was evaluated as key performance parameter to identify the minimum required S_{NH_3/N_2}.

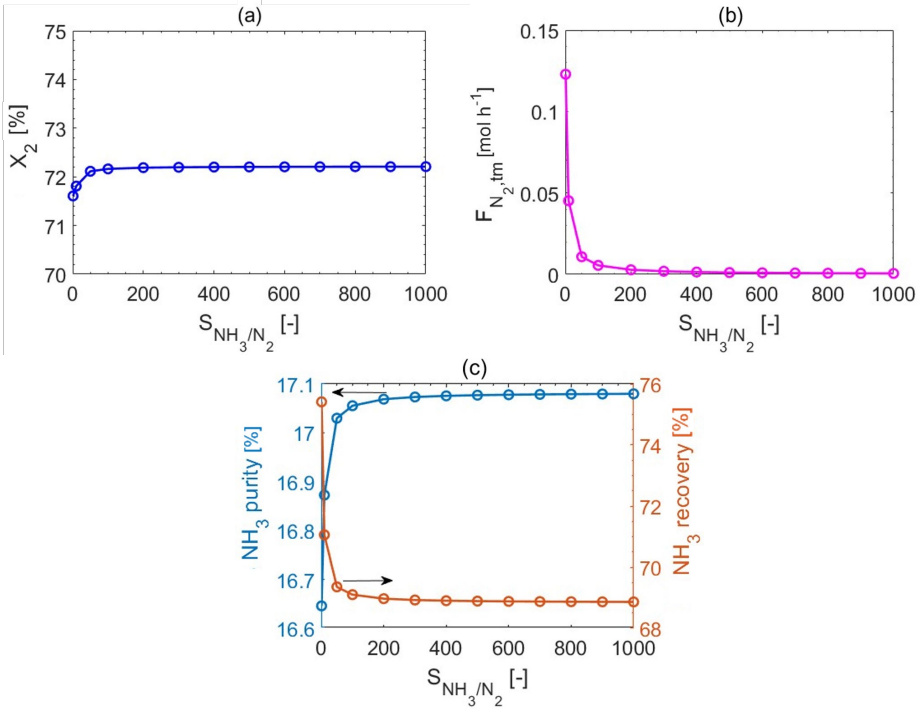


Figure 2.7 Study of the impact of membrane performance with respect to S_{NH_3/N_2} on (a) H_2 conversion, (b) N_2 transmembrane flow, (c) NH_3 purity and NH_3 recovery

The results reported in **Figure 2.7**(b) reveal that at low selectivity values, the nitrogen flow across the membrane decreases, and beyond a selectivity value of approximately 100, the decrease becomes less pronounced. Analysing the trends in NH_3 recovery and purity, shown in **Figure 2.7**(c), they exhibit an opposite behaviour. As S_{NH_3/N_2} increases, less nitrogen reaches the permeate side, which lowers the ammonia partial pressure in the retentate and makes it harder to drive ammonia through the membrane. At the same time, higher nitrogen concentration in the retentate favours ammonia synthesis, increasing production. This interplay results in an accumulation of ammonia in the retentate, some of which is not effectively removed, leading to a drop in NH_3 recovery. Purity, by contrast, increases with selectivity, as more ammonia is retained in permeate while less nitrogen crosses the membrane. Based on these findings, a minimum value of $S_{NH_3/N_2} = 100$ was set as required membrane performance criterion.

In **Figure 2.8**, H_2 conversion is plotted as a function of both S_{NH_3/H_2} and S_{NH_3/N_2} under three different NH_3 permeance scenarios. The result indicates that, at high S_{NH_3/H_2} selectivity, increasing NH_3 permeances raises H_2 conversion; at lower selectivities, including $S_{NH_3/H_2} = 50$, the value ultimately adopted, conversion is instead highest at $\mathcal{P}_{NH_3} = 10^{-8}$ mol·Pa^{-1}m^{-2}s^{-1} and decreases slightly at 10^{-7}, as

discussed below. For each S_{NH_3/H_2} value, the conversion consistently reaches a plateau at S_{NH_3/N_2} = 100. Similar trends are observed in NH_3 purity and recovery, as illustrated in **Figure A.2.2** and **Figure A.2.3** respectively.

When focusing on N_2 conversion (**Figure A.2.6**), a decreasing trend is observed with increase of S_{NH_3/H_2}. This behaviour can be attributed to the reduction in ammonia partial pressure in the retentate as selectivity increases, which enhances the driving force for nitrogen permeation. Consequently, the N_2 transmembrane flow increases with selectivity, leaving less N_2 available to react in the retentate side. On the other side, H_2 conversion increases with selectivity due to the diminishing back-permeation of hydrogen, which decreases as the membrane becomes more selective toward ammonia.

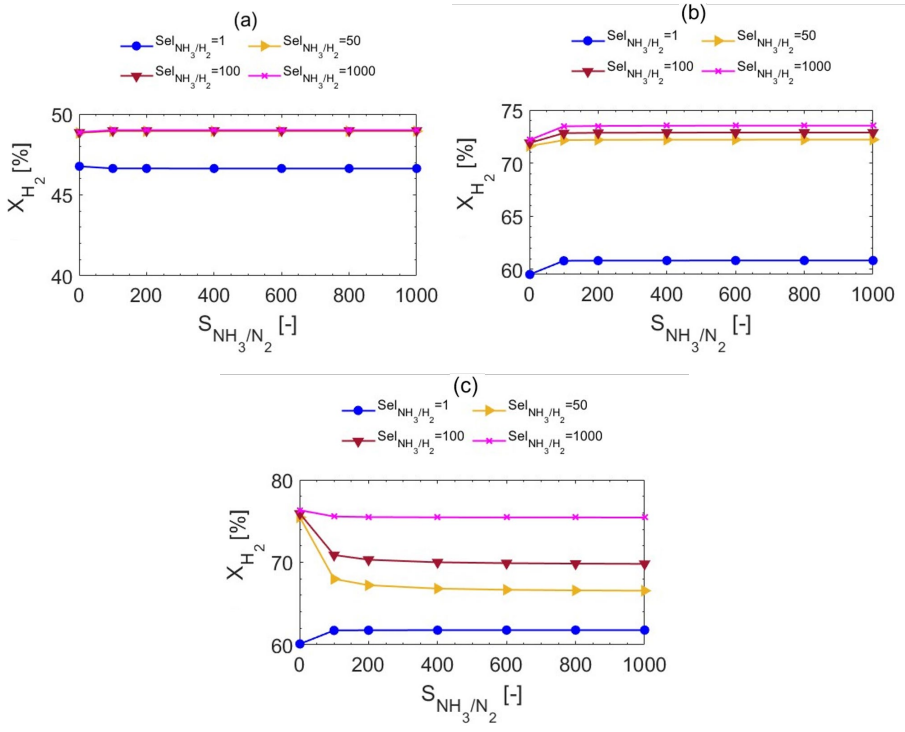


Figure 2.8 Study of the impact of membrane performance on H_2 conversion relative to S_{NH_3/N_2} and parametric to S_{NH_3/H_2} with (a) $\mathcal{P}_{NH_3}$ = 10^{-9} mol·Pa^{-1}m^{-2}s^{-1}, (b) $\mathcal{P}_{NH_3}$ = 10^{-8} mol·Pa^{-1}m^{-2}s^{-1} and (c) $\mathcal{P}_{NH_3}$ = 10^{-7} mol·Pa^{-1}m^{-2}s^{-1}

A similar effect is observed for stream purity, which decreases with S_{NH_3/H_2} increment, and eventually reaches a plateau at $\mathcal{P}_{NH_3}$ = 10^{-7} mol·Pa^{-1}m^{-2}s^{-1}. At this point, while nitrogen transmembrane flow remains sensitive to selectivity, the ammonia flux across the membrane becomes less dependent on selectivity and stabilises at this permeance value, as previously noted. Nevertheless, higher NH_3 recovery can still be achieved, as it depends solely on the ammonia molar flow

through the membrane, which increases with both NH_3 permeance and ammonia selectivity over nitrogen and hydrogen. As a result, $\mathcal{P}_{NH_3}$ = 10^{-7} mol·Pa^{-1}m^{-2}s^{-1} combined with a S_{NH_3/H_2} of approximately 50 and a S_{NH_3/N_2} of approximately 100, was adopted as the overall operating point. Although H_2 conversion at this selectivity is a few percentage points lower at this permeance than at the ten-fold lower value of 10^{-8} mol·Pa^{-1}m^{-2}s^{-1} (**Figure 2.8**(b)-(c)), NH_3 purity and recovery are both higher, representing a favourable trade-off between H_2 conversion, NH_3 purity, and NH_3 recovery overall.
Optimal membrane features determined at the end of this study are detailed in **Table 2.3**.

Table 2.3 Optimal membrane features determined at the end of this study

Membrane optimal conditions	Units	Value
$\mathcal{P}_{NH_3}$	mol·Pa^{-1}m^{-2}s^{-1}	10^{-7}
S_{NH_3/H_2}	-	50
S_{NH_3/N_2}	-	100

2.4.6 **Operating parameter study:** sweep-gas-to-feed flow ratio **and transmembrane pressure difference**

To maintain efficient ammonia separation, it is crucial to preserve a high partial pressure difference of ammonia across the membrane so as to enhance the driving force for permeation. A practical way to achieve this is to use a sweep gas in the permeate that keeps the ammonia partial pressure on that side as low as possible, while simultaneously ensuring that the partial pressures of the reactants remain high enough to limit their permeation. In this study, a sweep gas composed of the two reactants, H_2 and N_2, was considered.
The investigation initially focused on an adiabatic solution without considering heat exchange in shell and tube reactor configuration. Subsequently, the model was extended to include heat exchange between the retentate and the sweep gas streams, with Equations (2.5)-(2.6) implemented to compute the heat transfer between the two concentric tubes, accounting for all gas properties as temperature dependent functions, as detailed in the Appendix A.2.9. A parametric study was then carried out on the sweep-gas-to-feed flow ratio (SW) and the transmembrane pressure difference (ΔP) to evaluate their influence on reactor performance. As mentioned before, the inlet reaction temperature was fixed based on lower limit of the kinetic rate law. Thus, for simplicity the conditions of the reactor were kept the same as before, and the sweep gas inlet temperature was also set at 370 °C, while the permeate pressure was adjusted according to the chosen ΔP, up to 50 bar to match the pressure on the retentate side. The outcomes of this parametric study (yet without heat exchange) are presented in **Figure 2.9**(a) where H_2 conversion is

plotted as a function of SW between 0 and 50 for different ΔP values.
As SW increases, the conversion rises and eventually reaches a plateau. However, the rate at which this plateau is attained is determined by the ΔP: higher pressure differences lead to a stronger driving force for ammonia permeation and thus to a faster approach to the plateau together with higher conversion. This occurs because increasing SW reduces the ammonia partial pressure in the sweep stream, while increasing ΔP enhances the flux of ammonia from retentate to permeate.

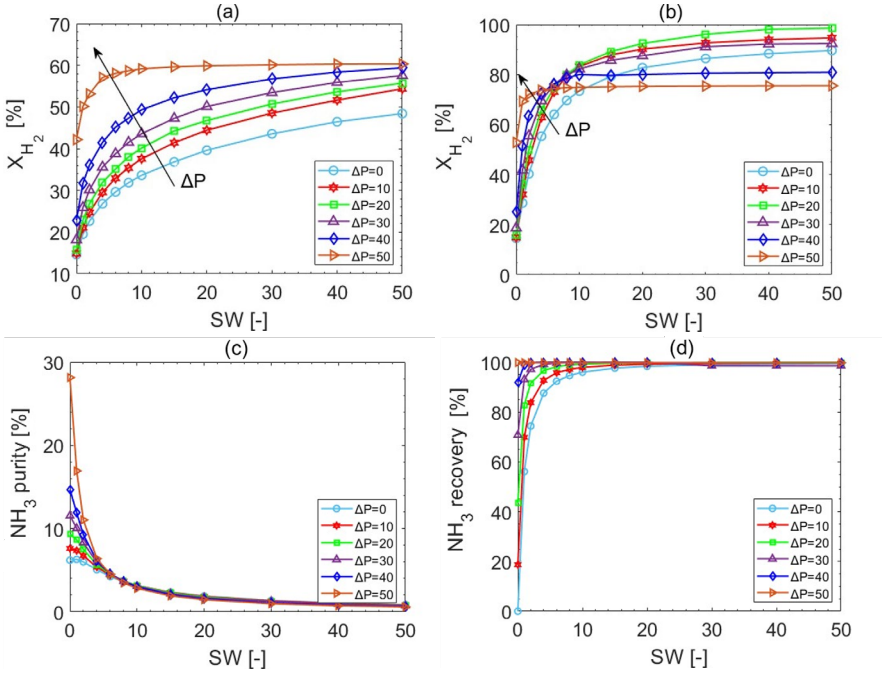


Figure 2.9 Effect of sweep-gas-to-feed flow ratio (SW) and transmembrane pressure difference (ΔP) under adiabatic conditions: (a) H_2 conversion without heat exchange, (b) H_2 conversion, (c) NH_3 purity and (d) NH_3 recovery both considering heat exchange between retentate and permeate

Once SW becomes sufficiently large, further increases barely reduce the ammonia partial pressure in the sweep gas, and H_2 conversion becomes insensitive to additional increments in SW.
When heat exchange between the retentate and permeate is included, as shown in **Figure 2.9**(b), the plateau is reached at a lower SW for each ΔP, and the overall trend is somewhat inverted. As SW increases, the residence time in the permeate side decreases, leading to faster removal of ammonia and a stronger driving force for reaction. At the same time, higher ΔP promotes additional ammonia separation, which accelerates the reaction rate but also increases the reactor temperature. Beyond a certain point, however, further increases in SW no longer improve conversion, and for larger ΔP values, the conversion eventually declines due to

overheating. Thus for SW ≤ 6, higher ΔP yields higher conversion, whereas as SW increases, the conversion trend rises with a decrease in ΔP. In all cases, the conversion with heat exchange exceeds that obtained without heat exchange. The temperature profile along the reactor is also more uniform when heat exchange between the two concentric tubes is considered (**Figure 2.10**(a)), since the sweep gas acts as a cooling fluid that mitigates the exothermicity of the ammonia synthesis reaction. As ΔP decreases, the driving force between the two sides weakens, which reduces the loss of sweep gas to the retentate and helps maintain a larger amount of cooling gas in the permeate.

Both NH_3 recovery and purity increase with the transmembrane pressure difference ΔP (**Figure 2.9**(c)-(d)), as expected, because a higher ΔP generates a larger ammonia partial-pressure difference and thus a higher permeation flux. In contrast, increasing the sweep-gas-to-feed flow ratio carries more hydrogen and nitrogen into the permeate, thereby reducing NH_3 purity. Furthermore, at lower driving forces less ammonia is removed from the retentate, resulting in decreased recovery.

Based on this analysis, ΔP = 40 bar and SW = 6 are identified as the best trade-off conditions for the membrane reactor, balancing high H_2 conversion, good NH_3 recovery, and acceptable purity while benefiting from the cooling effect of the sweep gas and heat-exchange integration.

2.4.7 Heat management study: effect of temperature

The mathematical model, incorporating all the discussed parameters, was further analysed with particular emphasis on heat management, considering the sweep gas as a cooling fluid. **Figure 2.10**(a) highlights two different cases: the dash-dotted lines represent the temperature profile of an adiabatic membrane reactor without considering heat exchange between retentate and sweep gases, whereas the solid ones show the temperature profile when heat transfer between these zones is included.

This comparison illustrates that the presence of the sweep gas leads to a more uniform and stable temperature profile, thereby promoting higher H_2 conversion.

Furthermore, **Figure 2.10**(b) displays the temperature profiles on both sides for the specific case of SW = 10, revealing that the sweep gas temperature gradually increases along the reactor. As the retentate transfers heat to the permeate, the temperature peaks in the retentate are attenuated, yielding a flatter temperature gradient and mitigating the risk of local overheating. Interestingly, by applying the optimised operating conditions identified in Subsection 2.4.8, and adjusting the sweep gas-to-feed inlet temperature on the permeate side, the final H_2 conversion can be further enhanced.

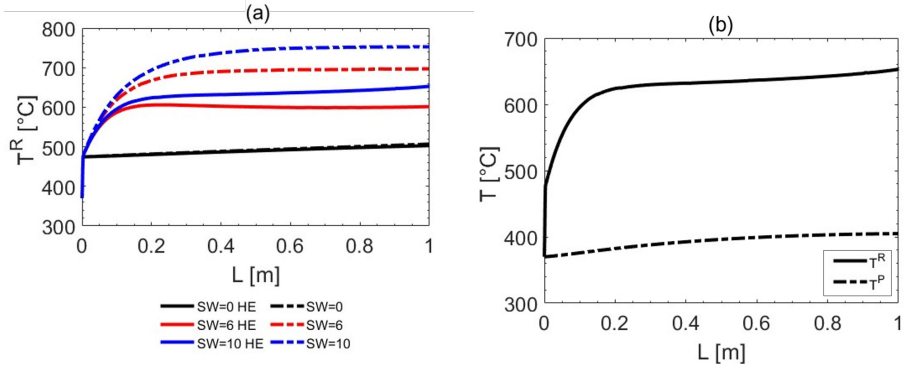


Figure 2.10 Temperature profile along the reactor length for: (a) an adiabatic packed bed membrane reactor with and without heat exchange (HE) between retentate and permeate side, (b) temperature profile in the retentate and permeate side for the case of SW = 10 and ΔP = 40 bar

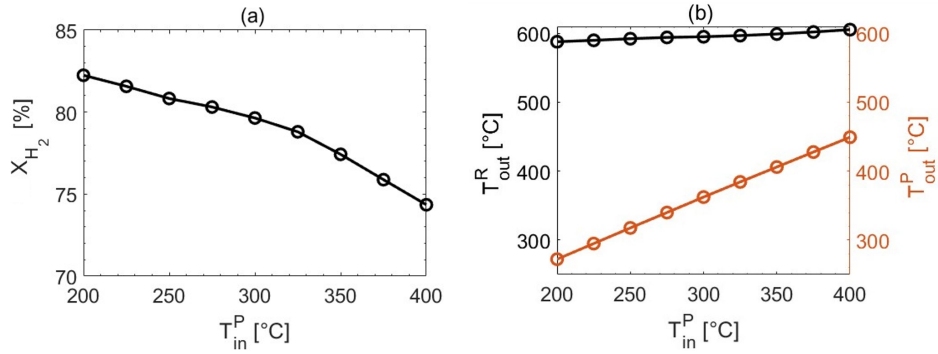


Figure 2.11 Study of the effect of the permeate inlet temperature (T_{in}^P) on: (a) H_2 conversion and (b) outlet temperature of permeate (T_{out}^P) and retentate(T_{out}^R)

Figure 2.11(a) illustrates this analysis, where the inlet permeate temperature is varied and the highest conversion is found at T_{in}^P = 200 °C. This result arises because, as the sweep-gas inlet temperature decreases, the sweep stream acts more effectively as a cooling fluid, reducing the temperature in the reaction zone and thereby shifting the equilibrium toward higher NH_3 yield. Conversely, as T_{in}^P increases, the driving force for heat transfer between the retentate and permeate sides diminishes, weakening the cooling effect.

Figure 2.11(b) shows the final temperatures reached in both retentate and permeate streams as a function of the inlet sweep gas temperature. The profiles indicate that the permeate side cannot fully remove the excess heat from the retentate, particularly at higher sweep-gas inlet temperatures. Hence, even with optimised SW and ΔP, an additional external cooling strategy would be required to fully control the reactor temperature and maximize conversion.

2.4.8 On the effect of sweep-gas H_2:N_2 molar ratio

A key factor influencing ammonia production is the H_2:N_2 feed ratio. In this work, a value of 1.5 was selected to leverage the favourable activity of the ruthenium-based catalyst under sub-stoichiometric conditions. The sweep-gas H_2:N_2 molar ratio was kept equal to that on the retentate side. This molar ratio is crucial because it directly affects both the efficiency of ammonia removal and the reaction equilibrium.

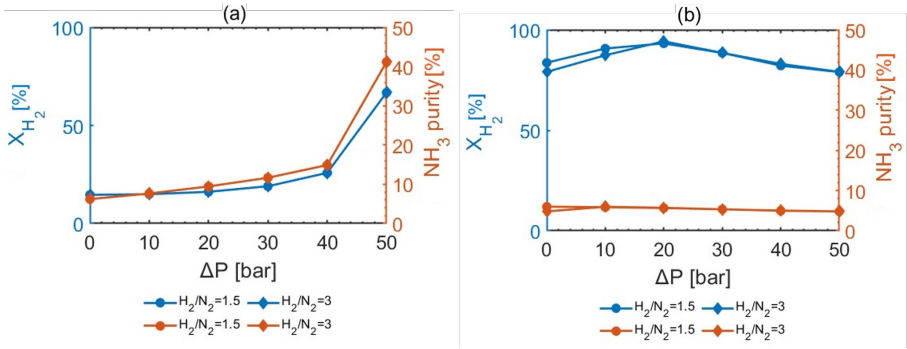


Figure 2.12 Effect of ΔP on H_2 conversion and NH_3 purity for: (a) SW = 0 and (b) SW = 6, with a parametric study of sweep gas H_2:N_2 molar ratio (1.5 and 3)

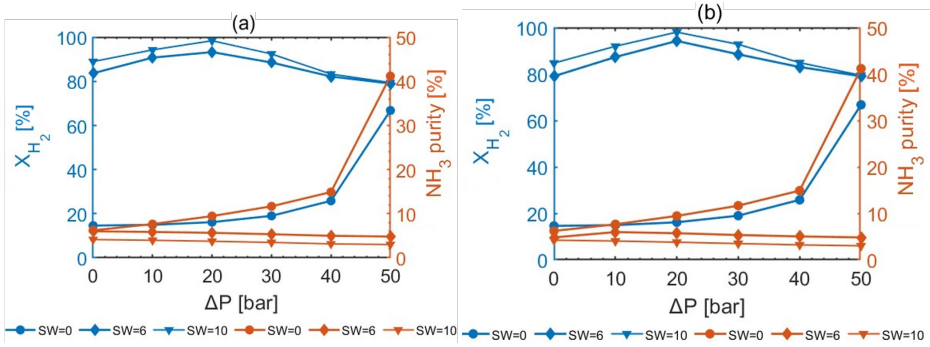


Figure 2.13 Effect of ΔP on H_2 conversion and NH_3 purity for different sweep gas H_2:N_2 molar ratios: (a) H_2:N_2 = 1.5 and (b) H_2:N_2 = 3, with a parametric study of SW = 0-6-10

Figure 2.12 compares two operating scenarios with different H_2:N_2 feed molar ratios in the permeate, and different sweep-gas-to-feed flow ratios, highlighting their impact on H_2 conversion and NH_3 purity as a function of ΔP. In **Figure 2.12**(a), for SW = 0, the feed ratio has no influence, as expected, and ΔP is the dominant parameter: increasing ΔP enhances H_2 conversion due to the larger ammonia partial pressure difference across the membrane, while NH_3 purity also increases because the permeate stream remains relatively undiluted. In **Figure 2.12**(b), for SW = 6, the maximum H_2 conversion occurs at ΔP = 20 bar. Below this value, conversion is slightly lower for H_2:N_2 = 3, which can be attributed to different reactant partial pressures (i.e., higher hydrogen content in the permeate) and the associated back-permeation of hydrogen. This difference diminishes as permeate pressure is

reduced, and conversion reaches a maximum before slightly decreasing at higher ΔP. **Figure 2.13**, which reports the cases with sweep gas H_2:N_2 ratios of 1.5 and 3, illustrates the reactor performance with a SW ranging from 0 to 10. In both cases, the highest conversion is achieved with SW = 6-10 at ΔP = 20 bar, with the trend reversing as ΔP increases further. As anticipated, SW = 0 yields the highest NH_3 purity but the lowest H_2 conversion. For the optimal parameter region, choosing SW = 6 or SW = 10 at high ΔP does not significantly alter conversion; however, SW = 6 provides an advantage in terms of NH_3 purity.
Therefore, SW = 6 was selected as the final value, independent of the sweep-gas H_2:N_2 molar ratio, together with ΔP = 20 bar. A rigorous determination of the absolute optimum would require an economic assessment to identify the most cost-effective operating point.

2.4.9 Packed bed membrane reactor vs. packed bed reactor

With the implementation of the membrane performance model, it became possible to study and compare two reactor configurations: a conventional packed bed reactor and a packed bed membrane reactor. The optimal operating conditions for the membrane reactor are summarised in **Table 2.4**.

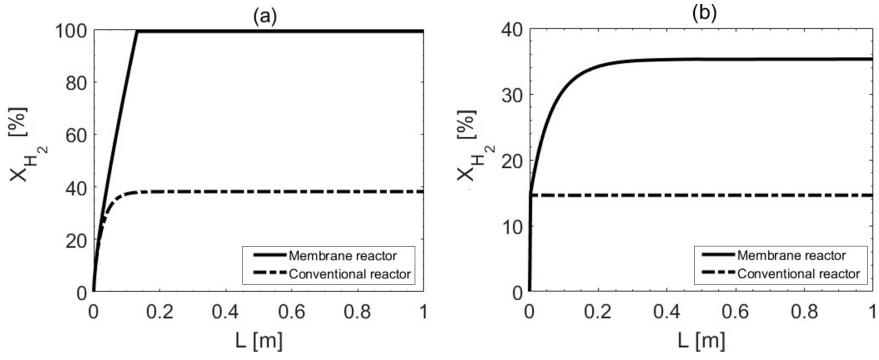


Figure 2.14 Comparison of H_2 conversion between a conventional packed bed reactor and a packed bed membrane reactor operated under: (a) isothermal and (b) adiabatic conditions

Figure 2.14(a) first presents the isothermal case, where the conversion profile along the reactor length clearly demonstrates the benefits of membrane integration. Under these conditions (T = 370 °C and P = 50 bar), the conventional packed bed reactor is constrained by thermodynamic equilibrium, whereas the membrane reactor configuration effectively alleviates this limitation. By selectively removing ammonia through the membrane, the equilibrium constraint on H_2 conversion is shifted, enabling higher overall conversion and improved NH_3 recovery.
Figure 2.14(b) compares the performance of a conventional packed bed reactor and a packed bed membrane reactor under adiabatic conditions. In the conventional reactor, where the operating conditions and design are chosen to reach equilibrium conversion, the H_2 conversion profile is almost flat, since the reaction essentially

reaches completion within the first few centimetres of the reactor.
In contrast, the adiabatic membrane reactor achieves a final conversion approximately 63% higher than that of the conventional adiabatic reactor, demonstrating the potential of membrane reactor technology for intensified ammonia synthesis.

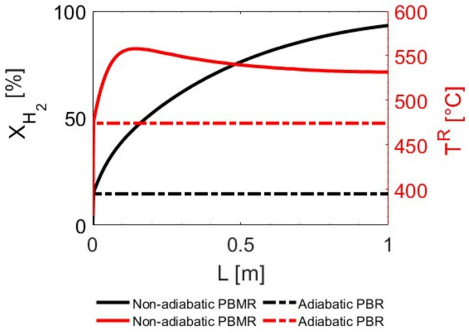


Figure 2.15 H_2 conversion and retentate temperature for the conventional adiabatic packed bed reactor (Adiabatic PBR) and the adiabatic membrane reactor with internal heat exchange between retentate and permeate (Adiabatic PBMR-HE)

For the adiabatic configurations in particular, the conversion trends of **Figure 2.14**(b) are best interpreted together with the corresponding retentate temperature profiles, since in an adiabatic reactor the local reaction rate, and hence the local conversion, is directly coupled to the local temperature through the exothermic heat of reaction. **Figure 2.15** provides this complementary information for the two cases of interest: the conventional adiabatic packed bed reactor (Adiabatic PBR), already shown in **Figure 2.14**(b), and the adiabatic membrane reactor with internal heat exchange between the retentate and the sweep gas on the permeate side (Adiabatic PBMR-HE), introduced in Section 2.4.7.
The effect of heat exchange between the retentate and permeate sides in the membrane reactor is illustrated in **Figure 2.15**. The red solid line indicates a pronounced temperature peak near the reactor inlet, caused by the high reaction rate in this region. The adoption of a co-current flow configuration ensures the highest driving force for both mass and heat transfer in this zone, thereby enhancing ammonia removal and improving overall conversion.

Table 2.4 Optimal operating conditions of the packed bed membrane reactor

Parameter	Symbol	Units	Value
Retentate temperature	T_{in}^{R}	°C	370
Permeate temperature	T_{in}^{P}	°C	200
Retentate pressure	P_{in}^{R}	bar	50
Pressure difference across the membrane	ΔP	bar	20
H_2:N_2 feed ratio (ret & perm)	q	$mol_{H_2} \cdot mol_{N_2}^{-1}$	1.5
Sweep-gas-to-feed flow ratio	SW	-	6
NH_3 permeance	$\mathcal{P}_{NH_3}$	$mol \cdot Pa^{-1}m^{-2}s^{-1}$	10^{-7}
NH_3 to H_2 selectivity	S_{NH_3/H_2}	-	50
NH_3 to N_2 selectivity	S_{NH_3/N_2}	-	100
Reactor length	L	m	1
Reactor diameter	D_r	m	0.033

2.5 CONCLUSIONS

This chapter investigated the impact of a membrane-enhanced process on ammonia production by developing a 1D phenomenological non-isothermal reactor model, to evaluate how the membrane's performance could influence the feasibility of the process. The mathematical model was first validated against experimental data obtained using a Ru/C catalyst. The membrane was then implemented in the isothermal reactor model to demonstrate the effect of in-situ ammonia separation on reactor performance. Under base conditions (T_{in}^{R} = 370 °C, P_{in}^{R} = 50 bar, H_2:N_2 = 1.5, SW = 1, ΔP = 0), introducing the membrane into the packed bed reactor led to a substantial enhancement in H_2 conversion. In particular, a S_{NH_3/H_2} = 50 and S_{NH_3/N_2} = 100, combined with a minimum $\mathcal{P}_{NH_3}$ = 10^{-7} $mol \cdot Pa^{-1}m^{-2}s^{-1}$, enabled H_2 conversions beyond the thermodynamic equilibrium limit of the conventional packed bed reactor.

The study delved into the influence of various process parameters. Simulations were performed for different co-current sweep-gas-to-feed flow ratios and transmembrane pressure differences, showing the possibility to further improve the reactor performance in terms of H_2 conversion. Once SW reached a sufficiently high value, however, further increases did not yield additional conversion gains, indicating a plateau behaviour. The optimal conditions from this study were identified as SW = 6 and ΔP = 20 bar. Treating the sweep gas as a cooling medium and including heat exchange between the retentate and permeate sides improved performance even further. Analysis of the axial temperature profiles emphasised the importance of heat management, demonstrating that adjusting the permeate-side inlet

temperature allows better control of the temperature profile and thus improves reactor performance.

The effect of the sweep-gas H_2:N_2 molar ratio was also explored. A feed ratio of H_2:N_2 = 1.5 and SW = 6 yielded a maximum H_2 conversion of 93%, together with an NH_3 purity of 5.7% and an NH_3 recovery of 99.2%. These findings highlight the trade-offs between conversion, purity, and recovery and confirm the potential of ammonia permeable membranes to intensify ammonia synthesis.

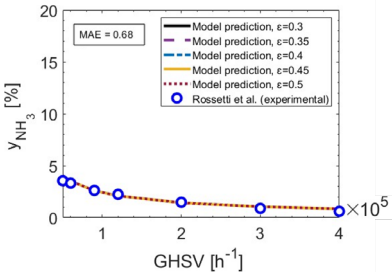
The results suggest that membrane reactors offer a promising route for improving the efficiency of the ammonia synthesis process, reducing overall energy consumption and operational costs. This can be achieved through lower operating pressures, equilibrium shifting via selective separation, reduced recycling and separation energy, enhanced heat integration, and decreased feedstock and catalyst usage, improving both efficiency and cost-effectiveness.

The present work relies on a one-dimensional pseudo-homogeneous model with ideal plug flow and steady-state operation, which is appropriate for small-diameter laboratory reactors but may not fully capture behaviour at larger scales. In Chapter 5, this modelling framework is extended to include axial and radial diffusion, in order to account for deviations from ideal flow and concentration profiles that may arise in larger or industrial-scale systems.

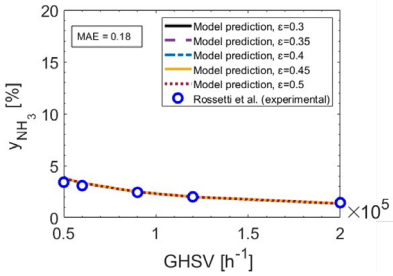
A.2 APPENDIX

A.2.1 Model validation using literature kinetic test from Rossetti et al.

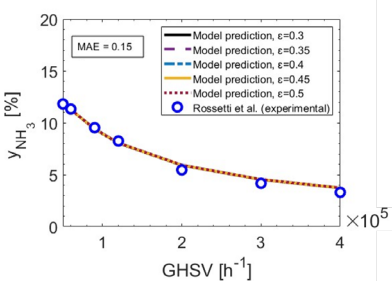
Kinetic test 2



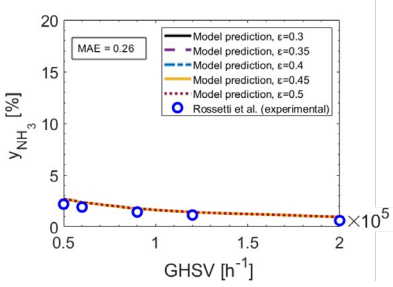
Kinetic test 3



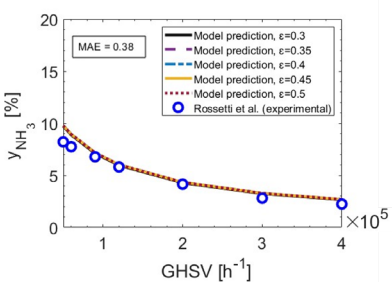
Kinetic test 4



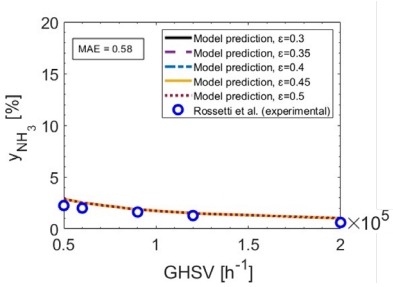
Kinetic test 7



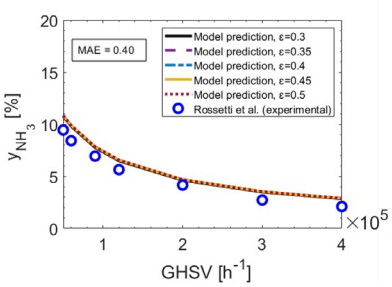
Kinetic test 8



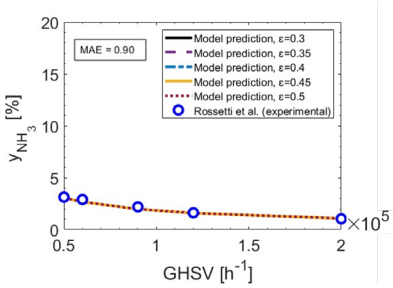
Kinetic test 10



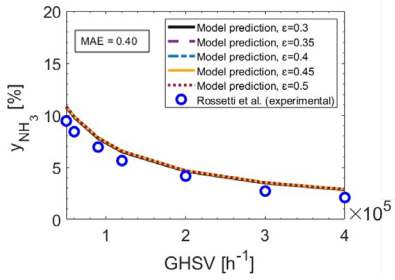
Kinetic test 11



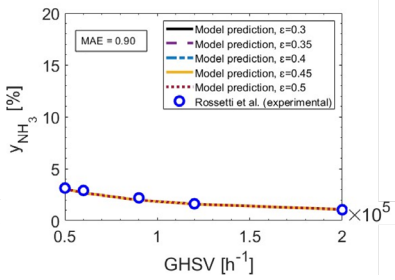
Kinetic test 13



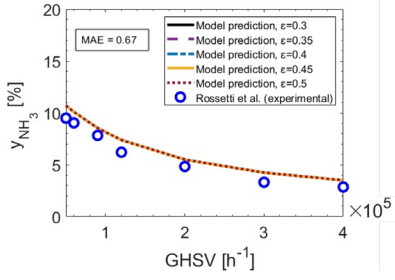
Kinetic test 15



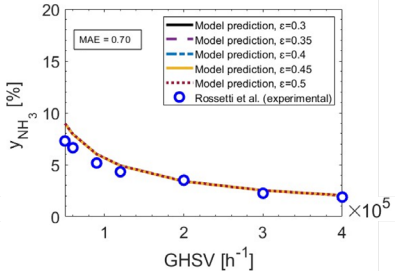
Kinetic test 17



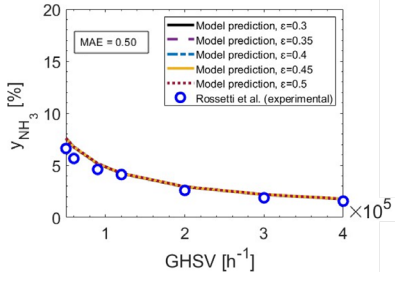
Kinetic test 18



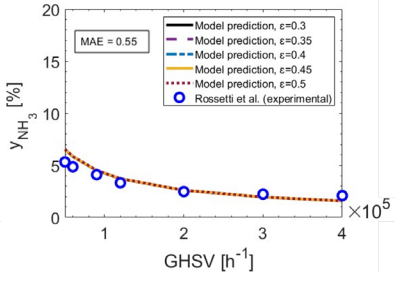
Kinetic test 19



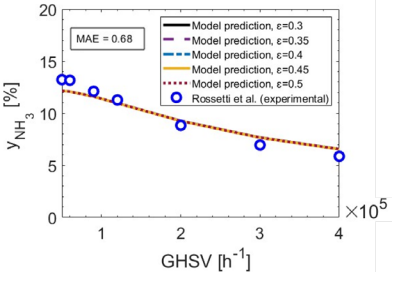
Kinetic test 20



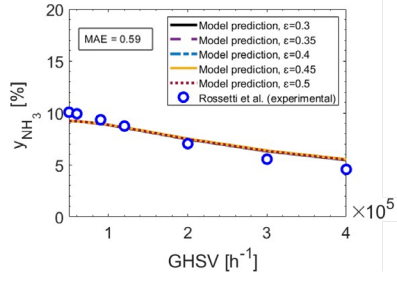
Kinetic test 21

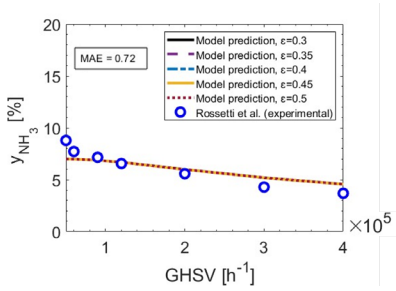


Kinetic test 22



Kinetic test 23





A.2.2 Pressure drops along the reactor in the retentate zone

In the reaction side, where the spherical catalyst particles with a diameter of $1.65 \cdot 10^{-3}$ m are packed, the pressure distribution along the reactor is determined using the Equation (2.16). The resulting axial pressure profile, shown in **Figure A.2.1**, indicates an overall pressure drop of approximately 0.001 bar, which can be regarded as negligible. This small pressure loss minimises the risk of significant back-permeation through the membrane and reduces the energy penalty associated with recompressing unconverted reactants for recycle to the retentate side.

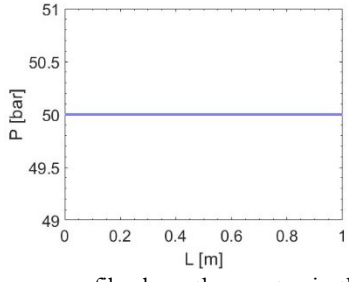
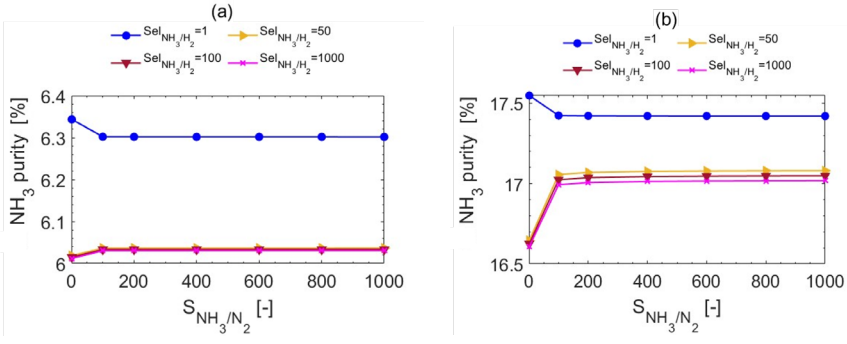


Figure A.2.1 Pressure profile along the reactor in the retentate side

A.2.3 Isothermal PBMR: NH_3 purity considering membrane real case study



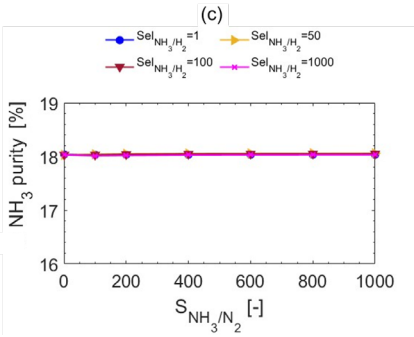


Figure A.2.2 Study of membrane performance impact on NH_3 purity in respect to S_{NH_3/N_2} and parametric to S_{NH_3/H_2} with: (a) $\mathcal{P}_{NH_3}$= 10^{-9} mol·Pa^{-1}m^{-2}s^{-1}, (b) $\mathcal{P}_{NH_3}$ = 10^{-8}mol·Pa^{-1}m^{-2}s^{-1} and (c) $\mathcal{P}_{NH_3}$ = 10^{-7} mol·Pa^{-1}m^{-2}s^{-1}

A.2.4 Isothermal PBMR: NH_3 recovery considering membrane real case study

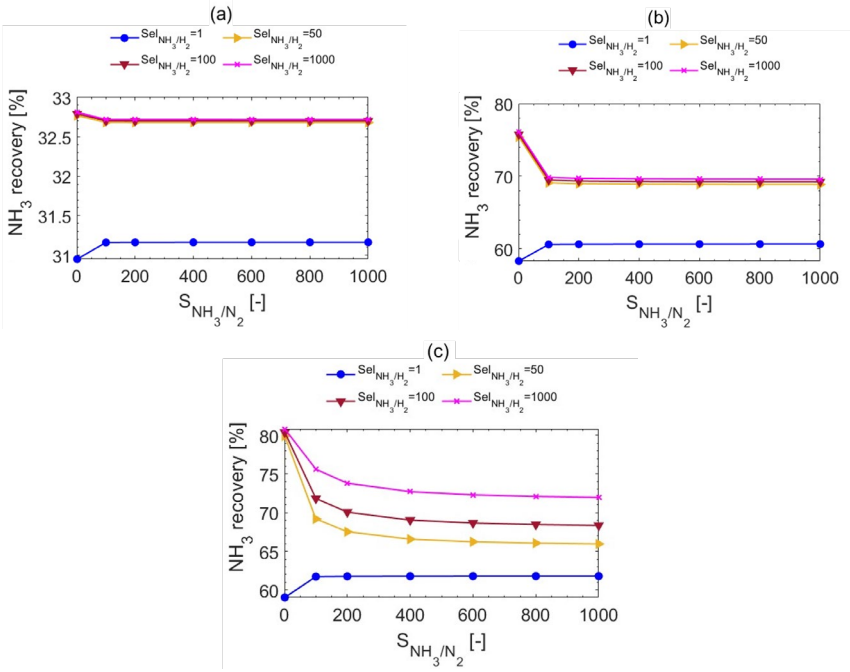


Figure A.2.3 Study of membrane performance impact on NH_3 recovery in respect to S_{NH_3/N_2} and parametric to S_{NH_3/H_2} with: (a) $\mathcal{P}_{NH_3}$= 10^{-9} mol·Pa^{-1}m^{-2}s^{-1}, (b) $\mathcal{P}_{NH_3}$ = 10^{-8} mol·Pa^{-1}m^{-2}s^{-1} and (c) $\mathcal{P}_{NH_3}$ = 10^{-7} mol·Pa^{-1}m^{-2}s^{-1}

A.2.5 Isothermal PBMR: Transmembrane nitrogen flow considering membrane real case study

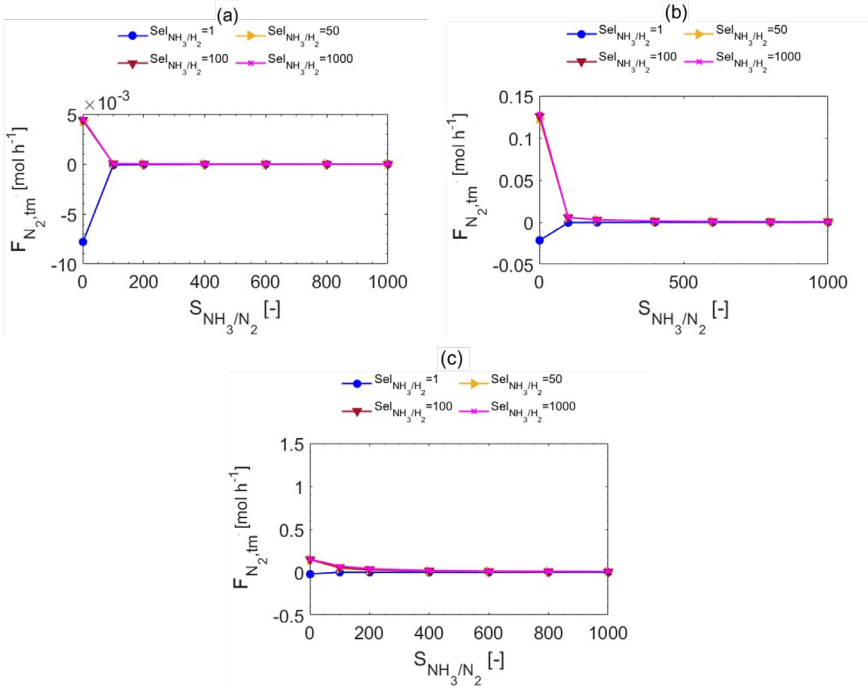
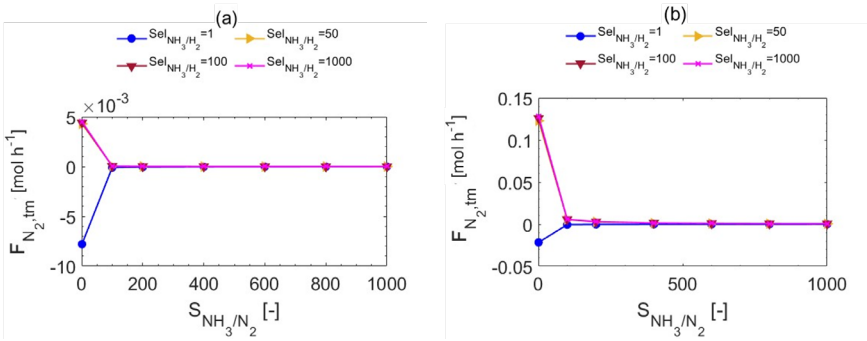


Figure A.2.4 Study of membrane performance impact on N_2 transmembrane flow in respect to S_{NH_3/N_2} and parametric to S_{NH_3/H_2} with: (a) $\mathcal{P}_{NH_3}$= 10^{-9} mol·Pa^{-1}m^{-2}s^{-1}, (b) $\mathcal{P}_{NH_3}$ = 10^{-8} mol·Pa^{-1}m^{-2}s^{-1} and (c) $\mathcal{P}_{NH_3}$ = 10^{-7} mol·Pa^{-1}m^{-2}s^{-1}

A.2.6 Isothermal PBMR: Back-permeating hydrogen considering membrane real case study



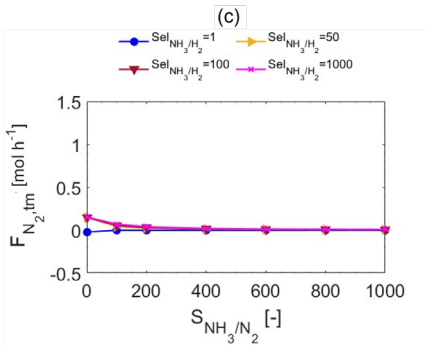


Figure A.2.5 Study of membrane performance impact on H_2 back-permeation in respect to S_{NH_3/N_2} and parametric to S_{NH_3/H_2} with: (a) $\mathcal{P}_{NH_3}$= 10^{-9} mol·Pa^{-1}m^{-2}s^{-1}, (b) $\mathcal{P}_{NH_3}$ = 10^{-8} mol·Pa^{-1}m^{-2}s^{-1} and (c) $\mathcal{P}_{NH_3}$ = 10^{-7} mol·Pa^{-1}m^{-2}s^{-1}

A.2.7 Isothermal PBMR: N_2 conversion considering membrane real case study

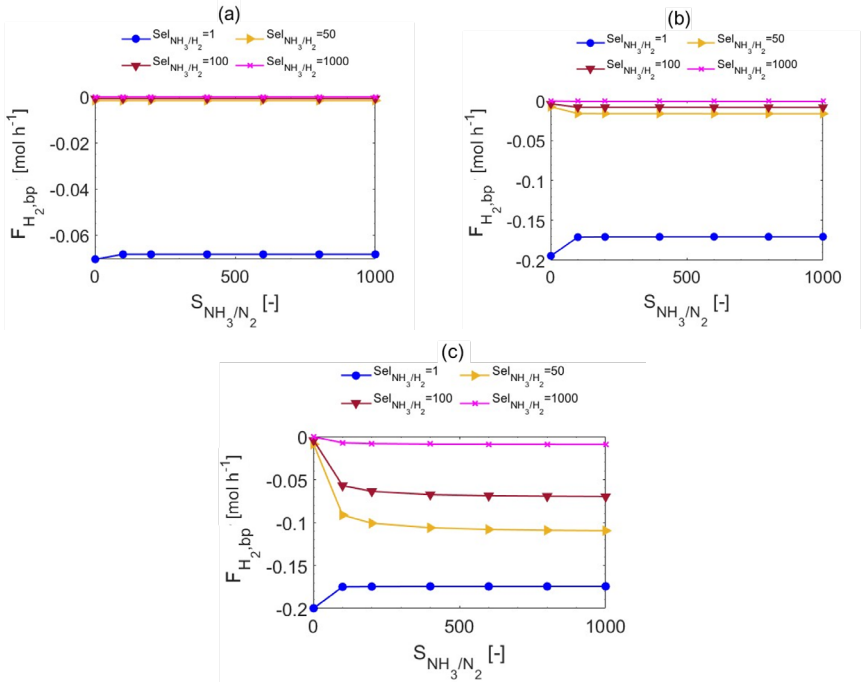


Figure A.2.6 Study of membrane performance impact on N_2 conversion in respect to S_{NH_3/N_2} and parametric to S_{NH_3/H_2} with: (a) $\mathcal{P}_{NH_3}$= 10^{-9} mol·Pa^{-1}m^{-2}s^{-1}, (b) $\mathcal{P}_{NH_3}$ = 10^{-8} mol·Pa^{-1}m^{-2}s^{-1} and (c) $\mathcal{P}_{NH_3}$ = 10^{-7} mol·Pa^{-1}m^{-2}s^{-1}

A.2.8 Non-isothermal PBMR: H_2 conversion vs. inlet volumetric flow

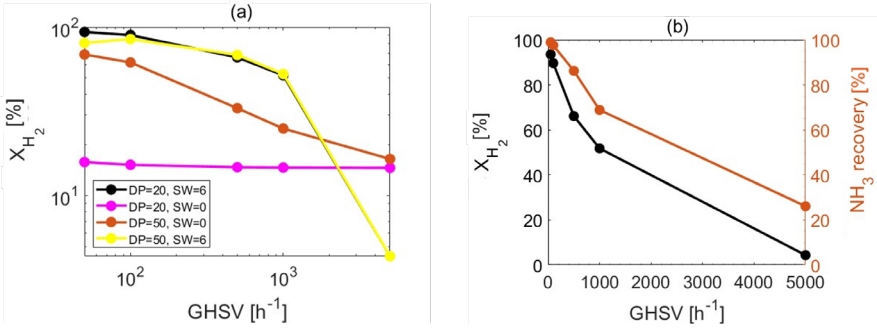


Figure A.2.7 Effect of the GHSV on: (a) H_2 conversion considering different ΔP and SW values and (b) H_2 conversion and NH_3 recovery for ΔP = 20 bar and SW = 6

A.2.9 Thermodynamic gas properties

❖ Density

The gas mixture density was calculated via Peng-Robinson cubic EoS, whose implicit form is expressed through the compressibility factor Z:

$$Z^3 - (1 - B)Z^2 + (A - 2B^2 - 2B)Z - (AB - B^3 - B^2) = 0 \quad \text{(A.2.1)}$$

Where the coefficients A and B are defined by Equation (A.2.2),(A.2.3), depending on the temperature and pressure of the system:

$$A = \frac{a \cdot P}{R^2 T^2} \quad \text{(A.2.2)}$$

$$B = \frac{b \cdot P}{RT} \quad \text{(A.2.3)}$$

The van der Waals one-fluid mixing rules are used for calculating the energy a and the volume b:

$$a = \sum_{i=1}^{N} \sum_{j=1}^{N} y_i y_j a_{ij} \quad \text{(A.2.4)}$$

$$b = \sum_{i=1}^{N} \sum_{j=1}^{N} y_i y_j b_{ij} \quad \text{(A.2.5)}$$

Where y_i and y_j is the molar fraction of each component in the gas phase, while the parameters a_{ij} and b_{ij} are defined by the critical properties of each gas, as expressed in the next equations.

$$a_{ij} = \sqrt{a_i a_j}\left(1 - k_{ij}\right) \quad \text{(A.2.6)}$$

$$b_{ij} = \frac{1}{2}\left(b_i + b_j\right)\left(1 - \delta_{ij}\right) \quad \text{(A.2.7)}$$

$$a_i = \Omega_a \frac{RP_{ri}}{{T_{ri}}^2}\left[1 + m_i\left(1 - \sqrt{\frac{T}{T_{ci}}}\right)\right]^2$$
$$= 0.457235529\ \frac{R^2T_{ci}^2}{P_{ci}}\left[1 + m_i\left(1 - \sqrt{\frac{T}{T_{ci}}}\right)\right]^2 \quad \text{(A.2.8)}$$

$$b_i = \Omega_b \frac{RP_{ri}}{T_{ri}} = 0.0777960739\ \frac{RT_{ci}}{P_{ci}} \quad \text{(A.2.9)}$$

Where Ω_a and Ω_b are constant with EoS, and P_{ri} and T_{ri} are reduced pressure and temperature of component i [14]. The factor m_i depends on the acentric factor ω_i [15].

If $\omega_i \leq 0.491, m_i = 0.37464 + 1.54226\omega_i - 0.26992\omega_i^2$ (A.2.10)

If $\omega_i > 0.491, m_i = 0.379642 + 1.48503\omega_i - 0.164423\omega_i^2 + 0.016666\omega_i^3$ (A.2.11)

The critical properties, T_{ci}, P_{ci} and ω_i, are the critical temperature, critical pressure and acentric factor respectively, which are shown in the table below (**Table A.2.1**) [16] (Table 2-106).

Table A.2.1 Critical properties in terms of each species

Species	T_{ci} [K]	P_{ci}[MPa]	V_{ci}	ω_i[-]
H_2	33.19	1.313	0.064147	-0.215993
N_2	126.2	3.4	0.08921	0.0377215
NH_3	405.65	11.28	0.07247	0.252608

The factor δ_{ij} and k_{ij} represent the binary interaction parameters between the different gas species. The first one is usually zero, while the second one can be calculated by the next equations, whose results are shown in the next table.

$$k_{ij} = \frac{1 - 8\sqrt{V_{ci}V_{cj}}}{({V_{ci}}^{1/3} + {V_{cj}}^{1/3})^3} \quad \text{(A.2.12)}$$

Table A.2.2 Binary interaction parameters of each gas

k_{ij}	H_2	N_2	NH_3
H_2	0	0.6495	0.8328
N_2	0.6495	0	0.5536
NH_3	0.8328	0.5536	0

❖ **Viscosity**

The viscosity of the gas mixture was calculated using the Wilke method [17], shown in the following equation:

$$\mu_{mix} = \sum_{i=1}^{N} \left(\frac{\mu_i y_i}{\sum_{j=1}^{N} y_i \phi_{ij}} \right) \quad \text{(A.2.13)}$$

Where μ_i is the viscosity of the single gas calculated with the following equation, retrieved from [16] (Table 2.138) together with the specific coefficient shown in the table below:

$$\mu = \frac{C_1 T^{C_2}}{1+\frac{C_3}{T}+\frac{C_4}{T^2}} \quad = \text{Pa·s with T [K]} \quad \text{(A.2.14)}$$

y_i and M_i are the molar fraction and molar mass of the single gas:

$$\phi_{ij} = \frac{\left[1+(\mu_i/\mu_j)^{1/2}+(M_i/M_j)^{1/4}\right]^2}{\left[8(1+M_i/M_j)\right]^{1/2}} \quad \text{(A.2.15)}$$

Table A.2.3 Specific coefficient of each species in the viscosity equation

Species	C_1	C_2	C_3	C_4
H_2	$1.797 \cdot 10^{-7}$	0.685	-0.59	140
N_2	$6.5592 \cdot 10^{-7}$	0.6081	54.714	0
NH_3	$4.1855 \cdot 10^{-8}$	0.9806	30.8	0

❖ **Specific heat**

The specific heat of the gas mixture was calculated as follows:

$$cp_{mix} = \sum_{i=1}^{N} y_i cp_i \quad \text{(A.2.16)}$$

Where c_{Pi} is the specific heat of the single species computed according to the correlation found in the [16] (Table 2.75)

$$cp = C_1 + C_2 \left[\frac{C_3/T}{sinh(C_3/T)}\right]^2 + C_4 \left[\frac{C_5/T}{cosh(C_5/T)}\right]^2 = \frac{\text{J}}{\text{kmol K}} \text{ with T [K]} \quad \text{(A.2.17)}$$

Table A.2.4 Specific coefficient of each species in the specific heat equation

Species	$C_1 \cdot 10^{-5}$	$C_2 \cdot 10^{-5}$	$C_3 \cdot 10^{-3}$	$C_4 \cdot 10^{-5}$	C_5
H_2	567.6	0.2761	0.0956	2.466	0.0376
N_2	909.79	0.29105	0.0816	1.7016	0.00103
NH_3	882	0.33427	0.4898	2.036	0.2256

❖ **Heat of reaction**

The heat of reaction was determined using the following correlation provided in [16] (Table 2.95), where T_{ref}=298 K.

$$\Delta H_r(T) = \Delta H_r(T_{ref}) + \int_{T_{ref}}^{T} \Delta c_P dT \quad \text{(A.2.18)}$$

❖ **Thermal conductivity**

The thermal conductivity of the gas mixture was calculated according to the general equation of Wassiljewa [17], which is expressed as follows:

$$\lambda_{mix} = \sum_{i=1}^{N} \frac{y_i \lambda_i}{\sum_{j=1}^{N} A_{ij} y_j} \quad \text{(A.2.19)}$$

Where λ_i is the thermal conductivity of each species, calculated via [16] correlation, where the single coefficient are reported in the table below:

$$\lambda = \frac{C_1 T^{C_2}}{1+\frac{C_3}{T}+\frac{C_4}{T^2}} = \frac{\text{W}}{\text{m K}} \text{ with T [K]} \quad \text{(A.2.20)}$$

Table A.2.5 Specific coefficient of each species in the thermal conductivity equation

Species	C_1	C_2	C_3	C_4
H_2	0.002653	0.7452	12	0
N_2	0.00033143	0.7722	16.323	373.72
NH_3	$9.66 \cdot 10^{-6}$	1.3799	0	0

While A_{ij} according to Mason and Saxena study [17] turns out to be exactly the same as ϕ_{ij}.

REFERENCES

[1] Z. Zhang, J.D. Way, C.A. Wolden, "Design and operational considerations of catalytic membrane reactors for ammonia synthesis", *AIChE Journal* 67 (2021). https://doi.org/10.1002/aic.17259.

[2] E. Kucuk, H. H. Koybasi, A.K. Avci, "Beyond equilibrium ammonia synthesis in a membrane and heat exchange integrated microreactor: A modeling study", *Fuel* 357 (2024) 129858. https://doi.org/10.1016/j.fuel.2023.129858.

[3] I. Rossetti, N. Pernicone, F. Ferrero, L. Forni, "Kinetic study of ammonia synthesis on a promoted Ru/C catalyst", *Ind. Eng. Chem. Res.* 45 (2006) 4150–4155. https://doi.org/10.1021/ie051398g.

[4] W. M. Rohsenow, J. P. Hartnett, Y. I. Cho, 3. "HEAT TRANSFER IN PACKED AND FLUIDIZED BEDS", in: Handbook of Heat Transfer, 1st Edition, 1998.

[5] J. Dirker, J.P. Meyer, "Heat Transfer Coefficients in Concentric Annuli", *J. Heat Transfer* 124 (2002) 1200–1203. https://doi.org/10.1115/1.1517266.

[6] S. Poto, F. Gallucci, M. Fernanda Neira d'Angelo, "Direct conversion of CO2 to dimethyl ether in a fixed bed membrane reactor: Influence of membrane properties and process conditions", *Fuel* 302 (2021). https://doi.org/10.1016/j.fuel.2021.121080.

[7] D. V. Laciak, G.P. Pez, P.M. Burban, "Molten salt facilitated transport membranes. Part 2. Separation of ammonia from nitrogen and hydrogen at high temperatures", *J. Memb. Sci.* 65 (1992) 31–38. https://doi.org/10.1016/0376-7388(92)87049-4.

[8] A. Bhown, E.L. Cussler, "Mechanism for Selective Ammonia Transport through Poly(vinylammoniumthiocyanate) Membranes", *J. Am. Chem. Soc* 113 (1991) 742-749. https://doi.org/10.1021/ja00003a002.

[9] Q. Wei, J.M. Lucero, J.M. Crawford, J. D. Way, C.A. Wolden, M.A. Carreon, "Ammonia separation from N2 and H2 over LTA zeolitic imidazolate framework membranes", *J. Memb. Sci.* 623 (2021). https://doi.org/10.1016/j.memsci.2021.119078.

[10] O. Camus, S. Perera, B. Crittenden, Y.C. Van Delft, D.F. Meyer, P.P.A.C. Pex, I. Kumakiri, S. Miachon, J.A. Dalmon, S. Tennison, P. Chanaud, E. Groensmit, W. Nobel, "Ceramic membranes for NH_3 recovery", *AIChE Journal* 52 (2006) 2055–2065. https://doi.org/10.1002/aic.10800.

[11] M. Kanezashi, A. Yamamoto, T. Yoshioka, T. Tsuru, "Characteristics of ammonia permeation through porous silica membranes", *AIChE Journal* 56 (2010) 1204–1212. https://doi.org/10.1002/aic.12059.

[12] J.A. Medrano, M.A. Llosa-Tanco, D.A. Pacheco-Tanaka, F. Gallucci, "Transport Mechanism and Modeling of Microporous Carbon Membranes", *Current Trends and Future Developments on (Bio-) Membranes: Microporous Membranes and Membrane Reactors*

(2019) 39–58. https://doi.org/10.1016/b978-0-12-816350-4.00002-7.

[13] A. Klinkenberg, H.J. Krajenbrink, H.A. Lauwerier, "Diffusion in a Fluid Moving at Uniform Velocity in a Tube", *Ind. Eng. Chem.* 45 (1953) 1202–1208. https://doi.org/10.1021/ie50522a024.

[14] J.S. Lopez-Echeverry, S. Reif-Acherman, E. Araujo-Lopez, "Peng-Robinson equation of state: 40 years through cubics", *Fluid Phase Equilib.* 447 (2017) 39–71. https://doi.org/10.1016/j.fluid.2017.05.007.

[15] J.N. Jaubert, F. Mutelet, "VLE predictions with the Peng-Robinson equation of state and temperature dependent kij calculated through a group contribution method", *Fluid Phase Equilib.* 224 (2004) 285–304. https://doi.org/10.1016/j.fluid.2004.06.059.

[16] D.W. Green, M.Z. Southard, Perry's Chemical Engineers' Handbook, McGraw-Hill Education, 2019. https://www.accessengineeringlibrary.com/content/book/9780071834087.

[17] R. C. Reid, J. M. Prausnitz, B. E. Poling, The Properties of Gases & Liquids, 4th Edition, (McGraw-Hill, 19

CHAPTER 3

Carbon molecular sieve (CMS) membranes for ammonia synthesis: experimental and theoretical analysis of transport mechanisms

ABSTRACT:
This chapter presents an experimental and theoretical investigation of phenolic-resin-derived CMS membranes, focusing on the effects of carbonisation temperature and transition-metal doping on membrane structure and gas transport. Tubular α-alumina supports were dip-coated with novolac-phenolic resin solution (11-13 wt%) containing formaldehyde (2.4 wt%) and ethylenediamine (0.4 wt%) in NMP; selected formulations also contained boehmite (0.6 wt%). Transition-metal dopants (Co, Cu, Ni, Zn) were added prior to coating to enhance ammonia selectivity, and the coated supports were pyrolysed at 500-700 °C under an oxygen-free atmosphere. Permeation experiments used pure gases (H_2, N_2, NH_3, He) and mixed-gas feeds at 150-350 °C up to 20 bar(g). Membrane characterisation included pore size distribution analysis via permporometry, surface morphology via confocal laser microscopy, and cross-sectional SEM imaging. Permporometry showed that higher carbonisation temperatures (700 °C) produce tighter ultramicroporous structures (~0.5 nm) with fewer surface adsorption sites, while lower temperatures (500-550 °C) yield more open, broader pore distribution. Arrhenius analysis confirmed that higher carbonisation temperatures favour molecular sieving, whereas lower temperatures promote surface diffusion. Mixed-gas experiments showed Cu-based membranes deliver superior overall permeance, though Ni- and Zn-doped membranes offer higher NH_3/H_2 selectivity (~2 at 150 °C).
A Gaussian pore-size/Langmuir adsorption model revealed distinct surface diffusion behaviours: at 150 °C, Cu showed the highest NH_3 surface diffusion contribution (~88%), followed by Ni (~70%); at 350 °C, Cu retained ~85% and Ni maintained >65%, demonstrating robust metal-NH_3 interactions. Zn-based membranes exhibited clear diffusion at 150 °C that declined sharply with temperature, while Co-based membranes lost almost all NH_3 surface diffusion at 350 °C. These findings establish that Cu-doped CMS membranes carbonised at the lower end of the temperature window (500-550 °C) are best suited for ammonia separation.

3.1 INTRODUCTION

A key element in the design of a membrane reactor is the membrane itself, since its properties largely determine the attainable permeation and separation performance and thus the reactor performance, as explained in Chapter 2. In the previous chapter, carbon molecular sieve (CMS) membranes were introduced at a general level; in this chapter, attention is focused on a detailed discussion of our investigation on CMS membranes, including their structure, transport mechanisms, and suitability for ammonia synthesis.

Carbon membranes are typically fabricated with an asymmetric architecture comprising at least two, and often three, porosity levels: a macroporous support (used for mechanical strength only, and frequently made of a ceramic material such as alumina) coated with a mesoporous intermediate layer that smooths the surface, followed by deposition of a thin microporous separation layer [1]. In fact, CMS membranes can achieve permeability-selectivity combinations that surpass the Robeson upper bound, which is representative of the best performance achieved by polymeric membranes [2]. To the best of current knowledge, however, there are no studies reporting the use of CMS membranes for ammonia synthesis. Nevertheless, several other membrane concepts have been investigated for ammonia separation under relevant catalytic conditions. Functionalised polymer and organosilica membranes (e.g. Poly(vinylammonium thiocyanate) [3], Nafion [4], Aquivion [5]) offer a favourable compromise between NH_3 permeability and selectivity and provide measurable performance improvements when integrated into ammonia membrane reactors. In parallel, novel inorganic or solvent-based systems exhibit very high intrinsic selectivities but are often limited by low permeance, stability issues, or challenges in scale-up, which restrict their suitability for large-scale ammonia production [6]. For instance, Na^+-gated nanochannel membranes display exceptional NH_3/H_2 and NH_3/N_2 selectivities (up to 10^3-10^4) but only moderate NH_3 permeance [7]. TPS-EtOH membranes can operate at approximately 300 °C with NH_3 permeance on the order of 10^{-7} mol·Pa^{-1}m^{-2}s^{-1} and NH_3/H_2 and NH_3/N_2 selectivities of about 7 and 266, respectively; yet their flux-selectivity balance still falls short of industrial requirements [8,9]. $ZnCl_2$-immobilised molten-salt (IMS) membranes exhibit outstanding ammonia separation performance at 300-350 °C, with NH_3/N_2 and NH_3/H_2 selectivities exceeding 10^4 and 10^7, but their long-term stability and durability under cyclic high-temperature operation remain uncertain [10].

These findings highlight the pressing need for NH_3-selective membranes that combine high permeance and selectivity with robust thermal and chemical stability and long lifetime at 300-350 °C. These requirements motivate the exploration of carbon molecular sieve membranes as alternative candidates for ammonia separation in membrane reactors.

As introduced in Section 1.5, CMS membranes are typically obtained by depositing a polymer precursor (e.g. phenolic resin) onto a porous support and subsequently carbonising it. Porous metallic supports (e.g., stainless steel or nickel-based alloys) could offer advantages in mechanical toughness, machinability, and heat transfer, which are attractive for reactor scale-up. However, their use may introduce challenges related to oxidation, corrosion, thermal-expansion mismatch, and potential interactions between the metal substrate and the polymer precursor during carbonisation.

The resulting pore size distribution and adsorption capacity, which governs gas separation selectivity, can be tuned by controlling the pyrolysis temperature, duration, and purge-gas flow rate during carbonisation [11]. During the pyrolysis of phenolic resins, pores begin to form around 500 °C and enlarge up to 700-800 °C; at higher temperatures, these pores shrink and eventually disappear near 1,000 °C [12]. Such structural evolution leads to pronounced differences in the gas separation properties of CMS membranes derived from phenolic resins [13]. For example, Poto et al. [14] studied the effect of carbonisation temperature between 450 °C and 750 °C, and reported that increasing carbonisation temperature gradually removes surface oxygen-containing groups. The -OH stretching band disappears at approximately 600 °C, reducing hydrophilicity, and between 600 °C and 700 °C ultramicropores emerge and molecular sieving becomes dominant, thereby increasing water permeance despite the reduced surface polarity. As a matter of fact, between approximately 300 and 500 °C, novolac-type phenolic resins undergo their primary decomposition step: the methylene and dimethylene-ether bridges, linking the phenolic rings, are progressively cleaved, releasing water, formaldehyde, CO, CO_2 and low-molecular-weight phenolic fragments as volatiles, while the aromatic rings largely persist [15]. In this range, the precursor has therefore lost much of its original cross-linked network but has not yet reorganised into the condensed, turbostratic sp^2-carbon skeleton that defines a molecular sieve: extensive dehydrogenative aromatic condensation, that knits the residual fragments into a stable carbon framework, only becomes significant from about 500 °C and proceeds progressively up to 700-900 °C [13,16]. Carbonisation confined to the 400-500 °C range is therefore inherently incomplete, leaving a solid that still contains a substantial fraction of uncondensed, oxygen- and hydrogen-rich fragments (residual -OH, C=O and aliphatic bridges) rather than a fully aromatised carbon matrix [17]. The retained oxygenated and aliphatic functionalities render the layer chemically metastable: such groups can continue to decompose, rearrange and outgas on further thermal or reactive exposure, and are known to interact strongly with reactive gases such as ammonia [18,19]. Consequently, the pore structure and separation performance of a membrane carbonised in this range would be expected to drift during operation rather than remain stable.

Given the risk of incomplete carbonisation and the resulting chemical instability below this range, the carbonisation temperatures explored in this study were therefore restricted to 500-700 °C, with 500 °C set as the lower bound.

Recent studies have also focused on developing metal-doped carbon membranes to further control pore size and adsorption capacity. For example, Teixeira et al. [20] doped a phenolic-resin precursor with boehmite (AlO(OH)) nanoparticles to form composite CMS membranes and investigated how this modification influences structure, adsorption, and gas transport. The embedded Al_2O_3 nanowires, derived from boehmite, altered the carbon microstructure, resulting in higher olefin/paraffin selectivity while maintaining practical permeance compared with undoped phenolic-derived CMS membranes. Rahimalimamaghani et al. [21] prepared aluminium-doped novolac-derived CMS membranes, by incorporating different amounts of aluminium acetylacetonate ($Al(acac)_3$). The aluminium was present in the membrane in the form of boehmite (γ-AlO(OH)) and/or γ-Al_2O_3, and the effect of Al content on H_2/N_2 transport was systematically evaluated. The permeances of H_2 and N_2 exhibited a volcano-type dependence on aluminium content, with the optimal performance observed at an $Al(acac)_3$ loading of approximately 4 wt%. Wu et al. demonstrated that using different combinations of small organic molecules and metal additives enables tuning of surface functionalities (N, O, S groups and metal doping), pore structure, morphology, and graphitic order [22]. Incorporation of metal species has long been known to affect gas transport by modifying surface-gas interactions and by introducing additional porosity or enlarged pore channels [23–25].

Although systematic studies of metal additives in CMS membranes remain limited, numerous investigations have examined the effect of metals in carbon-based adsorbents. For instance, Bandosz et al. explored the influence of metal chlorides and oxides impregnated into activated carbon for ammonia adsorption. They found that higher metal loadings (e.g., 10 wt% Zn, 5-10 wt% Cu) led to substantially enhanced NH_3 uptake, with adsorption capacities 43-70 times greater than those of pristine activated carbon [19]. In a follow-up work, the same authors reported that metal impregnation increased surface acidity, thereby further improving NH_3 sorption capacity [18].

Similar trends have been observed in the development of ammonia sensors. Li et al. investigated graphene oxide hybrids containing central metal atoms (Cu, Co, Ni) and found that stronger adsorption energies were correlated with shorter NH_3-metal bond lengths and higher net charge transfer. Among the tested metals, cobalt exhibited the strongest interaction with ammonia, followed by copper and nickel [26]. Enhancements related to metal incorporation were also noted in zinc-modified amphiphilic phthalocyanines [27], and copper-substituted phthalocyanines, both of which displayed improved sensing and adsorption performance [28].

These findings illustrate that metal additives can systematically tune the interaction

strength between ammonia and a solid surface, which in energetic terms corresponds to modifying the potential energy profile experienced by the permeating molecule. This concept is schematically depicted in **Figure 3.1**, where panel A represents the introduction of an attractive interaction and panel B a repulsive one. In the attractive case, the additional interaction lowers the potential energy near the pore wall, creating a deeper minimum and effectively reducing the activation barrier for permeation. In contrast, a repulsive interaction raises the energy in the vicinity of the wall, increasing the barrier and suppressing permeation. When such attractive interactions are selective for NH_3 relative to H_2 and N_2, they can be exploited to enhance ammonia separation in metal-doped CMS membranes.

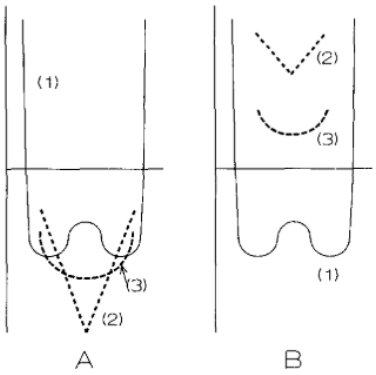


Figure 3.1 Schematic representation of the influence of attractive and repulsive interactions on the energy barrier encountered by a permeating molecule within a pore [29]

The role of pore size in shaping the potential energy profile is illustrated in **Figure 3.2**, which shows the potential energy function E of a permeating molecule as a function of pore size d_p. For wide pores ($d_p \geq 2$ nm), shallow minima near the walls arise from weak attractive interactions. The gas transport properties of CMS membranes arise from a bimodal pore size distribution consisting of larger micropores (7-20 Å) and smaller ultramicropores (< 7 Å). The micropores provide substantial pore volumes (> 0.1 $cm^3\ g^{-1}$) and high gas permeability, whereas the ultramicropores enable selective diffusion among closely sized penetrants, allowing precise molecular discrimination [16]. As the pore narrows to the nanometer and sub-nanometer range, the interaction potentials of opposing walls begin to overlap, deepening the potential wall and eventually generating a significant energy barrier that must be overcome for transport. This picture directly underpins the dominant gas-transport mechanisms in CMS membranes. Because CMS pores are typically smaller than 2 nm, transport is governed by activated diffusion, comprising molecular sieving and selective adsorption/surface diffusion. In molecular sieving, pore sizes are comparable to the kinetic diameters of NH_3, H_2, and N_2, so the overlapping wall potentials shown in **Figure 3.2** determine which species can enter

and traverse the pores. In selective adsorption/surface diffusion, metal dopants and surface functional groups modulate the attractive part of the potential, as in **Figure 3.1**, selectively lowering the energy barrier for ammonia and thereby enhancing its permeation relative to hydrogen and nitrogen. It is influenced by the interactions between molecules and pore wall, but also particle-particle interactions such as van der Waals and electrostatic forces [30]. When the pore size is in the same order of magnitude as the permeating molecule, the effect of the adsorbed layer on the permeation cannot be neglected [31].

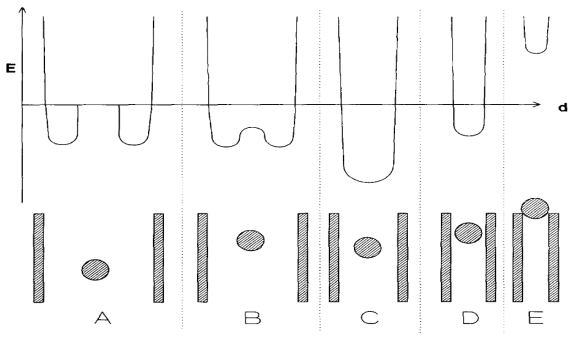


Figure 3.2 Schematic representation of the energy function E of the permeating molecule vs. the pore size d_p. A: $d_p \geq 2$ nm. B: d_p = 1-2 nm. C: d_p = 2-3 molecule diameters. D: d_p = 1-2 molecule diameters. E: $d_p \leq 1$ molecule diameter

This potential energy profile can be strategically tuned using doping materials, particularly transition metals such as Zn, Co, Ni, and Cu, which is the main motivation for investigating metal-doped CMS membranes in this work. By modifying molecule-wall interactions through their distinct oxidation states, thermal stability, and *d*-orbital configurations, these metals can selectively lower the energy barrier for ammonia.

It is important to note that when the pore size is comparable to the molecular dimensions of the permeating species, the contribution of the adsorbed layer to overall transport becomes significant, and both molecular sieving and surface diffusion may operate simultaneously. In practice, it is therefore important to discriminate which of these two activated mechanisms dominates under given conditions. This is commonly done by analysing the temperature dependence of the flux or permeability using an Arrhenius-type relation, from which an apparent activation energy for transport can be extracted. To formalise this analysis, the molar flux through the membrane pores can be expressed for each transport mechanism, and related to a temperature-dependent diffusion coefficient. Besides pore structure and surface chemistry, temperature is a key operating parameter determining which mechanism dominates [32].

The molar flux through the pore for each mechanism is defined as (Equation (3.1)):

$$J = -D_{Fick,i}\Gamma_i(T,P)\frac{\partial \mathrm{C}}{\partial \mathrm{x}} \tag{3.1}$$

Where J is expressed in mol·m^{-2}s^{-1}, $D_{Fick,i}$ is the Fickian diffusion coefficient, and $\Gamma_i(T,P)$ is a thermodynamic correction factor [33]; the specific form of $D_{Fick,i}$ depends on the prevailing transport mechanism.

For activated processes, the molar flux is expressed as in the following Equation:

$$J_i = \frac{\Delta P}{RTL} D_0(T) exp\left\{\frac{-(E_{a,i} - E_{ads})}{RT}\right\} \tag{3.2}$$

For pores in the microporous/ultra-microporous regime, the overall apparent activation energy combines the contributions from transport through the pore constriction and from adsorption. In activated surface diffusion, the energy difference $\Delta E_S = E_{a,S} - E_{ads}$ can be positive or negative, depending on whether the transport activation energy $E_{a,S}$ exceeds the heat of adsorption E_{ads} or not [33]. When $\Delta E_S < 0$, the surface diffusion contribution to flux decreases with increasing temperature, whereas for $\Delta E_S > 0$ it increases. By contrast, transport governed by molecular sieving through a pore constriction typically increases with temperature, since $E_{a,M} > E_{ads}$ [34].

In contrast to ultra-microporous CMS membranes, mesoporous membranes operating at low temperatures with gas mixtures containing both non-adsorbing permanent gases and condensable vapours can exhibit a condensation-permeation mechanism: separation is achieved by capillary condensation of the vapour in mesopores on the feed side and its release on the permeate side by vaporisation or desorption [35]. Because this mechanism relies on Kelvin equation-governed vapour-liquid equilibrium in mesopores, and the permeation experiments in this work were all conducted at 150-350 °C, above ammonia's bulk critical temperature (132 °C), classical capillary condensation as described above is not expected to occur in the ultramicroporous CMS membranes studied here. However, the strong overlap of pore-wall potentials in such narrow pores (**Figure 3.2**) can still enhance ammonia's local adsorption well beyond that of a flat surface, giving rise to an adsorption/surface diffusion dominated transport contribution rather than a true capillary-condensation mechanism, consistent with the pronounced adsorption-diffusion behaviour observed for NH_3 in Section 3.4.1. As temperature increases, condensed phases disappear and surface pores effectively become larger, allowing non-adsorbing molecules to enter and pass through more easily. The higher molecular energy and more frequent molecule-wall collisions give rise to Knudsen diffusion, whose effective diffusivity depends on the membrane geometry $\left(D_{K,c} = \frac{d_p}{3}\sqrt{\frac{8RT}{\pi M}}\right)$. Knudsen-type behaviour can also persist in the micropore range when adsorption diffusion contributes significantly. In such cases, membranes that exhibit high selectivity at low temperature may exhibit declining performance at

higher temperature, with the separation factor approaching the ideal Knudsen selectivity (Equation (3.3)) :

$$S_{i/j}^{Kn} = \sqrt{\frac{M_j}{M_i}} \tag{3.3}$$

where M_j and M_i are the molecular weights of components j and i.

With the development of CMS membranes, different transport models have been proposed to describe and predict the interplay of these mechanisms during gas permeation, providing a framework to interpret experimental activation energies and guide membrane design [33,36,37].

Several mechanistic descriptions of surface diffusion exist in the literature. The most common are: the hopping (site-to-site) model, in which molecules jump between discrete adsorption sites by overcoming an activation barrier; Fickian surface diffusion with a Darken (thermodynamic) correction, which treats the adsorbed phase as a continuous film and accounts for non-ideality via a concentration-dependent correction factor [38]; and Maxwell-Stefan surface diffusion, which formulates transport in terms of driving forces and friction coefficients and can, in principle, describe multicomponent coupling and coverage effects more rigorously [39]. The hopping model is physically intuitive for microporous solids with well-defined adsorption sites and leads to relatively simple expressions that can be coupled to Langmuir adsorption. In this picture, the system can be represented as a Langmuir lattice, where the lattice intersections correspond to surface atoms of the pore wall [40]. At these positions, the potential energy exhibits local maxima, whereas the lowest potential energy is found at the centres of the lattice cells, which represent adsorption sites (potential wells). To "hop" from one site to the next, the molecule must cross the potential barrier along the path connecting two adsorption sites, i.e. the saddle point between neighbouring wells. Within this framework, surface diffusion is strongly influenced by pressure, because in the Langmuir description the surface coverage and the density of the adsorbed phase increase with increasing pressure, thereby enhancing the contribution of surface diffusion to the overall flux [30].

In this chapter, two key parameters governing the performance of CMS membranes are investigated: the carbonisation temperature and the functionalisation of the polymer precursor. The influence of carbonisation temperature on the gas transport mechanism is first elucidated by an Arrhenius-type analysis of permeation data. Subsequently, metal-doped carbon membranes derived from functionalised polymers are examined, and their behaviour is interpreted using transport modelling to clarify how specific metal-molecule interactions affect membrane performance.

3.2 EXPERIMENTAL

3.2.1 Membrane preparation

The carbon membranes used in this study were prepared by TECNALIA via a one-step dip-dry-carbonisation procedure previously reported in [41], using novolac-phenolic resin as polymer precursor. The dipping solution, containing novolac-phenolic resin, formaldehyde, and ethylenediamine dissolved in N-methyl-2-pyrrolidone (NMP), was heated to 90 °C for 90 min to induce polymerisation/crosslinking. After completion of the polymerisation step, an aqueous metal-salt solution (nitrate or acetate) was added and the resulting solution was used for dip-coating the supports.

Table 3.1 Composition of dipping solutions and carbonisation temperatures for the carbon membranes prepared in this study

Code	Metal wt%	Boehmite wt%	Novolac wt%	Formaldehyde wt%	Ethylenediamine wt%	T_{carb} [°C]
T-99-Co	0.056	0.6	13	2.4	0.4	500
T-94-Co	0.02	0.6	13	2.4	0.4	500
T-116-Cu	0.088	0.6	13	2.4	0.4	500
T-112-Cu	0.049	0.6	13	2.4	0.4	500
U-37-Zn	0.11	0.6	13	2.4	0.4	500
U-33-Zn	0.07	0.6	13	2.4	0.4	500
U-26-Ni	0.07	0.6	13	2.4	0.4	500
U-24-Ni	0.05	0.6	11	2.4	0.4	500
U-99-Ni	0.15	0	11	2.4	0.4	550
U-101-Ni	0.15	0	11	2.4	0.4	700

Tubular α-alumina supports with outer/inner diameters of 10/7 mm, respectively, and a length of 7-15 cm were employed as supports for the membranes layer because, as previously mentioned, they combine high mechanical strength with excellent thermal and chemical stability. The support pore size (~200 nm) is much larger than the CMS pores, so transport resistance is dominated by the selective carbon layer rather than the substrate. One end of each tube was sealed, while the other was connected to a dense alumina tube using glass sealings for testing. The membranes produced, tested, and analysed in this chapter are summarised in **Table 3.1**.

It should be noted that the reported metal weight percentages refer to the composition of the dip-coating solution and not to the final metal loading in the carbonised membranes.

3.2.2 Gas permeation experimental setup

For the gas permeation experiments, two different experimental setups were employed, mainly depending on the pressure range investigated. Prior to describing the setups, the key performance indicators used to assess membrane performance are defined below.

❖ **Performance indicator**

Membrane performance was evaluated in terms of permeance and selectivity. Permeance quantifies how much material passes through the membrane per unit area and time, per unit driving force, and can be defined on a volumetric, mass, or molar basis. The permeation rate may be driven by gradients in total pressure, partial pressure, concentration, or, in some cases, electrical potential. For the pressure-driven experiments in this study, the gas permeance was calculated as in Equation (3.4):

$$\mathcal{P}_i = \frac{\Phi_{i,perm}}{\Delta p_i \, A_{mem} \, V_{m,i}} \tag{3.4}$$

Here, $\Phi_{i,perm}$ is the volumetric flow of species i in the permeate side, Δp_i is defined as the (total or partial) pressure gradient across the membrane, A_{mem} is the external area of the membrane and $V_{m,i}$ is the standard molar volume of species i. It is therefore important to specify whether Δp_i (Equation (3.5)) refers to total pressure or partial pressure when comparing permeance data.

$$\Delta p_i = p_i^R - p_i^P \tag{3.5}$$

Selectivity is the key parameter for assessing the quality of a separation, as higher selectivity generally leads to higher product purity [42]. Since the selectivity can deviate significantly between single-gas permeation tests and mixed-gas permeation test [43], a distinction is made between ideal selectivity (Equation (3.6)), calculated from pure gas permeances, and separation factor (Equation(3.7)), obtained directly under mixed conditions [44].

$$S_{i/j} = \frac{\mathcal{P}_i}{\mathcal{P}_j} \tag{3.6}$$

The separation factor $\alpha_{i/j}$ normalizes the permeate composition by the feed composition, as shown in the following equation.

$$\alpha_{i/j} = \frac{\left(\frac{y_i}{y_j}\right)_{permeate}}{\left(\frac{y_i}{y_j}\right)_{feed}} \tag{3.7}$$

Unless otherwise stated, all permeance and selectivity values reported in this chapter are averages of multiple chromatographic and/or film-flow-meter readings obtained

after steady state had been reached at each temperature and pressure; individual raw readings are not plotted.

❖ High-pressure permeation setup

A high-pressure, high-temperature membrane reactor was used for permeation experiments with pure hydrogen, nitrogen, and their mixtures. The setup can operate up to 60 bar(g) and 600 °C; a schematic is shown in **Figure 3.3**. Gas inflow is directed by pneumatic valves and the flow rate is controlled by mass flow controllers (MFCs) with maximum capacities of 50 $L \cdot min^{-1}$ for N_2 and 150 $L \cdot min^{-1}$ H_2, although the system can also handle CO, CO_2, and air, which were not used in this work. After the MFCs, the gas is preheated (up to 400 °C) and then fed from the bottom into the reactor.

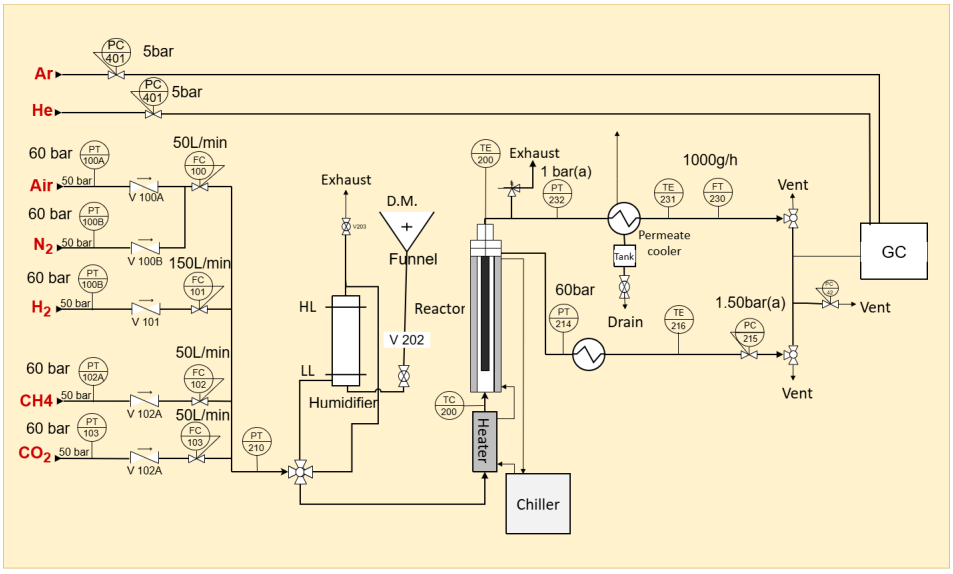


Figure 3.3 P&ID of the high-pressure setup

The reactor temperature is monitored and controlled using two thermocouples (TC-200, TC-201), located on the upper and lower parts of the reactor wall, while an internal thermocouple (TE 200) measures the gas temperature inside the reactor. The retentate pressure is regulated by a back-pressure regulator, and the permeate side is maintained at 1 bar(a). Flow rate and composition of both permeate and retentate streams are determined using a film flow meter (Horiba Stec VP1-VP2-VP4) and a gas chromatograph (490 MicroGC), respectively, after which the gas is vented. The experiments performed with this setup included pure hydrogen, pure nitrogen, and binary H_2:N_2 mixtures with volumetric ratios of 60:40 vol%. For each temperature level, beginning at 150 °C, the experimental protocol consisted of testing pure N_2 at 20, 15, 10, 5, and 1 bar(g) (in descending order), followed by pure

H_2 at the same pressures in the same order. This descending sequence was adopted for operational reasons: starting from the highest pressure and stepping down allowed the retentate pressure and permeate flow to reach a stable value. The same pressure sequence was then applied to the 60:40 vol% H_2:N_2 mixtures. After completion of the full pressure series for all gas compositions, the temperature was increased in steps of 50 °C and the procedure was repeated, until 350 °C.

❖ **Ammonia setup**

Experiments with ammonia were performed in a dedicated ammonia setup, schematically shown in **Figure 3.4**. The temperature range matched that of the high-pressure setup, while maximum pressure was limited to 8 bar(g) to prevent ammonia liquefaction under near-ambient conditions. N_2, H_2, He, NH_3 and CH_4 were supplied through mass flow controllers (MFC 100-101-102-104 from Bronkhorst) that could direct flows either to the reactor vessel or directly to the permeate side via a bypass line. The feed mixture flowed downward through a preheating coil surrounding the reactor within the oven, then entered the SS310 reactor tube (ID 4.5 cm, active length 28 cm) at the bottom and travelled upward. Along this path, part of the gas permeated to the permeate side (1 bar(a)) while the remaining gas exited through the retentate side, controlled via a back-pressure regulator.

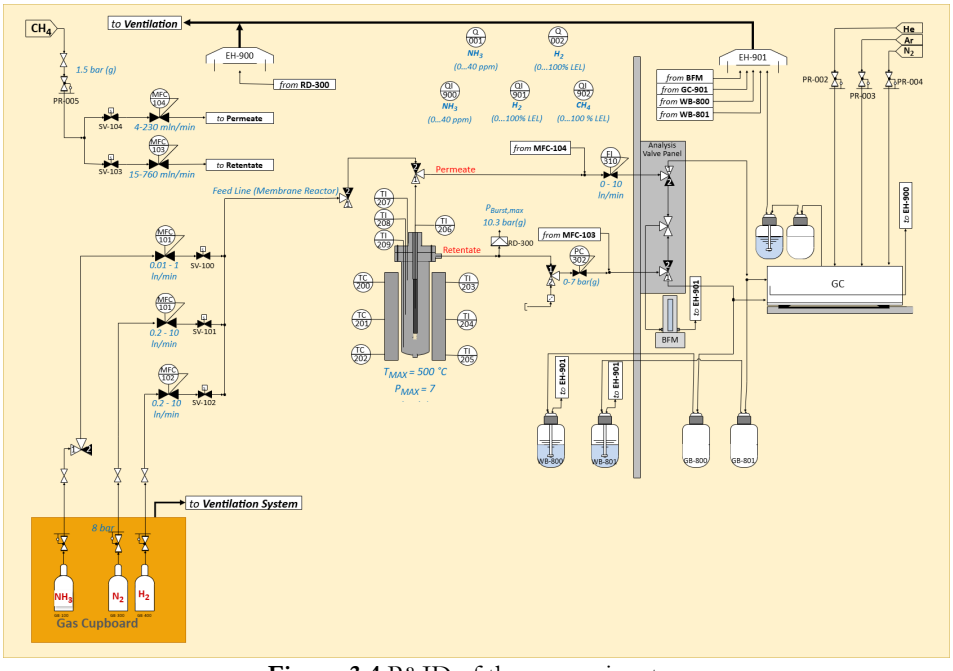


Figure 3.4 P&ID of the ammonia setup

The reactor assembly was housed in a three-zone electric split oven (top, middle, bottom), with independent thermocouples and controllers ensuring uniform

temperature distribution. Both retentate and permeate streams were fed into compact GC4.0 (Global Analyser Solutions) and Horiba STEC VP Series film flow meters (VP1-VP2-VP4) for composition and flow measurements respectively, selectable via hand valves (HV-402, HV-500, HV-302). Methane served as the GC internal standard. Film flow meters were also used to calibrate MFCs for N_2, H_2, He, CH_4, but were unsuitable for ammonia due to soap film dissolution. NH_3 MFC calibration used GC analysis of known CH_4 flows mixed with unknown ammonia quantities. Finally, water traps treated both streams before safe venting.

Tests covered 150-350 °C, at 5, 4, 2, 1 bar(g) using pure ammonia or a mixture simulating 20% H_2 conversion. For the latter, gas compositions matched expected concentrations after 20% H_2 conversion with H_2:N_2 = 1.5 feed ratio: 51.4% H_2, 40.0% N_2, and 8.6% NH_3.

In both the high-pressure and ammonia setups, the permeate side was operated at atmospheric pressure (1 bar(g)) and at the same temperature as the retentate, without sweep gas.

3.2.3 Permporometer setup

Pore size distribution was determined using a permporometry setup based on the method of Tsuru et al. [45] (**Figure 3.5**), which relies on capillary condensation principles described in Section 3.1. Prior to each experiment, membranes were dried at 300-400 °C under nitrogen carrier flow to remove pore-blocking residues. When the experiment started, two helium streams were fed to the tubular reactor (housed in a Carbolite Gero LHT 6/60 oven) at 70 °C: a dry He stream, and a wet stream where He carried water vapour generated by a Chemyx Fusion 200 syringe pump, and evaporated via preheater coil. A ΔP = 2 bar was maintained (retentate at 3 bar, permeate at 1 bar) and controlled via pressure sensor. Dry and wet He streams were set to fixed flow rates, with water injection rates calculated for targeted pore sizes using the Kelvin equation (Equation (3.8)) and Arden Buck saturation pressure correlation (P_{sat}). Permeate He flow was measured using Horiba STEC VP1/VP3 high precision film flow meters.

$$\ln\left(\frac{P}{P_{sat}}\right) = -\frac{2\gamma V_m}{r_p RT} \tag{3.8}$$

It is important to note that the use of helium as the carrier gas limits the detectable pore size range. Pores smaller than the kinetic diameter of helium (~0.26 nm) cannot be accessed by the condensing water vapour and are therefore not detected by this method. This constraint defines the lower boundary of the pore size measurement. Water injection rates were then incrementally increased to condense vapour in successively larger pores. After each step, the system stabilised for ≥ 30 min until permeate flow remained constant (checked every 5 min). Pore density at each radius was derived from stepwise permeate flow drops (Equation (3.9)):

$$n_{p,i} = \frac{F_{vol,i-1} - F_{vol,i}}{\frac{\pi}{4} r} \tag{3.9}$$

Cumulative analysis yielded the percentage distribution vs. pore radius, characterizing active membrane pores.

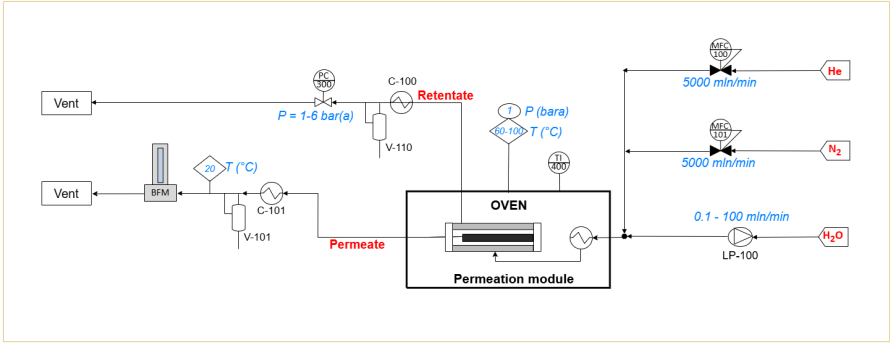


Figure 3.5 P&ID of the permporometer setup

3.2.4 Confocal laser microscope

Surface defects and irregularities on carbon membranes were characterised using confocal laser microscopy with the Keyence VK-X3000 Series 3D Surface Profiler. Variable objective lenses enabled selection of appropriate resolution and magnification for membrane imaging. From these measurements, key roughness parameters were extracted: arithmetic mean roughness R_a (average deviation from the mean plane) and R_z (average of five highest peaks and five deepest valleys).

3.2.5 Scanning electron microscopy (SEM)

The cross-sectional morphology of the membranes was examined using a FEI Quanta 3D FEG scanning electron microscope operated in high-vacuum mode with secondary electron detection. Images were collected at an accelerating voltage of 5-10 kV and a working distance of 10 mm. The membrane samples were prepared by razor-blade cutting, to expose the cross section.

3.3 MATHEMATICAL MODEL

For the investigation of the transport mechanisms associated with the metal-doped carbon membrane, the model developed and described by Sahin et al. [46] was employed.

In the development of this model, the following assumptions were taken into account:

- The (nano)porous membrane is represented as an assembly of parallel, perfectly cylindrical capillaries whose radii follow a normal (Gaussian) pore size distribution.
- Gas transport within these pores is driven by the pressure gradient across the membrane thickness and is coupled to adsorption-desorption equilibria at the internal pore surface.
- Macroscopic transport resistances outside the selective layer (such as concentration polarisation or resistance in the support) are assumed to be negligible.
- Exchange between gas-phase and adsorbed species within the membrane during permeation from retentate to permeate is considered insignificant and is therefore neglected.
- Each capillary is assumed to have a uniform diameter over its entire length.
- Transport through occasional voids or defects in the carbon matrix is considered minor compared to transport through the defined pore network.
- Phenomena related to capillary condensation and critical capillarity are not taken into account.

Based on these assumptions, the model is formulated for a total molar flux, expressed as the sum of a gas-phase contribution and a surface (adsorbed-phase) contribution, shown in Equation (3.10).

$$J_{tot} = J_{tot}^{g} + J_{tot}^{s} \tag{3.10}$$

In this framework, the gas-phase term accounts for the combined effect of viscous flow, slip flow, Knudsen diffusion, and molecular sieving. For carbon molecular sieve membranes, viscous and slip flow are not expected to contribute significantly due to the narrow pore size range; therefore, only Knudsen diffusion and molecular sieving are considered in the gas-phase transport term.

3.3.1 Modified Knudsen diffusion model

Knudsen diffusion typically becomes relevant for pores larger than about 2 nm. However, since this boundary is not absolute and pores close to 2 nm may be present, the possible contribution of micro-Knudsen diffusion in the 0.5-2 nm range was examined [33]. To capture this regime in the model, conventional Knudsen correlations are retained, but the pore diameter is replaced by an effective diameter (Equation (3.11)) defined as the actual pore size minus the kinetic diameter of the permeating molecule.

$$r_{eff} = r_p - r_{molecule} \tag{3.11}$$

In the model implementation, Knudsen diffusion was evaluated for pores with diameters between 0.5 nm (minimum relevant pore size) and 50 nm (ensuring complete coverage of the microporous range). Within this framework, tortuosity was used as a key fitting parameter to capture the Knudsen contribution to overall transport (Equation (3.12)).

$$J_{Kn}^{eff} = \frac{\varepsilon r_{eff}}{\tau}\sqrt{\frac{32}{9\pi RTM_W}}\frac{\Delta p}{\delta_{mem}^{act}} \tag{3.12}$$

3.3.2 Molecular sieving model

Permeation by molecular sieving for a component j is described by Equation (3.13), which includes a molecular sieving factor $C_{ms,j}$ (Equation (3.16)) and an activation energy, both of them as fitting parameters. However, the experimental data also allow an independent estimation of this activation energy, which substantially narrows the fitting window and improves the robustness of the parameter regression. For molecular sieving, the dominant fitting parameters are therefore the molecular sieving coefficient and the corresponding activation energy.

$$J_{ms}^{eff} = C_{ms,j} exp(-\frac{E_{act,ms,j}}{RT})\frac{\Delta p}{\delta_{mem}^{act}} \tag{3.13}$$

The overall expression for the molar flux is given in Equation (3.14), where the pore size distribution enters through a normal-distribution function (Equation (3.15)). This probability density function weights the contribution of pores of different radii to the total flux and thus links the structural PSD to the effective transport behaviour. It is evaluated using the pore radius r, the total number of pores n_p, and the standard deviation of the pore size σ_N, all of which are treated as fitting parameters. This expression is a Gaussian integral which can be solved algebraically.

$$J_{tot}^{g} = \sqrt{\frac{\pi}{2}}\frac{n_p}{\sigma_N A_{mem}}\frac{\Delta p}{\delta_{mem}^{act}}\left[\int_{r_{Kn}^{low}}^{r_{Kn}^{high}} \frac{Q_3(r)}{\tau}\sqrt{\frac{32}{9\pi RTM_W}}dr + \int_{r_{ms}^{low}}^{r_{ms}^{high}} Q_2(r)C_{ms}'\exp(-\frac{E_{act,ms}}{RT})dr\right] \tag{3.14}$$

$$Q_k(r) = r^k exp\left[-\frac{1}{2}\left(\frac{r-\bar{r}}{\sigma_N}\right)^2\right] \tag{3.15}$$

$$C_{ms}' = \frac{C_{ms}}{\varepsilon} = \frac{D_0 S_0}{\varepsilon} \tag{3.16}$$

The final integral form (Equation (3.17)) thus employs the above parameters together with the mean pore radius $\bar{r}$ and integration bounds a_k and b_k, which are themselves functions of r, $\bar{r}$, and σ_N. The subscript k indicates which set of fitting expressions must be used, corresponding to the particular gas transport mechanism under consideration and the original work provides a table specifying the appropriate forms of a_k and b_k for each case [46].

$$\int Q_k(r)dr = -\sigma_N \left[\sigma_N a_k \, exp\left[-\frac{1}{2}\left(\frac{r-\overline{r}}{\sigma_N} \right)^2 \right] + b_k \sqrt{\frac{\pi}{2}} \left(erf\left[\frac{\overline{r}-r}{\sigma_N \sqrt{2}} \right] - 1 \right) \right] \quad (3.13)$$

3.3.3 Surface diffusion model

Surface diffusion, which can become significant at low temperature and/or high pressure, was described using the model proposed in the same work, where several alternative formulations were evaluated. Ultimately, a simplified approach was selected in which the adsorbed phase is assumed to form a thin, uniform film on the pore walls; this choice was motivated by its lower number of fitting parameters compared to more complex surface diffusion models. In this framework, the total flux associated with surface transport is given by Equation (3.18), where the adsorbed amount per unit membrane mass q is described by an isotherm model, and the specific internal surface area S_S is calculated assuming perfect cylindrical capillaries (Equation (3.19)) with a shape-weight factor C_{sw}, combined with the pore size distribution expression (Equation (3.20)) to yield Equation (3.21).

$$J_{tot,j}^{S} = \frac{RT\rho_{mem}^{app}}{\tau^2 C_{R,j} S_S \delta_{mem}^{act}} p \int_{p_{perm,j}}^{p_{ret,j}} \frac{q_{ads,j}^2}{p} dp \quad (3.18)$$

$$S_S = 2\pi r_p l_p C_{sw} \quad (3.19)$$

$$N_N(r) = \frac{n_p}{\sqrt{2\pi}\sigma_N} \exp\left[-\frac{1}{2} \left(\frac{r-\overline{r}}{\sigma_N} \right)^2 \right] \quad (3.20)$$

$$S_S = \sqrt{2\pi} \frac{n_p}{\sigma_N} \delta_{mem}^{act} C_{sw} \int_{r_{su}^{low}}^{r_{su}^{high}} Q_1(r)dr \quad (3.21)$$

This leads to the final surface-transport flux expression in Equation (3.22), in which the adsorbed loading $q_{ads,j}$ is evaluated via a Langmuir isotherm (Equation (3.23)) and the corresponding equilibrium coefficient is expressed with an Arrhenius-type temperature dependence (Equation (3.24)).

$$J_{tot,j}^{S} = \frac{RT\rho_{mem}^{app}}{\tau^2 C_{R,j} C_{sw} (\delta_{mem}^{act})^2 \sqrt{2} \frac{n_p}{\sigma_N}} \frac{\int_{p_{perm,j}}^{p_{ret,j}} \frac{q_j^2}{p} dp}{\int_0^{r_{max}} Q_1(r)dr} \quad (3.22)$$

$$q_{ads,j} = q_{ads,m,j} \frac{C_{L,j} p_j}{1 + C_{L,j} p_j} \quad (3.23)$$

$$C_{L,j} = C_{L,j}^0 exp\left(-\frac{\Delta H_{ads,j}}{RT} \right) \quad (3.24)$$

Substituting these relations into the isotherm integral in Equation (3.22), it gives Equation (3.25); the resulting in the closed-form expression for the surface flux is reported in Equation (3.26).

$$\int_{p_{perm}}^{p_{ret}} \frac{q_m^2}{p}\left(\frac{C_L p}{1+C_L p}\right)^2 dp = q_m^2\left(\frac{1}{C_L p_{ret}+1} - \frac{1}{C_L p_{perm}+1} + \ln\left(\frac{C_L p_{ret}+1}{C_L p_{perm}+1}\right)\right) \quad (3.25)$$

$$J_{tot,j}^{S} = \frac{RT\rho_{mem}^{app}}{\tau^2 C_{R,j} C_{sw} (\delta_{mem}^{act})^2 \sqrt{2}\frac{n_p}{\sigma_N}} \frac{q_m^2\left(\frac{1}{C_L p_{ret}+1} - \frac{1}{C_L p_{perm}+1} + \ln\left(\frac{C_L p_{ret}+1}{C_L p_{perm}+1}\right)\right)}{\int_0^{r_{max}} Q_1(r)dr} \quad (3.26)$$

3.3.4 Fitting parameters

All governing equations described in the previous sections were implemented in the model and used in a comprehensive parameter estimation procedure. Three global optimisation algorithms were available (Global Search, Particle Swarm, and Genetic Algorithms) and Particle Swarm Optimisation (PSO) was selected as the most suitable for the relatively high-dimensional parameter space. In PSO, a population of particles with initial positions and velocities explores the parameter space; at each iteration, the objective function is evaluated for all particles, velocities are updated based on individual and global best positions, and the swarm is iteratively driven toward the optimum [47].

Parameter estimation was formulated as the minimization of the sum of squared residuals (SSR) between experimental and predicted molar fluxes (Equation (3.27)), a standard least-squares criterion that quantifies how well the model reproduces the measured data. The coefficient of determination R^2 (Equation (3.28)) was additionally calculated to assess the goodness of fit, providing a complementary measure of how much of the variance in the experimental fluxes is captured by the model.

$$SSR = \sum_{i=0}^{n} (J_{exp,i} - J_{num,i})^2 \quad (3.27)$$

$$R^2 = 1 - \frac{\sum_{i=0}^{n}(J_{exp,i} - J_{num,i})^2}{\sum_{i=0}^{n}(J_{exp,i} - \overline{J_{exp}})^2} \quad (3.28)$$

3.4 RESULTS AND DISCUSSION

To systematically investigate the performance of CMS membranes for ammonia separation, as already mentioned, two key design parameters were examined: carbonisation temperature and metal doping. The study was carried out in two parts. First, the effect of carbonisation temperature was examined by comparing two membranes of identical composition carbonised at 550 °C and 700 °C. Because only one membrane per temperature was tested, sample-to-sample variability cannot be fully separated from the temperature effect. The comparison should therefore be seen as indicative of a trend rather than a definitive optimum; additional temperatures and replicate membranes would be needed to confirm this finding. Second, metal-doped membranes prepared at the selected temperature were

characterised to elucidate the role of transition metal additives in enhancing ammonia selectivity.

3.4.1 Effect of carbonisation temperature on CMS membranes

The effect of carbonisation temperature on the performance of the CMS membranes was evaluated by comparing single-gas permeation data for membranes with the same composition but carbonised at different temperatures, specifically U-99-Ni (550 °C) and U-101-Ni (700 °C). Measurements were conducted at temperatures ranging from 150 to 350 °C and pressures of 1 to 5 bar(g). The results show that carbonisation temperature strongly influences both permeance and the apparent transport mechanism, indicating a shift in the membrane microstructure and pore network.

Figure 3.6 shows the permeance of the different gases as a function of temperature at constant $\Delta P = 2$ bar. The permeance values and their temperature dependence vary significantly with carbonisation temperature, confirming that the pyrolysis conditions strongly affect the final structure of the carbon selective layer. **Figure 3.6**(a) shows the NH_3 permeance as a function of temperature. Interestingly, the membrane carbonised at 700 °C exhibits a higher NH_3 permeance, despite the expected reduction in surface functional groups at higher carbonisation temperatures. This suggests that the pore size distribution at 700 °C (although tighter as shown in **Figure 3.7**) creates an optimal confinement regime that enhances molecule-wall interactions and promotes surface diffusion through stronger adsorption in the narrow pores. The decrease of permeance with increasing temperature is characteristic of an adsorption-diffusion transport contribution that weakens at higher temperatures. This interpretation is supported by the Arrhenius analysis presented in **Table 3.2**: ammonia displays the most negative apparent activation energy, confirming a strong adsorption-diffusion contribution. In contrast, U-99-Ni (550 °C) exhibits a comparatively more constant permeance over the same temperature range, suggesting that the two membranes differ not only in absolute permeance but also in the relative contributions of adsorption-diffusion and molecular sieving. In the lower temperature range (150-250 °C), the less negative activation energies observed for U-101-Ni indicate a partial compensation by positive contributions that can be attributed to molecular sieving. For a more rigorous comparison, helium (same kinetic diameter as ammonia) was also tested; its permeance trend is shown in **Figure 3.6**(c). The helium permeance is much lower than that of ammonia, which is consistent with the presence of an adsorption-related transport contribution for ammonia that cannot occur for an inert gas such as helium. For helium, the only relevant gas transport mechanism is therefore diffusion through the pores, dominated by molecular sieving, as confirmed by the Arrhenius analysis in **Table 3.2**, where helium exhibits the highest positive activation energy. Although Knudsen diffusion might also contribute, the NH_3/He

selectivity shown in **Figure 3.6**(e) ranges in value which are far from the ideal Knudsen selectivity of 0.48, indicating that Knudsen diffusion is not the dominant mechanism under the investigated conditions.

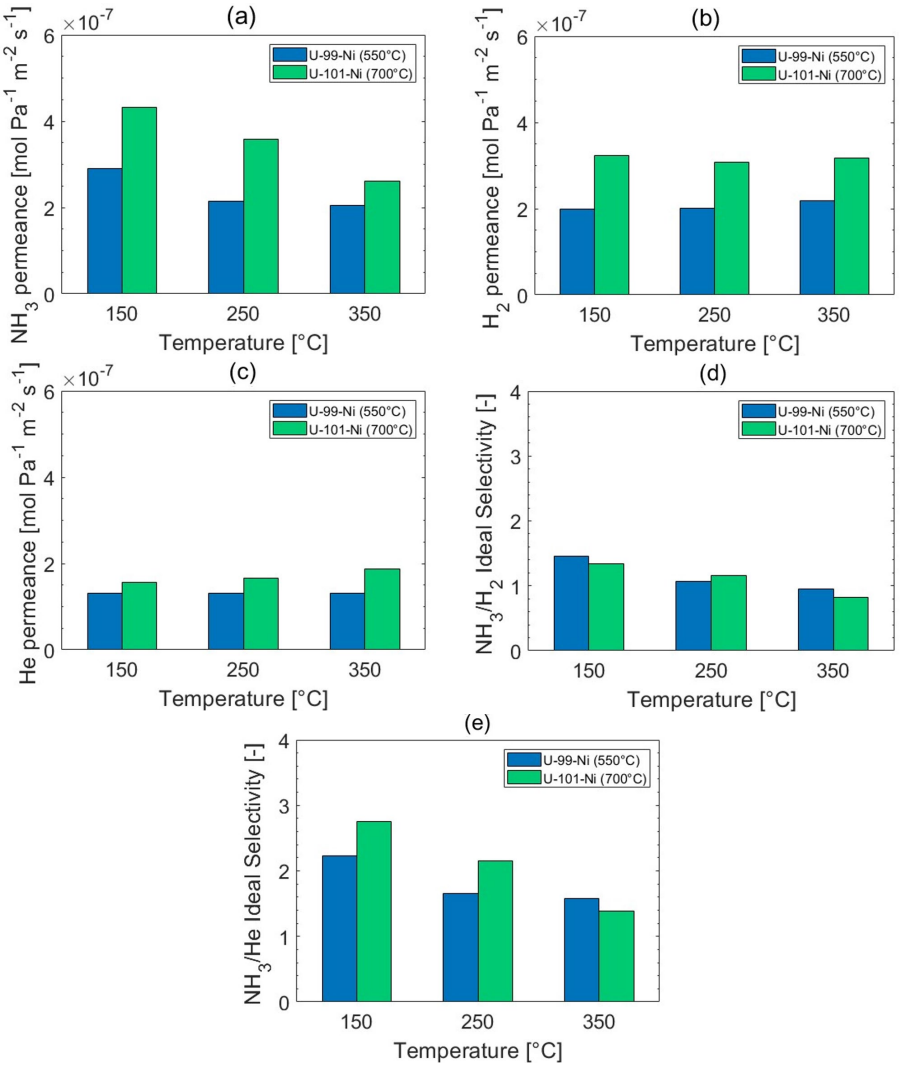


Figure 3.6 Single-gas permeation trend of CMS membranes U-99-Ni and U-101-Ni in temperature range 150-350 °C at ΔP = 2 bar: (a) NH_3 permeance, (b) H_2 permeance, (c) He permeance, (d) NH_3/H_2 ideal selectivity, (e) NH_3/He ideal selectivity

Hydrogen also shows a notable permeance, which remains higher in U-101-Ni, indicating significant interaction with the carbon structure. In both cases, however, the hydrogen permeance remains relatively constant with temperature, suggesting that its transport is less sensitive to the activated adsorption-diffusion processes that govern ammonia permeation. Instead, hydrogen transport reflects a strong balance

between molecular sieving and adsorption effects, as also indicated by near-zero activation energies reported in **Table 3.2**. Interestingly, the higher permeance observed for U-101-Ni is not reflected in the NH_3/H_2 selectivity trend shown in **Figure 3.6**(d), where both membranes display very similar values over the entire temperature range. This suggests that the higher carbonisation temperature increases the permeance of both ammonia and hydrogen proportionally, leaving their selectivity ratio largely unchanged.

The difference between the two membranes becomes particularly evident when considering nitrogen. The activation energies for N_2, reported in **Table 3.2**, differ more strongly between U-99-Ni and U-101-Ni. This is expected, since a smaller effective pore size increases the contribution of molecular sieving and therefore leads to a more positive apparent activation energy in the Arrhenius analysis. In other words, nitrogen transport is especially sensitive to pore constriction, and the higher carbonisation temperature reinforces this effect. Taken together, these results indicate that although the 700 °C membrane delivers higher absolute permeance, the 550 °C membrane retains a more consistently adsorption-diffusion-dominated transport regime for NH_3, as reflected in its more negative apparent activation energies across the full temperature range (**Table 3.2**), whereas the emerging molecular-sieving contribution at 700 °C partially compensates this interaction-driven signature, particularly at low temperature. Since the strategy pursued in this chapter relies on enhancing NH_3 selectivity through specific molecule-wall interactions rather than through pore-size sieving alone, the lower carbonisation temperature is preferred, consistent with the further reduction to 500 °C adopted for the metal-doped membranes examined in the remainder of this chapter.

Table 3.2 Apparent activation energies (E_a) obtained from Arrhenius fits of the permeance data for CMS membranes U-99-Ni and U-101-Ni; for each gas, the first value is calculated in the high-temperature interval 250-350 °C and the second in the low-temperature interval 150-250 °C. For NH_3 it was not possible to obtain permeance data at $\Delta P > 2$ bar

Code	ΔP [bar]	E_a H_2 [J·mol^{-1}]	E_a N_2 [J·mol^{-1}]	E_a NH_3 [J·mol^{-1}]	E_a He [J·mol^{-1}]
U-99-Ni	1	−661 – −471	−1779 – −789	−2682 – −1741	3234 – 2867
	2	−786 – −438	−1748 – −767	−2412 – −1508	3193 – 2642
	4	−652 – −463	−1695 – −755	-	-
	5	−807 – −437	−1753 – −701	-	-
U-101-Ni	1	283 – −129	2499 – 572	−2316 – −1125	2953 – 2174
	2	283 – −149	2452 – 688	−2316 – −587	2883 – 1995
	4	283 – −160	2380 – 597	-	-
	5	283 – −161	2300 – 598	-	-

The pore size distribution provides direct structural support for this interpretation. As shown in **Figure 3.7**, both membranes show a high fraction of pores around d_p = 0.5 nm, but the second peak in the distribution is shifted towards larger diameters for the membrane carbonised at the lower temperature. This suggests that the lower carbonisation temperature leads to less pore shrinkage and thus to a broader pore size distribution. By contrast, the higher carbonisation temperature produces a tighter ultramicroporous structure, which is more favourable for selective transport.

SEM cross-section images (**Figure 3.8**) indicate that the carbon layer is continuous and forms a homogeneous selective film with a thickness of approximately 1-2 µm, with a slight reduction in thickness for the membrane carbonised at higher temperature. Laser confocal microscopy analysis (**Figure 3.9**-**Figure 3.10**) reveals that the surface morphology also changes with carbonisation temperature.

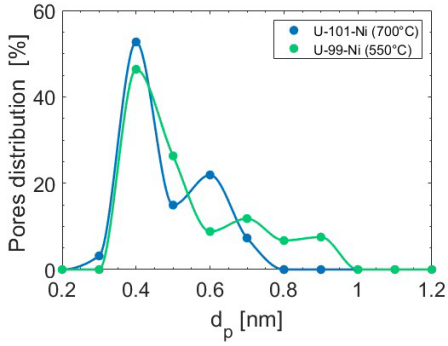


Figure 3.7 Pore size distribution of CMS membranes U-99-Ni and U-101-Ni, showing the fraction of pores as a function of pore diameter d_p

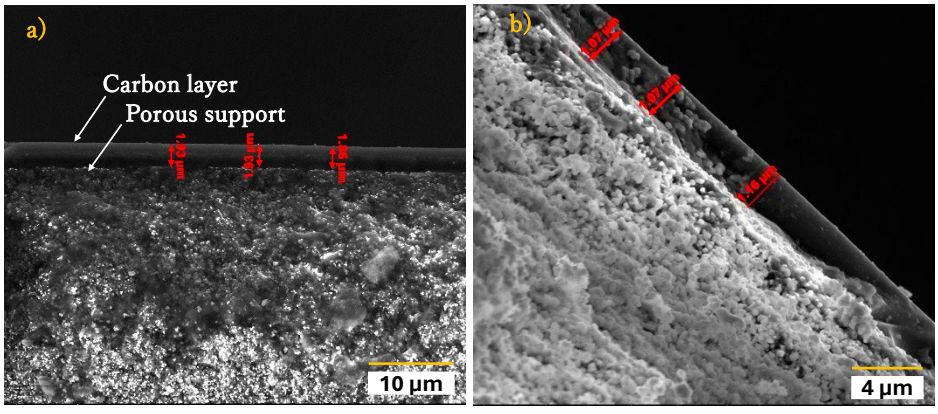


Figure 3.8 Cross-sectional SEM images of the CMS membranes: (a) U-99-Ni (magnification 5,000×, accelerating voltage 10.0 kV); (b) U-101-Ni (magnification 25,000×, accelerating voltage 5.0 kV), showing continuous carbon-selective layers with thicknesses of approximately 1-2 µm

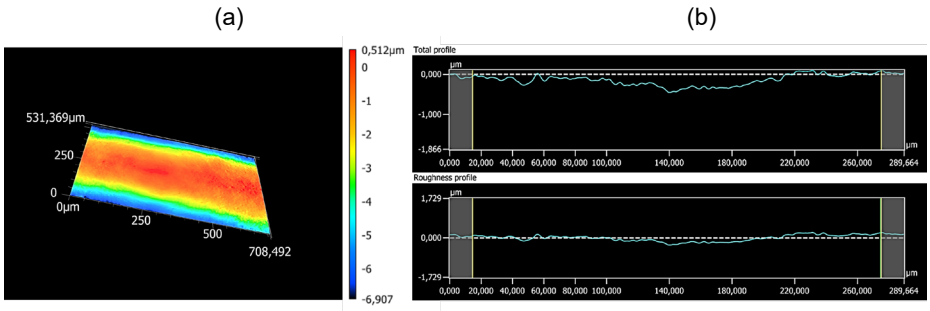


Figure 3.9 Laser microscopy image and roughness profile of CMS membrane U-99-Ni: (a) the 3D surface view and (b) corresponding line profile using 50× lens

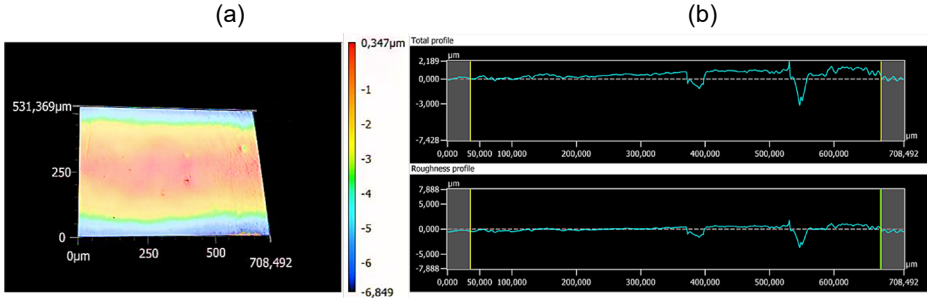


Figure 3.10 Laser microscopy image and roughness profile of CMS membrane U-101-Ni: (a) the 3D surface view and (b) corresponding line profile using 50× lens

The roughness parameters summarised in **Table 3.3** show that U-101-Ni exhibits a higher R_z and R_a value, indicating more pronounced local height variations and a rougher surface.

Table 3.3 Roughness parameters of the membrane surface profiles measured by 3D laser microscopy

Code	R_a [µm]	R_z [µm]
U-99-Ni	0.119	0.589
U-101-Ni	0.423	5.507

3.4.2 Effect of metal addition on CMS membranes: pure gas tests

In this section, the performance of the different CMS membranes doped with Co, Cu, Ni, and Zn is evaluated. An overview of the pure gas permeation results is presented together with preliminary interpretations, which will be examined in more detail in the modelling section. For all membranes, the pure H_2 and N_2 experiments show no noticeable dependence of permeance on pressure. Therefore, the pressure-dependent permeance and selectivity data are reported in the Appendix (**Figure A.3.1**(a),(b)) and the discussion here focuses on the temperature dependence

(excluding NH_3), summarised in **Figure 3.11**.

It should be noted that no metal-free (undoped) CMS membrane prepared under otherwise identical conditions was included in this study. Consequently, the observed differences in permeance and selectivity cannot be attributed unambiguously to a specific metal; the trends discussed should be interpreted as qualitative indications of dopant-dependent behaviour rather than as a rigorously controlled comparison. A metal-free reference and matched-loading series for each dopant would be required to isolate the effect of the metal species itself.

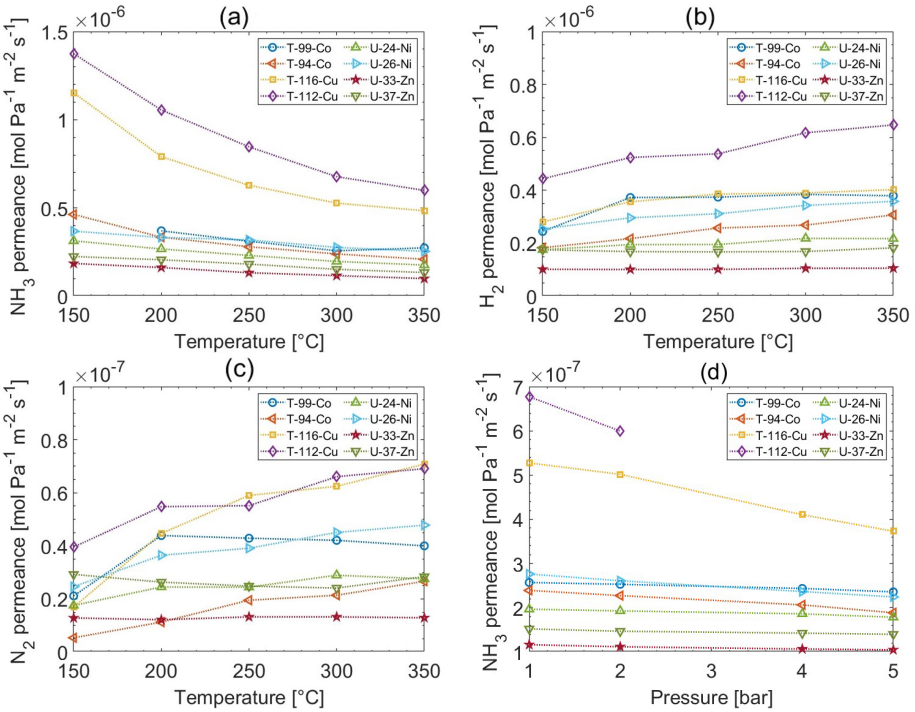


Figure 3.11 Single-gas permeation trend of CMS membranes: (a) NH_3 permeance 150-350 °C, ΔP = 1 bar, (b) H_2 permeance 150-350 °C, ΔP = 1 bar, (c) N_2 permeance 150-350 °C, ΔP = 1 bar, (d) NH_3 permeance ΔP = 1-5 bar, 300 °C

Figure 3.11(a) shows the NH_3 permeance as a function of temperature. For most membranes the NH_3 permeance exhibits only a mild dependence on temperature, with a slight decrease as temperature increases. In contrast, T-116-Cu and T-112-Cu display a much stronger temperature dependence: their NH_3 permeance decreases sharply with temperature, yet they still provide the highest NH_3 permeance over the entire temperature range. This behaviour is indicative of a strong adsorption-diffusion contribution, which is particularly important at low temperature and progressively weakens at higher temperature. **Figure 3.11**(d) also shows that the NH_3 permeance of the Cu-based membranes depends on pressure, suggesting that ammonia is also adsorbed within the pores. The Co- and Ni-based membranes (T-

99-Co, T-94-Co, U-24-Ni, U-26-Ni) form an intermediate group with moderate NH_3 permeance and relatively weak temperature dependence. The Zn-based membranes (U-33-Zn, U-37-Zn) exhibit the lowest NH_3 permeance and only a slight decrease with temperature, suggesting weaker specific ammonia surface interactions. The behaviour of H_2, shown in **Figure 3.11**(b), is essentially opposite to that of NH_3. For all membranes, H_2 permeance remains approximately constant or slightly increases with temperature, which is consistent with activated diffusion through narrow pores with a weaker adsorption contribution. Once again, T-112-Cu stands out, exhibiting both the highest H_2 permeance and the strongest positive temperature dependence, with a nearly monotonic increase from 150 °C to 350 °C. The Co- and Ni-based membranes show moderate H_2 permeance with a gentle upward trend, whereas the Zn-based membranes have the lowest H_2 permeance but follow the same qualitative increase with temperature. The much weaker and often positive temperature dependence of H_2 permeance compared with NH_3 confirms that H_2 transport is less governed by adsorption-diffusion and more by size-controlled diffusion (molecular sieving). Nitrogen shows a similar trend to hydrogen but with a stronger temperature dependence, reflecting its larger kinetic diameter and stronger sensitivity to pore constriction, as illustrated in **Figure 3.11**(c). As in the NH_3 and H_2 case, the Cu-based membranes exhibit the highest N_2 permeance, followed by the Co- and Ni-doped membranes, while the Zn-doped membranes show the lowest N_2 permeance across the full temperature range.

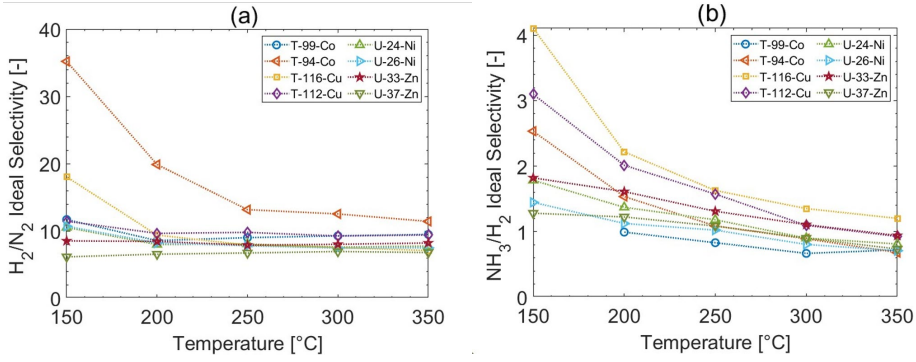


Figure 3.12 Ideal selectivity trend of CMS membranes in temperature range 150-350 °C: (a) H_2/N_2 at ΔP = 20 bar, (b) NH_3/H_2 at ΔP = 1 bar

The corresponding ideal selectivities are reported in **Figure 3.12**. **Figure 3.12**(a) presents the H_2/N_2 ideal selectivity. For most membranes, these values remain nearly constant both with pressure (here, results at ΔP = 20 bar are shown), and with temperature, with values in the range of 8-12. This behaviour indicates that both gases experience similar changes in transport resistance with increasing temperature. An exception is again observed for T-94-Co and, to a lesser extent, T-116-Cu, which show relatively high H_2/N_2 selectivity at 150 °C, followed by a pronounced decrease

with temperature. **Figure 3.12**(b) shows the NH_3/H_2 selectivity values is the highest at 150 °C for all membranes and decreases with increasing temperature. Cu- and Co-based membranes display the highest NH_3/H_2 selectivities at low temperature, with T-116-Cu and T-94-Co clearly standing out, whereas Ni- and Zn-based membranes exhibit more modest selectivities that evolve only slightly with temperature. By 350 °C, most membranes converge to NH_3/H_2 selectivity values close to unity, indicating that the advantage of NH_3 adsorption over H_2 is largely lost at high temperature. Also in this case it can be concluded that although the trend of the selectivity decreases with temperature, they have not reached the Knudsen diffusion mechanism yet. A detailed interpretation for the gas transport mechanism is provided in Section 3.4.4. This trend is consistent with a gradual transition from adsorption-dominated NH_3 transport at low temperature to more molecular sieving-controlled behaviour at higher temperatures.

3.4.3 Effect of metal addition on CMS membranes: mixed-gas tests

Mixed-gas permeation experiments were conducted in two stages: first, binary H_2:N_2 mixtures were tested to assess competitive transport effects between the reactant gases; subsequently, ternary $H_2/N_2/NH_3$ mixtures simulating ammonia synthesis conditions were evaluated.

Mixed-gas permeation tests with H_2/N_2 were performed initially using a molar feed ratio of H_2:N_2 = 3:2. At 300 °C, H_2 is consistently more permeant than N_2 for all membranes. From 5 to 20 bar, H_2 permeance (shown in **Figure 3.13**(a)) either slightly decreases or remains almost constant, depending on the membrane. T-112-Cu exhibits the highest H_2 permeance over the entire pressure range, followed by T-116-Cu and T-99-Co. The mild decrease in H_2 permeance with pressure for most membranes suggests some deviation from ideal diffusion, probably due to either partial site saturation or concentration- polarisation effects rather than simple pressure proportional transport. The absolute ordering (Cu > Co > Ni ~ Zn) indicates that Cu-based membranes provide the most open or H_2 affine transport pathways at 300 °C, while Zn-based ones are tighter for H_2 transport. This is consistent with the nearly flat H_2 permeance profile observed for the Zn-based membranes over the entire pressure range.

A similar hierarchy is observed for N_2, shown in **Figure 3.13**(b). T-116-Cu and T-112-Cu again stand out with the highest N_2 permeance, Co- and Ni-based membranes occupy an intermediate range, and Zn-based membranes show the lowest N_2 permeance. Overall the dependence on pressure is weaker for N_2 than for H_2, which suggests that N_2 transport is dominated by relatively pressure independent diffusion through the pores rather than by strong sorption effects. The very high permeance of the T-116-Cu membrane, however, results in a comparatively low H_2/N_2 separation factor (~2.5). This gives an advantage to the Co-based membranes, depicted in **Figure 3.13**(c), which display the strongest increase in

separation factor with pressure (from ~4.5 to near 6). The remaining membranes cluster in an intermediate range between about 3 and 4.5 over the same pressure interval.

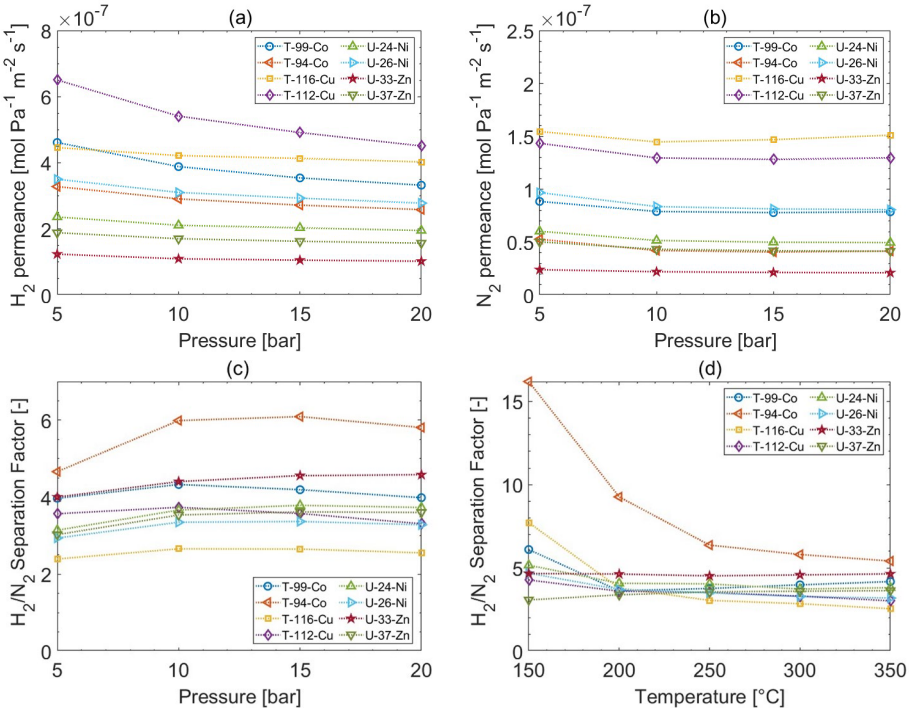


Figure 3.13 Mixed-gas permeation trend of CMS membranes in mixture H_2:N_2 = 3:2: (a) H_2 permeance ΔP = 5-20 bar, 300 °C (b) N_2 permeance ΔP = 5-20 bar, 300 °C, (c) H_2/N_2 separation factor ΔP = 5-20 bar, 300 °C, (d) H_2/N_2 separation factor 150-300 °C, ΔP = 20 bar

At 20 bar (**Figure 3.13**(d)), the temperature dependence of the H_2/N_2 separation factor is dominated by T-94-Co, which shows a very strong decrease in selectivity with increasing temperature, while the other membranes remain in a relatively narrow band. At 150 °C, T-94-Co reaches a relatively high separation factor (~16-17), whereas the other membranes lie mostly between ~4 and 7. With increasing temperature, the selectivity of T-94-Co drops steeply, T-116-Cu shows a similar but more gradual decline, and the remaining membranes display only a modest decrease in selectivity. This behaviour is consistent with strongly activated H_2 transport and/or pronounced low-temperature adsorption differences on Co- and Cu-doped surfaces: at low temperature, H_2 can be preferentially sorbed or activated relative to N_2, giving high separation factor; as the temperature increases, adsorption weakens and transport becomes more diffusion-controlled, so H_2 and N_2 permeances converge. Overall, at 300 °C, Cu-based membranes combine high H_2 and N_2 permeances with moderate H_2/N_2 separation factor, whereas the Co-based

membranes offer somewhat lower H_2 permeance but higher selectivity, particularly at elevated pressure. Zn- and Ni-based membranes show lower permeances but stable, mid-range selectivities that are relatively insensitive to both pressure and temperature, suggesting more purely diffusive transport with weaker specific interactions.

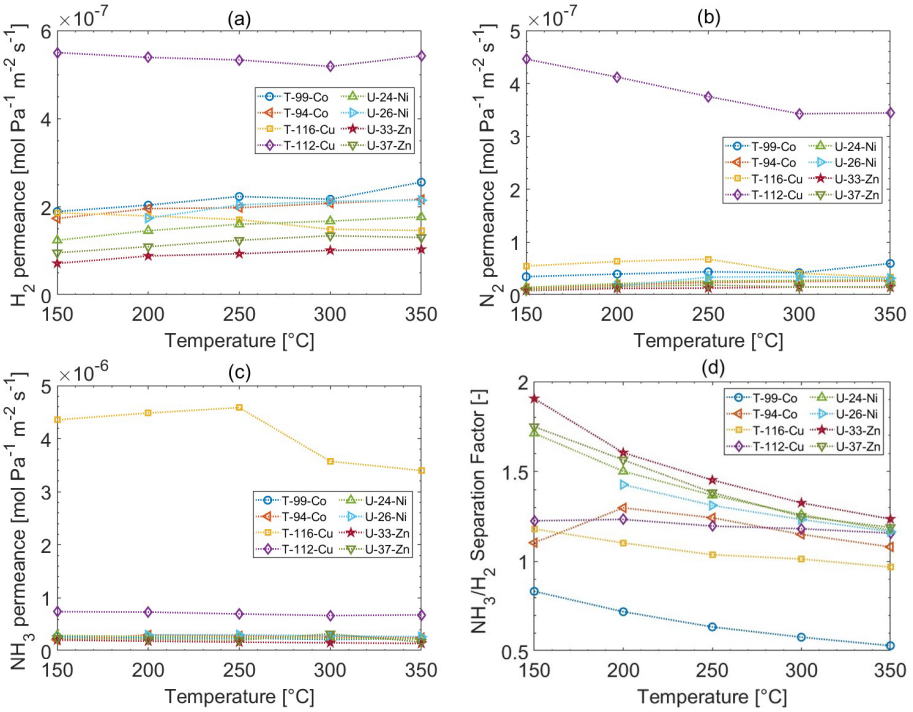


Figure 3.14 Mixed-gas permeation trend of CMS membranes in mixture simulating 20% conversion of H_2 (a) H_2 permeance 150-350 °C ΔP = 4 bar, (b) N_2 permeance 150-350 °C ΔP = 4 bar, (c) NH_3 permeance 150-350 °C ΔP = 4 bar, (d) NH_3/H_2 separation factor 150-350 °C, ΔP = 4 bar

In the Appendix (**Figure A.3.2**) the temperature dependence of both gases at 20 bar is also presented, showing that temperature modulates these trends with the same qualitative behaviour observed at all pressures. For clarity and to avoid overloading the main text, only representative datasets are discussed here. The omitted conditions follow the same qualitative trends. For instance, although the H_2/N_2 separation factor as a function of pressure is shown explicitly only at 300 °C, the behaviour at other temperatures is analogous.

Likewise, for both H_2 and N_2 the pressure dependence of permeance at each temperature consists of a slight decrease with increasing pressure, with the drop being consistently more pronounced for N_2 than for H_2. As a result, the H_2/N_2 separation factor exhibits a mild increase with pressure across the entire temperature range investigated. Following the binary H_2/N_2 experiments, mixed-gas permeation

tests were performed using a ternary $H_2/N_2/NH_3$ feed, chosen to simulate approximately 20% conversion of H_2. The overall trends are consistent with the behaviour observed previously for the binary H_2/N_2 mixture, but the presence of NH_3 introduces additional competitive transport effects, particularly for the Cu- and Co-based membranes. For H_2 (**Figure 3.14**(a)), the permeance increases moderately with temperature for most membranes, with T-112-Cu again exhibiting the highest H_2 permeance over the entire temperature range. Co-based membranes show intermediate H_2 permeances, followed by Ni- and Zn-based membranes, which remain the tightest for H_2 transport; this hierarchy mirrors the ordering observed in the binary H_2/N_2 tests. The N_2 permeance (**Figure 3.14**(b)) remains much lower than that of H_2 and exhibits only a small dependence on temperature for most compositions. T-112-Cu stands out with significantly higher N_2 permeance compared with the other membranes, whereas Co-, Ni- and Zn-based membranes cluster at substantially lower values with only small changes over the investigated temperature range. The most stable trend with temperature happens with NH_3, as shown in **Figure 3.14**(c). T-116-Cu exhibits by far the highest NH_3 permeance, with a maximum at intermediate temperature before decreasing again at higher temperature. Co-, Ni- and Zn-based membranes display much lower and relatively flat NH_3 permeances across the whole temperature interval. These observations indicate that ammonia interacts particularly strongly with Cu-based membranes, while its transport through Co-, Ni- and Zn-based membranes is more weakly affected by temperature and competitive sorption. The impact of these permeance trends on separation performance is captured by the NH_3/H_2 separation factor (**Figure 3.14**(d)). In this ternary mixture, the high permeance of all three gases over the Cu-based membranes leads to comparatively low NH_3/H_2 real selectivities, thereby shifting the advantage towards Ni- and Zn-based membranes. At 150 °C, the Zn- and Ni-based membranes exhibit relatively high NH_3/H_2 real selectivities, typically in the range 1.6-1.9, reflecting a pronounced preference for NH_3 over H_2 under cold conditions. Cu- and Co-based membranes start at lower selectivities, around 1.1-1.3, with T-94-Co showing a slight initial increase up to 200 °C. As temperature increases further, however, the NH_3/H_2 separation factor for all membranes decreases, and converges towards values close to unity at 350 °C.

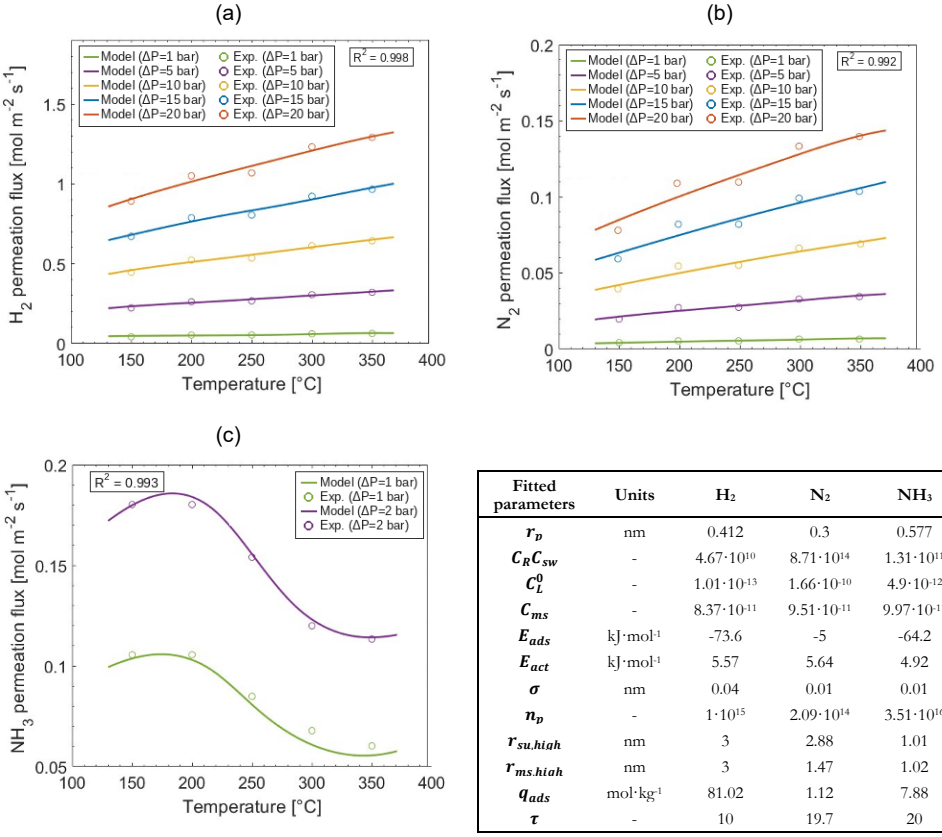
Taken together, the ternary $H_2/N_2/NH_3$ tests confirm the membrane hierarchy established in the binary experiments. Cu-based membranes (particularly T-116-Cu and T-112-Cu) deliver the highest overall permeances for all three gases, but their very high NH_3 and H_2 fluxes lead to only moderate NH_3/H_2 real selectivities, especially at elevated temperature. Co-based membranes provide a more balanced performance, with intermediate permeances and moderate selectivities that are less sensitive to temperature than those of the most NH_3 affine Cu sample. Ni- and Zn-based membranes, finally, exhibit lower permeances but comparatively high NH_3/H_2 real selectivities at low temperature and a more gradual decline with

increasing temperature, suggesting predominantly molecular sieving controlled transport with weaker specific interactions. These findings are consistent with the trends previously identified for the H_2/N_2 mixture and underline the strong role of Cu and Co in enhancing sorption-driven transport of NH_3 and H_2 under mixed-gas conditions.

3.4.4 Gas transport mechanism analysis

To elucidate the dominant transport mechanisms governing gas permeation in metal-doped CMS membranes, the transport model described in Section 3.3 was fitted to experimental single-gas flux data.

For clarity, only the results for membrane T-112-Cu are discussed here, as Cu-doped membranes were identified as the most promising candidates in the permeation study; fits for the other membranes are reported in the Appendix (**Figure A.3.3**-**Figure A.3.9**).



Fitted parameters	Units	H_2	N_2	NH_3
r_p	nm	0.412	0.3	0.577
$C_R C_{sw}$	-	$4.67 \cdot 10^{10}$	$8.71 \cdot 10^{14}$	$1.31 \cdot 10^{11}$
C_L^0	-	$1.01 \cdot 10^{-13}$	$1.66 \cdot 10^{-10}$	$4.9 \cdot 10^{-12}$
C_{ms}	-	$8.37 \cdot 10^{-11}$	$9.51 \cdot 10^{-11}$	$9.97 \cdot 10^{-11}$
E_{ads}	kJ·mol^{-1}	-73.6	-5	-64.2
E_{act}	kJ·mol^{-1}	5.57	5.64	4.92
σ	nm	0.04	0.01	0.01
n_p	-	$1 \cdot 10^{15}$	$2.09 \cdot 10^{14}$	$3.51 \cdot 10^{16}$
$r_{su,high}$	nm	3	2.88	1.01
$r_{ms,high}$	nm	3	1.47	1.02
q_{ads}	mol·kg^{-1}	81.02	1.12	7.88
τ	-	10	19.7	20

Figure 3.15 T-112-Cu membrane fit with experimental data over temperatures and different pressures for: (a) H_2 permeation flux, (b) N_2 permeation flux, (c) NH_3 permeation flux

Figure 3.15 shows the measured fluxes (symbols) and the corresponding model predictions (lines) for H_2, N_2 and NH_3 as a function of temperature at different pressure difference. The accuracy of the fit is also qualitatively determined with the R^2 value. The fitted parameter sets provide additional insight into the relative contributions of the individual transport mechanisms. For all three gases, the pore radii obtained from the fits lie in the sub-nanometer to few-nanometer range, consistent with a regime where molecular sieving/surface diffusion and micro/Knudsen diffusion are expected to play a role.

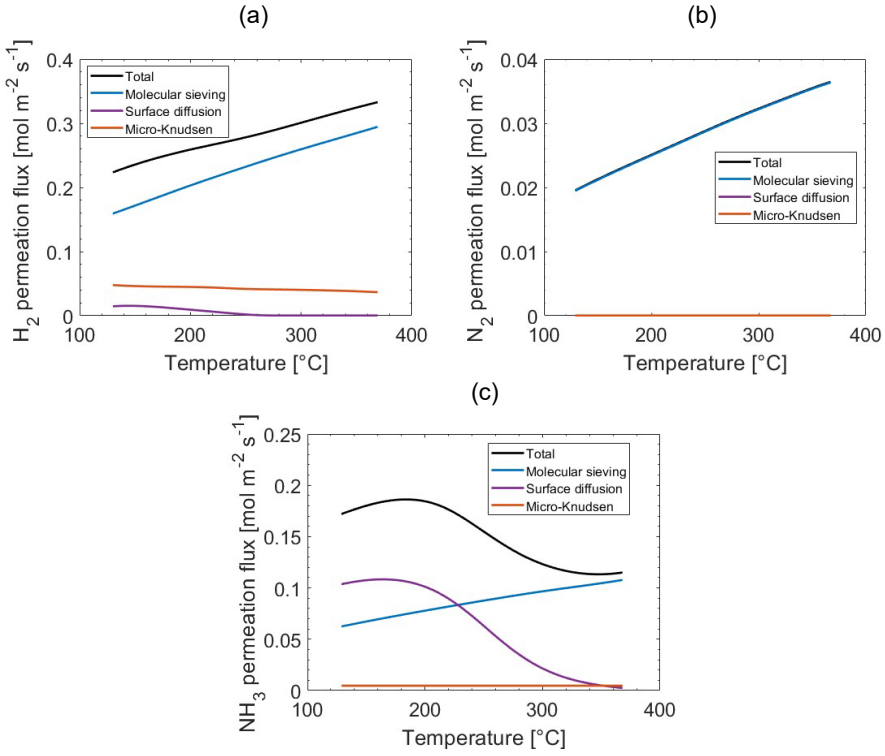


Figure 3.16 T-112-Cu contributions of different gas transport mechanism based on fitted parameters at ΔP = 5 bar for (a) H_2 permeation flux, (b) N_2 permeation flux, (c) NH_3 permeation flux

Figure 3.16 shows the predicted contribution of micro-Knudsen diffusion and surface diffusion for H_2, N_2 and NH_3 respectively. For H_2, the total permeation flux increases with temperature, and this trend is dominated by the molecular-sieving contribution, which rises almost linearly over the investigated range. Micro-Knudsen diffusion provides a smaller, nearly temperature-independent background, while the surface diffusion term is minor and slightly decreases with temperature. For N_2, the model predicts that the total flux is essentially identical to the molecular-sieving contribution over the entire temperature range, with negligible surface diffusion and

micro-Knudsen terms. The N_2 flux therefore increases constantly with temperature. By contrast, NH_3 exhibits a qualitatively different behaviour. The total NH_3 flux displays a pronounced maximum at intermediate temperature, which arises from the interplay between a strongly decreasing surface diffusion contribution and a moderately increasing molecular-sieving contribution.

At low temperature surface diffusion dominates, reflecting a strong adsorption on the Cu. As temperature increases the adsorption strength decreases and molecular sieving becomes progressively more important. For the remaining gas-transport mechanisms study in the other membranes, see the Appendix (**Figure A.3.10**-**Figure A.3.16**).

For a direct comparison, the influence of surface diffusion was evaluated for all membranes and gases at two representative temperatures, 150 °C and 350 °C, as shown in **Figure 3.17.** At 150 °C (**Figure 3.17**(a)), all three gases exhibit a clear surface diffusion contribution, with NH_3 showing the largest values across all compositions and particularly strong contributions for the Cu- and Ni-based membranes. At 350 °C (**Figure 3.17**(b)), by contrast, the surface diffusion contribution of H_2 and N_2 becomes negligible for every membrane, whereas NH_3 still retains a significant surface-controlled fraction, again most pronounced for the Cu-based samples. The only membranes that do not show a drastic loss of NH_3 surface diffusion between 150 and 350 °C are T-116-Cu and the two Ni-based membranes. For T-116-Cu, for example, the NH_3 surface diffusion contribution decreases only slightly, from about 88% at 150 °C to 85% at 350 °C, whereas U-26-Ni shows a similarly modest decline from 70% to 65%.

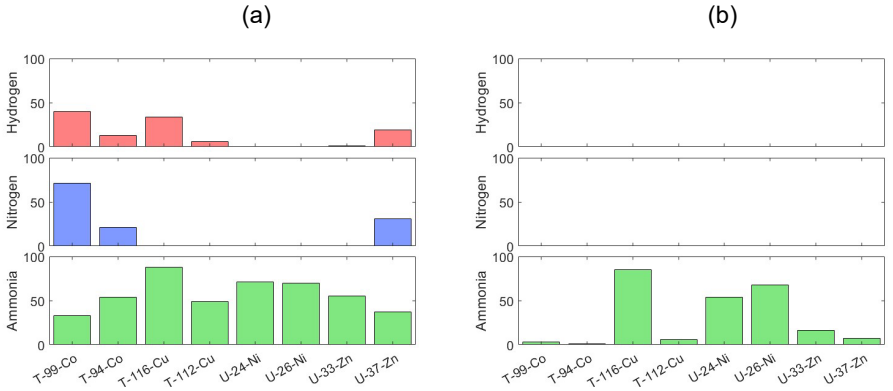


Figure 3.17 Relative contribution of surface diffusion to H_2, N_2 and NH_3 permeation for all membranes at ΔP = 5 bar and (a) 150 °C, (b) 350 °C

This behaviour contrasts sharply with that of T-94-Co, where the surface diffusion contribution essentially vanishes at 350 °C, suggesting that specific interactions between NH_3 and the Co-based membrane are largely lost at elevated temperature. Zn-based membranes lie in between: they show a clear surface contribution at 150

°C that strongly declines with temperature, but a small residual fraction persists at 350 °C. The comparatively strong and persistent NH_3 surface diffusion contribution observed for the Cu-based membranes, together with the behaviour of the other dopants (Co, Ni and Zn), can be rationalised in terms of transition-metal complex stability rather than bulk metallic bonding. In pyrolysed carbon membranes, the metal dopants are more realistically present as small, partially oxidised clusters or cationic sites coordinated to oxygen- and nitrogen-containing functionalities of the carbon matrix than as extended metallic surfaces. For such dispersed, oxidised metal centres interacting with a strongly σ-donating ligand such as NH_3, the relevant descriptor is the stability of the resulting metal-ammine complex. For divalent first-row transition metals, this follows the well-established Irving-Williams series [48]: Mn(II) < Fe(II) < Co(II) < Ni(II) < Cu(II) > Zn(II). In this series, Cu(II) forms the most stable complexes, benefiting from a d^9 configuration, whereas Zn(II) (d^{10}, no ligand-field stabilization) reverts to markedly lower stability. This ordering, Cu(II) > Ni(II) > Co(II) > Zn(II), is in good qualitative agreement with the trends observed in this chapter, where Cu-based membranes show the strongest and most temperature-persistent NH_3 surface diffusion contribution, Ni-based membranes retain a substantial fraction, and Co- and Zn-based membranes lose most of their NH_3 interaction at elevated temperature. This coordination-chemistry picture also aligns with a hopping-type surface diffusion mechanism: Cu(II) and Ni(II) sites, forming more stable complexes, can retain an appreciable adsorbed NH_3 population at high temperature while still allowing hopping between sites, whereas the weaker Co(II) and Zn(II) complexes are more readily depleted by thermal desorption, causing their surface diffusion contribution to collapse.

3.5 CONCLUSIONS

In this chapter, the effect of carbonisation temperature on membrane properties was first investigated by studying CMS membranes of identical composition but pyrolysed at two distinct temperatures: U-99-Ni (550 °C) and U-101-Ni (700 °C). While 550 °C carbonisation produced more open structures rich in adsorption sites, yielding high H_2 and NH_3 permeances dominated by surface diffusion, 700 °C treatment created tighter, more graphitic matrices with superior overall permeances across all gases due to optimised ultramicroporous windows (~0.5 nm) that enhance site interactions despite reduced functional groups, shifting non-adsorbing gases (H_2, N_2) toward molecular sieving mechanisms. Notably, NH_3 permeance in the 700 °C membrane still exhibits a strong adsorption-diffusion contribution, reflecting robust NH_3-Ni interactions that persist through the refined pore network.

Building on this baseline, the metal-doped membrane study focused on four different dopants: Co, Cu, Zn and Ni. These membranes were characterised by combining single- and mixed-gas permeation experiments (150-350 °C, 1-20 bar)

with detailed gas transport modelling. Single-gas tests show that Cu-based membranes provide the highest H_2 and NH_3 permeances with only moderate N_2 transport, and ternary feed experiments under ammonia-synthesis-like conditions confirm that Cu-based membranes deliver the highest overall fluxes for all three gases, whereas Ni- and Zn-based membranes reach higher NH_3/ H_2 selectivities (~1.6-1.9 at 150 °C).

The modelling results further reveal that Cu-based membranes exhibit the strongest NH_3 surface diffusion contribution, reflecting a robust interaction between ammonia and the Cu phase that persists even at elevated temperature, while H_2 transport is dominated by activated diffusion through a relatively open micropore network. In contrast, N_2 transport is essentially diffusion-controlled for all metals. Ni-based membranes also display a substantial NH_3 surface diffusion fraction (~65-70%), indicating a significant NH_3-Ni interaction, whereas Co- and Zn-based membranes lose most of their NH_3 surface diffusion contribution at high temperature and become largely insensitive to the presence of ammonia in the feed. Overall, these combined experimental and modelling results demonstrate that Cu-containing membranes carbonised towards the lower end of the studied temperature range may be particularly promising for ammonia-based separations because of their pronounced surface diffusion contribution. However, this observation is based on a single membrane at each carbonisation temperature and should therefore be interpreted as an indicative trend rather than evidence of a definitive optimum. Further investigation using additional carbonisation temperatures and replicate membranes is required to confirm the optimal conditions. Although the membrane performance is not yet fully optimised, the results establish a clear design framework that connects carbonisation conditions, metal-dopant selection, and gas-transport mechanisms, thereby providing useful guidance for future membrane development and process-level studies of ammonia membrane reactors.

A.3 APPENDIX

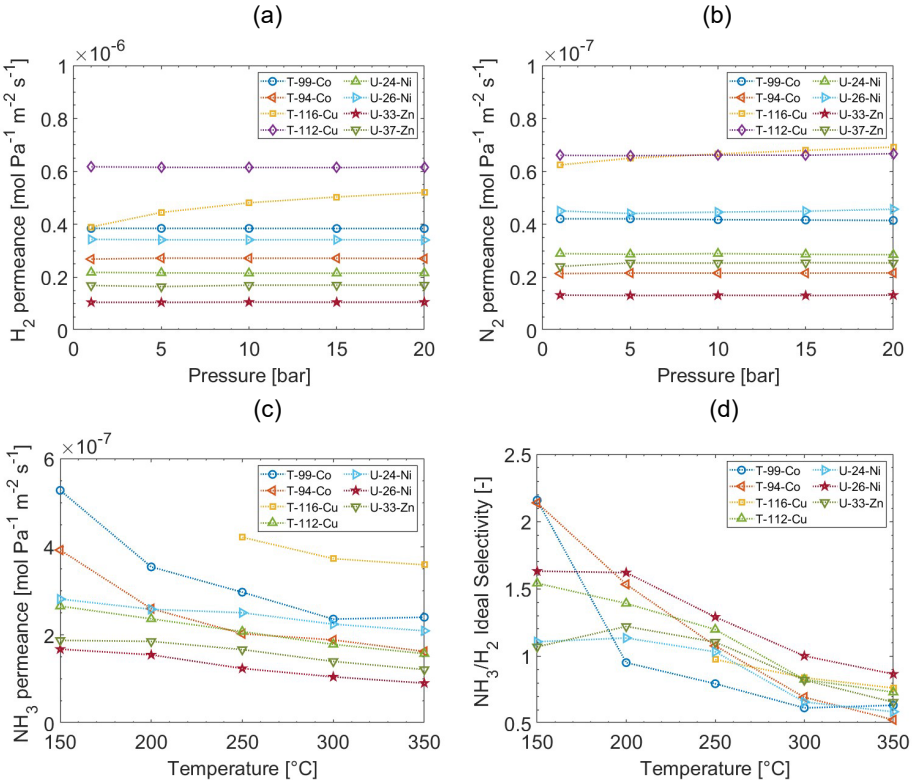


Figure A.3.1 Single-gas permeation trend of CMS membranes: (a) H_2 permeance ΔP = 1-20 bar, 300 °C (b) N_2 permeance ΔP = 1-20 bar 300 °C, (c) NH_3 permeance 150-350 °C, ΔP = 5 bar, (d) NH_3/H_2 ideal selectivity 150-350 °C, ΔP = 5 bar

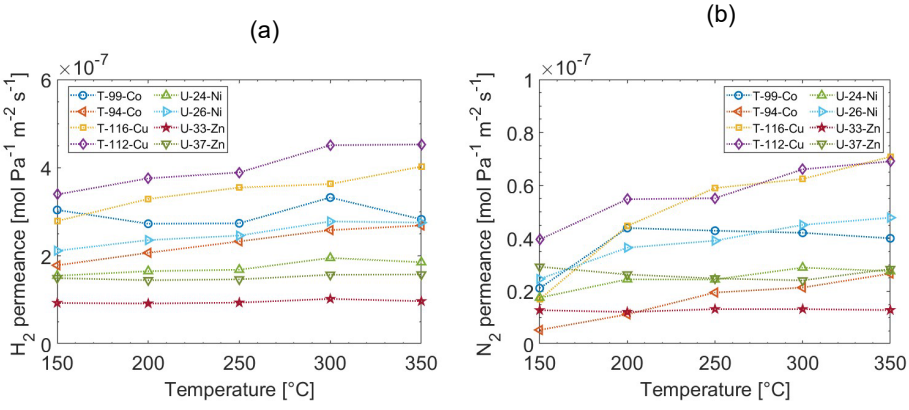
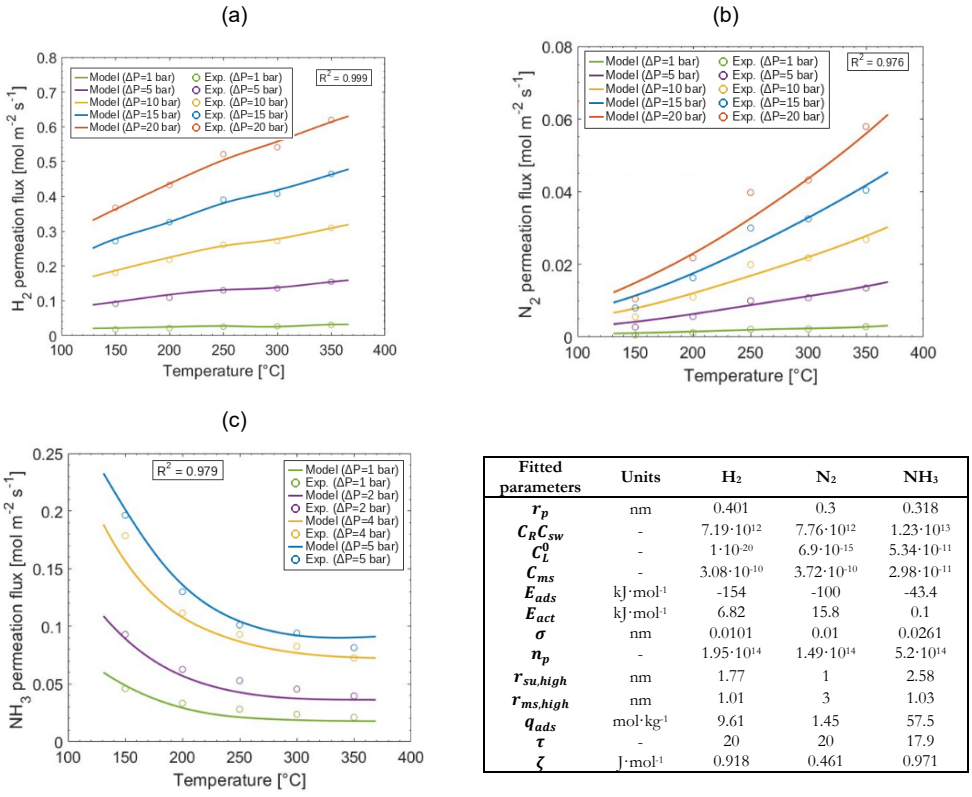
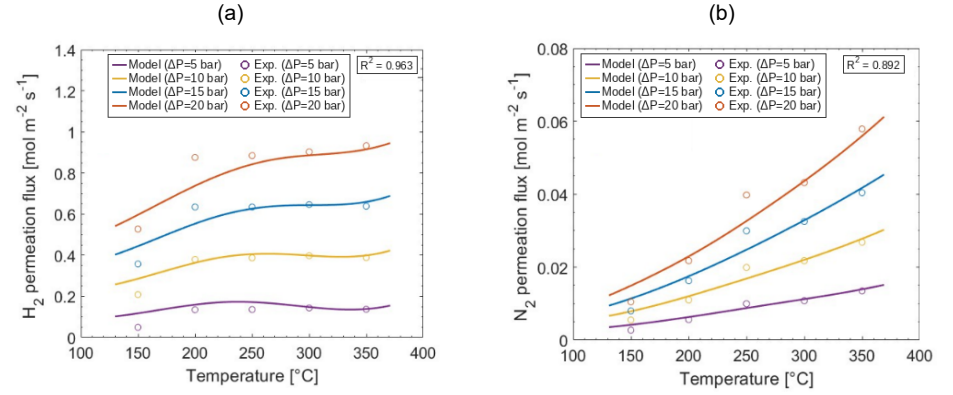


Figure A.3.2 Mixed-gas permeation trend of CMS membranes: (a) H_2 permeance 150-350 °C, ΔP = 20 bar, (b) N_2 150-350 °C, ΔP = 20 bar

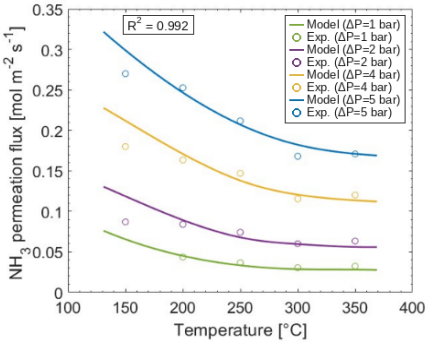


Fitted parameters	Units	H_2	N_2	NH_3
r_p	nm	0.401	0.3	0.318
$C_R C_{sw}$	-	$7.19 \cdot 10^{12}$	$7.76 \cdot 10^{12}$	$1.23 \cdot 10^{13}$
C_L^0	-	$1 \cdot 10^{-20}$	$6.9 \cdot 10^{-15}$	$5.34 \cdot 10^{-11}$
C_{ms}	-	$3.08 \cdot 10^{-10}$	$3.72 \cdot 10^{-10}$	$2.98 \cdot 10^{-11}$
E_{ads}	kJ·mol^{-1}	-154	-100	-43.4
E_{act}	kJ·mol^{-1}	6.82	15.8	0.1
σ	nm	0.0101	0.01	0.0261
n_p	-	$1.95 \cdot 10^{14}$	$1.49 \cdot 10^{14}$	$5.2 \cdot 10^{14}$
$r_{su,high}$	nm	1.77	1	2.58
$r_{ms,high}$	nm	1.01	3	1.03
q_{ads}	mol·kg^{-1}	9.61	1.45	57.5
τ	-	20	20	17.9
ζ	J·mol^{-1}	0.918	0.461	0.971

Figure A.3.3 T-94-Co membrane fit with experimental data over temperatures and different pressures for: (a) H_2 permeation flux, (b)N_2 permeation flux, (c) NH_3 permeation flux



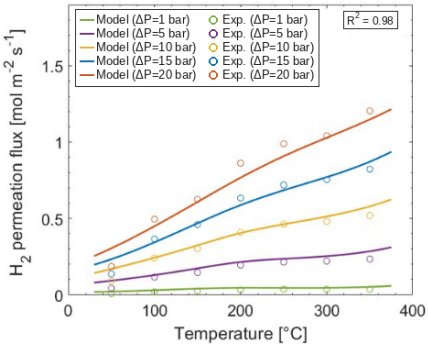
(c)



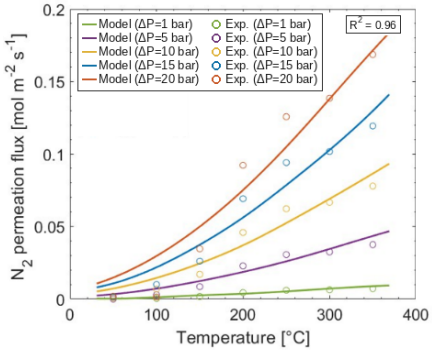
Fitted parameters	Units	H_2	N_2	NH_3
r_p	nm	0.3	0.3	0.6
$C_R C_{sw}$	-	$5.37 \cdot 10^{11}$	$1.21 \cdot 10^{12}$	$2.23 \cdot 10^{12}$
C_L^0	-	$1 \cdot 10^{-15}$	$3.06 \cdot 10^{-15}$	$1.82 \cdot 10^{-10}$
C_{ms}	-	$1.83 \cdot 10^{-10}$	$3.16 \cdot 10^{-10}$	$5.71 \cdot 10^{-12}$
E_{ads}	kJ·mol^{-1}	-105	-100	-41.9
E_{act}	kJ·mol^{-1}	6.91	9.23	1
σ	nm	0.01	0.01	0.0389
n_p	-	$8.9 \cdot 10^{14}$	$8.69 \cdot 10^{13}$	$8.29 \cdot 10^{14}$
$r_{su,high}$	nm	1	1.04	1.52
$r_{ms,high}$	nm	2.84	1	1
q_{ads}	mol·kg^{-1}	8.96	1.69	23.5
τ	-	20	20	10.4

Figure A.3.4 T-99-Co membrane fit with experimental data over temperatures and different pressures for: (a) H_2 permeation flux, (b)N_2 permeation flux, (c) NH_3 permeation flux

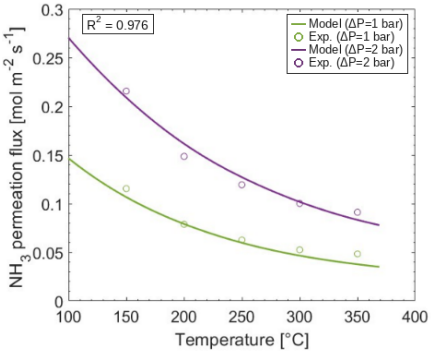
(a)



(b)

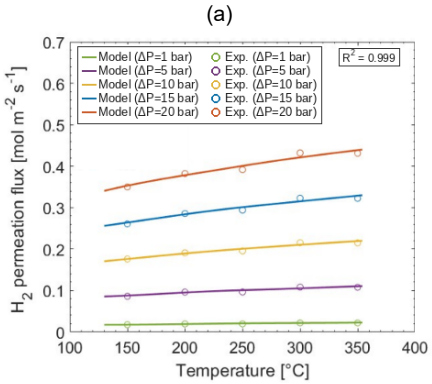


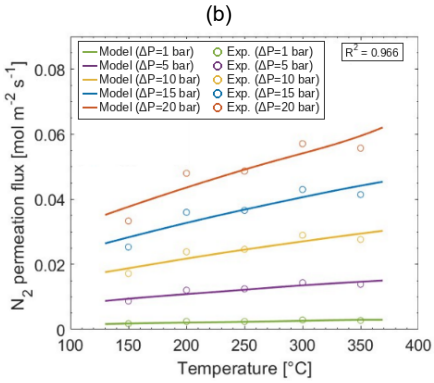
(c)

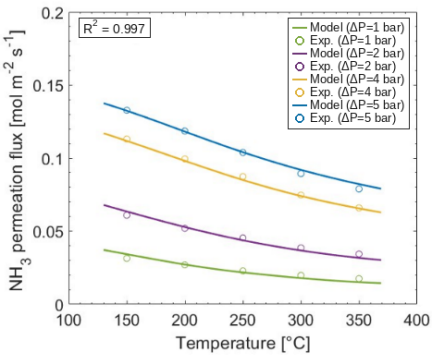


Fitted parameters	Units	H_2	N_2	NH_3
r_p	nm	0.5	0.442	0.5
$C_R C_{sw}$	-	$2.81 \cdot 10^{12}$	$7.49 \cdot 10^{16}$	$9.12 \cdot 10^{10}$
C_L^0	-	$1 \cdot 10^{-15}$	$6.39 \cdot 10^{-14}$	$1.58 \cdot 10^{-7}$
C_{ms}	-	$1.89 \cdot 10^{-8}$	$5.25 \cdot 10^{-5}$	$1 \cdot 10^{-16}$
E_{ads}	kJ·mol^{-1}	-100	-4.59	-13.2
E_{act}	kJ·mol^{-1}	8.61	13.6	0.1
σ	nm	0.01	0.01	0.04
n_p	-	$5.57 \cdot 10^{12}$	$1 \cdot 10^{9}$	$1 \cdot 10^{15}$
$r_{su,high}$	nm	3	1.03	3
$r_{ms,high}$	nm	1	1.95	1
q_{ads}	mol·kg^{-1}	2.13	1.6	12.6
τ	-	20	20	10

Figure A.3.5 T-116-Cu membrane fit with experimental data over temperatures and different pressures for: (a) H_2 permeation flux, (b) N_2 permeation flux, (c) NH_3 permeation flux

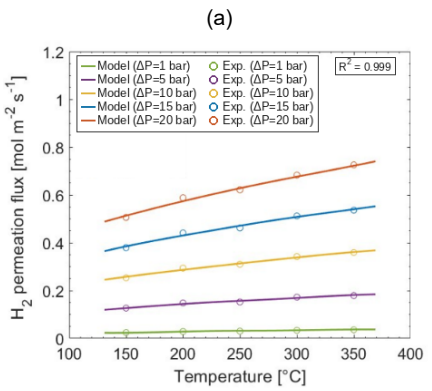


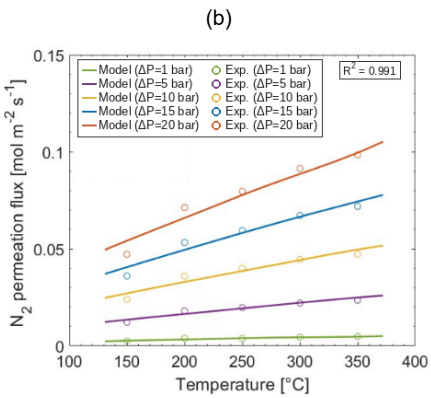




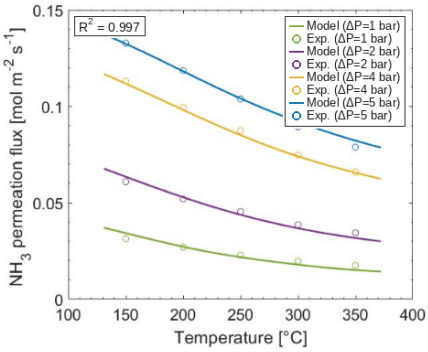
Fitted parameters	Units	H_2	N_2	NH_3
r_p	nm	0.317	0.3	0.4
$C_R C_{sw}$	-	$7.34 \cdot 10^{14}$	$8.86 \cdot 10^{17}$	$6.38 \cdot 10^{13}$
C_L^0	-	0.00671	$7.39 \cdot 10^{-12}$	$1.04 \cdot 10^{-7}$
C_{ms}	-	$8.7 \cdot 10^{-11}$	$7.23 \cdot 10^{-11}$	$2.4 \cdot 10^{-11}$
E_{ads}	kJ·mol^{-1}	-132	-96.8	-16.9
E_{act}	kJ·mol^{-1}	2.48	4.9	0.1
σ	nm	0.0341	0.0101	0.04
n_p	-	$3.35 \cdot 10^{14}$	$9.94 \cdot 10^{13}$	$1.65 \cdot 10^{14}$
$r_{su,high}$	nm	1.52	1.68	1.42
$r_{ms,high}$	nm	1.91	1.56	3
q_{ads}	mol·kg^{-1}	1.01	6.47	68.7
τ	-	20	20	14.4

Figure A.3.6 U-24-Ni membrane fit with experimental data over temperatures and different pressures for: (a) H_2 permeation flux, (b) N_2 permeation flux, (c) NH_3 permeation flux





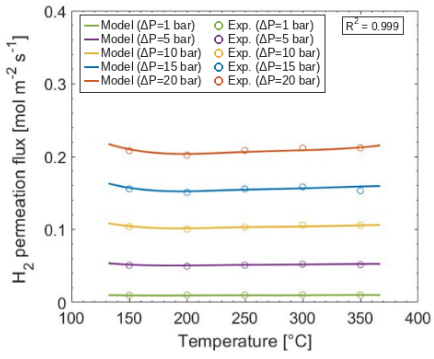
(c)



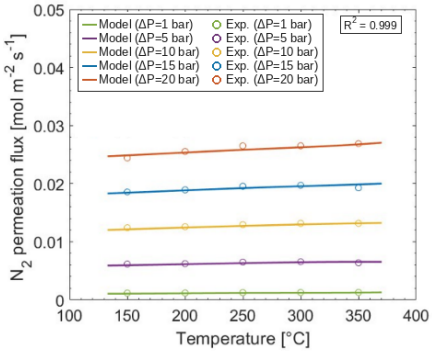
Fitted parameters	Units	H_2	N_2	NH_3
r_p	nm	0.3	0.301	0.5
$C_R C_{sw}$	-	$7.62 \cdot 10^{14}$	$8.43 \cdot 10^{14}$	$1.36 \cdot 10^{13}$
C_L^0	-	25	$9.95 \cdot 10^{-14}$	$3.26 \cdot 10^{-7}$
C_{ms}	-	$1.23 \cdot 10^{-10}$	$6.2 \cdot 10^{-11}$	$1 \cdot 10^{-15}$
E_{ads}	kJ·mol^{-1}	-340	-0.836	-15
E_{act}	kJ·mol^{-1}	3.78	6.72	1.31
σ	nm	0.01	0.01	0.04
n_p	-	$5.73 \cdot 10^{14}$	$2.75 \cdot 10^{14}$	$9.99 \cdot 10^{14}$
$r_{su,high}$	nm	2.73	2.66	2.63
$r_{ms,high}$	nm	1.04	2.09	2.77
q_{ads}	mol·kg^{-1}	7.6	1.03	55.5
τ	-	20	19.5	10

Figure A.3.7 U-26-Ni membrane fit with experimental data over temperatures and different pressures for: (a) H_2 permeation flux, (b) N_2 permeation flux, (c) NH_3 permeation flux

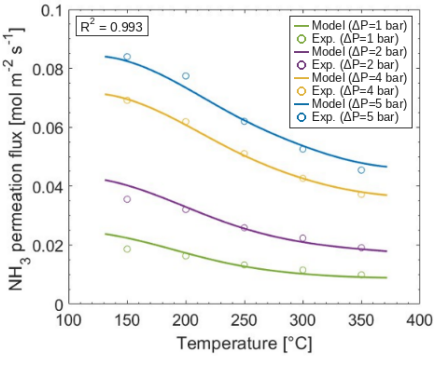
(a)



(b)

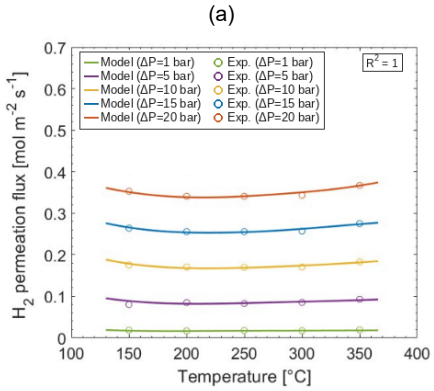


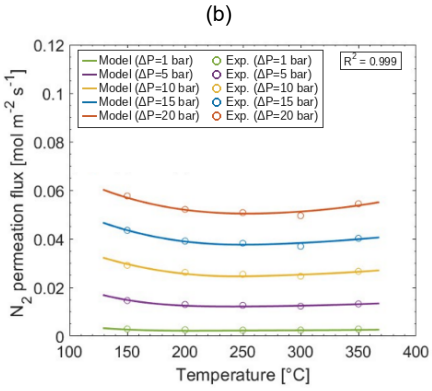
(c)

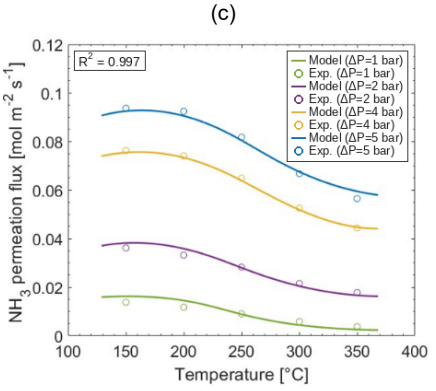


Fitted parameters	Units	H_2	N_2	NH_3
r_p	nm	0.4	0.328	0.306
$C_R C_{sw}$	-	$1.62 \cdot 10^{10}$	$1 \cdot 10^{10}$	$5.9 \cdot 10^{14}$
C_L^0	-	$1 \cdot 10^{-15}$	$7.85 \cdot 10^{-10}$	$2.44 \cdot 10^{-9}$
C_{ms}	-	$7.67 \cdot 10^{-12}$	$1.32 \cdot 10^{-9}$	$5.24 \cdot 10^{-12}$
E_{ads}	kJ·mol^{-1}	-70.7	-7.08	-33.2
E_{act}	kJ·mol^{-1}	6.37	1	1
σ	nm	0.01	0.01	0.04
n_p	-	$1 \cdot 10^{15}$	$9.58 \cdot 10^{11}$	$1.66 \cdot 10^{14}$
$r_{su,high}$	nm	1.08	1.19	2.12
$r_{ms,high}$	nm	2.75	1.75	2.42
q_{ads}	mol·kg^{-1}	1	1	70
τ	-	10	20	11.8

Figure A.3.8 U-33-Zn membrane fit with experimental data over temperatures and different pressures for: (a) H_2 permeation flux, (b) N_2 permeation flux, (c) NH_3 permeation flux







Fitted parameters	Units	H_2	N_2	NH_3
r_p	nm	0.4	0.399	0.4
$C_R C_{sw}$	-	$4.78 \cdot 10^{11}$	$2.18 \cdot 10^{11}$	$1 \cdot 10^{13}$
C_L^0	-	$1 \cdot 10^{-9}$	$7.57 \cdot 10^{-10}$	$2.78 \cdot 10^{-11}$
C_{ms}	-	$2.22 \cdot 10^{-11}$	$4.43 \cdot 10^{-12}$	$6.13 \cdot 10^{-12}$
E_{ads}	kJ·mol^{-1}	-26.2	-28.2	-56.2
E_{act}	kJ·mol^{-1}	6.84	9.06	1
σ	nm	0.04	0.04	0.04
n_p	-	$1 \cdot 10^{15}$	$1 \cdot 10^{15}$	$9.65 \cdot 10^{14}$
$r_{su,high}$	nm	1	1.22	1.05
$r_{ms,high}$	nm	3	1.17	3
q_{ads}	mol·kg^{-1}	10	3.03	21.2
τ	-	10	10	10

Figure A.3.9 U-37-Zn membrane fit with experimental data over temperatures and different pressures for: (a) H_2 permeation flux, (b) N_2 permeation flux, (c) NH_3 permeation flux

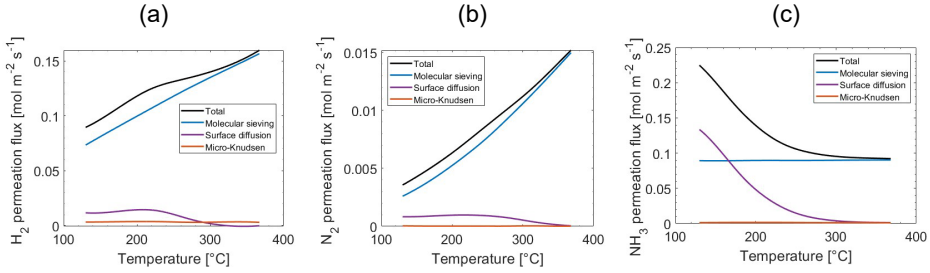


Figure A.3.10 T-94-Co contributions of different gas transport mechanism based on fitted parameters at ΔP = 5 bar for (a) H_2 permeation flux, (b) N_2 permeation flux, (c) NH_3 permeation flux

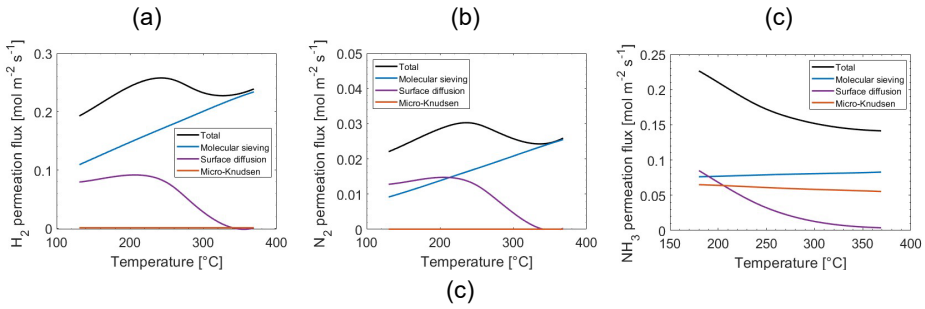


Figure A.3.11 T-99-Co contributions of different gas transport mechanism based on fitted parameters at ΔP = 5 bar for (a) H_2 permeation flux, (b) N_2 permeation flux, (c) NH_3 permeation flux

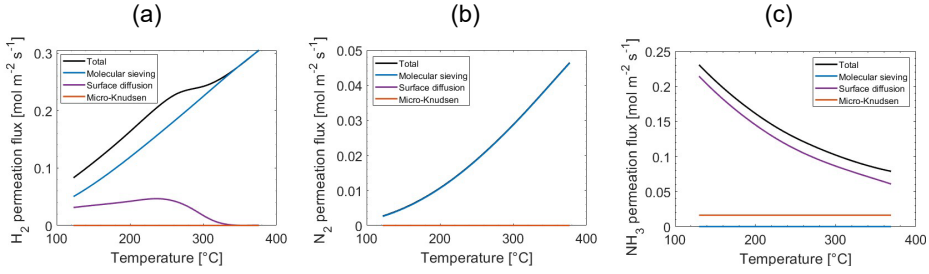


Figure A.3.12 T-116-Cu contributions of different gas transport mechanism based on fitted parameters at ΔP = 5 bar for (a) H_2 permeation flux, (b) N_2 permeation flux, (c) NH_3 permeation flux

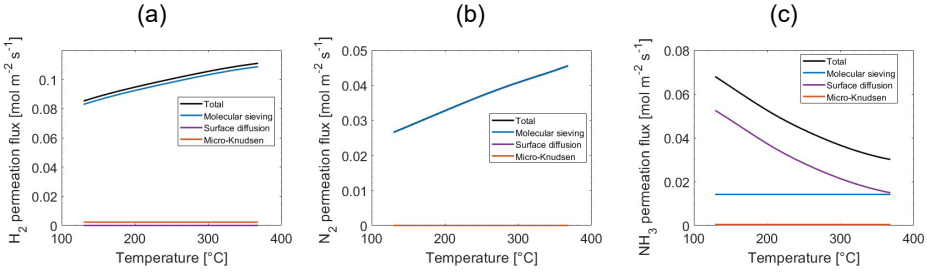


Figure A.3.13 U-24-Ni contributions of different gas transport mechanism based on fitted parameters at ΔP = 5 bar for (a) H_2 permeation flux, (b) N_2 permeation flux, (c) NH_3 permeation flux

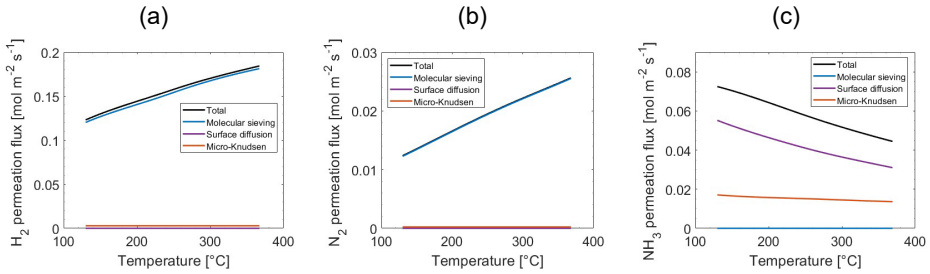


Figure A.3.14 U-26-Ni contributions of different gas transport mechanism based on fitted parameters at ΔP = 5 bar for (a) H_2 permeation flux, (b) N_2 permeation flux, (c) NH_3 permeation flux

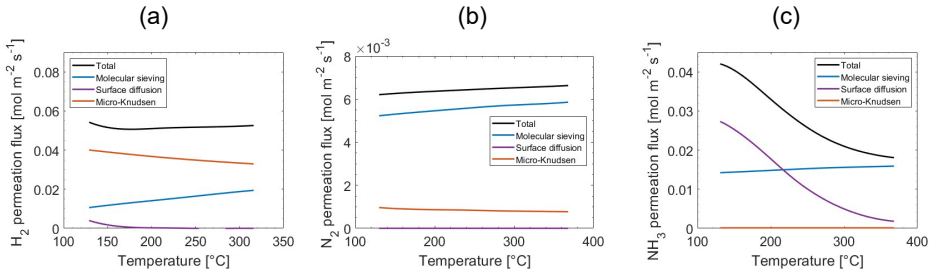


Figure A.3.15 U-33-Zn contributions of different gas transport mechanism based on fitted parameters at ΔP = 5 bar for (a) H_2 permeation flux, (b) N_2 permeation flux, (c) NH_3 permeation flux

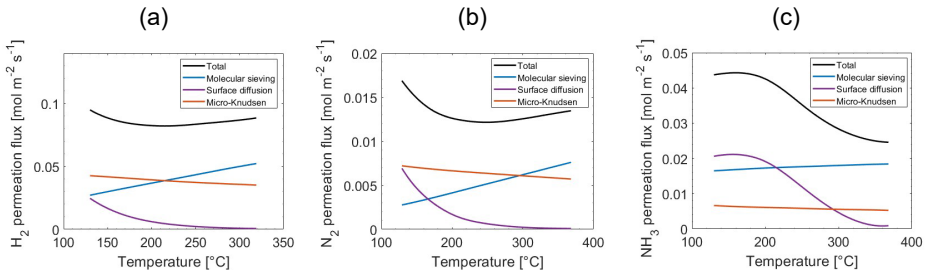


Figure A.3.16 U-37-Zn contributions of different gas transport mechanism based on fitted parameters at ΔP = 5 bar for (a) H_2 permeation flux, (b) N_2 permeation flux, (c) NH_3 permeation flux

REFERENCES

[1] K. Nath, "Membrane separation processes", Second edition, 2017.

[2] G. Genduso, W. Ogieglo, Y. Wang, I. Pinnau, "Carbon molecular sieve gas separation materials and membranes: A comprehensive review", *J. Memb. Sci.* 699 (2024) 122533. https://doi.org/10.1016/j.memsci.2024.122533.

[3] A. Bhown, E. L.Cussler, "Mechanism for Selective Ammonia Transport through Poly(vinylammoniumthiocyanate) Membranes", *J. Am. Chem. Soc* 113 (1991) 1059. https://pubs.acs.org/jacsat/article-pdf/113/3/742/7201546/ja00003a002.pdf.

[4] Y. He, E.L. Cussler, "Ammonia permeabilities of perfluorosulfonic membranes in various ionic forms", *J. Memb. Sci.* 68 (1992) 43–52. https://doi.org/10.1016/0376-7388(92)80148-d.

[5] K. Wakimoto, W.W. Yan, N. Moriyama, H. Nagasawa, M. Kanezashi, T. Tsuru, "Ammonia permeation of fluorinated sulfonic acid polymer/ceramic composite membranes", *J. Memb. Sci.* 658 (2022) 120718. https://doi.org/10.1016/j.memsci.2022.120718.

[6] W.W. Yan, T. Tsuru, "Overview: Insight into NH3 permselective membranes and their application to a membrane reactor for efficient ammonia production", *Sep. Purif. Technol.* 370 (2025) 133275. https://doi.org/10.1016/j.seppur.2025.133275.

[7] S. Padinjarekutt, H. Li, S. Ren, P. Ramesh, F. Zhou, S. Li, G. Belfort, M. Yu, "Na+-gated nanochannel membrane for highly selective ammonia (NH3) separation in the Haber-Bosch process", *Chemical Engineering Journal* 454 (2023) 139998. https://doi.org/10.1016/j.cej.2022.139998.

[8] W.W. Yan, K. Wakimoto, N. Moriyama, H. Nagasawa, M. Kanezashi, T. Tsuru, "Development of sulfonated (3-Mercaptopropyl)trimethoxysilane membranes with thermal stability and excellent NH3 perm-selectivity at 300 °C", *J. Memb. Sci.* 696 (2024) 122535. https://doi.org/10.1016/j.memsci.2024.122535.

[9] W.W. Yan, K. Wakimoto, N. Moriyama, H. Nagasawa, M. Kanezashi, T. Tsuru, "Fabrication of 3-(trihydroxysilyl)-1-propanesulfonic acid membranes with superior affinity and selectivity for NH3 permeation over H2 and N2 at 50–300 °C", *J. Memb. Sci.* 702 (2024) 122798. https://doi.org/10.1016/j.memsci.2024.122798.

[10] C. Zamfirescu, I. Dincer, "Innovative NH3 separation over immobilized molten salt membrane at high temperatures", *Chemical Engineering Journal* 479 (2024) 147434. https://doi.org/10.1016/j.cej.2023.147434.

[11] K. Briceño, R. Garcia-Valls, D. Montané, "State of the art of carbon molecular sieves supported on tubular ceramics for gas separation applications", *Asia-Pacific Journal of Chemical Engineering* 5 (2010) 169–178. https://doi.org/10.1002/apj.377.

[12] L. Forster, C. D'Agostino, M.A. Llosa-Tanco, V. Spallina, C. Brencio, F. Gallucci, M. Lindley, S.J. Haigh, D.A. Pacheco-Tanaka, "Tailoring pore structure and surface

chemistry of microporous Alumina-Carbon Molecular Sieve Membranes (Al-CMSMs) by altering carbonization temperature for optimal gas separation performance: An investigation using low-field NMR relaxation measurements", *Chemical Engineering Journal* 424 (2021) 129313. https://doi.org/10.1016/j.cej.2021.129313.

[13] T.A. Centeno, J.L. Vilas, A.B. Fuertes, "Effects of phenolic resin pyrolysis conditions on carbon membrane performance for gas separation", *J. Memb. Sci.* 228 (2004) 45–54. https://doi.org/10.1016/j.memsci.2003.09.010.

[14] S. Poto, A. Aguirre, F. Huigh, M.A. Llosa-Tanco, D.A. Pacheco-Tanaka, F. Gallucci, M.F. Neira d'Angelo, "Carbon molecular sieve membranes for water separation in CO2 hydrogenation reactions: Effect of the carbonization temperature", *J. Memb. Sci.* 677 (2023) 121613. https://doi.org/10.1016/j.memsci.2023.121613.

[15] K.A. Trick, T.E. Saliba, "Mechanisms of the pyrolysis of phenolic resin in a carbon/phenolic composite", *Carbon* 33 (1995) 1509–1515. https://doi.org/10.1016/0008-6223(95)00092-r.

[16] J.S. Adams, A.K. Itta, C. Zhang, G.B. Wenz, O. Sanyal, W.J. Koros, "New insights into structural evolution in carbon molecular sieve membranes during pyrolysis", *Carbon* 141 (2019) 238–246. https://doi.org/10.1016/j.carbon.2018.09.039.

[17] S.M. Saufi, A.F. Ismail, "Fabrication of carbon membranes for gas separation—a review", *Carbon* 42 (2004) 241–259. https://doi.org/10.1016/j.carbon.2003.10.022.

[18] L.M. Le Leuch, T.J. Bandosz, "The role of water and surface acidity on the reactive adsorption of ammonia on modified activated carbons", *Carbon* 45 (2007) 568–578. https://doi.org/10.1016/j.carbon.2006.10.016.

[19] T.J. Bandosz, C. Petit, "On the reactive adsorption of ammonia on activated carbons modified by impregnation with inorganic compounds", *J. Colloid Interface Sci.* 338 (2009) 329–345. https://doi.org/10.1016/j.jcis.2009.06.039.

[20] M. Teixeira, S.C. Rodrigues, M. Campo, D.A. Pacheco Tanaka, M.A. Llosa Tanco, L.M. Madeira, J.M. Sousa, A. Mendes, "Boehmite-phenolic resin carbon molecular sieve membranes—Permeation and adsorption studies", *Chemical Engineering Research and Design* 92 (2014) 2668–2680. https://doi.org/10.1016/j.cherd.2013.12.028.

[21] A. Rahimalimamaghani, D.A. Pacheco Tanaka, M.A. Llosa Tanco, F. Neira D'Angelo, F. Gallucci, "Effect of aluminium acetyl acetonate on the hydrogen and nitrogen permeation of carbon molecular sieves membranes", *Int. J. Hydrogen Energy* 47 (2022) 14570–14579. https://doi.org/10.1016/j.ijhydene.2022.02.198.

[22] Z.Y. Wu, S.L. Xu, Q.Q. Yan, Z.Q. Chen, Y.W. Ding, C. Li, H.W. Liang, S.H. Yu, "Transition metal–assisted carbonization of small organic molecules toward functional carbon materials", *Sci. Adv.* 4 (2018) 788–815. https://doi.org/10.1126/sciadv.aat0788.

[23] J.A. Lie, M.B. Hägg, "Carbon membranes from cellulose and metal loaded cellulose", *Carbon* 43 (2005) 2600–2607.

https://doi.org/10.1016/j.carbon.2005.05.018.

[24] T. Horiuchi, H. Hidaka, T. Fukui, Y. Kubo, M. Horio, K. Suzuki, T. Mori, "Effect of added basic metal oxides on CO2 adsorption on alumina at elevated temperatures", *Appl. Catal. A Gen.* 167 (1998) 195–202. https://doi.org/10.1016/s0926-860x(97)00318-9.

[25] M.-B. Hägg, X. He, Carbon Molecular Sieve Membranes for Gas Separation. https://doi.org/10.1039/9781849733489-00162.

[26] Y. Li, B. Wang, Z. Yu, X. Zhou, D. Kang, Y. Wu, Z. Chen, C. He, X. Zhou, "The effects of central metals on ammonia sensing of metallophthalocyanines covalently bonded to graphene oxide hybrids", *RSC Advances* 7 (2017) 34215–34225, doi:10.1039/c7ra06081e.

[27] X. Ding, H. Xu, L. Zhang, D. Jiang, A. Lu, "A novel amphiphilic zinc phthalocyanine LB flms as gas sensor material and its interaction with NH3", *Molecular Crystals and Liquid Crystals Science and Technology Section A: Molecular Crystals and Liquid Crystals* 337 (1999) 481–484. https://doi.org/10.1080/10587259908023482.

[28] D.P. Jiang, A.D. Lu, Y.J. Li, X.M. Pang, Y.L. Hua, "Interaction between copper tetra-4(2,4-ditert-amylphenoxy) phthalocyanine Langmuir-Blodgett films as a gas-sensitive sensor and NH3", *Thin Solid Films* 199 (1991) 173–179. https://doi.org/10.1016/0040-6090(91)90063-4.

[29] R.J.R. Uhlhorn, K. Keizer, A.J. Burggraaf, "Gas transport and separation with ceramic membranes. Part I. Multilayer diffusion and capillary condensation", *J. Memb. Sci.* 66 (1992) 259–269. https://doi.org/10.1016/0376-7388(92)87016-Q.

[30] K. Wu, X. Li, C. Wang, W. Yu, Z. Chen, "Model for Surface Diffusion of Adsorbed Gas in Nanopores of Shale Gas Reservoirs", *Ind. Eng. Chem. Res.* 54 (2015) 3225–3236. https://doi.org/10.1021/ie504030v.

[31] S. Huang, Y. Wu, L. Cheng, H. Liu, Y. Xue, G. Ding, "Apparent Permeability Model for Shale Gas Reservoirs Considering Multiple Transport Mechanisms", *Geofluids* 2018 (2018) 2186194. https://doi.org/10.1155/2018/2186194.

[32] S. Poto, J.G.H. Endepoel, M.A. Llosa-Tanco, D.A. Pacheco-Tanaka, F. Gallucci, M.F. Neira d'Angelo, "Vapor/gas separation through carbon molecular sieve membranes: Experimental and theoretical investigation", *Int. J. Hydrogen Energy* 47 (2022) 11385–11401. https://doi.org/10.1016/j.ijhydene.2021.10.155.

[33] J. Gilron, A. Soffer, "Knudsen diffusion in microporous carbon membranes with molecular sieving character", *J. Memb. Sci.* 209 (2002) 339–352. https://doi.org/10.1016/S0376-7388(02)00074-1.

[34] M.A. Llosa Tanco, D.A. Pacheco Tanaka, A. Mendes, "Composite-alumina-carbon molecular sieve membranes prepared from novolac resin and boehmite. Part II: Effect of the carbonization temperature on the gas permeation properties", *Int. J. Hydrogen Energy* 40 (2015) 3485–3496. https://doi.org/10.1016/j.ijhydene.2014.11.025.

[35] J. Dong, Y. S. Lin, M. Kanezashi, Z. Tang, "Microporous inorganic membranes for high temperature hydrogen purification", *J. Appl. Phys.* 104 (2008). https://doi.org/10.1063/1.3041061.

[36] Z.E. Sahin, D. Emmery, A.R. Mamaghani, M. Gazzani, F. Gallucci, "Mass transport in carbon membranes", (2023). https://doi.org/10.1016/j.coche.2022.100896.

[37] R. Rangarajan, M.A. Mazld, T. Matsuura, S. Sourirajan, "Permeation of pure gases under pressure through asymmetric porous membranes. Membrane characterization and prediction of performance", *Industrial & Engineering Chemistry Process Design and Development* 23 (1984) 79–87. https://doi.org/10.1021/I200024A014.

[38] D.M. Ruthven, Principles of adsorption and adsorption processes, Wiley; 433, (1984).

[39] R. Krishna, "The Maxwell–Stefan description of mixture diffusion in nanoporous crystalline materials", *Microporous and Mesoporous Materials* 185 (2014) 30–50. https://doi.org/10.1016/j.micromeso.2013.10.026.

[40] A.F. Ismail, D. Rana, T. Matsuura, H. C. Foley, "Carbon-based Membranes for Separation Processes".

[41] M.A. Llosa Tanco, D.A. Pacheco Tanaka, S.C. Rodrigues, M. Texeira, A. Mendes, "Composite-alumina-carbon molecular sieve membranes prepared from novolac resin and boehmite. Part I: Preparation, characterization and gas permeation studies", *Int. J. Hydrogen Energy* 40 (2015) 5653–5663. https://doi.org/10.1016/j.ijhydene.2015.02.112.

[42] L. Giorno, "Permselectivity", Encyclopedia of Membranes (2015) 1–2. https://doi.org/10.1007/978-3-642-40872-4_2245-1.

[43] N. Abdullah, M.A. Rahman, M.H.D. Othman, J. Jaafar, A.F. Ismail, "Membranes and Membrane Processes: Fundamentals", *Current Trends and Future Developments on (Bio-) Membranes: Photocatalytic Membranes and Photocatalytic Membrane Reactors* 3 (2018) 45–70. https://doi.org/10.1016/b978-0-12-813549-5.00002-5.

[44] Z. He, K. Wang, "The 'ideal selectivity' vs 'true selectivity' for permeation of gas mixture in nanoporous membranes", *IOP Conf. Ser. Mater. Sci. Eng.* 323 (2018) 012002. https://doi.org/10.1088/1757-899x/323/1/012002.

[45] T. Tsuru, T. Hino, T. Yoshioka, M. Asaeda, "Permporometry characterization of microporous ceramic membranes", J. Memb. Sci. 186 (2001) 257–265. https://doi.org/10.1016/S0376-7388(00)00692-X.

[46] Z.E. Sahin, A. Rahimalimamaghani, M. Gazzani, F. Gallucci, "Gas permeation through carbon membranes: Model development and experimental validation", *Int. J. Hydrogen Energy* 50 (2024) 561–581. https://doi.org/10.1016/j.ijhydene.2023.08.272.

[47] Particle Swarm Optimization Algorithm - MATLAB & Simulink. https://nl.mathworks.com/help/gads/particle-swarm-optimization-

algorithm.html.

[48] H. Irving, R.J.P. Williams, "The stability of transition-metal complexes", *Journal of the Chemical Society* 156 (1953) 3192–3210. https://doi.org/10.1039/jr9530003192/27862

CHAPTER 4

Activated triply periodic minimal surfaces (TPMS) Gyroid supports for efficient ammonia synthesis in membrane-integrated reactors

ABSTRACT:
In this chapter, a new membrane reactor concept is investigated: a CMS membrane embedded in an activated Triply Periodic Minimal Surface (TPMS) Gyroid support uniformly coated with a Ru-based catalytic layer. The most favourable baseline conditions were identified at the lowest weight hourly space velocity (WHSV = 715 $mLn \cdot g_{cat}^{-1} h^{-1}$) and an understoichiometric H_2:N_2 feed ratio of 2:1, reflecting proximity to thermodynamic equilibrium and the benefit of reduced hydrogen partial pressure on Ru-based catalysis. At 250 °C and 40 bar, increasing the sweep-gas-to-feed flow ratio (SW) to 10 enhanced NH_3 production rate by 43% and NH_3 yield by 15%, with an NH_3 recovery factor of 84%. At 30 bar and higher temperatures (350-450 °C), NH_3 production rate was still enhanced at reduced sweep-gas-to-feed flow ratios, with gains of 36-248% at SW = 1 and 41-133% at SW = 4 vs. the structured catalyst reactor (SCR). However, NH_3 recovery fell to 64-70% at SW = 1 and 41-66% at SW = 4, compared with 87-95% at 40 bar, demonstrating a trade-off between production rate and recovery. At 450 °C and 40 bar, with SW = 4, H_2 conversion exceeded equilibrium by 15-30%, while the conversion achieved at 400 °C in the SCR was already attained at 300 °C in the structured catalyst membrane reactor (SCMR). At 400 °C and 40 bar with SW = 4, H_2 conversion, NH_3 production rate, and NH_3 yield increased by 83%, 77%, and 53%, vs. the SCR. Gyroid and Body-centred cubic (BCC) geometries exhibit similar ammonia production performance. These findings provide a proof of concept for structured membrane reactors in ammonia synthesis: integrating Ru-based catalysts with carbon membranes can enhance efficiency and shift equilibrium under milder conditions, providing a basis for future scale-up.

This chapter is based on the following journal article:
"Activated Triply Periodic Minimal Surfaces (TPMS) Gyroid supports for efficient ammonia synthesis in membrane-integrated reactors", **I. Gargiulo**, A. Vita, C. Italiano, M. A. Llosa Tanco, D. A. Pacheco Tanaka, F. Gallucci, *Int. J. Hydrogen Energy*, 2026.

4.1 INTRODUCTION

Building on the background presented in Chapter 1, this chapter explores the use of structured catalyst architectures to address the thermodynamic and transport limitations of conventional packed bed systems. From the perspective of on-site ammonia production, structuring the catalyst can provide a more compact reactor configuration with improved transport characteristics [1]. In particular, triply periodic minimal surface (TPMS) structures are attractive because they provide interconnected flow pathways, high specific surface area, controllable pore-size distributions, low pressure drop, and good mechanical stability through efficient stress distribution [2].

In this chapter, these concepts are implemented in a structured catalyst membrane reactor (SCMR) that integrates a Cu-containing carbon molecular sieve (CMS) membrane within an activated TPMS Gyroid support coated with a Ru-based catalyst. The Cu-CMS membrane was selected based on the results presented in Chapter 3, where Cu-containing membranes were identified as promising candidates for ammonia separation. This configuration combines ammonia synthesis and in-situ product removal within a single structured reactor, enabling the influence of membrane integration on reactor performance to be assessed experimentally.

The SCMR was evaluated under a range of operating conditions, including temperature, pressure, H_2:N_2 feed ratio, weight hourly space velocity (WHSV), and sweep-gas-to-feed flow ratio (SW). The effects of these parameters on H_2 conversion, NH_3 production rate, NH_3 yield, and NH_3 recovery were investigated. The performance of the SCMR was compared with that of the corresponding structured catalyst reactor (SCR) without a membrane to quantify the contribution of membrane-assisted ammonia removal.

In addition, the performance of the Gyroid configuration was compared with that of a BCC structure under selected operating conditions. This comparison provides insight into the influence of POCS geometry on reactor performance and helps assess the potential of structured catalyst membrane reactors for further optimisation and scale-up.

4.2 EXPERIMENTAL: MATERIALS AND PREPARATION

4.2.1 TPMS Gyroid supports: manufacturing and catalytic activation by dip/spin coating

The Ni-alloy (IN625) Gyroid supports were manufactured using the Laser Powder Bed Fusion (LPBF) technique based on CAD files, resulting in cylindrical structures with a diameter of 26.66 mm and a length of 100 mm. The supports, incorporating a central channel (Ø = 15.1 mm), are specifically designed to host a CMS membrane. The Gyroid architecture was characterised by a cell size of 5 mm, a sheet diameter

of 0.34 mm, a specific surface area of 4.3 mm^{-1}, pore size of 2.16 mm and an overall porosity of 70%. **Figure 4.1** shows the support and its unit cell investigated in this work is reported.

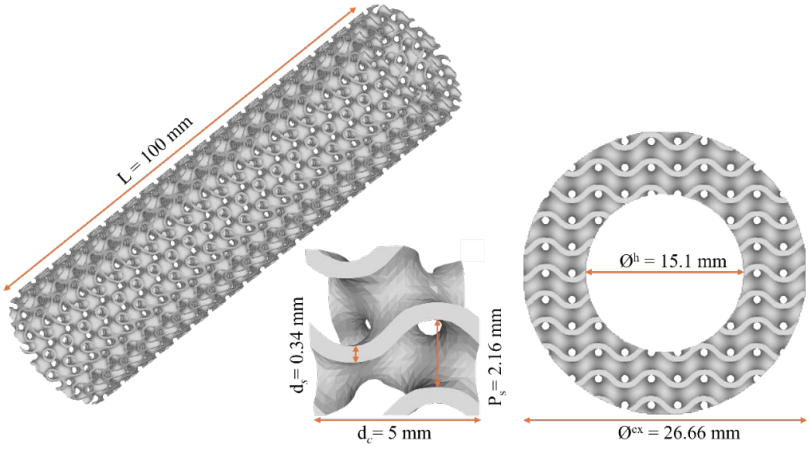


Figure 4.1 Rendering of Gyroid structure (L = length, $Ø^{ex}$ = external diameter, $Ø^h$ = hole diameter) and relative unit cell; d_c represents the cell dimension, d_s the thickness of the sheet and P_s the pore size dimension

A newly developed Ru-based (2.2 wt%) catalyst provided by Johnson Matthey (JM) in powder form was used to prepare a slurry mixture for activating the two identical Gyroid supports. The composition of the prepared slurry is reported in **Table 4.1**. The powder dispersions were prepared following a procedure described elsewhere [3].

Table 4.1 Composition of the prepared slurry

Catalyst [g]	Powder catalyst [wt%]	Glycerol [wt%]	PVA [wt%]	Water [wt%]	Slurry volume [mL]	Catalyst loaded [g]
2.2 wt% Ru-based 35	22.4	42.5	1.5	33.6	155	*Pc.1* = 6.54 *Pc.2* = 6.15

The dispersion medium was prepared by dissolving polyvinyl alcohol (PVA, 87-89% hydrolysed, Sigma-Aldrich) in distilled water, followed by the addition of glycerol (GLY, 99.5% bi-distilled, Analar Normapur®) under magnetic stirring at 85 °C. In this formulation, glycerol served as a dispersant, polyvinyl alcohol (PVA) as a rheology modifier, and distilled water as a solvent/diluent. The catalyst powder was homogenised by ball milling (Planetary Ball Mill BM40-POWTEQ) with zirconia spheres (1 cm diameter, mass ratio of spheres to catalyst powder = 7:1) for 24 h at 300 rpm in a 250 cm^3 zirconia jar. Before being added to the dispersion, the catalyst

powder itself was pre-milled in the same jar for 3 h at 300 rpm. After the milling process, the slurry underwent a 30 min sonication treatment to minimise foaming. Prior to deposition, the as-built Gyroid supports were cleaned by ultrasonic treatment in an acetone/water solution (50:50 vol%) for 30 min, thoroughly rinsed with water, and dried at 120 °C for 1 h. The structures were then calcined in air at 900 °C for 6 h. To ensure complete wetting of the porous network, samples were immersed in the slurry for about 10 s. Excess slurry was subsequently removed with a commercial spin-coater (Laurell WS-650Mz-23 NPPB) operated at 1,000 rpm, with 20 s rotation time and an acceleration of 1,000 rpm s^{-1}.



Figure 4.2 Images of bare (central) and coated Gyroid support (left and right)

After each coating step, samples were flash dried in air at 350 °C for 6 min. This process was repeated approximately 11 times to reach a washcoat load of ~6 g per piece, as reported in **Table 4.1**. The structures were then calcined at 500 °C for 6 h (heating rate: 5 °C·min^{-1}). Gravimetric analysis was performed after each drying and calcination step to monitor weight evolution and confirm washcoat loading. **Figure 4.2** shows images of the two activated Gyroid supports used in this study, compared with the bare one. Although a preliminary comparison between Gyroid and BCC geometries is presented in this chapter, a comprehensive characterisation and analysis of the BCC-based structured catalyst is presented in Chapter 6.

4.2.2 Carbon molecular sieve (CMS) membrane fabrication

Novolac resin was synthesised by the acid-catalysed condensation of phenol (99%) and formaldehyde (37%) following the procedure reported in [5]. A precursor solution containing novolac resin (16 wt%), formaldehyde (2.4 wt%) and ethylenediamine (0.4 wt%) dispersed in N-methyl-2-pyrrolidone (NMP) as a solvent, was prepared and heated at 90 °C for 90 minutes to form a novolac oligomer. After cooling, an appropriate amount of an aqueous $Cu(NO_3)_2$ solution (10 wt% of Cu^{2+}) was added to obtain 0.1 wt% of Cu^{2+} in the dipping solution. A 50 cm long asymmetric porous α-Al_2O_3 tube ($Ø^{in}$ = 7 mm, $Ø^{ex}$ = 10 mm), with 200 nm average pore size on the external surface was immersed in the dipping solution for 90

seconds. The coated support was placed vertically in an oven at 90 °C for 12 h to advance polymerisation and evaporate solvent. Finally, the membrane was carbonised at 550 °C for 2 h under N_2 atmosphere.



Figure 4.3 CMS membrane sealed using Swagelok fittings to enable connection to the reactor flange

The membrane was cut so that its overall length slightly exceeded that of the TPMS Gyroid catalyst. It was then sealed at both ends using Swagelok fittings with graphite rings to reduce mechanical stress. One end was closed with a dead-end Swagelok fitting, while the other remained open to allow connection to the flange, as shown in **Figure 4.3**.

4.3 CHARACTERISATION TECHNIQUES

4.3.1 TPMS Gyroid catalyst and coating slurry

A Keyence VHX-7000 digital optical microscope, characterised by a fully integrated head using stage shift technology and 4K mode for high-resolution imaging, was used for morphological measurements. Detailed images of the Gyroid catalyst were acquired with VHX-E20 (High-Resolution, Low-Magnification Objective Lens 20-100×) and VHX-E100 lenses (High-Resolution, Medium-Magnification Objective Lens 100-500×). Measurements were taken at various points on the struts and cells to identify any discrepancies from the CAD model.

The rheology of the slurry used for the coating of the structured catalyst was characterised using a rotational rheometer (Modular Compact Rheometer MCR 92, Anton Paar GmbH, Graz, Austria). Measurements were performed at 25 °C by using a double gap measuring system, and the slurry viscosity was measured in the 0.1-3000 s^{-1} shear-rate range.

4.3.2 CMS membrane

The membrane was first characterised in terms of its gas permeation performance. Permeance and selectivity were calculated from the measured permeate and feed compositions using Equations (3.4)-(3.7). Single- and mixed-gas permeation experiments were performed in the same setup as the catalytic tests, but without catalyst and under identical temperature and pressure conditions. Gas compositions were analysed using a Compact GC 4.0 micro-gas chromatograph (Global Analyser Solutions, GAS) equipped with two analytical channels and two thermal conductivity

detectors (TCDs). The first channel employed a Molsieve 5A column (7 m×0.32 mm) for the separation of N_2, H_2, and CH_4, using Ar as carrier gas at 100 °C, with an injection temperature of 130 °C and an inlet pressure of 110 kPa. The second channel used an Rtx-Volatile Amine column (30 m×0.32 mm) for NH_3 analysis, with He as carrier gas at 100 °C, an injection temperature of 130 °C, and an inlet pressure of 75 kPa.
Thermo Scientific™ Phenom Pharos™ G2 Desktop FEG-SEM which is a field-emission scanning electron microscope designed for high-resolution imaging of surfaces and cross-sections, was used to study the morphology of the membrane. It was operated at 10-15 kV, with magnifications in the range 20,000-35,000×, and elemental composition was analysed by energy-dispersive X-ray spectroscopy (EDX).

4.3.3 Experimental setup

The configuration of the experimental setup used to perform the tests is shown in **Figure 4.4**. The gas supply system includes nitrogen (N_2), hydrogen (H_2), ammonia (NH_3) and methane (CH_4). Gases are delivered either from high-pressure gas bottles (Linde) located in a gas cabinet equipped with pressure reducers (up to 66 bar for N_2 and H_2, and up to 8 bar for NH_3, limited by vapour-liquid equilibrium) or via a centralised feed line (N_2 for Pneumatic Valve Island and CH_4 for internal standard during analysis) operating at 6 bar. Flow rates are controlled by Bronkhorst mass-flow controllers (MFCs) with operating ranges of 20-1000 $mLn \cdot min^{-1}$ for N_2, 40-2000 $mLn \cdot min^{-1}$ for H_2, and 10-500 $mLn \cdot min^{-1}$ for NH_3. Pneumatically actuated Swagelok valves are used to automatically open and close the gas lines, while Swagelok check valves equipped with Kalrez® seals are installed downstream of the MFCs to prevent backflow. The reactor can be bypassed when required through three-way Swagelok valves. The reactor consists of an Inconel vessel ($Ø^{ex}$ = 33 mm, $Ø^{in}$ = 29 mm, L = 300 mm) that accommodates a TPMS unit, into which a CMS membrane is integrated. The assembly comprises two 10 cm TPMS segments stacked vertically, yielding a 20 cm total active length, as shown in **Figure 4.5**.
The membrane is sealed to the top flange, resulting in an overall membrane length of approximately 21 cm. To ensure thermal uniformity, the retentate and permeate feed lines, as well as the reactor body, are equipped with electrical heat tracing for preheating (IS-SP-H/230V/330W/KE1.5M). The retentate and permeate streams are physically separated: the retentate leaves the reactor laterally, whereas the permeate is withdrawn from the top flange. To ensure co-current operation, the reaction stream enters from the bottom of the reactor, while the sweep gas is introduced from the top via an internal capillary ($Ø^{ex}$ = 3 mm) that extends to the end of the membrane and then flows back along its length in the same axial direction as the retentate stream. Temperature is monitored using digital temperature transmitters: two thermocouples are installed inside the reactor (TE 502, TE 801E),

one control thermocouple is positioned externally on the reactor wall (TC 801A), and additional control thermocouples are located at the preheating sections of both the retentate and permeate lines (TC 501, TC 601). A thermocouple (TE 602) is also embedded within the membrane to monitor local conditions along the separation interface.

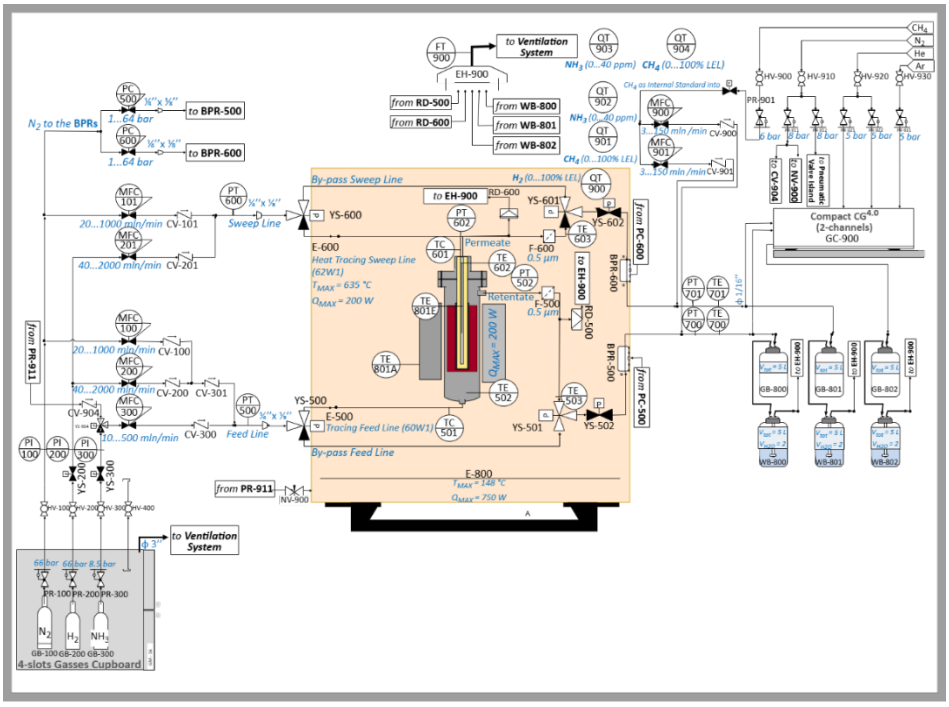


Figure 4.4 P&ID of the experimental setup used for the structured catalyst reactor (SCR)/structured catalyst membrane reactor (SCMR)

The entire reactor is enclosed within an electrical oven (247 Tailorsteel) to maintain isothermal conditions, and nitrogen is continuously flushed through the oven to ensure an inert atmosphere and prevent corrosion. Analogue pressure indicators (PI 100, PI 200, PI 300) are installed on the gas inlet lines, while electronic pressure transmitters (PT 502, PT 602 (Pressure Control Solutions)) are placed at the outlet of both retentate and permeate streams to monitor the actual system pressure. Back-pressure regulators (BPR-500, BPR-600, Equilibar LF, SS316, 69 bar, 150 °C) are used to regulate pressure separately on the two sides of the membrane. Rupture discs are installed at the outlets of both streams, set to relieve at a maximum pressure of 80 bar ± 5% at 20 °C to ensure safe operation. Upon leaving the reactor, gas streams can be directed to a Compact GC 4.0 micro-gas chromatograph (described in subsection 4.3.2) for compositional analysis. Methane is used as an internal standard to enable accurate determination of flow rates at both the retentate and

permeate outlets. Finally, all exhaust gases are passed through a scrubbing system to remove residual ammonia before being safely vented.

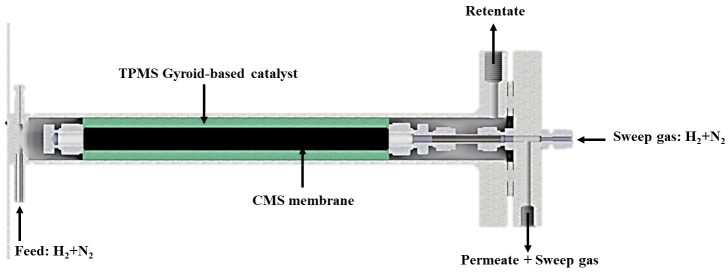


Figure 4.5 Internal sectional view of the tubular membrane reactor showing the TPMS catalyst support and central CMS membrane

4.4 OPERATING CONDITIONS AND KEY PERFORMANCE INDICATORS FOR REACTOR PERFORMANCE

The H_2 conversion and NH_3 recovery expressions introduced in Chapter 2, Equations (2.17)-(2.18), were also used in the present analysis. These equations account for hydrogen transport across the membrane, including both outward permeation and reverse transport, as well as the fraction of ammonia recovered on the permeate side. The following additional indicators were also considered:

$$\%\, Y_{NH_3} = \frac{F^R_{NH_3} + F^P_{NH_3}}{F^R_{H_2,in} - F^*_{H_2,tm}} \times 100 \tag{4.1}$$

$$NH_3\ production\ rate = \frac{F^R_{NH_3} + F^P_{NH_3}}{w_{cat}} \tag{4.2}$$

$$\%\ Improvement = \frac{KPI_i^{SCMR} - KPI_i^{SCR}}{KPI_i^{SCR}} \times 100 \tag{4.3}$$

The NH_3 yield (Y_{NH_3}) expresses the amount of ammonia formed with respect to the hydrogen available in the retentate, considering any co-fed hydrogen if applicable. The NH_3 production rate ($NH_3\ production\ rate$) considers the total ammonia formed within the system, normalised to the total catalyst used during the experiments, thus providing a consistent basis for production rate comparison. Finally, the percentage improvement quantifies the relative enhancement in performance achieved by the membrane-assisted configuration compared to the conventional reactor system.

The structured catalyst is evaluated under a range of operating conditions to quantify temperature, pressure, composition, and production rate profiles. To enable a direct comparison with the SCMR, all catalytic activity tests are performed using the same reactor configuration described in Section 4.3.3. In this configuration, a ceramic glass tube is inserted inside the structured catalyst in place of the CMS membrane in order

to isolate the permeate side while suppressing permeation. Before testing, the structured catalyst is reduced in situ using a 75% H_2/25% N_2 mixture, applying successive temperature steps from 200 °C to 550 °C. Subsequently, activity measurements are carried out in the temperature range 250-450 °C, at pressures between 10-40 bar, and with inlet molar feed ratios H_2:N_2 = 3:1/2:1. The weight hourly space velocity is varied between 715-14,273 $mL_N \cdot g_{cat}^{-1} h^{-1}$ to investigate the influence of contact time on reactor performance.

4.5 RESULTS AND DISCUSSION

4.5.1 TPMS Gyroid catalyst: morphological and rheological characterisation

Rheological characterisation (**Figure 4.6**) revealed that the slurry exhibited Newtonian behaviour. This property is particularly advantageous for coating applications, as it ensures the slurry maintains a stable viscosity across varying shear rates, allowing for predictable flow and easy application. As a result, uniform and defect-free coatings can be achieved, with the slurry readily penetrating small pores and conforming to the complex geometries of the support structure. Slurry deposition was carried out using a combined dip-spin coating procedure previously optimised [4].

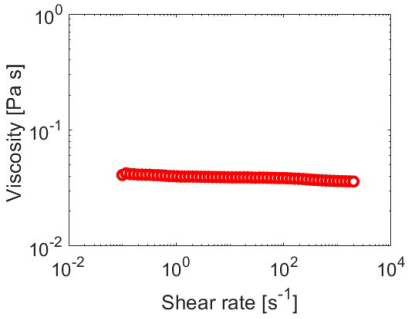


Figure 4.6 Slurry rheological behaviour

Figure 4.7 shows different optical images of the TPMS Gyroid structures. Sheet diameters and cell sizes of the uncoated Gyroid were measured using the dedicated software of the Keyence VHX-7000 microscope. Thanks to the high reproducibility of the adopted manufacturing technique, only minor variations in sheet dimensions were detected compared to the CAD model (**Figure 4.1**). Measurements performed on the as-built sample (**Figure 4.7**(a)) confirmed the high resolution of the process, with deviations remaining within narrow tolerances and thus demonstrating the reliability of the fabrication method in accurately reproducing the designed geometry. The coating process resulted in a uniform catalytic layer, with the porous network fully covered while preserving the open-cell architecture and preventing

clogging. Representative images (**Figure 4.7**(b)-(d)) highlight the homogeneous distribution of the catalyst throughout the Gyroid geometry. The spin-coating step was particularly critical in ensuring proper slurry distribution: at higher spinning speeds, excess slurry was effectively removed, leading to thinner layers and preventing pore occlusion.

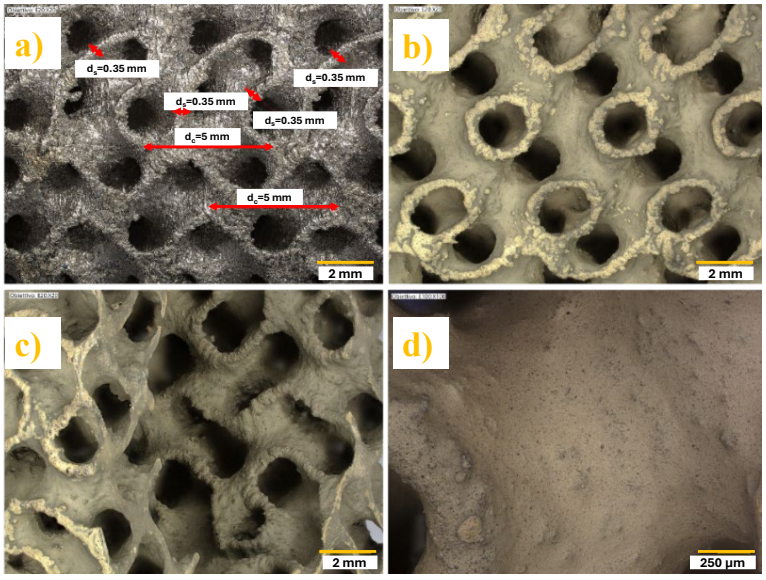


Figure 4.7 Optical images of: (a) external surface of the Gyroid support as built, (b) external surface of coated Gyroid support, (c) view of the activated internal hole zone, (d) magnification of the external coated surface

4.5.2 CMS membrane: separation performance and morphological characterisation

Single- and mixed-gas permeation experiments were carried out to discriminate the intrinsic behaviour of the membrane and assess how closely it approaches the targeted performance. All measurements were performed in the setup described in Section 4.3.3, over the full temperature range applied in the reaction tests and at pressures up to 40 bar. The results reported in **Figure 4.8** refer to a pressure of 8 bar, which corresponds to the maximum attainable ammonia pressure imposed by the equilibrium conditions in the gas cylinder; data at other pressures for hydrogen and nitrogen are provided in the Appendix. Across the full pressure range (**Figure A.4.1-Figure A.4.5**(a)), nitrogen permeance in single-gas tests remained essentially constant at each temperature, indicating negligible pressure dependence and thus the absence of large defects or cracks and of Poiseuille-type flow. The relatively high H_2 permeance and weak negative temperature dependence are consistent with transport through micropores, where activated diffusion and the temperature-dependent sorption of H_2 may partially compensate each other.

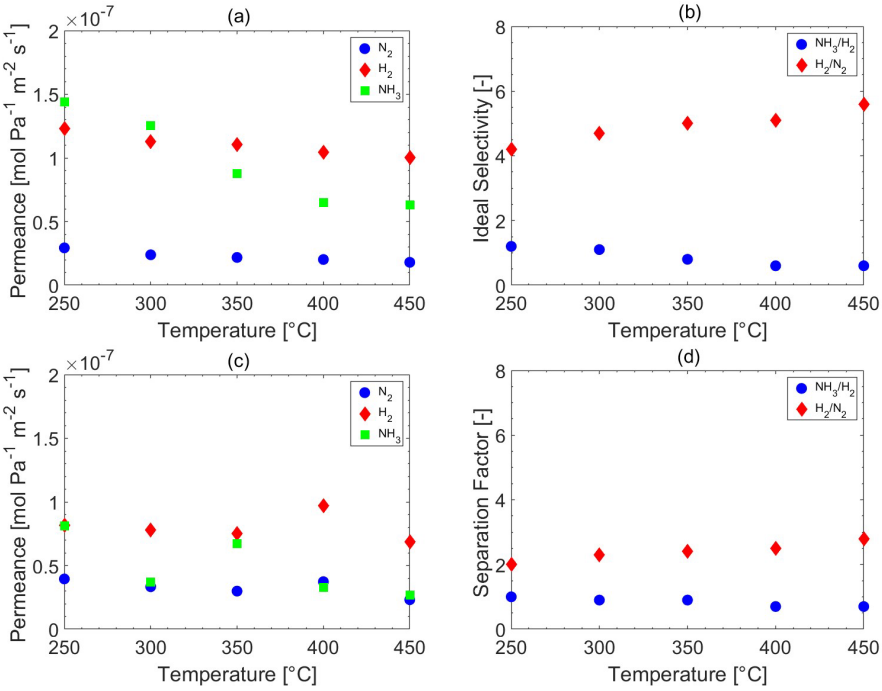


Figure 4.8 Membrane performance at different temperatures and ΔP = 8 bar: (a) single-gas permeance, (b) ideal selectivity, (c) mixed-gas permeance, (d) separation factor

Nevertheless, the plotted data alone do not allow the respective contributions of molecular sieving and surface diffusion to be quantified. Moreover, the permeance exhibits only a weak dependence on pressure across the investigated temperature range (**Figure A.4.1-Figure A.4.5**(a)). This behaviour can be attributed to the weakening of adsorption effects and the increasing dominance of diffusion through ultra-micropores as the rate-controlling step. At very high pressures (30-40 bar), the permeance becomes so high that it could not be accurately measured due to limitations in reactor pressurisation (**Figure A.4.5**).

For ammonia, the dependence on pressure is relatively weak over the investigated range, while permeance is predominantly governed by temperature (**Figure 4.8**(a)), and decreases markedly as the temperature increases, indicating adsorption-diffusion controlled transport with an apparent Arrhenius activation energy dominated by the loss of NH_3 adsorption sites at elevated temperature. Since the measured ideal selectivities (**Figure 4.8**(b)) exceed the corresponding Knudsen values (S_{NH_3/H_2}= 0.34, S_{H_2/N_2}= 3.74), gas transport mechanism is far from the Knudsen regime and dominated by the membrane pore structure and adsorption effects. As a matter of fact, the H_2/N_2 selectivity increased with temperature, consistent with a molecular sieving-dominated mechanism, whereas for NH_3/H_2 it decreases with temperature, reflecting the loss of adsorption-enhanced NH_3 transport relative to

Arrhenius-type, diffusion-dominated H_2 transport. At the highest temperatures, the ideal selectivities move closer to the Knudsen ratios, suggesting an approach towards a more Knudsen-like regime in which size-independent, collision-controlled transport partially replaces adsorption-dominated diffusion.

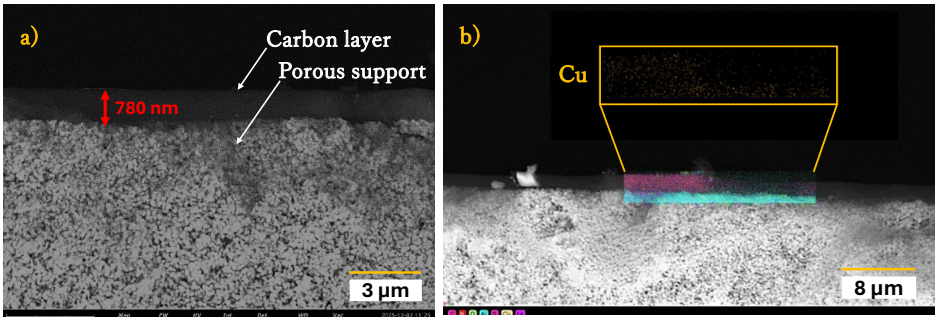


Figure 4.9 Cross-sectional SEM-EDX images of the CMS membrane showing the carbon layer and Cu distribution. Magnification: (a)35,000×- (b)20,000×; accelerating voltage: (a)10-(b)15 kV

In addition to single-gas measurements, mixed-gas permeation tests were conducted using a H_2:N_2 = 1.5:1 feed and a simulated 40% conversion, resulting in a gas composition of 38 vol% N_2, 42 vol% H_2, and 20 vol% NH_3, chosen to closely resemble the reaction environment. Mixed-gas tests at different pressures, shown in **Figure 4.8**(c)-**Figure A.4.6-Figure A.4.7**(a) reveal stronger competition between hydrogen, nitrogen and ammonia, leading to a reduction of the overall H_2/N_2 separation factor compared to the ideal single-gas selectivity. Moreover, the overall permeance of hydrogen and ammonia are lower than the single-gas tests, indicating that competitive adsorption of NH_3 partially blocks micropores available to H_2. As temperature rises, ammonia desorbs and H_2 transport becomes more diffusion-controlled. SEM-EDX analysis, shown in **Figure 4.9,** further confirmed the structural integrity of the selective layer, revealing a continuous ~800 nm thick film without defects and a homogeneous Cu distribution throughout the carbon matrix, as shown in **Table A.4.1**.

4.5.3 Effect of temperatures and pressures on the SCR

Temperature and pressure are the primary operating variables governing ammonia synthesis, because the reaction is simultaneously limited by kinetics and thermodynamics. As expected from Arrhenius behaviour, **Figure 4.10** shows the ammonia formation rate which increases with temperature due to faster surface reaction kinetics, up to the point where the equilibrium NH_3 yield starts to decline as a consequence of the exothermic nature of the reaction. Beyond this regime, further temperature increases lead to lower equilibrium conversions, so that thermodynamic constraints dominate and the observable rate no longer increases monotonically with temperature. Because the overall reaction proceeds with a net

decrease in the number of gas moles, increasing the total pressure shifts the equilibrium toward ammonia according to Le Châtelier's principle. This trend is clearly visible in **Figure 4.10**(a) (WHSV = 2,862 mLn·$g_{cat}^{-1}h^{-1}$), at intermediate residence times, where higher pressure consistently enhances ammonia production.

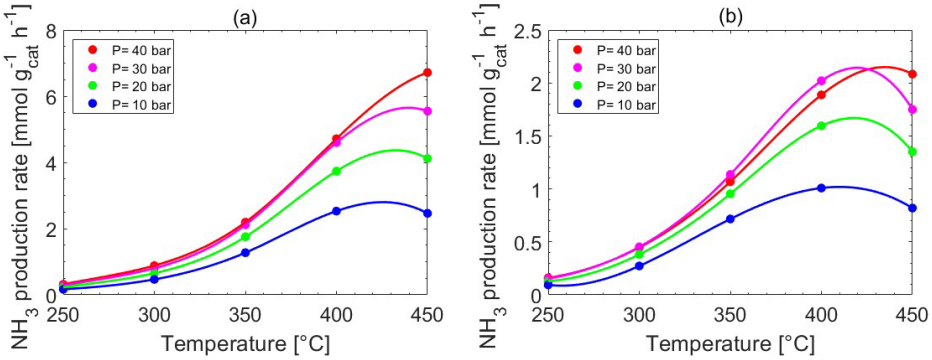


Figure 4.10 NH_3 production rate using inlet molar feed ratios H_2:N_2 = 2:1 as a function of temperature and pressure:(a) WHSV = 2,862 mLn·$g_{cat}^{-1}h^{-1}$, (b) WHSV = 715 mLn·$g_{cat}^{-1}h^{-1}$

At high residence times, (**Figure 4.10**(b) (WHSV = 715 mLn·$g_{cat}^{-1}h^{-1}$)), however, the reactor approaches thermodynamic equilibrium, and the benefit of increasing pressure from 30 to 40 bar becomes marginal or can even reverse for some temperatures, except at the highest temperature investigated (450 °C). This complex behaviour arises from the interplay between thermodynamic limitations and kinetic effects, including ammonia inhibition [6]. As temperature increases, the equilibrium constant decreases for this exothermic reaction, shifting equilibrium away from ammonia and making high pressure increasingly important to compensate for the loss in equilibrium yield. At the same time, higher temperatures accelerate the intrinsic kinetics and reduce the inhibitory effect of adsorbed ammonia on the catalyst, so that the system can benefit more from additional pressure driving the equilibrium toward product formation.

4.5.4 Effect of H_2:N_2 molar feed ratio on the SCR

To elucidate the influence of the hydrogen-to-nitrogen molar ratio on ammonia synthesis over the structured Ru-based catalyst, catalytic tests were performed at 40 bar while varying the H_2:N_2 ratio between 2:1 and the conventional stoichiometric value of 3:1. Prior studies have shown that deviations from the stoichiometric feed composition can markedly impact NH_3 production rate and overall catalyst utilisation efficiency, particularly for ruthenium catalysts that are prone to hydrogen poisoning under hydrogen-rich conditions [7–9]. In line with these findings, **Figure 4.11**(a)-(b) indicate that, across the investigated temperature range of 250-450 °C, the understoichiometric feed (H_2:N_2 = 2:1) generally delivers higher NH_3 production rates than the stoichiometric feed, with the notable exception of 400 °C where the

3:1 ratio becomes slightly more favourable.
This non-monotonic behaviour suggests a temperature-dependent balance between surface kinetics, hydrogen surface coverage, and thermodynamic constraints. For almost all temperatures, the lower H_2 partial pressure in the 2:1 feed likely mitigates hydrogen poisoning on Ru sites, enhancing N_2 activation and thus increasing the intrinsic reaction rate and effective catalyst production rate, despite the nominal hydrogen deficiency. Around 400 °C, however, the combination of accelerated surface kinetics and stronger equilibrium driving force at higher hydrogen partial pressure appears to outweigh the poisoning penalty, so that the stoichiometric 3:1 feed marginally outperforms the understoichiometric case, which is also in line with literature [10]. H_2 conversion increases with temperature for both feed compositions (**Figure 4.11**(c)-(d)), and the H_2: N_2 = 2:1 case consistently exhibits higher H_2 conversion than the 3:1 case, indicating that hydrogen is more completely utilised under understoichiometric conditions.

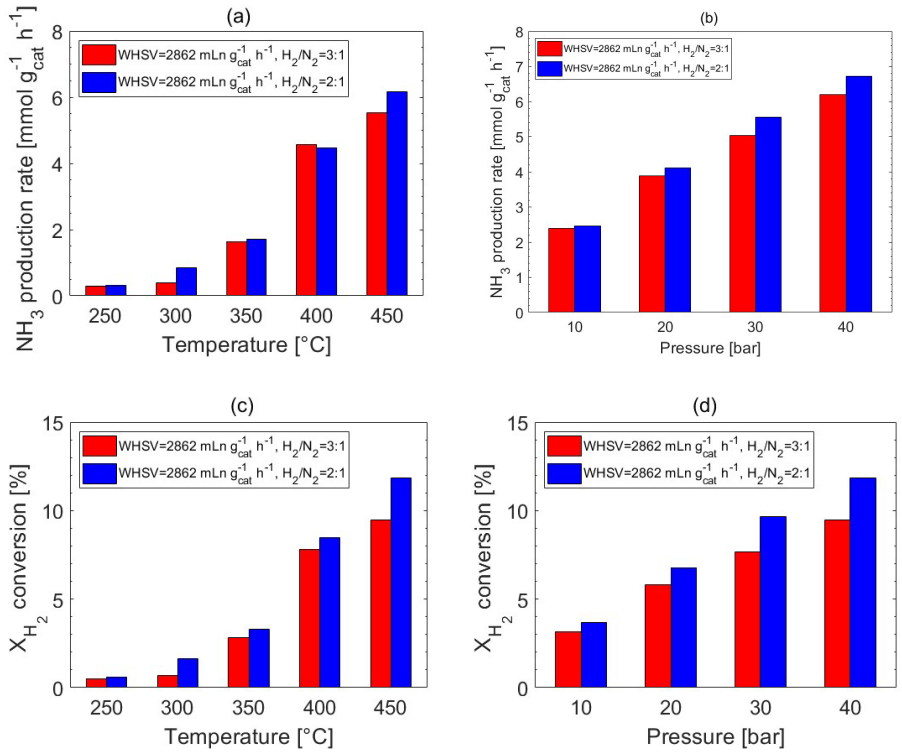


Figure 4.11 H_2:N_2 feed ratio investigation at WHSV = 2,862 mLn·$g_{cat}^{-1}h^{-1}$: NH_3 production rate as a function of: (a) Temperature at 40 bar (b) Pressure at 450 °C; H_2 conversion as a function of: (c) Temperature at 40 bar (d) Pressure at 450 °C

This reflects the complex interplay between reaction kinetics (enhanced at higher temperature and lower hydrogen coverage), equilibrium limitations (more severe at 2:1 when approaching high NH_3 yields), and reactor operation (fixed pressure and

residence time). In a kinetic regime the reaction rate rises with the temperature especially since all available hydrogen is consumed quickly [11].
At the same time, the reason of the non-monotonic behaviour of the NH_3 production rate is that at 2:1, the system is much more sensitive to equilibrium limitations because there is less excess hydrogen to drive the reaction forward.

4.5.5 Effect of WHSV on the SCR

In addition to varying the H_2:N_2 feed ratio, the influence of WHSV on ammonia synthesis was systematically investigated. WHSV is a critical operating parameter that governs the relationship between the molar feed rate, reactant conversion, and NH_3 production rate. The aim is to identify the optimal operating regimes suitable also for the membrane reactor system investigation.
The WHSV was varied in the range of 715-14,273 mLn·$g_{cat}^{-1}$$h^{-1}$ by adjusting the total flow rate of the reactants between 150 and 3,000 mLn·min^{-1}, along with changes in pressure and temperature. **Figure 4.12** presents the results at 450 °C. Increasing WHSV led to a pronounced enhancement in NH_3 production rate, particularly at higher pressures, due to the higher reactant throughput.

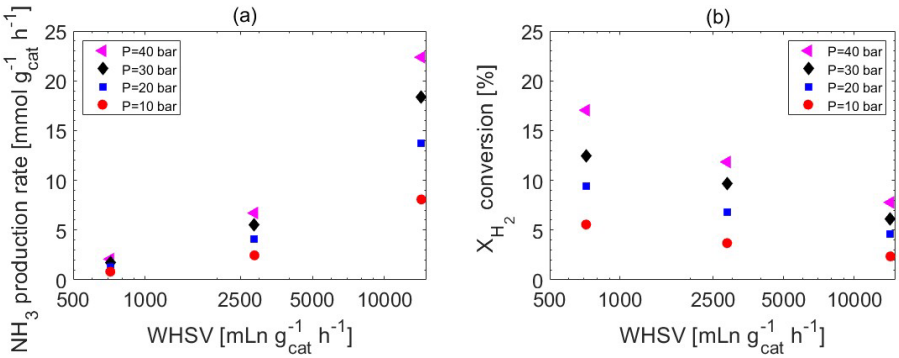


Figure 4.12 (a) NH_3 production rate (b) H_2 conversion as a function of WHSV at different pressures at 450 °C, H_2:N_2 = 2:1

However, as the WHSV increased, the H_2 conversion decreased, reflecting the reduced contact time between the gas phase and the catalyst surface. To ensure higher overall conversion, and allow for a reliable assessment of intrinsic catalytic performance as well as efficient ammonia permeation through the membrane [12], a low WHSV was selected for the membrane reactor experiments.

4.5.6 Effect of temperature, pressure and sweep-gas-to-feed flow ratio on the SCMR

The performance of the SCMR was systematically investigated to evaluate its potential for enhanced ammonia synthesis compared to the conventional SCR. In the following section, key reactor performance indicators, including NH_3 recovery,

yield, production rate, and H_2 conversion, were analysed as functions of temperature, pressure, WHSV, and SW. Comparative analysis with the conventional reactor was conducted using the improvement percentage defined in Equation (4.3) to quantify performance enhancement under varying reaction conditions. It should be noted that the catalyst is located on the retentate side of the membrane in all cases. Furthermore, the same catalyst amount and identical WHSV were used in both configurations to ensure a fair comparison.

The effect of SW on ammonia synthesis performance was systematically investigated using the SCMR. The SW value, defined as the ratio of sweep gas flow to the retentate feed gas flow, is a critical parameter governing the partial pressure gradient across the membrane and thereby influencing the reaction equilibrium. In Chapter 2 the significance of SW in enhancing overall conversion and NH_3 production rate was demonstrated.

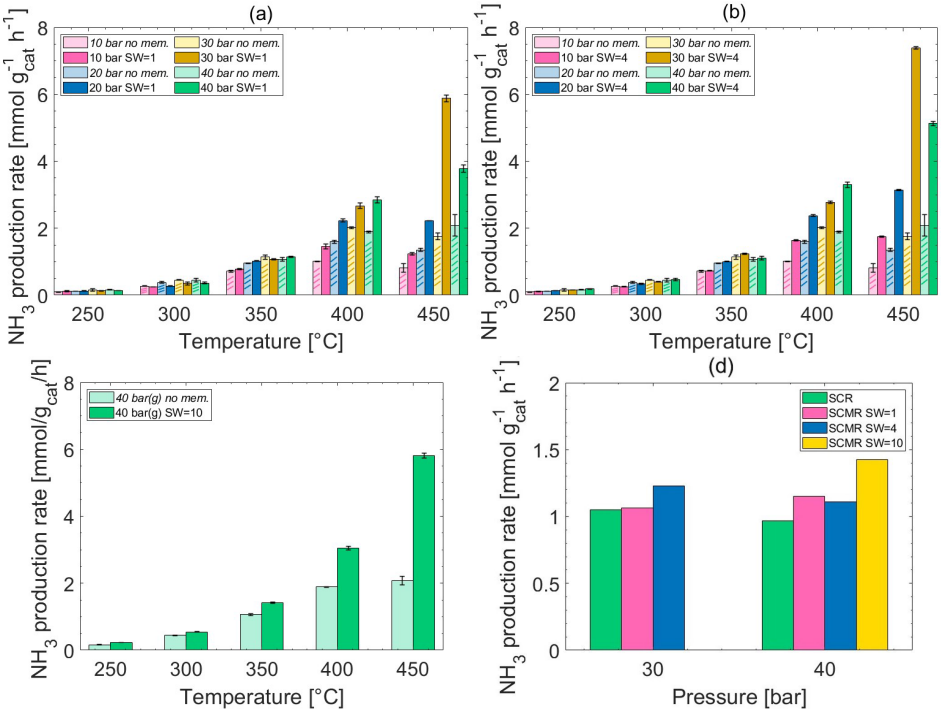


Figure 4.13 NH_3 production rate in the SCMR vs. SCR at 250-450 °C and different pressures for (a) SW = 1, (b) SW = 4, (c) SW = 10, (d) comparison at 30-40 bar for different SW at 350 °C

In this specific experimental investigation, the sweep gas composition was selected to match that of the feed gas, corresponding to a molar feed ratio H_2:N_2 = 2:1. Furthermore, to facilitate a direct comparison between operating conditions, the pressure difference across the membrane (ΔP) was maintained at zero, ensuring

equal pressure in both the retentate and permeate sides. This section evaluates the effect of varying SW ratios on H_2 conversion, NH_3 production rate, yield and recovery.

The effect of temperature on NH_3 production rate in the structured catalyst membrane reactor depends strongly on the sweep-gas conditions. As illustrated in **Figure 4.13**(a)-(b) at low temperatures (250-300 °C) and for SW = 1-4, the membrane configuration offers no advantage and may even slightly reduce NH_3 production rate compared to the conventional case, particularly at SW = 1. Under these conditions, the reaction is primarily governed by intrinsic kinetics, rendering the membrane-imposed driving force inadequate to overcome the intrinsically slow reaction rate; additionally, the introduction of sweep gas dilutes reactants at the membrane interface, further hindering the limited rate of ammonia formation. At the highest pressure examined (40 bar), this is compounded by hydrogen losses on the retentate side, which are particularly severe at SW = 1, where approximately 91% of the hydrogen is removed from the retentate, compared with only about 13% at SW = 4, as shown in **Figure 4.14**.

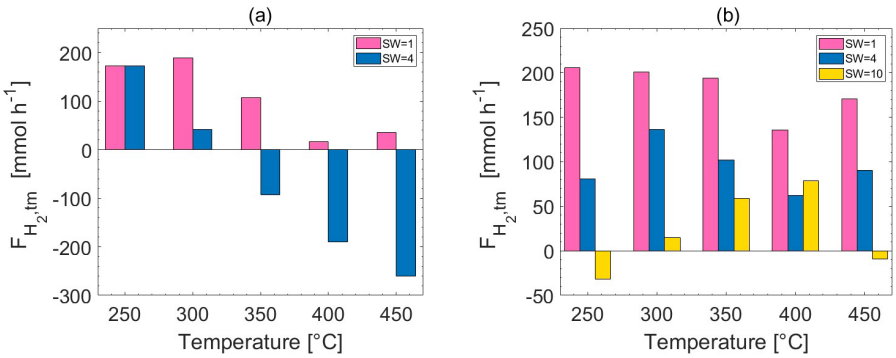


Figure 4.14 H_2 transmembrane flow at different temperatures: (a) 30 bar, SW = 1-4, (b) 40 bar, SW = 1-4-10

In **Figure 4.13**(a), this detrimental effect is marginally more pronounced, although still barely perceptible, because the small amount of ammonia formed is more difficult to continuously remove. As the temperature increases, the intrinsic reaction rate becomes higher and the process enters a regime where both kinetics and equilibrium effects become competitive, making the membrane-assisted configuration more effective. In this higher temperature window, the positive impact of in-situ ammonia removal becomes more pronounced, and the performance gap between SW = 1 and SW = 4 widens, with larger sweep-gas-to-feed flow ratios enabling substantially higher NH_3 production rates. At 350 °C and 30 bar, a SW = 4 leads to a clearly measurable improvement in NH_3 production rate of approximately 17%, whereas the corresponding gain at SW = 1 is negligible, as shown in **Figure 4.13**(d). As further evidence of the thermodynamic benefits of the

membrane-assisted configuration, the effect of sweep-gas-to-feed flow ratio at 40 bar clearly highlights a shift of the equilibrium limitation toward higher temperatures. In contrast to the conventional reactor (**Figure 4.10**), where thermodynamic constraints already depress NH_3 production rate at 400 °C and 40 bar, the membrane reactor delays this limitation to higher temperature, with the onset of pronounced equilibrium effects appearing only around 450 °C for SW = 1. At 450 °C and 30 bar, a sweep-gas-to-feed flow ratio of SW = 4 enables the membrane reactor to surpass the equilibrium conversion of the conventional configuration, achieving an improvement of approximately 94%. This behaviour is further clarified in **Figure 4.15**(a) which compares H_2 conversion in the conventional and membrane-based reactors and places these results in the context of the corresponding thermodynamic equilibrium conversion.
At 450 °C, raising the pressure to 40 bar leads to a clear performance gap, with improvements of 7.2% relative to the conventional case.

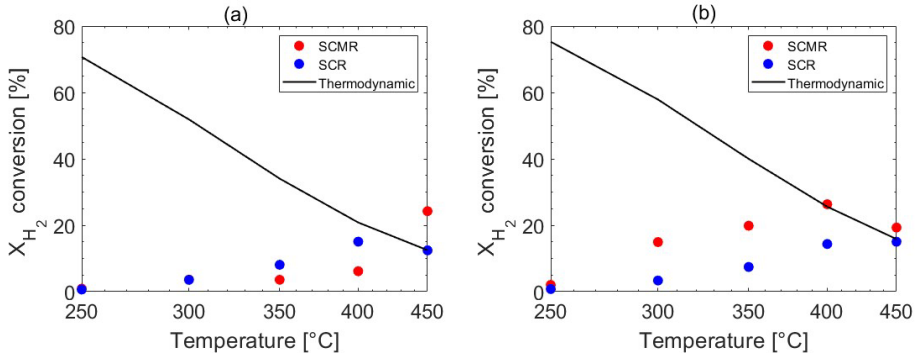


Figure 4.15 H_2 conversion of SCMR and SCR compared to the thermodynamic equilibrium at different temperature and SW = 4 at (a) 30 bar, (b) 40 bar

Figure 4.15(b) also illustrates the practical benefit of this shift: for a given conversion target, the membrane-based process can operate at significantly lower temperature than the conventional reactor. Specifically, the H_2 conversion attained at 400 °C in the conventional configuration, can already be reached at 300 °C in the membrane reactor. For a more detailed assessment, additional experiments were carried out at SW = 10 and 40 bar (**Figure 4.13**(c)) to enable a clearer comparison with lower sweep-gas-to-feed flow ratios. Under these conditions, it becomes evident that even in the kinetically controlled regime at low temperatures (250-300 °C), the membrane reactor already outperforms the conventional reactor, showing that more intense in-situ ammonia removal can partially offset the limitations imposed by slow intrinsic kinetics.
At 400 °C, however, **Figure 4.16**(b) reveals that SW = 10 yields lower performance than SW = 4; in this regime the system operates closer to thermodynamic equilibrium, and an excessively high sweep flow shortens the effective contact time

thereby reducing the efficiency of ammonia extraction from the retentate and diminishing the overall benefit of the membrane configuration.

Table 4.2 shows an overview of the SCMR improvement, if any, with respect to the SCR in terms of NH_3 production rate, H_2 conversion and NH_3 yield.

Temperature increase amplifies the beneficial effect of the membrane reactor on NH_3 production rate. Upon further increasing the temperature (450 °C), the positive impact of the membrane reactor on NH_3 production rate becomes more pronounced. At 40 bar, the performance differences between SW = 1, SW = 4 and SW = 10 become markedly clearer, and **Figure 4.16**(b) shows that the combination of 40 bar and 450 °C delivers the highest total production rate.

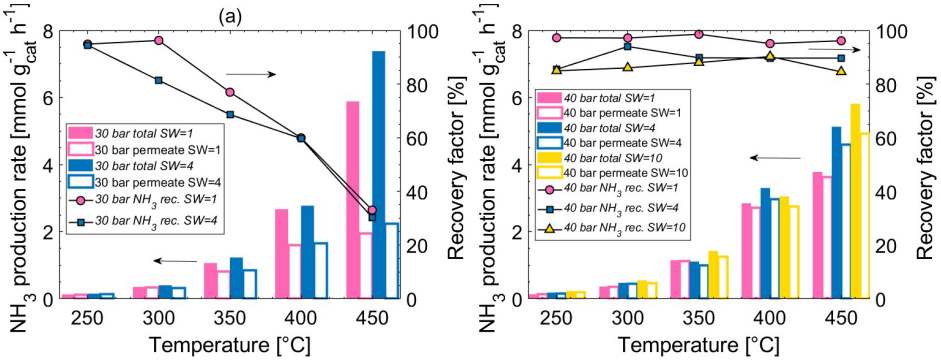


Figure 4.16 Total NH_3 production rate in the structured catalyst membrane reactor (SCMR) vs. recovery factor in the permeate at 250-450 °C (a) 30 bar, SW = 1-4, (b) 40 bar, SW = 1-4-10

Under these conditions, the membrane reactor attains an NH_3 production rate of 5.81 mmol·$g_{cat}^{-1}h^{-1}$ at SW = 10, compared to 2.21 mmol·$g_{cat}^{-1}h^{-1}$ in the conventional reactor, corresponding to a 162% increase in NH_3 production rate, with an NH_3 recovery factor of 84%.

Table 4.2 Improvement on H_2 conversion, NH_3 production rate, NH_3 yield compared to the conventional process at 400-450 °C, 40-30 bar for SW = 1-4-10

T [°C]	P [bar]	SW[-]	X_{H_2}[%]	NH_3 production rate[%]	Y_{NH_3}[%]
400	40	1	113.7	52.6	38.8
		4	83.3	76.8	53.4
		10	32.3	63.4	61.2
450		1	7.1	70.7	77.8
		4	7.2	131.5	123.4
		10	-70.3	162.5	148.6
400	30	1	80.1	36.4	23.7
		4	-79.0	41.7	46.1
450		1	16.3	248.4	120.7
		4	94.7	133.0	7.9

At 40 bar, the recovery factor remains comparatively high across the investigated temperature range (**Figure 4.16**(b)), although it gradually decreases with increasing SW, reflecting the combined effect of higher NH_3 production rates and a reduced effective residence time for permeation.
Conversely, at 30 bar (**Figure 4.16**(a)) the recovery factor declines more sharply with temperature for both sweep-gas conditions, indicating that, although the overall NH_3 production rate is still competitive, separation on the permeate side is less effective than at 40 bar. This behaviour highlights that, at lower pressure, the driving force for ammonia transport through the membrane is insufficient to sustain efficient separation of the produced ammonia. In other words, at 30 bar the membrane configuration maximizes production rate, whereas at 40 bar it favours NH_3 recovery and separation performance.

4.5.7 Effect of WHSV on the SCMR

The influence of WHSV is particularly relevant in membrane-assisted configurations, where separation performance depends on sufficient residence time for permeation. At high flow rates, the overall production rate can increase, but the shortened residence time may hinder effective product removal through the membrane, limiting the intensification potential of the system. Therefore, an additional set of experiments was performed at higher WHSV, maintaining a sweep-gas-to-feed flow ratio of SW = 4 and a total pressure of 40 bar, and the results were compared with those obtained at lower WHSV, shown in **Figure 4.17**.
In the investigated temperature range of 250-400 °C, the conventional reactor consistently exhibited higher production rate than the membrane integrated system at elevated WHSV, indicating that the benefit of product removal does not compensate for the kinetic and separation limitations under these conditions. At 450 °C the membrane reactor becomes competitive, achieving an increase in NH_3 production rate of approximately 15% relative to the conventional configuration. In this case the ammonia recovered in the permeate side was around 87% of the total produced amount.

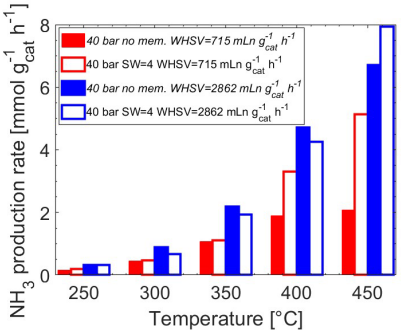


Figure 4.17 NH_3 production rate in SCMR vs. SCR at 40 bar, 250-450 °C, SW = 4 and different WHSV

4.5.8 Influence of POCS geometry: Gyroid vs. BCC

The influence of the internal POCS geometry is an additional design variable that must be considered when assessing the performance of the structured catalyst membrane reactor system. In this section, a comparison between Gyroid and BCC structured catalysts is presented. The BCC geometry was first evaluated in the conventional structured catalyst configuration (SCR) at the same reference pressures and temperatures and at the optimised space velocity, WHSV = 715 $mLn \cdot g_{cat}^{-1} h^{-1}$, used previously for the Gyroid-based system.

In the activity tests conducted without the membrane (**Figure 4.18**(a)), the Gyroid geometry appears marginally lower than BCC at low temperature; however, due to the very low absolute NH_3 production rates in this regime, it is not possible to draw robust conclusions about the differences between the two structures.

At intermediate temperatures (300-350 °C) and low pressures (10-20 bar), the Gyroid structure performs slightly better or comparably to BCC, while at higher temperatures the BCC geometry becomes superior at low pressures, and the Gyroid only shows a modest advantage at 40 bar. These trends suggest that both geometries provide broadly similar catalytic performance in the conventional reactor, with only subtle geometry driven differences in mass transfer and surface accessibility over the investigated operating window.

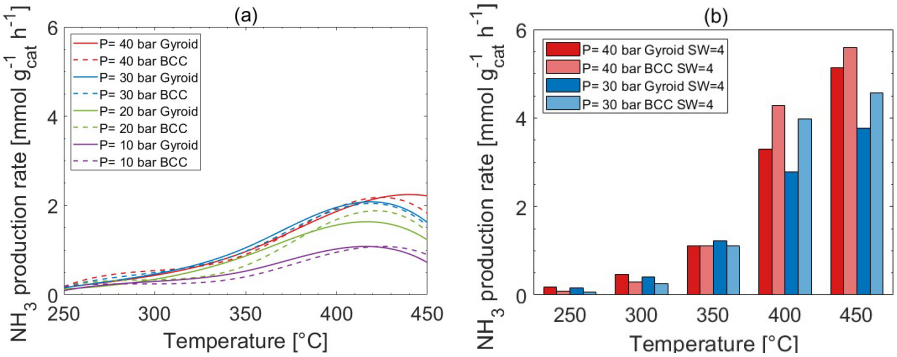


Figure 4.18 NH_3 production rates for Gyroid and BCC POCS structured catalysts at WHSV = 715 $mLn \cdot g_{cat}^{-1} h^{-1}$ as a function of temperature (250-450 °C): (a) SCR at 10-40 bar (b) SCMR at 30-40 bar, SW = 4

In the membrane reactor configuration, the comparison between the two geometries is slightly different. It is important to note that the BCC tests in the membrane reactor were conducted with a membrane of the same composition described in Section 4.2.2, but carbonised at a higher maximum temperature (800 °C). This modification was introduced to explore whether a higher carbonisation temperature could enhance overall reactor performance. Since the reference experiments without a membrane yielded very similar NH_3 production rates for Gyroid and BCC at the

same operating conditions, comparing the two membrane reactors despite the different carbonisation temperatures is still considered a fair benchmark of the combined geometry and membrane concept.

In the membrane reactor tests, the two configurations show essentially indistinguishable performance at low temperature; differences become apparent only at higher temperatures for both investigated pressures. Under these conditions, the BCC-based membrane reactor exhibits slightly higher NH_3 production rates than the Gyroid one, with improvements of approximately 10-15% at 400-450 °C and 40 bar and around 20-25% at 30 bar. Given the experimental scatter and the relatively modest magnitude of these differences, this should be interpreted as a minor advantage rather than a substantial performance boost, indicating that both geometries interact with the membrane in a broadly comparable way, and that geometry selection may play a secondary role compared to operating conditions and membrane properties.

4.6 COMPARISON BETWEEN MODEL PREDICTIONS AND EXPERIMENTAL RESULTS

The experimental NH_3 production rate trends at different pressures were compared with the predictions of the 1D non-isothermal packed bed membrane reactor model developed in Chapter 2.

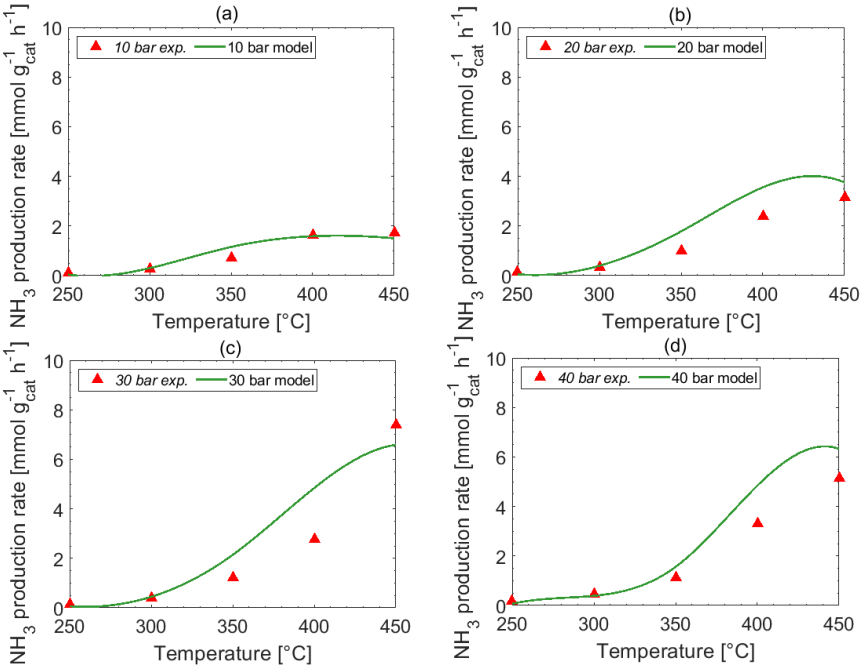


Figure 4.19 Model-experiment comparison of NH_3 production rate as a function of temperature at: (a) P = 10 bar; (b) P = 20 bar; (c) P = 30 bar; (d) P = 40 bar

As shown in **Figure 4.19**, the model captures the qualitative trends observed in all cases: NH_3 production rate increases with temperature and progressively improves as the pressure is raised from 10 to 40 bar. These trends are consistent with the combined kinetic and equilibrium effects observed experimentally. At the same time, noticeable quantitative deviations are present, especially at intermediate temperatures where the model tends to overpredict the measured rates, reflecting the fact that the current formulation was derived for a conventional particulate packed bed and does not explicitly represent the TPMS/BCC structured geometry and its associated transport characteristics.
These discrepancies suggest that, while the 1D model provides a useful first-order benchmark and confirms the overall trends, further refinement of the governing correlations, particularly those describing heat and mass transfer in structured supports, will be required to obtain quantitatively accurate predictions for membrane reactors based on complex POCS architectures.

4.7 CONCLUSIONS

The present chapter demonstrates that a structured Ru-based catalyst integrated into a membrane reactor can significantly enhance ammonia synthesis performance over a wide range of operating conditions. The Ru-based catalyst was successfully coated as a uniform catalytic layer onto an open-cellular 3D support. Its behaviour was first characterised in a structured catalyst reactor, assessing the effects of temperature, pressure, H_2:N_2 molar feed ratio, and feed flow rate. Under these conventional conditions, an understoichiometric feed ratio of H_2:N_2 = 2:1 almost always outperformed the traditional stoichiometric ratio of 3:1, reflecting the well-known susceptibility of Ru catalysts to hydrogen inhibition and the beneficial effect of reducing hydrogen partial pressure on intrinsic activity.
In the membrane reactor, the sweep-gas-to-feed flow ratio emerges as the key design variable governing the trade-off between reaction enhancement and hydrogen losses. A moderate sweep-gas-to-feed flow ratio (SW = 4) provides the most favourable balance between reaction and separation, enabling operation beyond the conventional thermodynamic equilibrium limit, with H_2 conversion exceeding equilibrium by ~15-30% at 450 °C and 40 bar. Under near optimal conditions (400 °C, 40 bar), SW = 4 delivers simultaneous improvements of 83% in H_2 conversion, 77% in NH_3 production rate, and 53.4% in NH_3 yield compared to a conventional reactor. In the low temperature regime (250-300 °C, 40 bar), a higher sweep-gas-to-feed flow ratio (SW = 10) enhances NH_3 production rates by 25-43% and yields by 15-19%. At more severe conditions (450 °C, 40 bar), SW = 10 maximizes absolute production rate, reaching 5.81 $mmol \cdot g_{cat}^{-1} h^{-1}$ and achieving up to 162% higher NH_3 production rates and 148% higher yields; however, it does not significantly promote equilibrium shifting. In contrast, at the same conditions, lower sweep-gas-to-feed

flow ratios (SW = 1-4) yield production rate improvements of approximately 70-131% while also enhancing conversion beyond equilibrium. These benefits, however, come at the expense of increased hydrogen permeation losses, particularly at low temperatures.

The influence of residence time, assessed via WHSV variation at SW = 4, shows that lower WHSV (i.e., longer residence time) improves performance by facilitating more effective in-situ ammonia removal. Notably, at 450 °C, the membrane reactor continues to outperform the conventional configuration even at higher WHSV, achieving ~15% higher NH_3 production rate and an NH_3 recovery factor of 87%. Overall, the results identify an optimal operating window characterised by moderate pressure (30-40 bar), and temperature (~400 °C), a moderate sweep-gas-to-feed flow ratio (SW = 4), and sufficiently low WHSV. This combination provides a robust compromise between kinetic enhancement, equilibrium shifting, and hydrogen utilisation. In contrast, very high sweep-gas-to-feed flow ratios (SW = 10) are more suitable for applications prioritizing maximum ammonia throughput over conversion efficiency and yield.

In addition, the comparison between Gyroid and BCC geometries shows that, under the identified optimal operating window, both structures deliver broadly comparable performance, with the BCC-based membrane reactor exhibiting only a modest (~10-25%) advantage in NH_3 production rate at high temperature and pressure, suggesting that internal geometry plays a secondary role compared to operating conditions and membrane properties in this system.

Finally, confronting the 1D membrane reactor model developed in Chapter 2 with the experimental NH_3 production rate data confirms that the model is able to predict the main temperature and pressure trends, but further refinements are required to achieve quantitative agreement for reactors based on structured catalyst supports.

A.4 APPENDIX

A.4.1 EDX

Table A.4.1 Elemental composition from EDX analysis of the carbon membrane cross-section

Element Number	Element Symbol	Element Name	Atomic Conc. [%]	Weight Conc. [%]
6	C	Carbon	49.61	36.80
7	N	Nitrogen	2.32	2.00
8	O	Oxygen	28.84	28.50
13	Al	Aluminium	19.09	31.80
16	S	Sulfur	0.05	0.10
29	Cu	Copper	0.03	0.10
57	La	Lanthanum	0.08	0.10

A.4.2 Gas permeation tests

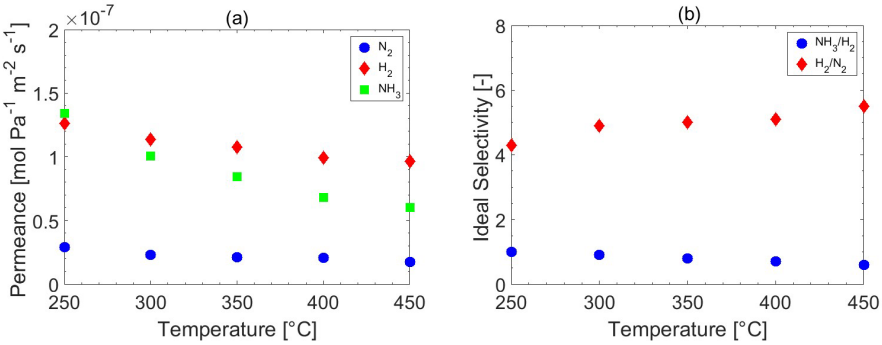


Figure A.4.1 Membrane performance at different temperatures and ΔP = 2 bar: (a) single-gas permeance, (b) ideal selectivities

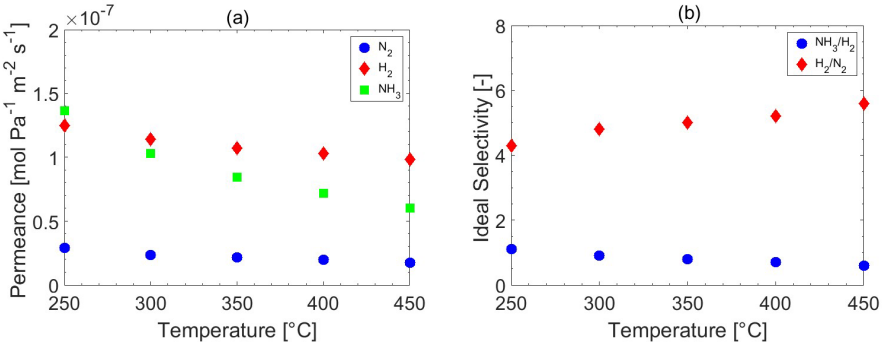


Figure A.4.2 Membrane performance at different temperatures and ΔP = 4 bar: (a) single-gas permeance, (b) ideal selectivities

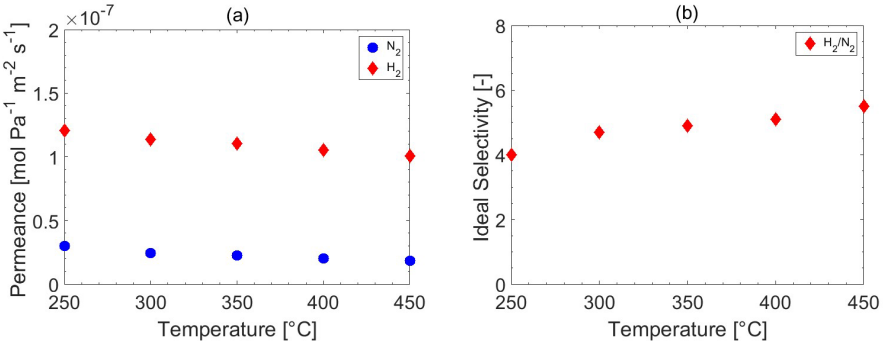


Figure A.4.3 Membrane performance at different temperatures and ΔP = 10 bar: (a) single-gas permeance, (b) ideal selectivity

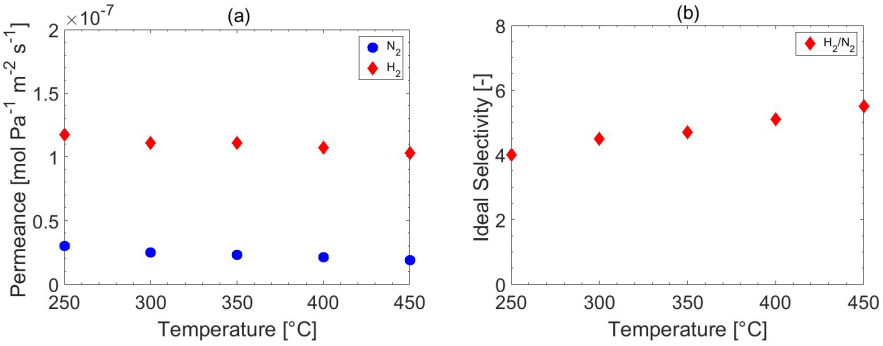


Figure A.4.4 Membrane performance at different temperatures and ΔP = 20 bar: (a) single-gas permeance, (b) ideal selectivity

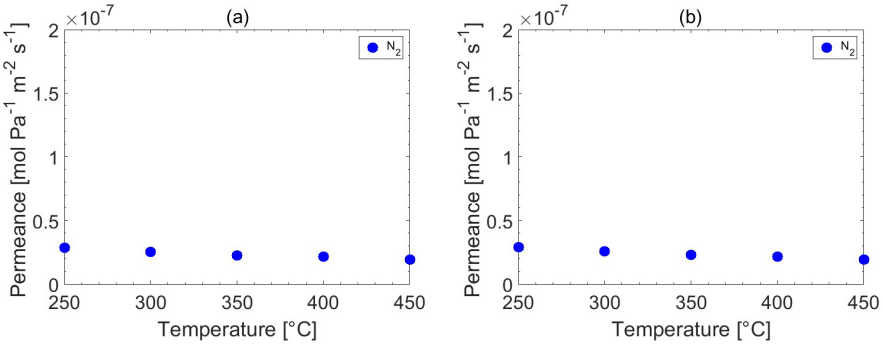


Figure A.4.5 Membrane performance at different temperatures: (a) single-gas permeance at ΔP = 30 bar, (b) single-gas permeance at ΔP = 40 bar

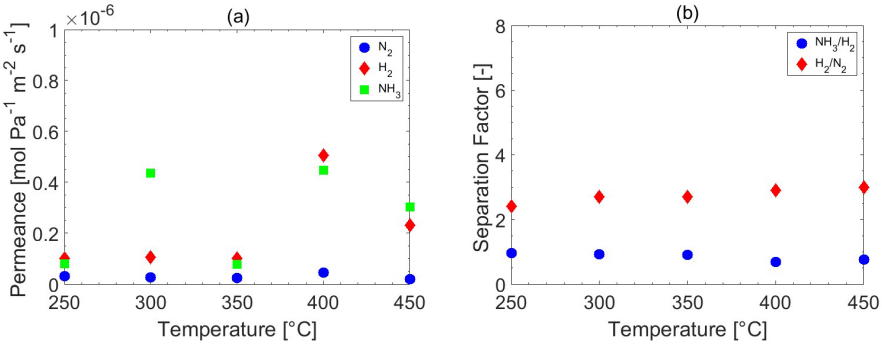


Figure A.4.6 Membrane performance at different temperatures and ΔP = 2 bar: (a) mixed-gas permeance, (b) separation factor

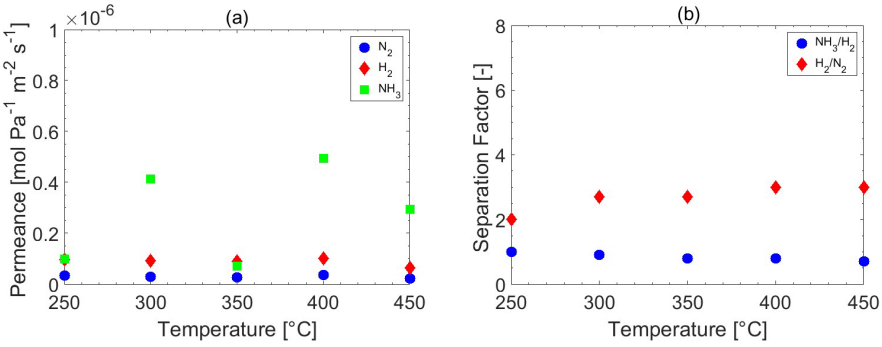


Figure A.4.7 Membrane performance at different temperatures and ΔP = 4 bar: (a) mixed-gas permeance, (b) separation factor

REFERENCES

[1] C. Plana, S. Armenise, A. Monzón, E. García-Bordejé, "Ni on alumina-coated cordierite monoliths for in situ generation of CO-free H2 from ammonia", *J. Catal.* 275 (2010) 228–235. https://doi.org/10.1016/j.jcat.2010.07.026.

[2] C. Italiano, G. Marino, M. Thomas, B. Hary, S. Nardone, S. Richard, A. Saker, D. Tasso, N. Meynet, P. Olivier, F. Gallucci, A. Vita, "Carbon-Free H2 Production from Ammonia Decomposition over 3D-Printed Ni-Alloy Structures Activated with a Ru/Al2O3 Catalyst", *Processes* 12 (2024). https://doi.org/10.3390/pr12122663.

[3] C. Italiano, G. Marino, M. Thomas, B. Hary, S. Nardone, S. Richard, A. Saker, D. Tasso, N. Meynet, P. Olivier, F. Gallucci, A. Vita, "Combined dip/spin coating deposition of Ni/CeO2 and Ni/CeO2-Al2O3 onto 3D printed AlSi10Mg Periodic Open Cellular Structures (POCS)", *Applied Surface Science Advances* 27 (2025) 100731. https://doi.org/10.1016/j.apsadv.2025.100731.

[4] S. Richard, D. Tasso, M. Rajana, A. Saker, N. Meynet, B. Hary, S. Nardone, G. Marino, C. Italiano, A. Vita, F. Gallucci, "Modelling the feasibility of membrane integration into periodic open cellular structures for ammonia decomposition", *Chemical Engineering Journal* 521 (2025) 166903. https://doi.org/10.1016/j.cej.2025.166903.

[5] D. Braun, H. Cherdron, H. Ritter, "Methods and techniques for synthesis, characterization, processing, and modification of polymers", Polymer Synthesis: Theory and Practice, 3rd ed., 2001, https://doi.org/10.1007/978-3-662-04573-2_2

[6] M. El-Shafie, "A comprehensive assessment of ammonia synthesis reaction kinetics and rate equations", *Int. J. Hydrogen Energy* 48 (2023) 35938–35952. https://doi.org/10.1016/j.ijhydene.2023.06.011.

[7] T. Cholewa, B. Steinbach, C. Heim, F. Nestler, T. Nanba, R. Güttel, O. Salem, "Reaction kinetics for ammonia synthesis using ruthenium and iron based catalysts under low temperature and pressure conditions", *Sustainable Energy & Fuels* 8 (2024), 2245–2255. https://doi:10.1039/d4se00254g.

[8] I. Rossetti, N. Pernicone, F. Ferrero, L. Forni, "Kinetic Study of Ammonia Synthesis on a Promoted Ru/C Catalyst", *Ind. Eng. Chem. Res.* 45 (2006) 4150–4155. https://doi.org/10.1021/ie051398g.

[9] A.B. Hamzah, H. Matsumoto, S. Ookawara, M. Kikugawa, Y. Goto, A. Sato, Y. Manaka, T. Nanba, "Simulation Analysis for Design of H2/N2 Ratio of Feed Gas to Ammonia Synthesis Process Using Ru/CeLaTiOx Catalyst", *Ind. Eng. Chem. Res.* 62 (2023) 12559–12570. https://doi.org/10.1021/acs.iecr.3C00384.

[10] A. Tripodi, M. Compagnoni, E. Bahadori, I. Rossetti, "Process simulation of ammonia synthesis over optimised Ru/C catalyst and multibed Fe + Ru configurations", *Journal of Industrial and Engineering Chemistry* (2018). https://doi.org/10.1016/j.jiec.2018.05.027.

[11] S. Nadiri, A. A. Moghaddam, J. Folke, H. Ruland, B. Shu, R. Fernandes, R. Schlögl, U. Krewer, "Ammonia Synthesis Rate Over a Wide Operating Range: From Experiments to Validated Kinetic Models", *ChemCatChem* 16 (2024). https://doi.org/10.1002/cctc.202400890.

[12] J.L. Cerrillo, N. Morlanés, S.R. Kulkarni, N. Realpe, A. Ramírez, S.P. Katikaneni, S.N. Paglieri, K. Lee, A. Harale, B. Solami, A. Jamal, S. Mani Sarathy, P. Castaño, J. Gascon, "High purity, self-sustained, pressurized hydrogen production from ammonia in a catalytic membrane reactor", *Chemical Engineering Journal* 431 (2022) 134310. https://doi.org/10.1016/j.cej.2021.13431.

CHAPTER 5

A 2D model for membrane reactors in ammonia synthesis: radial transport effects and scale-up design criteria

ABSTRACT:
This chapter presents the first fully coupled two-dimensional (2D), non-isothermal packed bed membrane reactor (PBMR) model for ammonia synthesis. The kinetic and membrane permeation models were validated separately against experimental data - kinetics against literature data (R^2 = 0.96) and permeation against measured NH_3, H_2, N_2 permeances - before integration into the full 2D model. The validated model was applied to 50 operating conditions over a Ru/C catalyst, spanning gas hourly space velocity (GHSV = 50-60,000 h^{-1}), pressure (30-80 bar), temperature (548-698 K), and annulus radius (0.02-0.06 m). A systematic comparison of 1D and 2D predictions across six performance indicators shows that the 1D model consistently overestimates H_2 conversion, NH_3 recovery, NH_3 yield, NH_3 purity, and peak temperature rise, with deviations up to 10 and 25 percentage points for H_2 conversion and NH_3 recovery, respectively. Discrepancies are largest at low GHSV and compact annulus geometry (r = 0.03 m), where a high membrane surface-to-volume ratio (S_M/V) drives the retentate near thermodynamic equilibrium and increases sensitivity to radial concentration gradients. Ammonia concentration polarisation transitions from a reaction-limited regime, where ammonia production cannot sustain membrane transport, to a permeation-dominated regime, where rapid ammonia removal outpaces radial mass transport. From the 2D dataset, a geometry-dependent, Reynolds-independent, reaction-enhanced Sherwood correction is derived: $Sh_{opt} = 1.49\kappa^{-0.912}$ (R^2 = 0.990, MAPE = 2.6%). Applied to a corrected 1D model, it reduces the mean absolute error in the predicted concentration-polarisation profile by over 75%. The correction originates from a reaction-screened diffusion layer: since kinetics are product-inhibited, wall depletion locally raises the net production rate and heals the deficit within a screening length set by the local ratio of diffusivity to kinetic sensitivity. A mechanistic closure reproduces the 2D KPIs nearly as well as the fitted power law.

This chapter is based on the following journal article:
"A two-dimensional model for membrane reactors in ammonia synthesis: concentration polarisation, radial transport effects, and scale-up design criteria", **I. Gargiulo**, E. A. J. F. Peters, A. E. Simpelaar, F. Gallucci, *Submitted to Chem. Eng. J.*.

5.1 INTRODUCTION

In Chapter 2, a non-isothermal 1D packed bed membrane reactor model incorporating a Ru/C catalyst with co-current sweep gas was developed, and it demonstrated that conversions exceeding the thermodynamic equilibrium of a conventional packed bed are achievable across a range of membrane permeances and selectivities.

Translating the PBMR concept to industrial scale, however, introduces transport phenomena that a 1D model cannot resolve. As reactor dimensions increase, the surface-area-to-volume (S_M/V) ratio decreases [1–3], and single-tube configurations give way to multi-membrane arrangements where tube spacing, flow distribution, and membrane-to-membrane interactions critically affect performance [4–6]. Modular reactor concepts, in which smaller membrane reactor modules are connected in parallel or series, have also been proposed as a scale-up strategy for decentralised ammonia production using renewable hydrogen [7–9].

A key limitation of conventional 1D membrane reactor models is their inability to capture concentration polarisation (CP), i.e. the radial depletion of permeating species adjacent to the membrane wall. In ammonia membrane reactors, continuous selective removal of ammonia establishes a radial concentration gradient between the bulk retentate and the membrane surface. When radial diffusion cannot replenish ammonia at the same rate as it is produced by reaction and removed by permeation, a product-depleted boundary layer develops, lowering the NH_3 partial pressure at the membrane interface, reducing the transmembrane driving force, and consequently limiting the permeation flux. Neglecting this external mass-transfer resistance therefore leads to an overestimation of NH_3 recovery and an underestimation of the membrane area required to achieve a given separation performance. Because these radial concentration gradients cannot be represented within a plug-flow framework, at least a two-dimensional reactor model is required to accurately predict membrane reactor behaviour [1]. Concentration polarisation also raises a second, closely related modelling challenge: the effective mass-transfer coefficient at the retentate-membrane interface is no longer a purely hydrodynamic quantity, but is altered by the coupled action of reaction, radial diffusion, selective permeation, and (in the present non-isothermal system) heat release. This effect is conveniently captured by a reaction-enhanced Sherwood correction, which provides a reduced description of membrane-side mass transfer for incorporation into lower-order models. A predictive Sherwood correction is therefore essential for embedding radial transport effects into computationally efficient 1D models, extending their applicability across a broad operating window without requiring repeated 2D simulations. Existing Sherwood correlations are not directly applicable to ammonia PBMRs. Classical packed bed correlations, such as the Wakao-Funazkri correlation [10], were developed for non-reactive systems and predict Sherwood numbers of

approximately 2-5 as functions of the Reynolds and Schmidt numbers. When applied to the present reactor, however, these correlations underpredict the Sherwood numbers extracted from the 2D simulations by factors of 6-15, highlighting their inability to capture reaction-enhanced mass transfer. More recently, Poto et al. [11] proposed the correlation $Sh = 0.4338\,Re^{0.3583}Sc^{1/3}$ for a CO_2/DME membrane reactor operating at $Re \gg 1$. This expression likewise underestimates mass transfer in the present low-Reynolds-number regime ($Re < 100$). Most recently, Ververs et al. fitted $Sh = 1.846\,Gz^{0.6}$ to H_2/N_2 permeation data on a Pd-Ag membrane in an empty vessel [12]. When evaluated using identical velocity and diffusivity fields from the 2D simulations, this correlation overestimates Sh by 100-400% in the reaction-limited regime and fails to reproduce the Re-independent plateau observed here, since without reaction the boundary layer thickens monotonically with z, whereas ammonia synthesis continuously regenerates ammonia at the wall, decoupling Sh from Re entirely. In contrast, Murmura et al. [13,14] demonstrated analytically that, under reaction-limited conditions at low Reynolds numbers, the enhanced Sherwood number becomes independent of both Reynolds and Schmidt numbers and depends only on reactor geometry ($L/r_1, r_2/r_1$). However, their analysis was derived for idealised isothermal reactors and has not been quantified for ammonia synthesis. The present reactor additionally incorporates the energy balance, introducing temperature gradients that couple heat release with reaction, permeation, and mass transport, thereby further modifying the effective mass-transfer coefficient.

Although two-dimensional modelling has been widely applied to membrane reactors for a variety of reactive systems [15–17], corresponding studies for ammonia synthesis remain limited, with only a few 2D models reported to date [18–21]. To the best of our knowledge, no previous study has presented a fully coupled two-dimensional, non-isothermal packed bed membrane reactor model for ammonia synthesis that simultaneously (i) resolves radial concentration and temperature fields, (ii) quantifies NH_3 concentration polarisation at the membrane interface, and (iii) derives a reaction-enhanced Sherwood correlation for incorporation into reduced-order 1D models. This absence represents a significant gap in the design and scale-up knowledge base for ammonia membrane reactors, particularly for multi-membrane configurations, where membrane spacing and tube geometry strongly influence reactor performance [22].

To address these limitations, this chapter develops a fully coupled two-dimensional (2D) non-isothermal PBMR model for ammonia synthesis that resolves both axial and radial transport phenomena. Rather than examining a limited number of operating conditions, the model is applied systematically to 50 cases spanning a wide operating window of gas hourly space velocity (GHSV), pressure, temperature, and annulus radius. This comprehensive dataset is used to identify the operating regimes

in which conventional 1D models fail, elucidate the mechanisms governing concentration polarisation, and derive a geometry-dependent reaction-enhanced Sherwood correlation that enables radial transport effects to be incorporated into computationally efficient 1D models. The specific objectives of this work are to:

1. Develop and validate a fully 2D non-isothermal PBMR model for ammonia synthesis;
2. Systematically quantify 1D-2D discrepancies across key performance indicators and identify the physical mechanisms responsible, including concentration polarisation and radial thermal stratification;
3. Characterize concentration polarisation metrics and derive a reaction-enhanced Sherwood correction from the 2D field data, and assess the applicability of existing literature correlations under low-Re, reaction-limited regime;
4. Translate the resulting mechanistic understanding into practical design guidelines for multi-membrane ammonia reactors, with particular emphasis on membrane spacing, annulus geometry, and operating conditions.

The chapter is structured as follows. Section 5.2 presents the reactor geometry, kinetic and membrane sub-models, governing equations, model assumptions, boundary conditions, and numerical implementation of the 2D non-isothermal PBMR model, together with a preliminary transport analysis used to justify the modelling choices and introduce the Sherwood/CP correction framework. Section 5.3 presents the experimental validation of the kinetic and membrane sub-models, followed by a systematic comparison between 1D and 2D predictions across the complete operating matrix, analysis of concentration polarisation, derivation of the reaction-enhanced Sherwood correction, and discussion of the resulting implications for reactor design and scale-up. Finally, Section 5.4 summarizes the main conclusions and translates the key findings into practical design guidance for multi-membrane reactor scale-up.

5.2 DEVELOPMENT OF THE 2D NON-ISOTHERMAL PBMR MODEL

5.2.1 Reactor geometry

The reactor investigated in this study, illustrated in **Figure 5.1**, is a multi-membrane packed bed reactor comprising a bundle of tubular membranes housed within a cylindrical shell. The retentate (shell-side) volume surrounding the membrane tubes is packed with a Ru/C catalyst bed. The feed gas (N_2 and H_2) enters the retentate side from the bottom, while sweep gas is introduced co-currently at the base of the permeate (tube) side. This co-current flow configuration maintains a sustained NH_3

partial pressure gradient across the membrane along the entire reactor length, thereby maximizing the driving force for ammonia removal. The permeated gases, predominantly NH_3 together with smaller amounts of unconverted N_2 and H_2, are transported by the sweep stream and collected at the top of the permeate tubes. The reactor operates under adiabatic conditions.

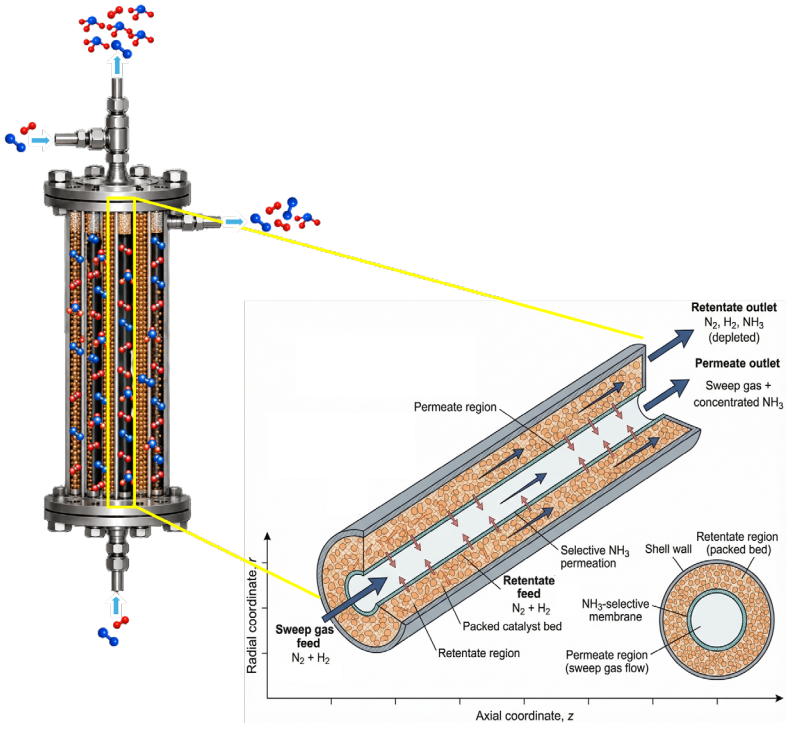


Figure 5.1 Schematic representation of the multi-membrane packed bed reactor for ammonia synthesis, showing the axial and radial coordinates, the retentate region with Ru/C packed catalyst bed, the permeate region carrying the sweep gas, and the NH_3-selective membranes that enable in-situ removal of ammonia from the retentate stream

To efficiently simulate the full multi-membrane array, the 2D model employs a single unit-cell domain that exploits the periodic geometric symmetry of a regular tube arrangement. In this framework, the geometry is strictly defined by the membrane outer radius (r_1), the outer unit-cell radius (r_2), the annular gap width ($l_c = r_2 - r_1$), and the dimensionless radius ratio ($\kappa = r_1/r_2$). The outer boundary at $r = r_2$ is governed by a zero-flux symmetry condition, representing the physical interface shared with adjacent unit cells. It must be noted that representing a multi-tube array as a continuous circular annulus is an equivalent-area approximation. In practice, multi-tube arrays are configured in specific lattice arrangements characterised by a centre-to-centre tube pitch (p). The circular annulus formulation mathematically

maps to these arrangements by equating the cross-sectional area of the circular unit cell (πr_2^2) to the area of the corresponding polygonal cell. For instance, the equivalent outer radius maps to $r_2 = p/\sqrt{\pi}$ for a square pitch and $r_2 = p[\sqrt{3}/(2\pi)]^{1/2}$ for a hexagonal pitch. Provided this area-equivalence mapping is applied, varying r_2 (and thus κ) in the parametric study is directly equivalent to altering the tube pitch p in the physical multi-membrane configuration. This justified approximation enables computationally efficient single tube results to be rigorously translated into multi-membrane design guidance.

5.2.2 Reaction kinetics and membrane flux

Ammonia synthesis over the promoted Ru/C catalyst is described by the modified Temkin rate expression reported by Rossetti et al. (Equation (2.1)). The kinetic parameters and activation energies adopted in this chapter are identical to those used in the non-isothermal 1D PBMR model of Chapter 2, ensuring consistency between the reactor simulations presented in the two chapters.

Because a porous membrane is considered in this study, it is assumed to be permeable to all species in the reaction mixture, with transport proceeding via a thermally activated mechanism wherein the permeance of each component follows an Arrhenius-type dependence on temperature (Equation (5.1)) [23]. To clarify the origin of the membrane parameters used in this work: the Arrhenius transport sub-model was implemented and validated by comparing its predictions directly against experimentally measured permeance data obtained from laboratory gas permeation tests on carbon molecular sieve (CMS) membranes. Meanwhile, the specific reference values for permeance and perm-selectivity used in the current 2D reactor simulations correspond to the optimised target values established in Chapter 2.

$$\mathcal{P}_i = \mathcal{P}_i^0 exp\left[\frac{-(E_{A,i})}{RT}\right] \tag{5.1}$$

Accordingly, the optimised membrane transport parameters used in this work are: $\mathcal{P}_{NH_3}$ = 1·10^{-7} mol·Pa^{-1}m^{-2}s^{-1}, S_{NH_3/H_2} = 50, S_{NH_3/N_2} = 100.

5.2.3 Preliminary transport analysis: screening negligible mass- and heat-transfer resistances

Before formulating the two-dimensional model equations, a systematic preliminary analysis of the relevant heat and mass transfer phenomena was carried out to identify which can be neglected without loss of accuracy. Rigorous multi-dimensional reactor modelling is computationally intensive and retaining resistances that are physically negligible at the scales of interest, would add complexity without improving predictive fidelity [11].

- **Intra-particle diffusion: Weisz-Prater criterion**

Diffusion resistance within catalyst pellets may reduce the effective reaction rate below its intrinsic value. The Weisz-Prater criterion (C_{WP}) provides a dimensionless comparison of the observed reaction rate with the capacity of intra-pore diffusion. When $C_{WP} \ll 1$, internal concentration gradients are negligible and the effectiveness factor approaches unity. For a spherical pellet with characteristic length defined as $L = \frac{r_{particle}}{3}$, the surface concentration (C_A^S) approximated by the bulk concentration [24], the criterion becomes:

$$C_{WP} = \frac{(-r_i)_{obs}\, r_{particle}^2}{D_{eff}\, C_i^S} \tag{5.2}$$

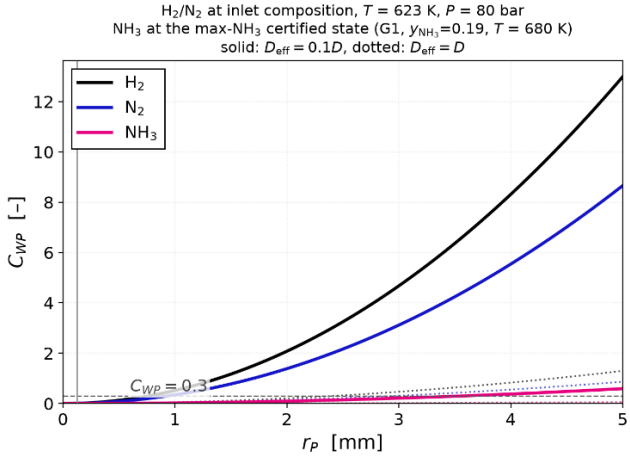


Figure 5.2 Weisz-Prater criterion (C_{WP}) as a function of particle radius ($r_{particle}$) for H_2, N_2, NH_3 at worst-case operating conditions (maximum pressure, optimal temperature, inlet composition)

The worst-case values are evaluated at the highest pressure and optimal temperature (reactor inlet, where the NH_3 mole fraction is lowest and the reaction rate is highest), and C^S is set to its minimum value. The effective diffusion D_{eff} is calculated as follow [25]:

$$D_{eff,i} = \frac{\varepsilon_{particle}}{\tau} D_{m,i} \tag{5.3}$$

$D_{m,i}$ is the individual molecular diffusion coefficient, which is calculated as detailed in the Appendix (Equation (A.5.7)). While tortuosity values of approximately 3-4 are commonly assumed in the literature, in this work it is instead determined following the methodology described in the referenced source [26]:

$$\tau = \frac{\varepsilon_{particle}}{1 - (1 - \varepsilon_{particle})^{2/3}} \tag{5.4}$$

A value of $\varepsilon_{particle}$ = 0.65 is adopted, consistent with activated-carbon supported Ru catalysts reported in the literature [27,28].

As shown in **Figure 5.2,** C_{WP} remains well below unity for all particle radii and species considered, confirming that intra-particle diffusion can be safely neglected across the full parameter space.

Beyond intra-particle diffusion, two additional criteria were evaluated to assess whether external (fluid-to-particle) mass- (Equation (A.5.16)) and heat- (Equation (A.5.17)) transfer resistances are significant.

❖ **Inter-phase radial transport: radial Péclet number**

The 1D plug-flow assumption is valid only when radial diffusion homogenises the annular cross-section on a timescale much shorter than axial convection. This condition is quantified by the radial Péclet number:

$$Pe_{r,i} = \frac{u_z l_c}{D_{m,ij}} \tag{5.5}$$

where u_z is the axial superficial velocity, $l_c = r_2 - r_1$ is the annular gap width (the characteristic radial length for the retentate), and $D_{m,ij}$ is the molecular diffusivity. When $Pe_r \ll 1$, radial diffusion is fast and the cross-section remains radially homogeneous; the 1D plug-flow formulation is therefore appropriate. When $Pe_r \gg 1$, radial diffusion is slow and radial gradients may develop; however, whether such gradients are large enough to significantly affect reactor performance depends on the strength of the source term relative to diffusion, quantified by the diffusive Damköhler number Da_{diff} :

$$Da_{diff,i} = \frac{r_i \, {l_c}^2}{D_{m,ij} \, c} \tag{5.6}$$

Where r is the absolute reaction rate, c is the absolute maximum concentration in the retentate side. When $Da_{diff} \gg 1$, reaction consumes or produces species faster than diffusion can equilibrate them, and steep radial concentration (and associated temperature) gradients arise that a 1D plug-flow model cannot capture.

The molecular diffusivity $D_{m,ij}$ used in the radial Péclet number is computed from the Chapman-Enskog relation (Equation (A.5.1)) for the H_2-N_2-NH_3 mixture. The use of molecular diffusivity D_m rather than a dispersion-corrected effective diffusivity is justified by the low Reynolds numbers across all simulated cases [29]. Both axial and radial dispersion contributions were evaluated explicitly: axial dispersion was assessed via Equation (A.5.9-A.5.13), confirming plug-flow behaviour along the reactor axis; radial dispersion was estimated using the Gunn correlation (Equation (A.5.14-A.5.15)) and found to be negligible relative to molecular diffusion across the full parameter space. Molecular diffusion therefore governs radial transport throughout this work, and no dispersion correction to D_m is required.

Evaluated across all 50 simulated cases, Pe_{r,H_2}^{max} spans more than three orders of

magnitude and scales as $Pe_r \propto GHSV^{1.06}$ and $Pe_r \propto r$, consistent with Equation 5.5 (**Figure A.5.2-A.5.3**). Critical space velocities at which $Pe_r = 1$ are $GHSV_{crit}$ = 55 h^{-1} for r = 0.06 m and 123 h^{-1} for r = 0.03 m; above these thresholds persistent radial gradients are expected. Of the 50 cases, only 7 satisfy $\langle Pe_{r,H_2} \rangle < 1$ and all 7 simultaneously satisfy $\langle Pe_{r,H_2} \rangle < 1$ and $Da_{diff} < 1$, conditions where the 1D plug-flow assumption is adequate. The remaining 43 cases operate at $\langle Pe_r \rangle \geq 10$, confirming that radial mass-transport non-uniformity is physically significant across the vast majority of the operating window investigated (**Figure A.5.5**). Furthermore, Da_{diff} scales as r^2, exhibiting a much stronger sensitivity to tube radius than Pe_r (which scales as r): increasing the annulus radius by a factor of three raises Da_{diff} by ~9× while Pe_r increases by only ~3×, providing the mechanistic basis for the strong geometry dependence of concentration polarisation reported in Section 5.3.3. Together, the Pe_r and Da_{diff} analysis confirms that radial concentration gradients are physically significant across the vast majority of the operating window, with with the potential for radial non-uniformity (Pe_r) increasing with GHSV and annulus radius. Whether this translates into strong concentration polarisation, however, depends on how fast the reaction replenishes the wall, as discussed in Section 5.3.3. A two-dimensional description is therefore necessary to accurately resolve these radial gradients and their consequences for predicted reactor performance. As shown in Section 5.3.2, the resulting 1D-2D discrepancies depend not only on the magnitude of Pe_r but also on the operating regime, with distinct failure mechanisms emerging at opposite ends of the GHSV range. The full dimensionless transport numbers scaling and regime maps are reported in the Appendix (Section A.5.3).

5.2.4 Model assumptions

Based on the transport analysis of Section 5.2.3, the following simplifying assumptions form the basis of the model development:

- Steady-state operation
- Reactions only occur on the retentate side (where catalyst is present)
- All reacting species are in the gas phase
- Uniform size, porosity, and activity of catalyst particles
- Newtonian fluid behaviour of the bulk gas mixture
- Adiabatic operation (no external heat loss through the outer reactor wall)
- Pseudo-homogeneous conditions: negligible temperature/concentration gradients between external particle surface and adjacent fluid as verified by the Biot number (Equation (A.5.16-A.5.17))
- Negligible axial heat and mass dispersion (plug flow behaviour along the reactor axis) and consistent with the criterion that axial diffusive back-mixing is negligible compared to axial convective transport [30]

5.2.5 Modelling equations

The two-dimensional model is formulated as a set of steady-state partial differential equations (PDEs) governing mass, energy, and momentum transport on the retentate and permeate sides. While the governing equations are formulated at steady state, a pseudo time-stepping method is utilised in the numerical solver to efficiently and stably reach the steady-state solution. Physical property correlations are taken from Chapter 2 and are reported in its Appendix.
The steady-state species continuity equations are given by:

$$\nabla \cdot \boldsymbol{u}^R c_i^R + \nabla \cdot (-D_{m,i} \nabla c_i^R) = r_i \tag{5.7}$$

$$\nabla \cdot \boldsymbol{u}^P c_i^P + \nabla \cdot (-D_{m,i} \nabla c_i^P) = 0 \tag{5.8}$$

Where $\boldsymbol{u}$ is the superficial velocity vector, c_i^R and c_i^P are the bulk molar concentrations of species i in the retentate and permeate, respectively, whereas $D_{m,i}$ is the individual molecular diffusivity coefficient for non-binary mixture, calculated as detailed in the Appendix (Equation (A.5.7)). The steady-state energy continuity equations are defined as:

$$\boldsymbol{u}^R \cdot \nabla T^R + \nabla \cdot (-\alpha_{mix}^R \nabla T^R) = \frac{r\,(-\Delta H)_{T^R}}{\rho_{mix} C_{P_{mix}}} \tag{5.9}$$

$$\boldsymbol{u}^P \cdot \nabla T^P + \nabla \cdot (-\alpha_{mix}^P \nabla T^P) = 0 \tag{5.10}$$

Where α_{mix}^R and α_{mix}^P are the thermal diffusivity of the gas mixture, depending on λ_{mix} which is the thermal conductivity through the gas mixture, $C_{P_{mix}}$ is the heat capacity of the gas mixture. In the retentate side (catalytic bed), the momentum balance is governed by the Ergun equation:

$$\boldsymbol{u}^R = -\left(\frac{150\,\mu_{mix}\,(1-\varepsilon)^2}{4\,\varepsilon^3\,r_{particle}^2} + \frac{1.75\,(1-\varepsilon)\,\rho_{mix}|\boldsymbol{u}^R|}{\varepsilon^3\,2\,r_{particle}}\right)^{-1} \nabla P^R \tag{5.11}$$

As expressed by this equation, the local pressure gradient drives the convective flow in both the axial and radial directions. The term within the brackets depends on the local velocity vector. During the numerical solution process, these non-linear velocity-dependent terms are updated iteratively via direct substitution (Picard iteration). The velocity profile on the permeate side is described by the Hagen-Poiseuille law for laminar flow in a cylindrical tube.
By utilizing the velocity expressions from the momentum equations within the convective terms of the species balances, the flow field is inherently linked to the local species concentrations. To fully close this set of equations, the pressure field (which dictates the driving force for the convective flow) is determined by coupling the system with the ideal gas law:

$$P = RT \sum_i c_i \tag{5.12}$$

The 1D model is derived as a limiting case of the 2D formulation by collapsing each domain, retentate and permeate, to a single radial cell. It shares the same coupled concentration-pressure-temperature field structure, the same ammonia synthesis kinetics, the same Peng-Robinson equation of state for mixture density, and the same Wilke-rule viscosity, thermal-conductivity, and diffusivity. Membrane heat transfer uses an overall resistance model with Nusselt-number correlations on both sides.

5.2.6 Boundary conditions

The boundary conditions applied to the 2D model are summarised in **Table 5.1.** All boundaries are either flux-specified (inlet) or zero-flux Neumann conditions (outer reactor wall, permeate centre axis). Inlet conditions are imposed as flux boundary conditions rather than Dirichlet (fixed-value) conditions, consistent with the flux formulation used for the species balances

Table 5.1 Summary of boundary conditions for the 2D membrane reactor model

Location	Variable	Retentate	Permeate
Inlet ($z = 0$)	Concentration	*Flux condition*	*Flux condition*
Inlet ($z = 0$)	Temperature	*Flux condition*	*Flux condition*
Membrane wall ($r = r_{mo}$ / $r = r_{mi}$)	Concentration (mass flux)	$-D_{m,i}^{R}\,\partial c_i^{R}/\partial r = -J_i = \mathcal{P}_i\,(P^R - P^P)$	$-D_{m,i}^{P}\,\partial c_i^{P}/\partial r = J_i \frac{r_{mi}}{r_{mo}}$
Membrane wall ($r = r_{mo}$ / $r = r_{mi}$)	Temperature (heat flux)	$\lambda^R \frac{dT^R}{dr} = -U(T^R - T^P)\frac{r_{mi}}{r_{mo}}$	$\lambda^P \frac{dT^P}{dr} = U(T^R - T^P)$
Outer reactor wall ($r = r_2$)	Concentration (no-flux)	$\frac{\partial c_i^R}{\partial r} = 0$	-
Outer reactor wall ($r = r_2$)	Temperature (adiabatic)	$\frac{dT^R}{dr} = 0$	-
Permeate centre ($r = 0$)	Concentration	-	$\frac{c_i^P}{\partial r} = 0$
Permeate centre ($r = 0$)	Temperature	-	$\frac{T^P}{\partial r} = 0$

5.2.7 Numerical implementation

The governing PDEs are discretised on a structured two-dimensional mesh in the (z, r) plane using a finite volume approach. Axial convective fluxes are treated with upwind differencing with TVD deferred correction, which ensures numerical stability at the cost of introducing a small degree of numerical diffusion along the reactor axis; axial and radial diffusive fluxes use second-order central differencing. The discretisation is staggered: velocities are defined on cell faces while scalar quantities (concentration and temperature) are collocated at cell centres. Temperature values at cell faces, required by the divergence operator in the energy balance, are obtained by TVD interpolation to prevent spurious oscillations near steep gradients. The pressure-velocity coupling follows the Ergun equation in the packed retentate and the Hagen-Poiseuille law in the permeate tube, and membrane species fluxes are incorporated implicitly in both the residual vector and a sparse Jacobian matrix. Furthermore, to handle the high non-linearity of the ammonia synthesis rate expression, the elements of the Jacobian corresponding to the reaction kinetics source terms are evaluated using numerical differentiation.

The discrete system is solved iteratively using a fully coupled, pseudo-transient Newton-Raphson algorithm with adaptive time-stepping, an Armijo line search for step-size control, and steady-state convergence monitoring. The species concentrations, total pressure, and temperature fields are coupled and resolved in a single-Newton-Raphson step at each iteration.

To ensure numerical stability across variables of drastically different magnitudes, residual scaling is applied within the solver; specifically, the energy balance residual is scaled by a factor of 0.1, while species mass and momentum residuals serve as the unscaled baseline (factor of 1.0). A solution is formally considered converged when the steady-state relative and absolute residual norms fall below $5 \cdot 10^{-2}$ and $1 \cdot 10^{-2}$, respectively. Although the solver permits a near-threshold acceptance rule for cases exhibiting asymptotic stalling, all reported simulations achieved strict convergence with a maximum recorded absolute residual norm of $0.99 \cdot 10^{-2}$, meaning this numerical relaxation was never required. Furthermore, to guarantee physical validity, a mandatory secondary check enforces global elemental mass-balance closure to within a relative tolerance of $1 \cdot 10^{-3}$ and an absolute tolerance of $1 \cdot 10^{-8}$ mol·s^{-1}. This strict adherence to macroscopic mass conservation ensures that the predicted key performance indicators (KPIs) remain highly accurate and completely unaffected by numerical artefacts.

5.2.8 Dimensionless framework: concentration polarisation and Sherwood correction

- **Concentration polarisation (CP) parameter**

The transmembrane driving force depends on the NH_3 partial pressure at the

retentate-membrane interface rather than on the cross-sectional bulk average. Any depletion of ammonia at the wall therefore directly reduces the permeation flux, causing the 1D model to overestimate reactor performance. The concentration polarisation (CP) parameter makes this gap explicit, providing a scalar diagnostic that quantifies the degree of wall depletion along the reactor axis and across the full parameter space.

The degree of NH_3 wall depletion at the membrane surface is quantified by the concentration polarisation parameter:

$$CP_{NH_3}(z) = \frac{y_{NH_3,mw}(z)}{\langle y_{NH_3} \rangle(z)} \tag{5.13}$$

Where $y_{NH_3,mw}$ is the NH_3 mole fraction at the membrane surface ($r = r_1$) and $\langle y_{NH_3} \rangle$ is the cross-sectionally averaged mole fraction. $CP_{NH_3} = 1$ corresponds to the 1D assumption; $CP_{NH_3} < 1$ indicates wall depletion and 1D overestimation of the driving force. $CP_{NH_3} > 1$ would indicate wall enrichment though this case is rare and its effect on integral performance is small. The parametric analysis of CP profiles across all operating conditions and geometries and the quantitative relationship between CP and the 1D-2D performance discrepancy is established in Section 5.3.

❖ **Reaction-enhanced Sherwood number**

The Sherwood analysis serves two complementary objectives. First, it provides a dimensionless characterisation of the effective membrane-side mass transfer, enabling comparison with existing Sherwood correlations while revealing the influence of reactor geometry and operating regime on concentration polarisation in the present non-isothermal system. Second, it yields a corrected membrane boundary condition for the 1D reactor model, thereby incorporating the effects of radial mass-transfer resistance without requiring a full 2D simulation. These objectives give rise to two Sherwood corrections: a field based correction, (Sh_{field}) extracted directly from the 2D concentration fields for mechanistic analysis and comparison with the literature, and an optimised correction, (Sh_{opt}), calibrated to minimise wall-concentration errors when implemented in the corrected 1D model. Although both corrections are obtained using the same fitting methodology, they are derived from different datasets, as described below.

The local mass-transfer coefficient $k_{CP,i}(z)$ at the retentate-membrane interface is extracted directly from the 2D concentration field:

$$k_{CP,NH_3} = \frac{J_{NH_3,mw}(z)}{\langle C_{NH_3} \rangle^R(z) - {C_{NH_3,mw}}^R(z)} \tag{5.14}$$

Where $J_{NH_3,mw}$ is the NH_3 permeation flux at the membrane wall, $\langle C_i \rangle^R$ area-weighted cross-sectional average molar concentration, ${C_{i,mw}}^R$ is the molar concentration at the membrane wall. The local Sherwood number follows directly:

$$Sh(z) = \frac{k_{CP,i}(z) l_c}{D_{m,i}} \tag{5.15}$$

To ensure physically meaningful Sherwood numbers, two filters were applied prior to the regression analysis. First, data with $z < 0.1$ m were excluded to eliminate the hydrodynamically developing region immediately downstream of the membrane inlet, where the radial concentration difference is negligible and the calculated Sherwood number becomes artificially large owing to the vanishing mass-transfer driving force. Second, only data satisfying (CP < 0.90) were retained, thereby excluding near-equilibrium conditions encountered at very low flow rates ($Re_{dh} <$ 5), for which the wall and bulk concentrations are nearly identical and the Sherwood number again becomes ill-conditioned. Because concentration polarisation is negligible under these conditions (CP~1), no correction is required. This criterion also explains the absence of a fitted correction at the lowest Reynolds numbers in the $Re_{dh} - Sh$ plot in Section 5.3.4. Application of these filters yielded 4,016 local Sherwood numbers, extracted from all resolved axial positions across the 50 converged simulation cases.

The extracted Sherwood numbers were first regressed against the complete set of dimensionless groups ($Re_{dh}, Sc, Da_{diff}, Da_{conv}, Pe_r$, and geometric ratios) to identify the controlling variables. This regression confirms that, within the operating regime considered (Re_{dh} < 8,000), Sh exhibits only a weak dependence on Reynolds number (Spearman (r = +0.23)) and no systematic dependence on the Schmidt number. Instead, the reactor geometry, expressed by the dimensionless ratio ($\kappa = r_1/r_2$), emerges as the dominant controlling parameter. Consequently, a reduced correction depending solely on κ is proposed. The resulting functional form is consistent with the analytical scaling derived by Murmura et al. [13,14], while extending it to non-isothermal NH_3 synthesis conditions.

Because only six distinct values of κ were investigated, corresponding to the six annulus geometries considered, the Sherwood numbers were grouped according to geometry. For each group, the median value was adopted as the representative Sherwood number, while the interquartile range (IQR = Q75 - Q25) was used to quantify the variability arising from changes in operating conditions (temperature, pressure, and GHSV). A power-law regression through the six median values yields the field-extracted Sherwood correction, Sh_{field}, reported in Section 5.3.4. The quality of this fit was quantitatively evaluated using the coefficient of determination R^2 and the Mean Absolute Percentage Error (*MAPE)*. While these metrics indicate a mathematically strong correction, the high statistical fit quality must be appropriately qualified. Because the regression is fitted exclusively to the six geometry-group medians, thereby suppressing the variance caused by individual operating variables, these metrics primarily reflect the accuracy of the correction in capturing the underlying geometric dependence of the Sherwood number. They do

not account for the underlying physical scatter caused by variations in temperature, pressure, and flow rate, nor do they reflect the uneven sampling density across different κ subsets.

The Sh_{field} correction represents the effective membrane-side mass transfer extracted directly from the 2D concentration fields and is therefore intended for mechanistic interpretation and comparison with existing Sherwood corrections. However, it does not necessarily provide the optimal correction when implemented in the coupled 1D boundary condition.

To obtain a Sherwood correction directly usable in the 1D correction, a scalar optimisation was performed independently for each of the 50 cases. For each case, Sh_{opt} was defined as the value for which the corrected 1D membrane law reproduces the 2D transmembrane NH_3 flux evaluated at the 2D cross-sectionally averaged state (flux matching), over all active axial locations (z > 0.10 m).

$$MAE(Sh) = \frac{1}{N_z}\sum_{i=1}^{N_z} \mid y_{mw}^{pred}(z;Sh) - y_{2D}^{pred}(z) \mid \tag{5.16}$$

The optimisation was performed using Brent's bounded scalar minimization algorithm, which combines golden-section search with inverse parabolic interpolation and does not require gradient information. For all 50 cases, the objective function was unimodal with a well-defined minimum, ensuring robust convergence within 24-31 function evaluations.

The resulting 50 optimal Sh values (Sh_{opt}) are then grouped by the 6 κ values and fitted by the same power-law procedure as Sh_{field}, giving the optimised correction Sh_{opt}, reported in 5.3.4.

The Sh_{opt} correction is incorporated into the 1D model by replacing the standard membrane boundary condition $y_{mw}^{pred} = \langle y \rangle$ with the following adjusted wall concentration, computed in a single-vectorised operation:

$$y_{mw}^{pred}(z_i) = \frac{k_{CP}\,\langle C^R\rangle(z_i)\,\langle y_{NH_3}^R\rangle(z_i) + \mathcal{P}\,P^P\,y_{NH_3}^P(z_i)}{k_{CP}\,\langle C^R\rangle(z_i) + \mathcal{P}\,P^R(z_i)} \tag{5.17}$$

The Sherwood correction is applied only when the mean CP_{NH_3} along the active reactor length is below 0.90; when CP_{NH_3}~1 (low-flow cases with Re_{dh} < 5), radial diffusion is sufficiently rapid relative to axial convection to maintain a well-mixed cross-section. From a pure mass-transfer perspective, the 1D assumption of uniform radial concentration is adequate in this regime, and applying a Sh correction would introduce unnecessary mathematical artefacts.

However, it is critical to distinguish this absence of concentration polarisation from the substantial divergence between 1D and 2D macroscopic KPI predictions frequently observed at these same low-flow conditions. At low GHSV, the long residence time drives the reactor close to thermodynamic equilibrium, causing the driving forces for both reaction and permeation to approach zero. In this near-

equilibrium regime, the macroscopic KPIs become mathematically hypersensitive. Even minute spatial variations in the 2D concentration and temperature fields result in highly amplified relative errors when compared to the perfectly averaged 1D predictions. Consequently, the 1D/2D divergence at low GHSV is not a failure of mass-transfer limitations (CP), but rather a direct manifestation of the extreme thermodynamic sensitivity near equilibrium. The performance of this correction is quantified in 5.3.5.

5.2.9 Mechanistic closure: the reaction-screened diffusion layer

While Sh_{field} and Sh_{opt} quantify the effective wall mass-transfer resistance, they remain empirical: the fit itself does not identify the physical mechanism that sets k_{cp}, and therefore does not delimit the conditions under which the κ-power law may be extrapolated. This subsection formulates a mechanistic closure built on the reaction-screening mechanism established from the 2D fields in Section 5.3.3, where three independent observations (flow independence of the extracted Sherwood number over the full GHSV span, a wall-deficit layer of nearly constant absolute thickness across all geometries, and weak permeation-induced radial suction) rule out a hydrodynamic boundary layer. Because ammonia synthesis is product-inhibited, local removal of ammonia at the membrane wall raises the local net production rate, and this kinetic response heals the wall deficit within a screening length set by local kinetics and diffusivity only:

$$\delta_i = \sqrt{D_i / s_i}, \qquad s_i = \max(-\partial R_i / \partial c_i,\ 0), \tag{5.18}$$

where D_i is the local mixture diffusivity and s_i the diagonal sensitivity of the net molar production rate R_i to the species' own concentration, both evaluated at the local bulk state. In the 1D model, $s_i(z)$ is obtained by a forward finite difference of the Temkin rate with respect to c_i, adding one vectorised rate evaluation per species to each residual assembly, a negligible cost.

To convert the screening length into a mass-transfer coefficient, the radial field is written as bulk plus deficit, $c_i(r,z) = \bar{c}_i(z) + c_i'(r,z)$, and the rate is linearised about the bulk state (diagonal approximation; cross-species couplings are absorbed in the calibration constant introduced below). The bulk balance carries $R_i(\bar{c})$, so the deficit obeys a modified Helmholtz equation in the annulus $r \in [r_{mem}, r_{max}]$ with no flux at the outer wall. Its solution in modified Bessel functions (full derivation in the Appendix A.5.4) yields the film coefficient of the screened channel:

$$k_{cp,i}^{screen} = \frac{D_i}{\delta_i} f_{ann}(x_a, x_b), \qquad f_{ann}(x_a, x_b) = \frac{K_1(x_a)\, I_1(x_b) - I_1(x_a)\, K_1(x_b)}{K_0(x_a)\, I_1(x_b) + I_0(x_a)\, K_1(x_b)} \tag{5.19}$$

with $x_a = r_{mem}/\delta_i$ and $x_b = r_{max}/\delta_i$, where I_n and K_n are modified Bessel

functions of the first and second kind. In the thin-layer limit ($\delta_i \ll d_h$) the factor reduces to $K_1(x_a)/K_0(x_a) \to 1$, the planar film-theory result, with a curvature enhancement of about 1.3 at the physically realised x_a~1.7; for $\delta_i \to \infty$ it vanishes, because without a kinetic response a pure deficit cannot sustain a steady flux.

For a species the kinetics cannot heal ($s_i \to 0$), the deficit is fed by the distributed background supply instead. Steady diffusion in the annulus with a uniform volumetric source, extracted entirely at the membrane with no flux at the outer wall, gives a closed-form shape factor $G(\kappa) = k_{cp}\, d_h/D$, the mass-transfer analogue of a fully developed Nusselt number (derivation in the Appendix-Section A.5.4). It decreases only weakly with geometry, from G = 6.24 at $\kappa = 0.083$ to G = 3.78 at κ = 0.25, i.e. approximately as $\kappa^{-0.46}$. Both channels feed the same deficit, so the better conductor controls, and the closure evaluated per axial cell and species from the current 1D state reads

$$k_{cp,i}(z) \;=\; \max\left(C\,\frac{D_i}{\delta_i}\, f_{ann}(r_{mem}/\delta_i,\, r_{max}/\delta_i),\; G(\kappa)\,\frac{D_i}{d_h} \right) \tag{5.20}$$

The maximum, rather than a sum, is deliberate: structure selection against the exact flux-matched closures shows that the screening term alone carries the full geometry dependence (per-κ calibration bias flat to within ± 5%, Section A.5.4), whereas any additive conduction admixture re-biases it. For the present chemistry the screened channel controls essentially everywhere (a factor ~2 above the conduction bound at the median); the bound exists so that a species without kinetic response retains a finite mass-transfer coefficient.

The closure contains a single calibrated constant. It follows in closed form as the flux-weighted logarithmic mean of the ratio between the exact flux-matched coefficient and the screened prediction over all active axial cells of the certified 2D dataset (4,923 samples):

$$\ln C \;=\; \left\langle \ln\left(k_{cp}^{exact}/k_{cp}^{screen}\right)\right\rangle_w, \qquad w = |J_{NH_3}|, \qquad \Rightarrow \qquad C = 0.464 \sim 1/2 \tag{5.21}$$

an $O(1)$ profile-shape factor that absorbs the linearisation, the diagonal approximation, and the effective-diffusivity convention. Because the chemistry enters only through the local sensitivity $\partial R_i/\partial c_i$, the closure evaluates along z and transfers to other product-inhibited chemistries, temperatures, and geometries, provided screening remains the dominant transport structure; it does not apply to inert, flow-dominated channels, for which a Graetz-Lévêque closure would be required instead.

5.2.10 Key performance indicators for 1D-2D model comparison

To systematically quantify discrepancies between the 1D and 2D models, six key performance indicators (KPIs) are monitored throughout this work, some of them already used in the previous chapters.

Bulk performance characterised by H_2 ($X_{H_2}(z)$), NH_3 yield ($Y_{NH_3}(z)$), and NH_3 recovery ($NH_3\ recovery\ (z)$), are evaluated as axial profiles from the retentate and permeate molar flows and reported in percentage points (pp):

$$\%\ X_{H_2}(z) = \frac{F^R_{H_2,in} - F^R_{H_2}(z) - F_{H_2,tm}(z)}{F^R_{H_2,in} - F_{H_2,tm}{}^*(z)} \times 100 \tag{5.22}$$

$$\%\ Y_{NH_3}(z) = \frac{F^R_{NH_3}(z) + F^P_{NH_3}(z)}{F^R_{H_2,in} - F_{H_2,tm}{}^*(z)} \times 100 \tag{5.23}$$

$$\%\ NH_3\ recovery\ (z) = \frac{F^P_{NH_3}(z)}{F^R_{NH_3}(z) + F^P_{NH_3}(z)} \times 100 \tag{5.24}$$

$$F_{H_2,tm}(z) = F^P_{H_2,out}(z) - F^P_{H_2,in} \tag{5.25}$$

$$F_{H_2,tm}{}^*(z) = F^P_{H_2,out}(z) - F^P_{H_2,in} \text{ only if } F_{H_2,tm}(z) \leq 0 \tag{5.26}$$

Separation performance is assessed by the NH_3 purity in the permeate stream, defined as the ammonia mole fraction at the permeate outlet:

$$\%\ NH_3\ purity = \frac{F^P_{NH_3}(z)}{F^P_{TOT}(z)} \times 100 \tag{5.27}$$

Thermal behaviour is characterised by the maximum temperature rise, defined as the maximum of the temperature field over the retentate domain relative to the inlet temperature:

$$\Delta T^R_{max} = T^R_{max} - T^R_{in} \tag{5.28}$$

Reactor production rate is measured as the ammonia space-time yield, defined as the NH_3 production rate per unit catalyst mass:

$$NH_3\ production\ rate(z) = \frac{F^R_{NH_3}(z) + F^P_{NH_3}(z)}{w_{cat}} \tag{5.29}$$

The discrepancy between the 1D and 2D models is quantified for each KPI by the absolute error:

$$\varepsilon_{1D-2D} = KPI_{1D} - KPI_{2D} \tag{5.30}$$

The base-case operating conditions and reactor geometry used throughout this work are summarised in the Appendix (**Table A.5.3**). For all simulations, a feed molar ratio H_2:N_2 = 2:1 is used. Furthermore, the catalyst particle radius is fixed at $r_{particle}$= 1.25·10^{-4} m the outer membrane radius is r_1 = 0.005 m; the catalyst bed porosity is ε = 0.4 and a catalyst dilution factor D_{cat} = 1/3 is applied.

5.3 RESULTS AND DISCUSSION

5.3.1 Verification and validation of sub-models

The 2D reactor model was first verified to ensure the correct implementation of two

constitutive sub-models: the ammonia synthesis kinetics and the membrane transport.

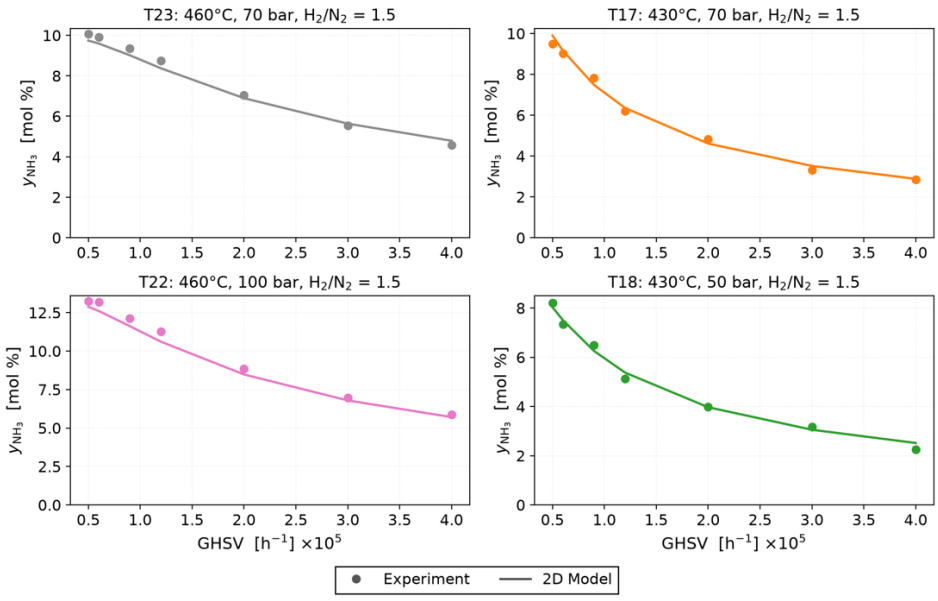


Figure 5.3 NH_3 outlet mole fraction as a function of gas hourly space velocity (GHSV) for four representative operating conditions. Symbols denote experimental data; solid lines represent 2D model predictions

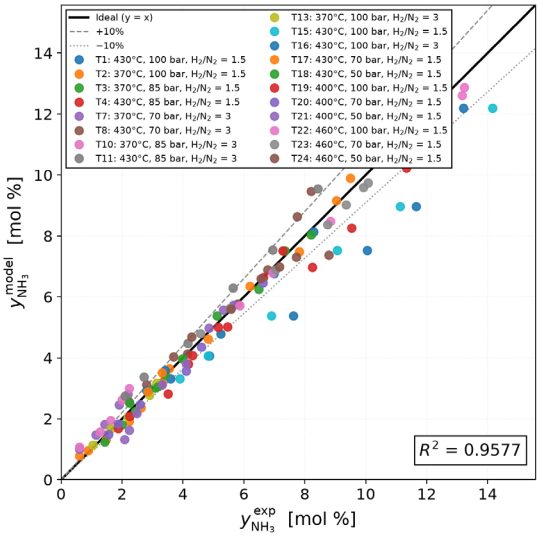


Figure 5.4 Parity plot comparing experimentally measured NH_3 outlet mole fractions with the predictions of the 2D pseudo-homogeneous reactor model for all 19 validation datasets (T1-T24). Conditions cover temperatures from 370 to 460 °C, pressures from 50 to 100 bar, and H_2N_2 feed ratios of 1.5 and 3.0

To verify the kinetic sub-model, isothermal simulations were performed across a broad range of operating conditions drawn from Rossetti et al. (as in Chapter 2), encompassing temperatures of 370-460 °C, pressures of 50-100 bar, H_2:N_2 feed ratios of 1.5 and 3.0, and gas hourly space velocities (GHSV) in the range of 50,000-400,000 h^{-1}.

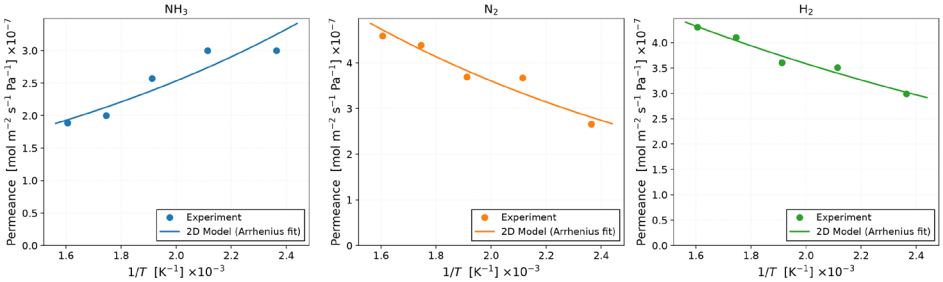


Figure 5.5 Arrhenius plots of single-gas membrane permeance for NH_3, N_2, and H_2. Symbols indicate experimental permeance data, while solid lines show the 2D membrane model predictions based on an Arrhenius-type temperature dependence

The predicted NH_3 outlet mole fraction was compared against the original dataset that Rossetti et al. used to derive their kinetic parameters. While this serves as a rigorous implementation check rather than an independent validation against unseen data, it is a crucial step to confirm the accurate coding and integration of the complex Temkin rate equations within our numerical solver.

Representative examples of this comparison are shown in **Figure 5.3** and the full set of the other 15 conditions is reported in **Figure A.5.7** of the Appendix. The overall agreement is summarised in the parity plot of **Figure 5.4**, which shows that all predicted values cluster tightly around the ideal y = x line across the entire range of NH_3 mole fractions from 0 to 18 mol%, with all points falling within the ±10% error band. This scatter-free agreement across such a wide and diverse set of conditions yields a coefficient of determination $R^2 = 0.9616$.

For the membrane transport sub-model, the permeance of NH_3, N_2, and H_2 was experimentally measured as a function of temperature and compared against the model predictions derived from an Arrhenius-type transport equation (**Figure 5.5**). The model accurately reproduces the measured temperature dependence for all three species. The satisfactory agreement obtained for both sub-models across independent experimental datasets provides confidence in the predictive capability of the assembled 2D model for the simulation of membrane reactor performance under industrially relevant conditions.

5.3.2 1D-2D discrepancies across key performance indicators (KPIs)

Standard 1D plug-flow model assumes that species concentrations are radially uniform across the retentate annulus at every axial position. In an annular membrane

reactor, this assumption is challenged by the continuous selective withdrawal of NH_3 at the inner wall, which creates a persistent near-wall depletion layer whose severity depends on the competition between permeation-driven removal, local reaction generation, and radial diffusive replenishment from the bulk. Whether this radial non-uniformity translates into meaningful errors in predicted reactor performance critically depends on which key performance indicator is considered, since concentration polarisation, thermal stratification, and membrane transport each respond differently to the same underlying flow conditions. The following subsections quantify this question systematically by comparing 1D and 2D model predictions across six KPIs. Throughout this section, errors are reported as the signed difference (1D - 2D), expressed in percentage points (pp) for dimensionless KPIs (X_{H_2}, Y_{NH_3}, $NH_3\ recovery$, $NH_3\ purity$) and in absolute units for dimensional quantities ($NH_3\ production\ rate$ in mmol·$g_{cat}^{-1}h^{-1}$, ΔT_{max}^{R} in K). Positive values indicate overestimation by the 1D model; negative values indicate underestimation.

Figure 5.6 compares 1D (dashed) and 2D (solid) predictions of all six KPIs as a function of GHSV for groups G1 (r = 0.06 m, blue) and G2 (r = 0.03 m, red) at P_{in}^{R} = 80 bar and T_{in}^{R} = 623 K. Three qualitatively distinct behaviours emerge. For H_2 conversion and NH_3 yield (panels (a) and (d)), the 1D and 2D curves converge at both ends of the GHSV range and diverge most strongly in between, though the two channel geometries do not converge at the same rate: the G1 (wider-channel) curves are effectively indistinguishable from GHSV~3,000-5,000 h^{-1} onward, whereas the G2 (narrower-channel) curves retain a visible gap up to GHSV~2-3·10^4 h^{-1}, only merging with the 1D prediction just before the sharp drop at the highest GHSV tested. The 1D model overpredicts both KPIs across most of the domain, though this reverses at the lowest GHSV for G2, where the 2D prediction is marginally higher. The magnitude of the 1D/2D discrepancy does not scale monotonically with annulus width: it is larger for G1 than G2 only at the two lowest GHSV values tested, while across the broad mid-to-high GHSV range the discrepancy is consistently larger for G2, the narrower channel, the reverse of what a longer radial diffusion path in G1 alone would predict. The signed KPI value is higher for G2 than G1 across most of the range (GHSV ≥ 500 h^{-1}), but this ordering reverses at the lowest GHSV, where the wider G1 channel achieves the higher conversion and yield.

NH_3 production rate (panel (b)) exhibits a qualitatively different pattern from the other KPIs: the 1D and 2D curves for both G1 and G2 remain essentially coincident across the entire GHSV range. Unlike conversion, yield, recovery, or purity, production rate shows no resolvable 1D/2D discrepancy at any point tested, indicating that the radial non-uniformities captured by the 2D model do not measurably affect this particular KPI. NH_3 recovery and purity (panels (c) and (e)) share a largely contrasting behaviour: the 1D model overpredicts both quantities

across essentially the entire GHSV range. For recovery, the gap is substantial through the middle of the range - on the order of 20-25 percentage points for both G1 and G2 around GHSV = 500-5,000 h^{-1} - and narrows toward the extremes, but even at the highest GHSV tested, where conversion errors have vanished, a gap of roughly 5 percentage points persists for G2. For purity, the 1D-2D gap is smaller in absolute terms throughout (roughly 1-3.5 percentage points across most of the range) and essentially closes by the highest GHSV tested. The one exception is NH_3 purity for G2 at the lowest GHSV tested, where the ordering briefly reverses and the 2D model gives the marginally higher value, by less than 1 percentage point.

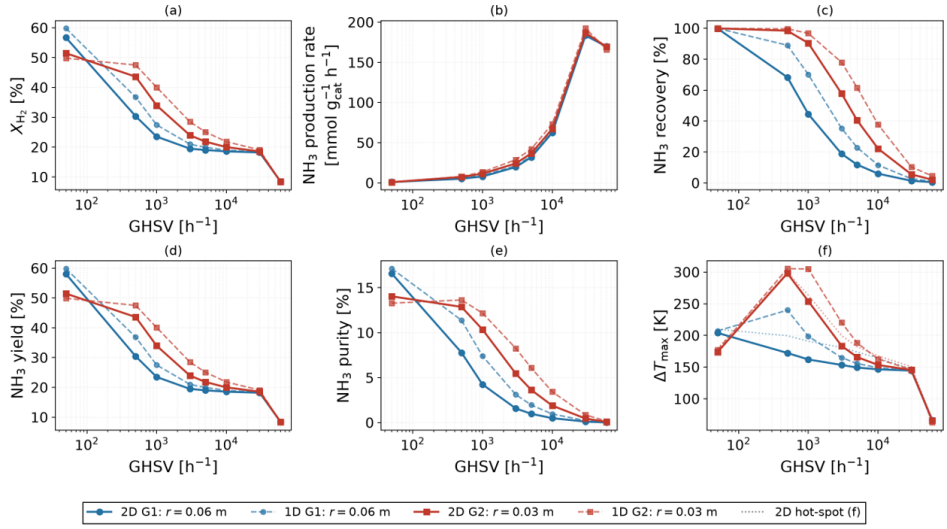


Figure 5.6 Comparison of 1D (dashed lines) and 2D (solid lines) model predictions as a function of GHSV for the GHSV groups G1 (r = 0.06 m, blue) and G2 (r = 0.03 m, red) at P_{in}^{R} = 80 bar and T_{in}^{R} = 623 K: (a) H_2 conversion; (b) NH_3 production rate; (c) NH_3 recovery; (d) NH_3 yield; (e) NH_3 purity; (f) maximum retentate temperature rise

The maximum retentate temperature rise ΔT_{max} (panel (f)) reveals a further layer of complexity. At the lowest GHSV tested, the 1D and 2D predictions are essentially coincident in both geometries; the overprediction instead peaks at the next GHSV tested (~500 h^{-1}), substantially for G1 (up to ~70 K) but only modestly for G2 (up to ~10 K), as the equilibrium-proximity mechanism amplifies the conversion overestimation and propagates it into a larger overestimation of cumulative heat release. At medium-high GHSV the overprediction essentially disappears: the 1D ΔT_{max}^{R} agrees with the radially averaged 2D value within a few kelvin, and slightly underpredicts the 2D hot-spot value by up to ~5 K. This reversal reflects a mechanistically distinct failure mode: persistent near-wall NH_3 depletion reduces local permeation flux, generates a localised thermal hot spot that the 2D model resolves but the radially averaged 1D model cannot. The wider annulus of G1

sustains a more pronounced radial thermal gradient over its longer diffusion path, explaining its larger underprediction at high GHSV. The two-dimensional temperature fields presented in Section 5.3.3 clearly demonstrate the hot-spot structure, with additional results provided in **Figures A.5.9-A.5.14**.

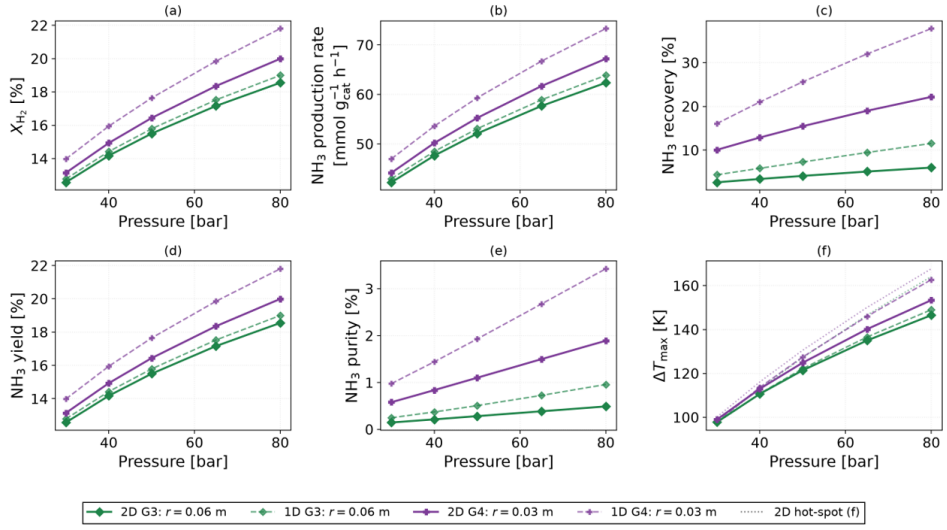


Figure 5.7 Comparison of 1D (dashed lines) and 2D (solid lines) model predictions as a function of pressure for the pressure groups G3 (r = 0.06 m, purple) and G4 (r = 0.03 m, green) at T_{in}^{R} = 623 K and GHSV = 10,000 h^{-1}: (a) H_2 conversion; (b) NH_3 production rate; (c) NH_3 recovery; (d) NH_3 yield; (e) NH_3 purity; (f) maximum retentate temperature rise

The pressure groups (**Figure 5.7**, G3: r = 0.06 m, G4: r = 0.03 m, GHSV = 10,000 h^{-1}) reinforce and extends these findings, by shifting the focus toward the higher-GHSV regime. Across all pressures, the 1D-2D discrepancies in conversion, yield, production rate, and purity (panels (a), (b), (d), (e)) are systematically larger for the compact annulus G4 than for the wider G3, and grow monotonically with pressure in both geometries. As in the GHSV analysis, this geometry dependence is not driven by stronger radial concentration gradients in G4: the 2D field analysis (Section 5.3.3) confirms that CP_{NH_3} profiles in G4 are intrinsically similar to those in G3. Rather, the equilibrium-proximity mechanism again dominates: the higher S_M/V ratio of G4 pushes the retentate closer to thermodynamic equilibrium, rendering the integrated KPIs hypersensitive to even modest near-wall concentration differences. The monotonic growth of this error with pressure reflects the progressive amplification of the permeation-induced equilibrium shift as the transmembrane driving force increases.

Unlike the conversion KPIs, recovery errors are geometry-selective: the 1D model overpredicts recovery for G4, with the gap growing from ~6 pp at P = 30 bar to

~16 pp at P = 80 bar, while G3 shows much less 1D-2D discrepancy across the full pressure range. This asymmetry is consistent with the surface-to-volume ratio argument: in G4, near-wall NH_3 depletion reduces the local transmembrane driving force below what the radially uniform 1D model assumes, causing the latter to overestimate recovery. For ΔT^R_{max}, the 1D and 2D models agree closely for G3 across the full pressure range, with the 2D model predicting a marginally higher hot spot at high pressure due to radially non-uniform heat release that the 1D model cannot resolve. For G4 the 2D model consistently predicts a larger ΔT^R_{max} than the 1D model across all pressures, with the gap growing with pressure, reflecting the more severe radial temperature gradients in the compact annulus where the higher membrane surface-to-volume ratio drives stronger localised heat release near the wall.

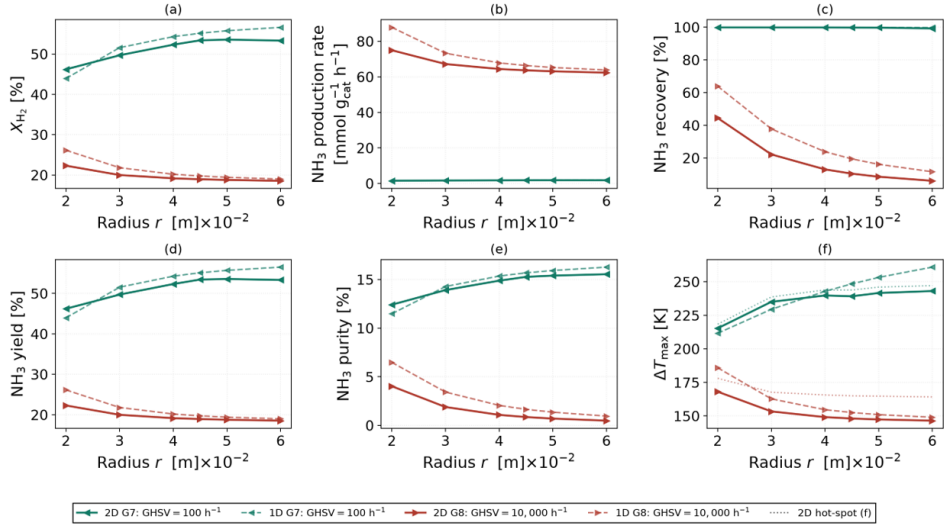


Figure 5.8 Comparison of 1D (dashed lines) and 2D (solid lines) model predictions as a function of annulus radius for the radius groups G7 (GHSV = 100 h^{-1}, green) and G8 (GHSV = 10,000 h^{-1}, red) at T^R_{in} = 623 K and P^R_{in} = 80 bar: (a) H_2 conversion; (b) NH_3 production rate; (c) NH_3 recovery; (d) NH_3 yield; (e) NH_3 purity; (f) maximum retentate temperature rise

The radius group (**Figure 5.8** G7: GHSV = 100 h^{-1}, G8: GHSV = 10,000 h^{-1}, P^R_{in} = 80 bar, T^R_{in} = 623 K) provides the most complete picture of geometry dependence by varying the annulus radius continuously across five values at both the low and high GHSV extremes. At high GHSV (G8), performances are more geometry-sensitive. H_2 conversion, NH_3 recovery, yield, and purity (panels (a), (c), (d), (e)) all decrease monotonically with increasing radius in the 2D model, directly reflecting the reduction in S_M/V ratio as the annulus widens and the permeation-driven equilibrium shift weakens. The 1D model overpredicts all four KPIs across the full

radius range, with the largest absolute errors at the smallest radius where equilibrium proximity is most acute: for recovery, the 1D/2D gap is approximately 20 percentage points at r = 0.02 m, narrowing to roughly 6 percentage points at r = 0.06 m as both predictions converge toward low recovery at large radius (the discrepancy shrinks with increasing radius rather than growing). NH_3 production rate (panel (b)) also decreases with radius under G8 conditions (from roughly 88 to 63 mmol·$g_{cat}^{-1}h^{-1}$), with the 1D and 2D predictions staying in reasonably close agreement throughout.

At low GHSV (G7), the picture is markedly different: H_2 conversion, NH_3 yield and purity (panels (a), (d), (e)) increase with radius rather than decrease (from roughly 44-46% to 53-57% for conversion and yield, and from roughly 12% to 16% for purity) while NH_3 recovery (panel (c)) sits essentially at its ceiling value (~99-100%) across the entire radius range, showing negligible geometry sensitivity. NH_3 production rate (panel (b)) is low across all radii at G7 conditions and remains nearly flat with radius, with only a slight decrease, reflecting the limited conversion achieved at these long residence times regardless of annulus width. ΔT_{max} (panel (f)) shows a more intricate pattern than a single-GHSV-dependent trend. At G8, the 2D model underpredicts ΔT_{max}^{R} relative to 1D at small radius, with a gap of roughly 19-20 K at r = 0.02 m that closes to near zero by r~0.04 m, consistent with the same near-wall depletion/hot-spot mechanism identified in **Figure 5.6**(f), where the radially averaged 1D model cannot resolve the localised thermal gradient that a compact, high-flux annulus produces. At G7, the two models track closely at small radius but diverge in the opposite direction as radius increases: 1D and 2D agree to within a few kelvin at r = 0.02 m, but 1D increasingly overpredicts ΔT_{max}^{R} at larger radius, reaching a gap of roughly 20 K by r = 0.06 m.

The temperature groups (G5, r = 0.06 m, G6, r = 0.03 m) exhibit KPI trends fully consistent with the mechanisms established above and are reported in **Figure A.5.8** of the Appendix. The detailed field analysis for the temperature groups, is presented in Appendix (**Figure A.5.22-A.5.31**).

The lower end of the temperature window deserves a remark. The steep rise in conversion and temperature rise between T_{in}^{R} = 548 K and 573 K (**Figure A.5.8**) marks the autothermal ignition of the bed, and in this transition region the model exhibits the steady-state multiplicity that is classical for ammonia synthesis reactors [31,32]: a low-conversion (extinguished) and an ignited steady state coexist, and which of the two a simulation approaches depends on its initial condition. The sensitivity is most pronounced at T_{in}^{R} = 598 K, where the ignited state was obtained reliably by continuation in the inlet temperature from neighbouring operating points; a linear stability analysis of the steady-state solutions confirms that both computed 598 K states (G5 and G6) are dynamically stable. Because performance inside a multiplicity window reflects the operating history and not the operating point alone

- behaviour documented for industrial ammonia converters [31] - these two cases are omitted from the parametric trend figures.

Taken together, the radius study reveals a critical bifurcation in the 1D model's limitations depending on the operating regime and target metric. For bulk conversion and yield, the 1D model is most unreliable at low GHSV and compact geometries, where high S_M/V and equilibrium proximity make integral KPIs hypersensitive to 1D volume-averaging. Conversely, for permeation-driven metrics like NH_3 recovery, the 1D model remains biased even at high GHSV, where the residual, weak concentration polarisation still reduces the permeation flux relative to the 1D prediction. This confirms that the 1D model requires correction across the entire operating window, though for entirely different physical reasons at opposite ends of the flow spectrum.

5.3.3 Physical origin of divergence from 2D fields

The KPI comparisons in Section 5.3.2 attribute 1D model errors to two root causes: thermodynamic hypersensitivity near equilibrium at low GHSV, and unresolved near-wall NH_3 depletion at high GHSV. Both originate from the same underlying field phenomenon, concentration polarisation, whose character shifts fundamentally depending on the competition between three local processes: permeation-driven wall removal, radial diffusive replenishment, and reaction-generated NH_3. Across all 50 simulated cases, the 2D fields reveal three qualitatively distinct CP regimes that govern this competition, and each examined operating variable (GHSV, geometry, pressure, and temperature) acts primarily by shifting the system between or within these regimes.

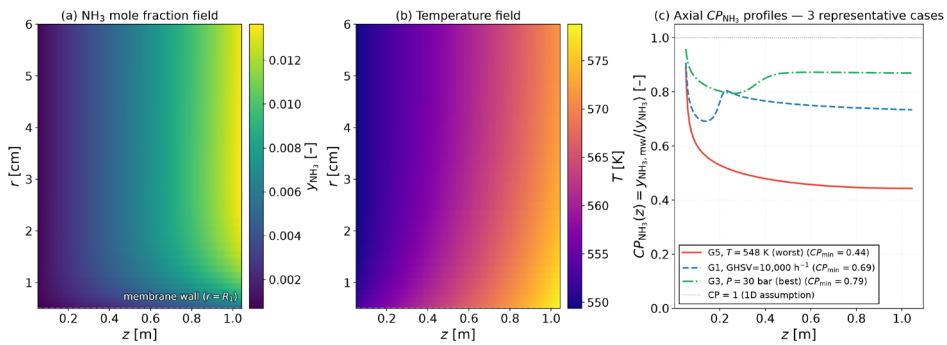


Figure 5.9 2D field of retentate NH_3 mole fraction (a) and retentate temperature (b) for the most severe CP case (G5, T_{in}^R = 548 K, r = 0.06 m, P_{in}^R = 80 bar, GHSV = 5,000 h^{-1}); (c) axial profiles of the NH_3 concentration polarisation factor, for three representative cases spanning the full parameter space

In the reaction-limited regime, typified by the most severely polarised case in the dataset (G5, T_{in}^R = 548 K, $CP_{NH_{3,min}}$ = 0.44, **Figure 5.9**) the reaction rate is too slow to supply ammonia at a rate sufficient to sustain both the bulk and the membrane

wall simultaneously. The membrane strips ammonia as rapidly as it is locally generated, leaving the wall continuously depleted (CP_{NH_3}~0.44-0.50) throughout the upstream 60% of the reactor, with a sharp recovery only at z~0.6 m once sufficient NH_3 has accumulated axially (**Figure 5.9**(c)). CP here is not driven by permeation outpacing diffusion (radial transport is largely adequate) but by the absence of a reaction source strong enough to feed the wall. The NH_3 mole fraction field (**Figure 5.9**(a)) reflects this: bulk concentrations remain below 0.005 over most of the reactor length, and the radial gradient is imposed on an already depleted bulk. The 2D fields for the intermediate case (G1, GHSV = 10,000 h^{-1}, $CP_{NH_{3,min}}$ = 0.75) and the least polarised case (G3, P_{in}^{R} = 30 bar, $CP_{NH_{3,min}}$ = 0.86) are presented in the Appendix (**Figure A.5.15, A.5.21**).

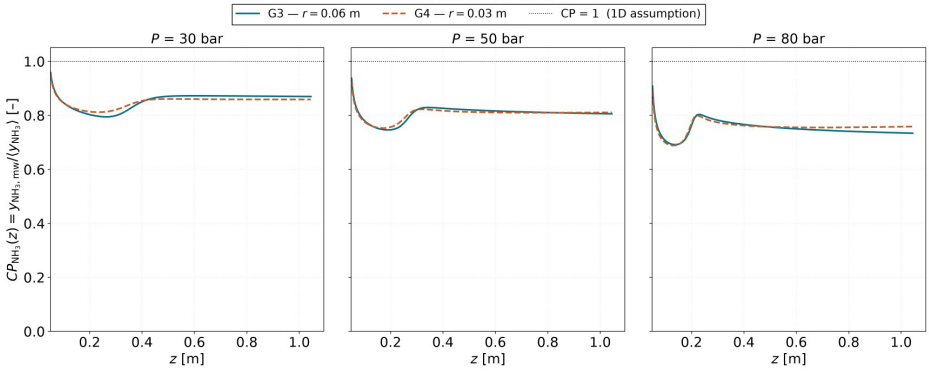


Figure 5.10 Axial profiles of the NH_3 concentration polarisation factor, CP_{NH_3}, for the pressure groups G3 (r = 0.06 m, solid blue) and G4 (r = 0.03 m, dashed orange) at three operating pressures (P_{in}^{R} = 30, 50, and 80 bar), with GHSV = 10,000 h^{-1} and T_{in}^{R} = 623 K; the dotted horizontal line at CP_{NH_3} = 1 represents the 1D plug-flow assumption of radial concentration uniformity

In the high-GHSV pressure group (G3/G4, GHSV = 10,000 h^{-1}, **Figure 5.10**), the high NH_3 production rate continuously replenishes the near-wall concentration, so that the CP_{NH_3} profiles for the wide and compact annuli nearly overlap at all pressures. This confirms that at these GHSV values the radial diffusion length is no longer the controlling variable; instead, the reaction source term dominates the radial mass balance. In this regime, CP severity is governed primarily by the local balance between permeation flux and reaction generation rate.this reaction-dominated, weak CP regime, pressure plays a dual role: increasing pressure deepens the CP minimum (from ~0.80 at 30 bar to ~0.70 at 80 bar) by enhancing permeation, while simultaneously accelerating axial recovery via the thermodynamic and kinetic intensification of NH_3 synthesis. The result is a sharper but more axially confined inlet depression at higher pressure, a tightening of the CP profile rather than a uniform worsening, so that reaction-generated NH_3 and radial diffusion together

keep the wall composition close to the bulk, and CP never becomes strongly diffusion-limited. This behaviour stands in contrast to the low-GHSV regime, where the reaction term can no longer compensate the permeation rate, radial diffusion becomes the controlling replenishment mechanism, and annulus geometry exerts a measurable influence on CP severity.

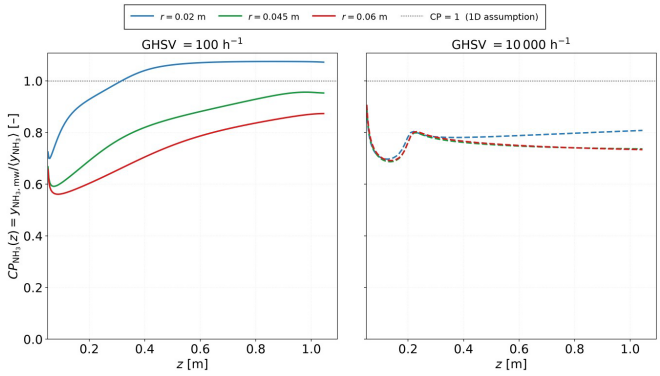


Figure 5.11 Axial profiles of the NH_3 concentration polarisation factor, CP_{NH_3}, for the radius groups G7 (GHSV = 100 h^{-1}, solid blue) and G8 (GHSV = 10,000 h^{-1}, dashed orange) at three annulus radius (r = 0.02, 0.045, 0.06 m), with T_{in}^{R} = 623 K, P_{in}^{R} = 80 bar. The dotted horizontal line at CP_{NH_3} = 1 represents the 1D plug-flow assumption of radial concentration uniformity

At low GHSV (**Figure 5.11**, G7, GHSV = 100 h^{-1}), the CP_{NH_3} profiles exhibit a pronounced geometry dependence. The largest radius (r = 0.06 m) shows the deepest and most persistent wall depletion throughout the reactor length, while decreasing the annulus width progressively reduces the depletion severity. At the smallest radius (r = 0.02 m), CP_{NH_3} does not remain below unity as in the classical concentration polarisation picture, instead it rises above 1.0 in the downstream section of the reactor, meaning the wall NH_3 concentration actually exceeds the bulk. This counter-intuitive behaviour arises from the interplay between the very high S_M/V ratio and the long residence time at low GHSV: as the system approaches thermodynamic equilibrium, permeation removes NH_3 from the bulk faster than from the near-wall region, where the local reaction-diffusion balance sustains a higher NH_3 concentration. At high GHSV (G8), this geometry sensitivity collapses and all radii produce nearly overlapping CP profiles, although the smallest radius recovers to a slightly higher plateau (CP_{NH_3}~0.80 vs. ~0.73 at r = 0.06 m), thereby sustaining a more uniform permeation driving force along the membrane length. Between the low-GHSV reaction-limited regime and the high-GHSV weak-CP limit lies a permeation-dominated crossover regime, most clearly illustrated by the GHSV-geometry group (**Figure A.5.9-A.5.10**).

In this regime, permeation begins to outpace radial diffusion and establishes a

measurable wall-depletion layer, while the reaction remains strong enough to partially replenish it. In the compact annulus G2 (**Figure A.5.10**), the higher S_M/V ratio concentrates permeation in the first reactor half, driving aggressive ammonia removal that exhausts the transmembrane driving force by z~0.8 m; downstream of this point, the retentate approaches depletion and the reactor operates in an effectively adiabatic mode, with temperatures exceeding 880 K. Despite this, G2 attains higher overall conversion and recovery than the wider annulus G1, because the permeation captured in the active first half more than compensates for the unused second half. This is the regime where geometry has the strongest influence: the reaction rate is still producing ammonia actively, the membrane is still selective, and yet radial concentration gradients are already significant enough that the annulus width becomes the key design variable. At GHSV ≥ 3,000 h^{-1} (**Figure A.5.11-A.5.20**), the system moves into the reaction-dominated, weak-CP regime. Although faster axial convection shortens the time available for radial diffusion, the higher local NH_3 production rate continuously replenishes the near-wall region, so the wall depletion becomes shallower and the CP profiles of different geometries converge.
Each parametric group can therefore be viewed as a trajectory through this three-regime space. Temperature provides the most direct lever (**Error! Reference source not found.A.5.32**): at T_{in}^{R} = 573 K the system is firmly in the reaction-limited regime, with CP_{NH_3} profiles that are nearly identical in shape for both geometries and exhibit very low, almost flat value (CP_{NH_3}~0.5) over the upstream section (z ≤ 0.6 m), reflecting severe and persistent wall depletion that the slow reaction cannot compensate. Raising the temperature to 623 K shifts the system into the permeation-dominated crossover regime, and at T_{in}^{R} ≥ 648 K faster kinetics drive it toward the reaction-dominated weak-CP regime: CP severity decreases further, although the simultaneous increase in permeation flux partially offsets this improvement.
It should be noted that the 880 K temperatures reached in the permeation-dominated crossover and reaction-dominated weak-CP regimes for the compact geometry exceed the validated range of standard ammonia synthesis catalysts and of the membrane-permeance correlations employed here, even though carbon molecular sieve membranes themselves can withstand such temperatures. These cases were retained to fully map the theoretical design space and to illustrate a key advantage of 2D modelling: its ability to capture localised thermal excursions that a 1D model would average out, thereby delineating the operational boundaries within which scale-up remains safe. Representative 2D fields for the smallest and largest radii in each group are provided in the Appendix (**Figure A.5.22-A.5.31**).

5.3.4 Empirical Sherwood number correction for radial mass transfer

The 2D concentration fields established in the previous section reveal systematic NH_3 depletion at the membrane wall relative to the cross-sectional average, quantified by the concentration polarisation ratio. To characterize this wall mass transfer resistance in a form compatible with 1D modelling, a local Sherwood number (Sh_{NH_3}) was extracted at each axial position from the 2D solution, according to Equation (5.14-5.15).

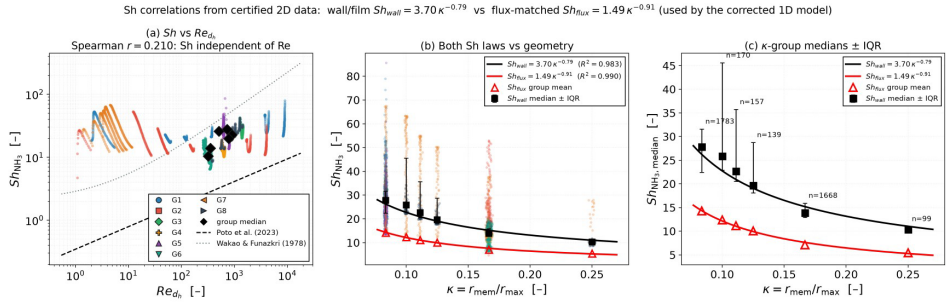


Figure 5.12 Reaction-enhanced Sherwood number correction for NH_3 concentration polarisation extracted from 50 2D simulation cases (4,016 axial data points; filters: z > 0.10 m, $CP_{NH_3} < 0.95$): (a) Sh vs. the hydraulic-diameter Reynolds number; (b) Sh vs. the geometry ratio $\kappa = r_1/r_2$ showing local data, group medians, and interquartile ranges; (c) κ-group medians ± IQR for both corrections, with the number of data points n per group indicated

Figure 5.12(a) reports all local Sh_{NH_3} values from the 50 simulated cases as a function of the hydraulic-diameter Reynolds number Re_{dh}, spanning nearly four orders of magnitude (Re_{dh}= 1.1 to 8,900). Despite this wide range, the Spearman rank correlation between Sh_{NH_3} and Re_{dh} is r~0.23, indicating that, for the present CMS membrane-based ammonia membrane reactor system and the explored operating window, the effective Sherwood number is weakly correlated with Reynolds number. The standard packed bed mass transfer correlations of Wakao and Funazkri [10] and Poto et al. [11], both plotted in **Figure 5.12**(a), increase monotonically with Re_{dh} misrepresent the observed Sh_{NH_3} by up to an order of magnitude or more at comparable Re_{dh}, confirming that these hydrodynamic correlations are not applicable in this reaction-enhanced regime. In this regime, both the permeation flux $J_{NH_3,mw}$ (numerator of Equation (5.14)) and the concentration difference $C^R_{i,bulk} - C^R_{i,mw}$ (denominator of Equation (5.14)) are governed by the local reaction-permeation balance: the synthesis reaction continuously replenishes ammonia in the bulk independently of flow velocity, fixing the effective mass transfer coefficient at a value determined by geometry rather than by convective hydrodynamic (Re or Sc). The absence of Sh_{NH_3} data at $Re_{dh} < 5$ (left side of

Figure 5.12(a)) is not a measurement gap: as established in Section 5.2.8, these operating points correspond to $CP_{NH_3} > 0.95$, where wall depletion is negligible and a Sherwood correction is neither needed nor meaningful.

Because Sh_{NH_3} is independent of the Reynold and Schmidt numbers in this low-Re, reaction-enhanced regime, the primary controlling variable becomes the reactor geometry, specifically the radii ratio $\kappa = r_1/r_2$. Because the radius ratio $\kappa = r_1/r_2$ maps directly onto the tube pitch in a multi-tube bundle via the equivalent-area unit-cell construction (Section 5.2.1), the present κ-scaling of Sh_{NH3} and CP can be applied directly to specify membrane spacing in modular PBMR designs.

Figure 5.12(b) shows all 4,016 local Sh_{NH_3} values plotted against κ, alongside the κ-group medians for both the field-extracted correction (Sh_{field}, black squares) and the wall-matching optimised correction (Sh_{opt}, red triangles). Both sets of medians follow the same power-law dependence on κ but are systematically offset by a factor of 1.8-2.1×. **Figure 5.12**(c) shows the κ-group medians ± IQR for both corrections, with the number of case *(n)* indicated per group. The IQR error bars quantify the within-group scatter due to secondary dependence on T, P, and GHSV, which accounts for ± 5-45% of the median value. Fitting through the 6 κ-group medians (standard procedure for grouped data, as described in 5.2.8) yields the following correction:

$$Sh_{field} = 3.70\left(\frac{r_1}{r_2}\right)^{-0.789} \quad R^2 = 0.983, MAPE = 3.6\% \tag{5.31}$$

$$Sh_{opt} = 1.49\left(\frac{r_1}{r_2}\right)^{-0.912} \quad R^2 = 0.990, MAPE = 2.6\% \tag{5.32}$$

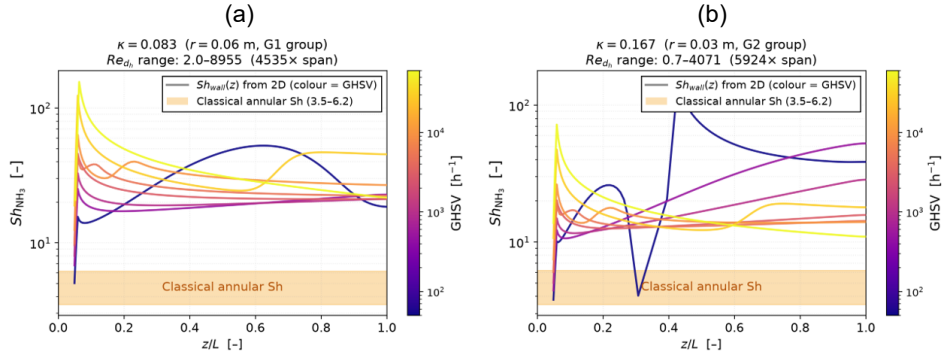


Figure 5.13 Axial profiles of the local ammonia Sherwood number (Sh_{NH_3}) along the dimensionless reactor length (z/L), for: (a) κ = 0.083; (b) κ = 0.167. Solid curves represent the computed $Sh_{field}(z)$ across the investigated GHSV; the shaded orange band indicates the theoretical limits for fully developed annular flow

The exponent of approximately -0.789 for Sh_{field} is consistent with the analytical

prediction of Murmura et al., who demonstrated that the reaction-enhanced Sherwood number scales as r_2/r_1 in the reaction-limited regime. The two best-sampled groups, κ = 0.083 (n = 21 cases) and κ = 0.167 (n = 21 cases), anchor the fit; the four intermediate groups at κ = 0.100, 0.111, 0.125 (n = 2 cases each) and κ = 0.250 (n = 2 case) confirm the power-law dependence but carry higher uncertainty, so the fitted exponent should be interpreted with this sampling in mind.

To interpret these Sherwood numbers, **Figure 5.13**-**Figure 5.14** compare the 2D-extracted $Sh_{NH3}(z)$ to analytical solutions for fully developed mass transfer in a concentric annulus with inner-wall removal and outer no-flux symmetry. The classical annular solutions yield $Sh_{classical}$ ~3.5-6.2 [32] over the present κ range when based on $r_2 - r_1$, whereas the median values extracted from the 2D simulations lie in the range $Sh_{field,median}$~14-30 (**Figure 5.13**), i.e. about 4-12 times larger. These fitted quantities must therefore be interpreted as effective reaction/permeation-enhanced Sherwood corrections, lumping reaction, permeation and radial diffusion, rather than as classical annular mass-transfer coefficients.

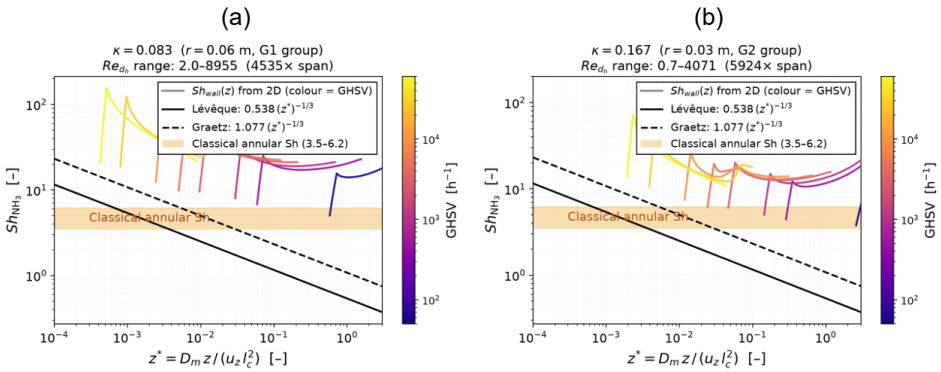


Figure 5.14 Axial profiles of the local ammonia Sherwood number (Sh_{NH_3}) as a function of the Graetz-type coordinate $z^* = D_m z/(u_z l_c^2)$, from 2D simulations. Results are shown for radius ratios of: (a) κ = 0.083; (b) κ = 0.167. Solid curves represent the computed $Sh_{field}(z)$ across the investigated GHSV

Figure 5.14 reports representative axial profiles $Sh_{field}(z)$ at fixed κ and varying GHSV/Re, together with the analytical developed-annulus band $Sh_{classical}$: the local $Sh_{field}(z)$ varies strongly near the inlet (e.g. 5-160 for r = 0.06 m) but rapidly converges to a nearly flat, geometry-controlled plateau that lies one order of magnitude above the classical annular band. The systematic factor of 1.8-2.1 between Sh_{opt} and $Sh_{field,median}$ arises from replacing this z-dependent profile by a single scalar in the nonlinear 1D correction formula, introducing a modest averaging bias. The two quantities are therefore complementary: $Sh_{field,median}$ characterizes the effective mass-transfer strength extracted from the

2D fields, whereas Sh_{opt} is the self-consistent scalar that, when used in the coupled 1D correction, most accurately reproduces the 2D wall concentration profile and is therefore adopted for practical 1D model correction. To examine whether the large effective Sherwood numbers originate from hydrodynamic entrance effects, **Figure 5.14** plots $Sh_{field}(z)$ at fixed κ and varying GHSV/Re both vs. z/L and vs. the Graetz-type coordinate $z^* = D_m z/(ul_c^2)$. If entrance effects were responsible, the profiles would be expected to collapse onto a universal z^*-controlled curve and decay towards the classical annular value at large z^*. Instead, after a short entrance region the curves converge to Re-insensitive plateaus that remain 4-12 times larger than $Sh_{classical}$ and do not collapse when plotted vs. z^*. Within the laminar regime investigated, this behaviour indicates that the effective Sherwood number is governed primarily by the local reaction-permeation balance rather than by classical hydrodynamic development, consistent with reaction-enhanced Sherwood concepts reported for membrane reactors. Conceptually, in the limit of vanishing membrane permeance the inner wall would approach a non-permeating annulus and the extracted Sherwood number would be expected to collapse toward $Sh_{classical}$; the fact that the present $Sh_{field,median}$ and Sh_{opt} remain well above this range under realistic CMS membranes permeances directly reflects the strong coupling between reaction and selective permeation at the membrane wall.

Similar behaviour has been reported for reactive hollow-fibre membrane contactors: at low Graetz numbers the mass-transfer boundary layer becomes fully developed, the Sherwood number approaches a flow-independent minimum, and effective Sh values can deviate significantly from classical hydrodynamic correlations. This is consistent with the Re-insensitive plateau and enhanced Sh_{field} observed here, which arise from the local reaction-permeation balance rather than from entrance-region hydrodynamics [33].

5.3.5 Application of Sherwood optimal correction for CP prediction

Figure 5.15 illustrates the impact of the Sherwood corrections on the CP profiles, showing one representative case per annulus geometry, spanning all six κ groups investigated (κ = 0.083-0.250, r = 0.02-0.06 m). For each geometry, the representative case is selected as the simulation with CP_{avg} closest to the group median.

The mean absolute errors (MAE) reported in the legends are evaluated over the active reactor length ($z/L > 0.10$) relative to the 2D reference, and each panel colour corresponds to the κ group colour used consistently throughout this chapter. In all six panels, the uncorrected 1D model (CP = 1, dotted line) substantially overestimates the wall concentration relative to the 2D reference (solid line), with a deviation from the 2D reference in the range of 0.05-0.25 depending on geometry and operating conditions. Applying the field-extracted correlation (Sh_{field} (dashed

line)) brings the predicted CP profile closer to the 2D reference but systematically underestimates the degree of wall depletion, particularly in the inlet region.
By contrast, the wall-matching correlation (Sh_{opt} (dash-dot line)) provides a substantially better approximation across all six geometries, confirming that the geometry-dependent power-law correlation generalises well beyond the two anchor geometries on which it was primarily fitted. Notably, the $\kappa = 0.250$ case ($r = 0.02$ m, bottom-right panel) exhibits $CP_{NH_3} > 1$ in the downstream half of the reactor, reflecting near-wall NH_3 accumulation driven by reaction faster than it is removed by permeation. In this regime, however, 2D solution itself converges toward CP_{NH_3}~1, meaning that the 1D model is already an adequate approximation and neither Sherwood correction is needed in practice.

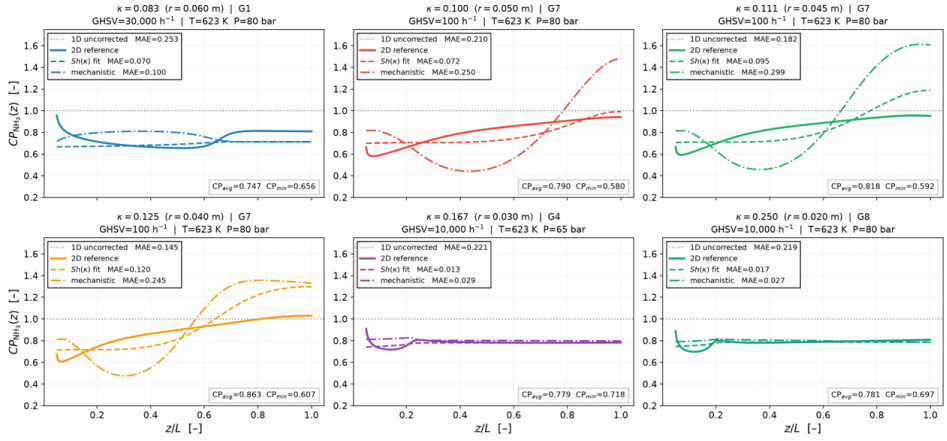


Figure 5.15 Axial CP_{NH_3} (z) profiles for one representative case per κ group, comparing the uncorrected 1D model (CP = 1, dotted grey), the 2D reference solution (solid), the Sh_{field} -corrected 1D prediction (dashed), and the Sh_{opt}-corrected 1D prediction (dash-dot)

5.3.6 Mechanistic validation: reaction screening, not hydrodynamics

Three independent measurements on the 2D fields identify the physics behind the κ-scaling established in Section 5.3.4 and quantify why hydrodynamic templates fail. First, within a fixed geometry the exact flux-matched Sherwood number moves by at most a factor of about 1.9 while GHSV spans a factor of 1,200; a developing Lévêque layer ($Sh \propto Pe^{1/3}$) or a packed-bed film correlation ($Sh \propto Re^{0.36}$) would move by an order of magnitude or more over the same span, consistent with the Reynolds-insensitivity of **Figure 5.14** (a). Second, the absolute thickness of the near-wall NH_3 deficit is nearly geometry-independent: the deficit halves within 1.8-4.3 mm of the membrane in all six geometries, while the gap width d_h varies by a factor of 3.7. Third, the permeation-induced radial Péclet number evaluated on the layer thickness is of order at most 0.14 (median 0.06), so suction is a correction, not

a mechanism. The mechanism consistent with all three observations is the kinetic screening formulated in Section 5.2.9: the deficit is localised not by the flow but by the product-inhibited kinetics themselves.

Figure 5.16(a) tests the resulting closure against the exact flux-matched Sherwood numbers of all reported cases. Evaluated with no geometric input beyond the annulus radii themselves, the screened closure lands on the exact values across all six κ groups: the flux-weighted calibration bias per geometry is flat to within ± 5% (**Table A.5.4**), and the per-case predictions scatter within the operating-condition spread of the exact values, widest at the sparsely sampled intermediate geometries. The predicted screening length, flux-weighted median 2.3 mm, matches the measured deficit thickness with no adjustable parameter. **Figure 5.16** (b) shows the closure along the reactor for a representative case: evaluated from the local state, it captures the entrance behaviour and the mid-reactor level through the local kinetic sensitivity, and overpredicts toward the outlet as the wall approaches equilibrium, point-wise scatter that largely averages out in the integral KPIs (**Table 5.2**).

The mechanism also explains the fitted exponent. With δ nearly constant, $Sh = k_{cp}\, d_h/D \sim d_h/\delta$ and $d_h = r_{mem}(1/\kappa - 1)$ give $Sh \sim \kappa^{-1}$; the fitted -0.91 is this geometric bookkeeping tempered by curvature. Conduction alone cannot reproduce it: the uniform-source annulus bound varies only as $\kappa^{-0.46}$ with magnitudes of 4-6, precisely the classical annular band of **Figure 5.13** that the extracted Sherwood numbers exceed by up to an order of magnitude. The localisation of the deficit by the kinetic response is therefore essential to both the magnitude and the geometry dependence of the correlation.

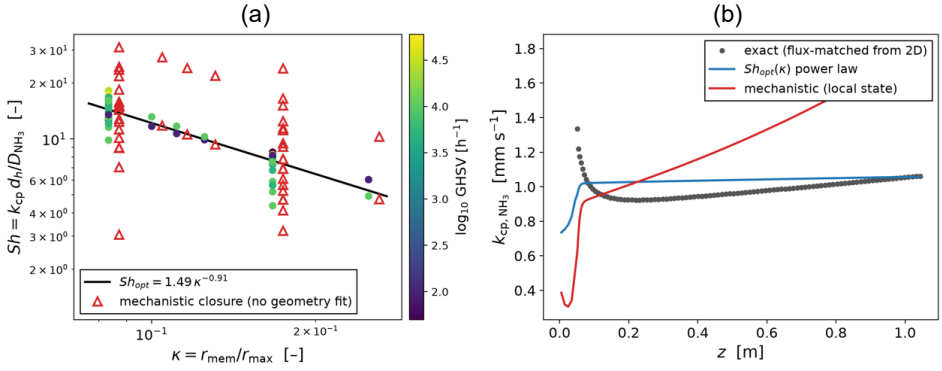


Figure 5.16 Mechanistic validation of the concentration-polarisation closure: (a) Exact flux-matched Sherwood numbers for 50 cases vs. the geometry ratio κ, compared with the fitted power law and the mechanistic closure without geometry fitting; (b) Axial comparison for case G2 (GHSV = 3,000 h^{-1}, r = 0.03 m), showing the exact profile, fitted correlation, and local-state mechanistic closure

Table 5.2 quantifies what the mechanistic closure delivers at the KPI level,

comparing the three 1D variants against the certified 2D results over the 50 reported cases (parity plots in **Figure A.5.6**). The two corrected variants are equivalent in practice: the fitted power law is marginally better in aggregate (median deviation 1.3% vs. 1.6% in X_{H_2}, 2.3% vs. 5.1% in NH_3 recovery), since its constant quietly absorbs temperature and profile effects, while the mechanistic closure is better on the radius family G7 (median 5.3% vs. 7.6% in X_{H_2}), exactly where geometry extrapolation is tested, and is the variant that would survive a change of catalyst. Both corrections repair the plain 1D model's recovery failure (median 70.5%) by more than an order of magnitude. The thermal rows of **Table 5.2** separate two observable definitions: a 1D model can only represent the cross-sectional mean temperature, and against the radially averaged 2D profile, the like-for-like reference, both corrected variants are within 1.9% (median), while the point-wise 2D hot spot exceeds that reference by 9.1% (median, up to 24%), which accounts for the apparent 11% thermal mismatch. Finally, re-running the corrected 1D model with the exact per-case $k_{cp}(z)$ closure reproduces the 2D recovery to 0.1% and X_{H_2} to 1.0% (median): with the species closure made exact, the residual 1D error is dominated by the radial averaging of the nonlinear kinetics ($\langle R(c,T)\rangle \neq R(\bar{c},\bar{T})$, which near equilibrium can even flip the sign of the cross-sectionally averaged rate), an error no transport closure can remove and the sharpest quantitative argument for the 2D model.

Table 5.2 Median and maximum relative deviations from the certified 2D KPIs across 50 cases for the plain 1D model and two corrected 1D variants. The final two rows distinguish the thermal references: the 1D model is compared with the radially averaged 2D temperature and with the point-wise 2D hot spot, which exceeds the average by 9.1% on average and up to 24%

KPI	Plain 1D (CP = 1)	Corrected 1D, $Sh_{opt}(\kappa)$	Corrected 1D, mechanistic
X_{H_2}	5.3% (31%)	1.3% (15%)	1.6% (12%)
NH_3 production	5.3% (31%)	1.3% (15%)	1.7% (12%)
NH_3 recovery	70.5% (208%)	2.3% (18%)	5.1% (43%)
NH_3 purity	79.3% (222%)	4.8% (31%)	6.0% (43%)
ΔT_{max} vs. 2D hot spot	3.6% (31%)	11.3% (29%)	10.9% (19%)
ΔT_{max} vs. 2D $\langle T\rangle$ profile	-	1.9% (27%)	1.7% (21%)

The idea that reaction enhances bed-to-membrane mass transfer has precedent, and the present result sharpens its regime classification. Murmura et al. [13] derive an enhanced Sherwood number for steam-reforming membrane reactors in the opposite kinetic limit: assuming local reaction equilibrium, a reaction invariant

removes the source term and the remaining Graetz problem yields a developing, flow- and position-dependent Sherwood number, whereas the flow independence measured here over a 1,200-fold GHSV span excludes that route for the present system. Sheintuch and Nekhamkina [34,35] identified a reaction boundary layer at the membrane in reforming separators but reduce it via assumed similarity profiles rather than a kinetics-derived length. The screened channel itself is classical film theory with a pseudo-first-order reaction, $k = \sqrt{Dk_1}$ [36], of which the present closure is the annular, finite-rate generalisation: the screening length follows from the linearised product-inhibition sensitivity of the actual kinetics, evaluated locally along the reactor inside the 1D solve. Its validity limits are equally explicit: the screening length is chemistry-specific, the calibration spans κ = 0.083-0.25, and the closure applies to product-inhibited systems far from the fast-reaction limit, not to inert, flow-dominated channels.

5.3.7 Towards scale-up: operating condition and geometry design criteria

The parametric analysis of Sections 5.3.2 and 5.3.3 provides a basis for translating the 2D field insights into practical design guidance. The compact annulus (r = 0.03 m) consistently outperforms the wide annulus (r = 0.06 m) in integral conversion and recovery across all operating conditions examined, owing to its higher membrane surface-to-volume ratio (S_M/V). This advantage is not fixed but grows monotonically with operating pressure: as the transmembrane NH_3 partial pressure driving force increases, both geometries experience higher permeation flux, but the compact geometry translates this enhanced flux into a proportionally larger equilibrium shift per unit reactor volume, progressively widening the conversion gap. At low temperature ($T_{in}^R \leq$ 573 K), where the system operates in the reaction-limited regime, the compact annulus carries an additional benefit: it reduces the severity of near-wall depletion relative to the wide annulus, making it the preferred geometric choice also in the kinetically starved operating range. More broadly, the smallest radius examined (r = 0.02 m) offers a coupled advantage at high GHSV: higher integral NH_3 recovery through elevated S_M/V, and a higher CP_{NH_3} plateau in the developed reactor section, meaning the transmembrane driving force is sustained more uniformly along the membrane length.

A direct design implication of the compact geometry emerges from the 2D concentration field at low space velocity: the NH_3 mole fraction at the membrane wall drops to near zero by z~0.4-0.5 m and remains effectively depleted throughout the downstream half of the reactor, rendering the membrane non-productive over approximately half its length. A truncated membrane of approximately 0.5 m would therefore retain all conversion and recovery benefits of the compact design while eliminating the unused downstream section, simultaneously improving membrane

utilisation efficiency, reducing peak temperature excursions, lowering capital cost, and mitigating the mechanical stress associated with highly non-uniform axial flux profiles.

The most critical and non-obvious finding for engineering practice is that the operating conditions most attractive from a performance standpoint are precisely those where 1D-based design tools are least reliable. At low GHSV and compact geometry, where S_M/V is highest and conversion is maximised, the 1D model suffers from thermodynamic hypersensitivity near equilibrium and overpredicts conversion most severely; a CP correction cannot remedy this failure mode since it acts on concentration gradients rather than on equilibrium sensitivity. At high GHSV, where throughput is maximised, unresolved near-wall depletion causes the 1D model to overpredict NH_3 recovery across all radii, with the error largest at the smallest radius: the 1D model is most unreliable for recovery exactly where the compact geometry is most attractive. These two failure modes are mechanistically independent and require distinct correction strategies: equilibrium-sensitivity corrections at low GHSV, and CP-based wall-concentration corrections at high GHSV, confirming that no single adjustment renders the 1D model universally reliable across the full operating window.

Design checklist for modular ammonia PBMRs:

- Geometry/pitch:
  - Prefer compact annuli (low κ, small pitch) to maximise S_M/V and NH_3 recovery; use the reaction-enhanced correction $Sh_{opt} = 1.49\,\kappa^{-0.912}$ when correcting 1D wall concentrations at high GHSV.
  - Avoid very wide annuli (high κ), which reduce S_M/V and effective Sh_{NH3}, especially at low GHSV.
- Reactor length:
  - For compact geometries at low GHSV, truncate the membrane once the wall NH_3 mole fraction remains near zero over the downstream half (e.g. $z/L \gtrsim 0.5$), to eliminate non-productive length and limit hot spots.
- Operating window:
  - Low GHSV/high conversion: 1D models fail mainly due to equilibrium hypersensitivity, not CP; Sherwood corrections alone are insufficient - use 2D analysis or explicit equilibrium-sensitivity corrections for design in this regime.
  - High GHSV/high throughput: CP dominates acting on recovery; incorporate $Sh_{opt} = 1.49\,\kappa^{-0.912}$ into 1D models to correct wall concentrations is sufficient to substantially reduce prediction errors and enables reliable membrane sizing without full 2D simulations.
- Safety margins:

- Avoid combinations of compact geometry, low GHSV, and high pressure that drive local temperatures toward 900 K unless catalyst and membrane stability are demonstrated; use 2D simulations to identify and exclude such hot-spot conditions during scale-up.

5.4 CONCLUSIONS

This work presented a fully two-dimensional, non-isothermal packed bed membrane reactor model for ammonia synthesis over a Ru/C catalyst, validated independently against experimental kinetic data and membrane permeance measurements. The full 2D model was then applied systematically across 50 simulated cases spanning GHSV = 50-60,000 h^{-1}, pressure = 30-80 bar, temperature = 548-698 K, and annulus radius = 0.02-0.06 m. Systematic comparison of 1D and 2D predictions across six key performance indicators - H_2 conversion, NH_3 production rate, NH_3 recovery, NH_3 yield, NH_3 purity, and peak temperature rise - demonstrated that the 1D model consistently overestimates reactor performance, with H_2 conversion overestimated by up to 10 percentage points, NH_3 recovery by up to 25 percentage points, and NH_3 purity by up to 5 percentage points. For NH_3 recovery, these discrepancies are primarily driven by unresolved concentration polarisation: the 1D model assumes a radially uniform NH_3 concentration equal to the bulk average, whereas the 2D fields reveal systematic near-wall depletion that reduces the transmembrane driving force and suppresses permeation relative to the 1D prediction. For conversion-, yield- and purity-related metrics, the errors are further amplified by operation close to thermodynamic equilibrium and by non-isothermal hot-spot formation that the 1D model cannot resolve.

The severity and axial distribution of concentration polarisation, and its impact on 1D-2D discrepancies, depend strongly on operating regime. At low GHSV, both geometries operate near thermodynamic equilibrium and exhibit diffusion-controlled CP: slow axial convection allows radial gradients to develop and persist, and annulus geometry exerts a strong influence on CP severity and on the associated 1D-2D deviations. At intermediate GHSV, the system enters a permeation-dominated crossover regime in which the compact annulus ($r = 0.03$ m) produces markedly larger discrepancies than the wide annulus: its elevated surface-to-volume ratio sustains aggressive ammonia removal, drives the retentate toward equilibrium, and causes membrane starvation and hot-spot formation in the downstream half of the reactor. At high GHSV, short residence times limit both conversion and radial gradients, and the reactor operates in a reaction-dominated, weak-CP regime: deviations between 1D and 2D shrink, geometry sensitivity collapses, and 1D predictions remain adequate for most bulk-based KPIs, although recovery still suffers from moderate CP-induced bias.

These mechanistic insights translate directly into design guidance. Low GHSV with

a compact annulus maximizes conversion, recovery, and purity by exploiting the full membrane-induced equilibrium shift, but at the cost of reduced catalyst production rate, membrane starvation risk, and the largest 1D-model errors; in this regime, 2D-informed design tools are essential. High GHSV delivers superior volumetric production rate and operational stability, and 1D predictions remain adequate for most bulk-based KPIs, but per-pass conversion and the geometric advantage of the compact annulus are sacrificed. Overall, the smallest radii examined (r = 0.02-0.03 m) provide the best combination of S_M/V and NH_3 recovery but also the strongest CP and largest recovery errors in uncorrected 1D models, so the optimal design depends on whether the process prioritises membrane-utilisation efficiency, favouring low GHSV with compact, potentially truncated annuli, or volumetric production rate, favouring high GHSV where geometry selection is less critical.

Classical literature correlations underpredict the Sherwood number extracted from the 2D fields. The analysis shows that, in the present reaction-enhanced regime, Sh_{NH3} is effectively independent of Reynolds number and controlled primarily by geometry via the radius ratio $\kappa = r_1/r_2$. Two new geometry-dependent, Reynolds-number-independent, reaction-enhanced Sherwood correction numbers are reported: one extracted directly from the 2D concentration fields (Sh_{field}) and one derived by minimizing the wall-concentration error between the corrected 1D model and the 2D solution (Sh_{opt}). The latter reduces the mean absolute error in the predicted CP profile by more than 75% relative to the uncorrected 1D assumption. Together, these correlations and geometry scaling relations provide the quantitative tools to identify where 1D model accuracy degrades, and to embed radial transport effects into 1D frameworks without requiring a full 2D simulation at every design point. The physical mechanism behind these correlations was identified as a reaction-screened diffusion layer. Three independent measurements on the 2D fields - the flow independence of the extracted Sherwood number across a 1,200-fold GHSV span, a wall-deficit layer of nearly constant absolute thickness (1.8-4.3 mm) in all geometries, and weak permeation-induced suction - rule out a hydrodynamic boundary layer: the deficit is localised by the product-inhibited kinetics themselves, within a screening length $\delta = \sqrt{D/s}$ set by the local diffusivity and rate sensitivity. A closed-form closure built on this mechanism, calibrated by a single-order-one constant ($C \sim 0.5$) with no geometry fit, reproduces the 2D KPIs nearly as well as the fitted correlation, performs best on the radius family where geometry extrapolation is actually tested, and explains the fitted exponent as the geometric ratio dh/δ tempered by curvature. Because the chemistry enters only through the local rate sensitivity, the closure transfers to other product-inhibited chemistries and geometries within the screening regime, turning the case-specific fitted correlation into a transferable design tool. With the species closure made exact, the remaining 1D error is dominated by the radial averaging of the nonlinear kinetics, an error no

transport closure can remove, and the strongest quantitative argument for full 2D modelling.

A.5 APPENDIX

A.5.1 Correlations

Any gas-mixture properties not explicitly reported in the following section are taken from Chapter 2.

- The molecular diffusion coefficients for a binary mixture ($D_{m,ij}$) at standard conditions were calculated using the Chapman-Enskog-Wilke-Lee model for binary diffusion coefficients [37]:

$$D_{m,ij} = (2.1989 \times 10^{-22} - 5.0665 \times 10^{-23} M_{ij}) \frac{T^{1.5} M_{ij}}{P \sigma_{ij}^2 \Omega_D} \quad \text{(A.5.1)}$$

$$M_{ij} = \sqrt{\frac{M_i + M_j}{M_i M_j}} \quad \text{(A.5.2)}$$

$$\sigma_{ij} = \frac{\sigma_i + \sigma_j}{2} \quad \text{(A.5.3)}$$

$$\Omega_D = \frac{A}{T^{*B}} + \frac{C}{\exp(DT^*)} + \frac{E}{\exp(FT^*)} + \frac{G}{\exp(HT^*)} \quad \text{(A.5.4)}$$

$$T^* = T \frac{k_b}{\epsilon_{ij}} \quad \text{(A.5.5)}$$

$$\epsilon_{ij} = \sqrt{\epsilon_i \epsilon_j} \quad \text{(A.5.6)}$$

The collision integral parameters are summarised in **Table A.5.1**. The Lennard-Jones parameters are summarised in **Table A.5.2**.

Table A.5.1 Empirical constants for the Chapman-Enskog collision integral used in the calculation of binary diffusion coefficients

Integral parameter	Value
A	1.06036
B	0.15610
C	0.19300
D	0.47635
E	1.03587
F	1.52996
G	1.76474
H	3.89411

Table A.5.2 Lennard-Jones size (σ) and energy ($\frac{\epsilon_{ij}}{k_b}$) parameters for H_2, N_2, and NH_3 used in the calculation of gas-phase diffusion coefficients

Species	σ [Å]	$\frac{\epsilon_{ij}}{k_b}$
H_2	2.827	59.7
N_2	3.798	71.4
NH_3	2.900	558.3

The individual molecular diffusion coefficient ($D_{m,i}$) is obtained from the binary diffusion coefficients D_{ij} and the gas-phase mole fractions using the following expression [38]:

$$D_{m,i} = \frac{1 - y_i}{\sum_{j=1}^{3} \left(\frac{y_i}{D_{ij}}\right) - \frac{y_i}{D_{ii}}} \tag{A.5.7}$$

Because the total molar concentration cancels (D_{ii}), its explicit value is not required for this calculation. To correct the binary diffusion coefficients for the actual reactor temperature and pressure, the following correlation is employed:

$$D_{ij} = D_{ij} \left(\frac{T}{273}\right)^{1.75} \frac{1e^5}{P} \tag{A.5.8}$$

The pressure dependence in Equation (A.5.8), is identical to that in Equation (A.5.1), whereas the temperature dependence differs because Ω_D depends on T.

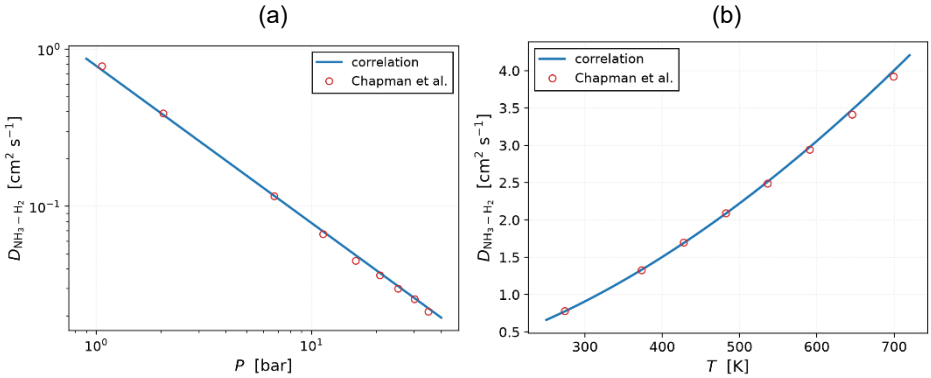


Figure A.5.1 (a) Effective binary diffusion coefficient of NH_3 in the gas mixture as a function of pressure at constant temperature: experimental data from Chapman et al. (symbols) vs. proposed correlation (solid line); (b) Effective binary diffusion coefficient of NH_3 in the gas mixture as a function of temperature at constant pressure: experimental values from Chapman et al. (symbols) vs. proposed correlation (solid line)

Accordingly, the correlation in Equation (A.5.8) was benchmarked against the full Chapman-Enskog expression (Equation (A.5.1)) over a wide range of temperatures and pressures. As illustrated in **Figure A.5.1**, the correlation provides excellent

approximation and, owing to its simpler implementation, is adopted throughout this work.

- The Bodenstein number (Bo) was then used to assess axial back-mixing. Bo represents the ratio of convective transport to axial diffusion and is equivalent to the reactor Péclet number, given by the product of the Reynolds number (based on reactor diameter) and the Schmidt number [39]:

$$Bo = Pe_r = \frac{u_z\, l_c}{D_{m,i}^{\ ax}} \tag{A.5.9}$$

Under the lowest gas velocity considered, Bo was found to be on the order of 10^2, indicating that convection strongly dominates and axial molecular diffusion can be neglected.

According to [39] when Bo is relatively low (up to about 100), the effective dispersion coefficient can be taken equal to the molecular diffusion coefficient. At very low fluid velocities, dispersion is governed primarily by molecular diffusion, whereas as the velocity increases, convective (hydrodynamic) dispersion becomes increasingly important [40]. Fogler (Chapter 15) reports that axial dispersion can be neglected when:

$$\frac{(-r_i)_{obs} r_{particle}}{u_z\, C_i^{bulk}} < \frac{u_z r_{particle}}{D_{ax,i}} \tag{A.5.10}$$

Where u_z is the superficial velocity and the D_{ax} is the axial dispersion coefficient, which in this work was calculated using the Gunn correlation [41]:

$$\frac{D_{ax}}{u_0\, r_{particle}} = \frac{Re\ Sc}{4\alpha^2(1-\varepsilon)}(1-P)^2 + \frac{Re^2 Sc^2}{16\alpha^4(1-\varepsilon)^2} P(1-P)^3 \times exp\left(\frac{-4(1-\varepsilon)\alpha^2}{P(1-P)Re\ Sc} - 1\right) + \frac{\varepsilon}{\tau\ Re\ Sc} \tag{A.5.11}$$

$$Re\ Sc = \frac{u_z\, r_{particle}\, \rho}{\mu} \frac{\mu}{D_{m,i}\, \rho} \tag{A.5.12}$$

$$P = 0.17 + 0.33\, exp(-\frac{24}{Re}) \tag{A.5.13}$$

where τ = 1.4 for spherical particles and α is the first root of $J_0(u)$.

- An analogous approach was used for radial dispersion, again applying the Gunn correlation [41].

$$\frac{1}{Pe} = \frac{1}{Pe_f} + \frac{\varepsilon}{\tau\ Re\ Sc} \tag{A.5.14}$$

Where Pe_f is the fluid-mechanical Peclet number for radial diffusion and is defined as:

$$Pe_f = 40 - 29\exp\left(-\frac{7}{Re}\right) \tag{A.5.15}$$

where $\tau = 1.2$ for spherical particles.

- According to [42], Biot number can also be used to assess whether intra-pellet mass transfer resistance is significant relative to the external boundary layer. When the pellet Biot number of a given species is below 10, the effectiveness factor is essentially unity and the gas concentration inside the pellet can be taken equal to the surface concentration.

$$Bi = \frac{k_{i,ext}\, r_{particle}}{D_{i,eff}} \tag{A.5.16}$$

In our case, the order of magnitude of $D_{i,eff}$ is ~10^{-6}, while the external mass-transfer coefficient is on the order of 10^{-3}, under high-GHSV conditions. Even for the largest catalyst size considered (as in the previous Weisz-Prater analysis), the resulting Biot number remains on the order of 10^{-3}, and is therefore negligible. The same conclusion holds for the thermal Biot number, which compares internal heat conduction in the particle to external convective heat transfer in the fluid. Using a solid thermal conductivity of 35 $W \cdot m^{-1}K^{-1}$ [43], the thermal Biot number was also found to be much smaller than 1.

$$Bi^T = \frac{h_{ext}\, r_{particle}}{\lambda_{cat}} \tag{A.5.17}$$

$$Nu = 0.17\, Re^{0.79} \left(\frac{Pr}{0.7}\right)^{1/3} = \frac{h_{ext} r_{particle}}{\lambda_f} \tag{A.5.18}$$

- Another criterion that was evaluated is the Mears criterion, which quantifies the importance of fluid-to-particle (external) mass transfer. When the Mears number is below 0.15, external mass-transfer limitations can be neglected and no significant concentration gradient exists between the bulk gas and the external surface of the catalyst pellet [44].

$$C_M = \frac{(-r_i)_{obs}\, r_p\, n}{k_{ext,i}\, C_i^{bulk}} \tag{A.5.19}$$

The external mass-transfer coefficient was estimated using the appropriate Sherwood number correlation [45] for $1 < Re < 10^4$:

$$\varepsilon_{bed} \frac{k_{ext,i}}{u_z} Sc^{2/3} = \frac{0.765}{Re^{0.82}} + \frac{0.365}{Re^{0.386}} \tag{A.5.20}$$

$$Sc = \frac{\mu_i}{\rho_i\, D_{m,i}} \tag{A.5.21}$$

$$Re = \frac{\rho_i\, u_z\, r_p}{\mu_i} \tag{A.5.22}$$

From this correlation, the resulting mass-transfer coefficient is sufficiently large that the Mears number is of the order of 10^{-4}. Since both external mass and heat transfer resistances are therefore negligible, a pseudo-homogeneous reactor model is justified. In other words, the reaction can be treated as occurring in the gas phase,

and the solid particles do not need to be modelled explicitly.

A.5.2 List of simulated cases

Table A.5.3 A complete listing of all 50 simulated cases

Case ID	P_{in}^{R} [bar]	T_{in}^{R} [K]	GHSV [h^{-1}]	r_2 [m]	SW [-]	P_{in}^{P} [bar]	T_{in}^{P} [K]	L_{mem} [m]
G1: GHSV	80	623	50	0.06	1	1	623	1
G1: GHSV	80	623	500	0.06	1	1	623	1
G1: GHSV	80	623	1,000	0.06	1	1	623	1
G1: GHSV	80	623	3,000	0.06	1	1	623	1
G1: GHSV	80	623	5,000	0.06	1	1	623	1
G1: GHSV	80	623	10,000	0.06	1	1	623	1
G1: GHSV	80	623	30,000	0.06	1	1	623	1
G1: GHSV	80	623	60,000	0.06	1	1	623	1
G2: GHSV	80	623	50	0.03	1	1	623	1
G2: GHSV	80	623	500	0.03	1	1	623	1
G2: GHSV	80	623	1,000	0.03	1	1	623	1
G2: GHSV	80	623	3,000	0.03	1	1	623	1
G2: GHSV	80	623	5,000	0.03	1	1	623	1
G2: GHSV	80	623	10,000	0.03	1	1	623	1
G2: GHSV	80	623	30,000	0.03	1	1	623	1
G2: GHSV	80	623	60,000	0.03	1	1	623	1
G3: Pressure	30	623	10,000	0.06	1	1	623	1
G3: Pressure	40	623	10,000	0.06	1	1	623	1
G3: Pressure	50	623	10,000	0.06	1	1	623	1
G3: Pressure	65	623	10,000	0.06	1	1	623	1
G3: Pressure	80	623	10,000	0.06	1	1	623	1
G4: Pressure	30	623	10,000	0.03	1	1	623	1
G4: Pressure	40	623	10,000	0.03	1	1	623	1
G4: Pressure	50	623	10,000	0.03	1	1	623	1
G4: Pressure	65	623	10,000	0.03	1	1	623	1
G4: Pressure	80	623	10,000	0.03	1	1	623	1
G5: Temp.	80	548	5,000	0.06	1	1	623	1
G5: Temp.	80	573	5,000	0.06	1	1	623	1
G5: Temp.	80	623	5,000	0.06	1	1	623	1
G5: Temp.	80	648	5,000	0.06	1	1	623	1
G5: Temp.	80	673	5,000	0.06	1	1	623	1

G5: Temp.	80	698	5,000	0.06	1	1	623	1
G6: Temp.	80	548	5,000	0.03	1	1	623	1
G6: Temp.	80	573	5,000	0.03	1	1	623	1
G6: Temp	80	623	5,000	0.03	1	1	623	1
G6: Temp	80	648	5,000	0.03	1	1	623	1
G6: Temp	80	673	5,000	0.03	1	1	623	1
G6: Temp	80	698	5,000	0.03	1	1	623	1
G7: Radius	80	623	100	0.02	1	1	623	1
G7: Radius	80	623	100	0.03	1	1	623	1
G7: Radius	80	623	100	0.04	1	1	623	1
G7: Radius	80	623	100	0.045	1	1	623	1
G7: Radius	80	623	100	0.05	1	1	623	1
G7: Radius	80	623	100	0.06	1	1	623	1
G8: Radius	80	623	10,000	0.02	1	1	623	1
G8: Radius	80	623	10,000	0.03	1	1	623	1
G8: Radius	80	623	10,000	0.04	1	1	623	1
G8: Radius	80	623	10,000	0.045	1	1	623	1
G8: Radius	80	623	10,000	0.05	1	1	623	1
G8: Radius	80	623	10,000	0.06	1	1	623	1

A.5.3 Dimensionless scaling and regime maps

This section provides the full quantitative support for the radial transport analysis summarised in Section 5.2.3.

❖ *Power-law scaling of dimensionless transport numbers*

Before constructing the regime maps, the dependence of the dimensionless transport groups on the primary design parameters was quantified by power-law regression on the GHSV groups (G1, G2) and the radius groups (G7, G8). For each case, the radial Péclet number Pe_r, the diffusive Damköhler number Da_{diff} are evaluated as maximum value over the active reactor length (z > 0.05 m); the sealed inlet region (z < 0.05 m) is excluded because the absence of membrane activity and the developing velocity profile in that zone yield artificially elevated Da_{conv} values that are not representative of the bulk transport regime. Pe_r is evaluated for H_2 as the limiting reactant, whereas Da_{diff} is evaluated for NH_3 as the permeating species of primary interest.

Figure A.5.2 shows the scaling of Pe_{r,H_2} and Da_{diff,H_2} with GHSV for the large tube (r = 0.06 m, left) and the small tube (r = 0.03 m, right) at 80 bar and 623 K. Both numbers exhibit near-perfect power-law behaviour over more than three orders of magnitude in GHSV, with fitted exponents $Pe_r \propto$

$GHSV^{1.06}$ and $Da_{diff} \propto GHSV^{1.30}$ for r = 0.06 m, and $Pe_r \propto GHSV^{1.06}$, $Da_{diff} \propto GHSV^{1.01}$ for r = 0.03 m, all with coefficients of determination $R^2 > 0.999$ for the Péclet fits and ~0.80 for the Damköhler fits. The superlinear deviations- from the ideal exponent of unity reflect the coupled variation of molecular diffusivity with temperature and composition as GHSV changes, an effect not captured in simple scaling arguments but consistent with the underlying physics.

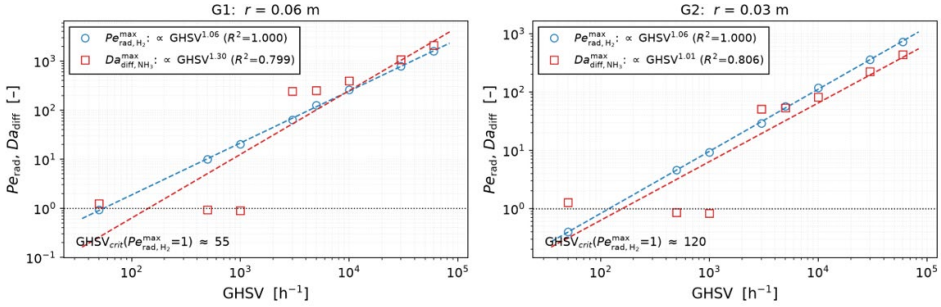


Figure A.5.2 Power-law scaling of the maximum radial Péclet number Pe_{r,H_2}^{max} and diffusive Damköhler number Da_{diff,H_2}^{max} with GHSV for the large tube (r = 0.06 m, left) and small tube (r = 0.03 m, right) at 80 bar and 623 K. Simulation data (symbols) follow near-ideal power-law trends (dashed lines), and the intersections with Pe_r = 1 indicate critical GHSV values below which the 1D plug-flow assumption remains valid

The intersections of the Pe_r fits with the threshold Pe_r = 1 define critical space velocities $GHSV_{crit}$ = 55 h^{-1} for r = 0.06 m and $GHSV_{crit}$ = 123 h^{-1} below these values radial mass homogenisation should be sufficiently fast that the 1D plug-flow assumption remains valid; above them persistent radial concentration gradients are expected and a 2D description becomes necessary.

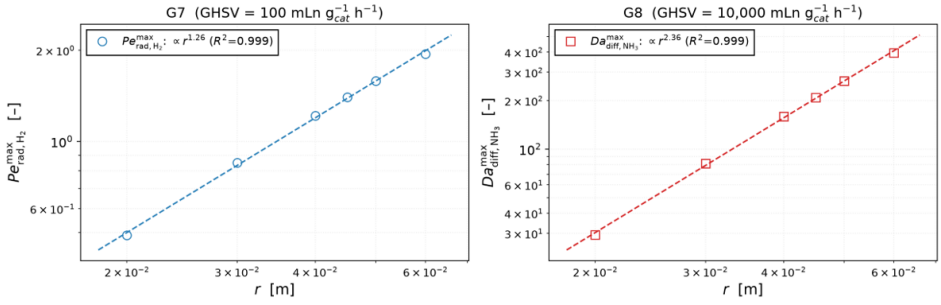


Figure A.5.3 Power-law scaling of the maximum radial Péclet number Pe_{r,H_2}^{max} (left) and diffusive Damköhler number Da_{diff,H_2}^{max} (right) with tube radius at fixed GHSV (100 and 10,000 h^{-1} respectively), 80 bar, and 623 K. Simulation data (symbols) follow near-ideal power laws trends (dashed line) highlighting the strong sensitivity of Da_{diff} to tube radius

Figure A.5.3 shows the corresponding scaling of Pe_{r,H_2} and Da_{diff,NH_3} with tube

radius at fixed GHSV. The fitted exponents are in close agreement with the theoretical $Pe_r \sim r^1$ and $Da_{diff} \sim r^2$ scaling; the modest deviations are attributable to the weak dependence of molecular diffusivity on local flow conditions at fixed throughput. The much stronger sensitivity of Da_{diff} to radius has direct practical implications: increasing r by a factor of three (from 0.02 to 0.06 m) raises Da_{diff} by approximately a factor of 13, while Pe_r increases by only a factor of about 4, consistent with the respective exponents. Scale-up via tube radius enlargement therefore rapidly pushes the system into a regime where near-inlet radial concentration gradients become severe, even when the overall axial throughput is held constant.

❖ *Regime map: mass transport validity*

Two distinct radial Péclet numbers are relevant for assessing 1D model validity in the membrane reactor. $\langle Pe_{r,H_2} \rangle$ governs radial homogenisation of the limiting reactant and controls the validity of the 1D bulk description, whereas $\langle Pe_{r,NH_3} \rangle$ governs radial homogenisation of the permeating product and therefore the accuracy of the 1D membrane boundary condition. Across all 50 simulated cases, $\langle Pe_{r,NH_3} \rangle$ is systematically larger than $\langle Pe_{r,H_2} \rangle$, with a mean ratio of approximately 1.6 and only modest scatter, reflecting the lower molecular diffusivity of NH_3 compared to H_2 in the H_2-N_2-NH_3 mixture (**Figure A.5.4**). The regime maps therefore use $\langle Pe_{r,H_2} \rangle$ as a single-x-axis that simultaneously identifies both failure modes: whenever $\langle Pe_{r,H_2} \rangle > 1$, $\langle Pe_{r,NH_3} \rangle$ is necessarily even larger, and the NH_3 concentration profile at the membrane wall is further from radial uniformity than the bulk H_2 field.

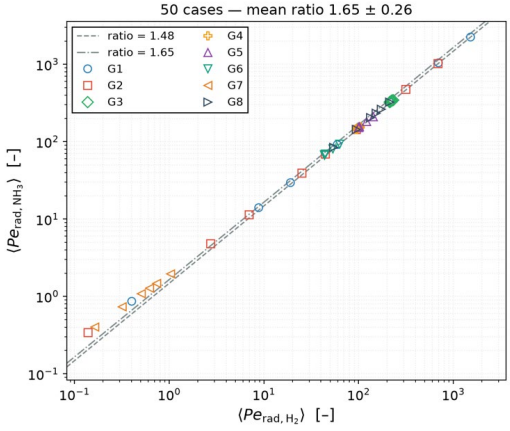


Figure A.5.4 $\langle Pe_{r,NH_3} \rangle$ vs. $\langle Pe_{r,H_2} \rangle$ for all 50 simulated cases: the dashed lines indicate constant ratios of 1.48 and 1.65; the mean ratio across all cases is 1.65 ± 0.26, confirming that NH_3 is consistently harder to radially homogenise than H_2 across the full parameter space

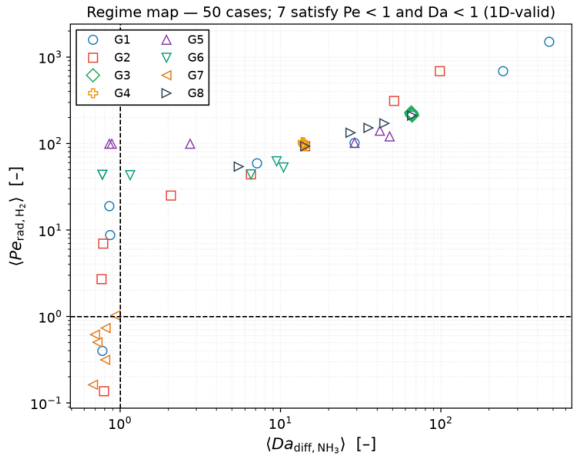


Figure A.5.5 Regime map of the radial Péclet number for hydrogen $\langle Pe_{r,H_2} \rangle$ vs. the diffusive Damköhler number for ammonia $\langle Da_{diff,NH_3} \rangle$ for all 50 simulated cases, grouped by GHSV, pressure, temperature, and tube radius; the vertical and horizontal dashed lines indicate $\langle Da_{diff,NH_3} \rangle$ = 1 and$\langle Pe_{r,H_2} \rangle$ = 1, respectively

Figure A.5.5 reveals a clear separation at the $\langle Pe_r \rangle$ = 1 threshold: only 7 of the 50 cases lie in the low-Péclet region $\langle Pe_r \rangle$ < 1, 4 fall in the transition band 1 ≤ $\langle Pe_r \rangle$ < 10, and the remaining 39 occupy a high-Péclet regime with $\langle Pe_r \rangle$ ≥ 10. Within this space, 7 cases simultaneously satisfy $\langle Pe_r \rangle$ < 1 and $\langle Da_{diff} \rangle$ < 1; these correspond to very low GHSV conditions where radial diffusion is fast enough to homogenise the cross-section and the reaction rate remains modest, so a 1D plug-flow model is adequate for mass transport. The GHSV groups (G1, G2) trace approximate power-law trajectories from the lower-left to the upper-right of the map, consistent with the simultaneous increase of both $\langle Pe_r \rangle$ and $\langle Da_{diff} \rangle$ with throughput, whereas the pressure groups (G3, G4) form nearly overlapping clusters: varying pressure from 30 to 80 bar changes $\langle Da_{diff} \rangle$ by less than about four percent and $\langle Pe_r \rangle$ by about ten percent, too little to move any case across the regime boundaries. This confirms that radial mass-transport validity depends primarily on GHSV and tube radius, with pressure exerting only a secondary influence through weak changes in density and diffusivity. Most importantly, the pressure sweep groups (G3, G4; 30-80 bar) form nearly overlapping clusters on the regime map, with $\langle Da_{diff} \rangle$ varying by less than 4% across the full pressure range confirming that $\langle Da_{diff} \rangle$ is effectively pressure-invariant and $\langle Pe_{r,H_2} \rangle$ changing by less than 11%.

A.5.4 Mechanistic closure: derivation, calibration, and KPI comparison

This section derives the reaction-screened concentration-polarisation closure of

Section 5.2.9, documents its calibration on the certified 2D dataset, and reports the KPI-level comparison of the three 1D model variants.

❖ The screened-deficit problem

The radial field of species i is decomposed into bulk and deficit, $c_i(r,z) = \bar{c}_i(z) + c_i'(r,z)$, and the net molar production rate is linearised about the bulk state, $R_i(c) \sim R_i(\bar{c}) + (\partial R_i/\partial c_i)\, c_i'$ (diagonal approximation; cross-species couplings are absorbed in the calibration constant C below). The bulk balance carries $R_i(\bar{c})$, so the deficit obeys a modified Helmholtz equation in the annulus $r \in [r_{mem}, r_{max}]$:

$$D_i \frac{1}{r}\frac{d}{dr}\left(r\,\frac{dc_i'}{dr}\right) = \frac{c_i'}{\delta_i^2}, \qquad \delta_i = \sqrt{D_i/s_i}, \qquad s_i = \max(-\partial R_i/\partial c_i,\ 0), \tag{A.5.23}$$

with no flux at the outer wall, $dc_i'/dr = 0$ at $r = r_{max}$. The general solution is a combination of modified Bessel functions, and the outer no-flux condition selects

$$c_i'(r) \ \propto\ K_0(r/\delta_i)I_1(r_{max}/\delta_i) + I_0(r/\delta_i)K_1(r_{max}/\delta_i), \tag{A.5.24}$$

which satisfies the boundary condition because $K_0' = -K_1$ and $I_0' = I_1$. The film coefficient is the wall gradient over the wall deficit, $k_{cp,i} = D_i\,|dc_i'/dr|/|c_i'|$ at $r = r_{mem}$, giving:

$$k_{cp,i}^{screen} = \frac{D_i}{\delta_i} f_{ann}(x_a, x_b), \qquad f_{ann}(x_a, x_b) = \frac{K_1(x_a)\,I_1(x_b) - I_1(x_a)\,K_1(x_b)}{K_0(x_a)\,I_1(x_b) + I_0(x_a)\,K_1(x_b)}, \tag{A.5.25}$$

with $x_a = r_{mem}/\delta_i$ and $x_b = r_{max}/\delta_i$. Two limits fix its interpretation. For a thin layer ($\delta_i \ll d_h$), $f_{ann} \to K_1(x_a)/K_0(x_a) \to 1$: the planar film-theory limit $k = D/\delta$, with a curvature enhancement K_1/K_0~1.3 at the physically realised x_a~1.7. For $\delta_i \to \infty$, $f_{ann} \to 0$: without a kinetic response, a pure deficit cannot sustain a steady flux, and the conduction channel below takes over. Numerically, f_{ann} is evaluated with exponentially scaled Bessel functions, so it is stable for arbitrarily thin layers.

❖ The conduction bound

For a species the kinetics cannot heal ($s_i \to 0$), the deficit is fed by the distributed background supply instead. Solving steady diffusion in the annulus with a uniform volumetric source S, all of it extracted at the membrane and no flux at the outer wall, gives the profile

$$c(r) - c(r_{mem}) = \frac{S}{2D}\left[r_{max}^2 \ln(r/r_{mem}) - \frac{r^2 - r_{mem}^2}{2}\right] \tag{A.5.26}$$

and, with $k_{cp} = J/(\bar{c} - c_{wall})$, the closed-form shape factor

$$G(\kappa) = \frac{k_{cp}\, d_h}{D} = \frac{(1-\kappa^2)^2(1-\kappa)}{2\kappa\, B(\kappa)}, \qquad B(\kappa) = \frac{1}{2}\ln\frac{1}{\kappa} - \frac{1-\kappa^2}{4} - \frac{1-\kappa^4}{8} + \frac{\kappa^2(1-\kappa^2)}{4} \tag{A.5.27}$$

in the scaled variable $\kappa = r_{mem}/r_{max}$. This is the mass-transfer analogue of a fully developed Nusselt number: G = 6.24 at κ = 0.083 and G = 3.78 at κ = 0.25, a weak dependence ($G \sim \kappa^{-0.46}$) that matches the classical annular band of **Figure 5.13** but cannot produce either the magnitude or the $\kappa^{-0.91}$ scaling of the extracted Sherwood numbers.

❖ Structure selection and calibration

The two channels feed the same deficit, so the closure takes the better conductor, $k_{cp,i}(z) = \max(C\,(D_i/\delta_i)\, f_{ann},\ G(\kappa)\, D_i/d_h)$, rather than their sum. This structure was selected against the exact flux-matched closures: with the maximum, the screening term alone carries the full geometry dependence, whereas any additive conduction admixture systematically re-biases the κ-dependence. For the present chemistry the screened channel controls essentially everywhere, lying a factor of about 2 (median) above the conduction bound; the bound guarantees a finite coefficient for a species without kinetic response.

The single constant C follows in closed form as the flux-weighted logarithmic mean of the ratio between the exact flux-matched coefficient and the screened prediction over all active axial cells of the certified 2D dataset (4,923 samples):

$$\ln C = \left\langle \ln\left(k_{cp}^{exact}/k_{cp}^{screen}\right)\right\rangle_w, \qquad w = |J_{NH_3}|, \qquad \Rightarrow \qquad C = 0.464 \sim 1/2 \tag{A.5.28}$$

an $O(1)$ profile-shape factor absorbing the linearisation, the diagonal approximation, and the effective-diffusivity convention; the weighted log-scatter about it is 0.43 (one standard deviation, i.e. a factor of about 1.5 point-wise). **Table A.5.4** reports the residual calibration bias per geometry group: it is flat to within ± 5% across all six κ values, which is the quantitative statement that the screening mechanism, not the calibration, carries the geometry dependence. The predicted screening length (flux-weighted median 2.3 mm) matches the measured deficit thickness (1.8-4.3 mm across all geometries) with no adjustable parameter.

❖ KPI comparison of the 1D variants

Figure A.5.6 shows parity plots of the three 1D variants against the certified 2D results for H_2 conversion and NH_3 recovery; the median and maximum deviations for all KPIs are collected in **Table 5.2**.

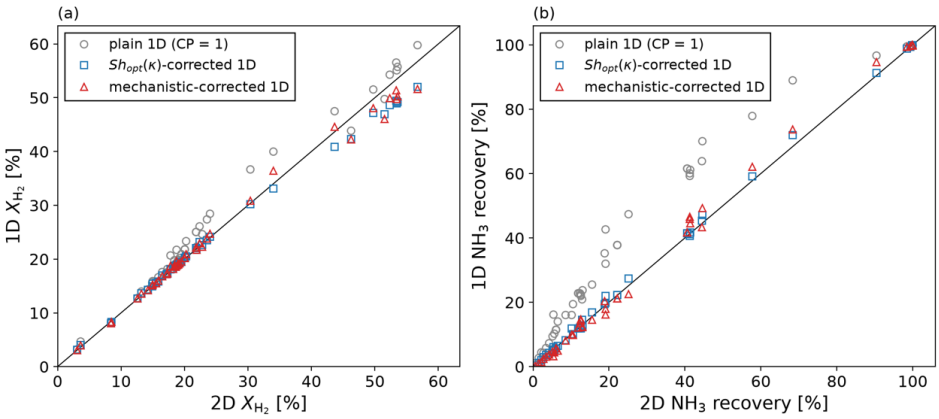


Figure A.5.6 Parity of the three 1D model variants against the certified 2D results for (a) H_2 conversion and (b) NH_3 recovery over the 50 reported cases. The recovery panel isolates the effect of the concentration-polarisation closure: the plain 1D model (CP = 1) overpredicts recovery by 70.5% (median); either corrected closure repairs it by more than an order of magnitude

The recovery panel isolates the effect of the concentration-polarisation closure: the plain 1D model (CP = 1) overpredicts recovery by 70.5% (median), and either corrected closure repairs this by more than an order of magnitude. The two corrected variants are equivalent in practice; the mechanistic closure is the better of the two on the radius family G7 (median 5.3% vs. 7.6% in X_{H_2}), where geometry extrapolation is tested.

Table A.5.4 Residual calibration bias of the screened closure per geometry group: the flux-weighted logarithmic mean of $k_{cp}^{exact}/\left(C\ k_{cp}^{screen}\right)$ within each κ group. A value of 1 means the calibrated closure is unbiased for that geometry

κ	0.083	0.100	0.111	0.125	0.167	0.250
bias	1.01	1.03	1.04	1.05	0.97	1.04

A.5.5 Kinetic model validation

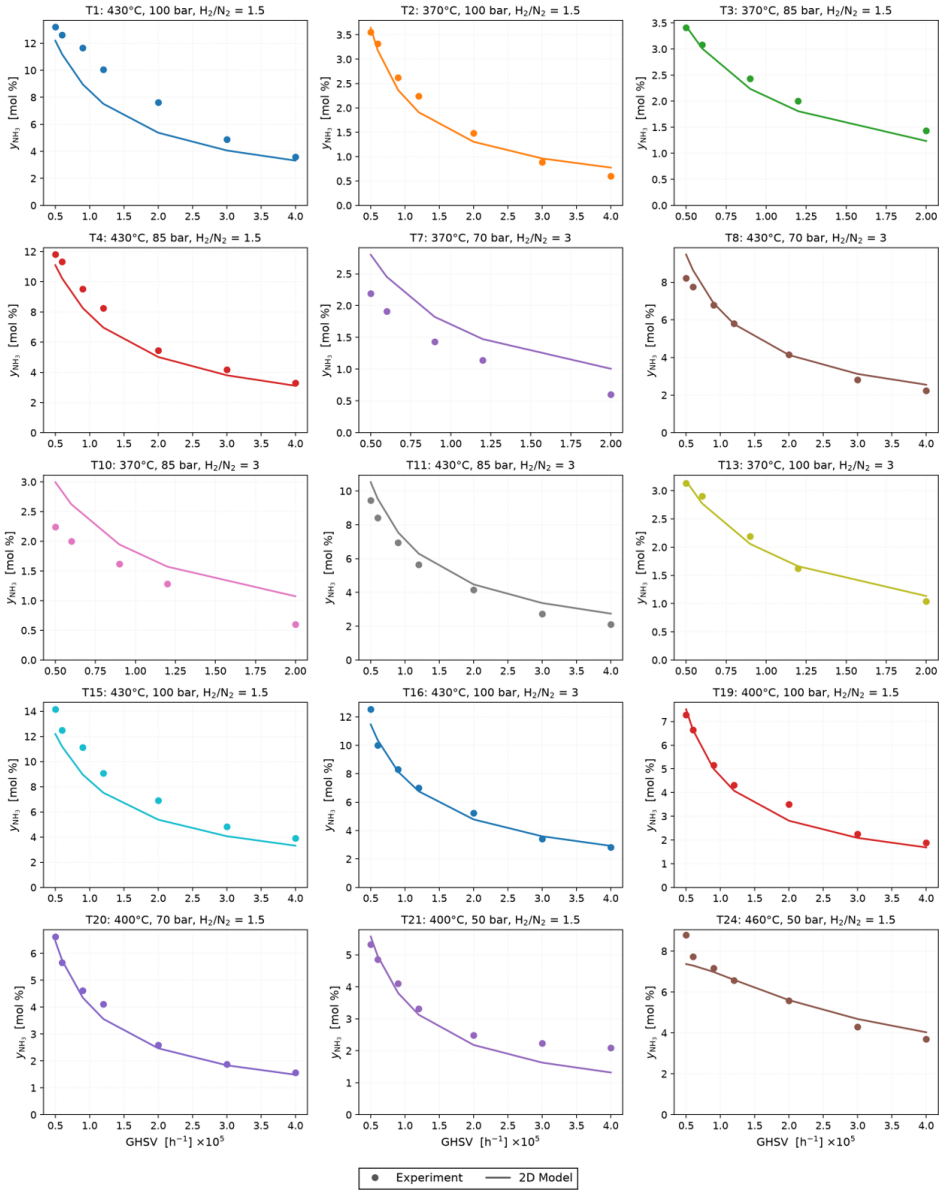


Figure A.5.7 NH_3 outlet mole fraction as a function of gas hourly space velocity (GHSV) for all other operating conditions. Symbols denote experimental data; solid lines represent 2D model predictions

A.5.6 1D-2D discrepancies across key performance indicators (KPIs): temperature effect

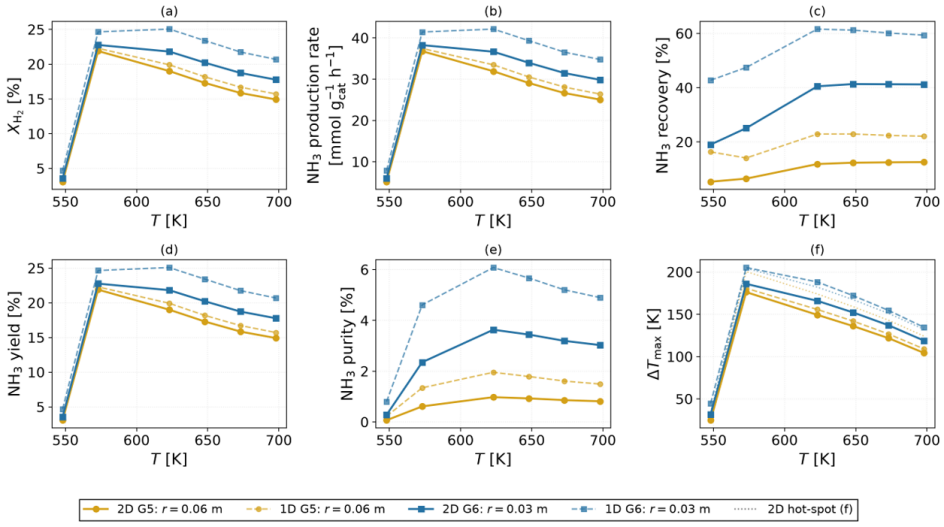


Figure A.5.8 Comparison of 1D (dashed lines) and 2D (solid lines) model predictions as a function of temperature for the temperature groups G5 (r = 0.06 m , yellow) and G6 (r = 0.03 m, blue) at P_{in}^{R} = 80 bar and GHSV = 5,000 h^{-1}: (a) H_2 conversion; (b) NH_3 production rate; (c) NH_3 recovery; (d) NH_3 yield; (e) NH_3 purity; (f) maximum retentate temperature rise

A.5.7 Concentration and temperature fields

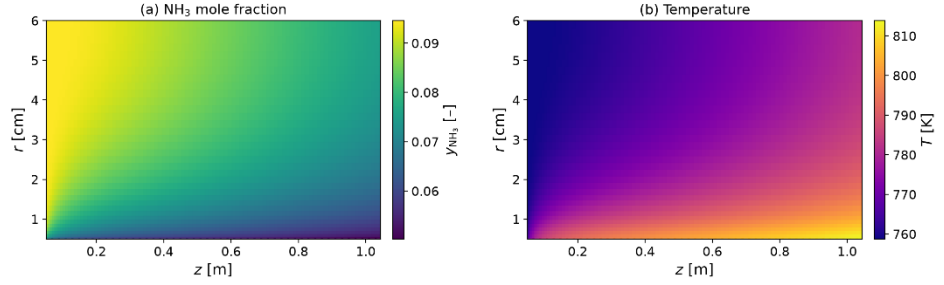


Figure A.5.9 2D fields of retentate NH_3 mole fraction (a) and retentate temperature (b) for case G1 (r = 0.06 m, T_{in}^{R} = 623 K, at P_{in}^{R} = 80 bar, GHSV = 1,000 h^{-1})

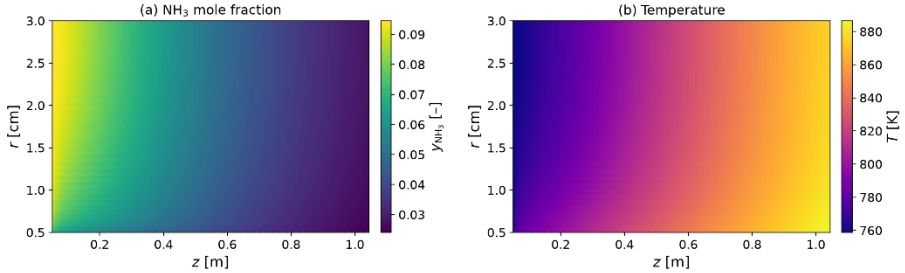


Figure A.5.10 2D fields of retentate NH_3 mole fraction (a) and retentate temperature (b) for case G2 (r = 0.03 m, T_{in}^{R} = 623 K, at P_{in}^{R} = 80 bar, GHSV = 1,000 h^{-1})

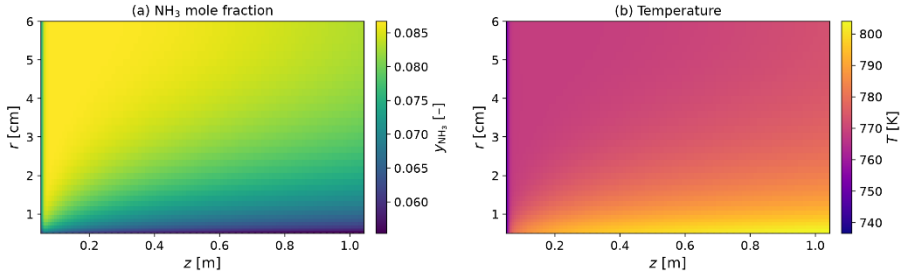


Figure A.5.11 2D fields of retentate NH_3 mole fraction (a) and retentate temperature (b) for case G1 (r = 0.06 m, T_{in}^{R} = 623 K, at P_{in}^{R} = 80 bar, GHSV = 3,000 h^{-1})

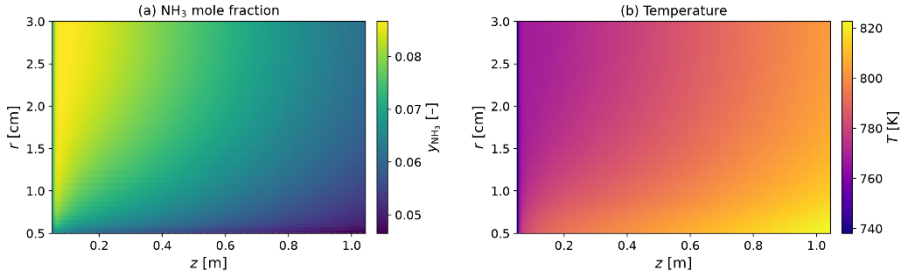


Figure A.5.12 2D fields of retentate NH_3 mole fraction (a) and retentate temperature (b) for case G2 (r = 0.03 m, T_{in}^{R} = 623 K, at P_{in}^{R} = 80 bar, GHSV = 3,000 h^{-1})

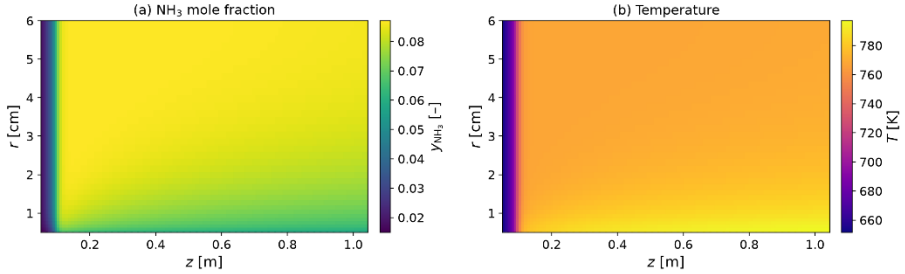


Figure A.5.13 2D fields of retentate NH_3 mole fraction (a) and retentate temperature (b) for case G1 (r = 0.06 m, T_{in}^{R} = 623 K, at P_{in}^{R} = 80 bar, GHSV = 5,000 h^{-1})

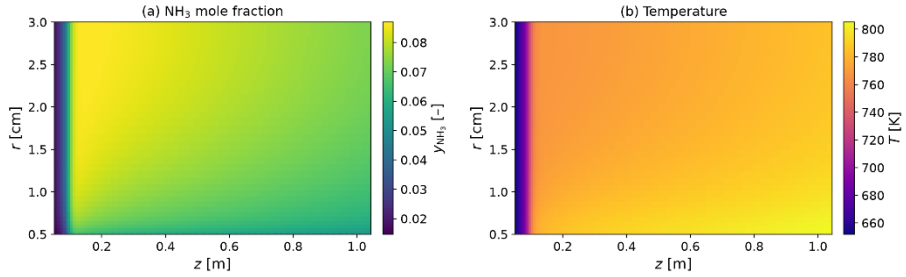


Figure A.5.14 2D fields of retentate NH_3 mole fraction (a) and retentate temperature (b) for case G2 (r = 0.03 m, T_{in}^{R} = 623 K, at P_{in}^{R} = 80 bar, GHSV = 5,000 h^{-1})

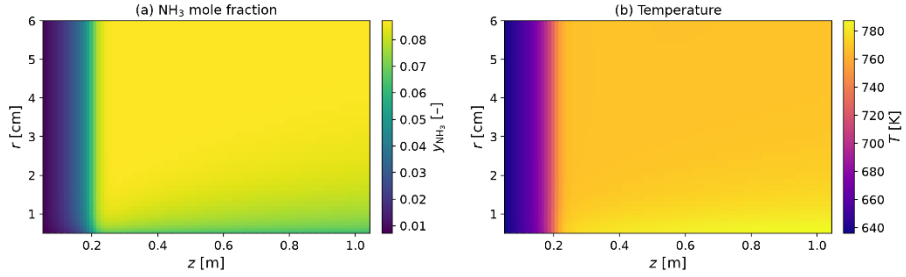


Figure A.5.15 2D fields of retentate NH_3 mole fraction (a) and retentate temperature (b) for case G1 (r = 0.06 m, T_{in}^{R} = 623 K, at P_{in}^{R} = 80 bar, GHSV = 10,000 h^{-1})

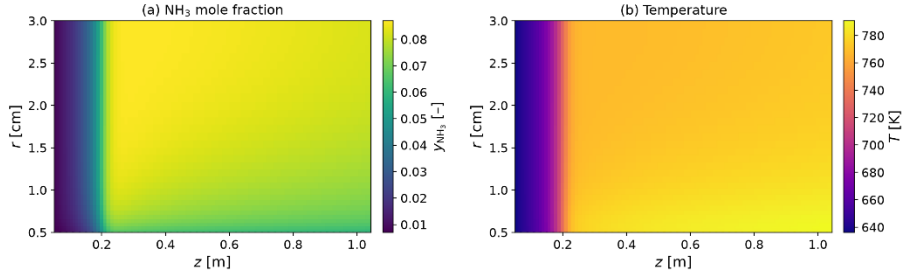


Figure A.5.16 2D fields of retentate NH_3 mole fraction (a) and retentate temperature (b) for case G2 (r = 0.03 m, T_{in}^{R} = 623 K, at P_{in}^{R} = 80 bar, GHSV = 10,000 h^{-1})

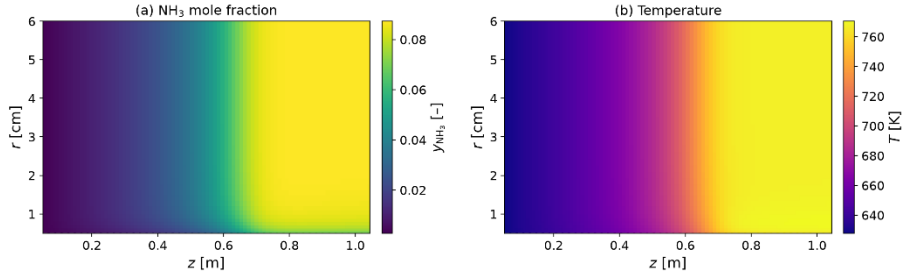


Figure A.5.17 2D fields of retentate NH_3 mole fraction (a) and retentate temperature (b) for case G1 (r = 0.06 m, T_{in}^{R} = 623 K, at P_{in}^{R} = 80 bar, GHSV = 30,000 h^{-1})

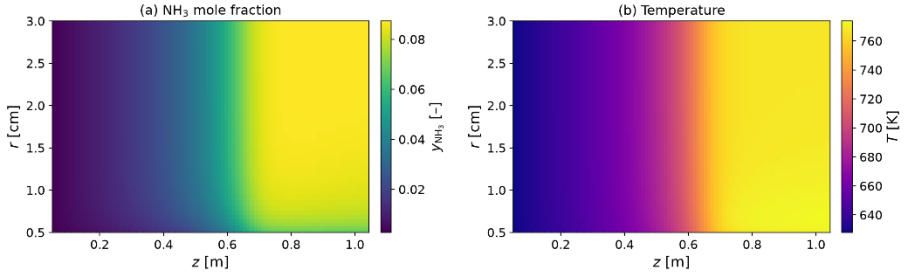


Figure A.5.18 2D fields of retentate NH_3 mole fraction (a) and retentate temperature (b) for case G2 (r = 0.03 m, T_{in}^{R} = 623 K, at P_{in}^{R} = 80 bar, GHSV = 30,000 h^{-1})

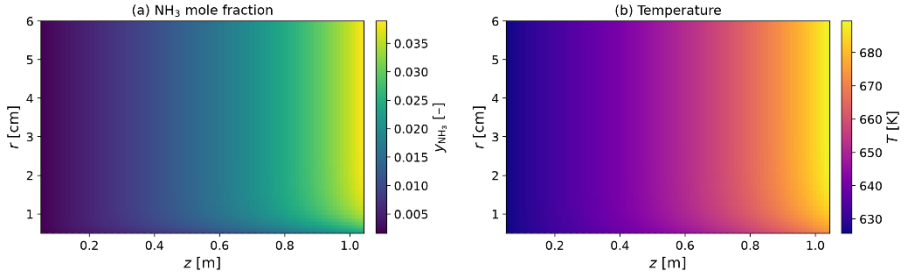


Figure A.5.19 2D fields of retentate NH_3 mole fraction (a) and retentate temperature (b) for case G1 (r = 0.06 m, T_{in}^{R} = 623 K, at P_{in}^{R} = 80 bar, GHSV = 60,000 h^{-1})

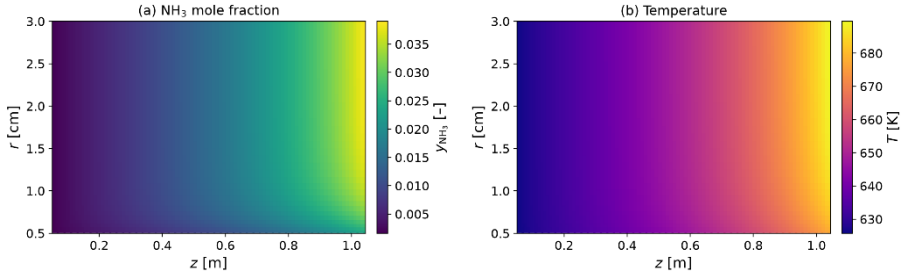


Figure A.5.20 2D fields of retentate NH_3 mole fraction (a) and retentate temperature (b) for case G2 (r = 0.03 m, T_{in}^{R} = 623 K, at P_{in}^{R} = 80 bar, GHSV = 60,000 h^{-1})

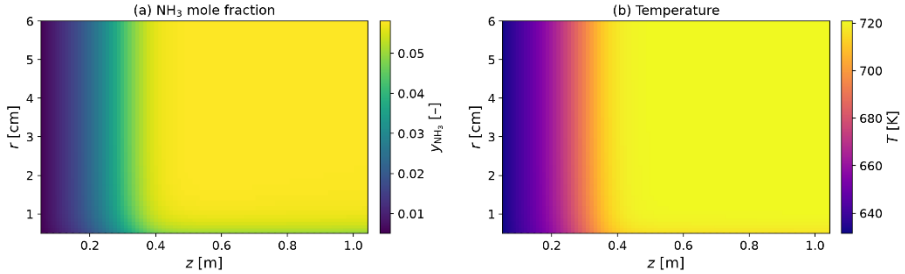


Figure A.5.21 2D fields of retentate NH_3 mole fraction (a) and retentate temperature (b) for case G3 (r = 0.06 m, T_{in}^{R} = 623 K, at P_{in}^{R} = 30 bar, GHSV = 10,000 h^{-1})

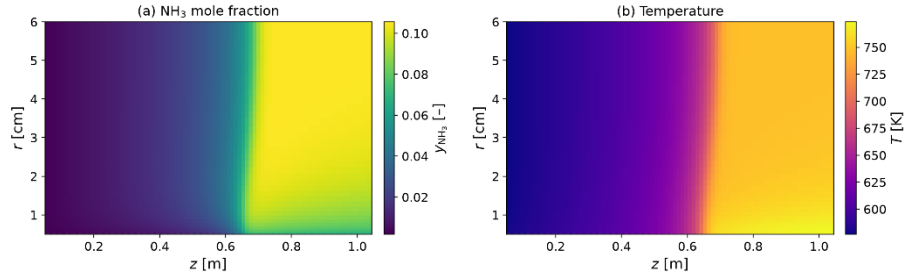


Figure A.5.22 2D fields of retentate NH_3 mole fraction (a) and retentate temperature (b) for case G5 (r = 0.06 m, T_{in}^{R} = 573 K, at P_{in}^{R} = 80 bar, GHSV = 5,000 h^{-1})

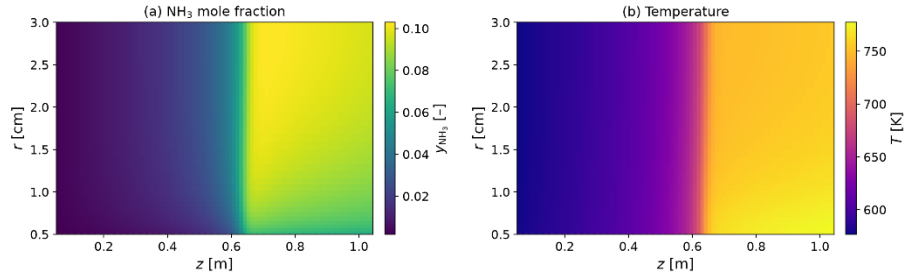


Figure A.5.23 2D fields of retentate NH_3 mole fraction (a) and retentate temperature (b) for case G5 (r = 0.06 m, T_{in}^{R} = 623 K, at P_{in}^{R} = 80 bar, GHSV = 5,000 h^{-1})

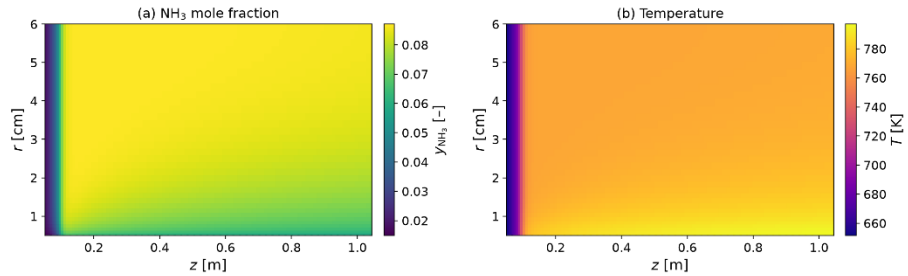


Figure A.5.24 2D fields of retentate NH_3 mole fraction (a) and retentate temperature (b) for case G5 (r = 0.06 m, T_{in}^{R} = 648 K, at P_{in}^{R} = 80 bar, GHSV = 5,000 h^{-1})

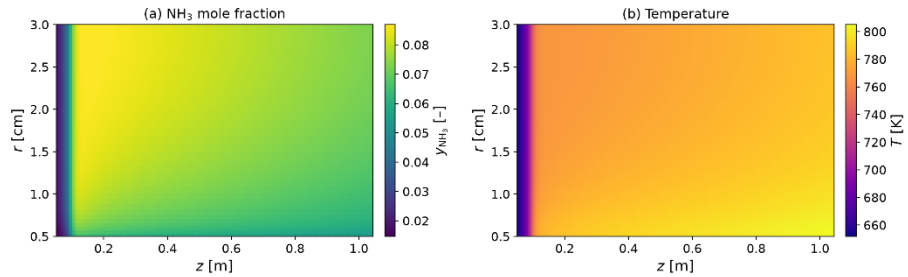


Figure A.5.25 2D fields of retentate NH_3 mole fraction (a) and retentate temperature (b) for case G5 (r = 0.06 m, T_{in}^{R} = 673 K, at P_{in}^{R} = 80 bar, GHSV = 5,000 h^{-1})

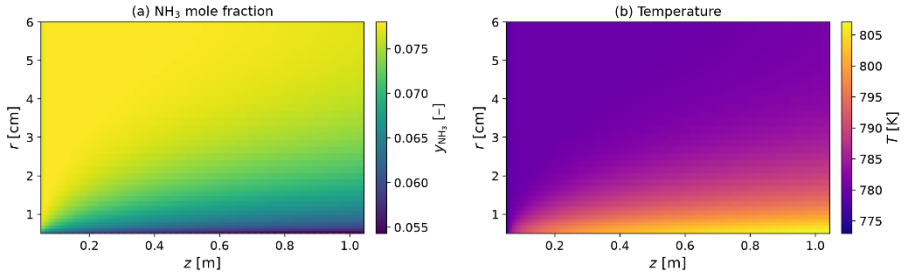


Figure A.5.26 2D fields of retentate NH_3 mole fraction (a) and retentate temperature (b) for case G5 (r = 0.06 m, T_{in}^{R} = 698 K, at P_{in}^{R} = 80 bar, GHSV = 5,000 h^{-1})

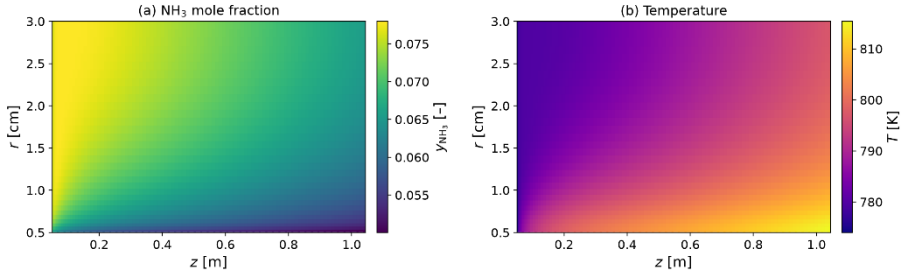


Figure A.5.27 2D fields of retentate NH_3 mole fraction (a) and retentate temperature (b) for case G6 (r = 0.03 m, T_{in}^{R} = 573 K, at P_{in}^{R} = 80 bar, GHSV = 5,000 h^{-1})

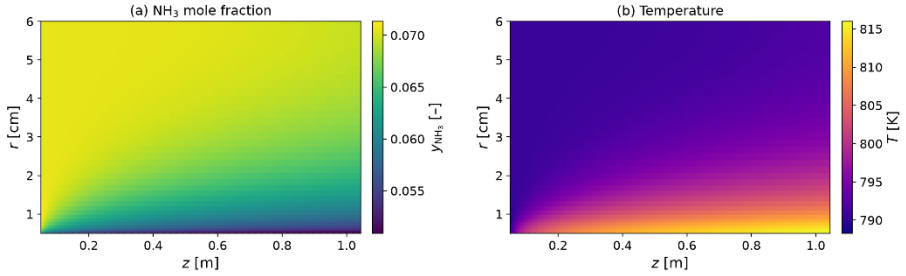


Figure A.5.28 2D fields of retentate NH3 mole fraction (a) and retentate temperature (b) for case G6 (r = 0.03 m, T_{in}^{R} = 623 K, at P_{in}^{R} = 80 bar, GHSV = 5,000 h^{-1})

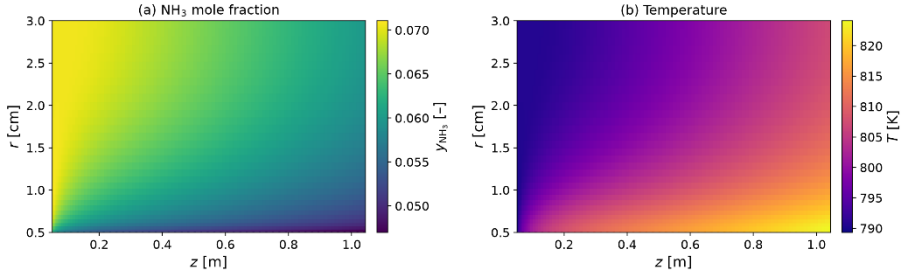


Figure A.5.29 2D fields of retentate NH3 mole fraction (a) and retentate temperature (b) for case G6 (r = 0.03 m, T_{in}^{R} = 648 K, at P_{in}^{R} = 80 bar, GHSV = 5,000 h-1)

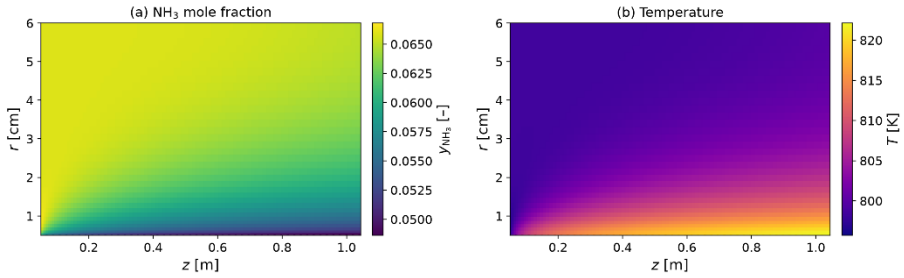


Figure A.5.30 2D fields of retentate NH_3 mole fraction (a) and retentate temperature (b) for case G6 (r = 0.03 m, T_{in}^{R} = 673 K, at P_{in}^{R} = 80 bar, GHSV = 5,000 h^{-1})

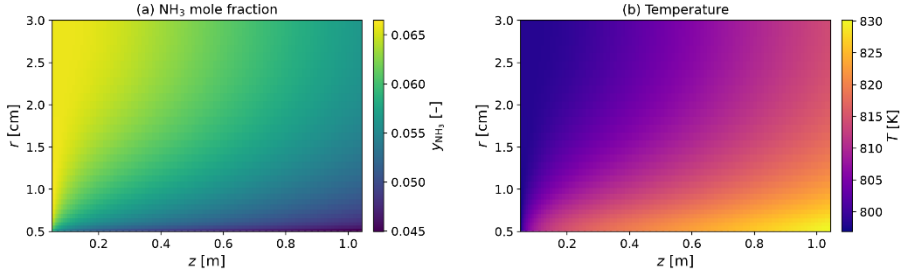


Figure A.5.31 2D fields of retentate NH_3 mole fraction (a) and retentate temperature (b) for case G6 (r = 0.03 m, T_{in}^{R}= 698 K, at P_{in}^{R} = 80 bar, GHSV = 5,000 h^{-1})

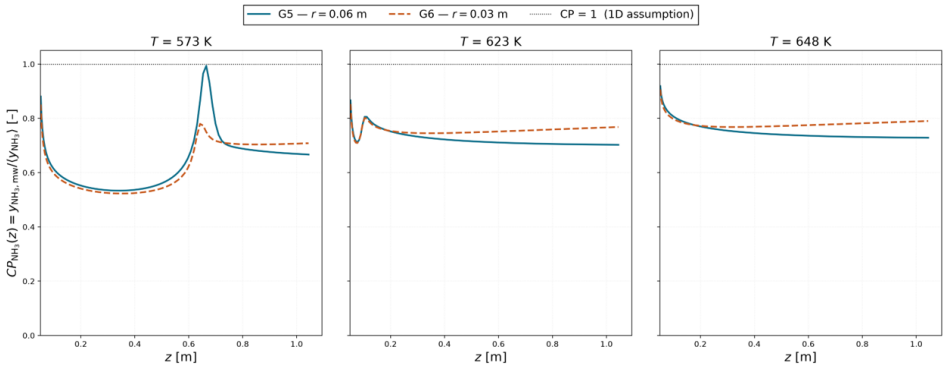


Figure A.5.32 Axial profiles of the NH_3 concentration polarisation factor, CP_{NH_3}, for the temperature groups G5 (r = 0.06 m, solid blue) and G6 (r = 0.03 m, dashed orange) at three operating temperature (T_{in}^{R} = 573, 623, 648 K), with GHSV = 5,000 h^{-1} and P_{in}^{R} = 80 bar. The dotted horizontal line at CP_{NH_3} = 1 represents the 1D plug-flow assumption of radial concentration uniformity

REFERENCES

[1] T. Chompupun, S. Limtrakul, T. Vatanatham, C. Kanhari, P.A. Ramachandran, "Experiments, modeling and scaling-up of membrane reactors for hydrogen production via steam methane reforming", *Chemical Engineering and Processing - Process Intensification* 134 (2018) 124–140. https://doi.org/10.1016/j.cep.2018.10.007.

[2] F. V. Lima, P. Daoutidis, M. Tsapatsis, J.J. Marano, "Modeling and optimization of membrane reactors for carbon capture in integrated gasification combined cycle units", *Ind. Eng. Chem. Res.* 51 (2012) 5480–5489. https://doi.org/10.1021/ie202234u.

[3] M.K. Koukou, N. Papayannakos, N.C. Markatos, M. Bracht, P.T. Alderliesten, "Simulation Tools for the Design of Industrial-Scale Membrane Reactors", *Chemical Engineering Research and Design* 76 (1998) 911–920. https://doi.org/10.1205/026387698525711.

[4] G. Donati, R. Paludetto, "Scale up of chemical reactors", *Catal. Today* 34 (1997) 483–533. https://doi.org/10.1016/S0920-5861(96)00069-7.

[5] R. Ma, B. Castro-Dominguez, A.G. Dixon, Y.H. Ma, "CFD study of heat and mass transfer in ethanol steam reforming in a catalytic membrane reactor", *Int. J. Hydrogen Energy* 43 (2018) 7662–7674. https://doi.org/10.1016/j.ijhydene.2017.08.173.

[6] A. Hussain, A. Seidel-Morgenstern, E. Tsotsas, "Heat and mass transfer in tubular ceramic membranes for membrane reactors", *Int. J. Heat Mass Transf.* 49 (2006) 2239–2253. https://doi.org/10.1016/j.ijheatmasstransfer.2005.12.006.

[7] Adris et al., "Fluidized bed reaction system for steam/hydrocarbon gas reforming to produce hydrogen", 1992. https://patents.google.com/patent/us5326550A/en.

[8] S. Guo, M. Mercangöz, "Design and Evaluation of a Multitubular Catalytic Membrane Reactor for Onboard Ammonia Cracking in Commercial Aviation", *ASME Open Journal of Engineering* 4 (2025). https://doi.org/10.1115/1.4069334.

[9] B.A. Bishop, F. V. Lima, "Novel module-based membrane reactor design approach for improved operability performance", *Membranes* 11 (2021) 1–18. https://doi.org/10.3390/membranes11020157.

[10] N. Wakao, T. Funazkri, "Effect of fluid dispersion coefficients on particle-to-fluid mass transfer coefficients in packed beds: Correlation of sherwood numbers", *Chem. Eng. Sci.* 33 (1978) 1375–1384. https://doi.org/10.1016/0009-2509(78)85120-3.

[11] S. Poto, H. van den Bogaard, F. Gallucci, M. Fernanda Neira d'Angelo, "Evaluation of the relevant mass and heat transfer phenomena in a packed bed membrane reactor for the direct conversion of CO2 to dimethyl ether", *Fuel* 350 (2023) 128783. https://doi.org/10.1016/j.fuel.2023.128783.

[12] W.J.R. Ververs, M. Ongis, A. Arratibel, L. Di Felice, F. Gallucci, "On the modeling of external mass transfer phenomena in Pd-based membrane separations", *Int. J.*

Hydrogen Energy 71 (2024) 1121–1133. https://doi.org/10.1016/j.ijhydene.2024.04.337.

[13] M.A. Murmura, C. Rocchetti, M.C. Annesini, "An Enhanced Sherwood Number to Model the Hydrogen Transport in Membrane Steam Reformers", *Membranes* 2021, Vol. 11, Page 805 (2021). https://doi.org/10.3390/membranes11110805.

[14] M.A. Murmura, S. Cerbelli, L. Manozzi, M.C. Annesini, "Toward Minimal Complexity Models of Membrane Reactors for Hydrogen Production," *Membranes* 2022, Vol. 12, Page 11-15 (2022). https://doi.org/10.3390/membranes12111115.

[15] M. Seiiedhoseiny, K. Ghasemzadeh, E. Jalilnejad, A. Iulianelli, "Computational fluid dynamics study on concentration polarization phenomena in silica membrane reactor during methanol steam reforming", *Chemical Engineering and Processing - Process Intensification* 183 (2023) 109249. https://doi.org/10.1016/j.cep.2022.109249.

[16] Y.H. Xiao, H.J. Xu, C.Y. Zhao, "Modeling the mass transfer process in membranes for carbon capture and separation with concentration polarization", *International Communications in Heat and Mass Transfer* 126 (2021) 105396. https://doi.org/10.1016/j.icheatmasstransfer.2021.105396.

[17] P.Y. Apel, P.M. Biesheuvel, O. V. Bobreshova, I.L. Borisov, V.I. Vasil'eva, V. V. Volkov, E.A. Grushevenko, V. V. Nikonenko, A. V. Parshina, N.D. Pismenskaya, I.I. Ryzhkov, M. V. Sharafan, A.B. Yaroslavtsev, "Concentration Polarization in Membrane Systems, Steady-state modeling and simulation of an axial-radial ammonia synthesis reactor", *Chem. Eng. Technol.* 26 (2003) 666–671. https://doi.org/10.1002/ceat.200390101.

[18] G. Chehade, I. Dincer, "Advanced kinetic modelling and simulation of a new small modular ammonia production unit", *Chem. Eng. Sci.* 236 (2021) 116512. https://doi.org/10.1016/j.ces.2021.116512.

[19] A. Mirvakili, Z. Eksiri, P. Biniaz, N. Mohaghegh, "Two-dimensional mathematical modeling of an industrial ammonia synthesis reactor with CFD analysis," *J. Taiwan Inst. Chem. Eng.* 121 (2021) 1–19. https://doi.org/10.1016/j.jtice.2021.03.032.

[20] F. Farivar, H.A. Ebrahim, "Simulation of an axial–radial ammonia synthesis reactor by linking COMSOL–MATLAB software", *RSC Adv.* 4 (2014) 48293–48298. https://doi.org/10.1039/c4ra05622a.

[21] H. Ma, M. Zhou, W. Ying, D. Fang, "Two-dimensional modeling of a plant-scale fixed-bed reactor for hydrogen production from methanol steam reforming", *Int. J. Hydrogen Energy* 41 (2016) 16932–16943. https://doi.org/10.1016/j.ijhydene.2016.07.117.

[22] J.A. Medrano, M.A. Llosa-Tanco, D.A. Pacheco-Tanaka, F. Gallucci, "Transport Mechanism and Modeling of Microporous Carbon Membranes", *Current Trends and Future Developments on (Bio-) Membranes: Microporous Membranes and Membrane Reactors* (2019) 39–58. https://doi.org/10.1016/b978-0-12-816350-4.00002-7.

[23] K. Ountaksinkul, S. Wannakao, P. Praserthdam, S. Assabumrungrat, "Intrinsic

kinetic study of 1-butene isomerization over magnesium oxide catalyst via a Berty stationary catalyst basket reactor", *RSC Adv.* 10 (2020) 36667–36677. https://doi.org/10.1039/d0ra05453d.

[24] S.T.B. Lundin, W.J. Movick, A. Ikeda, Y. Hasegawa, C.A. Wolden, J.D. Way, "Modeling of an ammonia decomposition membrane reactor including purity with complex geometry and non-isothermal behavior", *J. Memb. Sci.* 693 (2024) 122345. https://doi.org/10.1016/j.memsci.2023.122345.

[25] W. Sobieski, S. Lipiński, "The analysis of the relations between porosity and tortuosity in granular beds", 2017.

[26] J. K. Chinthaginjala, J.H. Bitter, L. Lefferts, "Thin layer of carbon-nano-fibers (CNFs) as catalyst support for fast mass transfer in hydrogenation of nitrite", *Appl. Catal. A Gen.* 383 (2010) 24–32. https://doi.org/10.1016/j.apcata.2010.05.013.

[27] E. Peter, O. Olafadehan, "Mass transfer effect on steam reforming of glycerol over ruthenium-alumina (Ru/Al 2O3)" *Catalyst*. https://www.researchgate.net/publication/339741887.

[28] J.M.P.Q. Delgado, "A critical review of dispersion in packed beds", *Heat and Mass Transfer* 42, (2006). https://doi.org/10.1007/s00231-005-0019-0.

[29] L.L. Raja, R.J. Kee, O. Deutschmann, J. Warnatz, L.D. Schmidt, "A critical evaluation of Navier–Stokes, boundary-layer, and plug-flow models of the flow and chemistry in a catalytic-combustion monolith", *Catal. Today* 59 (2000) 47–60. https://doi.org/10.1016/S0920-5861(00)00271-6.

[30] C. van Heerden, "Autothermic Processes", *Ind. Eng. Chem.* 45 (1953) 1242–1247. https://doi.org/10.1021/ie50522A030.

[31] J.C. Morud, S. Skogestad, "Analysis of Instability in an Industrial Ammonia Reactor", *AIChE Journal* 44 (1998) 888–895. https://doi.org/10.1002/AIC.690440414.

[32] R.K. Shah, A. L. London, "Laminar Flow Forced Convection in Ducts", (2014). https://books.google.com/books/about/Laminar_Flow_Forced_Convection_in_Ducts.html?hl=it&id=D-JbAwAAQBAJ.

[33] D. Albarracin-Zaidiza, B. Belaissaoui, S. Rode, "Hybrid amine-based PCC processes, membrane contactors for PCC", *Absorption-Based Post-Combustion Capture of Carbon Dioxide* (2016) 365–395. https://doi.org/10.1016/b978-0-08-100514-9.00015-9.

[34] O. Nekhamkina, M. Sheintuch, "Effective approximations for concentration-polarization in Pd-membrane separators", *Chemical Engineering Journal* 260 (2015) 835–845. https://doi.org/10.1016/j.cej.2014.09.049.

[35] O. Nekhamkina, M. Sheintuch, "Approximate models of concentration-polarization in Pd-membrane separators. Fast numerical analysis", *J. Memb. Sci.* 500 (2016) 136–150. https://doi.org/10.1016/j.memsci.2015.11.027.

[36] P. V Danckwerts, Gas-liquid reactions, (1970).

https://journals.flvc.org/cee/article/download/126566/126054/.

[37] R. C. Reid, J. M. Prausnits, B. E. Poling, The Properties of Gases & Liquids, 4th Edition, https://www.scribd.com/document/386010207/The-Properties-of-Gases-Liquids-4th-Edition-R-C-Reid-J-M-Prausnitz-B-E-Poling.

[38] D.C. Dyson, J.M. Simon, "A kinetic expression with diffusion correction for ammonia synthesis on industrial catalyst", *Industrial and Engineering Chemistry Fundamentals* 7 (1968) 605–610. https://doi.org/10.1021/I160028A013.

[39] O. Levenspiel, J. Wiley, Chemical Reaction Engineering Third Edition, 1999.

[40] M. Gaeini, R. Wind, P.A.J. Donkers, H.A. Zondag, C.C.M. Rindt, "Development of a validated 2D model for flow, moisture and heat transport in a packed bed reactor using MRI experiment and a lab-scale reactor setup", *Int. J. Heat Mass Transf.* 113 (2017) 1116–1129. https://doi.org/10.1016/j.ijheatmasstransfer.2017.06.034.

[41] D.J. Gunn, "Axial and Radial dispersion in fixed beds", *Chemical Engineering Sector* 42 (1987) 363–373.

[42] C.D. A. Srinivasan, "One-Dimensional Pseudo-Homogeneous Packed-Bed Reactor Modeling: I. Chemical Species Equation and Effective Diffusivity, *Chemical Engineering Technology* (2013). https://doi.org/10.1002/ceat.201200458.

[43] E.M. Petersen, R.G. Rao, B.C. Vance, J.P. Tessonnier, "SiO2/SiC supports with tailored thermal conductivity to reveal the effect of surface temperature on Ru-catalyzed CO2 methanation", *Appl. Catal. B* 286 (2021) 119904. https://doi.org/10.1016/j.apcatb.2021.119904.

[44] H. Scott Fogler, Elements of Chemical Reaction Engineering.

[45] P.N. Dwivedi, S.N. Upadhyay, "Particle-Fluid Mass Transfer in Fixed and Fluidized Beds", *Industrial and Engineering Chemistry Process Design and Development* 16 (1977) 157–165. https://doi.org/10.1021/I260062A001

CHAPTER 6

On the scaling-up of 3D-printed metallic POCS structured catalysts membrane reactors

ABSTRACT

This chapter reports the first experimental demonstration of a scaled-up, multi-membrane reactor for ammonia synthesis, integrating four tubular CMS membranes with two 3D-printed metallic Periodic Open Cellular Structure (POCS) supports featuring Gyroid and Body-centred cubic (BCC) geometry. The supports were manufactured from Inconel 625 by Laser Powder Bed Fusion and washcoated with a Ru-based catalyst via a scaled-up dip-spin coating procedure. The dip-spin coating protocol was transferred to both POCS topologies at larger scale without modification, and optical microscopy confirmed uniform, crack-free catalyst coverage in both geometries. The previously characterised CMS membrane was carbonised at 550 °C and analysed by organic elemental analysis, X-ray photoelectron spectroscopy, and Raman spectroscopy. The results confirmed a defect-rich, turbostratic sp^2 carbon matrix with a microporous architecture. Baseline testing in the conventional reactor over the range of 350-450 °C and 20-40 bar demonstrated that the Gyroid and BCC configurations delivered identical catalytic performance under all investigated conditions. Upon membrane integration, this geometry-independence was preserved, and the membrane consistently enhanced the NH_3 production rates across all operating conditions. Operation beyond thermodynamic equilibrium, indicated by H_2 conversion and NH_3 yields exceeding their equilibrium values, was achieved exclusively at low WHSV with a sweep-gas-to-feed flow ratio of SW = 4. Under these conditions, H_2 conversion exceeded the equilibrium limit by 30% at 400 °C and 110% at 450 °C, while NH_3 yield increased by 65% and 170%, respectively, compared with the conventional reactor. Increasing the number of membranes from one to four resulted in a membrane-area-normalised production rate improvement of up to 424% at 350 °C and 40 bar. These results provide a strong basis for further scale-up of membrane reactors for ammonia synthesis.

This chapter is based on the following journal article:

"On the scaling-up of 3D-printed metallic POCS structured catalysts membrane reactors", **I. Gargiulo**, A. Vita, C. Italiano, C. Coiana, F. Gallucci, *Accepted in Chem. Eng. J.*.

6.1 INTRODUCTION

Building on the structured catalyst membrane reactor concept developed in Chapter 4, this chapter investigates its extension to a larger-scale, multi-membrane configuration. In Chapter 4, Gyroid and BCC POCS supports were evaluated as structured catalyst supports in a single-membrane reactor. Here, the same lattice geometries are integrated with four carbon molecular sieve membranes to assess their performance under scaled-up operating conditions. The two-dimensional modelling and scale-up analysis presented in Chapter 5 provided additional guidance for the reactor design. Although the exact optimum operating conditions and geometries identified in that chapter were not quantitatively reproduced here, the modelling insights informed the qualitative design choices, including membrane spacing, annulus compactness, and operating pressure.

To the best of our knowledge, no previous study has reported the integration of 3D-printed metallic POCS catalysts with carbon molecular sieve membranes for ammonia synthesis beyond the proof of concept scale represented by TRL 3-4. In addition, the systematic comparison of POCS lattice geometries within an operational ammonia-synthesis membrane reactor remains unexplored. This work therefore provides, to the best of our knowledge, the first demonstration of dual process intensification through the integration of structured catalytic supports and membrane-assisted separation in a multi-membrane reactor configuration relevant to TRL-5 development. Two complementary 3D-printed metallic POCS architectures, Gyroid and BCC, were manufactured in nickel alloy (IN625) with dimensions 5.1×10 cm (~130 cm^3 per piece). Both geometries were then activated with the same Ru-based catalyst through a scaled-up dip-spin coating procedure, designed to meet the higher slurry demand. The coated structures were subsequently integrated with four tubular CMS membranes in a multi-membrane reactor.

Thus, the objectives of the study are: (i) to demonstrate that the dip-spin coating protocol previously optimised at the lab scale can be reproducibly transferred to larger supports of different lattice topology, without modification of the slurry formulation, or the spinning parameters; (ii) to provide a direct comparison of the Gyroid and BCC geometries when integrated with CMS membranes in the membrane reactor; (iii) to quantify the enhancement in NH_3 production rate, H_2 conversion and NH_3 yield attributable to membrane-assisted equilibrium shift, including the influence of increased membrane area, and to identify the operating conditions under which this synergy between structured catalytic supports and CMS membranes is maximised.

6.2 EXPERIMENTAL: MATERIALS AND PREPARATION

6.2.1 POCS design and fabrication: Gyroid and BCC geometry

Periodic open cellular structures with Gyroid and Body-centred cubic (BCC) geometries were manufactured by ENGIE from Ni-alloy (IN625) using Laser Powder Bed Fusion (LPBF) starting from CAD-designed architectures. Cylindrical supports with an external diameter of 51.1 mm and a length of 100 mm were produced. For each geometry, two identical pieces were stacked axially in series within the reactor, yielding a total catalytic bed length of 200 mm per geometry. Two Gyroid and two BCC structures were fabricated to accommodate a total of four tubular CMS membranes within the multi-tubular membrane reactor configuration. Each structure incorporated four longitudinal channels (Ø = 15.1 mm) aligned along the axial direction; when the two pieces of the same geometry are assembled in series, these channels form continuous passages of 200 mm that house the CMS membranes (220 mm in active length), which extend slightly beyond the POCS assembly to span the full reactor housing.

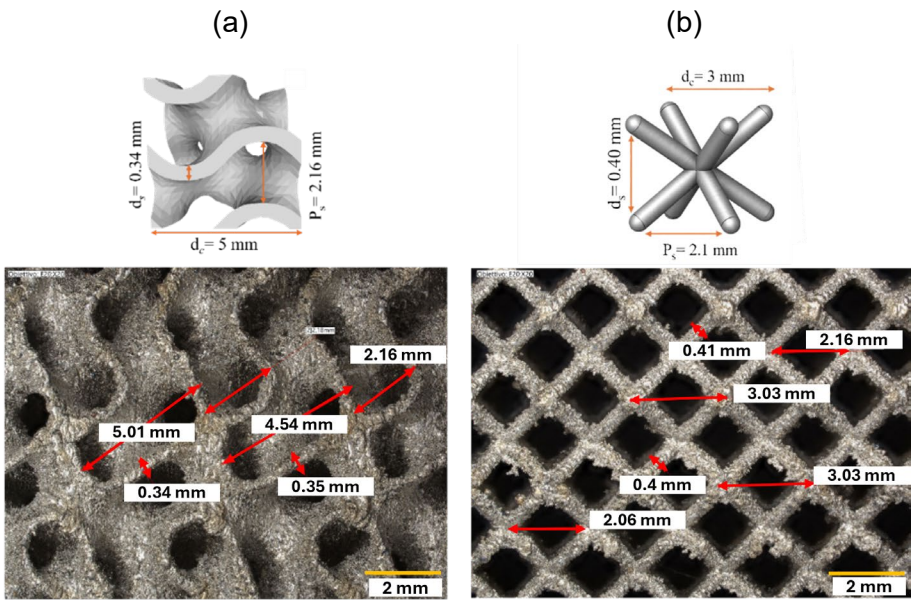


Figure 6.1 Unit cells rendering and optical images of Gyroid (a) and BCC (b); d_c represents the cell dimension, d_s the thickness of the sheet and P_s the equivalent pore size dimension

The Gyroid architecture was characterised by a cell size of 5 mm and a sheet thickness of 0.34 mm, whereas the BCC structure exhibited a cell size of 3 mm and a strut diameter of 0.40 mm. Both geometries present high void fractions (ε~0.72-0.82). **Figure 6.1** shows a rendering of the single-unit cells corresponding to both Gyroid and BCC supports, together with optical microscope images of

representative portions of their bare surfaces. Dimensional measurements revealed good agreement between the CAD-designed geometries and the resulting additively manufactured structures, confirming the fidelity and reproducibility of the printing process.

Prior to catalyst deposition, each as-built support was degreased under ultrasonic agitation in a 50:50 vol% acetone/water mixture for 30 min, rinsed with abundant distilled water, and oven-dried at 120 °C for 1 h. A pre-oxidation treatment in static air at 900 °C for 6 h was then applied to all supports to develop a thin, adherent oxide scale on the metallic surface, thereby improving the adhesion of the subsequent washcoat layer [1].

6.2.2 Catalyst slurry preparation

A developmental Ru-based catalyst (2.2 wt% Ru) supplied by Johnson Matthey in powder form was used to prepare the washcoat slurry employed for activating the four POCS supports. The target catalyst loading was set at 0.21 $g \cdot cm^{-3}$.

Four slurry batches (I-IV) were prepared to meet the catalyst demand associated with the larger support volume of about 130 cm^3 each, corresponding to the structure envelope excluding the four membrane channels, each with a volume of approximately 150 mL. The slurry composition was kept unchanged with respect to the formulation reported in Chapter 4: 35 g (22.4 wt%) catalyst, 66.5 g (42.5 wt%) glycerol, 2.38 g (1.5 wt%) polyvinyl alcohol (PVA) and 33.6 wt% distilled water. The dispersion medium was prepared by dissolving PVA (87-89% hydrolysed, Sigma-Aldrich) in distilled water, under magnetic stirring at 85 °C, followed by the addition of glycerol (99.5% bi-distilled, Analar Normapur®). In this formulation, glycerol acts as a dispersant, PVA as a rheology modifier, and distilled water as solvent and diluent. Prior to incorporation into the slurry, the catalyst powder was pre-milled in zirconia jars for 3 h at 300 rpm to reduce particle size and improve dispersion. The catalyst powder was then added to the dispersion medium, and the resulting slurry was homogenised by ball milling (BM40-POWTEQ) with zirconia spheres (1 cm diameter, sphere-to-powder mass ratio = 7:1) for 24 h at 300 rpm. To increase throughput at this scale, four 250 cm^3 zirconia jars were loaded and operated simultaneously in the planetary mill, allowing batches I-IV to be processed in a single milling run. After milling, each batch underwent a 30 min sonication treatment to minimise foaming prior to coating.

The rheological behaviour of all four slurry batches was characterised over the shear-rate range 0.1-2000 s^{-1}; the results are reported and discussed in Section 6.5.1. All four batches exhibited equivalent pseudoplastic, shear-thinning behaviour across the full shear-rate window investigated, confirming excellent batch-to-batch reproducibility of the scaled-up preparation procedure.

6.2.3 POCS activation by dip-spin coating

The activation of the four POCS supports - two Gyroid and two BCC - was carried out by a combined dip-spin coating route, developed and optimised in Chapter 4. In each coating cycle, the support was fully immersed in the slurry for approximately 10 s to ensure complete wetting of the open-cell network. The wet sample was immediately transferred to a commercial spin-coater (Laurell WS-650Mz-23 NPPB), where the excess slurry was removed by rotating the piece at 1,000 rpm for 20 s, with a ramp acceleration of 1,000 rpm s^{-1}. To accommodate the larger POCS dimensions, a dedicated cylindrical specimen holder was designed and integrated into the spin-coating system, ensuring mechanical stability and alignment during high-speed rotation. Immediately after spinning, the support was flash-dried in air at 450 °C for 10 min to consolidate the freshly deposited layer before the next dipping step.

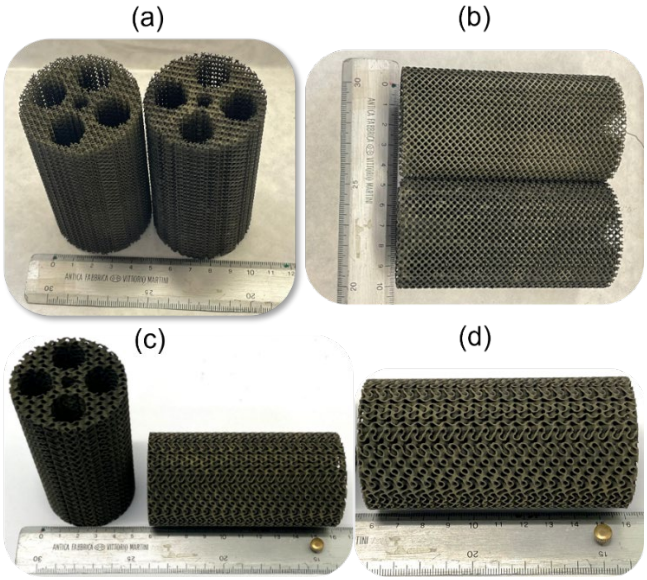


Figure 6.2 Images of 3D-printed washcoated structured catalysts: (a)-(b) Gyroid topology and (c)-(d) Body-centred cubic (BCC) topology supports after coating deposition

The dip-spin-flash-dry sequence was iterated 16 times per support until the gravimetric uptake matched the target loading of 0.21 g·cm^{-3} (~27 g of washcoat per piece). The progression of the coating was monitored gravimetrically throughout: each sample was weighed before and after every drying and calcination step, so that the build-up of the washcoat could be tracked cycle-by-cycle and the nominal loading verified at the end of the process.

Once the target loading was achieved, all four supports underwent a final calcination in static air at 500 °C for 6 h (heating rate 5 °C·min^{-1}) to remove residual organic additives (PVA and glycerol) and stabilise the catalyst layer. The Gyroid and BCC

supports obtained at the end of the activation procedure are shown in **Figure 6.2**.

6.2.4 Membrane fabrication

A novolac-based precursor for the CMS membranes was prepared according to the method described in Chapter 4, using the same phenol-formaldehyde monomer ratio, acid catalyst, Cu addition, and thermal treatment conditions up to the polymerisation stage. This synthesis route was employed by TECNALIA to obtain both supported CMS membranes for catalyst-integrated reactor experiments and unsupported membrane material for *ex situ* characterisation.
For the supported membranes, the precursor solution was deposited onto asymmetric porous α-Al_2O_3 tubes ($Ø^{in}$ = 7 mm, $Ø^{ex}$ = 10 mm, outer surface pore size ~200 nm), geometry, surface preparation, and coating conditions as described in Chapter 4. After deposition, the coated tubes were subjected to the same polymerisation and subsequent carbonisation protocol, carried out under a non-oxidising atmosphere at 550 °C. Unsupported membrane samples were prepared in parallel from the same novolac-based precursor, in the absence of any ceramic substrate. Two sample states were produced: a non-carbonised sample, obtained by polymerisation at 90 °C without any subsequent thermal treatment, and a carbonised sample, produced by applying the same carbonisation protocol as the supported membranes.

6.3 CHARACTERISATION TECHNIQUES

6.3.1 Morphological and rheological characterisation of POCS supports and washcoat slurry

The surface morphology and geometric fidelity of the as-built and washcoated Gyroid and BCC supports were assessed by optical microscopy using a Keyence VHX-7000 digital microscope. Images were acquired with VHX-E20 (High-Resolution, Low-Magnification Objective Lens 20-100×) and VHX-E100 (High-Resolution, Medium-Magnification Objective Lens 100-500×) objective lenses at multiple locations across the strut and sheet surfaces and cell interiors. Cell size, strut diameter, sheet thickness, and channel diameter were measured and compared against the nominal CAD dimensions to quantify the dimensional deviations introduced by the LPBF process.
The rheological behaviour of the washcoat slurry was characterised using a modular compact rotational rheometer (Modular Compact Rheometer MCR 92, Anton Paar GmbH, Graz, Austria) equipped with a double-gap measuring geometry. Flow curves were acquired at 25 °C over a shear-rate range of 0.1-3000 s^{-1}.

6.3.2 Unsupported carbon membrane material characterisation

The unsupported CMS membrane material was characterised in both its non-

carbonised and carbonised (550 °C) forms, using organic elemental analysis (OEA), X-ray photoelectron spectroscopy (XPS), and Raman spectroscopy, to track the chemical and structural transformation induced by pyrolysis.
The elemental composition of the membrane material, including carbon, hydrogen, nitrogen, and oxygen, was determined by organic elemental analysis using a Thermo Scientific Flash Smart CHNS/O analyser (Waltham, MA, USA).
X-ray photoelectron spectroscopy (XPS) measurements were conducted under ultra-high-vacuum conditions using a K-Alpha spectrometer. The acquired spectra were processed in CasaXPS, applying a Shirley-type background subtraction prior to peak fitting. Component fitting was performed following the methodology reported in [2].
Raman spectroscopy was carried out using a WITec WMT 50 confocal Raman microscope equipped with a 532 nm excitation laser under confocal conditions, providing high spatial resolution. Spectra were collected for both the non-carbonised precursor and the carbonised membrane (550 °C) to assess the changes in carbon ordering and bonding structure induced by thermal treatment. The spectra were baseline-corrected before analysis to remove background fluorescence and isolate the intrinsic Raman signal.

6.3.3 Experimental setup for multi-membrane reactor testing

The experimental test rig used for multi-membrane reactor testing has been described in detail in Chapter 4, to which the reader is referred for a comprehensive description of the gas supply system, flow control instrumentation, thermal management, pressure regulation, and analytical equipment. Briefly, the setup comprises Bronkhorst mass-flow controllers for N_2, H_2, and NH_3, pneumatically actuated Swagelok valves, independent back-pressure regulators on the retentate and permeate sides, and a Compact GC 4.0 micro-gas chromatograph (Global Analyser Solutions) for multi-component gas analysis, with methane as internal standard. The P&ID of the complete setup is shown in **Figure 6.3**, illustrating the gas feed lines, MFC network, reactor section, back-pressure regulators, and downstream GC analysis system.
The present study introduces a scaled-up multi-membrane reactor configuration, designed to accommodate four tubular CMS membranes integrated with the POCS catalyst unit. The reactor consists of a 316Ti stainless steel pressure vessel ($Ø^{ext}$ = 60 mm, $Ø^{int}$ = 51.3 mm, L = 350 mm), sealed at the top flange via a LEADER Ring Joint R Oval sealing ring (316L, R24, API 6A/ISO 10423), selected for its mechanical and chemical compatibility with high-pressure ammonia service.
The four membranes are individually sealed to the top flange via Swagelok connections incorporating graphite rings to mitigate mechanical stress on the membrane tubes, resulting in an overall active membrane length of approximately 220-225 mm. Two POCS segments are stacked axially in series within the vessel,

yielding a total active bed length of 200 mm.

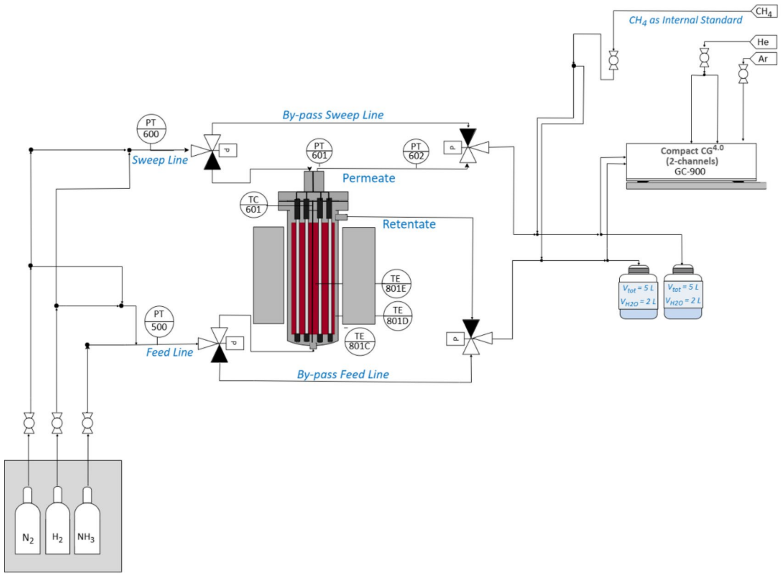


Figure 6.3 P&ID of the experimental setup

A multipoint thermocouple is embedded within the POCS bed along its central axis to monitor the axial temperature profile across the full catalytic zone and to detect any thermal gradients arising during reaction.

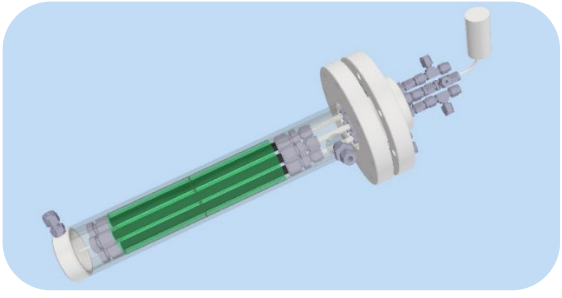


Figure 6.4 3D CAD render of the multi-membrane reactor showing the four tubular CMS membranes running axially through the POCS catalyst body (green) housed within the cylindrical pressure vessel, with the top flange and Swagelok membrane fittings

A 3D render of the multi-membrane reactor design, together with the as-built demonstrator unit and the metallic sealing components, is shown in **Figure 6.4**.
To ensure co-current operation, the reaction stream enters from the bottom of the reactor, while the sweep gas is introduced from the top via four individual internal capillaries ($Ø^{ex}$ = 3.3 mm), each inserted into one of the four membranes, extending to the end of the respective membrane and then flowing back along its length in the same axial direction as the retentate stream. The permeate stream is collected at the

top flange and withdrawn independently from the retentate. **Figure 6.5**(a) shows the four CMS membranes extending from the top flange with their individual Swagelok fittings, while **Figure 6.5**(b) illustrates the subsequent assembly step in which the POCS catalyst unit has been positioned over the membranes prior to insertion into the pressure vessel.



Figure 6.5 (a) Assembly of four tubular CMS membranes connected to the reactor flange, (b) Assembly with POCS catalyst structures fitted over the membrane tubes

6.4 OPERATING CONDITIONS AND KEY PERFORMANCE INDICATORS FOR REACTOR PERFORMANCE

The operating conditions explored in this study are summarised in **Table 6.1**. For each experimental condition, reactor performance was assessed using the set of metrics defined in Chapter 4 (Equations (2.17, 2.18, 4.1-4.3)), with the addition of the following metric:

Table 6.1 Operating conditions used during the experimental campaign

Case ID	WHSV [mLn·$g_{cat}^{-1}h^{-1}$]	T [°C]	P [bar]	ΔP [bar]	SW [-]	H_2:N_2
SCR	715	350, 400, 450	20, 30, 40	-	-	2
SCR	3,285	350, 400, 450	30, 40	-	-	2
SCMR	715	350, 400, 450	30, 40	0	1	2
SCMR	715	350, 400, 450	20, 30, 40	0	4	2
SCMR	3,285	350, 400, 450	30, 40	0, 1, 2, 3	1	2

$$\%\ Reactant\ loss = \frac{F_{i,tm}}{F_{i,0}^{R}} \times 100 \tag{6.1}$$

$$NH_3\ production\ rate\ -\ membrane-based\ = \frac{F^R_{NH_3} + F^P_{NH_3}}{A_{mem}} \quad (6.2)$$

$$\%\ Improvement\ of\ membrane\ area\ normalised\ NH_3\ productivity = \frac{F^{tot}_{NH_3,4\ mem.} - F^{tot}_{NH_3,1\ mem.}}{F^{tot}_{NH_3,1\ mem.}} \times 100 \quad (6.3)$$

The membrane-area-normalised production rate (Equation (6.2)) provides an additional performance metric that quantifies the NH_3 output per unit of membrane surface area deployed, particularly important during the scaling of membrane reactor. All catalyst-normalised NH_3 production rate data are reported with error bars representing the standard deviation computed from five consecutive gas chromatography measurements acquired under steady-state conditions at each operating point.

The relative performance improvement of the membrane reactor over the conventional reactor is defined as Equation (4.3) at identical operating condition, whereas the incremental gain attributable to increasing the number of integrated membranes from one to four is quantified by the membrane-area-normalised production rate improvement in Equation (6.3), using the NH_3 membrane area based production rate (Equation (6.2)).

These metrics are used in Section 6.5 to assess the performance of the four-membrane reactor configuration and to compare it against the single membrane baseline reported in Chapter 4. It should be noted that the two configurations differ in both membrane number and catalyst mass, with the catalyst amount and membrane area scaled approximately in proportion.

6.5 RESULTS AND DISCUSSION

6.5.1 POCS catalysts: slurry rheology and batch reproducibility

The rheological behaviour of the four slurry batches was investigated over the shear-rate range 0.1-2000 s^{-1}; the resulting dynamic viscosity curves are reported in **Figure 6.6**. All four batches exhibit a consistent pseudoplastic, shear-thinning response. At very low shear rates (~0.1-0.2 s^{-1}), the viscosity passes through a local maximum of approximately 0.08-0.10 Pa·s, attributed to the progressive breakdown of the weakly structured polymer-solvent network formed at rest. With increasing shear rate, the viscosity decreases monotonically by nearly one order of magnitude, approaching a Newtonian-like plateau of ~0.02 Pa·s above ~100 s^{-1}. This flow profile is well matched to the dip-spin coating procedure adopted in this work. The comparatively higher viscosity at low shear promotes sufficient slurry retention on the POCS struts during the dipping step, while the low plateau viscosity at high shear, representative of the spinning stage, allows excess slurry to drain freely, preventing channel blockage within the open-cell architecture and promoting a uniform catalyst

distribution across the lattice.

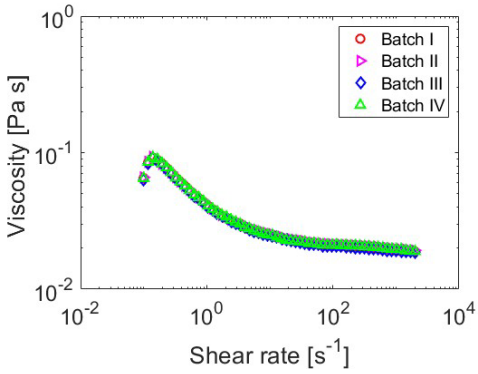


Figure 6.6 Slurry rheological behaviour

Most importantly, the curves measured for batches I-IV are superimposable across the entire shear-rate window investigated, confirming the excellent batch-to-batch reproducibility achieved by operating four 250 cm^3 zirconia jars simultaneously in the planetary mill.

6.5.2 POCS catalysts: optical characterisation

Representative optical images of the external surface of the activated POCS supports, acquired with a digital optical microscope (Keyence VHX-7000), are reported in **Figure 6.7**: the top panel refers to the Gyroid geometry and the bottom panel to the BCC. In both cases, the catalyst layer appears uniformly distributed over the metallic struts, with full surface coverage and no evidence of cracking, delamination, or localised slurry accumulation within the channels. The native architecture of each support, the smoothly curving cells of the Gyroid and the more angular periodically arranged windows of the BCC, is fully preserved after activation, and all open-cell pathways remain clearly accessible to gas flow.

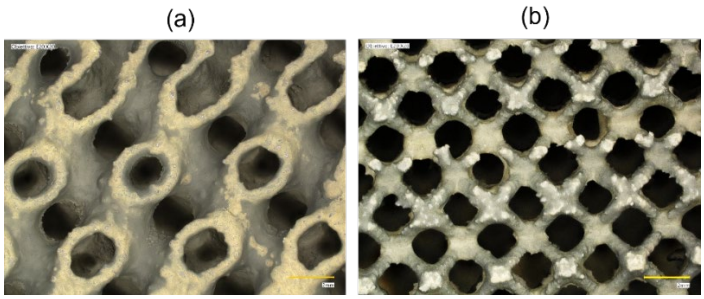


Figure 6.7 Optical images of the washcoated surface of structured catalyst supports: (a) Gyroid topology and (b) Body-centred cubic (BCC) topology

These observations confirm the effectiveness of the dip-spin coating procedure in

producing a thin, conformal washcoat on both POCS architectures. The spin-coating step proved particularly critical in this regard: rotating the wet support at 1,000 rpm efficiently removed excess slurry retained within the lattice, yielding a coating layer thick enough to meet the target loading yet thin enough to avoid pore occlusion, which would otherwise penalise flow distribution and active-site accessibility.

Notably, an identical protocol - i.e. slurry formulation, dipping time, spinning rate and acceleration, number of dip-spin cycles, and flash-drying conditions - was applied without modification to both POCS geometries, despite their markedly different topologies, and yielded comparable coating quality in both architectures. This geometry-independence demonstrates that the proposed dip-spin coating route is robust with respect to support topology and scale, and constitutes a viable and readily transferable strategy for the catalytic activation of complex metallic 3D-printed structures.

6.5.3 Chemical and structural characterisation of the CMS membrane material

The chemical composition of the novolac-based membrane material was investigated before and after carbonisation at 550 °C by organic elemental analysis, X-ray photoelectron spectroscopy (XPS), and Raman spectroscopy. The three techniques provide complementary and mutually consistent evidence of the polymer-to-carbon transformation, and their findings are discussed jointly below.

OEA reveals a marked compositional shift upon carbonisation, as summarised in **Table 6.2**. The pre-carbonised sample exhibits a carbon content of 73.9 wt%, with substantial contributions from hydrogen (6.7 wt%), oxygen (14.7 wt%), and nitrogen (4.7 wt%), consistent with the composition expected for a novolac resin incorporating an ethylenediamine crosslinker and residual NMP solvent. After carbonisation, the carbon content rises to 92.0 wt%, while hydrogen, oxygen, and nitrogen decrease sharply to 3.3, 3.8, and 0.9 wt%, respectively. The near-complete elimination of hydrogen is indicative of extensive dehydrogenation and condensation reactions during pyrolysis, while the reduction in oxygen and nitrogen reflects the thermal decomposition of phenolic hydroxyl groups, methylene ether bridges, and amine-based functionalities. The residual heteroatom content in the carbonised sample suggests that a fraction of surface oxygen and nitrogen groups survives pyrolysis. The OEA findings are corroborated by the elemental composition of the samples determined through XPS analysis (**Table 6.2**). The XPS C1s spectra provide surface-specific confirmation of the bulk compositional changes observed by the elemental analysis. In the pre-carbonised sample (**Figure 6.8**(a)), the C1s envelope is broad and asymmetric, comprising a dominant C-C component at ~284.8 eV together with C-O contribution at ~286.2 eV attributed to aliphatic esters, phenolic hydroxyl groups, and methylene ether bridges of the novolac

backbone. The C=O component at ~288.2 eV reflects carbonyl-type species, mainly the lactam carbonyl of NMP along with possible oxidised carbonyl groups formed within the phenolic backbone [2–4]. A weak shake-up satellite at ~290.5 eV, arising from $\pi \rightarrow \pi^*$ transitions in which the photoionised system is left in an electronically excited state a few electron volts above the ground state [5], confirms the presence of aromatic rings within the novolac structure. After carbonisation **Figure 6.8**(d), the C1s envelope undergoes a marked transformation: the C-C component becomes dominant, reflecting the conversion of the sp^3-rich polymer matrix to a predominantly sp^2 graphitic-like carbon network, while the C-O contribution is now positioned at ~285.6 eV and shows reduced intensity, in full agreement with the oxygen elimination observed by elemental analysis. Additionally, the C=O component is replaced by a very weak COO contribution at ~288.6 eV, indicating the evaporation of NMP and the emergence of carboxyl/ester groups formed through thermally induced rearrangements during pyrolysis [6]. The O1s spectra are coherent with the C1s curve fitting and further support the compositional changes.

Table 6.2 Elemental composition of novolac-based unsupported membrane samples before and after carbonisation at 550 °C acquired via Organic Elemental Analysis (OEA) and X-ray Photoelectron Spectroscopy (XPS). They are expressed in weight percentages (wt%) and atomic percentages (at%), respectively

Sample type	OEA wt%				XPS at%			
	N	C	H	O	C	O	N	Cu
Pre-carbonisation	4.65	73.88	6.72	14.72	74.36	22.34	3.26	0.03
Post-carbonisation	0.92	92.02	3.28	3.77	93.90	5.50	0.40	0.20

In the pre-carbonised sample **Figure 6.8**(b) the spectrum comprises the C-O contribution at ~532.9 eV associated with phenolic O-H groups and possible methylene-ether bridges, and the C=O component at ~531.5 eV corresponding to amide/lactam carbonyls from NMP together with oxidised carbonyl species formed within the novolac matrix [7,8]. After carbonisation, the total oxygen signal decreases substantially (**Figure 6.8**(e)), consistent with the reduction from 14.7 to 3.8 wt% measured by OEA and from 22.3 at% to 5.5 at% determined by XPS. The shape of the O1s spectrum changes markedly, displaying a double-peaked structure whose curve fitting resolves four distinct contributions. These include oxidised copper species (Cu_xO) at ~531 eV, a C-OH/C-O-C/C-OR component at ~532.2 eV, a COOR contribution at ~533.7 eV, and a high binding energy feature at ~534.7 eV attributed to adsorbed O_2 or moisture [9,10]. This evolution reveals the emergence of oxidised copper species, absent in the pre-carbonised sample, along with oxygen-containing surface functionalities generated during pyrolysis. Despite the very low atomic percentage of Cu in the non-carbonised sample, the Cu 2p spectrum (**Figure 6.8**(c)) still exhibits the characteristic Cu $2p_{3/2}$ and Cu $2p_{1/2}$ features [11]. The Cu

$2p_{3/2}$ peak can be satisfactorily fitted with a single component at ~933.4 eV, which is most likely associated with oxidised copper species (Cu_xO) [12].

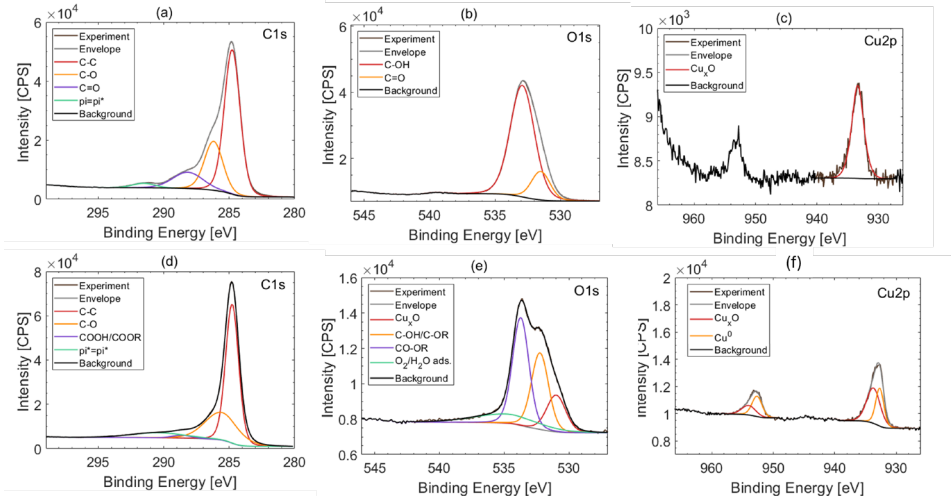


Figure 6.8 XPS spectra of pre-carbonised unsupported membrane sample of (a) Carbon, (b) Oxygen, (c) Copper and post-carbonised unsupported membrane sample of (d) Carbon, (e) Oxygen, (f) Copper

After carbonisation, the intensity of the Cu 2p peaks increases slightly, consistent with the higher Cu atomic percentage detected in the carbon matrix after pyrolysis (**Table 6.2**). The Cu 2p spectrum of the carbonised samples again displays the Cu $2p_{3/2}$ and Cu $2p_{1/2}$ doublet; however, each component now requires two sub-peaks for an adequate fit, revealing the coexistence of both metallic copper (Cu^0) and oxidised copper species (Cu_xO). According to literature assignments [9], the peaks at ~932.7 eV and ~952.6 eV correspond to Cu^0, whereas the components at ~933.7 eV and ~954.0 eV are attributed to Cu_xO. The appearance of Cu^0 components at ~932.7 eV and ~952.6 eV in the carbonised sample indicates that copper undergoes partial reduction during pyrolysis, likely promoted by the carbonaceous environment and the oxygen depleting conditions of the carbonisation process.

The degree of graphitic ordering in the two samples was assessed by Raman spectroscopy (**Figure 6.9**). The non-carbonised novolac resin exhibits only a very weak, broad hump in the 1200-1600 cm^{-1} region [13], confirming the amorphous, non-graphitic nature of the precursor and the complete absence of any sp^2 carbon ordering prior to pyrolysis. After carbonisation at 550 °C, two well-resolved bands emerge: the G band at ~1582 cm^{-1}, symbolising the presence of graphitic-like layers (in line with increase of C-C bonds in C1s spectra) and the D band at ~1357 cm^{-1}, associated with structural disorder and defects. The D band intensity is directly related to the density of aromatic sp^2 bonds located at defect sites [14]. The I_D/I_G ratio close to unity indicates a turbostratic, defect-rich carbon structure. A fully

graphitic material would exhibit a suppressed D band and a collapsed micropore network; the high D band intensity observed here confirms that the carbonisation temperature of 550 °C has been deliberately selected to produce a disordered sp^2 carbon matrix that preserves the defect-rich microporous architecture.
Taken together, the OEA, XPS, and Raman data provide a fully consistent picture of the carbonisation process: pyrolysis at 550 °C converts the oxygen- and hydrogen-rich novolac precursor into a predominantly sp^2 carbon matrix through dehydrogenation and condensation reactions.

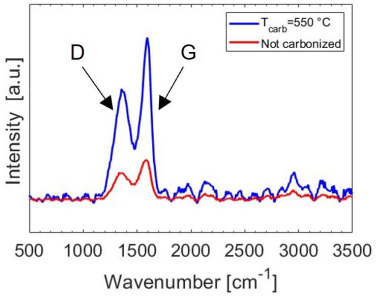


Figure 6.9 Raman spectra of pre-carbonised and post-carbonised novolac-based unsupported membrane samples

6.5.4 POCS geometry comparison in a conventional reactor: Gyroid vs. BCC performance

Prior to membrane reactor testing, the intrinsic catalytic performance of the two POCS geometries - Gyroid and BCC - was systematically assessed in the absence of membranes under two distinct space velocity conditions: WHSV = 715 $mLn \cdot g_{cat}^{-1} h^{-1}$, consistent with the operating window employed in Chapter 4, and WHSV = 3,285 $mLn \cdot g_{cat}^{-1} h^{-1}$ at higher throughput. All experiments were conducted with an understoichiometric H_2:N_2 = 2:1 molar feed ratio, across a temperature range of 350-450 °C and at operating pressures of 20-40 bar, depending on the condition.
The Ru-based catalyst washcoated onto the POCS supports was activated in situ under a H_2:N_2= 2:1 molar feed ratio at 30 bar. The activation protocol consisted of stepwise heating from ambient temperature to 200, 300, 400 and finally 550 °C, with isothermal holds at each plateau to ensure complete and reproducible reduction of the active phase before cooling to the target reaction temperature.
Under high WHSV conditions (**Figure 6.10**(a)), the NH_3 production rate increases monotonically with temperature at 40 bar for both geometries, reaching values of approximately 8 $mmol \cdot g_{cat}^{-1} h^{-1}$ at 40 bar and 450 °C, indicative of operation in a predominantly kinetically controlled regime in which the system remains appreciably far from thermodynamic equilibrium across the full temperature window investigated. At 30 bar, however, a modest but reproducible decline in production rate is observed at 450 °C for both Gyroid and BCC configurations, suggesting that

the reduced operating pressure is sufficient to bring the system into closer proximity to the thermodynamic equilibrium limit at elevated temperatures. Under low WHSV conditions (**Figure 6.10**(b)), this behaviour is markedly amplified across all pressures tested.

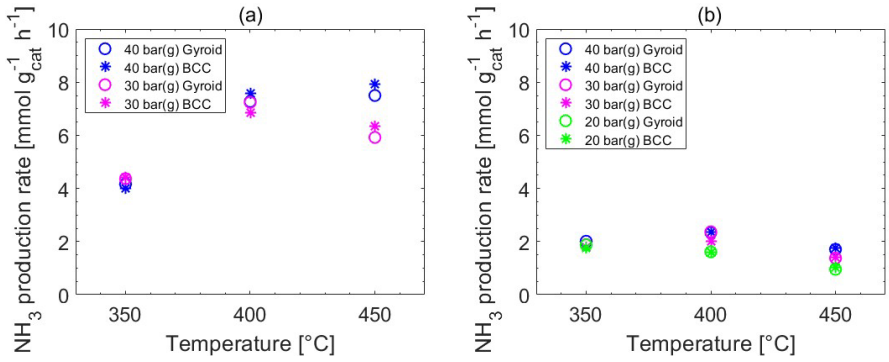


Figure 6.10 NH_3 production rate of Gyroid and BCC catalyst structures in a conventional reactor as a function of reaction temperature and pressure: (a) WHSV = 3,285 mLn·$g_{cat}^{-1}h^{-1}$; (b) WHSV = 715 mLn·$g_{cat}^{-1}h^{-1}$

A well-defined maximum in NH_3 production rate is observed at 400 °C, followed by a pronounced decline at 450 °C, a trend that is characteristic of thermodynamic control: the extended catalyst contact time associated with the lower space velocity allows the gas-phase composition to approach the equilibrium conversion, beyond which the increasingly unfavourable thermodynamics at elevated temperatures dominates over any kinetic gains. Collectively, these results demonstrate that the transition from a kinetically controlled to a thermodynamically-limited regime is governed by the compound effect of WHSV and operating pressure, with reduced pressure accelerating this transition even at conditions of elevated space velocity.

The H_2 conversion trends, reported as a function of temperature and pressure for both WHSV conditions in **Figure A.6.1**(a) and **Figure A.6.1**(b) of the Appendix, are fully consistent with the NH_3 production rate behaviour described above. Under high WHSV (**Figure A.6.1**(a)), H_2 conversion increases from approximately 5% at 350 °C to 9-10% at 400 °C, before exhibiting a slight decline at 450 °C (particularly at 30 bar), in agreement with the onset of thermodynamic limitation at lower pressures. Under low WHSV (**Figure A.6.1**(b)), conversion values are substantially higher, reaching 12-14% at 350-400 °C before declining to 6-11% at 450 °C depending on pressure, with the 20 bar condition exhibiting the most pronounced drop, consistent with the equilibrium limit being reached earliest at lower operating pressure. In both regimes, the conversion increases systematically with pressure, reflecting the thermodynamic favourability of NH_3 synthesis at elevated pressures as predicted by Le Châtelier's principle, and decreases with increasing WHSV, as the reduced residence time limits the extent of reaction.

6.5.5 POCS geometry comparison in a membrane reactor: Gyroid vs. BCC performance

The same POCS catalyst configurations were subsequently tested in the integrated membrane reactor under the two different WHSV conditions and different sweep-gas-to-feed flow ratio (SW = 1 and SW = 4), enabling continuous in-situ removal of ammonia from the reaction side and thus shifting the equilibrium beyond the thermodynamic limit of the conventional system.

Under high WHSV conditions with SW = 1 (**Figure 6.11**(a)), NH_3 production rate increases substantially compared to the conventional case, reaching values of approximately 11 mmol·$g_{cat}^{-1}h^{-1}$ at 40 bar and 450 °C, representing a relative enhancement of approximately 50% over the corresponding non-membrane case.

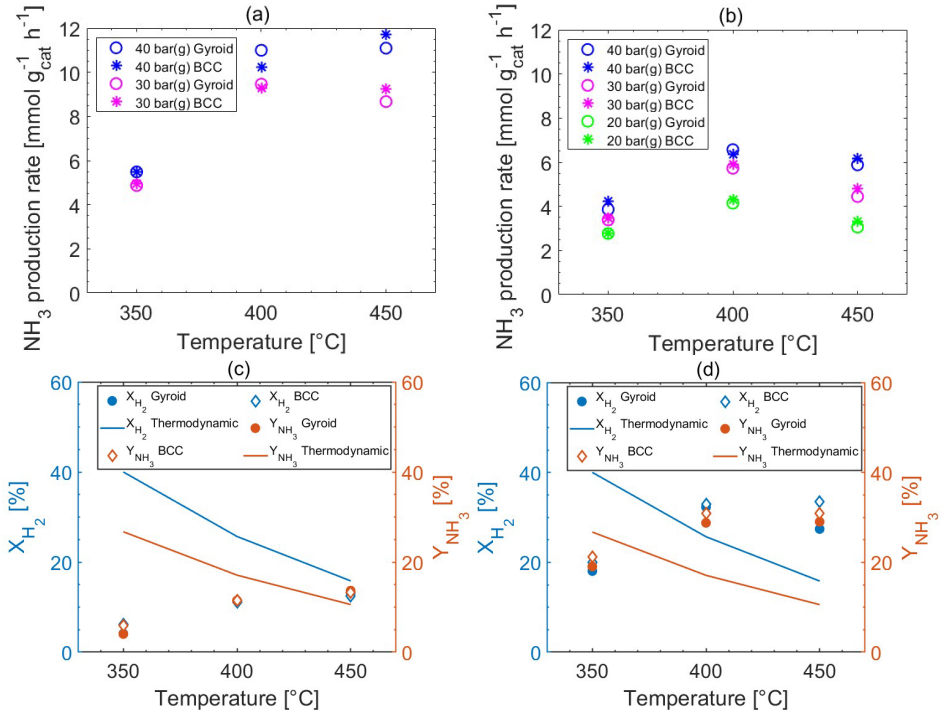


Figure 6.11 NH_3 production rate, H_2 conversion and NH_3 yield of Gyroid and BCC catalyst structures in a membrane reactor as a function of reaction temperature: (a) WHSV = 3,285 mLn·$g_{cat}^{-1}h^{-1}$, SW = 1, P = 30, 40 bar; (b) WHSV = 715 mLn·$g_{cat}^{-1}h^{-1}$, SW = 4, P = 20, 30, 40 bar; (c) WHSV = 3,285 mLn·$g_{cat}^{-1}h^{-1}$, SW = 1, P = 40 bar; (d) WHSV = 715 mLn·$g_{cat}^{-1}h^{-1}$, SW = 4, P = 40 bar

Rates increase monotonically with temperature across the full 350-450 °C range, and the physical origin of this trend is clarified by the conversion and yield data in **Figure 6.11**(c). At 350 °C, the experimental H_2 conversion is approximately 5%, against a thermodynamic equilibrium value of approximately 40%, confirming that the high

space velocity imposes insufficient contact time for the gas-phase composition to approach equilibrium. As temperature increases toward 450 °C, the experimental conversion rises to approximately 13-14%, representing an approximately 40% relative improvement over the conventional case at the same conditions, and converging toward, but remaining marginally below, the equilibrium value of approximately 15%. The operative regime shifts fundamentally under low WHSV with SW = 4 (**Figure 6.11**(b)). Although absolute production rates are lower owing to the reduced gas throughput, the H_2 conversion and NH_3 yield (**Figure 6.11**(d)) not only approach but clearly and reproducibly exceed the thermodynamic equilibrium curves at 400 °C and 450 °C. At 400 °C, the experimental H_2 conversion reaches approximately 32%, compared with an equilibrium prediction of approximately 25%, while at 450 °C the experimental conversion of approximately 30-33% stands well above the equilibrium value of approximately 16%. Expressed as relative improvements over the corresponding conventional reactor, these gains correspond to approximately 30% at 400 °C and 110% at 450 °C. The enhancement was most pronounced at the highest temperature because the equilibrium conversion was lowest under these conditions, making each increment of ammonia removed by the membrane proportionally more effective in driving the reaction forward. The consequence in terms of production rate is equally evident in **Figure 6.11**(b): the maximum rate previously observed at 400 °C in the conventional tests is substantially attenuated, and production rates remain more sustained toward 450 °C, further evidence of equilibrium displacement by the membrane.

Figure A.6.2(a)-(c) report the H_2 conversion and NH_3 yield as a function of temperature for Gyroid and BCC configurations at pressures of 20 and 30 bar, compared against the thermodynamic equilibrium curves. At high WHSV (**Figure A.6.2**(a)), all experimental values lie below the thermodynamic equilibrium across the full temperature range, confirming kinetically controlled operation at this space velocity, with the sole exception of the BCC's NH_3 yield at 450 °C, which marginally exceeds the equilibrium curve. At low WHSV and 30 bar (**Figure A.6.2**(b)), the conversion and yield values approach the equilibrium curve, while the NH_3 yield surpasses them in some cases. At a pressure of 20 bar under low WHSV (**Figure A.6.2**(c)), the approach to equilibrium is progressively reduced relative to the 30-40 bar case, as the lower operating pressure weakens the transmembrane NH_3 partial pressure gradient and therefore limits the extent of equilibrium displacement achievable by the membrane.

As observed in the conventional reactor benchmarking, reported in Subsection 6.5.4 no significant difference in NH_3 production rate, H_2 conversion, or NH_3 yield is detected between the Gyroid and BCC geometries under membrane reactor operation across any of the conditions investigated. This geometry-independence under reactive membrane conditions further confirms that both POCS architectures deliver equivalent catalytic performance because the system operates in a regime

governed by intrinsic reaction kinetics and thermodynamics rather than by geometry-dependent heat or mass transfer resistances. Consequently, the complete BCC dataset is reported in the Appendix, and the following discussion focuses exclusively on the Gyroid geometry.

6.5.6 Effect of sweep gas configuration and pressure on membrane reactor performance

To isolate and quantify the individual and combined contributions of space velocity, operating pressure, and sweep configuration on the membrane reactor performance, the Gyroid geometry is analysed in detail in this section. **Figure 6.12**(a) presents a direct comparison between conventional and membrane reactor operation under two WHSV conditions at P = 40 bar with SW = 1. At low WHSV, the membrane enhancement is already clearly established across the entire temperature range, with the membrane system consistently outperforming the conventional reactor. At high WHSV, the benefit is equally pronounced: production rates increase by approximately 35% and 47% at 400 and 450 °C, respectively, relative to the conventional baseline, with the enhancement growing with temperature as the thermodynamic driving force for NH_3 removal intensifies. Reducing the operating pressure to 30 bar (**Figure 6.12**(b)), high WHSV still yields a visible membrane benefit, with production rate increments of approximately 35% and 45% at 400 and 450 °C, respectively, confirming that the equilibrium-shift effect of the membrane persists across the explored pressure range. The recovery factor is plotted on the secondary axis of **Figure 6.12**(b) and remains in the range of approximately 35-40% across all conditions, with 40 bar operation producing a marginally higher recovery than 30 bar, owing to the greater transmembrane partial pressure gradient driving NH_3 permeation. This higher recovery directly translates into a higher total NH_3 production rate on the permeate side, confirming that operating pressure is an effective lever for maximising the membrane contribution. The corresponding trends for the BCC geometry are provided in Appendix (**Figure A.6.3**).

The reactant loss and co-feeding behaviour, quantified as the net molar imbalance of H_2 and N_2 between retentate inlet and outlet and reported in **Figure 6.12**(c), provides important additional insight into the selectivity of the membrane and the internal consistency of the mass balance. Positive values indicate net permeation of reactants from the retentate to the permeate side (reactant loss), while negative values indicate co-feeding, whereby reactants present in the sweep stream enter the retentate side through the membrane in the direction opposing the desired NH_3 flux. At low temperatures and high WHSV, the reactant loss is slightly negative (indicating co-feeding) which is physically consistent with the low NH_3 partial pressure generated at high space velocity and low temperature, where the driving force for NH_3 permeation is limited. The N_2 loss is systematically higher than the H_2 loss across all conditions, a consequence of the understoichiometric H_2:N_2 = 2:1 feed

ratio employed in this study: the higher N_2 partial pressure in the retentate relative to H_2 creates a larger transmembrane driving force for N_2 permeation, while the lower H_2 partial pressure reduces the tendency for H_2 to permeate. At 400 °C, the reactant loss increases relative to 350 °C, and the low WHSV condition exhibits a higher reactant loss than the high WHSV case, which is directly consistent with the higher conversion achieved at low WHSV (**Figure 6.12**(d)). At 450 °C, this behaviour is reversed: the high WHSV condition exhibits a slightly lower reactant loss than the low WHSV case, particularly for H_2 at 40 bar. This reversal is reflected in the convergence of the conversion values between the two WHSV conditions at 450 °C, as the low WHSV system approaches equilibrium and its conversion begins to track that of the high WHSV case.

The conversion and yield data, compared against the thermodynamic equilibrium curves in **Figure 6.12**(d), corroborate these observations. The low WHSV condition approaches the equilibrium conversion more rapidly with increasing temperature than the high WHSV case, and at 400 °C the NH_3 yield for low WHSV already surpasses the thermodynamic equilibrium value, corresponding to a 17% improvement relative to the conventional reactor at the same conditions. At 450 °C, this yield enhancement grows to approximately 44% for low WHSV, while the H_2 conversion under all conditions converges toward the equilibrium curve, with both WHSV cases approaching comparable values as the thermodynamic constraint becomes the dominant limiting factor.

The high WHSV yield approaches but does not exceed the equilibrium line, consistent with the more limited contact time and therefore less complete NH_3 permeation in the high space velocity case. Taken together, **Figure 6.12**(a)-(d) demonstrate that the membrane reactor performance is governed by a compound interplay between space velocity, operating pressure, and the thermodynamic state of the system. The results discussed so far were obtained at a sweep-gas-to-feed flow ratio of SW = 1. Because the transmembrane driving force for NH_3 permeation depends on the NH_3 partial pressure difference between the retentate and permeate sides, increasing the sweep-gas-to-feed flow ratio to SW = 4 is expected to dilute the permeate stream, maintain a larger concentration gradient across the membrane, and enhance the equilibrium-shifting effect. The effect of increasing the sweep-gas-to-feed flow ratio is examined in **Figure 6.13**(a). **Figure 6.13**(a) presents the performance of the Gyroid membrane reactor at low WHSV and SW = 4 over a broader pressure range of 20-40 bar. Across all temperatures, the conventional-reactor baseline increases modestly with pressure. The membrane enhancement is observed at every pressure and temperature and becomes more pronounced as the pressure increases from 20 to 40 bar. This pressure dependence arises from the transmembrane driving force: at higher retentate-side total pressure, the NH_3 partial pressure increases, enhancing the permeation flux through the CMS membrane and resulting in more efficient NH_3 removal.

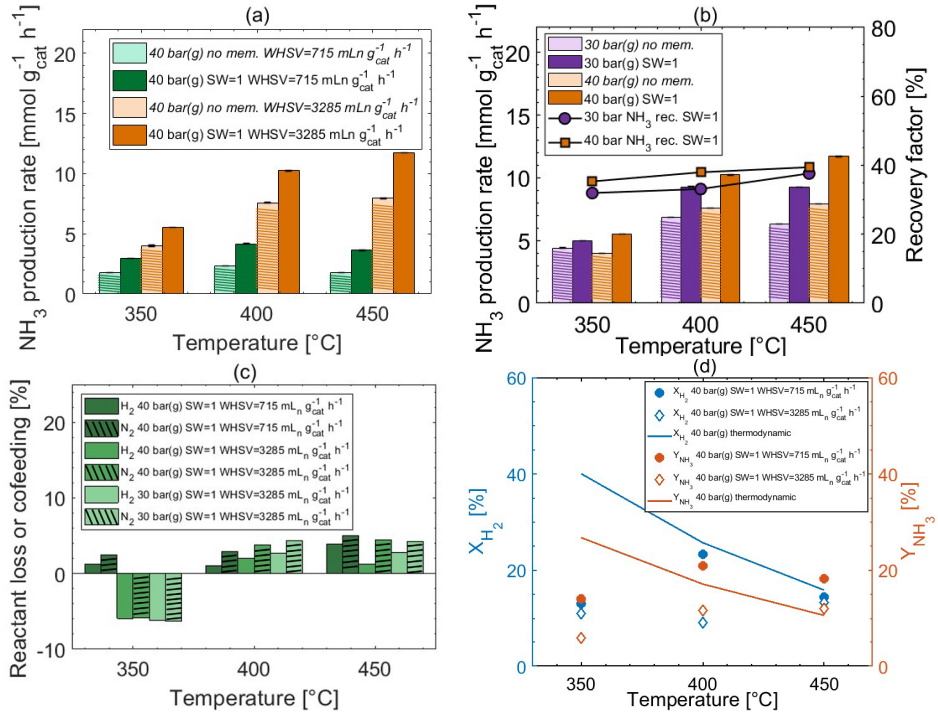


Figure 6.12 NH_3 production rate and NH_3 recovery factor of Gyroid catalyst structures as a function of temperature: comparison between conventional and membrane reactor at SW = 1 (a) Effect of WHSV at P = 40 bar; (b) Effect of operating pressure at WHSV = 3,285 $mLn \cdot g_{cat}^{-1} h^{-1}$, with NH_3 recovery factor reported on the secondary axis; (c) Effect of WHSV on reactant loss or cofeeding at P = 30, 40 bar; (d) Effect of WHSV on H_2 conversion and NH_3 yield at P = 40 bar

A non-monotonic temperature dependence is observed in the membrane reactor cases, most prominently at 40 bar, where the production rate reaches a maximum at 400 °C and slightly declines at 450 °C. This behaviour reflects the competing effects of reaction kinetics and thermodynamics: at 350 °C, slow kinetics limit conversion; at 400 °C, sufficiently fast kinetics combine with effective membrane removal to maximise production rate; at 450 °C, the unfavourable shift of the exothermic equilibrium lowers the thermodynamic driving force, partially offsetting the kinetic gain even in the presence of the membrane. The BCC analysis shows the same overall trend (**Figure A.6.4**). **Figure 6.13**(b) isolates the effect of sweep-gas-to-feed flow ratio at fixed operating conditions (P = 40 bar, low WHSV), comparing SW = 1 and SW = 4 against the conventional case. Increasing the sweep-gas-to-feed flow ratio from 1 to 4 yields a substantial enhancement in NH_3 production rate across all temperatures, with the largest absolute gain observed at 400 °C. This confirms that the permeate-side NH_3 partial pressure, governed by the sweep flow rate, is the primary rate-limiting factor for membrane-assisted equilibrium displacement under these conditions, and that further optimisation of sweep gas utilisation represents

the most impactful lever for improving membrane reactor performance. Crucially, the recovery factor reported on the secondary axis of **Figure 6.13**(b) reveals that the benefit of a higher sweep-gas-to-feed flow ratio extends beyond the reaction side: SW = 4 not only increases the production rate in the retentate but simultaneously raises the NH_3 recovery to the permeate side to approximately 75-80%, compared with approximately 55-60% at SW = 1.

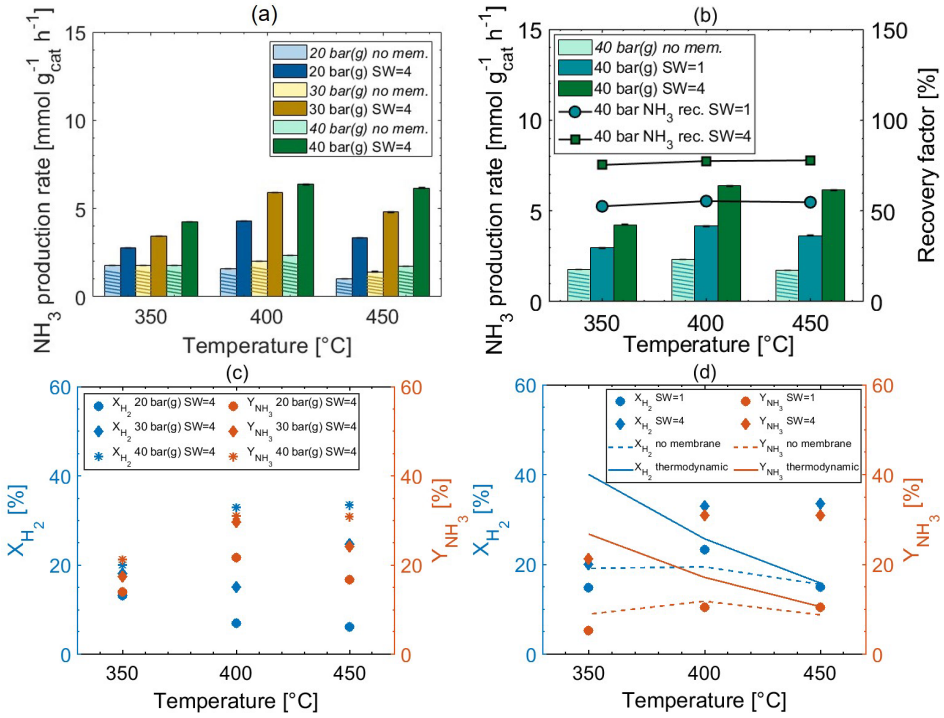


Figure 6.13 NH_3 production rate, H_2 conversion and NH_3 yield of Gyroid catalyst structures as a function of temperature at WHSV = 715 $mL_N \cdot g_{cat}^{-1} h^{-1}$: (a) effect of operating pressure at SW = 4; (b) effect of sweep-gas-to-feed flow ratio at P = 40 bar, with NH_3 recovery factor reported on the secondary axis; H_2 conversion and NH_3 yield as a function of: (c) operating pressure at SW = 4; (d) P = 40 bar, SW = 1-4, comparing the conventional membrane-free case, and the thermodynamic equilibrium limit

The H_2 conversion and NH_3 yield data, shown in **Figure 6.13**(c) as a function of temperature across the three pressure conditions at SW = 4, provide quantitative confirmation of the pressure dependence observed in the production rate trend. Both parameters increase systematically with operating pressure at all temperatures, consistent with the thermodynamic favourability of NH_3 synthesis at elevated pressures. The conversion improvement between 20 and 40 bar is most pronounced at 400 and 450 °C, where the system is thermodynamically most sensitive to pressure, while at 350 °C the kinetic limitation constrains conversion regardless of pressure and the differences between conditions are correspondingly smaller.

Figure 6.13(d) provides the most complete picture of the membrane contribution by comparing, at 40 bar, the H_2 conversion and NH_3 yield achieved under SW = 1 and SW = 4 conditions, against both the calculated thermodynamic equilibrium curves and the conventional case.

At 350 °C, none of the membrane configurations exceeds the thermodynamic equilibrium. Nevertheless, SW = 4 already delivers an NH_3 yield improvement of approximately 136% relative to the conventional case at 350 °C, while SW = 1 remains closer to the conventional case. At 400 °C, the divergence between SW = 1 and SW = 4 becomes dramatically more pronounced. The SW = 4 condition achieves an H_2 conversion improvement of approximately 30% and an NH_3 yield improvement of approximately 65% relative to the conventional reactor, with both metrics clearly surpassing not only the conventional case but also the thermodynamic equilibrium curve. By contrast, SW = 1 at 400 °C remains marginally below the thermodynamic equilibrium and performs in close proximity to the conventional reactor, confirming that a sweep-gas-to-feed flow ratio of unity is insufficient to generate the permeate-side concentration gradient necessary to drive the system beyond its thermodynamic limit. At 450 °C, both the thermodynamic equilibrium conversion and yield decrease, causing all curves to converge toward lower absolute values. In this regime, the conventional reactor and SW = 1 membrane reactor approach the equilibrium boundary from below, while the SW = 4 condition continues to track the same equilibrium trend established at 400 °C, maintaining both conversion and yield above the thermodynamic limit.

6.5.7 Influence of transmembrane ΔP on membrane reactor performance

The transmembrane pressure difference (ΔP) represents a critical additional degree of freedom in the optimisation of membrane reactor operating conditions, as it directly governs the convective contribution to the total NH_3 permeation flux. It is important to note, however, that the applicable range of ΔP in this study was subject to a significant experimental constraint arising from the high permeance and low selectivities of the CMS membrane employed. When a positive transmembrane pressure difference is imposed, the high membrane permeability induces rapid permeation of all gas species from the retentate to the permeate zone, generating a sharp pressure drop on the reaction side until the two pressures equilibrate [15]. To maintain stable operation and preserve the desired ΔP throughout each experiment, it was necessary to operate at the highest space velocity condition used in this study (WHSV = 3,285 $mLn \cdot g_{cat}^{-1} h^{-1}$), as the elevated feed flow rate provides a sufficient and continuous gas supply to the retentate zone to compensate for the permeation losses through the membrane and sustain the imposed pressure differential. For the same reason and additionally owing to the flow rate limitations of the mass flow controllers available in the experimental setup, the transmembrane pressure

difference study was conducted exclusively under SW = 1 conditions.

Figure 6.14(a) shows that at ΔP = 0 bar, the membrane reactor consistently outperforms the conventional baseline across the entire temperature range investigated, confirming the equilibrium-shift benefit of diffusion-driven NH_3 removal through the CMS membrane in the absence of any convective driving force. As ΔP increases from 0 to 3 bar, however, the NH_3 production rate decreases monotonically, and at ΔP = 3 bar it falls to values comparable to, or marginally below, the conventional reactor at 350 °C. This counterintuitive trend is attributed to the NH_3/H_2 and NH_3/N_2 non-ideal selectivity of the CMS membrane: while a positive ΔP enhances convective permeation of NH_3, it simultaneously promotes the loss of H_2 and N_2 reactants to the permeate side, depleting the reactive mixture within the retentate and reducing overall production rate. **Figure 6.14**(b) quantifies this trade-off by reporting the fractional loss of H_2 and N_2 to the permeate side as a function of ΔP and temperature.

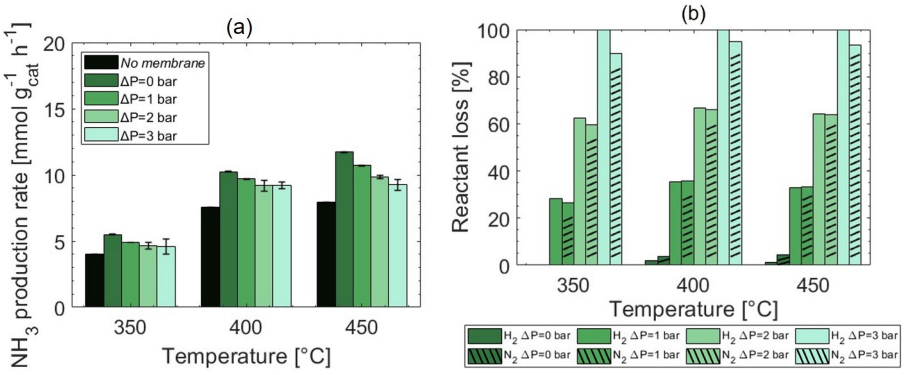


Figure 6.14 Effect of transmembrane pressure difference on the performance of Gyroid catalyst structures in a membrane reactor: (a) NH_3 production rate as a function of reaction temperature; (b) Fractional loss of H_2 and N_2 reactants to the permeate side as a function of reaction temperature. WHSV = 3,285 mLn·$g_{cat}^{-1}h^{-1}$, SW = 1, P = 40 bar, ΔP = 0-3 bar

Consistent with the relative permeance hierarchy of the CMS membrane, the fraction of H_2 lost to the permeate side is systematically higher than that of N_2 across all conditions, a consequence of the smaller kinetic diameter of H_2 (0.289 nm) relative to N_2 (0.364 nm). At ΔP = 3 bar, this non-selective convective permeation becomes severe: H_2 losses approach 100% and N_2 losses reach approximately 90%, implying that the vast majority of the reactants introduced into the retentate zone permeate through the membrane before they can participate in the catalytic synthesis reaction. The resulting stoichiometric depletion and severe imbalance of the reactive mixture in the retentate constitutes the primary cause of the NH_3 production rate decline observed in **Figure 6.14**(a). Taken together, **Figure 6.14**(a)-(b) demonstrate that, for the CMS membranes with the permeance and selectivity characteristics

employed in this study, operation at $\Delta P = 0$ represents the optimal strategy for maximising membrane reactor performance. For the BCC analysis, these tests were performed at a single pressure difference to verify whether the same trend held, and this was indeed the case: because the membrane properties were identical, the best results were again obtained at $\Delta P = 0$ (**Figure A.6.5**).

6.5.8 Scaling the membrane contribution: 1 vs. 4 membrane configuration

This section investigates the effect of scaling the integrated membrane-reactor system from one to four CMS membranes. The analysis assesses the change in total NH_3 production rate, membrane-area-normalised NH_3 production rate, and NH_3 recovery factor over the investigated operating range. The catalyst inventory and active membrane area were scaled approximately proportionally from the single- to the four-membrane configuration, thereby maintaining an approximately constant catalyst-to-membrane-area ratio. Nevertheless, the comparison represents a scale-up assessment rather than an isolated study of membrane number, because catalyst mass, membrane area, and reactor-scale transport conditions changed simultaneously.

Figure 6.15(a) reports the catalyst-normalised NH_3 production rate at SW = 4 across the full pressure range (P = 20, 30, and 40 bar), comparing the single- and four-membrane configurations. The four-membrane configuration exhibits a higher catalyst-normalised production rate throughout the investigated temperature and pressure ranges. The relative gain is most pronounced at 350 °C and decreases progressively with increasing temperature, a trend that reflects the compound effect of simultaneously increasing both the catalytic capacity and the membrane area during scale-up. In the single-membrane configuration, both the available catalytic capacity and the membrane area are lower. In the four-membrane configuration, the increased catalyst inventory provides a larger reaction capacity, while the increased membrane area provides additional NH_3-removal capacity. The resulting change in performance should therefore be interpreted as the combined outcome of these two scale-up effects and any associated changes in reactor transport. At higher temperatures, the intrinsic reaction rate increases for both configurations, and both progressively approach the same thermodynamic equilibrium. However, because the two configurations also differ in reactor geometry, flow distribution, heat transfer, and radial transport, the individual contributions of these effects cannot be isolated from the present experiments.

For the BCC geometry, experiments were conducted only at 40 bar, yet the same qualitative trend was retained, with the four-membrane configuration outperforming the single-membrane case in terms of production rate (**Figure A.6.6**).

Figure 6.15(b) extends the analysis by reporting the NH_3 production rate normalised by the total active membrane area. For each pressure condition, the four-

membrane configuration exhibits a higher membrane-area-normalised production rate than the single-membrane configuration over the investigated temperature range. Interpretation of this result requires consideration of the simultaneous changes in catalyst mass and membrane area. Although the catalyst-to-membrane-area ratio was approximately conserved, the total catalyst inventory and total membrane area were both increased during scale-up. Consequently, the higher area-normalised production rate indicates that the four-membrane configuration achieved a different overall reaction-separation performance, but it does not by itself establish an independent membrane-number effect.

The membrane-area-normalised production rate increases systematically with both temperature and pressure across both configurations, consistent with the stronger NH_3 partial pressure gradient and the higher absolute reaction rates attained at elevated operating conditions.

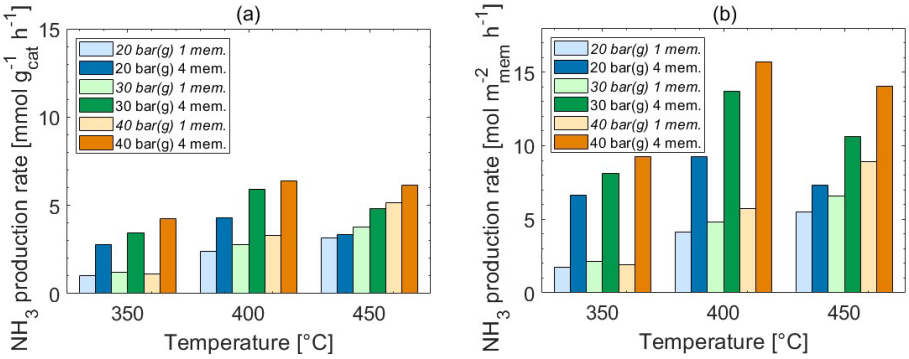


Figure 6.15 NH_3 production rate of Gyroid catalyst structures as a function of reaction temperature. Effect of scaling the number of membranes from 1 to 4: (a) Effect of pressure on catalyst-normalised production rate; (b) Membrane-area-normalised NH_3 production rate at P = 20, 30, 40 bar, SW = 4, WHSV = 715 $mLn \cdot g_{cat}^{-1} h^{-1}$ for all conditions

Table 6.3 summarises these results by reporting the percentage improvement in membrane-area-normalised NH_3 production rate and the NH_3 recovery factor upon increasing the membrane number from one to four across all explored conditions.

At P = 20 bar and SW = 4, the improvement in area-normalised production rate was 281.8% at 350 °C, 148.2% at 400 °C and 45.3% at 450 °C. The recovery factor for the four-membrane configuration increased from 51.9% to 70.3% at 350 °C and from 43.6% to 72.1% at 450 °C. At P = 30 bar, the area-normalised production rate increased by 285.6%, 192.0%, and 74.6% at 350, 400, and 450 °C, respectively. The recovery factor ranged from 59.1% to 75.6%, corresponding to a variation of less than 15 percentage points across the full temperature range. This relatively limited variation indicates that the four-membrane configuration maintained a comparatively stable NH_3 recovery as the temperature changed.

At P = 40 bar, the area-normalised production rate improvement was the highest

among the investigated pressure conditions, reaching 423.7% at 350 °C, 165.1% at 400 °C, and 64.6% at 450 °C. The recovery factor was also highest at this pressure, ranging from approximately 77.8% to 89.7% across the temperature range. This behaviour is consistent with the higher NH_3 partial pressure in the retentate and the greater transmembrane driving force at elevated pressure.

At all pressures, the percentage improvement in area-normalised production rate decreased with increasing temperature. The largest relative benefit of the four-membrane configuration was therefore observed at 350 °C, whereas the difference between the configurations became smaller at higher temperatures. This trend suggests that the single-membrane configuration already achieves greater NH_3 production and recovery at elevated temperature, leaving less scope for further improvement through the addition of three membranes. Because the catalyst inventory and membrane area were increased simultaneously, these results represent the combined effect of the scale-up and should not be interpreted as an isolated membrane-number effect.

Table 6.3 Percentage improvement in membrane-area-normalised NH_3 production rate and NH_3 recovery factor upon increasing the number of membranes from 1 to 4, as a function of temperature, pressure, and sweep-gas-to-feed flow ratio. WHSV = 715 $mLn \cdot g_{cat}^{-1} h^{-1}$

T [°C]	**P** [bar]	**SW** [−]	***Improvement of membrane area normalised NH_3 productivity*** **[%]**	***NH_3 Recovery factor*** **[%]**
350			281.8	51.9-70.3
400	20	4	148.2	43.5-72.4
450			45.3	43.6-72.1
350			285.6	68.6-72.9
400	30	4	192.0	59.7-75.6
450			74.6	59.1-74.7
350			423.7	89.7-77.3
400	40	4	165.1	89.8-77.5
450			64.6	89.7-77.8

6.6 CONCLUSIONS

This work demonstrates, for the first time, a scaled-up multi-membrane reactor for ammonia synthesis that integrates four tubular CMS membranes with two complementary 3D-printed metallic Periodic Open Cellular Structure (POCS) geometries (Gyroid and Body-centred cubic (BCC)) manufactured in Inconel 625 by Laser Powder Bed Fusion and activated with a Ru-based catalyst. This study represents a step towards higher technology readiness for dual process

intensification in ammonia synthesis. Relative to the laboratory-scale proof of concept reactor presented in Chapter 4, both the catalyst inventory and membrane area were increased, with the two quantities scaled approximately proportionally. The scalability of the dip-spin coating protocol, previously optimised on smaller Gyroid geometries, was successfully demonstrated at the larger scale for both POCS topologies, using an identical protocol for the two geometries; the larger support volume required an increased number of coating cycles to reach the higher target loading, with optical microscopy confirming the absence of cracking and delamination. The CMS membranes were produced and characterised by OEA, XPS, and Raman spectroscopy. Carbonisation at 550 °C was confirmed to convert the oxygen- and hydrogen-rich novolac precursor into a predominantly sp^2 carbon matrix through dehydrogenation and condensation reactions. XPS additionally confirmed the partial reduction of Cu^{2+} to Cu^0 during pyrolysis and the survival of thermally stable carbonyl and Cu_xO surface groups in the final membrane.

Baseline testing in the conventional reactor, conducted over a temperature range of 350-450 °C and pressures of 20-40 bar, demonstrated that the Gyroid and BCC POCS configurations deliver virtually identical catalytic performance under all explored conditions. At WHSV = 3,285 $mLn \cdot g_{cat}^{-1} h^{-1}$, NH_3 production rates increase monotonically with temperature at 40 bar, consistent with kinetically controlled operation, while a slight decline at 450 °C under 30 bar signals the onset of thermodynamic limitation at lower pressure. At WHSV = 715 $mLn \cdot g_{cat}^{-1} h^{-1}$, this thermodynamic limit is more clearly exposed at 400 °C.

Upon integration of the CMS membranes into the membrane reactor, the same geometry-independence was confirmed. The membrane consistently enhanced NH_3 production rates relative to the conventional baseline across all operating conditions. At high WHSV = 3,285 $mLn \cdot g_{cat}^{-1} h^{-1}$ with SW = 1, production rate improvements of approximately 35-47% were achieved at 400-450 °C and 30-40 bar, with the 40 bar condition delivering a marginally higher NH_3 recovery factor owing to the stronger transmembrane partial pressure gradient. However, super-equilibrium operation, in which both H_2 conversion and NH_3 yield exceeded the thermodynamic equilibrium curves, was achievable exclusively at WHSV = 715 $mLn \cdot g_{cat}^{-1} h^{-1}$ with SW = 4. Under these conditions, the H_2 conversion exceeded the thermodynamic equilibrium limit by about 30% at 400 °C and 110% at 450 °C. At the same temperature, NH_3 yield increased by 65% and 170% relative to the conventional, respectively, indicating that SW = 4 is the critical operating condition needed to unlock the full equilibrium-displacement potential of the POCS-CMS membrane reactor system. The systematic investigation of sweep-gas-to-feed flow ratio also revealed that increasing SW from 1 to 4 not only amplifies the NH_3 production rate but simultaneously raises the NH_3 recovery factor to approximately 75-80%, compared with 55-60% at SW = 1, confirming that permeate-side dilution of NH_3 is the primary lever governing the strength of equilibrium displacement.

Finally, the direct comparison between the single-membrane and four-membrane reactor configurations demonstrated clear and systematic performance improvements across all metrics. The membrane-area-normalised NH_3 production rate was consistently higher in the four-membrane configuration than in the single-membrane case at all temperatures and pressures, confirming that the system operates in a reaction-limited rather than permeation-limited regime even when four membranes are deployed simultaneously. The largest absolute improvement was recorded at 350 °C and 40 bar, where the membrane-area-normalised production rate increased by 424% relative to the single-membrane baseline.

A.6 APPENDIX

A.6.1 Supplementary tests

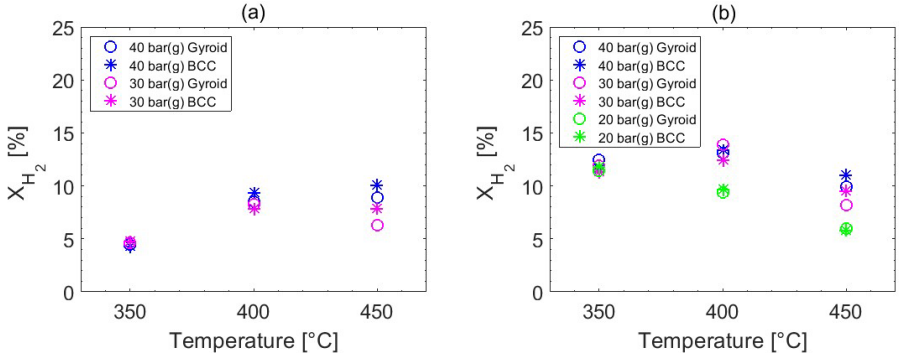


Figure A.6.1 H_2 conversion of Gyroid and BCC catalyst structures in a conventional reactor as a function of reaction temperature and pressure: (a) WHSV = 3,285 $mLn \cdot g_{cat}^{-1} h^{-1}$, (b) WHSV = 715 $\cdot mLn \cdot g_{cat}^{-1}\ h^{-1}$

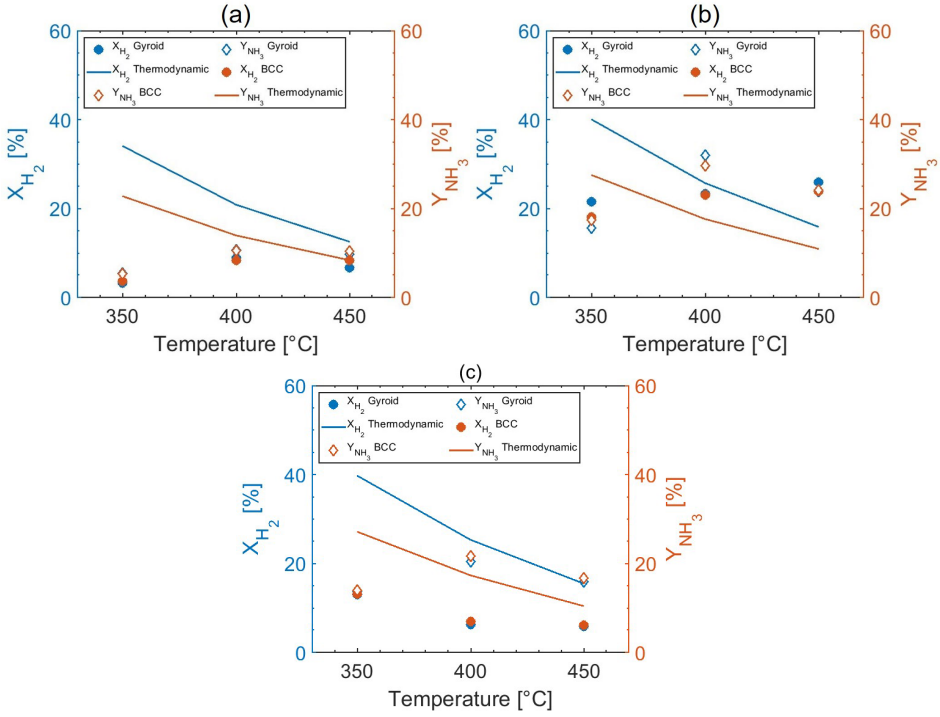


Figure A.6.2 H_2 conversion of Gyroid and BCC catalyst structures in a membrane reactor as a function of reaction temperature: (a) WHSV = 3,285 $mLn \cdot g_{cat}^{-1} h^{-1}$, SW = 1, P = 30 bar; (b) WHSV = 715 $mLn \cdot g_{cat}^{-1} h^{-1}$, SW = 4, P = 30 bar; (c) WHSV = 715 $mLn \cdot g_{cat}^{-1} h^{-1}$, SW = 4, P = 20 bar

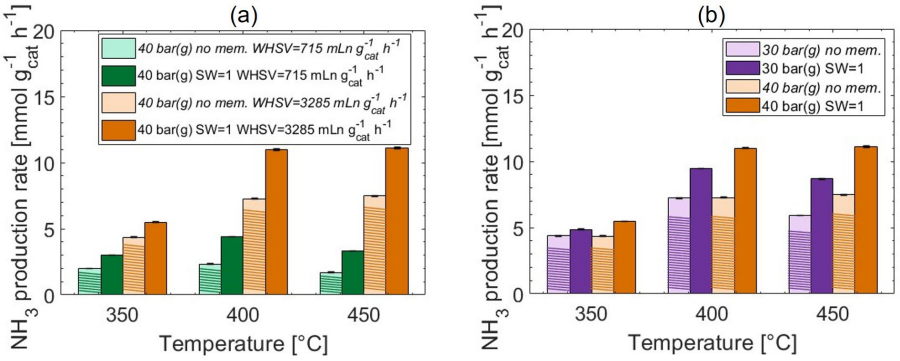


Figure A.6.3 NH_3 production rate of BCC catalyst structures as a function of temperature: comparison between conventional and membrane reactor at SW = 1 (a) Effect of WHSV at P = 40 bar; (b) Effect of operating pressure at WHSV = 3,285 mLn·$g_{cat}^{-1}h^{-1}$, with NH_3 recovery factor reported on the secondary axis

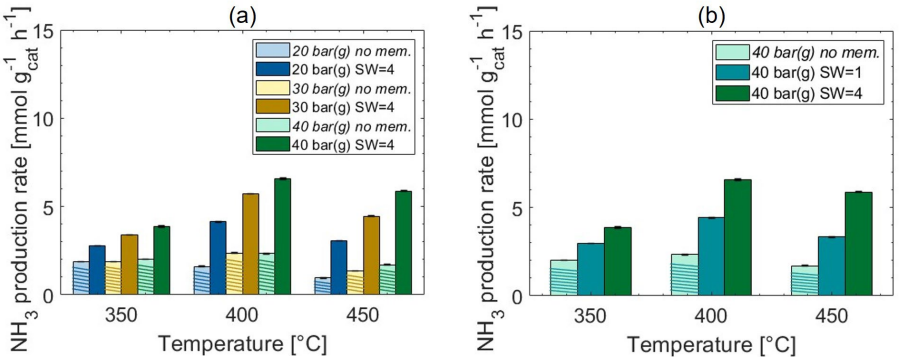


Figure A.6.4 NH_3 production rate of BCC catalyst structures as a function of temperature at WHSV = 715 mLn·$g_{cat}^{-1}h^{-1}$: (a) Effect of operating pressure at SW = 4; (b) Effect of sweep-gas-to-feed flow ratio at P = 40 bar

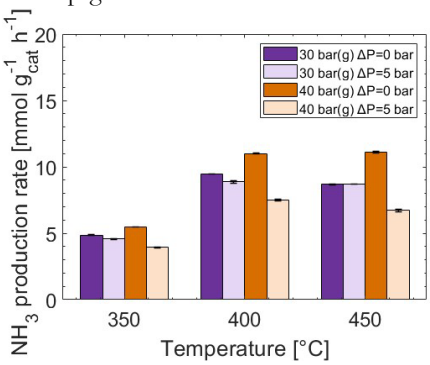


Figure A.6.5 NH_3 production rate of BCC catalyst structures as a function of transmembrane pressure difference and temperature at WHSV = 3,285 mLn·$g_{cat}^{-1}h^{-1}$, SW = 1 , P = 40 bar

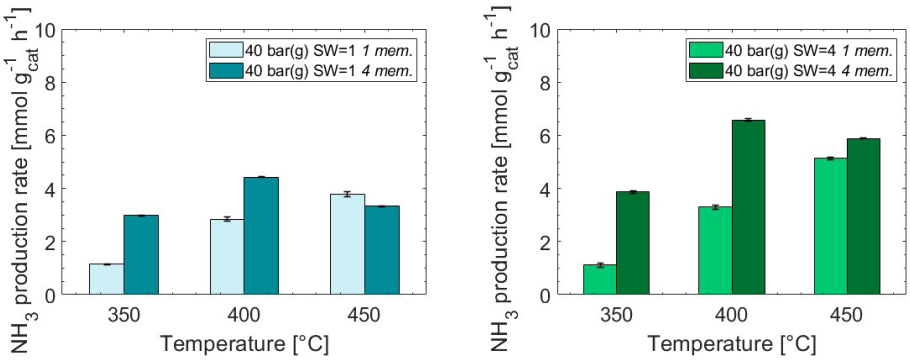


Figure A.6.6 NH_3 production rate of BCC catalyst structures as a function of reaction temperature. Effect of scaling the number of membranes from 1 to 4: (a) SW = 1 , P = 40 bar, WHSV = 715 mLn·$g_{cat}^{-1}h^{-1}$; (b) SW = 4 , P = 40 bar, WHSV = 715 mLn·$g_{cat}^{-1}h^{-1}$

REFERENCES

[1] C. Italiano, G. Marino, M. Thomas, B. Hary, S. Nardone, S. Richard, A. Saker, D. Tasso, N. Meynet, P. Olivier, F. Gallucci, A. Vita, "Carbon-Free H2 Production from Ammonia Decomposition over 3D-Printed Ni-Alloy Structures Activated with a Ru/Al2O3 Catalyst", *Processes* 2024, Vol. 12, Page 2663 12 (2024) 2663. https://doi.org/10.3390/pr12122663.

[2] X. Chen, X. Wang, D. Fang, "A review on C1s XPS-spectra for some kinds of carbon materials", *Fullerenes Nanotubes and Carbon Nanostructures* 28 (2020) 1048–1058. https://doi.org/ 10.1080/1536383X.2020.1794851.

[3] M. Quintana, K. Spyrou, M. Grzelczak, W.R. Browne, P. Rudolf, M. Prato, "Functionalization of Graphene via 1,3-Dipolar Cycloaddition", *ACS Nano* 4 (2010) 3527–3533. https://doi.org/10.1021/nn100883p.

[4] P. Stathi, D. Gournis, Y. Deligiannakis, P. Rudolf, "Stabilization of Phenolic Radicals on Graphene Oxide: An XPS and EPR Study", *Langmuir* 31 (2015) 10508–10516. https://doi.org/10.1021/acs.langmuir.5B01248.

[5] J. Moulder, W. Stickle, W. Sobol, K.D. Bomben, Handbook of X-Ray Photoelectron Spectroscopy, (1992).

[6] M. Smith, L. Scudiero, J. Espinal, J.S. McEwen, M. Garcia-Perez, "Improving the deconvolution and interpretation of XPS spectra from chars by ab initio calculations", *Carbon*, 110 (2016) 155–171. https://doi.org/10.1016/j.carbon.2016.09.012.

[7] T. Kato, Y. Yamada, Y. Nishikawa, H. Ishikawa, S. Sato, "Carbonization mechanisms of polyimide: Methodology to analyze carbon materials with nitrogen, oxygen, pentagons, and heptagons", *Carbon,* 178 (2021) 58–80. https://doi.org/10.1016/j.carbon.2021.02.090.

[8] K. Ishimaru, T. Hata, P. Bronsveld, D. Meier, Y. Imamura, "Spectroscopic analysis of carbonization behavior of wood, cellulose and lignin", *Journal of Materials Science* 1 42 (2006) 122–129. https://doi.org/10.1007/S10853-006-1042-3.

[9] A. Roy, A.K. Mukhopadhyay, S.C. Das, G. Bhattacharjee, A. Majumdar, R. Hippler, "Surface Stoichiometry and Optical Properties of Cux–TiyCz Thin Films Deposited by Magnetron Sputtering", *Coatings* 9, (2019) 551. https://doi.org/10.3390/coatings9090551.

[10] A. Hu, G. Chen, A. Huang, Z. Cai, T. Yang, C. Ma, L. Li, H. Gao, J. Gu, C. Zhu, Y. Wu, X. Qiu, J. Xu, J. Shen, L. Zhong, "o-phenylenediamine Derived Fluorescent Carbon Quantum dots for Detection of Hg(II) in Environmental Water", *Journal of Fluorescence* 34 (2023) 905–913. https://doi.org/10.1007/S10895-023-03331-Y.

[11] T. Ghodselahi, M.A. Vesaghi, A. Shafiekhani, A. Baghizadeh, M. Lameii, "XPS study of the Cu@Cu2O core-shell nanoparticles", *Appl. Surf. Sci.* 255 (2008) 2730–2734.

https://doi.org/10.1016/j.apsusc.2008.08.110.

[12] D. V. Sivkov, O. V. Petrova, S. V. Nekipelov, A.S. Vinogradov, R.N. Skandakov, S.I. Isaenko, A.M. Ob'edkov, B.S. Kaverin, I. V. Vilkov, R.I. Korolev, V.N. Sivkov, "The identification of cu–o–c bond in cu/mwcnts hybrid nanocomposite by xps and nexafs spectroscopy", *Nanomaterials* 11 (2021) 2993. https://doi.org/10.3390/nano11112993.

[13] T.H. Ko, W.S. Kuo, Y.H. Chang, "Raman study of the microstructure changes of phenolic resin during pyrolysis", *Polym. Compos.* 21 (2000) 745–750. https://doi.org/10.1002/pc.10229.

[14] S. Theodoropoulou, D. Papadimitriou, L. Zoumpoulakis, J. Simitzis, "Optical properties of carbon materials formed by pyrolysis of novolac-resin/biomass composites", *Diam. Relat. Mater.* 13 (2004) 371–375. https://doi.org/10.1016/j.diamond.2003.11.057.

[15] S. Poto, M.A. Llosa Tanco, D.A. Pacheco Tanaka, M.F. Neira d'Angelo, F. Gallucci, "Experimental investigation of a packed bed membrane reactor for the direct conversion of CO2 to dimethyl ether", *Journal of CO2 Utilization* 72 (2023) 102513. https://doi.org/10.1016/j.jcou.2023.102513.

CHAPTER 7

Techno-economic analysis of a small-scale green ammonia plant: conventional vs. membrane-assisted process

ABSTRACT:
Building on earlier work showing that PBMR can enhance PtA efficiency but are still constrained by a condensation-dominated separation section, the present chapter examines a PBMR coupled with Zeolite-13X adsorption as an alternative for small-scale, low-pressure green ammonia production. A conventional PBR and a PBMR flowsheet are each optimised in two stages: first with respect to operating window and reactor geometry, and then with respect to membrane- and adsorption-specific parameters, using a techno-economic framework that combines the 1D reactor model from Chapter 2 with process-level mass and energy balances. The final PBMR design (L_r/D_r^i = 3, SW = 0.67, $y_{H_2,in}^P$ = 0.9) achieves a levelized cost of ammonia (LCOA) of 2,793 €·$t_{NH_3}^{-1}$, representing a 5.6% reduction relative to the optimised PBR, which yields 2,958 €·$t_{NH_3}^{-1}$. The PBMR also improves power-to-ammonia efficiency by 20% (32.4 vs. 26.9) and increases per-pass H_2 conversion (20.1% vs. 15.6%). These gains arise from moderate reductions in both capital cost (4.3%) and operating cost (7.1%), particularly in the separation section. The identical Cold Gas Efficiency of both configurations (84.3%) indicates that the PBMR advantage results from reduced separation loads and improved loop performance rather than differences in whole-plant feedstock utilisation. At the production scale considered, both LCOA values remain above green-ammonia benchmarks but are comparable to those reported for similarly sized plants. Sensitivity analysis identifies hydrogen price as the principal economic driver, with LCOA varying by approximately ±55%, highlighting the importance of renewable-hydrogen costs for small-scale green ammonia systems incorporating membrane reactors.

This chapter is based on the following journal article:
"Techno-economic analysis of a small-scale green ammonia plant: conventional vs. membrane-assisted process", **I. Gargiulo**, M. den Hartog, A. Evtimova, V. Cechetto, F. Gallucci, *In preparation.*

7.1 INTRODUCTION

The integration of selective membranes in catalytic membrane reactors (CMRs) has been widely proposed as a strategy to intensify ammonia synthesis and reduce the energy demand of Haber-Bosch-type processes. However, despite substantial work at the material and reactor scale, only a limited number of studies have assessed membrane-assisted ammonia synthesis at the process level. At industrial scale, ammonia is conventionally separated by condensation at the process operating pressure of typically 100-200 bar [1]. Condensation temperatures range from about 11.5 °C at 300 bar to -10.5 °C at 100 bar and -26.0 °C at 50 bar [2], implying large temperature or pressure swings between the reactor outlet and the separation section in small-scale, lower-pressure plants. For the small-scale ammonia synthesis plant considered here (reactor outlet around 400 °C and 50 bar), such drastic changes would significantly increase both operating and capital costs. In our previous work investigating green ammonia synthesis process with membrane reactors [3], we showed that integrating a packed bed membrane reactor within the synthesis loop can increase the overall PtA efficiency by approximately 8% with respect to a conventional PEM-based reference process, and by up to about 15% when combined with solid-oxide electrolysis, while maintaining a comparable levelized cost of ammonia (LCOA) when condensation is retained as the final purification step. These results confirm that membrane reactors are a promising option for green ammonia production from renewable hydrogen but also highlight that their full potential is not yet realised at the process scale, as conventional cryogenic condensation still dominates the separation section. That work recommended that future work should explore separation techniques compatible with milder operating conditions, such as adsorption. Building on these insights, the present chapter investigates adsorption-based separations as a complement to membrane reactors, with the aim of replacing the condensation step in small-scale, low pressure PtA plants. Several authors have identified the separation step as a key economic bottleneck in lower-pressure or small-scale ammonia plants. Yoshida et al. showed that, at small production scales, the economic trade-off of operating at lower pressure is dominated by the cost of the ammonia separation section, particularly at low capacities [2]. Lin et al. compared a conventional small-scale Haber-Bosch flowsheet, with condensation at 150 bar, to an alternative configuration using absorption at about 20 bar, and reported CAPEX reductions exceeding 2.5 M$ and OPEX reductions above 1.5 M$ due to the avoidance of very high pressures [1]. Regarding sorbent choice, experimental and modelling studies on ammonia adsorption indicate that zeolitic materials offer high capacity and good stability under relevant conditions. Tokushige and co-workers [4] investigated ammonia adsorption-desorption on various zeolites at 473 K using a pressure-swing protocol between 1 and 5 bar, and found that larger pore size increases adsorption capacity

and that sodium cations strongly promote NH_3 uptake. Numerical simulations of different zeolite frameworks show that structures with larger pore volume, such as FAU or LTA, exhibit higher NH_3 capacities, with FAU-type materials recommended when maximizing NH_3 recovery. Helminen et al. [5] compared several isotherm models for ammonia adsorption on common sorbents over 1-100 kPa and 298-393 K, concluding that the Langmuir-Freundlich model combined with van 't Hoff and thermal expansion expressions provides the most accurate fit for Zeolite-13X. Yuan et al. showed that ammonia reversibility on zeolites with Brønsted and Brønsted/Lewis acid sites improves at temperatures above 423 K, meaning chemisorbed ammonia can desorb more readily in the absence of gas-phase ammonia [6]. Molecular simulations by Patel et al. reported NH_3 selectivities of 13-16 over H_2/N_2 mixtures in bulk MFI zeolite at 373 K and 1-8 bar, with selectivity increasing at higher pressures [7]. Considering commercial availability, thermal stability, and reported selectivity, Zeolite-13X is chosen as the sorbent material in this study.

This chapter presents a techno-economic comparison between a conventional packed bed ammonia synthesis process and a multi-membrane reactor as an alternative for small-scale green ammonia production.

7.2 METHODOLOGY

The overall process layouts were developed in Aspen Plus V14 to determine mass and energy balances, while the reactor units were modelled using the 1D model developed in Chapter 2 and implemented in Python. In both the process and reactor simulations, the Peng-Robinson equation of state was adopted, consistent with previous studies on ammonia synthesis systems [3,8,9]. The analysis investigates key process-intensification strategies - namely the sweep-gas-to-feed flow ratio, the pressure difference across the membrane, and the adsorption-based separation conditions (adsorption and desorption temperatures) - to identify the operating conditions that maximize NH_3 recovery and plant efficiency while minimizing the levelized cost of ammonia (LCOA). Subsequently, the impact of capital investment (CAPEX) and operating expenses (OPEX) on the LCOA is quantified, and sensitivity analyses on key cost drivers, such as hydrogen price, membrane cost, and adsorption-based separation strategy, are performed to identify the conditions under which the membrane-assisted process could become competitive. Finally, the resulting LCOA is benchmarked against current and projected ammonia market prices to assess the commercial viability of the proposed process.

7.2.1 Process design choice and system boundaries

The aim of this chapter is to design a green ammonia production plant with a nominal capacity of 350 $kmol \cdot h^{-1}$ NH_3, operated for 8,000 $h \cdot y^{-1}$ (capacity factor

~0.91) with a plant lifetime of 25 years. The process considered is a small-scale ammonia synthesis plant using either a conventional packed bed reactor or a multi-membrane reactor configuration.

- **Plant capacity and product purity:** according to the Ammonia Energy Association, commercial/agricultural-grade ammonia (C-grade) requires 99.5% purity, while refrigerant-grade (R-grade) requires 99.98%; fuel applications are expected to tolerate lower purity, so targeting 99.5 vol% ensures that the product meets C-grade requirements and remains suitable for fuel use [10].
- **Scale rationale and green-hydrogen constraint:** Yoshida et al. [2] reported the total cost of ammonia plants as a function of production capacity, operating pressure, and catalyst type, and showed that, for a facility operated at 50 bar with a ruthenium catalyst, the economic optimum lies around 100 $t \cdot d^{-1}$ (~33 $kton \cdot y^{-1}$) roughly one-third of the maximum capacity that could be reached with the available green hydrogen. For comparison, one of the largest installed electrolysers to date is an alkaline unit in China with a capacity of 300 MW, corresponding to approximately 20 $kton_{H_2} \cdot y^{-1}$ [11]; this highlights that truly large-scale green hydrogen supply remains limited and supports focusing on distributed, lower-capacity ammonia plants like the one studied here.
- **Location and cooling utilities**: the plant is assumed to be in Germany, selected for its high installed renewable energy capacity and the availability of detailed techno-economic data. As of 2025, Germany has by far the largest renewable capacity in the European Union (160 GW), more than double that of Spain (88 GW), which provides a realistic context for sourcing green electricity to produce hydrogen [12]. The site is assumed to be adjacent to a river supplying cooling water at 20 °C, with cooling water returned at 25 °C.
- **Feed streams and inlet conditions**: green hydrogen is treated as an external feedstock to the ammonia synthesis plant. Hydrogen production (electrolysis) is therefore excluded from the scope of the process model, and the cost of hydrogen is incorporated as a fixed contribution to the operating expenses (OPEX) based on the 2025 average price for renewable-powered electrolysis in Germany (8.6 $€ \cdot kg^{-1}$) [13]. Hydrogen is produced externally, stored on site with a buffer capacity of 24 hours, and fed to the ammonia synthesis section at 30 bar and 342 K. Nitrogen is produced on site via a cryogenic distillation air separation unit, designed following literature proposals for small-scale ammonia plants, and is fed to the process at 50 bar and 273 K, consistent with typical cryogenic distillation outlet conditions.
- **Inside battery limits (ISBL)**: within this process scope, the modelled plant includes hydrogen storage, on-site nitrogen production, the conventional or membrane reactor section, ammonia purification from both retentate and permeate streams via adsorption columns, the heat-exchanger network, ammonia storage container, and reactant recycle loops on both sides of the membrane.

- **Outside battery limits (OSBL)**: the supporting utilities outside the core process scope comprise the cooling-water system and the high-pressure steam generation system. Electricity is assumed to be supplied from the grid and its cost is accounted for in the OPEX; no maintenance for the container for ammonia is considered.

7.2.2 Process design modelling

- **Reactor design and sizing**: The reactor models for both the conventional and membrane-assisted configurations are based on a one-dimensional, steady-state pseudo-homogeneous plug-flow formulation implemented in Python, directly adapted from the model developed in Chapter 2 and coupled to the process model in Aspen Plus. The model assumes no internal diffusion limitations, no external mass-transfer limitations, and no temperature gradients at the particle scale or in the radial direction of the reactor, assumptions that are supported by the analysis reported in Chapter 5. In line with these assumptions, the radial phenomena are simplified by adopting a square geometry for the tube arrangement and a tube-pitch spacing of 0.04 m, which limits radial maldistribution and justifies treating the reactor as radially uniform at the scale of the model. The reaction kinetics follow the Temkin-type rate expression reported in Equation (2.1), accounting for the Ru/C catalyst [14]. Axial material balances for each component in the retentate and permeate phases are described by Equation (2.2-2.3), with the membrane transport represented through a permeance-based flux expression; the flux is calculated according to Equation (2.4) with a positive pressure difference defined from the retentate to the permeate side so that the model captures generic pressure-driven membrane separations for NH_3 recovery. The dimensionless groups used to characterize heat and mass transfer (Reynolds, Prandtl, Nusselt, and related correlations) are defined in Equation (2.8-2.13) and all thermophysical properties of the gas mixtures (density, viscosity, heat capacity, and thermal conductivity) are evaluated as specified in Appendix A.2.9. Pressure drop along the catalytic bed is estimated using the Ergun equation, (Equation (2.16)), applied to the retentate side only, while the permeate pressure is assumed constant; the full set of modelling assumptions adopted for the reactor description is summarised in Chapter 2. To mitigate hot spots, quartz particles are added to the catalyst bed with a volumetric dilution factor of 2/3, and an average particle diameter (d_p) of 3 mm is assumed for both catalyst and diluent. The solid volume distribution (ε_S) is set to 0.6 m^3_{solid} $m^{-3}_{reactor}$. The membrane module of the PBMR consists of CMS membranes which have been already investigated in previous chapters. Chapter 3 showed that the experimentally obtained CMS membrane performance for ammonia synthesis conditions was still sub-optimal and that further membrane development is required before a fully realistic industrial implementation is possible; nevertheless, the permeance values targeted in Chapter 2 are used here as a representative

performance target for the techno-economic assessment. Furthermore, in our previous study [3], we already found out that the recovery factor and the degree of conversion tend to be independent from the ammonia/hydrogen selectivity beyond a threshold of 10-20. In this study, the membrane permeances of H_2, N_2 and NH_3 are therefore taken from the Chapter 2 characterisation and applied as idealised membrane properties within the PBMR model.

The base-case operating pressure for the conventional reactor is set to 50 bar, in line with the techno-economic reference by Yoshida et al., who showed that Ru-based catalysts perform significantly better than iron catalysts under milder pressures, and with the conditions analysed in Chapter 2. The conventional process differs from the industrial Haber-Bosch process since the synthesis section consists of a single packed bed reactor rather than three beds in series; this simplification allows a more direct and fair comparison with the multi-tubular membrane reactor configuration. Matching one conventional bed with one membrane-reactor module provides a suitable basis for assessing the effect of membrane integration, while keeping all other unit operations unchanged. This choice is also consistent with the small, distributed scale targeted throughout the chapter: the interstage cooling and quenching hardware that justifies multi-bed staging pays off once the resulting efficiency gain, which scales with total reactor throughput, outweighs the added heat-exchanger, piping and control complexity, a trade-off that is markedly more favourable at world-scale single-train capacities (2,000-3,670 $t \cdot day^{-1}$ [15,16]) than at the scale considered here. Industrial multi-bed Haber-Bosch converters use this staging because ammonia synthesis is an equilibrium-limited, exothermic reaction. As conversion increases, the temperature corresponding to the maximum reaction rate decreases, defining a "locus of maximum reaction rates" that a single adiabatic bed cannot follow because its temperature increases monotonically along the reactor length [17]. In this chapter, both configurations are operated adiabatically at the shell level, while heat transfer between the retentate and permeate sides is explicitly accounted for in the PBMR.

For the PBMR, an initial low gradient in total pressure $\Delta P = 20$ bar between reaction and permeation zones is selected to ensure selective removal of ammonia while retaining reactants in the reaction zone. To the same end, the reactants (with an overall understoichiometric ratio of 1.5:1 in the feed) are circulated in the permeation zone as a co-current sweep gas, increasing the driving force for permeation without excessively depleting the retentate. The sweep-gas-to-feed flow ratio SW, is another parameter controlling the driving force for ammonia removal: in Chapter 2 a value of SW = 6 was found to be effective for simultaneous removal of ammonia and heat from the reaction

environment, but it required excessive H_2 make-up for sweep-gas recirculation. Since hydrogen has been identified as a critical cost driver in ammonia synthesis processes, this study adopts lower sweep-gas ratios to reduce hydrogen consumption while relying on heat exchange and reactor design to manage temperature.

Both the PBR and PBMR are sized to achieve the target production rate. The reactor operating conditions (pressure, temperature and geometry) are first optimised for the conventional packed bed reactor; the PBMR is then evaluated under the same inlet conditions, and a sensitivity analysis is performed to determine the optimal normalised membrane area and sweep-gas configuration. In the Python implementation, the gas hourly space velocity (GHSV) is adjusted iteratively to meet the desired plant-scale productivity, ensuring consistency between the detailed reactor model and the overall process design.

- **Nitrogen production**: Nitrogen production technologies are well researched and industrially available. Cameli et al. performed a SWOT analysis of cryogenic distillation, Pressure Swing Adsorption (PSA) and Polymeric Membranes (PM) for N_2 production in a small-scale NH_3 synthesis plant. A key requirement for the nitrogen feed is very high purity, since even small amounts of oxygen can contaminate and deactivate the synthesis catalyst; this condition effectively excludes PM, because the achievable purity is insufficient, and makes PSA less attractive due to its transient operation, which does not match the continuous nature of the ammonia process. In contrast, cryogenic distillation is a mature technology that can deliver high-purity N_2 and valuable side products such as pure O_2, and is therefore selected in this work as the nitrogen-production route [18].

  The production capacity of the cryogenic distillation section (**Figure 7.1**) is sized to supply the required N_2 feed for both the conventional and membrane-assisted process configurations. The column design is based on the proposal by Cameli et al. for a similar production scale, including approximately 30 stages, a per-stage pressure drop of 0.005 bar, a condenser pressure of 5.5 bar, feed introduction above stage 25, and a boil-up ratio of 6.83. Their reference column operates at 6 bar, which leads to a condenser outlet temperature of −177.9 °C and would require a refrigerant at least 5 °C colder, severely limiting the choice of refrigerants and necessitating an additional deep-cold refrigeration step. To alleviate this constraint, the distillation column in this study is operated at somewhat higher pressure, which increases the condenser temperature to -163 °C and reduces the severity of the refrigeration requirements.

  Refrigerants for the cryogenic system are selected based on both thermodynamic properties and environmental impact. Potential refrigerants capable of reaching -168 °C (i.e., a 5 °C temperature approach to the -163 °C

condenser) include N_2 (critical temperature -146.96 °C, boiling point -195.81 °C), CH_4 (critical temperature -82.55 °C, boiling point -161.95 °C) and CF_4 (critical temperature -45.65 °C, boiling point -128.05 °C). Based on their boiling points, CH_4 and CF_4 would need to be operated under vacuum to reach the required low temperature, while the critical temperature of N_2 is only 15 °C above the condenser temperature, implying that a first refrigeration loop using N_2 would provide a limited temperature lift and is therefore not considered further as a refrigerant. Among CH_4 and CF_4, both have zero ozone-depletion potential (ODP), but CF_4 has a global warming potential (GWP) more than 200 times higher than CH_4, making methane the preferred choice from an environmental perspective [19]. Following the three-stage refrigeration concept proposed by Johnson et al. [20], methane, ethane/ethylene and propylene are used as refrigerants in successive loops to reach -163 °C. In the first loop, methane is chosen as the refrigerant, with its evaporator pressure further reduced relative to the Johnson et al. design to achieve the required low temperature for the N_2 condenser. For the second loop, ethane and ethylene are both viable options; Johnson et al. recommend ethylene, but ethane has a slightly higher latent heat of vaporisation ($\Delta H_{vap}^{-88.3°C}$ = 488 kJ·kg^{-1}) compared to ethylene ($\Delta H_{vap}^{-104°C}$ = 483 kJ·kg^{-1}), which means less ethane is required to deliver the same cooling duty, reducing compression work despite its higher boiling point and the associated need for vacuum operation. Given their low GWP and zero ODP, ethane is selected as the second-loop refrigerant [21,22]. For the third loop, propylene is chosen as the refrigerant; it is an established industrial refrigerant with zero ODP, low GWP [23], and is recommended by Johnson et al. for reaching -163 °C in a three-stage cycle [20].

In industrial applications, refrigerants are efficiently utilised through closed refrigeration loops to optimize their performance. These loops typically consist of four stages: evaporation, compression, condensation and expansion. A low-temperature, low-pressure liquid refrigerant first passes through an evaporator (heat exchanger), where it absorbs heat from the process stream and undergoes a phase change to vapour. The vapour is then compressed to a higher pressure, at which its condensation temperature is correspondingly higher, and subsequently condensed in a condenser (heat exchanger), releasing heat to a cooling medium such as air or cooling water. Finally, the condensed refrigerant is expanded through a throttle or expansion valve back to the original low pressure at the evaporator, closing the cycle.

In this work, the three-stage refrigeration system for the air-separation unit is implemented as three distinct vapour-compression loops, each using a different refrigerant and represented in Aspen Plus by a dedicated process flow diagram (PFD) (**Figure A.7.1**). In the PFD, the loops are distinguished

by colour coding corresponding to the specific refrigerant, and phase transitions are indicated by additional colour cues (green for liquid streams and yellow for vapour streams). Consistent with the ASU flowsheet, the stream passing through EVAP-201 represents the total cooling duty required for HX-106 and HX-107. The main refrigeration duties in the methane loop are modelled through heat exchangers HX-201, HX-202 and HX-203, while the ethane loop is represented as a single equivalent unit in Aspen Plus, capturing its combined cooling effect at the intermediate temperature level; the propylene loop provides the final cold duty at the lowest temperature level.

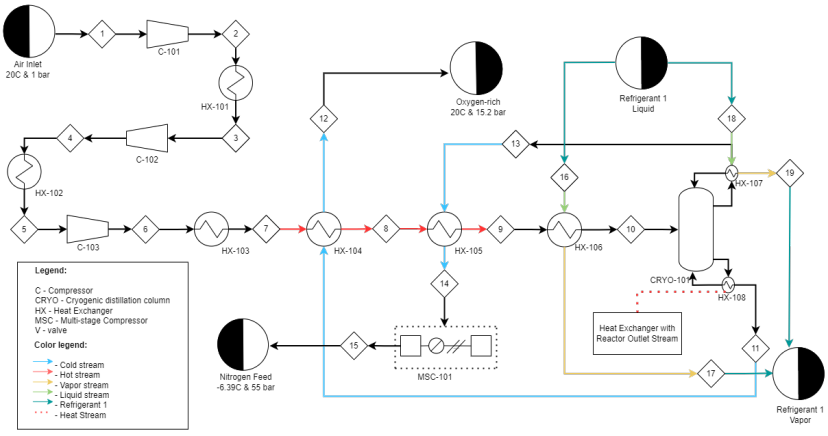


Figure 7.1 Process flow diagram of the ASU

- **<u>Adsorption column configuration and cycle design</u>**: ammonia separation from the reactor outlet streams (retentate and permeate) is carried out in a zeolite-based adsorption system. The adsorption section is modelled as a simplified temperature-swing adsorption (TSA) cycle in a fed-batch configuration, using two columns per stage operating alternately in adsorption and desorption (regeneration) mode to ensure continuous operation. During the adsorption step, one column receives the feed stream and delivers a recycle stream containing the non-adsorbed fraction, while the second column is in desorption mode, releasing the adsorbed ammonia to the product stream. The adsorption model is designed to exhibit dynamic behaviour based on adsorption-specific design parameters that can be varied in the input dataset, while responding to changes in the reactor outlet conditions if the reactor design is modified. The adsorber model, implemented in Python, estimates the required number of adsorption stages to reach the target product purity of 99.5 vol% NH_3. For each stage, it calculates the working capacities of the sorbent, component flow rates in the feed, recycle and product streams, the required sorbent mass and column dimensions, and the associated heating and cooling duties. To keep the model

easy for process-wide techno-economic analysis, several simplifying assumptions are adopted:

- Two columns per stage, operating only in adsorption or desorption mode, with a one-hour adsorption step and a one-hour desorption step; every hour, the columns alternate their mode.
- Changes in temperature and pressure between adsorption and desorption steps (heating from T_{ads} to T_{des}, depressurising from P_{ads} to P_{des}, and the reverse cooling and repressurising) are treated as part of the regeneration step and included in the estimated heating and cooling duties.
- Pressure drop along the adsorption columns is neglected.
- Adsorption and desorption selectivities are assumed constant over the range of partial pressures and temperatures considered.

Adsorption model: Each adsorption stage consists of the two alternating columns and three streams: feed, recycle and product. The material balance over a single stage is given by:

$$F_i^{feed} = F_i^{recycle} + F_i^{product} \tag{7.1}$$

where F_i^{feed} is the molar flow rate of component i entering the stage during adsorption, $F_i^{recycle}$ is the non-adsorbed fraction leaving the column during adsorption and returned to the process, and $F_i^{product}$ is the adsorbed material released during desorption.

To close the material balance, it is assumed that 99% of the ammonia is captured and released in the product stream during regeneration:

$$F_{NH_3}^{product} = 0.99\, F_{NH_3}^{feed} \tag{7.2}$$

This recovery assumption allows the ammonia product flow rate to be calculated directly from the feed; flow rates of H_2 and N_2 in the recycle and product streams then follow from the overall mass balance and the relative working capacities of the sorbent. The total sorbent mass required per stage is proportional to the ammonia working capacity, defined as the difference between the equilibrium loading at adsorption and desorption conditions.

The adsorption capacity model describes the equilibrium loading of H_2, N_2 and NH_3 on Zeolite-13X as a function of temperature, pressure and gas-phase composition. Because multicomponent isotherm data for the H_2-N_2-NH_3 mixture over the full operating window are limited, a slightly customised extended competitive Langmuir approach is used.

First, the saturation adsorption capacity of Zeolite-13X for NH_3 decreases with increasing temperature and is described by an empirical exponential decay as Langmuir-Freundlich isotherm reported by J. Helminen et al. [5]:

$$q_{NH_3}^{sat} = q_{NH_3}^{0} exp\,[-\alpha(T - T_0)] \tag{7.3}$$

Where $q_{NH_3}^{sat}$ is the temperature-dependent saturation capacity (mol·kg^{-1}), $q_{NH_3}^{0}$ is the saturation capacity at reference temperature T_0 (mol·kg^{-1}), α is a temperature coefficient (K^{-1}), T is the adsorption or desorption temperature (K), and T_0 = 298 K.

The extended competitive Langmuir isotherm is then used to represent simultaneous adsorption of H_2-N_2-NH_3:

$$q_{H_2} = \frac{q_{sat} b_{H_2} p_{H_2}}{1 + b_{H_2} p_{H_2} + b_{N_2} p_{N_2} + b_{NH_3} p_{NH_3}} \tag{7.4}$$

$$q_{N_2} = \frac{q_{sat} b_{N_2} p_{N_2}}{1 + b_{H_2} p_{H_2} + b_{N_2} p_{N_2} + b_{NH_3} p_{NH_3}} \tag{7.5}$$

$$q_{NH_3} = \frac{q_{sat} b_{NH_3} p_{NH_3}}{1 + b_{H_2} p_{H_2} + b_{N_2} p_{N_2} + b_{NH_3} p_{NH_3}} \tag{7.6}$$

where q_{sat} is the shared saturation capacity (mol·kg^{-1}), b_i is the Langmuir affinity constant of component i (bar^{-1}), and p_i is the partial pressure of component i (bar). Unlike the standard extended Langmuir formulation, in which each component has its own saturation capacity, this model uses a single shared q_{sat} derived exclusively from pure-component NH_3 isotherms. As a result, absolute loading values for H_2 and N_2 are governed by their affinity constants relative to NH_3, rather than by independently fitted saturation capacities.

The temperature dependence of the NH_3 affinity constant is described by the van 't Hoff equation:

$$b^{NH_3}(T) = b_0^{NH_3} \exp\left(-\frac{\Delta H_{ads}}{RT}\right) \tag{7.7}$$

where $b_0^{NH_3}$ is the pre-exponential constant in bar^{-1}, ΔH_{ads} is the enthalpy of adsorption in J·mol^{-1}, R is the universal gas constant in J·mol^{-1} K^{-1}, and T is the temperature in K. The adsorption enthalpy ΔH_{ads} is a negative quantity for exothermic adsorption processes.

Affinity constants for H_2 and N_2 are derived from the NH_3 affinity via fixed adsorption selectivity factors:

$$b^{H_2} = \frac{b^{NH_3}}{S_{ads,H_2}} \tag{7.8}$$

$$b^{N_2} = \frac{b^{NH_3}}{S_{ads,N_2}} \tag{7.9}$$

where S_{ads,H_2} = 30 and S_{ads,N_2} = 10, retrieved from data reported by Helminen et al., according to the expected molar fraction in the adsorption

columns [5].

The working capacity Δq_i of the sorbent for each component is defined as the difference between the equilibrium loadings at adsorption and desorption conditions:

$$\Delta q_i = q_i(T_{ads}, P_{ads}, y_{ads}) - q_i\,(T_{des}, P_{des}, y_{des}) \quad (7.10)$$

where T, P and y denote temperature, total pressure and average gas-phase molar composition during the adsorption and desorption steps, respectively. The gas composition y_{des} used to evaluate desorption loading has a meaningful effect on the computed working capacity: during regeneration, released ammonia increases its gas-phase concentration and reduces the driving force for further desorption. In this model, y_{des} is taken as a fixed assumed composition rather than being updated dynamically during desorption.

Operating conditions and energy balance: The adsorption temperature T_{ads} = 308 K and desorption temperature T_{des} = 423 K were selected based on an optimisation carried out during the techno-economic assessment. The adsorption pressure P_{ads} = 15 bar was selected considering experimental isotherm data for sodium-containing aluminosilicate zeolites such as Na-X under conditions directly relevant to ammonia synthesis separations. Aristizabal-Gonzalez et al. [24] measured equilibrium NH_3 adsorption on commercial Na-X up to 15 bar and across temperatures 323-473 K, identifying 323 K and 15 bar as the lowest temperatures and highest pressures combination investigated, which corresponds to the highest achievable equilibrium loading and thus the most favourable adsorption capacity. Selecting these conditions as the adsorption step maximizes the working capacity per cycle, reducing the required sorbent mass and column size, while ensuring that ammonia remains in the vapour phase. Tokushige and Ryu [4] investigated ammonia adsorption and desorption on several zeolite types at 473 K using a PSA method and observed high durability over repeated cycles with no significant degradation in particle morphology. Both adsorption and desorption steps are carried out at the same pressure $P_{ads} = P_{des}$ = 15 bar, yielding a pure TSA cycle without pressure swing; this avoids additional compression/expansion equipment required for PSA-based regeneration.

The energy balance for the adsorption system accounts for both sensible heat of the bed and heats of adsorption/desorption. The total heating duty of a column during desorption is calculated as the sum of the sensible heat required to raise the bed temperature from T_{ads} to T_{des} and the endothermic heat of desorption:

$$Q_{column}^{heat} = Q_{bed}^{heat} + Q_{des} \tag{7.11}$$

$$Q_{bed}^{heat} = W_{sorbent}\, Cp_{bed}\, (T_{des} - T_{ads}) \tag{7.12}$$

$$Q_{des} = \sum_i F_i^{product} \mid \Delta H_{des,i} \mid \tag{7.13}$$

with $W_{sorbent}$ the total sorbent mass (kg), Cp_{bed} the bed heat capacity ($J \cdot kg^{-1} \cdot K^{-1}$), and $\Delta H_{des,i}$ the enthalpy of desorption ($J \cdot mol^{-1}$) for component i. The total cooling duty during adsorption is calculated analogously:

$$Q_{column}^{cool} = Q_{bed}^{cool} + Q_{ads} \tag{7.14}$$

$$Q_{bed}^{cool} = W_{sorbent}\, Cp_{bed}\, (T_{des} - T_{ads}) \tag{7.15}$$

$$Q_{ads} = \sum_i F_i^{product} \mid \Delta H_{ads,i} \mid \tag{7.16}$$

These expressions reflect the physical symmetry: the energy released during adsorption equals the energy required for desorption, since desorption is the thermodynamic reverse of adsorption, but they contribute to opposite duties (cooling vs. heating). Constant values for the heats of adsorption of each component are taken from literature. The value for NH_3 (-75.0 $kJ \cdot mol^{-1}$) is consistent with the experimental data reported by Helminen et al. for NH_3 adsorption on Zeolite-13X across 298-393 K [5]. For H_2 and N_2, heats of adsorption are taken from Azzan et al. for Y-type zeolites and are set to -10.7 $kJ \cdot mol^{-1}$ and -13.5 $kJ \cdot mol^{-1}$ respectively [25].

Table 7.1 Key design and operating parameters used in the adsorption model

Parameter	Unit	Value	Reference
T_{ads}	K	308	[24]- Optimisation
P_{ads}	bar	15	[24]
T_{des}	K	423	[24]-Optimisation
P_{des}	bar	15	[4]
L_r/D_r^i	-	3	[27]
ε_s	$m^3_{solid} \cdot m^{-3}_{column}$	0.55	[-]
$\rho_{sorbent}$	$kg \cdot m^{-3}_{column}$	700	[28]
Cp_{bed}	$J \cdot kg^{-1} \cdot K^{-1}$	900	[29]
S_{ads,H_2}	-	30	[5]
S_{ads,N_2}	-	10	[5]

The heating duty required for desorption is supplied by high-pressure steam at approximately 30 bar (liquefaction 505 K), which falls within standard HP-steam conditions [26] in industrial process plants and can be generated by an electric boiler to remain consistent with the renewable-electricity basis of the overall process. Cooling duty during adsorption is assumed to be provided by cooling water. The heat required to heat or cool the vessel shell is neglected, and heat dissipation during non-adsorption parts of the cycle is assumed to be accommodated by the utility systems. All the parameters are shown in **Table 7.1**.

- **Heat exchangers**: the heat-exchanger network (HEN) was designed using pinch analysis to minimise utility consumption. All process heat exchangers are modelled in Aspen Plus as counter-current shell-and-tube units using the shortcut design method, with a minimum temperature approach of 10 °C, apart the last condenser used to liquefy ammonia (5 °C).
- **Compressors:** all compressors in the flowsheet are modelled in Aspen Plus with an isentropic efficiency of 0.70 and a mechanical efficiency of 0.85 [3].

7.2.3 Technical key performance indicators (KPIs)

The definition of the conversion in the reactor follows the expressions reported in Chapter 2, in particular Equation (2.17), and is evaluated for both the conventional PBR and the PBMR. The NH_3 recovery factor, defined in Equation (2.18) as the fraction of ammonia removed through the membrane relative to the amount produced in the reaction zone, is only meaningful for the membrane-assisted configuration and is therefore reported exclusively for the PBMR.

At the plant level, a power-to-ammonia (PtA) efficiency, denoted η_{PtA} (Equation (7.17)), is defined as the ratio between the chemical energy associated with the produced ammonia and the total energy input required to operate the process. The numerator is calculated from the lower heating value of ammonia (LHV = 18.6 $MJ \cdot kg^{-1}$) and the net NH_3 production rate, while the denominator includes the electrical consumption of all compressors (for hydrogen compression, nitrogen/air separation, recycle compression and product handling), together with the equivalent electrical energy associated with the heating and cooling duties required for ammonia separation and product conditioning.

$$\eta_{PtA} = \frac{F_{NH_3,produced} \times LHV_{NH_3}}{Energy\ consumption} \tag{7.17}$$

Cold Gas Efficiency (CGE) is another metric used here (Equation (7.18)), defined as the ratio between the energy content of the valuable product (ammonia) and the energy content of the feedstock (hydrogen), where the energy content of each stream is evaluated using its lower heating value (LHV):

$$CGE = \frac{F_{NH_3,produced} \times LHV_{NH_3}}{F_{H_2,fresh} \times LHV_{H_2}} \quad (7.18)$$

7.2.4 Economic parameters

The objective of the economic assessment is to obtain the levelized cost of ammonia (LCOA) for all of the proposed processes (conventional reactor and membrane-assisted process).

The economic assessment was performed using the methodology suggested by Equation (7.19), where the levelized cost of ammonia (LCOA) is calculated using capital expenditures (CAPEX) and operating expenditures (OPEX). In particular, Equation (7.19) expresses LCOA as:

$$LCOA = \frac{(TOC\ CCF) + OPEX_{fixed} + (OPEX_{variable}\ h_{eq})}{\dot{m}_{NH_3}\ h_{eq}} \quad (7.19)$$

where TOC is the total overnight cost, CCF is the capital charge factor, $\dot{m}_{NH_3}$ is the NH_3 production rate ($t \cdot y^{-1}$), and h_{eq} is the equivalent operating hours per year. The CAPEX term appears in the numerator in the form of TOC multiplied by CCF (annualised capital cost), while the fixed OPEX comprises maintenance, insurance and labour, and the variable OPEX includes utilities (electricity, steam, cooling water, etc.) and consumables, such as chemicals, catalysts and adsorbents make-up.

CAPEX

The total overnight cost (TOC) is calculated using the procedure summarised in **Table 7.2**, which combines bare erected equipment costs, direct installation costs and indirect costs into a single CAPEX figure. These costs do not take into account interest and escalation during construction. The TOC calculation proceeds as follows: the Bare Erected Cost (BEC) is obtained by summing the individual costs of all equipment; direct costs are calculated as a percentage of BEC and grouped into the Total Installation Cost (TIC); these are summed in the Engineering procurement and construction (EPC). Finally, the contingencies and owner's costs (C&OC) are calculated based on the EPC. The TOC is equal to the sum of EPC and C&OC.

Equipment purchase costs are estimated using capacity-based correlations from Smith [30]:

$$C_E = C_B \left(\frac{Q}{Q_B}\right)^M \quad (7.20)$$

where C_E is the cost of equipment at capacity Q, C_B is the base cost at capacity Q_B, and M is a cost exponent for the specific equipment type.

Table 7.2 Procedure for calculating the total overnight cost (TOC)

Plant Component	Cost (M€)
Component A	A
Component B	B
Component C	C
Bare Erected Cost (BEC)	A+B+C
Direct Costs as percentage BEC	
Total Installation Cost (TIC)	80% BEC
Total Direct Plant Cost (TDPC)	BEC + TIC
Indirect Cost (IC)	14%TDPC
Engineering procurement and construction (EPC)	TDPC + IC
Contingencies and owner's costs (C&OC)	
Contingency	10% EPC
Owner's cost	5% EPC
Total contingencies & OC (C&OC)	15% EPC
Total Overnight Cost (TOC)	EPC + C&OC

The base equipment types and capacity measures are shown in **Table 7.3**.
For pressure vessels (reactors, adsorption columns), the equipment mass is calculated from the wall volume and material density, using 8,000 kg·m^{-3} for 316 stainless steel [31]. Wall thickness t (Equation (7.21)) is computed as a function of operating pressure, allowable tensile stress and vessel radius, with an additional 3 mm corrosion allowance [32]; tensile strength (S in Equation (7.21)) is taken as interpolation from literature considering the highest operating temperature of the vessel [33]. **Table 7.3** shows the specific conditions for each equipment type. For the equipment items with a maximum operating pressure of 15 bar (e.g. adsorption stage), the allowable stress was evaluated at 30 bar to account for the presence of 30-bar steam in the heating jacket. The same mechanical design approach was applied consistently to pressure vessels, compressors and shell-and-tube heat exchangers, including those equipped with heating jackets, as well as to the distillation column shell in the ASU section.

$$t = \frac{p\,R}{0.9\,S - 0.6\,p} \tag{7.21}$$

Notably, the capacity for each equipment type is expressed in terms of different characteristics (mass for pressure vessels and distillation columns, shaft power for compressors, and heat-transfer area for shell-and-tube heat exchangers). Aspen Plus provides the required power for compressors and the required heat-transfer area for

heat exchangers directly from the process simulations, which are used as capacity inputs Q in the cost correlations of Equation (7.20).

Table 7.3 Overview of base equipment types

Base material of construction	Capacity measure	Size range	Base size	Base cost (€)	Cost exponent
Pressure vessel (SS)	Mass (t)	6-100	6	98400	0.82
Compressor	Power (kW)	250-10,000	250	98400	0.46
Shell-and-tube heat exchanger (CS)	Heat transfer area (m^2)	80-40,000	80	32800	0.68
Distillation column (Empty shell) (CS)	Mass (t)	8-300	8	65600	0.89

Next, the calculated base equipment cost is corrected to account for the specific construction material and the operating pressure and temperature. Smith [30] provides multiplicative cost factors for material of construction, design temperature and design pressure, which are applied to the base cost obtained from Equation (7.20). The material cost factors (f_M) used in this work (e.g. carbon steel, stainless steel 316) are listed in **Table 7.4**.

Table 7.4 Material cost correction factors

Material	Correction factor f_M
Carbon Steel (CS)	1
Stainless Steel (SS, low grades)	2.4
Stainless Steel (SS, high grades)	3.4
CS shell and tubes	1
SS (low grade) shell and tubes	2.9
Inconel (Reboiler ASU)	4.4

The material of construction for the air-separation unit and the associated refrigeration cycles is low-grade stainless steel, selected to mitigate corrosion risks arising from moisture in the air feed and to withstand cryogenic temperatures [34]. For the reaction and adsorption sections, high-grade stainless steel is adopted due to the significant hydrogen and ammonia content in the feed, in order to account for potential hydrogen embrittlement and ammonia corrosion. Because no specific material cost factors are available for high-grade stainless steel heat exchangers, the generic material correction factor f_M = 3.4 is applied in their cost estimation. Conversely, the base cost correlation for pressure vessels already assumes low-grade stainless steel, so the reactor vessel cost is corrected by multiplying the base cost by

the ratio of the high-grade to low-grade stainless steel cost factors, ensuring consistency between the material selection and the economic evaluation.

Table 7.5 Correction factor as a function of operating temperature

Operating temperature	Correction factor
0-100	1.0
300	1.6
500	2.1

Table 7.6 Correction factor as a function of operating pressure

Operating pressure (bar absolute)	Correction factor
0.01	2
0.1	1.3
0.5 to 7	1
50	1.5

The ASU reboiler operates with a large temperature difference of about 350 °C between the process stream and the heating medium and is also used to pre-heat the N_2 feed to approximately 270 °C, which can induce significant thermal stresses and therefore requires materials with low thermal expansion and high thermal-fatigue resistance. For this reason, it is constructed in Inconel, a nickel-based alloy widely used in aerospace and jet-engine components and in oil and gas, particularly in LNG service, demonstrating its ability to withstand substantial temperature gradients [35]. **Table 7.5** and **Table 7.6** show the cost factors for the operating temperatures and pressure.

Due to the absence of dedicated cost correlations at cryogenic temperatures, the lowest available temperature range is used for cryogenic equipment. For operating temperatures between 100 °C and 300 °C, the correction factor corresponding to 300 °C is applied. The same approach is adopted for temperatures above 300 °C and for pressure. When an equipment item operates across two temperature or pressure ranges (for example, certain heat exchangers), the higher cost factor is used to obtain a conservative estimate.

The cost of the equipment is actualised to the reference year of this study. Equipment costs are updated using the Chemical Engineering Plant Cost Index (CEPCI), taking the index value for November 2025 as reference [36]. Base equipment costs reported by Smith correspond to January 2000 values in $ [30] and are converted to € using a currency exchange rate of 0.86 €·$$^{-1}$ for May 2026 [37]. The final purchase cost of each equipment item C_i (Equation (7.22)) is thus obtained by multiplying the base cost by the relevant material, temperature and pressure correction factors, by the CEPCI ratio, and by the currency conversion factor.

$$C_i^{2025} = C_E f_M f_T f_p \frac{CEPCI_{2025}}{CEPCI_{2000}} \cdot CER \tag{7.22}$$

$$CCF = \sum_{j=1}^{n} \frac{1}{(1+i)^j} = \frac{i(1+i)^n}{(1+i)^n - 1} \tag{7.23}$$

The Capital Charge Factor (CCF) is the second CAPEX-related term in the LCOA expression and represents the annualised capital charge associated with the TOC. CCF is calculated from the plant lifetime and discount rate using Equation (7.23), and its product with TOC yields the annual capital cost used in the LCOA numerator.

OPEX

The operating expenditures (OPEX) are divided into fixed and variable components. Fixed expenses include maintenance, insurance and labour; maintenance and insurance are expressed as fractions of the total overnight cost (TOC), as summarised in **Table 7.7**.

Table 7.7 Procedure for calculating $OPEX_{fixed}$

Cost component	Value	Reference
Maintenance costs	2.5% TOC	[38]
Insurance	2.0% TOC	[38]
Labour	$4.5 \cdot N_{OL} \cdot$ Annual Salary	[38]
Number of operators required (N_{OL})	$(6.29+0.23 \cdot N_{np})^{0.5}$	[39]
Total amount of operators per year	$4.5 \cdot N_{OL}$	[39]
Annual salary per operator	€45,793.00	[40]

The calculation of the labour cost is based on the number of non-particulate processing steps N_{np} (compression, heat exchange, reaction, separation, etc.), using the correlation reported in **Table 7.7** to relate N_{np} to the number of operators required per shift. The total number of operators per year is then obtained by comparing the annual plant operating hours to the working hours of a single operator, leading to 4.5 shifts; this number is rounded up and multiplied by the annual salary of a machine operator in Germany in 2026 to obtain the total labour cost [40].

The variable operating costs include chemicals (catalyst, adsorbent, refrigerants), electricity, cooling water and membrane replacement in the case of the membrane-assisted process, as detailed in **Table 7.8**. The cost of hydrogen is taken as 8.6 €·kg^{-1} for green hydrogen at the plant boundary and does not include transportation cost.

Table 7.8 Variable operating costs

Material	Price	Unit	Reference
Green hydrogen	8.6	[€·kg^{-1}]	[13]
Catalyst (Ru/C)	864	[€·kg^{-1}]	[41]
Quartz	0.2	[€·kg^{-1}]	[42]
Zeolite-13X	2	[€·kg^{-1}]	[43]
Refrigerant 1	233	[€·GJ^{-1}]	[44]
Refrigerant 2	69	[€·GJ^{-1}]	[44]
Refrigerant 3	16	[€·GJ^{-1}]	[44]
Membranes	1950	[€·m^{-2}]	[3]
Electricity	160	[€·MWh^{-1}]	[45]
HP steam	17.7	[€·GJ^{-1}]	[46]
Cooling water	0.2	[€·t^{-1}]	[47]

Since the refrigeration cycles are modelled as closed loops, the same refrigerant is assumed to circulate continuously without significant make-up; consequently, the required refrigerant inventory is approximated as the inlet refrigerant feed needed to operate the cycle for 1 hour, and this amount is used to estimate the refrigerant cost. For the membrane-assisted process, the cost of fresh hydrogen used as sweep gas is treated as a recurring variable OPEX term.

Throughout the economic analysis, chemicals such as catalyst, adsorbent and refrigerants are assumed to have a lifetime of 5 years, while membranes are replaced every 3 years [3], as summarised in **Table 7.9**.

Table 7.9 Economic assumptions

Plant lifetime	25 yr
Location	Germany
Discount rate	8%
Currency exchange rate	0.86 €·\$$^{-1}$
Operational year (h_{eq})	8,000 hr
Catalyst lifetime	5 yr
Adsorbent lifetime	5 yr
Refrigerants lifetime	5 yr
Membrane lifetime	3 yr
Cooling water $T_{w,in}$	20 °C
Cooling water $T_{w,out}$	25 °C

7.3 RESULTS AND DISCUSSION

7.3.1 Traditional ammonia synthesis process: PBR design

The conventional configuration is based on a single adiabatic packed bed reactor with a Ru/C catalyst, sized to achieve the target NH_3 production rate. The design objective was to identify the combination of temperature, pressure and reactor geometry that minimises the levelized cost of ammonia (LCOA), while maximising ammonia production per unit catalyst and overall process efficiency.

Before presenting the optimisation results, it is worth noting that both the reaction kinetics and the membrane permeation model underlying the reactor simulations were validated: the kinetic model was validated against literature data [14], while the membrane permeation model was validated against experimental data. In both cases further details of the models are presented in Chapter 2 and 5. The corresponding kinetic validation results are reported in Appendix (**Figure A.7.2**).

Reactor geometry was parametrised through the reactor length, L_r, and the aspect ratio, L_r/D_r^i. For each candidate geometry, the inlet flow rate and gas hourly space velocity (GHSV) were adjusted to meet the target plant capacity. Because GHSV is defined with respect to the catalyst bed volume, changes in L_r and L_r/D_r^i simultaneously change the total catalyst mass and the space velocity; the parametric study therefore explores, for each geometry, a different combination of catalyst loading and reactor size. The resulting LCOA and η_{PtA} values reflect the combined effect of operating conditions and catalyst loading.

The following decision variables were varied: aspect ratio $L_r/D_r^i \in$ {2.0, 2.5, 3.0, 3.5}; reactor length $L_r \in$ {6, 7, 8, 9} m; inlet temperature $T_{in}^R \in$ {625, 650, 675} K; and pressure $P_{in}^R \in$ {50, 55, 60, 65, 70} bar. These ranges were chosen on practical grounds: shorter reactors would require unrealistically large diameters to meet the production target at the imposed GHSV, while longer reactors would increase pressure drop, axial temperature gradients and fabrication cost. The pressure range reflects the favourable activity of Ru-based catalysts at moderate pressure relative to iron-based catalysts, avoiding the additional compression stages that higher pressures would require. The temperature range balances kinetic and thermal constraints: lower temperatures reduce the reaction rate and increase the required reactor size, while higher temperatures reduce equilibrium conversion and risk catalyst deactivation.

The optimisation proceeded in two steps: the operating window (T_{in}^R, P_{in}^R) was first explored at fixed geometry L_r, and the reactor geometry (L_r, L_r/D_r^i) was subsequently optimised at the selected operating point.

At fixed geometry (L_r = 7 m), X_{H_2}, η_{PtA} and LCOA respond differently to T_{in}^R and P_{in}^R (**Figure 7.2**). LCOA varies only weakly across the domain (2,955-3,060 €·$t_{NH_3}^{-1}$,

a spread below 3.5%), increasing gently with both temperature and pressure; its minimum lies at the low-temperature, low-pressure corner of the domain. This indicates that, for a fixed reactor size, the operating point is a secondary cost driver compared with reactor geometry. It is worth noting that these absolute LCOA values are considerably higher than those typically reported for large-scale green ammonia plants. As shown later in this chapter, this gap is attributable partly to the production scale and, more significantly, to the assumed hydrogen feedstock price and the separation technology used in this study. Their effects are quantified in the economic analysis and literature comparison presented in Section 7.6.

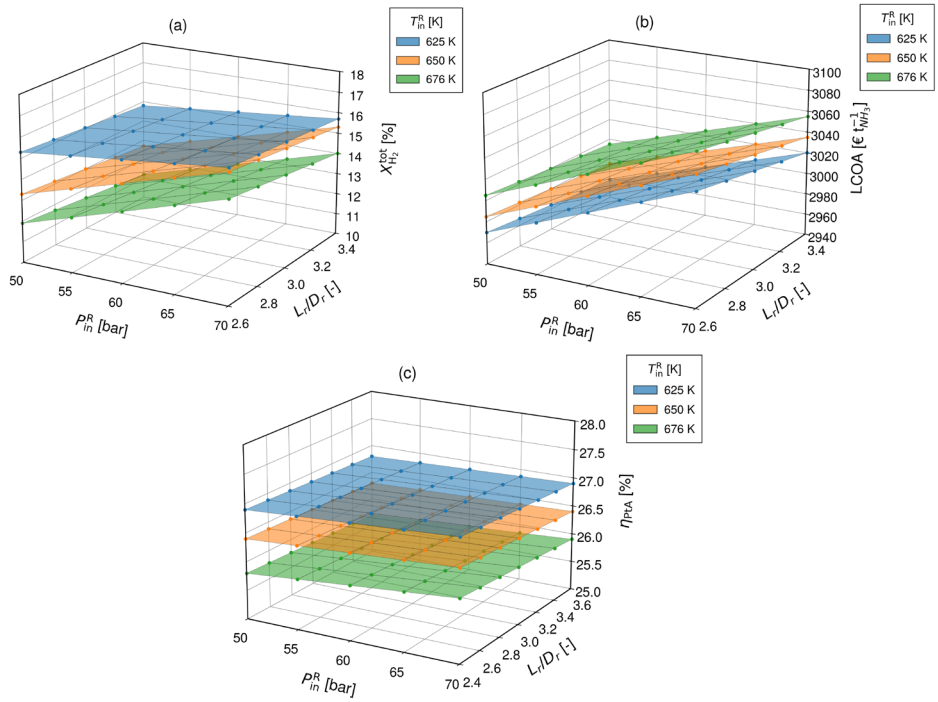


Figure 7.2 Effect of the retentate inlet pressure (P_{in}^R) and reactor aspect ratio (L_r/D_r^i) on: (a) H_2 conversion, (b) LCOA, (c) PtA, shown for three retentate inlet temperature (T_{in}^R = 625-650-675 K) at L_r = 7 m

Power-to-ammonia efficiency, η_{PtA}, varies between 26.4% and 27.0% and depends mainly on pressure, increasing as P_{in}^R decreases; the temperature dependence is comparatively weak. H_2 conversion shows the largest variation of the three indicators (13-17%, a relative change of about 30%), increasing as both temperature and pressure decreases, and reaching its maximum at the low-temperature, low-pressure corner of the operating window. The temperature dependence follows directly from the exothermic, equilibrium-limited nature of the ammonia synthesis reaction, which favours lower temperatures. The operating window reveals no single optimum that simultaneously minimises LCOA and maximizes performances, since

the trends are not aligned: increasing pressure improves conversion, but it also increases the LCOA. The point at 625 K and 50 bar was therefore chosen as a compromise operating condition for the subsequent geometry study.

At the selected operating point (T_{in}^{R} = 625 K, P_{in}^{R}= 50 bar), LCOA increases monotonically with L_r (**Table 7.10**) for every L_r/D_r^i (e.g. from 2,956 to 3,043 €·$t_{NH_3}^{-1}$ as L_r increases from 6 to 9 m at L_r/D_r^i = 2.5), because catalyst mass and reactor volume increase over this range without a corresponding gain in conversion. This behaviour indicates that the reactor is already sized with sufficient catalyst at L_r = 6 m, so additional catalyst does not provide an economic benefit. At fixed L_r, increasing the aspect ratio reduces LCOA: at L_r = 7 m, LCOA decreases from 2,977 to 2,961 to 2,952 €·$t_{NH_3}^{-1}$ as L_r/D_r increases from 2.5 to 3.0 to 3.5, together with a reduction in catalyst mass (from 5,086 to 3,532 to 2,595 $kg_{Ru/C}$) and reactor volume (from 43.1 to 29.9, to 22.0 m^3), and an increase in GHSV (from 15,783 to 22,761 to 31,132 h^{-1}). Slender reactors therefore achieve the same production target with less catalyst and a smaller volume.

Table 7.10 Summary of PBR process performance indicators for L_r = 6, 7, 8, 9 m and L_r/D_r^i = 2.5, 3, 3.5. The fixed operating conditions are T_{in}^{R} = 625 K, P_{in}^{R} = 50 bar

L_r [m]	T_{in}^{R} [K]	P_{in}^{R} [bar]	LCOA [€·$t_{NH_3}^{-1}$]	η_{PtA} [%]	X_{H_2} [%]	W_{cat} [$kg_{Ru/C}$]	V_{tot} [m^3]	GHSV [h^{-1}]
L_r/D_r^i = 2.5								
6	625	50	2,956.4	27.0	15.6	3,203	27.1	25,058
7	625	50	2,977.7	27.0	15.6	5,086	43.1	15,783
8	625	50	3,007.1	27.0	15.7	7,592	64.3	10,552
9	625	50	3,043.6	27.0	15.7	10,810	91.6	7,413
L_r/D_r^i = 3.0								
6	625	50	2,954.2	26.8	15.3	2,224	18.8	36,441
7	625	50	2,961.4	26.8	15.6	3,532	29.9	22,761
8	625	50	2,980.6	27.0	15.6	5,272	44.6	15,240
9	625	50	3,006.8	27.0	15.6	7,507	63.6	10,680
L_r/D_r^i = 3.5								
6	625	50	-	-	-	-	-	-
7	625	50	2,952.2	26.9	15.5	2,595	21.9	31,132
8	625	50	2,967.2	26.9	15.6	3,874	32.8	20,778
9	625	50	2,985.0	26.9	15.6	5,515	46.7	14,566

Across the entire geometry investigation, X_{H_2} (15.3%-15.7%) and η_{PtA} (26.8%-27.0%) remain nearly constant. Reactor sizing therefore trades capital intensity (catalyst mass and reactor volume) against LCOA, with little effect on conversion or efficiency; this is the opposite of the T_{in}^{R}-P_{in}^{R} behaviour, where the operating point

strongly affected the technical indicators but not the cost.

This trend is limited by reactor feasibility: at L_r = 6 m and L_r/D_r^i = 3.5, no converged solution was obtained, indicating that residence time becomes insufficient to reach the target production below a minimum reactor size. The shortest feasible reactor at the highest aspect ratio is therefore L_r= 7 m.

Combining the two optimisation steps identifies T_{in}^R = 625 K, P_{in}^R = 50 bar, L_r = 7 m and L_r/D_r^i= 3.5 as the reference configuration for the conventional reactor, with LCOA = 2,952 €·$t_{NH_3}^{-1}$, η_{PtA} ~26.9 and X_{H_2} ~15.5. The final optimal geometry properties and reaction conditions are shown in **Table 7.11**.

Table 7.11 PBR geometry properties and reaction conditions

Parameter	Unit	Value
Number of reaction units	-	1
Reactor length (L_r)	m	7
Reactor internal diameter (D_r^i)	m	2
Reactor external diameter (D_r^o)	m	2.33
Catalyst mass per reactor (W_{cat})	kg	2,595
Inlet temperature (T_{in}^R)	K	625
Inlet pressure (P_{in})	bar	50
Bed porosity (ε)	$m^3_{void}·m^{-3}_{reac}$	0.4
Catalyst particle size (d_p)	mm	3
Catalyst dilution factor	$m^3_{cat}·m^{-3}_{quartz}$	1/3
Gas hourly space velocity (GHSV)	h^{-1}	31,132
H_2:N_2 feed molar ratio	mol·mol^{-1}	1.5

7.3.2 Traditional ammonia synthesis process: process implementation

Figure 7.3 shows the process flow diagram of the traditional process. The fresh nitrogen and hydrogen feeds (N2RET1 and H2RET1) are supplied by the upstream units: nitrogen (N2RET1) is produced in the air-separation unit (ASU), while hydrogen (H2RET1) is delivered from the hydrogen storage system. These streams enter the synthesis loop as the fresh make-up feeds and are preheated using the hot reactor effluent in a three-stage feed-effluent heat exchanger train (STHER1, STHER2, STHER3), arranged as a cascade: the reactor product stream enters STHER1 first, is progressively cooled as it exchanges heat sequentially with the fresh N_2 stream (STHER1), the fresh H_2 stream (STHER2), and finally the recompressed recycle stream (STHER3), exiting as RH1OUT, RH2OUT and RH3OUT at each stage respectively. On the cold side, N2RET1 is heated to N2RET2 in STHER1, H2RET1 is heated to H2RET2 in STHER2, and the recycle stream RETRECN is

heated to RETREC in STHER3. This arrangement recovers sensible heat from the reactor effluent to minimise the external heating duty on the fresh feed and recycle streams before they enter the reactor. The preheated fresh nitrogen (N2RET2), fresh hydrogen (H2RET2) and preheated recycle stream (RETREC) are combined in the main feed mixer, and the resulting combined stream (RETIN) is fed to the adiabatic packed bed reactor (REACTOR), where the ammonia synthesis reaction proceeds over the Ru/C catalyst bed. The reactor effluent (RETOUT), a mixture of unconverted H_2, N_2, and NH_3, is routed back through the STHER1-STHER3 train described above, providing the hot-side heat source for preheating the incoming feeds, before continuing to a final cooler, B1, which brings the stream to the temperature required for the downstream separation train.

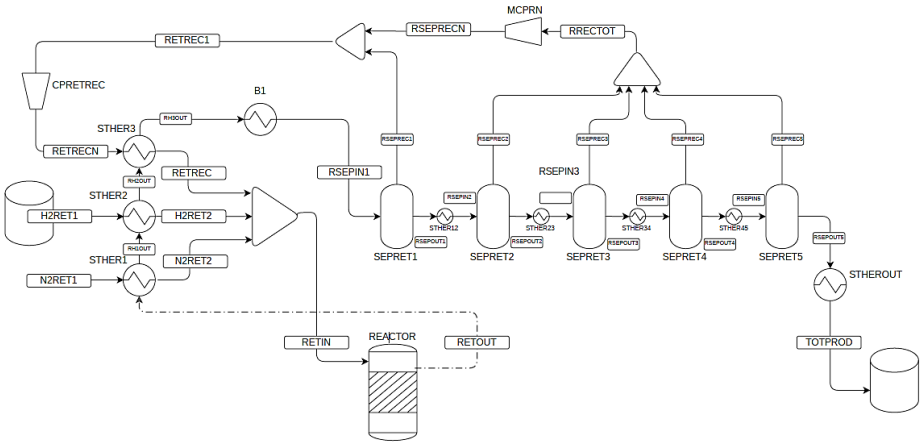


Figure 7.3 Process flow diagram of the packed bed reactor configuration

The cooled reactor effluent (RSEPIN1) enters the first of a series of adsorption stages (SEPRET1–SEPRET5), where ammonia is selectively captured on the Zeolite-13X sorbent bed. The model is configured to accommodate up to five stages in series, allowing the number of active columns to be adjusted dynamically depending on the required separation performance; in the present case, four stages (SEPRET1–SEPRET4) proved sufficient to achieve the target ammonia recovery, with the fifth stage included in the model architecture for flexibility but not required under these operating conditions. In the first adsorption stage, the column operates at the reactor outlet pressure, whereas all subsequent stages are maintained at a constant pressure of 15 bar. At each stage, the NH_3-rich stream leaving the desorption step is cooled in an intercooler (STHER12, STHER23, STHER34, STHER45) before entering the next adsorption column (RSEPIN2-RSEPIN5). The ammonia recovered in each stage is withdrawn as product via desorption (RSEPOUT1-RSEPOUT4 for stages 1-4, and RSEPOUT5 at the final stage). This cascade progressively lowers the temperature and recovers additional ammonia at

each step, improving overall recovery beyond what a single flash stage could achieve. The unreacted gas streams leaving separators 2 through 5 (RSEPREC2-RSEPREC5) are collected into a single recycle stream (RRECTOT) and recompressed in compressor MCPRN, producing RSEPRECN. This recompressed stream is combined with the gas leaving the first separator stage (RSEPREC1) which, being closest to reactor pressure, requires no intermediate recompression, to form the total recycle stream, RETREC1. This combined recycle is boosted to the required reactor inlet pressure by a second compressor, CPRETREC, producing RETRECN, which is returned to the STHER3 preheat stage described above before rejoining the fresh feed at the main mixer.

The liquid ammonia product from the final separator stage (RSEPOUT5) is subcooled in STHEROUT and withdrawn as the total product stream, TOTPROD, which is sent to ammonia storage.

7.3.3 Membrane-assisted ammonia synthesis process: PBMR design

The membrane reactor was optimised following the same two-step logic as the traditional reactor, extended to account for the additional membrane-related degrees of freedom: (1) the operating window and reactor geometry were screened jointly, and (2) the membrane-specific parameters were subsequently optimised at the resulting geometry and operating point.

The PBMR model was first run at the same operating point identified as optimal for the traditional reactor (T_{in}^{R} = 625 K, P_{in}^{R} = 50 bar), to confirm that the membrane-assisted configuration converges to a physically consistent solution before its own geometry was optimised independently. At this exact geometry, however, the target production rate could not be reached: the reduced catalyst residence time introduced by the membrane bundle was insufficient to close the mass balance at the traditional reactor's volume. A nearby, marginally larger geometry (L_r = 7.61 m, L_r/D_r^i = 3.50, V_{tot} = 28.27 m^3) was therefore identified as the closest feasible case to the traditional reactor's design, and is reported as PBMR (initial) in **Table 7.12**. In parallel, the PBR model was re-evaluated under comparable operating conditions to enable a more equitable performance and economic comparison.

At this base case, the membrane-assisted process gives an LCOA of 3,052 €·$t_{NH_3}^{-1}$, higher than the traditional reactor's 2,958 €·$t_{NH_3}^{-1}$, which was re-simulated at the closest matching operating conditions to those of the PBMR to ensure a consistent comparison. The membrane reactor is therefore not competitive at this stage, using an unoptimised sweep-gas-to-feed flow ratio (SW = 1) and a geometry chosen only for feasibility rather than performance. For this reason, a further study was performed across a range of aspect ratios, to identify the L_r/D_r^i that minimises LCOA at this scale, before the sweep-gas-to-feed flow ratio and other membrane parameters were optimised in turn.

Table 7.12 Baseline comparison of PBR and PBMR (initial)

Variable	Unit	PBR	PBMR (initial)
T_{in}^{R}	[K]	625	625
P_{in}^{R}	[bar]	50	50
L_r/D_r^i	[-]	3.50	3.50
L_r	[m]	7.50	7.61
D_r^i	[m]	2.14	2.17
V_{tot}	[m^3]	27.05	28.27
W_{cat}	[$kg_{Ru/C}$]	3,191	3,173
GHSV	[h^{-1}]	25,273	19,546
ΔT_{ret}	[K]	110.46	71.37
ΔP_{ret}	[bar]	-1.14	-0.69
$n_{stage,ret}$	[-]	4	4
$n_{stage,perm}$	[-]	-	4
n_{mem}	[-]	-	2,300
SW	[-]	-	1.00
$y_{H_2,in}^{P}$	[-]	-	0.60
ΔP_{mem}	[bar]	-	20
X_{H_2}	[%]	15.6	15.5
$NH_3\ recovery\ factor$	[%]	-	10.7
$y_{NH_3,product}$	[mol%]	99.94%	99.90%
$F_{NH_3,product}$	[$kmol \cdot h^{-1}$]	342.27	327.66
η_{PtA}	[%]	26.9	25.7
LCOA	[$€ \cdot t_{NH_3}^{-1}$]	2,958	3,052

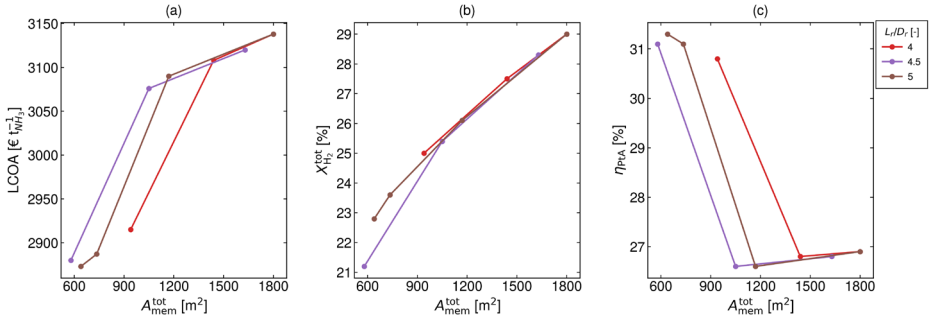


Figure 7.4 Effect of total membrane area (A_{mem}^{tot}) at T_{in}^{R} = 625 K, P_{in}^{R} = 50 bar and SW = 1 for L_r/D_r^i = 4.0, 4.5, 5.0: (a) LCOA, (b) H_2 conversion, (c) PtA

The volume constraint was then relaxed: at T_{in}^{R} = 625 K, P_{in}^{R} = 50 bar, the total membrane area (and hence n_{mem}) was varied freely for L_r/D_r^i = 4.0, 4.5 and 5.0; reactor length and diameter were not independently specified in this step, but

followed directly from n_{mem} (via the membrane packing) and the target aspect ratio L_r/D_r^i, so that V_{tot} varied as a consequence rather than as a controlled input (**Figure 7.4**).

The range of aspect ratios tested was itself restricted by feasibility: at SW = 1, lower values of L_r/D_r^i (2.5, 3, 3.5) did not reach the target production rate at any membrane area within the range explored, and are therefore absent from this screening. Under this design, LCOA increases monotonically with membrane area for every aspect ratio tested (**Figure 7.4**(a)), with the lowest values occurring at the smallest membrane areas rather than at an interior optimum; X_{H_2} increases correspondingly with membrane area (**Figure 7.4**(b)), while η_{PtA} falls sharply from its low-area values before levelling off (**Figure 7.4**(c)). Among the feasible aspect ratios, L_r/D_r^i = 5.0 gives the lowest LCOA, marginally outperforming 4.5 and 4.0 throughout the range tested. The best configuration found in this screening, (L_r/D_r^i = 5.0, A_{mem} = 600 m², n_{mem} = 2000, V_{tot} = 32.8 m³), gives an LCOA of 2,873 €·$t_{NH_3}^{-1}$, a 2.9% reduction relative to the PBR base case (2,958 €·$t_{NH_3}^{-1}$). An analogous study was carried out at an increased pressure of 60 bar (**Figure A.7.3**), which shows that raising the operating pressure simply leads to a higher LCOA, as shown for the PBR process.

To further explore the sensitivity of the optimal membrane-assisted configuration, the number of membranes was fixed at the optimal value (n_{mem} = 2000) and the model was re-run at higher reactor inlet temperature (T_{in}^R = 650 K) and varying pressures.

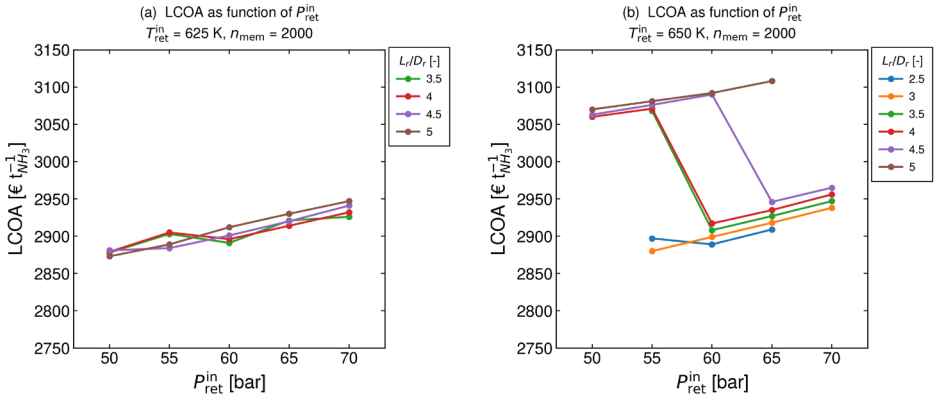


Figure 7.5 Effect of inlet retentate pressure P_{in}^R with n_{mem} = 2000 on LCOA, for various reactor aspect ratios L_r/D_r^i: (a) T_{in}^R= 625 K; (b) T_{in}^R= 650 K

At 625 K (**Figure 7.5**(a)), the LCOA increases almost monotonically with P_{in}^R for all feasible aspect ratios, with only minor differences between L_r/D_r^i = 3.5, 4.0, 4.5 and 5.0, indicating that pressure mainly penalises the process via higher compression

work rather than significantly improving conversion. In contrast, at 650 K a pronounced drop in LCOA is observed around P_{in}^{R} = 60 bar for the higher aspect ratios, particularly L_r/D_r= 4.5 and 5.0, followed by an increase at higher pressures. This behaviour reflects a more favourable compromise between reaction rate, membrane driving force and compression cost at intermediate pressures: for sufficiently long reactors (high L_r/D_r^i), the additional volume and catalyst inventory are fully exploited at 60 bar, yielding a step reduction in LCOA. At this pressure, the required number of adsorption stages also decreases, which further lowers both capital and operating costs; beyond 60 bar, however, the reduction in stages is exhausted and the extra compression work is no longer offset by gains in conversion, so the LCOA rises again.

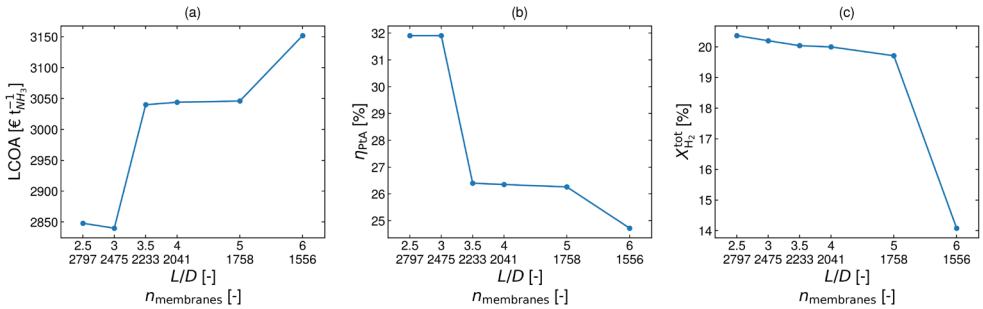


Figure 7.6 Effect of L_r/D_r^i and the corresponding number of membranes, at fixed total reactor volume (V_{tot} = 27 m³) and sweep-gas-to-feed flow ratio (SW = 0.67) at T_{in}^{R} = 625 K, P_{in}^{R} = 50 bar: (a) LCOA, (b) PtA, (c) H_2 conversion

In a subsequent step, the sweep-gas-to-feed flow ratio was adjusted to SW = 0.67 so that a truly direct comparison with the optimal traditional reactor (same empty volume and target productivity) was possible. Under these constraints, the reactor aspect ratio was varied over L_r/D_r^i= 2.5-6.0 to assess its influence on process performance and LCOA. The number of membranes follows directly from the resulting reactor diameter rather than being chosen independently. LCOA remains low for L_r/D_r^i= 2.5-3, then rises sharply from L_r/D_r^i = 3.5 onward, a step attributed to the separation section requiring an additional stage once the membrane number falls below a critical threshold at this fixed volume. L_r/D_r^i= 3 gives the lowest LCOA within this screening, corresponding to a total membrane area of 536 m² and an LCOA of 2,837 €·$t_{NH_3}^{-1}$, a 4.1% reduction relative to the PBR base case (2,958 €·$t_{NH_3}^{-1}$), and also lower than the best result obtained in the free-volume, SW = 1 screening above (2,873.4 €·$t_{NH_3}^{-1}$ at L_r/D_r^i= 5.0).

This is notably smaller than the traditional reactor's optimal aspect ratio (L_r/D_r^i = 3.50), consistent with a more compact, larger-diameter geometry being preferable for the membrane reactor: a lower L_r/D_r^i increases the reactor's cross-sectional

circumference relative to its length, providing more radial surface for membrane placement per unit reactor volume.

7.3.4 Membrane parameter sensitivity analysis

The membrane parameter sensitivity analysis presented below was carried out at L_r/D_r^i = 5.0 rather than at L_r/D_r^i = 3.0, the aspect ratio identified as most cost-effective in the fixed-volume screening above. This choice reflects the feasibility pattern already established: at SW = 1, L_r/D_r^i = 2.5-3.5 failed to reach the target productivity, and only converged once SW was decreased to 0.67. Since the present sensitivity analysis deliberately explores different sweep-gas-to-feed flow ratios, running the same grid at L_r/D_r^i = 3.0 would risk losing convergence at the lower end of the SW range being tested, before any comparison of SW values could even be made. L_r/D_r^i = 5.0 was therefore retained as the geometry for this analysis because it remains feasible across the full range of sweep-gas-to-feed flow ratios investigated, allowing the effect of SW itself to be isolated cleanly.

Table 7.13 Best performing SW and minimum LCOA for each combination of $y_{H_2,in}^P$ and n_{mem}, at fixed L_r/D_r^i= 5.0, T_{in}^R = 625 K, P_{in}^R = 50 bar

$y_{H_2,in}^P$ [-]	n_{mem} [-]	Best SW [-]	Best ΔP [bar]	Min LCOA [€·$t_{NH_3}^{-1}$]
0.50	1900	0.67	20	2,863
0.50	2000	0.67	30	2,869
0.50	2100	0.83	20	2,886
0.60	1900	0.67	5	2,847
0.60	2000	0.67	5	2,851
0.60	2100	0.83	5	2,867
0.75	1900	0.67	10	2,828
0.75	2000	0.67	10	2,832
0.75	2100	0.67	10	2,825
0.90	1900	0.67	20	2,807
0.90	2000	0.67	20	2,811
0.90	2100	0.67	10	2,816

With the geometry fixed at L_r/D_r^i = 5.0 (T_{in}^R = 625 K, P_{in}^R = 50 bar), the sweep-gas-to-feed flow ratio, the transmembrane pressure difference (ΔP), the permeate-side hydrogen molar fraction ($y_{H_2,in}^P$) and the membrane number (n_{mem}) were investigated jointly, to identify the best performing combination. The optimal sets of operating parameters resulting from this screening are summarised in **Table 7.13**. This screening was restricted to $n_{mem} \geq 1900$. Below this value, the required GHSV exceeded 150,000 h^{-1}, and the model was unable to reach the target production rate;

n_{mem} = 1900 therefore represents the practical feasibility limit at this geometry and operating point rather than an arbitrary lower bound or a converged interior optimum. To confirm that SW = 0.67 is not an artefact of the particular $y^P_{H_2,in}$ and n_{mem} values used above, the full sweep-ratio and ΔP screening was repeated across every combination of $y^P_{H_2,in}$ (0.5, 0.6, 0.75, 0.9) and n_{mem} (1900, 2000, 2100) considered in the reactor-design optimisation (**Table 7.13**).

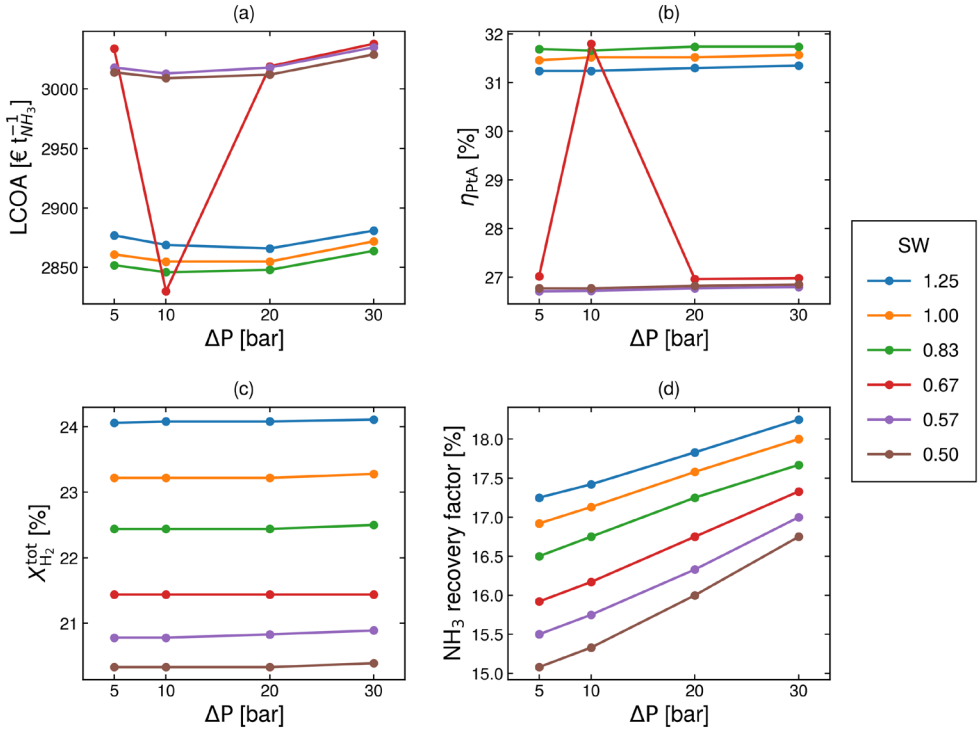


Figure 7.7 Effect of ΔP at different SW (0.5, 0.57, 0.67, 0.83, 1, 1.25) at $y^P_{H_2,in}$ = 0.75, n_{mem} = 2100: (a) LCOA; (b) PtA; (c) H_2 conversion; (d) NH_3 recovery factor

The permeate hydrogen fraction has a clear, monotonic effect on LCOA: across the full grid (**Table 7.13**), the lowest achievable LCOA falls from 2,863 €·t$^{-1}_{NH_3}$ at $y^P_{H_2,in}$ = 0.5 to 2,847 at 0.6, 2,825 at 0.75, and 2,807 at 0.90, the highest value tested remains the best, with no sign of a turning point. η_{PtA} slightly improves correspondingly, from ~31% to ~32%. This trend holds independently of n_{mem}.

The sweep-gas-to-feed flow ratio shows an interior optimum rather than a monotonic trend: LCOA falls from 2,837 €·t$^{-1}_{NH_3}$ at SW = 1.25 to a minimum of 2,807 at SW = 0.67, then rises sharply to 2,990 at SW = 0.57. The transmembrane pressure difference, by contrast, is a comparatively minor, second-order variable: LCOA varies between 2,807 (ΔP = 20 bar) and 2,823 €·t$^{-1}_{NH_3}$ (ΔP = 30 bar) across

the full range tested.

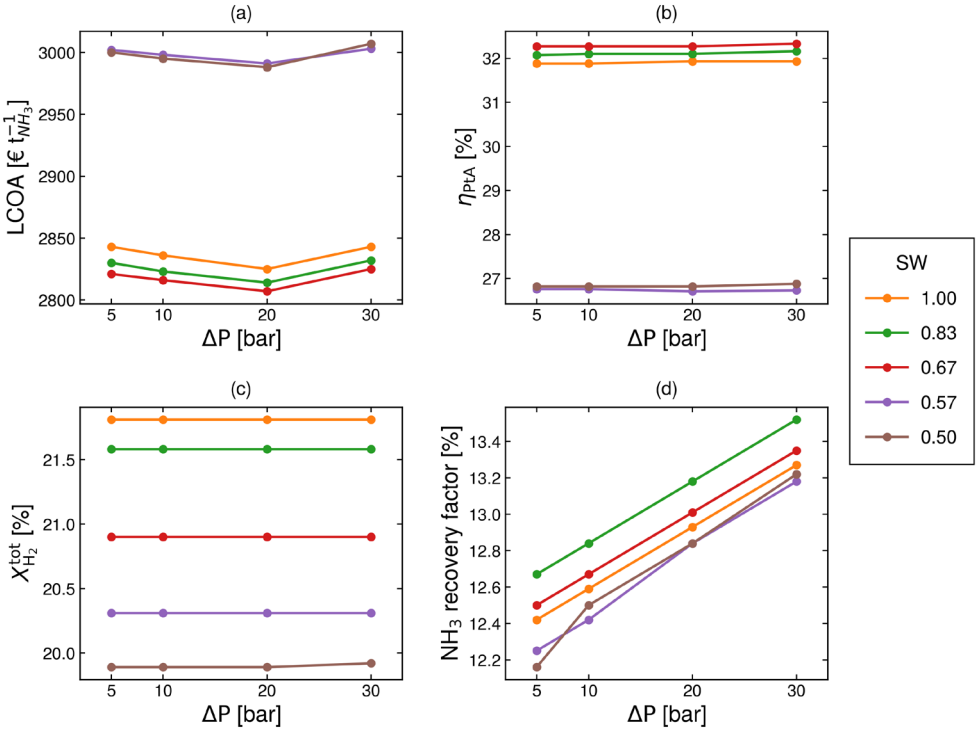


Figure 7.8 Effect of ΔP at different SW (0.5, 0.57, 0.67, 0.83, 1, 1.25) at $y^P_{H_2,in}$ = 0.90, n_{mem} = 1900: (a) LCOA; (b) PtA; (c) H_2 conversion; (d) NH_3 recovery factor

SW = 0.67 gives the lowest LCOA in 10 of the 12 combinations tested, confirming the robustness of this choice; the two exceptions, both at n_{mem} = 2100 and the lowest permeate compositions ($y^P_{H_2,in}$ = 0.5 and 0.6), are won marginally, by only 3-4 €·t$^{-1}_{NH_3}$, by SW = 0.83 instead.

In every case, the minimum corresponds to a reduction in the number of retentate-side separation stages from four to three ($n_{stage,ret}$), the same discrete transition identified elsewhere in this chapter. Where this transition falls, as a function of ΔP, depends on the specific combination of SW, $y^P_{H_2,in}$ and n_{mem}, which explains the sharp, non-monotonic LCOA response with ΔP observed at n_{mem} = 2100 for $y^P_{H_2,in}$ = 0.75 (**Figure 7.7**): at these conditions, SW = 0.67 sits close enough to the stage boundary that a change in ΔP from 5 to 10 bar alone is sufficient to cross it, causing LCOA to drop from ~3,020-3,035 to 2,825 €·t$^{-1}_{NH_3}$ ($y^P_{H_2,in}$ = 0.75) or 2,816 €·t$^{-1}_{NH_3}$ ($y^P_{H_2,in}$ = 0.90) (**Figure 7.8**) at that single point, before returning to the four-stage regime at ΔP ≥ 20 bar.

Table 7.14 PBMR geometry properties and reaction conditions

Parameter	Unit	Value
Number of reaction units	-	1
Reactor length (L_r)	m	6.77
Reactor internal diameter (D_r^i)	m	2.26
Reactor external diameter (D_r^o)	m	2.56
Catalyst mass per reactor (W_{cat})	kg	3,003
Membrane inner diameter (D_m^i)	m	0.007
Membrane outer diameter (D_m^o)	m	0.01
Membrane length (L_m)	m	6.77
Number of membranes (n_{mem})	-	2,475
Inlet temperature reaction zone (T_{in}^R)	K	625
Inlet temperature permeation zone (T_{in}^P)	K	625
Inlet pressure reaction zone (P_{in}^R)	bar	50
Transmembrane pressure gradient (ΔP)	bar	20
Bed porosity (ε)	$m^3_{void} \cdot m^{-3}_{reac}$	0.4
Catalyst particle size (d_p)	mm	3
Gas hourly space velocity (GHSV)	h^{-1}	20,338
Sweep-gas-to-feed flow ratio (SW)	$mol \cdot mol^{-1}$	0.67
H_2:N_2 feed molar ratio sweep gas (ret.)	$mol \cdot mol^{-1}$	1.5
H_2:N_2 feed molar ratio sweep gas (perm.)	$mol \cdot mol^{-1}$	9

The adopted operating point ($y_{H_2,in}^P$ = 0.90, n_{mem} = 1900, **Figure 7.8**) sits well clear of this boundary: SW = 0.67 is the smooth, stable minimum across the full ΔP range at this combination, with no stage-count discontinuity, making it a robust choice rather than one that happens to benefit from a narrow, coincidental threshold crossing. The remaining combinations, at n_{mem} = 1900, are reported in the Appendix **Figure A.7.4-A.7.6**.

Taken together, the membrane parameter screening identifies SW = 0.67, n_{mem} = 1900, $y_{H_2,in}^P$ = 0.90, ΔP = 20 bar as the best-performing and most robust combination, giving LCOA = 2,807 €·$t_{NH_3}^{-1}$, η_{PtA} = 32.3 and X_{H_2} = 20.9, a 5.1% reduction in LCOA and a 20.0% increase in η_{PtA} relative to the traditional reactor. These membrane parameters were then applied at L_r/D_r^i = 3.0, previously established as the best-performing aspect ratio in the fixed-volume geometry screening; this combined configuration achieved an even lower LCOA of 2,793 €·$t_{NH_3}^{-1}$, confirming that the geometry and membrane-parameter optimisations are compatible and that their combined effect is at least as favourable as either optimisation performed independently.

7.3.5 Adsorption and desorption temperature optimisation

During the optimisation study, in parallel, the adsorption and desorption temperatures were varied to quantify their impact on LCOA, overall η_{PtA}, and recycle compressor duty. The LCOA plot (**Figure 7.9**(a)) shows that, for all adsorption temperatures, increasing the desorption temperature from 350 K to around 400-450 K yields a significant reduction in LCOA, after which the improvement becomes marginal. This trend reflects the trade-off between higher NH_3 working capacity at elevated T_{des} (which reduces adsorbent amount and cycle frequency) and the additional heat required for desorption; at intermediate desorption temperatures the gain in separation performance and reduced equipment sizing outweigh the extra thermal duty, while at the highest T_{des} the incremental benefit on LCOA diminishes. At fixed T_{des}, lower adsorption temperatures systematically lead to lower LCOA, consistent with higher equilibrium loadings and better NH_3 selectivity at lower T_{ads}.

The PtA efficiency (**Figure 7.9**(b)) decreases almost linearly with increasing desorption temperature for all adsorption temperatures, indicating that the additional heat input required for regeneration is not fully compensated by improvements in separation performance. As T_{des} rises, more heat is consumed in the adsorption unit, which reduces the net electrical and thermal efficiency of the overall PtA chain, even though the adsorbent working capacity increases. Differences between adsorption temperatures appear as small vertical offsets: higher T_{ads} slightly improves efficiency at given T_{des}, suggesting a modest benefit of warmer adsorption conditions on the integration with the upstream reactor and heat-recovery network. In contrast, the recycle compressor duty is essentially insensitive to the desorption temperature and is mainly dictated by the adsorption temperature, as shown by the nearly flat lines: for each T_{ads}, the compressor power remains almost constant over the investigated T_{des} range, whereas higher T_{ads} leads to a systematically higher duty. This behaviour is consistent with the compressor being sized and operated primarily according to the gas conditions at the end of adsorption and the recycle flowrate, which are only weakly affected by desorption temperature in the optimised cycles.

Because the adsorption and desorption steps alternate between columns on an hourly cycle, there is in principle an opportunity to use the heat removed from a column transitioning from desorption back to adsorption conditions to pre-heat a column transitioning in the opposite direction. This internal heat recovery between columns could substantially reduce the external heating and cooling utility requirements. No heat integration was performed in this study, and this is identified as a recommendation for future work.

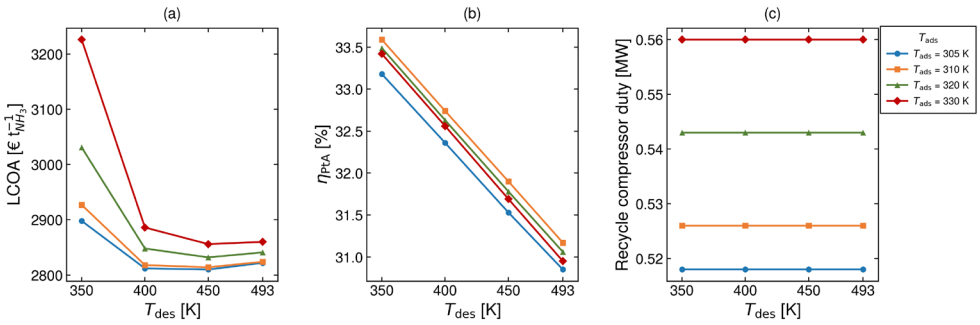


Figure 7.9 Effect of adsorption and desorption temperatures on (a) LCOA, (b) PtA, (c) recycle compressor duty

7.3.6 Membrane-assisted ammonia synthesis process: process implementation

The membrane-assisted process flowsheet (**Figure 7.10**) extends the traditional reactor loop with a second, parallel process train on the permeate side of the reactor, sweeping the membrane with a separate nitrogen/hydrogen feed to continuously remove the permeating species from the reaction zone. The retentate-side loop (fresh feed preheat, reactor, cascade separation, recycle recompression) is structurally identical to the traditional reactor described above; the permeate-side loop mirrors this structure independently, and the two product streams are combined only at the very end of the process.

The fresh nitrogen and hydrogen feeds (N2RET1, H2RET1), together with the recycle (RETRECN) are preheated against the reactor's retentate effluent in the three-stage heat exchanger train (STHER1, STHER2, STHER3), following the same cascade arrangement as the traditional reactor.

The preheated fresh feeds and recycle (N2RET2, H2RET2, RETREC) are combined in the main retentate-side mixer, and the resulting stream (RETIN) enters the retentate side of the membrane reactor. Independently, a separate nitrogen and hydrogen feed (N2PERM1, H2PERM1) together with the recycle (PSEPRECN) are preheated in an analogous three-stage exchanger train on the permeate side (STHEP1, STHEP2, STHEP3), following the same cascade logic: the permeate-side effluent stream is progressively cooled as it exchanges heat with the fresh N_2 and H_2 sweep-gas feeds, producing preheated streams N2PERM2, H2PERM2 and PERREC. These are combined in the permeate-side mixer, and the resulting stream (PERMIN) enters the permeate side of the reactor as the sweep gas.

The membrane reactor (REACTOR) operates with two co-existing zones separated by the membrane: the retentate (reaction) side, where the ammonia synthesis reaction proceeds over the catalyst bed fed by RETIN, and the permeate (sweep) side, fed by PERMIN, across which permeating species (primarily NH_3, and H_2/N_2 according to the membrane's selectivity) are continuously withdrawn from the

reaction zone. Two effluent streams leave the reactor: the retentate outlet (RETOUT), which provides the hot-side heat source for the STHER1-STHER3 preheat train as in the traditional reactor, and the permeate outlet (PERMOUT), which correspondingly provides the hot-side heat source for the STHEP1-STHEP3 preheat train on the permeate side.

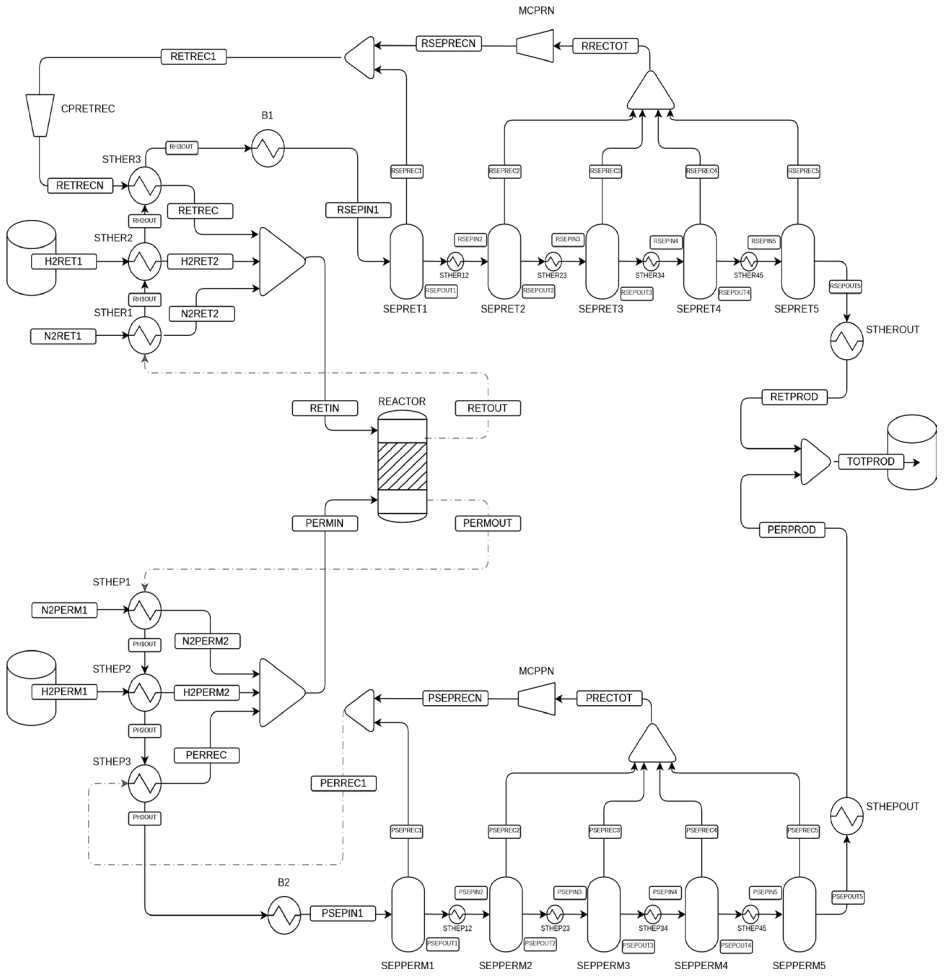


Figure 7.10 Process flow diagram of the packed bed membrane reactor configuration

After leaving the STHER train, the retentate effluent is cooled to the separation temperature in cooler B1 and then fed to the same five-stage cascade separation train as the traditional reactor (SEPRET1-SEPRET5), with intercoolers STHER12-STHER45 between the stages. Ammonia product is recovered at each stage (RSEPOUT1-RSEPOUT5), while the remaining gas is returned to the recycle loop. The gas from SEPRET2-SEPRET5 is collected and recompressed in the compressor MCPRN (RRECTOT to RSEPRECN), then combined with the gas

from SEPRET1 (RSEPREC1, which bypasses recompression as it remains closest to reactor pressure) to form the total retentate recycle, RETREC1, which is pressurised to reactor pressure in CPRETREC and returned to the STHER3 preheat stage as RETRECN. The permeate-side effluent follows the identical pattern after cooling in B2: a five-stage cascade separation train (SEPPERM1-SEPPERM5, with intercoolers STHEP12-STHEP45) recovers ammonia product at each stage (PSEPOUT1-PSEPOUT5), while the uncaptured gas from SEPPERM2-SEPPERM5 is collected and recompressed in MCPPN (PRECTOT to PSEPRECN), then combined with the SEPPERM1 gas (PSEPREC1) to form the total permeate recycle, PERREC1, which is boosted to pressure in the permeate-side recycle compressor and returned to the STHEP train as PERREC.
The ammonia recovered from the final stage of each train (RSEPOUT5 in retentate and PSEPOUT5 in permeate) is subcooled in STHEROUT (retentate side) and in STHEPOUT (permeate side), producing the retentate-side product stream (RETPROD) and the permeate-side product stream (PERPROD). These two streams are combined in a final mixer, and the total combined product (TOTPROD) is sent to ammonia storage.

7.4 TECHNICAL ANALYSIS

The PBR and PBMR were evaluated at both reactor and process scale under identical operating conditions (625 K, 50 bar) (**Table 7.15**). In this direct comparison the PBMR exhibits a slightly larger reactor volume (26.75 m^3 vs. 21.9 m^3) and a higher Ru/C catalyst inventory (3,003 vs. 2,595 kg), accompanied by a reduction in GHSV from 31,132 to 20,338 h^{-1}. This combination of membrane presence, higher catalyst loading, and lower space velocity leads to a higher per-pass ammonia conversion, with the conversion increasing from 15.6 in the PBR to 20.1 in the PBMR, and the NH_3 mole fraction at the reactor outlet rising from 6.89 to 8.22 mol%. The integration of the membrane bundle (2,475 tubes, 526.2 m^2) further intensifies the loop by enabling in-situ ammonia removal at a sweep-gas-to-feed flow ratio SW = 0.67, a permeate-side hydrogen mole fraction of approximately 0.90, and a transmembrane pressure difference of 20 bar, yielding an NH_3 recovery of 10.5%. As a result, the PBMR configuration requires only three adsorption stages instead of four, while maintaining a comparable product purity (99.94 vs. 99.54 mol% NH_3) and slightly lower feed rates and thermal input (H_2: 1,037.2 vs. 1,021.7 $kg \cdot h^{-1}$; N_2: 4,804.9 vs. 4,732.3 $kg \cdot h^{-1}$; thermal input: 34.57 vs. 34.06 MW).

Table 7.15 Key operating conditions, design parameters and performance indicators for the conventional packed bed reactor (PBR) and the membrane-assisted reactor (PBMR)

Variable/KPI	Unit	PBR	PBMR
Operating conditions			
T_{in}^{R}	K	625	625
P_{in}^{R}	bar	50	50
Geometry and catalyst			
L_r	m	7.5	6.77
D_r^i	m	2.14	2.26
L_r/D_r^i	-	3.50	3.0
V_{tot}	m^3	27.05	26.75
W_{cat}	$kg_{Ru/C}$	3,191	3,003
GHSV	h^{-1}	25,273	20,338
Reactor performance			
X_{H_2}	%	15.6	20.1
$y_{NH_3,out}^{R}$	mol%	6.89	8.22
$y_{NH_3,out}^{P}$	mol%	-	1.30
ΔT_{ret}	K	110.46	87.17
ΔP_{ret}	bar	-1.14	-0.37
Separation/Adsorption			
$n_{stage,ret}$	-	4	3
$n_{stage,perm}$	-	-	4
Membranes			
n_{mem}	-	-	2,475
A_{mem}	m^2	-	526.2
SW	-	-	0.67
$y_{H_2,in}^{P}$	-	-	0.9
ΔP	bar	-	20
$NH_3\ recovery\ factor$	%	-	10.5
Feedstock			
H_2 fresh feed ($\dot{m}_{H_2}^{in}$)	$kg \cdot h^{-1}$	1037.2	1021.7
N_2 fresh feed ($\dot{m}_{N_2}^{in}$)	$kg \cdot h^{-1}$	4804.9	4732.3
Thermal input (W_{feed})	MW	34.57	34.06
Product			
$y_{NH_3,product}$	mol%	99.94%	99.54%
$F_{NH_3,product}$	$kmol \cdot h^{-1}$	343	337.87
Thermal output (W_{chem})	MW	29.16	28.72
Cold Gas Efficiency(CGE)	%	84.3	84.3
η_{PtA}	%	26.9	32.4

Importantly, the Cold Gas Efficiency remains unchanged at 84.3% for both designs, indicating that the overall thermodynamic performance of the power-to-ammonia chain is preserved. The net effect of these changes is reflected in the power-to-ammonia efficiency KPI, which increases from 26.9% for the PBR to 32.4% for the PBMR. This improvement demonstrates that, the membrane-assisted configuration converts electrical power and feedstocks into ammonia more effectively at the system level, and thus constitutes a technically advantageous intensification of the synthesis loop under the small-scale conditions considered.

7.5 ECONOMIC ANALYSIS

The results of the economic analysis are summarised in **Table 7.16**. The total capital expenditure is 4.3% lower for the PBMR than for the conventional process (103.60 M€ vs. 108.21 M€). This reduction is driven almost entirely by the separation section: the Sepblocks contribution falls from 55.22 M€ (51.03% of CAPEX) in the PBR to 50.33 M€ (48.58%) in the PBMR, consistent with part of the separation duty being carried out in situ by the membrane, reducing the size and cost of the downstream adsorption train.

Table 7.16 CAPEX & OPEX distribution for PBR and PBMR

Component	Unit	PBR		PBMR	
		Raw value	Share [%]	Raw value	Share [%]
		CAPEX			
ASU	M€	17.03	15.74	17.03	16.44
STHE	M€	2.57	2.37	3.08	2.98
Compressors	M€	3.70	3.42	3.73	3.60
Sepblocks	M€	55.22	51.03	50.33	48.58
Reactor	M€	8.05	7.44	8.07	7.79
Storage	M€	21.64	20.00	21.36	20.62
Total	**M€**	**108.21**	**100.00**	**103.60**	**100.00**
		OPEX			
H_2 feed	M€·yr^{-1}	73.68	58.98	72.29	62.29
Electricity	M€·yr^{-1}	12.45	9.97	12.26	10.56
Cooling water	M€·yr^{-1}	16.77	13.42	13.71	11.81
Steam	M€·yr^{-1}	21.33	17.07	16.81	14.48
Catalyst	M€·yr^{-1}	0.55	0.44	0.52	0.45
Membranes	M€·yr^{-1}	-	-	0.34	0.29
Sorbent	M€·yr^{-1}	0.15	0.12	0.13	0.11
Total	**M€·yr^{-1}**	**124.83**	**100.00**	**115.95**	**100.00**

This reduction is partly counterbalanced by two smaller increases elsewhere: the heat exchanger network (STHE) rises from 2.57 M€ (2.37%) to 3.08 M€ (2.98%),

reflecting the additional heat integration duty introduced by the membrane's permeate-side stream, and the compressor cost rises marginally from 3.70 to 3.73 M€, consistent with the extra recompression stage required to return the permeate-side recycle to reactor pressure. The ASU and storage contributions are effectively identical in both cases (17.03 M€ and ~21.5 M€ respectively), as neither depends on the reactor configuration. Across both cases, the Sepblocks remain the dominant CAPEX contributor (51.03% PBR, 48.58% PBMR), followed by Storage (20.00%, 20.62%) and ASU (15.74%, 16.44%), with the Reactor (7.44%, 7.79%) and Compressors (3.42%, 3.60%) contributing comparatively little (**Figure 7.11**).

Considering the operating costs, the PBMR process has a total variable cost of 124.83 M€·yr^{-1} vs. 124.83 M€·yr^{-1} for the conventional process, a 7.1% reduction, in line with its higher conversion and lower utility requirement. As shown in **Figure 7.11**, the largest contributor to OPEX in both cases is the hydrogen feedstock, which accounts for 58.98% of PBR OPEX and rises to 62.29% for the PBMR, a larger share despite a slightly lower absolute cost (72.29 M€·yr^{-1} vs. 73.68 M€·yr^{-1}), since the other OPEX components fall by more. Steam is the second-largest contributor in both cases, falling from 17.07% (21.33 M€·yr^{-1}) in the PBR to 14.48% (16.81 M€·yr^{-1}) in the PBMR, followed by cooling water (13.42% to 11.81%; 16.77 to 13.71 M€·yr^{-1}) and electricity (9.97% to 10.56%; 12.45 to 12.26 M€·yr^{-1}).

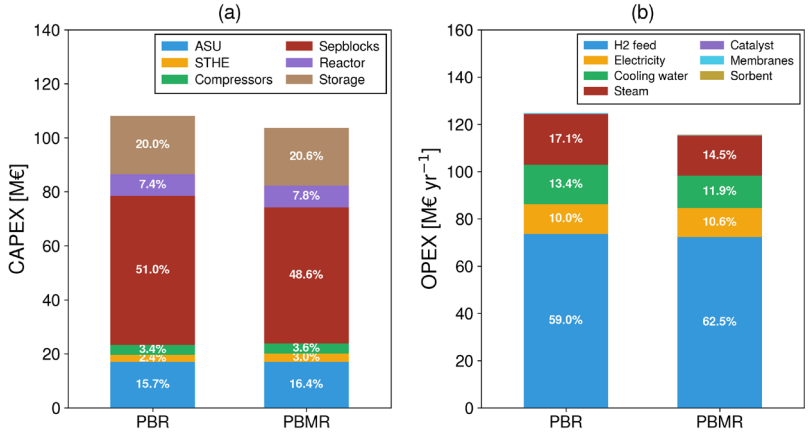


Figure 7.11 Comparison of CAPEX and OPEX component contributions for the PBR and PBMR design cases: (a) CAPEX distribution (M€), by component: ASU, STHE, Compressors, Sepblocks, Reactor, Storage; (b) OPEX distribution (M€·yr^{-1}), by component: H_2 feed, Electricity, Cooling water, Steam, Catalyst, Membranes, Sorbent

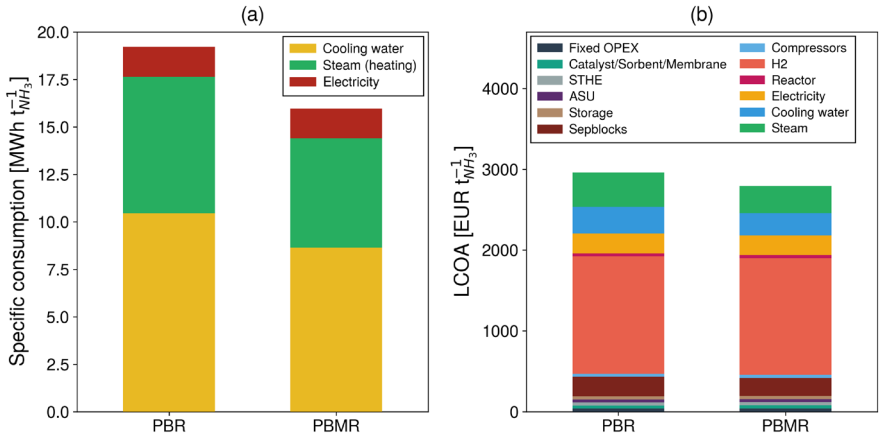


Figure 7.12 (a) Specific consumption breakdown (electricity, steam, cooling water) and (b) LCOA breakdown by cost component, comparing the PBR and the optimised PBMR configurations

Catalyst, membranes and sorbent costs are negligible in both cases (below 0.4% each). As with the capital cost comparison, this pattern reflects a general characteristic of the membrane-assisted design: rather than a single dominant cost saving, the PBMR achieves a broad, moderate reduction across nearly every utility category simultaneously. The combined effect of the lower CAPEX and lower OPEX is reflected directly in the levelized cost of ammonia, which falls from 2,958 €·$t_{NH_3}^{-1}$ for the PBR to 2,793 €·$t_{NH_3}^{-1}$ for the PBMR, a 5.6% reduction. **Figure 7.12**(a) presents the distribution of specific energy consumption in MWh·$t_{NH_3}^{-1}$. Steam and cooling water together dominate the specific consumption in both configurations, accounting for approximately 92% of the total for the PBR and 90% for the PBMR, while electricity contributes only a minor share (~8-10%) in both cases. Focusing on the benefit of the membrane reactor, the PBMR reduces the cooling water duty by 17.2% (10.44 to 8.64 MWh·$t_{NH_3}^{-1}$) and the steam/heating duty by 20.1% (7.20 to 5.75 MWh·$t_{NH_3}^{-1}$), driven by the smaller separation burden associated with the reduction from four to three retentate-side adsorption stages.

This yields a total specific energy consumption ranging from 19.20 MWh·t_{NH3}^{-1} for the PBR to 15.96 MWh·t_{NH3}^{-1} for the MR, a 16.9% reduction. Economically, **Figure 7.12**(b) shows that, under the present assumptions, the LCOA for the PBMR process is 5.6% lower than the reference PBR process (2,793 vs. 2,958 €·$t_{NH_3}^{-1}$), a more favourable outcome than our own previous work [3], in which the condensation-based membrane reactor's LCOA came out close to, or slightly higher than, its own reference case. This reversal is attributable to the change in separation technology: replacing condensation with adsorption-based separation reduces both the cooling and heating load simultaneously, translating the membrane reactor's established

efficiency gain into a genuine economic benefit rather than a cost-neutral or unfavourable trade-off.

7.6 SENSITIVITY ANALYSIS

To assess how sensitive the adsorption-based separation step is to sorbent performance, a sensitivity study was performed, in which the ideal adsorption selectivity of the sorbent toward NH_3 (relative to H_2 and N_2) was scaled by a multiplicative factor applied to the base-case values (**Table 7.17**), ranging from 1× up to 1000× the base case.

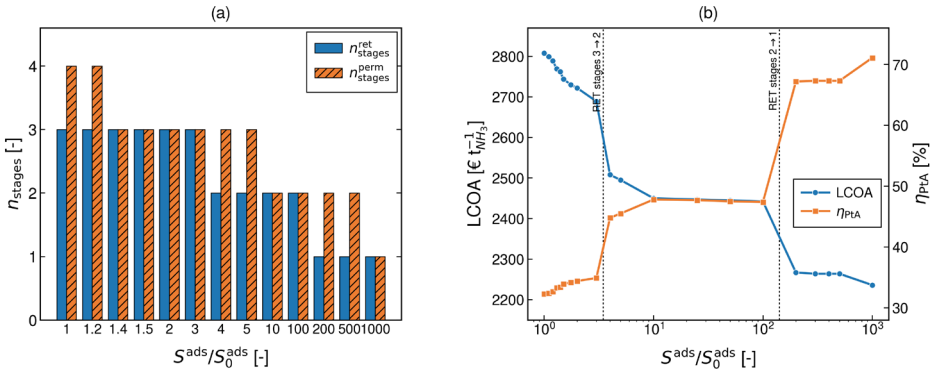


Figure 7.13 Effect of the multiplicative adsorption-selectivity factor on (a) the theoretical separation stages required on the retentate and permeate sides and (b) LCOA and η_{PtA} for the optimal membrane-reactor configuration; dotted lines indicate selectivity factors at which the required retentate-side stages decrease

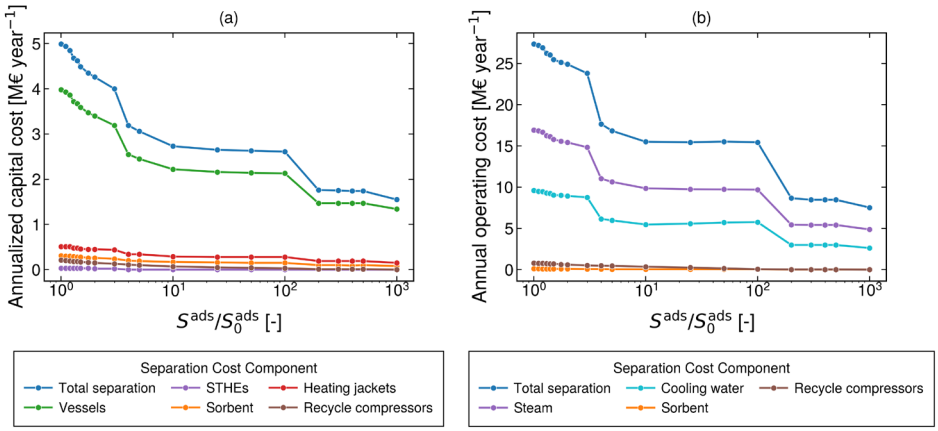


Figure 7.14 Influence of the adsorption-selectivity factor on the annualised cost of the separation step: (a) capital cost and (b) operating cost, broken down by cost component

At the base case, the optimal membrane-reactor configuration required three adsorption stages on the retentate side and four on the permeate side to reach the

target product purity.
Increasing the selectivity progressively reduced this stage count on both sides, with the retentate stages dropping from three to two at a selectivity factor of around 4, and further to one stage above a factor of roughly 150; the permeate side showed an analogous, earlier reduction (**Figure 7.13**(a)).

Table 7.17 Ideal adsorption selectivities for H_2 and N_2 with respect to NH_3, at each multiplicative selectivity factor relative to the base-case sorbent ($S_{ads}/S^0_{ads} = 1$)

S_{ads}/S^0_{ads} [-]	$S^{ideal}_{NH_3/H_2}$ [-]	$S^{ideal}_{NH_3/N_2}$ [-]
1	30	10
1.1	33	11
1.2	36	12
1.3	39	13
1.4	42	14
1.5	45	15
1.75	52.5	17.5
2	60	20
3	90	30
4	120	40
5	150	50
10	300	100
25	750	250
50	1500	500
100	3000	1000
200	6000	2000
300	9000	3000
400	12000	4000
500	15000	5000
1000	30000	10000

Because the number of separation stages is the dominant driver of both the capital and operating cost of the separation step, this reduction translated directly into a lower LCOA and a higher η_{PtA}: LCOA decreased from approximately 2,810 to 2,240 €·$t^{-1}_{NH_3}$ (roughly 20%) across the investigated selectivity range, while the η_{PtA} rose from about 32% to 71%, with the largest single improvements occurring exactly at the two stage-reduction thresholds (**Figure 7.13**(b)).
Breaking down the separation step's annualised cost by component confirms that

this improvement is driven almost entirely by the vessel (capital) and steam and cooling-water (operating) contributions, which fall in step with the reduced stage count, while the sorbent, heating-jacket, and recycle-compressor contributions remain comparatively small throughout the investigated range (**Figure 7.14**).
It should be noted that this analysis assumed a constant sorbent price regardless of selectivity; since more selective sorbent materials are in practice likely to be more expensive, the LCOA improvements reported at high selectivity factors should be regarded as an optimistic bound rather than an achievable target with currently available, cost-competitive sorbents.
The sensitivity of LCOA to variations in the price of each major cost input was assessed for both the PBR and PBMR configurations by scaling each price component individually by a factor of 0.25-2.00 relative to its own base case value, with all other prices held fixed (**Figure 7.15**(a)-(b)). Hydrogen price is by far the dominant driver of LCOA in both configurations: varying it alone across this range shifts LCOA from approximately 1,500 to 4,350 €·$t_{NH_3}^{-1}$ for the PBR and from approximately 1,550 to 4,250 €·$t_{NH_3}^{-1}$ for the PBMR, consistent with hydrogen feedstock accounting for 59.0% and 62.3% of total variable OPEX, respectively (**Table 7.16**).

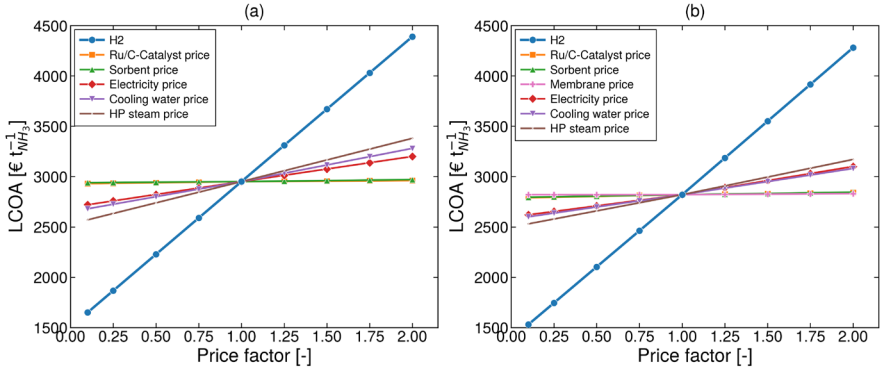


Figure 7.15 Sensitivity of LCOA to individual price components for: (a) PBR; (b) PBMR configurations. Each component was varied from 0.25 to 2.00 times its base-case value while all other prices were held constant

Every other price component produces a comparatively minor effect in both configurations, with LCOA remaining within a narrow band of the base-case value (2,958 €·$t_{NH_3}^{-1}$ for the PBR, 2,793 €·$t_{NH_3}^{-1}$ for the PBMR) across the same range. Excluding hydrogen to resolve the remaining trends, a clear secondary ranking emerges: HP steam price has the largest remaining effect, followed by cooling water and electricity price, which show comparable, moderate sensitivity; Ru/C catalyst and sorbent prices are, by contrast, nearly insensitive parameters in both configurations, consistent with their combined negligible share of total OPEX

(about 0.5% in each case).

For the PBMR, membrane price is also included in this comparison and proves to be the least sensitive parameter of all (visibly flatter across the full range than even catalyst and sorbent price) consistent with the negligible membrane OPEX share established above. This ranking mirrors the OPEX composition established in the economic analysis directly: the components with the largest OPEX share (H_2, steam) are also those to which LCOA is most sensitive in both configurations, while components with negligible OPEX share (catalyst, sorbent, membrane) leave LCOA essentially unchanged regardless of price. This confirms that securing low-cost green hydrogen, rather than catalyst, sorbent, membrane, or utility costs, remains the single most important economic lever for both the conventional and membrane-assisted processes. The LCOA values obtained in this study, 2,958 €·$t_{NH_3}^{-1}$ for the PBR and 2,793 €·$t_{NH_3}^{-1}$ for the PBMR, sit well above the range typically reported for commercial-scale green ammonia plants, which spans roughly 300-900 €·$t_{NH_3}^{-1}$ depending on location, renewable energy cost, and plant scale. Techno-economic evaluations of renewable-energy-driven ammonia synthesis report LCOA values of 772.1 €·$t_{NH_3}^{-1}$ in Northern Germany, 569.3 €·$t_{NH_3}^{-1}$ in Southern Spain, and 484.7 €·$t_{NH_3}^{-1}$ in Saudi Arabia [48], while other assessments report an LCOA of 332.1 €·$t_{NH_3}^{-1}$ for a gas-switching reforming concept against 385.1-385.9 €·$t_{NH_3}^{-1}$ for conventional plants at European energy prices [49]. Production scale explains part, but not all, of this gap. A recent techno-economic assessment of a small-scale, 2.4 t_{NH_3}·day^{-1} offshore e-ammonia plant reports an LCOA in the range of approximately 2,000-2,600 €·$t_{NH_3}^{-1}$ [50], superficially similar in magnitude to the present study; however, the plant considered here produces approximately 140 t_{NH_3}·day^{-1}, and its specific capital cost (462 €·$t_{NH_3}^{-1}$) is correspondingly lower than that reference plant's (662 €·$t_{NH_3}^{-1}$), consistent with the expected economy-of-scale advantage of the larger configuration. This remaining gap is attributable primarily to the hydrogen feedstock price assumed in this work (8.6 €·$kg_{H_2}^{-1}$): the reference offshore plant generates hydrogen on-site via electrolysis powered by a dedicated wind electricity price of 0.0199 €·kWh^{-1}, corresponding to an effective hydrogen cost of approximately 1.12 €·$kg_{H_2}^{-1}$, roughly 7.7 times lower than the externally purchased hydrogen price assumed here. Re-evaluating the present study's LCOA at this lower effective hydrogen cost yields 1,537-1,695 €·$t_{NH_3}^{-1}$, below the reference plant's own LCOA, confirming that the scale advantage of the configuration considered here is real but is masked in a direct comparison by the substantially more favourable hydrogen cost basis assumed in the reference study.

Conventional (grey) ammonia, produced via steam-methane reforming or autothermal reforming and ammonia synthesised via a conventional Haber-Bosch

process, delivered to Northwest Europe, was assessed at approximately 609 €·$t_{NH_3}^{-1}$ in late 2025 [51]. In contrast, green ammonia, based on hydrogen from PEM or alkaline electrolysis using renewable electricity and a conventional Haber-Bosch process, traded in the first quarter of 2026 in the range 705 €·$t_{NH_3}^{-1}$ in India to 764 €·$t_{NH_3}^{-1}$ in Canada, with Germany (the only European country in this scenario) at around 722 €·$t_{NH_3}^{-1}$. Both the PBR and PBMR LCOA values obtained in this work (2,958 and 2,793 €·$t_{NH_3}^{-1}$, respectively) are therefore more than three times higher than current market prices for either grey or green ammonia, consistent with the scale and hydrogen-price effects established above rather than any general shortcoming of the membrane-reactor concept. No prices are reported for ammonia exported from Europe to other regions, indicating that large-scale export of European green ammonia is not yet established as a commercial practice. In the techno-economic analysis presented here, the conventional configuration (single packed bed reactor with adsorption-based separation) is taken as the reference case, and the cost of ammonia (COA) for the membrane-assisted process is compared directly against this baseline. The primary objective is thus to quantify the relative cost penalty or benefit of integrating a PBMR, rather than to reproduce prevailing market prices.

7.7 REGULATORY AND POLICY SCENARIO ANALYSIS

The techno-economic assessment presented above holds hydrogen and ammonia prices fixed at their early 2026 levels. In practice, both are moving targets: in April 2026 alone, the closure of the Strait of Hormuz disrupted an estimated 35% of global ammonia and urea trade, contributing to a 71% spike in EU nitrogen-fertiliser prices and prompting the European Commission to adopt an EU Fertiliser Action Plan that explicitly links food-security concerns to support for domestic, decarbonised ammonia capacity [52].

This illustrates that the competitiveness of the PBR/PBMR concept should be assessed not only against current spot prices, but against a small number of plausible regulatory and policy trajectories that could alter the cost of the grey-ammonia benchmark, the cost of renewable hydrogen, and the price the plant's product could command.

Carbon pricing affects this study indirectly, via the grey-ammonia benchmark, since the process modelled here uses purchased renewable hydrogen and reports no direct CO_2 emissions. Since the CBAM entered its definitive phase in January 2026, fertilisers are covered, with the certificate price tied to the weekly EU Emissions Trading System (ETS) allowance price, which fluctuated around 72-83 €·$t_{CO_2}^{-1}$ over 2026 [53,54]. Conventional (grey) ammonia carries process emissions of approximately 2.16 t_{CO_2eq}·$t_{NH_3}^{-1}$ [55]; at a representative 80 €·$t_{CO_2}^{-1}$ price, full exposure

would add about 173 €·$t_{NH_3}^{-1}$ to the 609 €·$t_{NH_3}^{-1}$ grey-ammonia benchmark, raising it to roughly 780 €·$t_{NH_3}^{-1}$ (+28%). This closes less than 8% of the more than 2,180 €·$t_{NH_3}^{-1}$ gap to the PBMR LCOA (2,793 €·$t_{NH_3}^{-1}$). Carbon pricing is therefore a real but second-order lever here: it gradually reduces the cost advantage of grey ammonia, but even doubling the current carbon price would not be enough to eliminate the difference.

Hydrogen subsidies help reduce the cost gap between renewable and grey ammonia instead of increasing the cost of grey ammonia through taxation. The European Hydrogen Bank has held two auctions, offering support of 0.20-0.60 €·$kg_{H_2}^{-1}$ for general projects and up to 1.88 €·$kg_{H_2}^{-1}$ for maritime projects over ten years, using a budget of more than €900 million [56].

On the demand side, buyers are beginning to pay a premium for green ammonia, although public information remains limited. In January 2026, Uniper and AM Green signed an agreement for the purchase of up to 500,000 t_{NH_3}·y^{-1} from 2028, but the price was not disclosed.

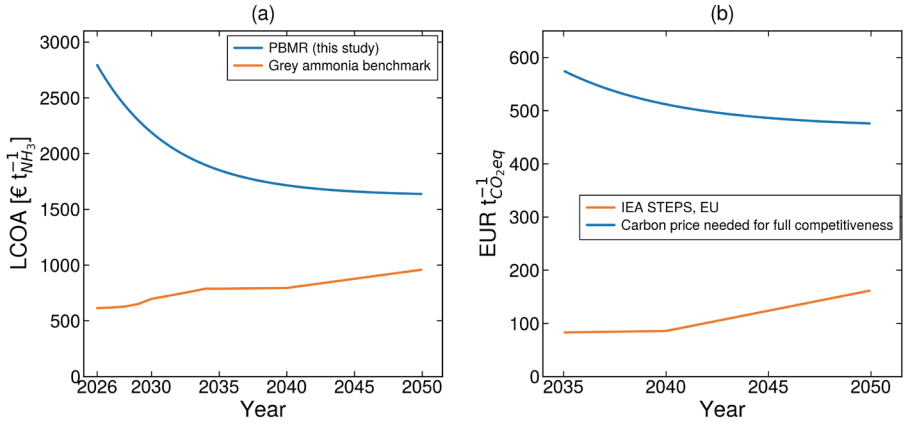


Figure 7.16 Projected cost competitiveness of the PBMR ammonia route vs. the grey-ammonia benchmark, 2026-2050: (a) PBMR and grey-ammonia LCOA, including the EU carbon costs applied during CBAM phase-in; (b) Projected EU carbon price under the IEA Stated Policies Scenario (STEPS) vs. the price required for the grey-ammonia benchmark to achieve cost parity with the PBMR route

The measures discussed above are evaluated using 2026 values. To extend the analysis to 2050, the hydrogen price, PBMR LCOA, and grey-ammonia benchmark are projected using three external forecasts. This approach follows standard practice for estimating when a low-carbon process may reach cost parity with its conventional counterpart. First, the hydrogen-price projection is rescaled from the renewable-hydrogen reported by Detz et al. [57]. The base-case value of 8.6 €·$kg_{H_2}^{-1}$ used in this study (**Table 7.8**) is consistent with the system boundary of the source

learning curve, which includes hydrogen production and on-site storage but excludes compression and downstream delivery. The projection is cross-checked against an independent estimate of 5.2 €·$kg_{H_2}^{-1}$ for EU hydrogen in 2030 [58].

Figure 7.16 compares the projected LCOA for the PBMR route (calibrated against ICCT's 2030 EU hydrogen production cost estimate [59]) against a CBAM-adjusted grey-ammonia benchmark. The benchmark assumes an emission factor of 2.16 $t_{CO_2} \cdot t_{NH_3}^{-1}$ for conventional ammonia production [55], and its cost rises over time as the EU CBAM charge phases in fully by 2034 (Regulation (EU) 2023/956, Art. 31 [60]) and as the underlying EU carbon price increases, taken here from the IEA's Stated Policies Scenario (STEPS) for the European Union [61].

As **Figure 7.16**(a) shows, the cost gap between the two routes narrows steadily, from roughly 2,180 €·$t_{NH_3}^{-1}$ in 2026 to about 680 €·$t_{NH_3}^{-1}$ by 2050, but does not close within this horizon. **Figure 7.16**(b) presents the result from the perspective of carbon pricing. Under the IEA STEPS scenario, the projected carbon price remains well below the approximately 470-575 €·$t_{CO_2}^{-1}$ required to achieve full cost parity throughout the period. This represents a more conservative outlook than scenarios based on stronger carbon-price growth, reflecting the STEPS scenario's focus on current and stated policies rather than aspirational targets. More ambitious scenarios, such as APS and NZE, would imply faster convergence and could be included as sensitivity cases.

7.8 CONCLUSIONS

This chapter has presented a techno-economic comparison between a conventional packed bed reactor (PBR) and a packed bed membrane reactor (PBMR) coupled with adsorption-based separation, for small-scale green ammonia synthesis from renewable hydrogen. Both configurations were optimised independently, following a consistent two-step approach: first screening the operating window (T_{in}^{R}, P_{in}^{R}) and reactor geometry (L_r, L_r/D_r^i), then optimizing the configuration-specific parameters at the resulting design point, i.e. reactor length and aspect ratio for the PBR, and sweep-gas-to-feed flow ratio, transmembrane pressure difference, permeate composition and membrane number for the PBMR.

The optimised PBR reaches its lowest LCOA (2,958 €·$t_{NH_3}^{-1}$) at T_{in}^{R} = 625 K, P_{in}^{R} = 50 bar, L_r = 7.50 m, L_r/D_r^i = 3.50, an operating point at the lower boundary of the temperature range considered, reflecting the trade-off between equilibrium conversion, compression work and intrinsic reaction rate inherent to a fixed-bed configuration. The optimised PBMR reaches a lower LCOA (2,793 €·$t_{NH_3}^{-1}$, a 5.6% reduction) at a more compact aspect ratio (L_r/D_r^i = 3.0), combined with a SW = 0.67 and a hydrogen-rich permeate stream ($y_{H_2,in}^{P}$ = 0.90). This improvement is

accompanied by a 20% relative increase in power-to-ammonia efficiency (26.9% vs. 32.4%) and substantially higher per-pass H_2 conversion (15.6% vs. 20.1%), confirming that in-situ ammonia removal via the membrane relaxes the equilibrium constraint that otherwise forces the traditional reactor toward its slowest, least productive operating regime. at an almost identical reactor volume (27.05 vs. 26.75 m^3) and with a slightly lower catalyst loading (3,191 vs. 3,003 kg), and despite an essentially identical Cold Gas Efficiency between the two configurations (84.3%).

Economically, the PBMR's advantage is broad rather than concentrated: total CAPEX falls by 4.3%, driven primarily by a smaller separation section as part of the separation duty shifts to the membrane itself, while total OPEX falls by 7.1% across hydrogen feedstock, steam and cooling water consumption simultaneously, rather than through any single dominant saving. Sensitivity analysis confirms that hydrogen price remains, by a wide margin, the single most important economic lever for both configurations, with LCOA varying by roughly ±55% across the price range tested, while sensitivity to catalyst, sorbent and membrane costs is negligible by comparison, indicating that further reductions in the cost of renewable hydrogen would benefit both configurations proportionally, without changing their relative ranking.

Placed in the context of the wider literature, the LCOA values obtained here remain substantially above those reported for utility-scale green ammonia plants (roughly 300-900 $€\cdot t_{NH_3}^{-1}$), but align closely with the limited number of studies addressing small-scale, low-pressure plants of comparable capacity, confirming that the elevated cost obtained in this study is primarily a consequence of production scale. Both PBR and PBMR LCOA values remain more than three times higher than current market ammonia prices (approximately 609 $€\cdot t_{NH_3}^{-1}$ for grey ammonia in late 2025, and 705-764 $€\cdot t_{NH_3}^{-1}$ for green ammonia across major markets in Q1 2026). Relative to our own previous work, a membrane-reactor PtA process retaining condensation for final purification, which achieved an efficiency gain without a corresponding cost reduction, the present adsorption-assisted configuration achieves both a technical and an economic improvement simultaneously, directly confirming the motivation stated in the introduction: replacing condensation with a milder, adsorption-based separation step unlocks more of the membrane reactor's intrinsic potential than was possible with condensation alone.

Several aspects of the optimisation were not pursued to full joint convergence within the scope of this work and are noted here as directions for future refinement. The membrane-specific parameter screening was carried out at a fixed geometry established earlier in the optimisation sequence, rather than being re-optimised jointly at every candidate aspect ratio; similarly, the adsorption/desorption temperature optimisation was performed using membrane parameters close to, but not identical to, the final adopted configuration. A fully joint optimisation across geometry, membrane operation, and adsorption conditions was outside the scope of

the present study, but the consistency observed between these partially independent optimisations suggests any further gain from closing this gap is likely to be modest rather than transformative. More significant potential for improvement lies in production scale: given the strong sensitivity of LCOA to plant capacity observed when comparing this study to the wider literature, extending the present model to larger production scales represents the most promising direction for narrowing the gap between the LCOA obtained here and current or anticipated market ammonia prices.

A.7 APPENDIX

A.7.1. ASU refrigeration loop

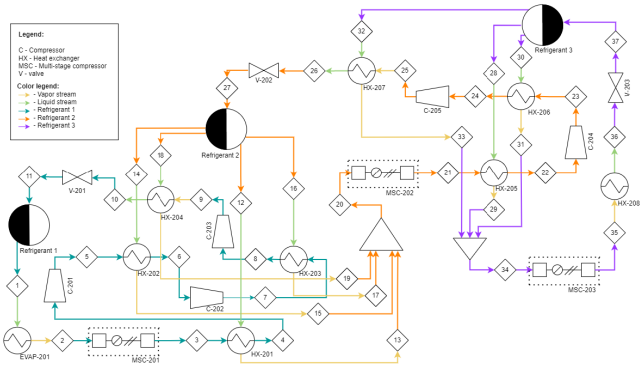


Figure A.7.1 Process flow diagram for Refrigeration Loops

Table A.7.1 Design parameters for refrigeration loops

	Loop 1-Methane		Loop 2-Ethane		Loop 3-Propylene	
	Evap. 1	Cond. 1	Evap. 2	Cond. 2	Evap. 3	Cond. 3
T [°C]	-168	-97.90	-103.00	-20.29	-25.58	25.19
P [bar]	0.57	28	0.43	14.1	2.5	11.6
Vapour Inlet	ASU Str.	Methane	Methane	Ethane	Ethane	Propylene
Liquid Inlet	Methane	Ethane	Ethane	Propylene	Propylene	Cool. Water
Comp. stages	5		4		2	
Pres. ratio	2.18		2.39		2.15	

A.7.2 Kinetic model validation

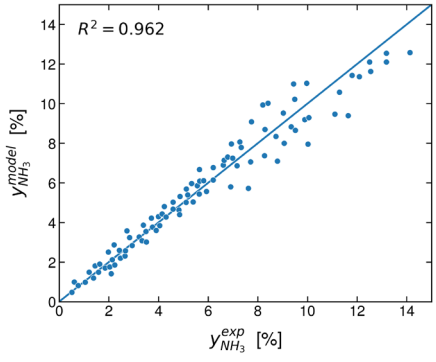


Figure A.7.2 Parity plot comparing simulated and experimental NH_3 mole fractions, $y_{NH_3}^{exp}$ vs. $y_{NH_3}^{model}$

A.7.3 PBMR sensitivity analysis

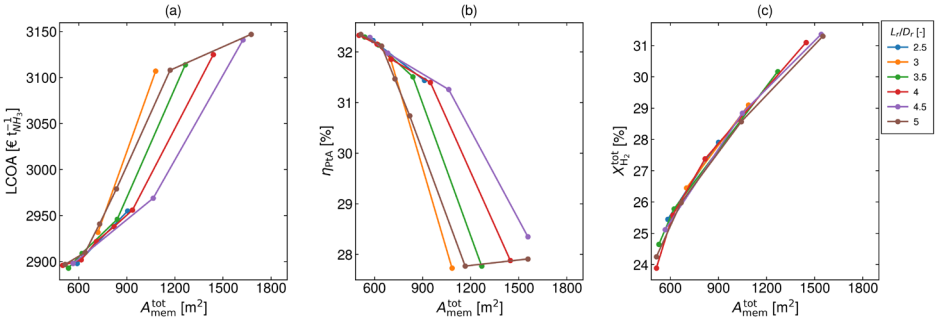


Figure A.7.3 Effect of total membrane area (A_{mem}^{tot}) at T_{in}^{R} = 625 K, P_{in}^{R} = 60 bar and SW = 1 for L_r/D_r^i = 2.5, 3.0, 3.5, 4.0, 4.5, 5.0: (a) LCOA, (b) H_2 conversion,(c) PtA

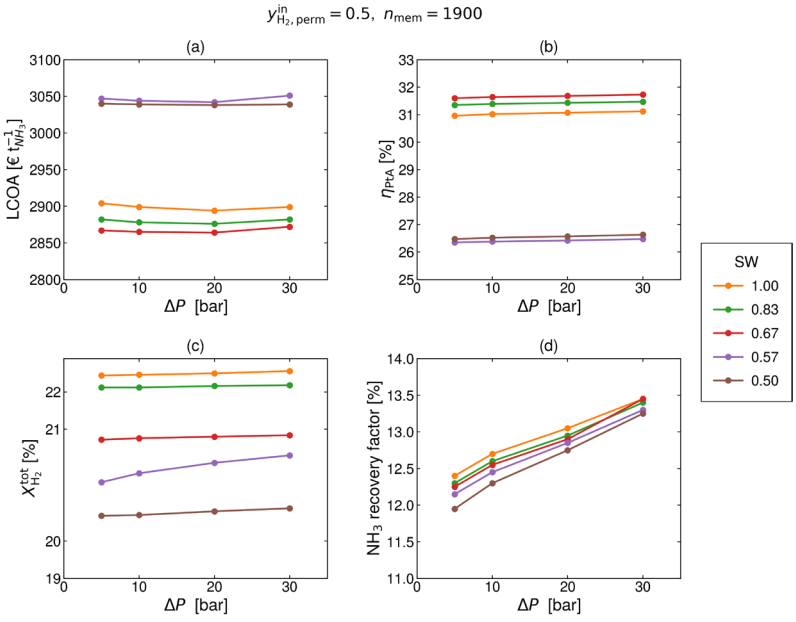


Figure A.7.4 Effect of ΔP at different SW (0.5, 0.57, 0.67, 0.83, 1, 1.25) at $y_{H_2,in}^{P}$ = 0.50, n_{mem} = 1900: (a) LCOA, (b) PtA,(c) H_2 conversion, (d) NH_3 recovery factor

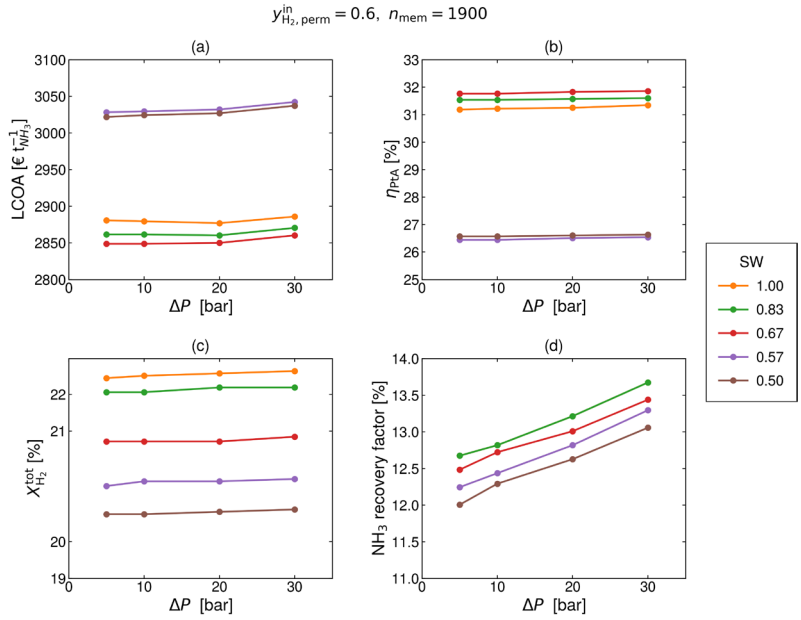


Figure A.7.5 Effect of ΔP at different SW (0.5, 0.57, 0.67, 0.83, 1, 1.25) at $y^{P}_{H_2,in} = 0.60$, $n_{mem} = 1900$: (a) LCOA, (b) PtA,(c) H_2 conversion, (d) NH_3 recovery factor

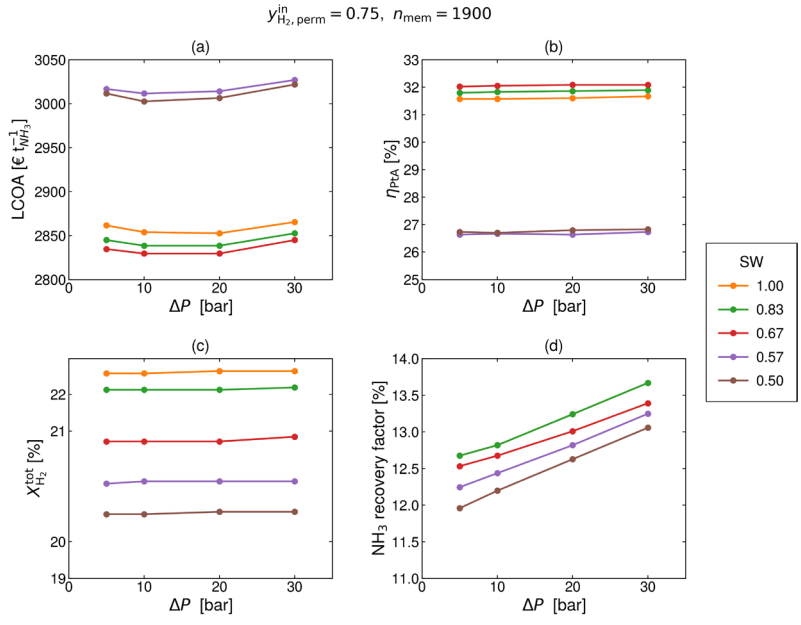


Figure A.7.6 Effect of ΔP at different SW (0.5, 0.57, 0.67, 0.83, 1, 1.25) at $y^{P}_{H_2,in} = 0.75$, $n_{mem} = 1900$: (a) LCOA, (b) PtA,(c) H_2 conversion, (d) NH_3 recovery factor

REFERENCES

[1] B. Lin, T. Wiesner, M. Malmali, "Performance of a Small-Scale Haber Process: A Techno-Economic Analysis", *ACS Sustain. Chem. Eng.* 8 (2020) 15517–15531. https://doi.org/10.1021/acssuschemeng.0C04313.

[2] M. Yoshida, T. Ogawa, Y. Imamura, K.N. Ishihara, "Economies of scale in ammonia synthesis loops embedded with iron- and ruthenium-based catalysts", *Int. J. Hydrogen Energy* 46 (2021) 28840–28854. https://doi.org/10.1016/j.ijhydene.2020.12.081.

[3] S. Richard, V. Verde, N. Kezibri, C. Makhloufi, A. Saker, I. Gargiulo, F. Gallucci, "Power-to-ammonia synthesis process with membrane reactors: Techno-economic study", *Int. J. Hydrogen Energy* 73 (2024) 462–474. https://doi.org/10.1016/J.ijhydene.2024.06.041.

[4] M. Tokushige, J. Ryu, "Adsorption and Desorption Behaviors of Ammonia on Zeolites at 473 K by the Pressure-Swing Method", *ACS Omega* 8 (2023) 32536–32543. https://doi.org/10.1021/acsomega.3C02882.

[5] J. Helminen, J. Helenius, E. Paatero, I. Turunen, "Comparison of sorbents and isotherm models for NH3-gas separation by adsorption", *AIChE Journal* 46 (2000) 1541–1555. https://doi.org/10.1002/aic.690460807.

[6] Z. Yuan, Y. Bai, K. Gong, W. Huang, "Accurate Measurements of NH3 Differential Adsorption Heat Unveil Structural Sensitivity of Brønsted Acid and Brønsted/Lewis Acid Synergy in Zeolites", *J. Phys. Chem. Lett.* 15 (2024) 863–868. https://doi.org/10.1021/acs.jpclett.3C03336.

[7] R. Patel, J. Castro, M. Tsapatsis, J.I. Siepmann, "Molecular Simulations Probing the Adsorption and Diffusion of Ammonia, Nitrogen, Hydrogen, and Their Mixtures in Bulk MFI Zeolite and MFI Nanosheets at High Temperature and Pressure", *J. Chem. Eng. Data* 67 (2022) 1779–1791. https://doi.org/10.1021/acs.jced.2C00086.

[8] A. Tripodi, M. Compagnoni, E. Bahadori, I. Rossetti, "Process simulation of ammonia synthesis over optimized Ru/C catalyst and multibed Fe + Ru configurations", *Journal of Industrial and Engineering Chemistry* 66 (2018) 176–186. https://doi.org/10.1016/j.jiec.2018.05.027.

[9] O. Osman, S. Sgouridis, A. Sleptchenko, "Scaling the production of renewable ammonia: A techno-economic optimization applied in regions with high insolation", *J. Clean. Prod.* 271 (2020) 121627. https://doi.org/10.1016/j.jclepro.2020.121627.

[10] "A Fuel Standard for Ammonia: panel wrap-up from the Ammonia Energy Conference 2020" - Ammonia Energy Association,. https://ammoniaenergy.org/articles/a-fuel-standard-for-ammonia-panel-wrap-up-from-the-ammonia-energy-conference-2020/.

[11] I. Yin, E. Yep, "China's hydrogen ambitions may ride on Sinopec's Kuqa project in Xinjiang", *S and P Global* (2024).

[12] International Renewable Energy Agency (IRENA), Renewable Capacity Highlights 2025, (2025). https://unstats.un.org/unsd/methodology/m49/.

[13] Cost of hydrogen production | European Hydrogen Observatory. https://observatory.clean-hydrogen.europa.eu/hydrogen-landscape/production-trade-and-cost/cost-hydrogen-production.

[14] I. Rossetti, N. Pernicone, F. Ferrero, L. Forni, "Kinetic study of ammonia synthesis on a promoted Ru/C catalyst", *Ind. Eng. Chem. Res.* 45 (2006) 4150–4155. https://doi.org/10.1021/ie051398g.

[15] V. Pattabathula, J. Richardson, "Introduction to Ammonia Production", *Chem. Eng. Prog.* 112 (2016) 69–75. https://www.aiche.org/sites/default/files/cep/20160969.pdf.

[16] KBR Ammonia Energy Association. https://ammoniaenergy.org/organization/kbr/.

[17] O. Levenspiel, "Chemical Reaction Engineering", 3rd Edition, (1999)

[18] F. Cameli, A. Kourou, V. Rosa, E. Delikonstantis, V. Galvita, K.M. Van Geem, G.D. Stefanidis, "Conceptual process design and technoeconomic analysis of an e-ammonia plant: Green H2 and cryogenic air separation coupled with Haber-Bosch process", *Int. J. Hydrogen Energy* 49 (2024) 1416–1425. https://doi.org/10.1016/j.ijhydene.2023.10.020.

[19] S. Russell, "A recommended methodology for estimating and reporting the potential greenhouse gas emissions from fossil fuel reserves", *World Resources Institute*.

[20] N. Johnson, J. Baltrusaitis, W.L. Luyben, "Design and control of a cryogenic multi-stage compression refrigeration process", *Chemical Engineering Research and Design* 121 (2017) 360–367. https://doi.org/10.1016/j.cherd.2017.03.018.

[21] Ethane - Thermophysical Properties. https://www.engineeringtoolbox.com/ethane-d_1417.html.

[22] Ethylene - Thermophysical Properties. https://www.engineeringtoolbox.com/ethylene-ethene-C2H4-properties-d_2104.html.

[23] Linde, R1270 Propylene,. https://static.prd.echannel.linde.com/wcsstore/NO_REN_Industrial_Gas_Store/pdf/EN/Natural_refrigerant_R1270_CARE_45_Product_data_EN_tcm639-661326.pdf.

[24] C. Aristizabal-González, J.C. Muñoz-Senmache, N. Prerna, J.I. Siepmann, M. Tsapatsis, A.J. Hernández-Maldonado, "Ammonia Adsorption at High Temperature and Pressure Using Sodium Containing Aluminosilicates: Selectivity over Nitrogen and Multicycle Working Capacities", *Ind. Eng. Chem. Res.* 64 (2025) 4027–4039. https://doi.org/10.1021/acs.iecr.4c04621.

[25] H. Azzan, D. Danaci, C. Petit, R. Pini, "Unary Adsorption Equilibria of Hydrogen,

Nitrogen, and Carbon Dioxide on Y-Type Zeolites at Temperatures from 298 to 393 K and at Pressures up to 3 MPa", *J. Chem. Eng. Data* 68 (2023) 3512–3524. https://doi.org/10.1021/acs.jced.3c00504.

[26] "Saturated steam table pressure/temperature". https://www.kitzus-kca.com/wp-content/uploads/BIV-58.pdf.

[27] E. Bérut, M. Ondarts, F. Delachaux, M. Chhay, J. Outin, S. Bennici, N. Le Pierrès, "Simulation of a zeolite thermochemical heat storage reactor: Impact assessment of isotherm model selection", *Int. J. Heat Mass Transf.* 231 (2024) 125796. https://doi.org/10.1016/j.ijheatmasstransfer.2024.125796.

[28] M.I. Hossain, C.E. Holland, A.D. Ebner, J.A. Ritter, Mass "Transfer Mechanisms and Rates of CO2 and N2 in 13X Zeolite from Volumetric Frequency Response", *Ind. Eng. Chem. Res.* 58 (2019) 21679–21690. https://doi.org/10.1021/acs.iecr.9b04756.

[29] L. Qiu, V. Murashov, M.A. White, "Zeolite 4A: Heat capacity and thermodynamic properties", *Solid State Sci.* 2 (2000) 841–846. https://doi.org/10.1016/S1293-2558(00)01102-X.

[30] R. Smith, Chemical process: design and integration; Chapter 2: Process Economics, Wiley (2005) 17–33.

[31] Density of stainless steel 316 - Amardeep Steel.

[32] G.D. Ulrich, P. T. Vasudevan, Chemical engineering process design and economics a practical guide second edition, 2004.

[33] SECTION II: ASME Boiler and Pressure Vessel Code An International Code. www.asme.org/cer.

[34] AIGA 056/23 Safe Practice Guide for Cryogenic Air Separation Plants, 2023.

[35] 5 applications of INCONEL alloys, (2024). https://www.corrotherm.co.uk/blog/5-applications-of-inconel-alloys.

[36] Economic Indicators: March 2026 - Chemical Engineering | Page 1. https://www.chemengonline.com/2025-cepci-updates-november-prelim-and-october-final/.

[37] Currency Converter | Foreign Exchange Rates | OANDA, (n.d.). https://www.oanda.com/currency-converter/en/?from=EUR&to=USD&amount=0.87431.

[38] V. Spallina, D. Pandolfo, A. Battistella, M.C. Romano, M. Van Sint Annaland, F. Gallucci, "Techno-economic assessment of membrane assisted fluidized bed reactors for pure H2 production with CO2 capture", *Energy Convers. Manag.* 120 (2016) 257–273. https://doi.org/10.1016/j.enconman.2016.04.073.

[39] R. Turton, J.A. Shaeiwitz, D. Bhattacharyya, W.B. Whiting, "Analysis, Synthesis, and Design of Chemical Processes", Fifth Edition.

[40] Machine Operator Salary in Germany (2026). https://www.erieri.com/salary/job/machine-operator/germany.

[41] Ruthenium price | Umicore Precious Metals Management. https://pmm.umicore.com/en/prices/ruthenium.

[42] Quartz Granules, https://dir.indiamart.com/impcat/quartz-granules.html.

[43] China Zeolite 13x Apg Molecular Sieve, Zeolite 13x Apg Molecular Sieve Wholesale, Manufacturers, Price. https://www.made-in-china.com/products-search/hot-china-products/Zeolite_13x_Apg_Molecular_Sieve.html.

[44] W.L. Luyben, "Estimating refrigeration costs at cryogenic temperatures", *Comput. Chem. Eng.* 103 (2017) 144–150. https://doi.org/10.1016/j.compchemeng.2017.03.013.

[45] Germany Electricity Price - Quote - Chart - Historical Data - News. https://tradingeconomics.com/germany/electricity-price.

[46] Gas sales - German Federal Statistical Office. https://www.destatis.de/EN/Themes/Economic-Sectors-Enterprises/Energy/Use/Tables/gas-sales.html.

[47] A. Boulamanti, J.A. Moya, "Production costs of the chemical industry in the EU and other countries: Ammonia, methanol and light olefins", *Renewable and Sustainable Energy Reviews* 68 (2017) 1205–1212. https://doi.org/10.1016/j.rser.2016.02.021.

[48] R. Sun, L. Sun, J. Li, "Techno-economic evaluation of green ammonia synthesis for renewable energy storage using rigorous models", *Energy* 336 (2025) 138068. https://doi.org/10.1016/j.energy.2025.138068.

[49] C. Arnaiz del Pozo, S. Cloete, "Techno-economic assessment of blue and green ammonia as energy carriers in a low-carbon future", *Energy Convers. Manag.* 255 (2022) 115312. https://doi.org/10.1016/j.enconman.2022.115312.

[50] L. Pérez-Gandarillas, B. Galán, J.R. Viguri, "Techno-Economic Analysis of Small-Scale Electro-Ammonia Production in a Port Platform for Maritime Transport", *Clean Technologies* 8 (2026) 65. https://doi.org/10.3390/cleantechnol8030065.

[51] Interactive: Ammonia price chart | S&P Global. https://www.spglobal.com/energy/en/news-research/latest-news/energy-transition/051023-interactive-ammonia-price-chart-natural-gas-feedstock-europe-usgc-black-sea.

[52] After a 71% nitrogen price spike, the EU adopts | Wikifarmer. https://wikifarmer.com/library/en/article/eu-fertiliser-action-plan-2026.

[53] EU carbon market outlook: How politics is shaping carbon prices in 2026 | INSIGHT. https://www.reccessary.com/en/insight/eu-carbon-price-outlook-2026-ets-reform.

[54] Carbon Border Adjustment Mechanism - Taxation and Customs Union.

https://taxation-customs.ec.europa.eu/carbon-border-adjustment-mechanism_en.

[55] S. Ghavam, M. Vahdati, I.A.G. Wilson, P. Styring, "Sustainable Ammonia Production Processes", *Front. Energy Res.* 9 (2021). https://doi.org/10.3389/fenrg.2021.580808.

[56] European Hydrogen Bank - European Commission. https://energy.ec.europa.eu/topics/eus-energy-system/hydrogen/european-hydrogen-bank_en.

[57] R.J. Detz, J.N.H. Reek, B.C.C. Van Der Zwaan, "The future of solar fuels: when could they become competitive?", *Energy Environ. Sci.* (2018). https://doi.org/10.1039/c8ee00111a.

[58] G. Glenk, S. Reichelstein, "Economics of converting renewable power to hydrogen", *Nat. Energy* 4 (2019) 216–222. https://doi.org/10.1038/S41560-019-0326-1.

[59] International Council on Clean Transportation (ICCT), 20 May 2024. https://theicct.org/the-price-of-green-hydrogen-estimate-future-production-costs-may24/

[60] Regulation - 2023/956 - EN - cbam regulation - EUR-Lex. https://eur-lex.europa.eu/eli/reg/2023/956/oj/en

[61] International Energy Agency (IEA), World Energy Outlook 2025 – Stated Policies Scenario (STEPS), IEA, Paris, 2025. https://www.iea.org/reports/world-energy-outlook-2025.

CHAPTER 8

Conclusions & Outlook

8.1 CONCLUSIONS

In this thesis, membrane reactor technology for ammonia synthesis was investigated across multiple scales, with the overarching aim of elucidating how coupled reaction-separation and transport phenomena shape reactor performance from lab-scale systems up to multi-membrane configurations.

In **Chapter 2** a non-isothermal one-dimensional packed bed membrane reactor model for ammonia synthesis over Ru/C was developed and validated, with the objective of identifying operating conditions under which the process can surpass the equilibrium limitations of the conventional Haber-Bosch reactor. The analysis showed that membrane performance requirements are close to the current state of the art, but that the optimal operating window is shifted toward lower temperatures than typical industrial practice, leading to the proposal of carbon molecular sieve membranes as promising candidates due to their thermal and chemical stability over a wide range of pressures and temperatures. Under isothermal conditions, the model identified quantitative benchmarks of $\mathcal{P}_{NH_3} > 10^{-7}$ mol m^{-2}Pa^{-1}s^{-1}, $S_{NH_3/H_2} = 50$ and $S_{NH_3/N_2} = 100$ as necessary to significantly enhance H_2 conversion while balancing NH_3 purity and recovery. Parametric studies confirmed sweep-gas-to-feed flow ratio (SW) and transmembrane pressure difference (ΔP) as key design variables, identifying optimal isothermal operation at a sweep-gas-to-feed flow ratio SW = 6 and ΔP = 20 bar, and showing in the adiabatic configuration that integrated feed-permeate heat exchange with sweep-gas cooling can achieve H_2 conversion of 93.0%, NH_3 recovery of 99.2%, and NH_3 purity of 5.7% at a permeate inlet temperature of 200 °C.

Based on the membrane performance requirements established in Chapter 2, **Chapter 3** investigated phenolic-derived carbon molecular sieve (CMS) membranes as NH_3-selective candidates by systematically varying two key synthesis parameters: carbonisation temperature and transition-metal doping (Co, Cu, Ni, Zn). Through permporometry, SEM and confocal laser microscopy, the study showed that lower carbonisation temperatures (500-550 °C) generate broader pore size distributions with a second peak shifted toward larger diameters, forming more open ultra-microporous structures, whereas higher temperatures (~700 °C) produce tighter ultra-micropores centred around ~0.5 nm and slightly thinner carbon layers with increased surface roughness. Pure- and mixed-gas permeation experiments with NH_3, H_2 and N_2 at 150-350 °C revealed that these structural changes translate directly into distinct transport regimes. At low temperature, Cu- and Ni-doped CMS

membranes exhibit high NH_3 permeance with a strong negative temperature dependence and very large NH_3 surface diffusion fractions (~88% for Cu and ~70% for Ni at 150 °C), while H_2 and N_2 permeances remain nearly constant or increase with temperature, indicating size-controlled, sieving-dominated transport through narrow pores. As temperature rises to 350 °C, Cu and Ni membranes retain substantial NH_3 surface diffusion (~85% and > 65%, respectively), demonstrating robust metal-NH_3 interactions across the relevant reaction window, whereas Zn- and especially Co-doped membranes show weak or vanishing NH_3 surface diffusion and behave predominantly as molecular sieves. To formalise this mechanistic picture, an established transport model combining Gaussian pore size distributions, Langmuir adsorption and parallel contributions of molecular sieving, micro-Knudsen diffusion and surface diffusion was fitted against the experimental flux data across all gases and operating conditions. The fitted model was then used to decompose the total flux into its underlying mechanisms, quantitatively confirming that NH_3 transport in Cu- and Ni-based CMS membranes is dominated by adsorption-diffusion in the broader ultra-micropore population at lower carbonisation temperatures, while H_2 and N_2 transport remains governed by activated sieving and micro-Knudsen diffusion in the tighter pores. When these mechanistic insights are compared with the permeance and perm-selectivity targets derived in Chapter 2, Cu-doped CMS membranes carbonised at 500-550 °C emerge as the most promising membranes for ammonia synthesis, offering the best compromise between high NH_3 permeance and favourable NH_3/H_2 and NH_3/N_2 selectivities under mixed-gas conditions; however, while the achieved NH_3 permeance is already in line with the Chapter 2 benchmarks, further improvement in NH_3/H_2 and NH_3/N_2 perm-selectivities remains necessary to fully meet the membrane performance targets for intensified reactor operation.

In **Chapter 4**, the Cu-based CMS membrane identified in Chapter 3 was integrated with a Ru-activated POCS Gyroid (and BCC) structured catalyst to realise a membrane-intensified reactor for ammonia synthesis and experimentally evaluate its performance under relevant operating conditions. Unlike conventional packed bed catalysts, the POCS-based structured supports were deliberately employed to simultaneously investigate how enhanced heat and mass transfer, improved thermal management, and reduced pressure drop in the catalytic bed influence the synergy between Ru catalysis and in-situ ammonia removal, and to assess whether internal geometry (Gyroid vs. BCC) could further affect reactor performance. The results showed that, within the identified optimal operating window, both geometries deliver essentially comparable NH_3 production rates and equilibrium shifting, indicating that in this system the details of the POCS architecture play a minor role compared with operating conditions and membrane properties. Importantly, even though the membrane permeance-selectivity combination did not fully reach the ideal targets defined in Chapter 2, appropriate tuning of pressure, temperature,

sweep-gas-to-feed flow ratio and residence time in this lab-scale reactor still enabled the structured membrane reactor to outperform the corresponding structured reactor without a membrane, demonstrating that non-ideal NH_3-selective membranes can nevertheless deliver a significantly intensified process when embedded in a carefully optimised operating window. In particular, the experiments showed that an understoichiometric H_2:N_2 feed ratio of 2:1 systematically improves Ru-catalyst performance relative to the conventional 3:1 ratio, that a moderate sweep-gas-to-feed flow ratio (SW~4) offers the best compromise between equilibrium shifting and hydrogen losses, and that pressures in the range 30-40 bar combined with intermediate temperatures around 400 °C maximize the synergy between in-situ ammonia removal and Ru kinetics; under these near-optimal conditions, H_2 conversion exceeded the corresponding equilibrium value by roughly 15-30%, while NH_3 production rate and NH_3 yield increased by about 77% and 53%, respectively, compared to the structured reactor without a membrane.

In **Chapter 5**, the membrane reactor concept developed in Chapters 2-4 was extended to multi-membrane configurations by analysing a two-dimensional, non-isothermal packed bed membrane reactor that accounts for radial transport and concentration polarisation, with the primary objective of elucidating the transport phenomena that will arise upon scale-up of ammonia membrane reactors. Comparison between the 2D fields and 1D plug-flow predictions showed that the 1D model systematically overestimates H_2 conversion, NH_3 recovery, NH_3 yield and peak temperature rise, and that these discrepancies originate from the combined effect of concentration polarisation at the membrane wall and the strong thermodynamic sensitivity near equilibrium in compact, high-surface-to-volume geometries. The 2D analysis shows that compact annuli (small tube pitch, high surface-to-volume ratio) consistently outperform wider annuli in terms of H_2 conversion and NH_3 recovery, and that this advantage increases as pressure is raised. However, it also demonstrates that continuous ammonia removal unavoidably generates concentration polarisation at the membrane wall in all operating regimes, with its impact on performance becoming particularly severe in compact geometries and at low GHSV where the retentate approaches equilibrium and reactor behaviour is highly sensitive to radial concentration gradients. Under these conditions, radial diffusion cannot replenish ammonia at the same rate as it is produced and permeated, causing the NH_3 mole fraction at the membrane surface to collapse to near zero over the downstream half of the reactor and rendering that section effectively non-productive. This leads to a clear design implication: in compact multi-membrane geometries operated close to equilibrium, membrane length should be intentionally truncated once the wall NH_3 concentration remains depleted, so that the reactor retains the conversion benefits of high surface-to-volume ratio while limiting concentration-polarisation losses, reducing hot spots, and improving membrane utilisation. In parallel, a geometry-dependent reaction-enhanced

Sherwood correlation was derived from the 2D concentration fields, which can be embedded into reduced 1D PBMR models to correct wall concentrations and capture concentration-polarisation effects when designing multi-membrane ammonia reactors without resorting to full 2D simulations.

Following up on the multi-membrane reactor scale-up analysis developed in Chapter 5, **Chapter 6** experimentally investigated a multi-membrane structured catalyst reactor as a direct scale-up of the single-membrane TPMS/POCS concept introduced in Chapter 4, assessing how ammonia synthesis performance evolves when the membrane area and the number of membranes are increased under comparable operating conditions. Baseline tests of Gyroid and BCC POCS supports operated without membranes confirmed that the two geometries provide essentially identical catalytic performance at larger scale, in line with the single-membrane observations of Chapter 4. Membrane-integrated experiments, including comparisons at the same WHSV used in Chapter 4, showed that increasing membrane area and the number of membranes systematically enhances ammonia production and equilibrium shifting under otherwise identical conditions; beyond-equilibrium operation, in which H_2 conversion and NH_3 yield reproducibly exceeded the thermodynamic equilibrium, was achieved exclusively at low WHSV with a sweep-gas-to-feed flow ratio of SW = 4, with H_2 conversion surpassing the equilibrium limit by about 30% at 400 °C and 110% at 450 °C, and NH_3 yield improvements of roughly 65% and 170% over the corresponding structured reactor at the same temperatures. Scaling from one to four membranes further yielded a membrane-area-normalised production rate improvement of up to ~424% at 350 °C and 40 bar, providing a strong experimental foundation for continued scale-up toward larger-scale membrane reactors for ammonia synthesis.

In **Chapter 7**, the membrane reactor concept was evaluated at process scale using a rigorous techno-economic assessment that compares two reactor configurations: a single conventional packed bed reactor and a multi-membrane packed bed membrane reactor. To link the reactor-level intensification demonstrated in Chapters 2-6 to system level costs, a small-scale power-to-ammonia (PtA) plant was modelled in which renewable hydrogen (from electrolysis) and nitrogen (from air separation) feed either a traditional PBR or a PBMR. Adsorption was investigated as an alternative ammonia separation step, building on our previous work in which a condensation-based separation section was analysed and identified as a key limitation to further process intensification. Both flowsheets were optimised in two stages: first, with respect to operating conditions and reactor geometry, and second, with respect to membrane and adsorption parameters, including sweep-gas-to-feed flow ratio, transmembrane pressure difference, permeate-side hydrogen composition, adsorption and desorption temperatures, and the number of adsorption stages.

The optimised PBMR configuration (L_r/D_r = 3, SW = 0.67, $y^P_{H_2,in}$ = 0.90) achieves a levelized cost of ammonia (LCOA) of 2,793 €·$t^{-1}_{NH_3}$, representing a 5.6% reduction relative to the optimised PBR, which yields 2,958 €·$t^{-1}_{NH_3}$. At the same time, the PBMR delivers a 20% relative improvement in power-to-ammonia efficiency (32.4 vs. 26.9) and higher per-pass H_2 conversion (20.1 vs. 15.6). The cost reduction is not dominated by a single item, but arises from a broad, moderate decrease in both capital expenditure (~4.3% lower overall, with the main savings in the separation section due to fewer adsorption stages) and operating expenditure (~7.1% lower, spread across hydrogen, steam and cooling-water consumption).

8.2 OUTLOOK AND RECOMMENDATIONS FOR FUTURE WORK

This work shows that membrane reactors for ammonia synthesis are a promising technology for process intensification, offering the possibility to improve both reaction performance and overall process efficiency; at the same time, there are several limitations that will be briefly addressed in this section.

The results obtained in this thesis indicate that integrating NH_3-selective CMS membranes with advanced structured catalysts can significantly enhance ammonia synthesis under milder operating conditions, suggesting a viable pathway for membrane-assisted ammonia production from renewable hydrogen and, ultimately, for decentralised power-to-ammonia schemes.

From a technology-readiness perspective, the carbon molecular sieve membranes investigated in this thesis remain the most critical element for further development, as their NH_3 permeance already approaches the targets derived in Chapter 2, whereas NH_3/H_2 and NH_3/N_2 perm-selectivities still remain limited, and the presence of larger pores limits true molecular-sieving behaviour. Future work should therefore concentrate on a more detailed optimisation of metal doping, including systematic studies of metal dispersion and loading, so that metal-NH_3 interactions selectively enhance ammonia adsorption and surface diffusion without opening non-selective transport pathways for hydrogen and nitrogen. In parallel, rheological characterisation of the precursor slurry and a deeper analysis of viscosity-coating relationships are needed to better control film formation and layer thickness, enabling the fabrication and systematic assessment of both thinner defect-free selective layers and deliberately thicker layers with tighter pore size distributions and reduced macro-porosity. Exploring alternative dopant metals and co-dopant combinations beyond the current Cu, Ni, Zn, and Co formulations may further tune adsorption energetics and pore architecture [1]. Finally, further investigation is required regarding the reproducibility of CMS membrane fabrication and performance, so that membrane properties and separation behaviour can be reliably

reproduced across different batches.
In addition, the relatively high sweep-gas flow rates required by the current membranes are not convenient from an energy-demand perspective, and improved perm-selectivity would enable operation with lower sweep-gas loads, reducing auxiliary compression and heating duties while facilitating downstream purification toward higher NH_3 purity.
From a practical standpoint, scaling up the membrane reactor exposed significant mechanical integration challenges, as sealing the CMS membrane to the reactor flange proved labour-intensive and technically demanding. These difficulties mainly arise because membrane end-sealing still requires further optimisation and, in structured reactors, the catalyst geometry imposes very tight tolerances, so tsealed tubular membranes must be exceptionally straight and dimensionally accurate in order to be inserted smoothly into the internal channels without inducing misalignment or mechanical stress. To mitigate these issues, future designs should allow the structured catalyst to slide down along the membrane without interference, and make use of dedicated insertion tools to place the catalyst accurately while avoiding contact that could scratch or damage the membrane selective layer.
Beyond the experimental work, the reactor modelling tools and scale-up methodology also present important opportunities for improvement, particularly in coupling detailed 1D/2D simulations with targeted validation campaigns on multi-membrane TPMS reactors. Experiments in units with larger characteristic diameters and multi-tube bundles, where appreciable radial concentration gradients can develop at both the structured-support and reactor scale, would be especially valuable for testing the CP and transport assumptions embedded in these models. In parallel, the non-isothermal 1D and 2D reactor formulations should be extended to explicitly represent POCS structured supports rather than a conventional particulate bed, enabling the same modelling framework to interpret the membrane-integrated POCS experiments reported in this thesis and to serve as a robust quantitative basis for further development of the new reactor concept [2].
Lastly, the techno-economic analysis shows that membrane-assisted reactors can already deliver a meaningful LCOA and PtA-efficiency improvement at small scale, but that the economics are dominated by hydrogen cost and scale effects. Future work should therefore target larger, more industrially relevant PBMR plants, using the same adsorption-based separation concept while investigating more selective sorbent materials, in order to quantify how the relative LCOA benefit evolves with capacity and whether membrane reactors remain advantageous once economies of scale are fully exploited.

REFERENCES

[1] W. W. Yan and T. Tsuru, "Overview: Insight into NH3 permselective membranes and their application to a membrane reactor for efficient ammonia production," *Sep. Purif. Technol.*, vol. 370, p. 133275, Oct. 2025, doi: 10.1016/J.SEPPUR.2025.133275.

[2] S. Richard *et al.*, "Modelling the feasibility of membrane integration into periodic open cellular structures for ammonia decomposition," *Chemical Engineering Journal*, vol. 521, p. 166903, Oct. 2025, doi: 10.1016/J.CEJ.2025.166903

LIST OF PUBLICATIONS

JOURNAL ARTICLES

- **I. Gargiulo**, G. Anello, S. Richard, and F. Gallucci, "Modelling of a packed bed membrane reactor for ammonia synthesis: on the role of membrane performance and operating conditions", *Int. J. Hydrogen Energy*, vol. 166, p. 150995, Sep. 2025.

- **I. Gargiulo**, A. Vita, C. Italiano, M. A. Llosa Tanco, D. A. Pacheco Tanaka, and F. Gallucci, "Activated Triply Periodic Minimal Surfaces (TPMS) gyroid supports for efficient ammonia synthesis in membrane-integrated reactors", *Int. J. Hydrogen Energy*, vol. 235, p. 155170, May 2026.

- **I. Gargiulo**, A. Vita, C. Italiano, C. Coiana and F. Gallucci, "On the scaling-up of 3D-printed metallic POCS structured catalysts membrane reactors", *Accepted in Chem. Eng. J.*.

- **I. Gargiulo**, E. A. J. F. Peters, A. E. Simpelaar, and F. Gallucci, "A two-dimensional model for membrane reactors in ammonia synthesis: concentration polarisation, radial transport effects, and scale-up design criteria", *Submitted to Chem. Eng. J.*.

- **I. Gargiulo**, M. den Hartog, A. Evtimova, V. Cechetto, F. Gallucci, "Techno-economic analysis of a small-scale green ammonia plant: conventional vs. membrane-assisted process", *In preparation.*

JOURNAL ARTICLES OUT OF THE SCOPE OF THE THESIS

- S. Richard, V. Verde, N. Kezibri, C. Makhloufi, A. Saker, **I. Gargiulo**, F. Gallucci, "Power-to-ammonia synthesis process with membrane reactors: Techno- economic study," *Int. J. Hydrogen Energy*, vol. 73, pp. 462–474, Jul. 2024.

ORAL PRESENTATIONS

- **I. Gargiulo**, A. Rahimalimamaghani, and F. Gallucci, "Development of long-term Hydrogen storage technologies through green ammonia production in innovative Catalytic Membrane Reactor (CMR)", 18th edition of the Netherlands Process Technology Symposium (NPS2023), July, 6-7, 2023, Twente (The Netherlands).

- **I. Gargiulo**, G. Anello, L. De Felice, and F. Gallucci, "Simulation and optimisation of an ammonia synthesis catalytic membrane reactor", 2nd Symposium on AMMONIA ENERGY (SoAE), July, 11-13, 2023, Orléans (France).

- **I. Gargiulo**, G. Anello, L. De Felice, and F. Gallucci, "Simulation and optimisation of an ammonia synthesis catalytic membrane reactor", 16th International Conference on Catalysis in Membrane Reactors (ICCMR-16), October, 16-18, 2023, Donostia-San Sebastián (Spain).

- **I. Gargiulo**, M.A. Llosa Tanco, D.A. Pacheco Tanaka, and F. Gallucci, "Carbon molecular sieve membrane (CMSM) for ammonia synthesis: study on the effect of carbonisation and permeation temperature", 9th Symposium on Hydrogen, Fuel Cells and Advanced Batteries (HYCELTEC24), 30 June - 3 July, 2024, Milazzo (Italy).

- **I. Gargiulo**, E. A. J. F. Peters, A. E. Simpelaar, and F. Gallucci, "2D mathematical model study of a packed bed membrane reactor for ammonia synthesis: optimisation, design and scale-up", 3rd Symposium on AMMONIA ENERGY (SoAE), September, 23-26, 2024, Shanghai (China).

- **I. Gargiulo**, A. Evtimova, V. Cechetto, and F. Gallucci, "A Techno-Economic Analysis on a small-scale ammonia synthesis plant: conventional vs. membrane-assisted reactor system", 15th European Congress of Chemical Engineering (ECCE) & 8th European Congress of Applied Biotechnology (ECAB) & 3rd Iberoamerican Congress on Chemical

Engineering (CIBIQ), September, 8-10, 2025, Lisbon (Portugal).

- **I. Gargiulo**, A. Vita, C. Italiano, M. A. Llosa Tanco, D. A. Pacheco Tanaka, and F. Gallucci, "A novel CMSM-based membrane reactor for ammonia synthesis integrating POCS: a proof of concept", Sustainable Energy and Process Technologies Conference (SEPTech), October, 21-23, 2025, Eindhoven (The Netherlands). Awarded: "*Best oral presentation*".

- **I. Gargiulo**, A.E. Simpelaar, E.A.J.F. Peters, G. Anello, S. Richard, and F. Gallucci, "Advancing membrane reactor modelling for ammonia synthesis: from 1D to 2D frameworks", 17th International Conference on Catalysis in Membrane Reactors (ICCMR-17), October, 27-29, 2025, Nanjing (China). Awarded: "*Best oral presentation*".

POSTER PRESENTATIONS

- **I. Gargiulo**, A.E. Simpelaar, E.A.J.F. Peters, G. Anello, S. Richard, and F. Gallucci, "Two-dimensional model in a packed bed membrane reactor for ammonia production considering diffusion limitation phenomena: optimisation, design and scale-up", 19th edition of the Netherlands Process Technology Symposium (NPS2024), October, 8-9, 2024, Groningen (The Netherlands).

- **I. Gargiulo**, A.E. Simpelaar, E.A.J.F. Peters, G. Anello, S. Richard, and F. Gallucci, "Two-dimensional model in a packed bed membrane reactor for ammonia production considering diffusion limitation phenomena: optimisation, design and scale-up", NMG/BMG/DGMT Symposium and Poster Day, October, 11, 2024, Veldhoven (The Netherlands)

ACKNOWLEDGEMENTS

I still find it difficult to believe that, after almost four years, I am finally putting pen to paper on these pages. These words mark the end of a journey that, at times, felt as though it would never end, and yet now seems to have passed in the blink of an eye. With these final lines, I close not only the pages of this thesis, but also a chapter of my life - a chapter filled with discoveries, challenges, unexpected turns, laughter, frustration, and, above all, people who have left a mark on me.

If you are wondering what the cover of this thesis represents, perhaps this is the right place to explain it. More than an illustration of the work contained in these pages, it is a representation of my journey. It begins with Vesuvius, my origin, my roots, and my home. It represents the part of me that travelled from Naples to this country, carrying everything that came before. Far from home, I found a country that welcomed me, challenged me, and gave me the opportunity to build a new life and, along the way, another family. Then comes the windmill, marking the beginning of something new. Its blades turning in the wind are a small tribute to the work, energy, and ideas that have shaped these four years. From there, the path crosses the sea - perhaps the best representation of a PhD. There were calm and sunny days, but also storms when the horizon disappeared, and I had to keep moving forward without knowing where I would arrive. There were moments of certainty and doubt, excitement and frustration, but the journey was never still. Perhaps this journey was never about leaving one place behind and arriving somewhere else, but about discovering how far I could go without losing where I came from. These pages therefore carry much more than the work of a PhD. They carry a small piece of the journey that brought me here.

First and foremost, I would like to express my deepest gratitude to my promoter and supervisor, Prof. Fausto Gallucci, who made this journey possible. Thank you for welcoming me into your group and for giving me the opportunity to grow into the researcher I am today. I am grateful for all the formative discussions, the questions that pushed me to think further, and, above all, for the many moments you made time for me despite your always busy schedule. Most of all, I am grateful for the trust you placed in me from the very beginning. You saw something in me that I could not always see myself, and you always found a gentle and kind way to push me forward and remind me that I was capable of doing it. I would also like to take this opportunity to thank my second promoter, Prof. John van der Schaaf. Although our discussions about my research were not as frequent, many other conversations took place around the coffee machine. What usually started as a simple exchange about everyday life could, almost effortlessly, turn into the most philosophical discussions about life, people, society, or simply the world around us.

I would also like to thank all the members of the committee who are here today and who have taken the time to read, evaluate, and discuss my work: Prof. Martin van

Sint Annaland, whose way of communicating science I have always greatly admired. I still remember attending one of his presentations and feeling as though I were watching an episode of one of my favourite series. His ability to explain complex ideas so naturally, while making the audience feel part of the story and of the conversation, is something I have always found remarkable; Dr. Fernanda Neira D'Angelo, with whom I have had the pleasure of sharing many interesting conversations over these years. Our discussions could range from personal matters to scientific topics, and I always found it remarkably easy to move from one to the other; Prof. Efrem Curcio, whom I had the opportunity to meet on some occasions over the past years, including during some of his presentations. I always appreciated his openness and the welcoming attitude that made it easy to feel comfortable when talking with him; Prof. David Alique Amor, whom I had the pleasure of meeting on a few occasions over the past years. I particularly appreciated the conversation we had during one of my last conferences, where we could exchange ideas about science and his work. Last but not least, I would like to thank Antonio Vita, my advisor, with whom I first came into contact through the AMBHER project. Looking back at these four years, I realise how much of my PhD journey is closely connected to you. Professionally, you have always been there for discussions, always open to collaboration and generous with your time and ideas. Your presence is also quite literally part of this thesis, with two chapters reflecting the work we carried out together. But you have been much more than a partner in the consortium. You have been a colleague, and, along the way, a friend with whom I could share not only scientific thoughts, but also many personal matters. I sincerely hope that this will not be the end of our journey together, and that we will stay in touch and continue to share thoughts, ideas, and perhaps a few more conversations in the years to come. I would also like to deeply thank Prof. Frank Peters, with whom I had the opportunity to start a collaboration halfway through my PhD. Although we began working together relatively late in this journey, I am truly grateful that our paths crossed and that I had the chance to have you as part of this work. Your professionalism, dedication, and meticulous approach have contributed so much to Chapter 5 and, in many ways, helped elevate it to another level. Working with you made me realise how much these qualities can shape not only the quality of the work, but also the way in which it is carried out. I am sincerely grateful for everything you brought to this chapter and to my journey.

And now it is time to turn to the big group that I have been part of throughout these four years: the SPE group. I would first like to thank the staff, starting with the person who has been by my side through so much of this journey: Joris. I will never be able to thank you enough for all the effort, work, and, at times, sheer dedication you put into helping me succeed in this project. I will never forget our endless discussions about designs, solutions, and the many decisions that had to be made to make everything work. Your motivation pushed me forward even in the moments

when I thought there was no solution left. But beyond all the technical discussions, I am equally grateful for all the laughs and jokes we shared, which made this journey feel much lighter. Thank you for always welcoming me into your office, for the occasional candy, and for the countless silly moments shared with you and Roberto. And thank you, Roberto, for always being there to help, even when my project was not your responsibility. For all the times I would come to you with a quick question or ask for a favour, you were always willing to help and somehow, almost effortlessly, find a solution. I would also like to thank Erik, who, although not directly involved in my project, was always there whenever he saw me struggling. Often without me even having to ask, you would already be there, ready to help me out and, more importantly, to teach me something along the way. I will never forget our discussions about imperial and metric fittings, which somehow managed to turn even the simplest practical problem into a lesson. And then there is Peter, my gas-bottle mate. I do not know how many times I have bothered you with transporting gas bottles, or how many times we walked through the rain carrying them around. What I do know is that we probably built quite a few muscles along the way! I would also like to thank Carlo. I must admit that, at the beginning, I was a little scared of you! But over the years, you taught me a great deal about safety and made me realise how important it is to approach research with the right mindset. Then there are the two mothers of the group, Saskia and Marlies. Thank you for always being there for every little problem and for welcoming me, and all of us, as if we were your children. I will never forget our escape from a group outing for that spontaneous girls' shopping session in Maastricht! Marlies, thank you also for the countless times you helped me with GC, always patiently. And Saskia, thank you for always being so proactive, helpful, and ready to make things easier throughout this journey. I am very grateful to have had you both looking after us.

Beyond the staff, I want to thank all the colleagues I have met along the way, many of whom gradually became a small family to me.

To my office mate, Claudia: you entered my life so quietly and naturally that, before I realised it, you had become much more than a colleague. Your kindness and care have made these two years so special, and I am truly grateful for the friendship we built. Thank you for sharing your food, your gym sessions, and your healthy lifestyle with me, always pushing me to do a little better. I am so happy you found your way into my life. To Negar, one of the most sensitive and kind-hearted people I have ever met. Your warmth and gentle way of looking after people made a real difference to my time here. I will always be grateful for the way you opened the door to Persian culture for me and shared it so naturally and generously. Every dish you cooked felt like an invitation into your world, and the countless little gestures of care made me feel truly at home. I will carry a little piece of your culture and our friendship with me wherever I go. Thank you to Valentina, my conference partner throughout this journey. From travelling to conferences and preparing presentations to all the

conversations, laughs, and little adventures in between, sharing these experiences with you always made them more enjoyable. Thank you also for all the advice you gave me, especially during your brief period of supervision, which I truly appreciated. Thank you to Gaetano, who was one of the first people to welcome me to the PhD and into my project. Thank you for introducing the little me to the lab, patiently showing me the way, and for always looking out for me. I will always remember those first days and how much your presence helped me feel at home. And, of course, thank you for all the delicious pizzas you have shared with me along the way! Riccardo, thank you for being one of the last to join, but somehow one of the first to make an impression on me. Your happiness and cheerful way of approaching things made the final part of my PhD a little lighter. Alberto, thank you for always making me feel that, even though we did not work closely together, I could count on you whenever I needed a hand. And thank you for all the gossip, which at times made this journey a little lighter! Roberto, thank you for the moments we had the chance to work together and for the knowledge we shared along the way. I also truly enjoyed our conversations, not only about research but also about life outside the lab, especially because we come from the same place and could share that connection. Alessia, thank you for being part of these years and for all the moments we shared as colleagues. I truly appreciated your kindness and the ease of working alongside you. A special thank you to Huub, Daniel and Zancat, my Dutch guides in the group, for introducing me to little pieces of Dutch culture and life and for helping me feel more at home in a country that was once completely new to me.
I would also like to thank the previous generation of the group, those who were here before me and have since moved on to new adventures. Serena 2, in particular, I owe you a special thank you, because if I am here today, it is also thanks to you. You were one of the first people to truly believe in me and to convince me that I was capable of doing this PhD. I will always remember that trust and the confidence you gave me when I was still unsure of myself. Beyond that, I am even more grateful for the friendship we built along the way. I will never forget our countless Thursdays in Stratum, the laughs, the fun, and all the evenings that made these years so much more than just a PhD. And thank you, Giulia. You have been a truly precious presence throughout this journey. Thank you for welcoming me from the very beginning and for showing me the way in a country where, at the time, I knew nobody. You helped me find my feet, not only within the university but also in everyday life, and made everything feel a little less unfamiliar. I will always remember how much at home you made me feel when everything around me was still new. Thank you for being there whenever I needed you, and for being one of the people who made this country feel like home. And then there is Serena 1, my first real office mate. You welcomed me so warmly and, in many ways, became my guiding soul through the first part of my PhD. Although we shared an office for less than a year, you taught me so much, both professionally and personally. I have always admired

your perseverance and the calm and thoughtful way in which you approach things. I am especially happy that, beyond being colleagues, our paths turned into a friendship that I truly cherish. And alongside you, I am also grateful to have had Camilla. You have been a genuine presence throughout my PhD, always there with your support and kindness, even after you left the group. And to all the other members of the SPE group: Shilpa, Goktug, Sierd, Alessia De Gregorio, Stefan, Anouk, Thijs, Wout, Adarsh, Arash and Amin. Thank you for all the conversations, coffees, laughs, help, and everyday moments that, together, made these four years richer and more enjoyable. Each of you has contributed in your own way to making SPE feel like more than just a workplace, and I am grateful to have been part of this group with you.

Last but not least, I would like to thank my two paranymphs, because your presence by my side today reflects the truly central role you have played in this journey.

Clara, you are the one who has been there since day zero, even before this journey officially began. You have known me from the very beginning, before the PhD and before I even knew where this path would take me, and that is what makes our friendship so special to me. You have seen every version of me through these years: the excitement, the doubts, the struggles and the little victories. How lucky I have been to have someone beside me who knew where I came from and could recognise the person I was becoming, even when I was still trying to find her myself. You believed in me and reminded me what I was capable of, especially in the moments when I could no longer see it. And you did it so naturally, without ever needing to be asked. You were simply there, ready to listen, to encourage me, or just to make things feel a little lighter. I will always carry with me the way you opened not only your door, but your home and your life to me. Far from where I started, you gave me warmth, trust and a sense of belonging, and those moments meant more than I probably ever told you. In a place that was once completely new to me, you became one of the reasons it started to feel like home. You have become woven into so many memories of these years, and into who I am. Wherever life takes us, I hope you always know how much you mean to me, and that our friendship remains one of the great constants in my life.

And then there is Pranav, one of the most beautiful discoveries of this journey. Little by little, you became such an important presence in my life. As you slowly came out of your shell, I had the chance to discover your genuineness, your values, your way of thinking, and the kindness with which you are always willing to help. We spent so much time talking about life, about the things we believe in, and, especially, about our cultures. I will always be grateful for how sincerely you appreciated my roots, my culture, and where I came from. At the same time, you welcomed me into your own world and let me discover South Indian culture through our conversations, your stories, and the pieces of your life you shared with me. You once told me how close you felt to my home, and that stayed with me. It made me realise that sometimes

there are no real boundaries between countries unless we choose to create them. Our roots may be different, but our values made us feel incredibly close. Somewhere along the way, you became much more than a friend: you became a little brother to me. I am truly grateful that this journey brought you into my life, and I hope that, wherever life takes us from here, this bond will always remain.

A special thank you to Orlando, who was only briefly part of SPE but somehow became the group's adopted son. You were part of an important part of my PhD, sharing with me and Serena 2 all those Thursdays in Stratum. From that moment, our friendship only grew stronger. You are one of those people with whom, even if time passes without a message, the moment we speak again, everything feels genuine, easy, and unchanged. I am very grateful that this part of my journey brought you into my life.

I would also like to thank all the students I had the pleasure of supervising throughout these years. Each of you, in your own way, became part of my journey as a researcher and as a supervisor, and I am grateful for everything you taught me along the way. Zinovia, you were the very beginning. As my first BEP student, you gave me the opportunity to discover what it meant to supervise someone and to take my first steps as a supervisor. I will always remember that first experience and the excitement of seeing someone else's work grow under my guidance. Joost, thank you for all the memories we made along the way, for our conversations about our two cultures, and for the countless times we simply found ourselves talking at the F.O.R.T., often about everything and nothing at all. Without your contribution, the third chapter of this thesis would not exist, but beyond the work itself, I am grateful for the person I got to know through all those conversations. Bram, thank you for being so deeply immersed in modelling and for all our formative discussions. You taught me a lot throughout our time working together, and I am genuinely grateful for everything I learned from you. Your curiosity, questions, and way of thinking challenged me in the best way and helped shape the ideas that eventually became the fifth chapter of this thesis. Aleksandra, thank you for your calm and meticulous way of working. You taught me that things can be done thoroughly and effectively without rushing, and I truly appreciated the care you brought to your work. Mika, thank you for believing in my project and for the enthusiasm and fresh perspective you brought to it. It was a pleasure to see you engage with the work and bring your own ideas into it. Fred, thank you for your dedication and patience. Even when the project became challenging, you kept going and remained committed to it. I truly appreciated your perseverance and the trust you placed in the work we were doing together. And Max, thank you for the energy, curiosity, and openness you brought to our collaboration. Seeing the work continue to grow through the people I had the chance to supervise has been one of the most rewarding parts of this journey.

Coming to this country also meant meeting so many new people, and among all those encounters, one of the most beautiful discoveries was you, Ilaria. From the

very beginning, your kindness made me feel that our friendship was something genuine and special. I have always admired your willingness to be there for others, your generosity, and the way you are always ready to help without hesitation. Over time, our friendship grew into something even more special, eventually becoming the little family we created together with Clara. Coming so far from home, I never expected to find people who would feel like family, but somehow, I did.
And of course, this also means thanking the whole Pescado family. Thank you for all the dinners, drinks, laughs, conversations, and spontaneous plans that made these years so much more than just work and research. I am grateful for the warmth with which you welcomed me and for all the memories we created together. And then there is Ciro. Thank you for always being genuinely willing to help, no matter the problem. You have always been someone I could count on, and I truly appreciated the way you were there without ever making it feel like a favour.
Prima di guardare avanti, sento il bisogno di fare un passo indietro e ringraziare i miei amici di sempre in Italia, quelle persone speciali che so di ritrovare intatte ogni volta che torno a casa. Annachiara, siamo insieme da quando avevamo tre anni. Siamo cresciute fianco a fianco e, nonostante la distanza e le strade diverse che abbiamo preso, sapere che ci sei sempre è una delle mie certezze più belle. Ilde, grazie per essere una di quelle amicizie che il tempo e la distanza non cambiano mai. Ogni volta che ci ritroviamo, sembra di non esserci mai lasciate. Alessia, grazie per essere sempre rimasta una presenza importante nella mia vita e per essere ormai una delle nostre "adottate". Anche se non ci vediamo spesso, ogni volta che ci ritroviamo è come se il tempo non fosse mai passato. E poi c'è Antonella, che occupa un posto davvero speciale nel mio cuore: sei entrata nella mia vita come amica e, attraverso mio fratello, sei diventata anche parte della mia famiglia. Sono felice che queste due parti così importanti della mia vita si siano incontrate proprio in te, e ancora di più di averti avuta accanto in entrambi questi ruoli.
Poi ci sono le mie due stelle, Simona e Mary, che ho incontrato nel percorso della mia vita universitaria e che, senza quasi accorgercene, sono diventate parte integrante della mia vita. Amiche mie, grazie per la vostra presenza così preziosa e costante, per aver reso sempre tutto un po' più speciale. Ricordo quanto fosse bello andare all'università sapendo di avere voi ad aspettarmi per il nostro caffè delle 8:30 del mattino.Simona, grazie per la persona che sei: sempre pronta ad aiutare, sempre pronta a capire, così sensibile e, allo stesso tempo, sempre capace di trovare una soluzione a tutto. Mary, grazie per tutta la giovinezza, la leggerezza e la spensieratezza che mi hai regalato durante tutti quei weekend trascorsi insieme. Ad entrambe, grazie perché nemmeno la distanza è mai riuscita a scalfire il nostro legame. Sapere che, nonostante gli anni e i chilometri, siete ancora qui e che oggi siete parte di questo momento significa davvero tantissimo per me.
Coming to this country not only gave me colleagues and friends, but it also blessed

me with an unexpected gift: finding a second family thousands of kilometres away from home. Through you, Param, your family welcomed me with open arms and slowly became an essential part of my life. Neha, thank you for welcoming me into your family with such openness and warmth, despite the distance and the cultural differences between us. From the very first moment, you made me feel like I truly belonged. Thank you for all the love, care, and kindness you have given me, and for always making me feel at home. A special thank you to Vatsal, whom I would have loved to have here with us today, knowing how much joy this moment would have brought him. I am sure that, wherever he is, he is watching over us, cheering for me, and celebrating this milestone. I will always be deeply grateful for the genuine warmth with which you embraced me into your family. And Tiru, my little sister. You constantly reminded me of my own sister, and perhaps that is why our bond felt so natural from the beginning. Thank you for the love, spontaneity, and generosity you have always shown me, and for making me feel like a sister. I am truly grateful to have found you along the way, and to Purva too, for his kindness and for always making me feel so welcome with you both. You are one of the most genuine people I know, sincere and true in everything you do!

E adesso è il momento di tornare dove tutto è iniziato: alla mia famiglia. A voi che siete le fondamenta di tutto quello che sono. Vorrei ringraziare tutti i miei cugini, che, in modi diversi, hanno sempre fatto parte della mia vita e dei miei ricordi più belli. Crescere insieme ha significato condividere una parte importante della mia storia, fatta di estati, feste, risate e tanti momenti che porterò sempre con me. In particolare, grazie Michela, che in un certo senso, sei stata il mio spirito guida. Sei stata la prima della famiglia ad avere il coraggio di andare via, inseguire i tuoi sogni e costruire la tua strada lontano da casa. Senza forse rendertene conto, mi hai insegnato che partire non significa lasciare indietro le proprie radici, ma portarle con sé ovunque si vada. E anche con la distanza, sei sempre stata presente, e sapere di poterti avere accanto ha significato davvero tanto per me. Generoso, grazie per la tua sensibilità, per tutte le pazzie della nostra infanzia che oggi sono diventate infiniti racconti da ricordare e raccontare, e per tutti gli anni che abbiamo condiviso. Sei parte di tanti dei miei ricordi più belli, quelli più semplici e spensierati, che ancora oggi riescono a farmi sorridere. Mimmo e Carmine, grazie per essere stati parte della mia crescita, per le risate, la complicità e tutti i momenti condivisi. Anche se la vita ci ha portati in direzioni diverse, è bello sapere che, quando ci ritroviamo, quel senso di famiglia è ancora lì. A tutti voi, grazie per essere parte della mia storia e per aver lasciato, ciascuno a modo suo, un pezzo di voi nei miei ricordi.

Desidero ringraziare anche tutti i miei zii, che ogni volta che tornavo erano lì per trascorrere del tempo con me e che, ogni volta che ripartivo, erano già lì a chiedermi quando sarei tornata. Anche attraverso questi piccoli gesti mi avete sempre fatto sentire quanto fossi importante per voi.

Un grazie speciale va ai miei nonni, a quelli che ci sono ancora e a quelli che oggi,

purtroppo, non possono essere qui con me. A tutti voi devo una parte di ciò che sono, per l'amore che mi avete dato, per le attenzioni, per i piccoli gesti e per tutto ciò che avete fatto per me nel corso degli anni. A chi oggi non può condividere con me questo momento, voglio dire che mi piace pensare che, se foste qui, sareste stati i primi ad esultare per me e con me, con quella gioia semplice e sincera che solo i nonni sanno avere. Mi piace pensare che, in qualche modo, una parte di voi sia comunque qui, in questo giorno così importante, perché tutto l'amore che mi avete dato non è mai andato via.

E poi ci siete voi, mio fratello e mia sorella. Siete forse le persone che mi sono mancate di più in questi anni, ma anche quelle presenze che, nonostante la distanza, ho sentito sempre accanto a me e che nessuno potrebbe mai sostituire. Nicola, tu sei colui che mi ha accompagnata fin da quando ero piccola, camminando al mio fianco attraverso ogni fase della mia vita. Abbiamo avuto la fortuna di essere fratelli, ma anche amici, colleghi, complici e molto altro. Sei sempre stato la mia spalla, quella persona che so di poter chiamare in qualsiasi momento, anche nel cuore della notte, sapendo che dall'altra parte troverei sempre te, pronto ad aiutarmi. Mi hai insegnato che a volte si può amare profondamente anche senza bisogno di dirlo, semplicemente attraverso il modo in cui ci si è sempre l'uno per l'altro. E anche quando la distanza ci ha separati, non ho mai avuto la sensazione di essere davvero sola, perché ho sempre saputo che, se ne avessi avuto bisogno, tu ci saresti stato. Chiara, la piccola della famiglia, sei stata l'energia e l'amore che più mi sono mancati durante questi anni lontano da casa. Mi hai insegnato cosa significa amare incondizionatamente, ma anche cosa significa avere una sorella più piccola e sentire naturalmente il bisogno di proteggerla, di prendermi cura di lei e di esserci. Grazie per essere quella che riempie la nostra famiglia di felicità, spensieratezza e giovinezza. La tua presenza ha sempre portato luce nella nostra casa, e ogni volta che torno mi ricorda quanto è bello ritrovare quella parte di me che è rimasta lì con voi.

E infine ci siete voi, mamma e papà. Voi che avete creduto in me più di chiunque altro, spesso anche più di quanto io riuscissi a fare. Voi che vi siete messi in discussione tante volte per me, che avete fatto sacrifici e rinunce, spesso in silenzio, pur di vedermi sorridere, realizzarmi e diventare la persona che desideravo essere. Mi avete insegnato cosa significano davvero l'affetto, l'amore e la cura. Mi avete insegnato che si può essere presenti anche quando si è lontani e, soprattutto, che amare qualcuno significa anche avere il coraggio di lasciarlo andare. Mi avete sempre raccolta quando ne avevo bisogno, ma allo stesso tempo mi avete incoraggiata a partire, a sognare e ad avere il coraggio di vivere ogni avventura, soprattutto questa. E forse è proprio questo il regalo più grande che mi avete fatto: mi avete dato delle radici abbastanza forti da permettermi di andare lontano. In questi anni ho imparato che posso cambiare Paese, costruire una nuova vita e sentirmi a casa in luoghi che un tempo mi erano completamente sconosciuti. Ho imparato a costruirmi nuove radici, nuove amicizie e una nuova quotidianità lontano da voi. Ma più sono andata

lontano, più ho capito una cosa: la mia vera casa è sempre rimasta lì, con voi. È nelle stanze in cui sono cresciuta, nelle abitudini di ogni giorno, nelle risate, nei piccoli momenti che allora sembravano così normali e che oggi, ripensandoci da lontano, hanno un valore immenso. È nel sapere che, per quanto lontano io possa andare, esiste sempre un posto in cui posso tornare ed essere semplicemente Iolanda. Ai vostri sacrifici silenziosi che siete rimasti a casa, per permettermi di arrivare fin qui.

And finally, to the person who fills my life today: Param. You were an unexpected discovery in the middle of a storm, and somehow you became the person who helped me walk through it. It is almost incredible to think that everything started in the lab. In the middle of experiments, long days, and endless conversations, I met you without ever imagining where that first encounter would take us. What started between the walls of the lab slowly became something much bigger, until you were no longer simply part of my PhD, but part of my life. Since the moment we met, we have shared beautiful days and difficult ones, moments of joy and moments when things were not so easy. We have grown together and, through all of this, learned what it really means to stay beside each other. You have seen me from every possible perspective - at work, at home, on my best days and on my worst ones. Looking back now, it still feels incredible that one of the most important things I found during my PhD was not something I discovered in the lab, but you. After everything these years have brought me, finding someone with whom I can share not only my dreams and ambitions, but also the quiet, ordinary moments of everyday life, is the greatest gift I could have asked for. Thank you for being my anchor, my partner, and the person with whom I can simply be myself. Thank you for choosing me, every day, and for making me understand that home does not always have to be a place. Sometimes, home is a person. And after finding mine in you, I only hope that, wherever life takes us, I will always get to share it with you.

With this thesis, one journey comes to an end, but the most beautiful part of life is that every ending is simply the beginning of something new. Thank you to everyone who walked beside me, believed in me, and made this journey unforgettable.

Here is to the next chapter.

Con questa tesi si conclude un viaggio, ma la parte più bella della vita è che ogni fine non è altro che l'inizio di qualcosa di nuovo. Grazie a tutti coloro che hanno camminato al mio fianco, hanno creduto in me e hanno reso questo viaggio indimenticabile.

Al prossimo capitolo.

With love and gratitude,

Iolanda
Eindhoven, October 2026

CURRICULUM VITAE



Iolanda Gargiulo was born on June 15, 1996, in Castellammare di Stabia, Italy. She completed her secondary education (high school) in 2015 at Liceo Scientifico Don L. Milani in Gragnano, Italy. She then pursued a Bachelor's degree in Chemical Engineering at the University of Salerno, graduating in March 2019 with a thesis titled "Supercritical Antisolvent Extraction (SAE) of Astaxanthin from *H. pluvialis* and polymer encapsulation strategies: optimisation of operating conditions and evaluation of antioxidant activity". Remaining at the University of Salerno, she enrolled in the Chemical Engineering Master's programme, specialising in the Energy and Environment track. During her Master's studies, Iolanda completed an Erasmus exchange at the Eindhoven University of Technology (TU/e) in the Sustainable Process Engineering group, researching palladium membranes under the supervision of Prof.dr.ir. F. Gallucci and Dr. S. Agnolin. She received her Master's degree *cum laude* in May 2022 for her thesis entitled "Development of novel metallic-supported Pd based membrane - Influence of YSZ alumina addition on interdiffusion layer".

In September 2022, she started her PhD in the same group at TU/e, under the primary supervision of Prof.dr.ir. F. Gallucci. As part of the European AMBHER project, her doctoral research focuses on developing membrane reactors for ammonia synthesis as a solution for long-term hydrogen storage. This dissertation is a culmination of the results obtained within her PhD project.